Neuroscience Bulletin

The Official Journal of The Chinese Neuroscience Society
神经科学通报

Volume 37
Number 8
August 2021

Hormone Function in Female Patients with Major Depressive Disorder

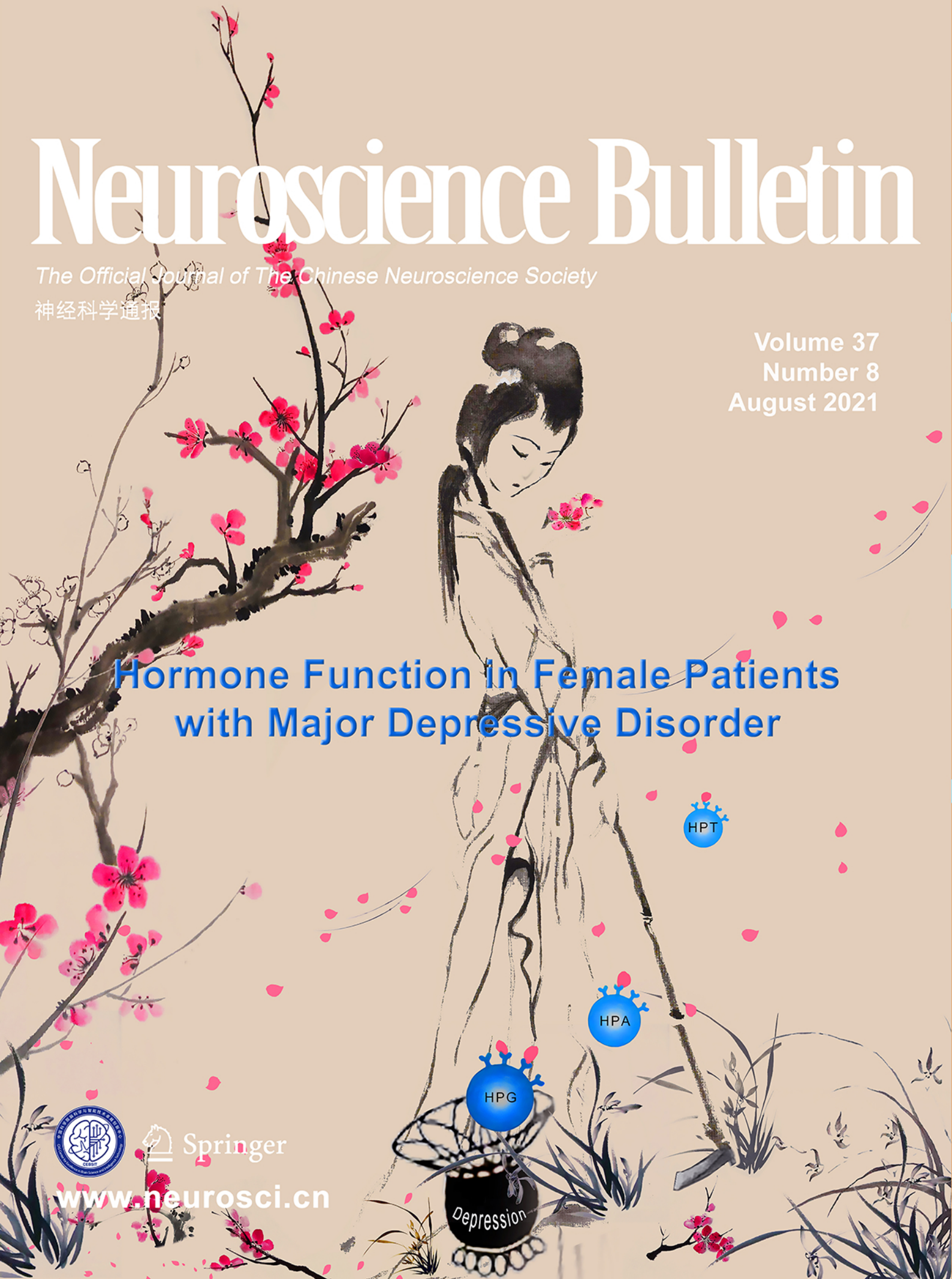

Springer
www.neurosci.cn

CONTENTS

Neuroscience Bulletin

About the Cover

Major depressive disorder (MDD) is a severe mental disorder that contributes to a significant worldwide disease burden, with unknown etiology, unclear pathogenesis and significant gender differences. This review focuses on the hypothalamic-pituitary-end organ feedback loops (HPT, HPA, and HPG) associated with the neuroendocrine and immune systems of female patients suffering from MDD. In this cover image, the theme of "Daiyu Burying Fallen Flower Petals" (黛玉葬花) is used to express the melancholic temperament of these patients. The peach blossom symbolizes hormones, and the wind symbolizes stress. When the wind blows, the petals are blown to the three receptors, which increase the likelihood of depression, especially in females. See pages 1176–1187. (Cover designed by Yuncheng Zhu, Xiaohui Wu, and Zhiang Niu, and made by Yushuo Design Co., Ltd.)

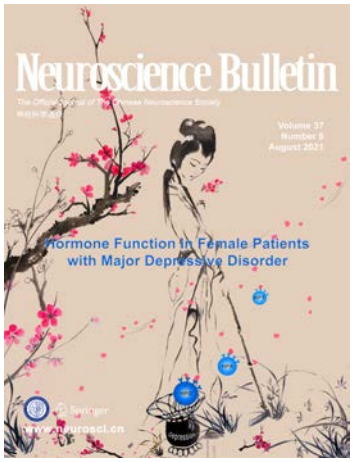

Volume 37 Number 8
August 2021

Original Articles

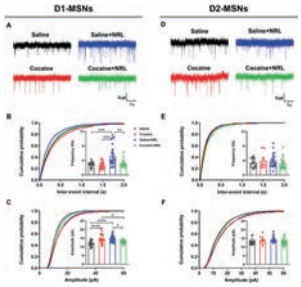

p 1125

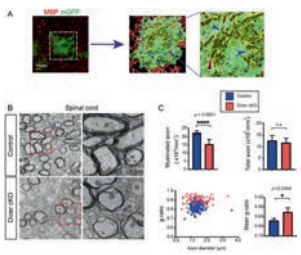

p 1140

www.neurosci.cn

CONTENTS

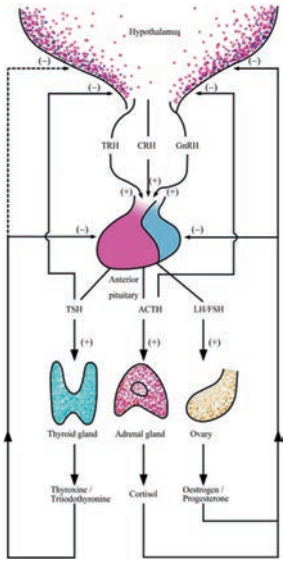

p 1177

Reviews

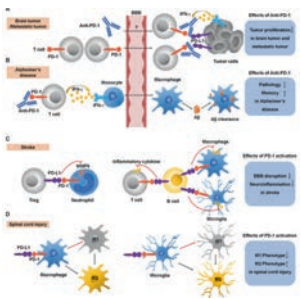

p 1194

Letters to the Editor

CONTENTS

Neuroscience Bulletin

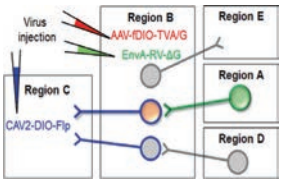

p 1206

Research Highlights

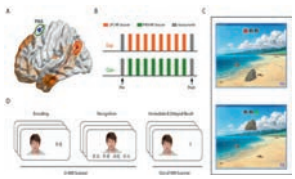

p 1253

Neurosci. Bull. August, 2021, 37(8):1091–1106
https://doi.org/10.1007/s12264-021-00685-w

www.neurosci.cn
www.springer.com/12264

ORIGINAL ARTICLE

An Intronic Variant of *CHD7* Identified in Autism Patients Interferes with Neuronal Differentiation and Development

Ran Zhang[1,2,3] · Hui He[1,2,3] · Bo Yuan[1,2,3] · Ziyan Wu[1,2,3] · Xiuzhen Wang[1,2,3] · Yasong Du[4] · Yuejun Chen[1,2,3] · Zilong Qiu[1,2,3]

Received: 25 August 2020 / Accepted: 27 December 2020 / Published online: 4 May 2021

Abstract Genetic composition plays critical roles in the pathogenesis of autism spectrum disorder (ASD). Especially, inherited and *de novo* intronic variants are often seen in patients with ASD. However, the biological significance of intronic variants is difficult to address. Here, among a Chinese ASD cohort, we identified a recurrent inherited intronic variant in the *CHD7* gene, which is specifically enriched in East Asian populations. *CHD7* has been implicated in numerous developmental disorders including CHARGE syndrome and ASD. To investigate whether the ASD-associated *CHD7* intronic variant affects neural development, we established human embryonic stem cells carrying this variant using CRISPR/Cas9 methods and found that the level of *CHD7* mRNA significantly decreased compared to control. Upon differentiation towards the forebrain neuronal lineage, we found that neural cells carrying the *CHD7* intronic variant exhibited developmental delay and maturity defects. Importantly, we found that *TBR1*, a gene also implicated in ASD, was significantly increased in neurons carrying the *CHD7* intronic variant, suggesting the intrinsic relevance among ASD genes. Furthermore, the morphological defects found in neurons carrying *CHD7* intronic mutations were rescued by knocking down *TBR1*, indicating that *TBR1* may be responsible for the defects in *CHD7*-related disorders. Finally, the *CHD7* intronic variant generated three abnormal forms of transcripts through alternative splicing, which all exhibited loss-of-function in functional assays. Our study provides crucial evidence supporting the notion that the intronic variant of *CHD7* is potentially an autism susceptibility site, shedding new light on identifying the functions of intronic variants in genetic studies of autism.

Keywords Autism · *CHD7* · Intronic variant · Inherited variant · *TBR1*

Ran Zhang, Hui He and Bo Yuan have contributed equally to this work.

Supplementary Information The online version contains supplementary material available at https://doi.org/10.1007/s12264-021-00685-w.

✉ Yasong Du
yasongdu@163.com

✉ Yuejun Chen
yuejunchen@ion.ac.cn

✉ Zilong Qiu
zqiu@ion.ac.cn

[1] Institute of Neuroscience, State Key Laboratory of Neuroscience, Key Laboratory of Primate Neurobiology, Center for Excellence in Brain Science and Intelligence Technology, Chinese Academy of Sciences, Shanghai 200031, China

[2] Shanghai Center for Brain Science and Brain-Inspired Intelligence Technology, Shanghai 201210, China

[3] University of the Chinese Academy of Sciences, Beijing 100049, China

[4] Shanghai Mental Health Center, School of Medicine, Shanghai Jiao Tong University, Shanghai 200030, China

Introduction

Autism spectrum disorder (ASD) is known as a specific group of neurodevelopmental disorders characterized by impairments in social interaction and stereotyped behaviors [1]. Although both genetic and environmental factors may contribute to the autistic symptoms, recent genome-wide analyses indicate that genetic composition is the dominant cause of ASD [2–4]. The genetic architecture of ASD is

highly heterogeneous as > 100 risk genes have been found [5, 6]. Analysis of *de novo* and inherited rare variations linked to ASD has identified convergent functional themes, such as neuronal development and axon guidance, signaling pathways, and chromatin and transcription regulation [7–9].

Due to the genetic heterogeneity, one strategy is to perform genome sequencing for a large number of ASD families and identify risk genes more comprehensively. As a result of the increasing resolution and decreasing cost of DNA sequencing technology such as karyotyping, microarrays, whole-exome sequencing, and whole-genome sequencing, nearly 20% of ASD cases can be explained by identifiable genetic causes, while the rest remain unclear. So far, most efforts have been focused on rare deleterious *de novo* single-nucleotide variants (likely gene-disrupting variants) on coding regions or splicing sites. However, multiple common inherited variants are clearly suspect factors for ASD [10]. Since inherited variants are also present in unaffected parents, identifying the causal relationship between inherited variations and ASD pathogenesis requires neurobiological evidence as well as genetic evidence [11, 12].

The current largest genetic sequencing projects for ASD cohorts are from Europe and the USA, which are mostly composed of Caucasian, Latino, Ashkenazi Jewish, and African–American populations. Due to the genetic and geographical differences between Caucasians and Asians, the potential genetic causes for Asians population may incompletely overlap with those in the western world. Considering the vast population of China, there is no doubt that a large population of individuals with ASD exist in the Chinese population. Identification of the ASD risk genes based on the Chinese population is not only critical to provide precise diagnoses and specific interventions for Chinese ASD patients, but also to provide an important missing piece for a comprehensive and in-depth understanding of autism [13].

Therefore, we set out performing whole-exome sequencing for Chinese ASD probands along with their parents to identify mutations that do not exist in common databases and to explore the new pathogenesis of ASD.

Materials and Methods

Ethics Statement

We obtained assent from the Institutional Review Board (IRB), Shanghai Mental Health Center of Shanghai Jiao Tong University (Federalwide Assurance Number: 00003065; IRB Organization Number: 0002202). Dr. Yi-Feng Xu approved and signed our study with ethical review number 2016–4. Written informed consent was given by parents since all patients were minors. All participants were screened using the appropriate protocol approved by the IRB of Shanghai Mental Health Center, Shanghai Jiao Tong University School of Medicine.

Participants

A total of 168 core families with probands diagnosed with ASD were recruited from among the outpatients in the Department of the Child and Adolescent Psychiatry, Shanghai Mental Health Center. All patients were diagnosed on the basis of the fifth edition of the Diagnostic and Statistical Manual of Mental Disorders. All patients were Han Chinese and their ages ranged from 2 to 18 years.

Human H9 Embryonic Stem Cells (hESCs)

hESCs (H9, line WA09 (WiCell), passages 20–40) were cultured on a feeder layer of irradiated mouse embryonic fibroblasts in a humidified incubator with 5% CO_2 at 37 °C. The hESC medium containing DMEM/F12 (Gibco), 20% Knock Serum Replacement (Gibco, 10828010), 0.1 mmol/L beta-mercaptoethanol (Sigma), 1% (v/v) Non-Essential Amino Acids (NEAA, Life Technologies), and 0.5% (v/v) GlutaMAX (Life Technologies). The medium was changed every day with 10 ng/mL of basic fibroblast growth factor (PeproTech). hESCs were passaged every 7 days. hESCs with an intronic mutation (8-61757392-C-T) were transformed from H9 hESCs by introducing an intronic mutation and two synonymous mutations by homology-mediated end joining-based targeted integration using CRISPR/Cas9. The editor vector (Addgene #48138) containing the small guiding RNA (sgRNA) that targeting exon sequence of *CHD7*, together with the donor vector containing a 1.6 kB homologous sequence of *CHD7* and carrying an intronic mutation and two synonymous mutations, were transfected into H9 hESCs by liposome. Single GFP^+ cells were isolated using flow cytometry and cultured. The cells with an intronic point mutation were identified by DNA sequencing.

Human Embryonic Kidney (HEK) 293 Cells

HEK293 cells were purchased from Cell Bank of the Chinese Academy of Sciences (Shanghai, China). HEK293 cells with the intronic mutation (8-61757392-C-T) were transformed from HEK293 cells by introducing an intronic mutation and two synonymous mutations by homology-mediated end joining-based targeted integration using CRISPR/Cas9. The editor vector (Addgene #48138) containing the small guiding RNA (sgRNA) that targeting exon sequence of *CHD7*, together with the donor vector

containing a 1.6 kB homologous sequence of *CHD7* and carrying an intronic mutation and two synonymous mutations, were transfected into H9 hESCs by liposome. Single GFP^+ cells were isolated using flow cytometry and cultured. The cells with the intronic point mutation were identified by DNA sequencing. HEK293 synonymous control cells were similar to HEK293 intronic mutation cells with two synonymous mutations but without the intronic mutation. All the HEK293 cells were cultured in DMEM (Gibco/Life Technologies) with 10% FBS (Gibco/Life Technologies) at 37 °C in a 5% CO_2 incubator (Thermo Scientific Heraeus).

The primers for cell genotypes were as follows:
CHD7-forward: GAAGTTCACAGGAGCCAGAG
CHD7-reverse: CAGAAAGTAGAATGGTGATTGCCAG

Primary Cultures of Cortical Neurons

Mouse cortical neurons were cultured from E14.5 C57BL/6J of either sex. Cerebral cortices were dissected, dissociated, and cultured in 0.5 mL/well Neurobasal medium (Gibco, 21103-049) with 2% B27 (Gibco, 17504-044) and 2 mmol/L Glutamax-I (Gibco, 35050-061) on Lab-Tek II Chamber Slides (Thermo Fisher Scientific, 154941) at 100,000 cells/cm^2. For the axon and dendrite experiments, the neurons were transfected by Lipo3000 (Invitrogen, L3000075) with 0.9 μg vector, following the Lipofectamine™ 3000 Reagent Protocol, 24 h after plating. After transfection, the cultures were fed with new medium every 2 days.

Plasmid Construct

The gene editor vector was an sgRNA targeting sequence cloned in CRISPR/Cas9 vector (Addgene #48138). The donor vector was the homologous arm cloned in pUC57. The vector that expressed GFP was FUGW (Addgene #14883). The control expression vector was FUGW with GFP removed. The vector expressing CHD7 was a gift from Prof. Wei-Jun Feng (Institutes of Biomedical Sciences Fudan University, Shanghai, China). The vectors expressing alternative forms of *CHD7* (exons 22–23 deletion and exons 22–23 duplication) were modified by enzyme ligation and homologous recombination from the vector expressing *CHD7*. The shRNAs for mouse *Chd7*, human *CHD7*, and human *TBR1* were cloned into the FUGW-H1 vector (Addgene #25870); the shRNA for control was *DsRed*.

The shRNA sequences were as follows:
mouse *Chd7*: GCAGCAGCCTCGTTCGTTTAT
human *CHD7*: GCAGCAGTCTCGTCCATTTAT
human *TBR1*: GCCTTTCTCCTTCTATCATGC
DsRed: AGTTCCAGTACGGCTCCAA

Whole-Exome Sequencing

DNA was extracted from the peripheral blood of patients and their parents using the DNeasy Blood & Tissue Kit (Qiagen, 69506, Germany), following the manufacturer's instructions. For each sample to be sequenced, individual library preparation, hybridization, and capture were performed following the protocol of the Agilent SureSelect capture kit (V5) or the IDT XGen Exome Research Panel. Sequencing was performed on an Illumina HiSeq X-10 instrument (Illumina) following the manufacturer's protocol (HiSeq X-10 System User Guide).

Variation Identification by Sanger Sequencing

Based on the data from whole-exome sequencing (WES), all families with probands carrying *CHD7* variations were selected for Sanger sequencing to validate whether the variations were *de novo* or inherited from parents. The primers for Sanger sequencing were as follows:
CHD7-forward: CCAGGGTTAGCTTTGTGGGT
CHD7-reverse: TGGCTTTGTGACCCTGTAGC

RNA Isolation and Reverse Transcription

Each group of cells was dissociation in 1 mL TRIzol (Invitrogen, 15596018). Total RNA was isolated using the method in the user guide for TRIzol™ Reagent. Reverse transcription used the Reverse Transcriptase M-MLV kit (TaKaRa, D2639B). One microgram of total mRNA and 50 nmol oligo dT were used as primers in the reverse transcription.

Quantitative Real-Time RT-PCR (qPCR)

For qPCR analysis, the gene expression of cDNA samples was analyzed using SYBR green (Toyobo, QPK-201). The qPCR program was three steps with melting as follows: 95 °C denaturation for 10 min, followed by 40 cycles of 95 °C for 10 s, 60 °C for 15 s, and 72 °C for 20 s. The RNA level was calculated and standardized using the ΔCt method and the GAPDH expression level as control.

The primers for qPCR were as follows:
CHD7 exon 19-forward: ACGAAAAGGGGCCTATG GTG
CHD7 exon 20-reverse: TTCAGCCTTCTTAGCCCA CT
CHD7 exon 25-forward: TCCCTGAACCTTTCCATG CT
CHD7 exon 26-reverse: TCCCTGAACCTTT CCATGCT
CHD7 exon 35-forward: ATGGCTGAAGCTGCACC CTA

CHD7 exon 38-reverse: AGGCGGTCAAACATCGACTC

CHD7 intronic retention-forward: TGGAGAAGAATCTGCTTGTCTATGGG

CHD7 intronic retention-reverse: TCTGGGCTTTCACCTTCTTT

CHD7 exon 22–23 deletion-forward: AATCTGCTTGTCTATGGGGTCC

CHD7 exon 22–23 deletion-reverse: TCCCTGAACCTTTCCATGCT

CHD7 exon 22–23 duplication-forward: CAACCATTCCGGTTTGTCAGC

CHD7 exon 22–23 duplication-reverse: TCTGGGCTTTCACCTTCTTT

TBR1-forward: GACTCAGTTCATCGCCGTCA

TBR1-reverse: TGCTCACGAACTGGTCCTG

GAPDH-forward: CATCGCTCAGACACCATGGG

GAPDH-reverse: CCTTGACGGTGCCATGGAAT

Chd7-forward: TCCACATTTGCTAAGGCCAG

Chd7-reverse: TTCAGCCTTCTTAGCCCACT

Gapdh-forward: GTGAAGGTCGGTGTGAACGG

Gapdh-reverse: CGCTCCTGGAAGATGGTGAT

Differentiation of Dorsal Forebrain Glutamate Neurons

hESC colonies were cultured with daily medium changes until they reached approximately 80% confluence. Then, the colonies were detached from the feeder layer by digestion with dispase (Life Technologies), and re-suspended in hESC medium for 4 days to form embryoid bodies (EBs). For neural induction, the EBs were cultured in neural induction medium [DMEM/F12, 1% (v/v) N2 supplement, 5% (v/v) B27 without RA, 1% (v/v) NEAA, all from Life Technologies (NIM)] supplemented with SB-431542 (2 μmol/L, Stemgent) and DMH-1 (2 μmol/L, Tocris) for 3 days. The EBs were then attached to a 6-well plate in NIM supplemented with 5% fetal bovine serum. The cells were fed with NIM every other day until neural tube-like rosette formation at around day 16. Then, the rosettes were blown off using a 1-mL pipette and cultured in suspension. After 2 days, the cell clusters formed neurospheres, and then the medium was changed every other day. On day 26, the neurospheres were digested into single cells using accutase, and seeded at ~ 40,000 cells/cm^2 on coverslips pre-coated with Matrigel. After 5 h–6 h, neuronal differentiation medium [neural basal media, 1% (v/v) N2, BDNF (10 ng/mL, PeproTech), GDNF (10 ng/mL, PeproTech), cAMP (1 μmol/L, Sigma), IGF-I (10 ng/mL, PeproTech), and AA (200 μmol/L, Sigma)] was added to the wells, and the medium was changed weekly.

Immunohistochemical Staining

Cultured cells were washed with PBS for 5 min, fixed in 4% PFA at room temperature for 30 min, then washed twice with PBS every 10 min. The cells were blocked with 5% BSA and 0.3% TritonX-100 in PBS at room temperature for 2 h, then incubated overnight at 4 °C with primary antibody in 3% BSA and 0.1% TritonX-100 in PBS. After washing 3 times with PBS every 10 min, they were incubated at room temperature with secondary antibody and DAPI in PBS for 2 h, then washed 3 times with PBS every 10 min.

The primary antibodies and dilutions were as follows:

Anti-SOX2 (R&D, AF2018, 1:500)

Anti-PAX6 (DSHB, AB-528427, 1:10)

Anti-TUJ1 (Sigma, T8660, 1:5000)

Anti-KI67 (Abcam, ab15580, 1:800)

Anti-CHD7 (CST, #6505, 1:1000)

Anti-GFP (Abcam, ab6673, 1:400)

Anti-MAP2 (Millipore, MAB3418, 1:1000)

Anti-SMI312 (Biolegend, 837904, 1:1000)

Anti-TBR1 (Abcam, ab31940, 1:1000)

Anti-CTIP2 (Abcam, ab18465, 1:200)

Hoechst (Life-tech/3570, 1:2000)

DAPI (Sigma, D9542, 1:1000)

Western Blot

SDS-polyacrylamide gradient gel (4%–20%) was used in the Western blot; the electrophoresis program was 80 V for 30 min and then 120 V for 180 min. Proteins were transferred onto Immobilon polyvinylidene difluoride membranes (Millipore) for 210 min at 200 mA. The membrane was blocked by TBST (50 mmol/L Tris-HCl, pH 7.5, 150 mmol/L NaCl, and 0.1% Tween 20) with 5% BSA for 2 h at room temperature, incubated overnight at 4 °C with primary antibody in 3% BSA, then washed 3 times with TBST every 10 min. The membrane was treated with secondary antibody for 2 h at room temperature, then washed 3 times with TBST every 10 min. The reaction was analyzed using imaging film.

The primary antibodies and dilutions were as follows:

Anti-CHD7 (CST, #6505, 1:1000)

Anti-GAPDH (ab8245, 1:5000)

Analysis of Dendrites and Axons

About 40–50 GFP-positive (GFP$^+$) neurons were picked up randomly from each group. The searcher was blinded until statistical analysis was completed. The images were analyzed using Fiji software: all dendritic branches and secondary branches, the longest axon and secondary branches, and the total length of all neurites were taken

into account. At least three independent experiments were performed,

Alternative Splicing Analysis

cDNA was segmentally amplified by PCR. The products were separated by agarose gel electrophoresis and retrieved, then ligated with pGEM-T Easy Vector (Promega). The ligation products were transformed into *Escherichia coli* Top10 and monoclonal culture. At least 40 monoclonals were sequenced per sample.

Transcriptome Analysis (RNAseq)

For RNA-sequencing, total RNA was extracted and subsequently a sequencing library was prepared using the Illumina TrueSeq Total RNA Sample Prep Kit and sequenced on the Illumina Hi-Seq 2000. The clean reads were aligned to 9606 (NCBI Taxonomy ID) genome (version: GRCh38) using Hisat2. We applied HTseq to calculate the counts of genes. Reads/Fragments Per Kilobase Million Reads was used to standardize the expression data. We applied the DEseq2 algorithm to filter the differentially-expressed genes, then we filtered fold-change (FC) and false discovery rate (FDR) under the following criteria: (a) $\log_2(FC) > 0.585$ or < -0.585; (b) FDR < 0.05. For Gene ontology (GO) analysis, we downloaded the GO annotations from NCBI (http://www.ncbi.nlm.nih.gov/), UniProt (http://www.uniprot.org/) and GO (http://www.geneontology.org/). Fisher's exact test was applied to identify the significant GO categories and FDR was used to correct the *P*-values.

Statistical Analysis

Statistical tests were carried out using GraphPad Prism 6 (GraphPad Software, Inc., RRID:SCR_002798). Two-tailed Student's *t*-test was used for sample pairs, one-way ANOVA followed by Tukey's multiple comparison tests was used for 3 or more groups. Data distribution was tested by the Kolmogorov–Smirnov and Shapiro–Wilk tests in SPSS software (IBM, RRID:SCR_002865). The data distribution was normal. Results are shown as the mean ± SEM, and "*n*" represents either the number of neurons (for morphological analysis) or the number of repeated experiments (for qPCR and RNAseq). Mouse cortical neurons were independently obtained at least 3 times from 3 different litters. Stem cell differentiation was carried out independently in at least 3 batches. All data analyses were performed blinded to the experimental conditions. All conditions statistically different from the control are indicated as: $*P < 0.05$; $**P < 0.01$; $***P < 0.001$; $****P < 0.0001$. If the data were not in the 95% confidence interval of the group, they were excluded.

Results

An Intronic Variant of the *CHD7* Gene Found in Chinese Patients with ASD Leads to Down-Regulation of *CHD7* mRNA

After whole-exome sequencing for 167 ASD probands and their parents from Shanghai Mental Health Center, we identified an intronic variation in the *CHD7* gene (NM_017780.3:c.4851-31C>T, het) in 6 probands (Fig. 1A). Variants of five probands were inherited paternally, and one variant was inherited maternally and his non-carrier brother was unaffected (Fig. 1B). Sanger sequencing was carried out to confirm the presence of the variant (Fig. 1C).

When we examined the frequency of this variant (rs149348445) in various populations in the gnomAD database, we surprisingly found that this variant only existed in East Asia populations as a common variant with relatively low frequency (0.39%), and not in Caucasian or other populations. However, this variant had a nearly 10-times enriched frequency (3.6%, 6/167) in our ASD cohort, strongly suggesting that this variant is implicated in ASD.

The CHD7 protein belongs to the CHD family of chromatin remodelers and catalyzes the translocation of nucleosomes along DNA in chromatin [14]. Mutations of the *CHD7* gene are the major cause of CHARGE syndrome, which is characterized by coloboma of the eye, heart defects, atresia of the choanae, retardation of growth and development, genital abnormalities, and ear abnormalities [15]. Children with CHARGE syndrome frequently exhibit autistic-like deficits in vocalization, social responsiveness, and repetitive behaviors, suggesting that *CHD7* has a direct impact on autism [16].

Due to the high variability of non-coding regions between rodents and humans, the mouse *Chd7* gene does not contain similar sites with which we could make mouse models to mimic the condition. Therefore, to investigate whether this intronic variant affects the expression of the *CHD7* gene, we set out to perform mutagenesis in hESCs.

The point mutation was introduced into hESCs (H9) by homology-mediated end joining-based targeted integration with CRISPR/Cas9 technology [17]. Two synonymous mutations were also introduced into the sgRNA target region within exon 22 to avoid unwanted digestion by Cas9 after recombination (Fig. 1D). Two sub-clones (hom1-H9-hESCs and hom2-H9-hESCs) were successfully established, which carried the intronic mutations in a

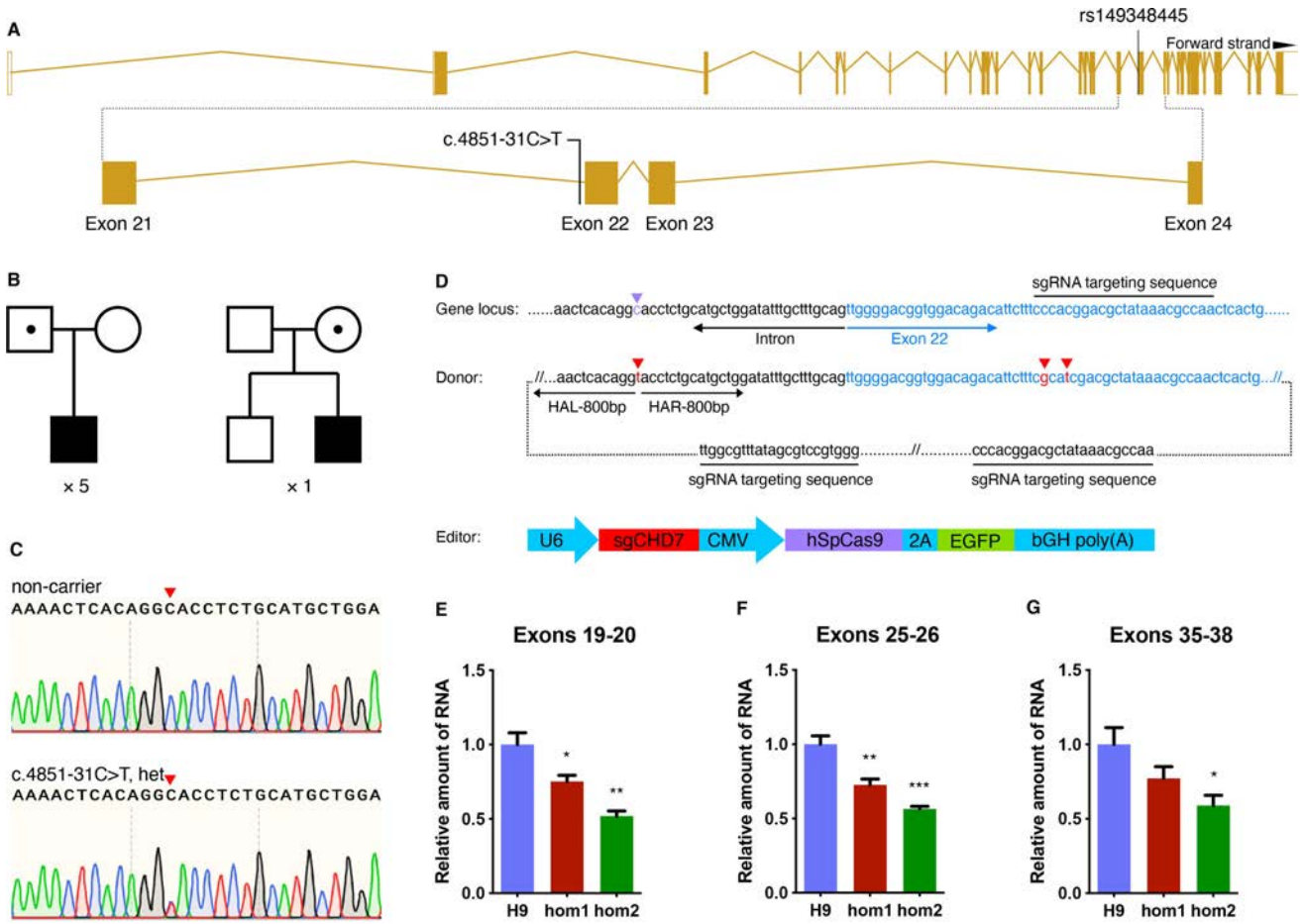

Fig. 1. An intronic variation of *CHD7* found in Chinese ASD patients leads to down-regulation of *CHD7* mRNA. **A** Position of the intronic variation in the genomic structure of the *CHD7* gene. **B** Genogram of the six families with probands carrying the *CHD7* variation (blank, non-carrier; blank with dot, asymptomatic carrier; solid, affected carrier; squares and circles represent males and females, respectively). **C** Sanger sequencing to verify the intronic variation in the *CHD7* gene (red arrowheads, variant base). **D** Schematic of gene editing (purple arrowhead, normal base; red arrowheads, introduced mutant bases; HAL/HAR, left/right homology arm). **E–G** mRNA levels assessed by RT-qPCR for *CHD7* in cell lines carrying homozygous mutants (hom1 and hom2) with primers located in exons 19–20 (**E**); exons 25–26 (**F**); and exons 35–38 (**G**). Values represent the mean ± SEM ($n = 3$, $^{*}P < 0.05$, $^{**}P < 0.01$, $^{***}P < 0.001$, $^{****}P < 0.0001$; one-way ANOVA). See also Fig. S1.

homozygous manner (hom; Fig. S1A). Unfortunately, heterozygous mutations (het) failed to be established.

In order to eliminate the risk of off-target effects, the sgRNA used was not matched with any regions outside the target. Nevertheless, we verified the top five predicted high risks (Fig. S1B) and no off-targets were found.

To determine whether the point mutation affected the expression of *CHD7*, we analyzed the mRNA expression using real-time qPCR with multiple primer pairs amplifying exons adjacent to the intronic variant site and the mRNA terminus. We found that the relative amount of *CHD7* mRNA was down-regulated in both cell lines carrying homozygous mutants (hom1-H9-hESCs and hom2-H9-hESCs) compared to H9 wild-type cells, using primer pairs amplified upstream (exons 19–20) or downstream exons (exons 25–26) of the point mutation, as well as a primer pair amplifying the 3' end of mRNA (exons 35–38) (Fig. 1E–G). This evidence indicated that the intronic variant (ch8-61757392-C-T) in the *CHD7* gene affects the expression of *CHD7* in human cells.

Intronic Variation of *CHD7* Delays Neuronal Differentiation of Human ESCs

Chd7 has been implicated in adult neurogenesis and the neural differentiation of cerebellar granule cells in mice [18, 19]. In order to study whether the intronic variation of *CHD7* found in autistic patients affects neuronal differentiation, we differentiated hESCs into dorsal forebrain glutamate neurons according to an established protocol (Fig. S2A).

On day 28 (D28) of neural differentiation, we first examined whether the proliferation of NPCs was affected by the intronic variant of *CHD7*. We performed

immunostaining using antibodies against the proliferation marker KI67 and the neural stem cell marker SOX2. We found that the percentage of KI67-positive cells among SOX2-positive cells were similar in NPCs derived from wild-type H9 cells and the two cell lines (hom1-H9-hESCs and hom2-H9-hESCs) carrying homozygous variants (Fig. 2A, B), suggesting that the intronic variation has no effect on the proliferation of human NPCs.

In order to further examine the process of neural differentiation, we performed immunostaining for SOX2 (an early neural stem cell marker), PAX6 (an intermediate neural stem cell marker), and TUJ1 (a neuronal marker) on D28 (Fig. 2C). We first found that most of the neuronal cells derived from wild-type or mutant hESCs expressed the dorsal forebrain progenitor marker PAX6 in a similar proportion, suggesting that the intronic mutation of *CHD7* did not affect the dorsal forebrain progenitor differentiation of hESCs (Fig. 2D). Interestingly, there were more SOX2-positive cells in the culture derived from both mutant hESC lines than in those from wild-type hESCs (Fig. 2E). In contrast, the proportion of TUJ1-positive cells derived from mutant hESCs was much lower than that in wild-type hESCs (Fig. 2F). These results are consistent with the previous report that a lack of Chd7 in mouse neural stem cells causes delayed neural differentiation [18].

Taken together, this evidence strongly suggests that the increase of SOX2-positive cells in hESCs-derived neurons carrying the intronic variant is most likely due to the delayed differentiation of forebrain stem cells, rather than increased proliferative capacity.

Chd7 plays a critical role in chromatin remodeling, and it has been shown that loss of Chd7 leads to dramatic changes in gene expression [19]. To further determine the molecular mechanism by which CHD7 regulates neural differentiation, we performed RNA-seq with RNA collected from neural precursor cells at D26 after the initiation of neural differentiation. We found that the expression of numerous genes changed significantly in NPCs carrying *CHD7* intronic variants comparing to wild-type NPCs (Fig. 2G, H). Altered genes were involved in biological processes including dopaminergic neuron differentiation, dentate gyrus development, and the Wnt signaling pathway (Fig. S2B). Genes closely associated with neural differentiation and development are of great interest, (marked with an asterisk in Fig. 2G, H) and we carried out real-time qPCR to verify the expression change (Fig. S2C–J). Among them, *LMX1A* is required for proper ear histogenesis and morphogenesis [20], and loss of hearing is a pivotal defect of the CHARGE syndrome. *WNT5A*, a critical gene in the Wnt signaling pathway, favors bone marrow MSC differentiation into osteoblasts by inhibiting the function of activated PPARγ through complex formation between NLK, SETDB1, and CHD7 [21]. *LAMB1* is one of the risk genes for ASD [22]. This evidence indicates that the intronic variant in the *CHD7* gene leads to the dysregulation of a series of critical genes that are implicated in neural developmental disorders, and the effect is similar to that caused by gene deletion.

Intronic Variation of *CHD7* Impairs Neurite Development and Dendritic Morphology

Cortical glutamatergic neurons comprise the major excitatory network in the central nervous system [23]. Glutamatergic neurons play critical roles in controlling cognition, emotion, language, and motor function. Dysfunction of cortical glutamatergic neurons may be relevant to autism [24]. Several of the known genetic disorders associated with autism have important implications for glutamatergic deficits in the disorder.

It has been reported that the development of newborn neurons in the subgranular zone of adult *Chd7*-null mice is severely compromised, showing less complex dendritic morphology than wild-type newborn neurons [18]. In order to study whether the intronic variation of *CHD7* found in autistic patients affects neuronal development, we differentiated hESCs into dorsal forebrain glutamate neurons using an established protocol (Fig. S2A). The cortical deeper-layer markers of glutamatergic neurons, TBR1 and CTIP2, were observed on D40 (Fig. S3).

During the differentiation of NPCs towards mature neurons, neurites including axons and dendrites start to develop and form functional synapses. Thus, to determine whether neuronal development is affected by an intronic variant of *CHD7*, we measured the neurites growth of differentiated neurons derived from hESCs. To visualize the morphology of neurons, we transfected GFP-expressing plasmids on D38 after neural differentiation. On D43, we performed immunostaining using antibodies against GFP and MAP2 (protein marker for dendrites) and found that the signals of GFP and MAP2 fully overlapped (Fig. 3A), suggesting that the polarity of neurons has not been established as axonal differentiation has not accomplished. Although neuronal differentiation is ongoing on D43, we still found that total neurite length and branch number was lower in neurons carrying homozygous mutations than in wild-type neurons derived from H9 ESCs, although the difference was not significant (Fig. 3B, C).

To determine whether intronic variation of *CHD7* affects mature neurons, we transfected GFP-expressing plasmid into mature neurons derived from human embryonic stem cells on D68 from the initiation of neural differentiation. On D72, we immunostained intronic variant and wild-type neurons, and found that the long axons labeled by GFP could not be marked by MAP2 (Fig. 3D), suggesting that axonal differentiation was finished, and

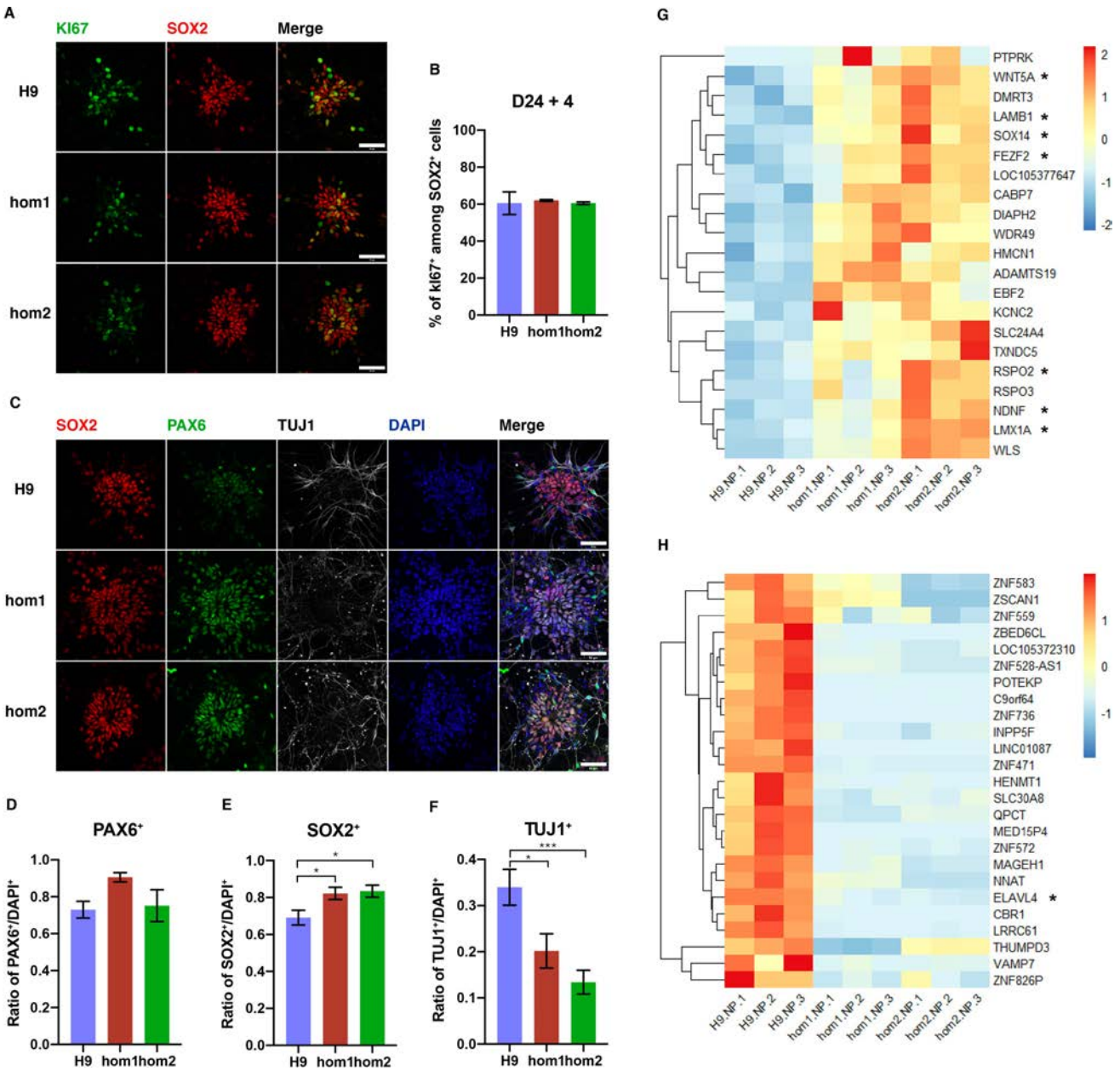

Fig. 2. Intronic variation of *CHD7* delays neuronal differentiation of hESCs. **A** Confocal images of differentiated human neural precursor cells (H9 control, hom1, and hom2) on D28 co-immunostained for Ki67 and SOX2 (scale bars, 50 μm). **B** Proportions of Ki67-positive cells among SOX2-positive cells (at least 1000 cells in 8 fields were analyzed for each group). **C** Confocal images of differentiated human neural precursor cells (H9 control, hom1, and hom2) on D28 co-immunostained for SOX2, PAX6, TUJ1, and DAPI (scale bars, 50 μm). **D–F** Statistical ratios of PAX6 (**D**), SOX2 (**E**), and TUJ1 (**F**) to DAPI (at least 1,000 cells in 8 fields were analyzed for each group; $*P < 0.05$, $**P < 0.01$, $***P < 0.001$, $****P < 0.0001$; one-way ANOVA). **G**, **H** Heatmaps showing significantly up-regulated genes (**G**) and down-regulated genes (**H**) (fold change > 1.5, FDR < 0.05) in differentiated neural precursor hom1 and hom2 cells compared to H9 control on D26 (color scale on right; *genes involved in neural differentiation and development; see also Fig. S2).

mature dendrites were labeled by MAP2. We found that both dendritic length and branch number were significantly lower in neurons carrying the intronic variant than in wild-type neurons derived from H9 ESCs (Fig. 3E, F), suggesting that the intronic variation of *CHD7* impairs the formation of dendritic morphology.

The Morphological Defects Caused by Intronic Variation are Rescued by Knocking Down its Up-Regulated Gene *TBR1*

To investigate whether the intronic variation of *CHD7* interferes with the gene expression profile during neuronal development, we performed RNA-seq on RNA from

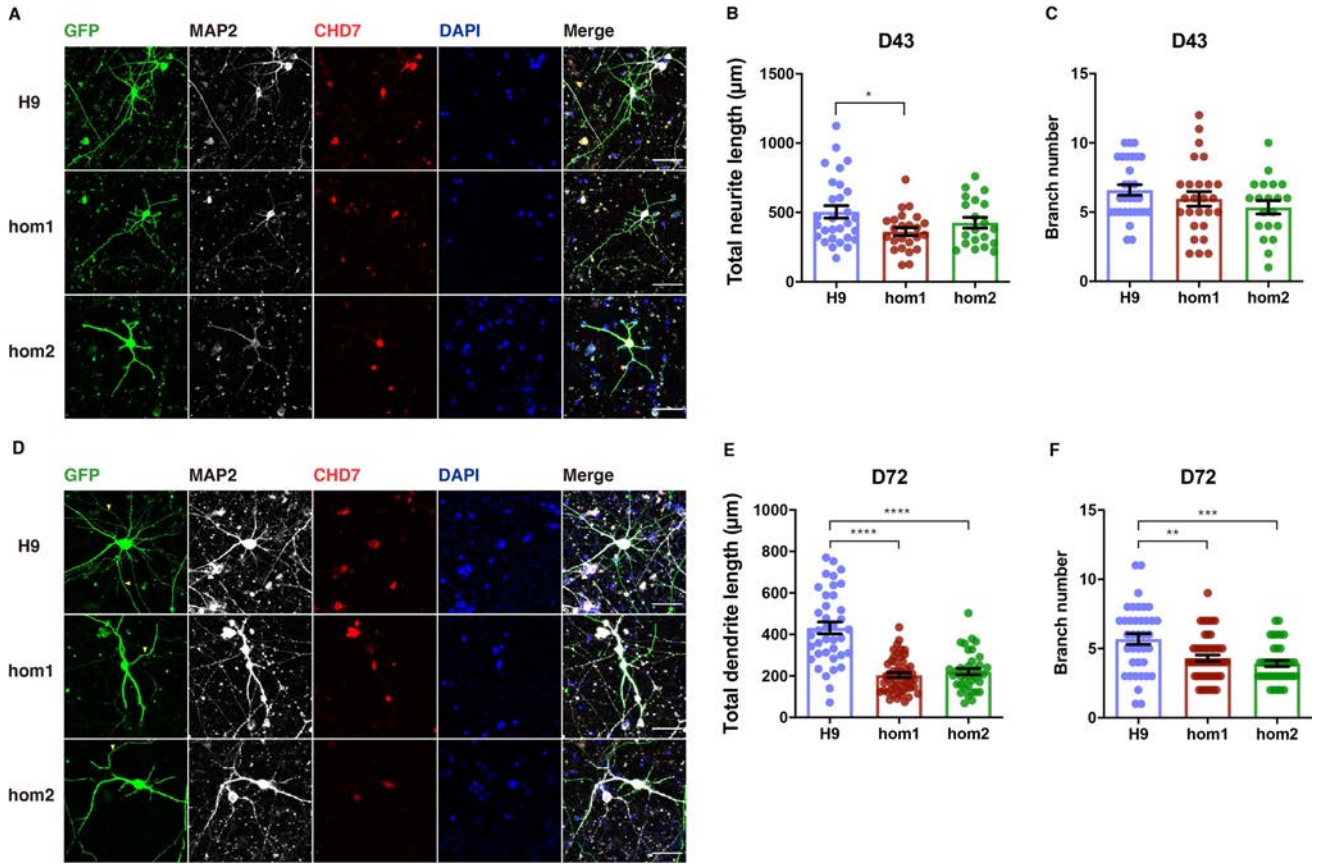

Fig. 3. Intronic variation of *CHD7* impairs neurite development and dendritic morphology. **A** Representative images of differentiated neurons (H9 control, hom1, and hom2) on D43 transfected with GFP, co-immunostained for GFP, MAP2, CHD7, and DAPI (scale bars, 50 μm). **B**, **C** Quantification of total neurite length (**B**) and branch number of differentiated neurons (**C**) (H9 control hom1, and hom2) on D43 (25–30 neurons were analyzed for each group; $*P < 0.05$, $**P < 0.01$, $***P < 0.001$, $****P < 0.0001$; one-way ANOVA). **D** Representative images of differentiated neurons (H9 control, hom1, and hom2) on D72, co-immunostained for GFP, MAP2, CHD7, and DAPI (yellow arrowheads, axons labeled by GFP but not MAP2; scale bars, 50 μm). **E**, **F** Quantification of total dendrite length (**E**) and branch number (**F**) of differentiated neurons (H9 control, hom1, and hom2) on D72 (25–30 neurons were analyzed per group; $*P < 0.05$, $**P < 0.01$, $***P < 0.001$, $****P < 0.0001$; one-way ANOVA; see also Fig. S3).

differentiated neurons on D40 after the initiation of neural differentiation. Interestingly, we found that the genes that were up-regulated in neurons derived from both hom1-H9-hESCs and hom2-H9-hESCs compared to the wild-type, were much more numerous than down-regulated genes (Figs. 4A, B, S4A), strongly suggesting that CHD7 plays a negative role in regulating gene expression in neurons (genes closely associated with neural development are marked with asterisks in Fig. 4A, B). We further validated these findings using real-time qPCR in neurons on D40 (Figs. 4C, S4B, C). We found that *TBR1*, a critical gene implicated in autism, was strongly up-regulated in neurons carrying the intronic variation, comparing to wild-type neurons (Fig. 4A).

The *TBR1* gene has been implicated in amygdala development and the laminar patterning of retinal ganglion cells as well as cortical neurons [25–27]. Interestingly, TBR1 is a putative transcription factor that is strongly expressed in glutamatergic early-born cortical neurons and regulates differentiation of the preplate and layer VI neurons [28]. Another up-regulated gene *EOMES* (*TBR2*), and *TBR1* are expressed sequentially by intermediate progenitor cells and postmitotic neurons in developing neocortex [29]. Given the function of TBR1 in regulating neuron projection development, as well as the association of several of the regulated genes with TBR1, we considered whether the morphological defects could be improved by restoring the expression of *TBR1*.

We transfected shRNAs for *TBR1* and GFP-expressing plasmid into differentiated neurons with the *CHD7* intronic variant on D60. As controls, shRNAs for *DsRed* and GFP-expressing plasmid were transfected into D60 differentiated wild-type neurons. On D72, we immunostained neurons with anti-GFP (Fig. 4D). From the results, both the dendritic length and branch number in neurons with the intronic variant transfected with shRNA for *TBR1* were

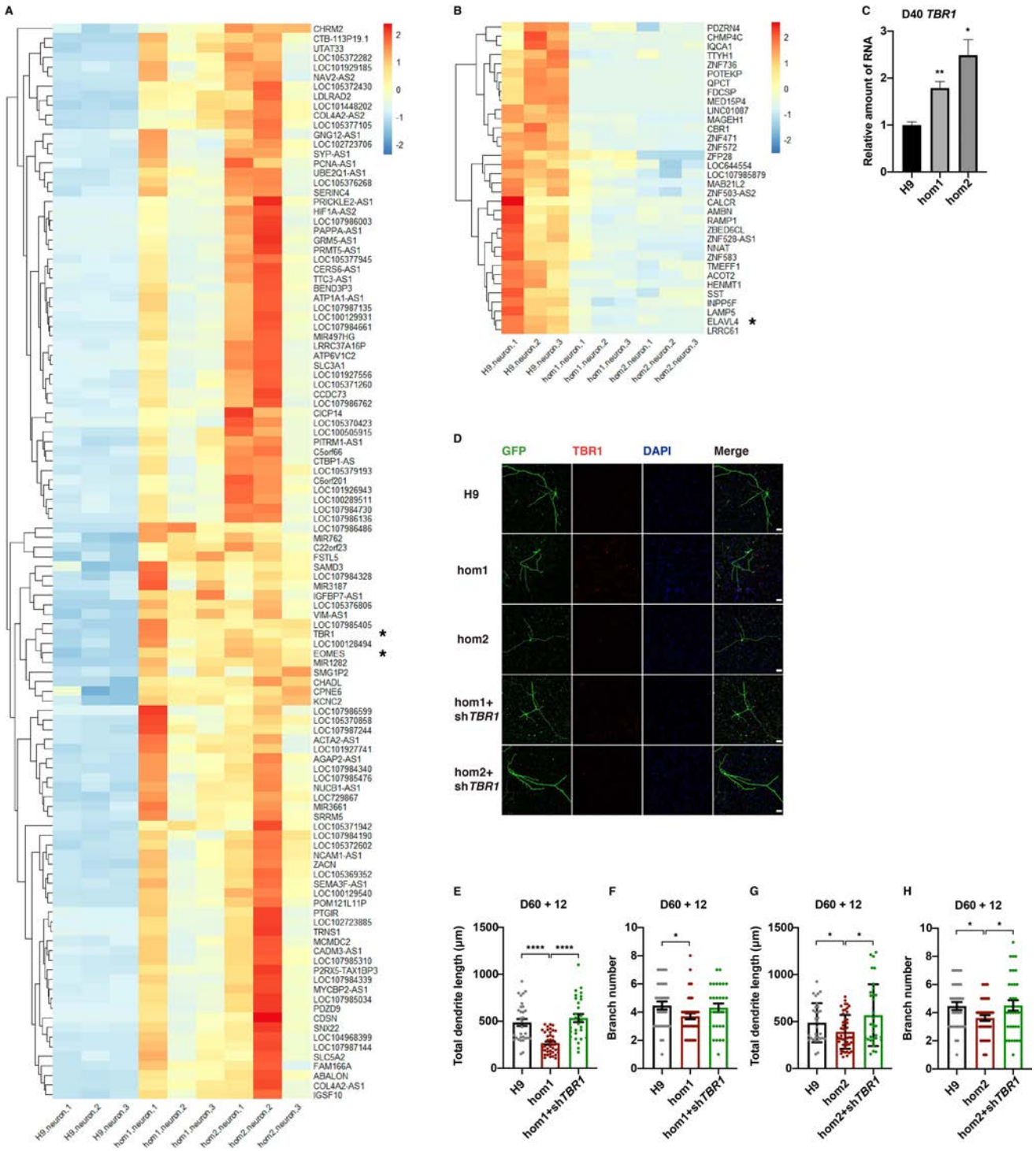

Fig. 4. The morphological defects caused by intronic variation are rescued by knocking down its up-regulated gene *TBR1*. **A**, **B** Heatmaps showing up-regulated genes (**A**) and down-regulated genes (**B**) (fold change > 1.5, FDR < 0.05) in differentiated hom1 and hom2 neurons compared to H9 controls on D40. (color scale on right; *genes involved in neural differentiation and development). **C** *TBR1* mRNA levels assessed by RT-qPCR in H9 and cell lines carrying homozygous mutants (hom1 and hom2). Values represent the mean ± SEM ($n = 3$, $^{*}P < 0.05$, $^{**}P < 0.01$, $^{***}P < 0.001$, $^{****}P < 0.0001$; *t*-test). **D** Representative images of differentiated neurons (H9 control, hom1, and hom2) on day D72 transfected with GFP and shRNA, co-immunostained for GFP, MAP2, TBR1, and DAPI (scale bars, 50 μm). **E–H** Quantification of the total dendrite length (**E** and **G**) and branch number (**F** and **H**) of differentiated neurons (H9 control, hom1, and hom2) on D72 (at least 30 neurons were analyzed for each group; $^{*}P < 0.05$, $^{**}P < 0.01$, $^{***}P < 0.001$, $^{****}P < 0.0001$; one-way ANOVA; see also Fig. S4).

improved over those transfected with shRNA for *DsRed*, and did not differ from the wild-type (Fig. 4E–H). This evidence indicated that *TBR1* is an important downstream gene of CHD7.

Intronic Variation of *CHD7* Affects Alternative Splicing, Resulting in Three Abnormal Transcripts that are Functionally Deficient

The precise excision of introns is catalyzed by a sophisticated ribonucleoprotein machinery called the spliceosome [30]. Intron–exon boundaries are delimited by short consensus sequences at the 5′ (donor) and 3′ (acceptor) splicing sites that are recognized by the spliceosome. In addition, the spliceosome interacts with a catalytic adenosine (the branch point) and a polypyrimidine tract (PyT) located between the branch point adenosine and the 3′ splicing sites [31].

Since the intronic variation of the *CHD7* gene is located adjacent to the branch point and may form a new splicing site, it would be intriguing to determine whether alternative splicing processes are altered in cells carrying the intronic variant.

Since the intronic variant (ch8-61757392-C-T) was located in the intron between exons 21 and 22 (Fig. 1A), in order to examine potential transcripts, we amplified mRNA segments of *CHD7* from exon 21 to exon 24 with PCR in wild-type hESCs and cells carrying the homozygous intronic variant (Fig. 5A). The amplification products were ligated with the T-vector followed by monoclonal sequencing. Interestingly, we found that, besides wild-type transcripts found in wild-type hESCs, there were three novel transcripts in hESCs carrying the intronic variant: a transcript with deletion of exons 22–23 (del), a transcript with duplication of exons 22–23 (dup), and a transcript with retention of 32 bp of an intronic fragment with seamless connection upstream to exon 22 (Fig. 5B).

To further determine the expression level of each novel transcript in wild-type hESCs and hESCs carrying the intronic variant, we assessed the level of each transcript using real-time qPCR with specific primers in RNA samples from corresponding cell lines (arrows in Fig. 5B). Importantly, we found that the expression levels of the three novel transcripts were significantly higher in hESCs with the intronic variant than in H9 wild-type hESCs (Fig. 5C–E), suggesting that the intronic variant compromises the alternative splicing of *CHD7* mRNA.

In order to further verify that the intronic variant affects the alternative splicing of *CHD7* in other cell lines, we also constructed cell lines with the intronic point mutation using HEK293 cells, and successfully screened heterozygotes and homozygotes including three point mutations (an intronic mutation and two synonymous mutations, abbreviated as 3PM het and 3PM hom, respectively), as well as heterozygotes and homozygotes with only two synonymous mutations (abbreviated as 2PM het and 2PM hom, respectively) as controls. Synonymous mutations were introduced in the exonic sites using the same strategy as in hESCs, to avoid unwanted digestion of Cas9 after homologous recombination. We found that intronic variants led to increases in the three abnormal transcripts in HEK293 cells as well, consistent with findings in hESCs (Fig. S5A–C).

The proportion of each transcript in hESCs and HEK293 cells was analyzed based on the cycle threshold from real-time qPCR (Fig. S5D, E). The dup transcript accounted for a considerable proportion of the total transcripts in hESCs and HEK293 cells. In contrast, the dup transcript was replaced by the del transcript in 3PM het HEK293 cells. The intronic retention transcript took up a very small proportion. These results suggest that the intronic variation regulates the alternative splicing of exons 22–23 by unknown mechanisms, and produces novel splicing forms by changing the selection of splicing sites.

Combined with the results from hESCs and HEK293 cells, the three novel transcripts were significantly increased with intronic variation, but the degree was different in each strain. This may be because the effect of intronic variation is not limited to what we observed, making dominant selection of splicing sites randomly, which in turn further deepens the differences.

To further determine whether these abnormal types of alternative splicing occur in differentiated neural precursors and neurons, we performed real-time qPCR experiments in NPCs and neurons derived from hESCs. Briefly, we amplified mRNA segments of *CHD7* from exon 21 to exon 24 by PCR on D26 and D40 in differentiated wild-type H9 cells and cells carrying homozygous intronic variants. We found that the three types of abnormal transcript were all present in hESCs and consistently, the expression levels of these transcripts were significantly higher in cells with the intronic variant on D26 and D40 than in H9 wild-type cells at the same stage (Fig. S5F–K). Based on these results, we were curious about the existence of the three novel transcripts in the mRNA of variant carriers. Unfortunately, it was difficult to obtain samples from patients.

We then set out to further address whether the three abnormal transcripts of *CHD7* caused by the intronic variant are functional. The transcript containing extra 32 bp of the intronic fragment would have a frameshift during translation, and thus be functionally deficient. Since exons 22 and 23 together contain 360 bp, the del transcript lacking these exons and the dup transcript containing two copies of these exons could be translated to full-length proteins with fewer or more amino-acids encoded by exons

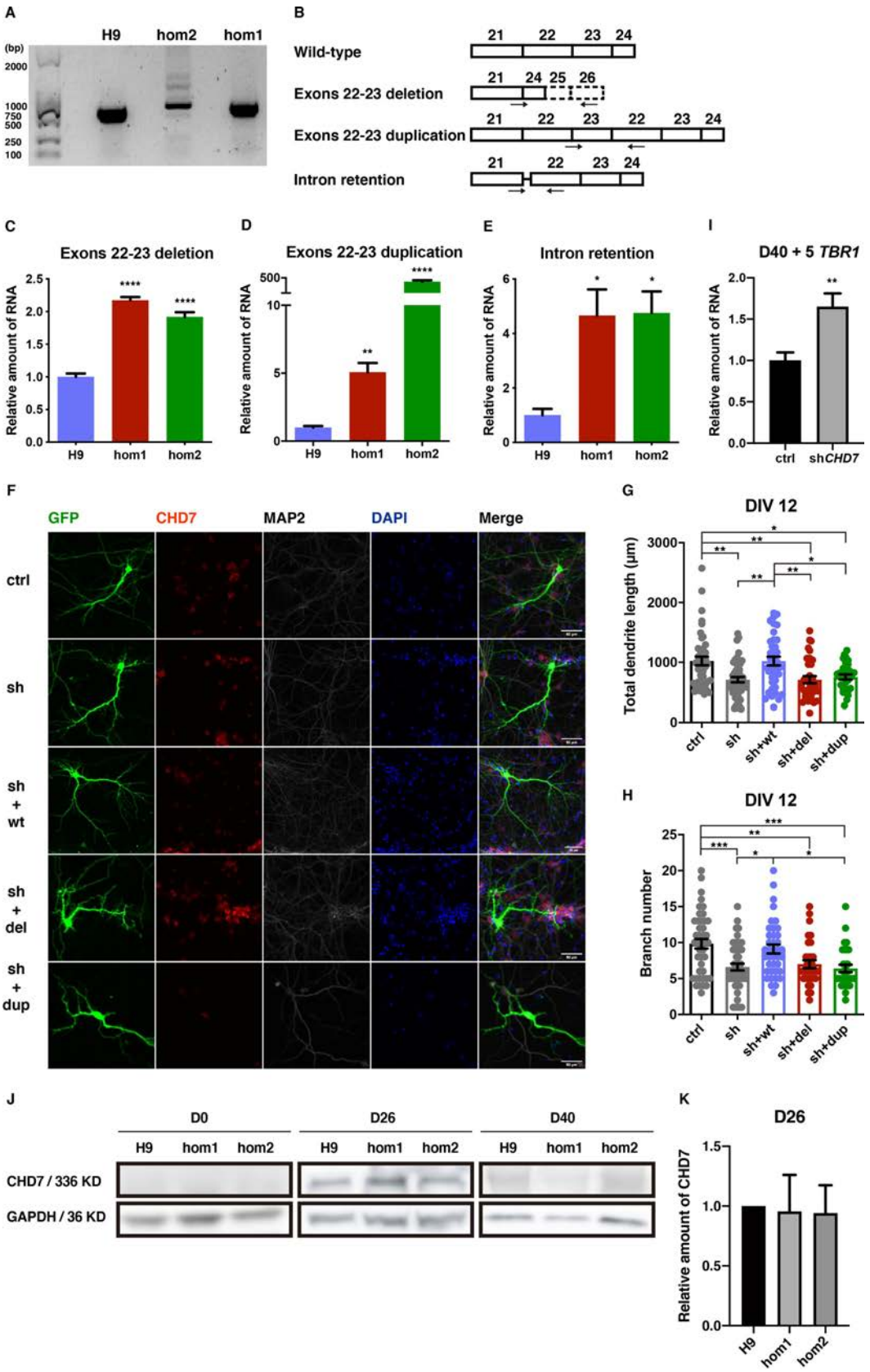
A
H9
hom2
hom1
(bp)
2000
1000
750
500
250
100
B
Wild-type
Exons 22-23 deletion
Exons 22-23 duplication
Intron retention
21
22
23
24
25
26
C
Exons 22-23 deletion
Relative amount of RNA
H9
hom1
hom2
D
Exons 22-23 duplication
E
Intron retention
I
D40 + 5 TBR1
ctrl
shCHD7
F
GFP
CHD7
MAP2
DAPI
Merge
ctrl
sh
sh + wt
sh + del
sh + dup
G
DIV 12
Total dendrite length (μm)
sh+wt
sh+del
sh+dup
H
Branch number
J
D0
D26
D40
CHD7 / 336 KD
GAPDH / 36 KD
K
D26
Relative amount of CHD7

◀**Fig. 5.** Intronic variation of *CHD7* affects alternative splicing, resulting in three abnormal transcripts that are functionally deficient. **A** Agarose gel electrophoresis illustrating PCR products of exons 21–24 from cDNA of H9 control, hom1, and hom2. **B** Schematic of alternative splicing around the intronic mutation. **C–E** mRNA levels assessed by RT-qPCR for the transcripts with exons 22–23 deletion (**C**), exons 22–23 duplication (**D**), and intron retention (**E**) in H9 control and two point-mutant cell lines. Values represent the mean ± SEM ($n = 3$, $^{*}P < 0.05$, $^{**}P < 0.01$, $^{***}P < 0.001$, $^{****}P < 0.0001$; one-way ANOVA). **F** Representative images of E14.5 mouse primary cortical neurons transfected with GFP, together with shRNA for DsRed as control or shRNA for mouse *Chd7*, and with human *CHD7* transcript wild-type, del or dup at DIV 12, co-immunostained for GFP, CHD7, MAP2, and DAPI (scale bars, 50 μm). **G**, **H** Quantification of total dendrite length (**G**) and branch number (**H**) of DIV 12 neurons (at least 30 neurons were analyzed for each group; $^{*}P < 0.05$, $^{**}P < 0.01$, $^{***}P < 0.001$, $^{****}P < 0.0001$; one-way ANOVA). **I** *TBR1* mRNA levels assessed by RT-qPCR in differentiated neurons after transfection with shRNA for *CHD7* at D40 for 5 days. Values represent the mean ± SEM ($n = 8$, $^{*}P < 0.05$, $^{**}P < 0.01$, $^{***}P < 0.001$, $^{****}P < 0.0001$; *t*-test). **J** Western blot analysis of CHD7 protein expression on D0, D26, and D40 of differentiation. **K** Quantification of CHD7 protein expression on D26 of differentiation. Values represent the mean ± SEM ($n = 3$, $^{*}P < 0.05$, $^{**}P < 0.01$, $^{***}P < 0.001$, $^{****}P < 0.0001$; *t*-test; see also Fig. S5).

22 and 23. To determine whether the protein products translated from the del and dup transcripts function differently from the wild-type CHD7 protein, we constructed the del and dup CHD7 expression vectors and assessed the expression of wild-type, del and dup CHD7 in HEK293 cells by Western blot. We found that the protein products generated from the del and dup transcripts were comparable to the wild-type CHD7 protein, at ~ 336 kD (Fig. S5L).

To determine whether the proteins carrying duplication of exons 22 and 23 or without exons 22 and 23 have function normally like wild-type CHD7, we knocked down endogenous *Chd7* in cultured cortical neurons from E14.5 mice using shRNA that only targeted mouse *Chd7* and not human *CHD7* (Fig. S5M, N). Meanwhile, we performed rescue experiments, by co-expressing wild-type CHD7, del and dup CHD7 constructs, along with shRNA against *Chd7*.

We first measured axonal growth at 3 days *in vitro* (DIV) and found that the total axonal length decreased significantly after *Chd7* knockdown. This was fully rescued by wild-type human *CHD7*, but not the del or dup form of *CHD7*, suggesting that the del and dup forms of *CHD7* are loss-of-function transcripts (Fig. S5O, P).

At 12 DIV, we found that the dendritic length and branch number significantly decreased after *Chd7* knockdown (Fig. 5F–H), indicating that *Chd7* plays a critical role in the normal development of cortical neurons. Importantly, the defects of dendritic growth were fully rescued by wild-type human *CHD7*, but not the del or dup transcripts (Fig. 5F–H). Together, this evidence demonstrates that the del and dup *CHD7* transcripts caused by the intronic variant act in a loss-of-function manner.

In the previous results, we found that the intronic variant led to an increase of *TBR1* expression (Fig. 4C) and defective neuronal morphology (Fig. 4E–H). In order to investigate whether this was caused by the decrease of CHD7, we analyzed the expression of *TBR1* 5 days after knockdown of *CHD7* by shRNA in differentiated neurons on D40. The results showed that *CHD7* mRNA was knockdown by 40% (Fig. S5Q) and *TBR1* was significant up-regulated (Fig. 5I). It is worth noting that the protein expression of CHD7 was predominantly in neural precursors during differentiation and rarely in hESCs and neurons (Fig. 5J). There was no significant difference in the high expression period on D26 (Fig. 5K), so it may be that the subsequent effect caused by the intronic variant is through *CHD7* mRNA rather than the protein, if the factor that the protein with high molecular weight cannot be quantified accurately using Western blot could be excluded. If this is the case, mRNA accumulation in hESCs and neurons is functional rather than redundant.

Based on the above results, we found that the intronic variant produced three novel transcripts, especially a huge increase of the del transcript in 3PM het of HEK293 cells (Fig. S5A), the dup transcript in 3PM hom of HEK293 cells (Fig. S5B), and in hom2 of H9 cells (Fig. 5D; Fig. S5G, J), indicating that the intronic variant leads to instability of exons 22–23 splicing. Moreover, both transcripts did not function normally, it can be concluded that this further reduced the content of normal transcripts to varying degrees due to alternative splicing. This may partly explain the phenotypic difference of the intronic variant carriers.

Thus, the intronic variant identified in autism patients indeed plays a critical role in regulating the function of *CHD7* by down-regulating the mRNA level and disrupted alternative splicing patterns. The proper neural differentiation and development of human NPCs and neurons were severely affected by the intronic variant, providing crucial evidence supporting the notion that the intronic variant site of *CHD7* is a potential autism susceptibility site.

Discussion

Genes implicated in autism have provided critical insights into the pathogenesis of the disease. Some of the well-documented autism risk factors include genes associated with rare syndromic forms of ASD (*MECP2*, *FMR1*, and *PTEN*), synaptic cell adhesion and scaffolding molecules (NLGN3, NLGN4, NRXN1, CNTNAP2, and SHANK3), and genes with *de novo* mutations (*CHD8*, *SCN2A*, and *DYRK1A* among others) identified in whole-exome

sequencing studies [5]. Due to the high heterogeneity of autism, the phenotype of patients varies from mild to severe and is affected by the genetic background of the family. Therefore, according to the unified criteria for autism diagnosis, large-scale family analysis with family members as controls is very important for the screening of risk mutations. Deleterious mutations are usually screened for in coding regions and splicing sites, because such mutations can result in the loss of gene function. Even so, at most 25% of ASD cases can be shown to have a genetic cause. Understanding of the genetic basis of autism has evolved from high-load disruption caused by a single mutation to a complex of multi-genes\ variation with low-load effects. These mutations alone are not enough to cause the phenotype, but can act as helpers. For this, some carriers become ill while others are asymptomatic, making it difficult to present a comprehensive picture of genetic variation in ASD patients.

Many introns contain highly conserved sequence elements, including the consensus splice site sequences and the binding sites for regulatory proteins, as well as the sequences of non-coding RNA genes [32]. Alternative splicing increases the diversity of the transcriptome by generating multiple mRNA isoforms from a single gene. A pre-mRNA molecule can be alternatively spliced through exon-skipping, alternative splice-site selection, and intron retention [33]. Mutations in intronic regions have been documented in various diseases. For example, a mutation that creates a novel donor splice site leads to the inclusion of a 95-nucleotide intronic sequence in *BRCA2* mRNA [31, 34]. A mutation that creates a novel binding site for SRSF1 activating a splicing enhancer element thus leads to inclusion of a 147-nucleotide pseudo-exon in *COL4A5* mRNA [31, 35]. In addition, genetic variants have been reported to cause disease through inactivation of intron-encoded RNA genes [36]. In our study, intronic variation created a novel acceptor splice site and led to the inclusion of a 32-nucleotide intronic sequence in *CHD7* mRNA (Fig. 5B, E). Interestingly, two abnormal transcripts with deletion of exons 22–23 and duplication of exons 22–23 were also found (Fig. 5B–D). We have not further explored the mechanism of mutation disturbing the splicing stability of exons 22–23. Nevertheless, the results provide a new form of alternative splicing. If exon deletion is caused by the selection of splicing sites and leads to exon-skipping, the mechanism of exon duplication is much more complicated; for example, the sequence repeat process may be a combination of transcription and splicing.

As evidence we present in this study, we found that intronic variation of *CHD7* has critical effects on neural differentiation and morphological development. In our study, transcriptome sequencing was performed in three stages of differentiation (hESCs, NPCs, and neurons). The genes with significant differences between the wild-type H9 cells and those carrying *CHD7* intronic variants on D26 and D40 were listed for analysis (Figs. 2G, H and 4A, B). Few genes were regulated during the ESC period (data not show). Moreover, results showed that *CHD7* mRNA was expressed in hESCs while protein expression was scarce, suggesting that the function of CHD7 in stem cells is limited. In NPCs, the affected genes participate in dopaminergic neuronal differentiation, dentate gyrus development, and the Wnt signaling pathway (Figs. 2G, H, S2B). In neurons, the affected genes are involved in cell metabolism, signal transduction pathways, synaptic transmission, and axon guidance (Figs. 4A, B, S4A).

In a comprehensive analysis of three stages, we found that the up-regulated genes in each period were highly specific and regulated only in the specific period, suggesting that the inhibitory action of *CHD7* on its target genes is stage-specific. Among the down-regulated genes, there were not only highly specific genes, but also genes that were continuously regulated. For example, some genes were down-regulated in stem cells and precursor cells such as *ZNF826P*; some genes were down-regulated in precursor cells and neurons such as *ELAVL4*; and some genes were down-regulated in all three stages such as *LINC01087*, *MED15P4*, and *ZNF528-AS1*. In addition, although some genes were regulated only in a specific period, there were direct interactions between regulated genes in different periods. For example, *FEZF2* that was up-regulated in the precursor phase can be inhibited by *TBR1* that is up-regulated in neurons during neocortical development [37]. Based on the above results, CHD7 begins to accumulate in stem cells, but plays a role mainly in neural differentiation and development. Its function is partly period-specific and partly continuous, which suggests that different treatments should be given at different stages in the development of the defects caused by *CHD7* mutation.

Conclusions

In conclusion, the level of *CHD7* mRNA significantly decreased in cell lines carrying homozygous mutants compared to control. Upon differentiation towards the forebrain neuronal lineage, neural cells carrying the *CHD7* intronic variant exhibited developmental delay and maturity defects. *TBR1*, a gene also implicated in ASD, significantly increased in neurons carrying the *CHD7* intronic variant. Furthermore, the morphological defects in neurons carrying *CHD7* intronic mutations were rescued by knocking down *TBR1*, indicating that *TBR1* may be responsible for the defects in *CHD7*-related disorders. Finally, the *CHD7* intronic variant generated three

abnormal forms of transcripts through alternative splicing, all of which exhibited loss-of-function in functional assays. Our study provides crucial evidence to support the notion that the intronic variant site of *CHD7* is a potential autism susceptibility site, shedding new light on identifying the functions of intronic variants in genetic studies of autism.

Acknowledgements We thank Weijun Feng, Institutes of Biomedical Sciences Fudan University, for providing the *CHD7*-expressing plasmid. This work was supported by the National Key R&D Program of China (2018YFA0108000), the National Natural Science Foundation of China (31625013, 81941405, 31771137, 31722024, 91732302, and 32000726), a Shanghai Brain-Intelligence Project from the Science and Technology Commission of Shanghai Municipality (16JC1420501), the Strategic Priority Research Program of the Chinese Academy of Sciences (XDBS01060200 and XDA16010310), a Shanghai Municipal Science and Technology Major Project (2018SHZDZX05), and the Shanghai Pujiang Program (17PJ1410200), and the research was supported by the Open Large Infrastructure Research of the Chinese Academy of Sciences.

Conflict of interest The authors declare no competing interests.

References

1. Kanner L. Autistic disturbances of affective contact. Nervous Child 1943, 2: 217–250.
2. Ronald A, Hoekstra RA. Autism spectrum disorders and autistic traits: a decade of new twin studies. Am J Med Genet B Neuropsychiatr Genet 2011, 156b: 255–274.
3. Sandin S, Lichtenstein P, Kuja-Halkola R, Larsson H, Hultman CM, Reichenberg A. The familial risk of autism. JAMA 2014, 311: 1770–1777.
4. Tick B, Bolton P, Happé F, Rutter M, Rijsdijk F. Heritability of autism spectrum disorders: a meta-analysis of twin studies. J Child Psychol Psychiatry 2016, 57: 585–595.
5. Huguet G, Bourgeron T. Genetic causes of autism spectrum disorders. In: Neuronal and synaptic dysfunction in autism spectrum disorder and intellectual disability. Academic Press, 2016: 13–24.
6. Satterstrom FK, Kosmicki JA, Wang J, Breen MS, De Rubeis S, An JY. Large-scale exome sequencing study implicates both developmental and functional changes in the neurobiology of autism. Cell 2020, 180: 568–584.e523.
7. Pinto D, Delaby E, Merico D, Barbosa M, Merikangas A, Klei L, *et al.* Convergence of genes and cellular pathways dysregulated in autism spectrum disorders. Am J Hum Genet 2014, 94: 677–694.
8. Bourgeron T. From the genetic architecture to synaptic plasticity in autism spectrum disorder. Nat Rev Neurosci 2015, 16: 551–563.
9. Yu X, Yang L, Li J, Li W, Li D, Wang R, *et al.* De novo and inherited SETD1A variants in early-onset epilepsy. Neurosci Bull 2019, 35: 1045–1057.
10. Gaugler T, Klei L, Sanders SJ, Bodea CA, Goldberg AP, Lee AB, *et al.* Most genetic risk for autism resides with common variation. Nat Genet 2014, 46: 881–885.
11. Guo H, Wang T, Wu H, Long M, Coe BP, Li H, *et al.* Inherited and multiple *de novo* mutations in autism/developmental delay risk genes suggest a multifactorial model. Mol Autism 2018, 9: 64.
12. Jiang YH, Yuen RK, Jin X, Wang M, Chen N, Wu X, *et al.* Detection of clinically relevant genetic variants in autism spectrum disorder by whole-genome sequencing. Am J Hum Genet 2013, 93: 249–263.
13. Qiu Z, Yuan B. Towards the framework of understanding autism spectrum disorders. Neurosci Bull 2019, 35: 1110–1112.
14. Petty E, Pillus L. Balancing chromatin remodeling and histone modifications in transcription. Trends Genet 2013, 29: 621–629.
15. Vissers LE, van Ravenswaaij CM, Admiraal R, Hurst JA, de Vries BB, Janssen IM, *et al.* Mutations in a new member of the chromodomain gene family cause CHARGE syndrome. Nat Genet 2004, 36: 955–957.
16 Hartshorne TS, Grialou TL, Parker KR. Autistic-like behavior in CHARGE syndrome. Am J Med Genet A 2005, 133a: 257–261.
17. Yao X, Wang X, Hu X, Liu Z, Liu J, Zhou H, *et al.* Homology-mediated end joining-based targeted integration using CRISPR/Cas9. Cell Res 2017, 27: 801–814.
18. Feng W, Khan MA, Bellvis P, Zhu Z, Bernhardt O, Herold-Mende C, *et al.* The chromatin remodeler CHD7 regulates adult neurogenesis *via* activation of SoxC transcription factors. Cell Stem Cell 2013, 13: 62–72.
19. Feng W, Kawauchi D, Körkel-Qu H, Deng H, Serger E, Sieber L, *et al.* Chd7 is indispensable for mammalian brain development through activation of a neuronal differentiation programme. Nat Commun 2017, 8: 14758.
20. Nichols DH, Pauley S, Jahan I, Beisel KW, Millen KJ, Fritzsch B. Lmx1a is required for segregation of sensory epithelia and normal ear histogenesis and morphogenesis. Cell Tissue Res 2008, 334: 339–358.
21. Takada I, Kouzmenko AP, Kato S. Wnt and PPARγ signaling in osteoblastogenesis and adipogenesis. Nat Rev Rheumatol 2009, 5: 442–447.
22. Takata A, Miyake N, Tsurusaki Y, Fukai R, Miyatake S, Koshimizu E, *et al.* Integrative analyses of de novo mutations provide deeper biological insights into autism spectrum disorder. Cell Rep 2018, 22: 734–747.
23. Molyneaux BJ, Arlotta P, Menezes JR, Macklis JD. Neuronal subtype specification in the cerebral cortex. Nat Rev Neurosci 2007, 8: 427–437.
24. DeVito TJ, Drost DJ, Neufeld RW, Rajakumar N, Pavlosky W, Williamson P, *et al.* Evidence for cortical dysfunction in autism: a proton magnetic resonance spectroscopic imaging study. Biol Psychiatry 2007, 61: 465–473.
25. Huang TN, Chuang HC, Chou WH, Chen CY, Wang HF, Chou SJ, *et al.* Tbr1 haploinsufficiency impairs amygdalar axonal projections and results in cognitive abnormality. Nat Neurosci 2014, 17: 240–247.
26. Liu J, Reggiani JDS, Laboulaye MA, Pandey S, Chen B, Rubenstein JLR, *et al.* Tbr1 instructs laminar patterning of retinal ganglion cell dendrites. Nat Neurosci 2018, 21: 659–670.

27. Darbandi SF, Schwartz SER, Qi Q, Catta-Preta R, Pai EL-L, Mandell JD, *et al.* Neonatal Tbr1 dosage controls cortical layer 6 connectivity. Neuron 2018, 100: 831–845.
28. Hevner RF, Shi L, Justice NJ, Hsueh Y, Sheng M, Smiga S, *et al.* Tbr1 regulates differentiation of the preplate and layer 6. Neuron 2001, 29: 353–366.
29. Englund C, Fink A, Lau C, Pham D, Daza RA, Bulfone A, *et al.* Pax6, Tbr2, and Tbr1 are expressed sequentially by radial glia, intermediate progenitor cells, and postmitotic neurons in developing neocortex. J Neurosci 2005, 25: 247–251.
30. Papasaikas P, Valcárcel J. The spliceosome: the ultimate RNA chaperone and sculptor. Trends Biochem Sci 2016, 41: 33–45.
31. Vaz-Drago R, Custódio N, Carmo-Fonseca M. Deep intronic mutations and human disease. Hum Genet 2017, 136: 1093–1111.
32. Kelly S, Georgomanolis T, Zirkel A, Diermeier S, O'Reilly D, Murphy S, *et al.* Splicing of many human genes involves sites embedded within introns. Nucleic Acids Res 2015, 43: 4721–4732.
33. Chen M, Manley JL. Mechanisms of alternative splicing regulation: insights from molecular and genomics approaches. Nat Rev Mol Cell Biol 2009, 10: 741–754.
34. Anczuków O, Buisson M, Léoné M, Coutanson C, Lasset C, Calender A, *et al.* BRCA2 deep intronic mutation causing activation of a cryptic exon: opening toward a new preventive therapeutic strategy. Clin Cancer Res 2012, 18: 4903–4909.
35. King K, Flinter FA, Nihalani V, Green PM. Unusual deep intronic mutations in the COL4A5 gene cause X linked Alport syndrome. Hum Genet 2002, 111: 548–554
36. He H, Liyanarachchi S, Akagi K, Nagy R, Li J, Dietrich RC, *et al.* Mutations in U4atac snRNA, a component of the minor spliceosome, in the developmental disorder MOPD I. Science 2011, 332: 238–240
37. McKenna WL, Betancourt J, Larkin KA, Abrams B, Guo C, Rubenstein JL, *et al.* Tbr1 and Fezf2 regulate alternate corticofugal neuronal identities during neocortical development. J Neurosci 2011, 31: 549–564

Neurosci. Bull. August, 2021, 37(8):1107–1118
https://doi.org/10.1007/s12264-021-00699-4

www.neurosci.cn
www.springer.com/12264

ORIGINAL ARTICLE

The Amygdala Responds Rapidly to Flashes Linked to Direct Retinal Innervation: A Flash-evoked Potential Study Across Cortical and Subcortical Visual Pathways

Yanmei Chen[1] · Yiling Ni[1] · Jianhong Zhou[1] · Hua Zhou[1] · Qian Zhong[2] · Xinyue Li[2] · Jichuan Zhang[1] · Yuanye Ma[2] · Jingkuan Wei[2]

Received: 29 August 2020 / Accepted: 27 February 2021 / Published online: 4 June 2021

Abstract Rapid detection and response to visual threats are critical for survival in animals. The amygdala (AMY) is hypothesized to be involved in this process, but how it interacts with the visual system to do this remains unclear. By recording flash-evoked potentials simultaneously from the superior colliculus (SC), lateral posterior nucleus of the thalamus, AMY, lateral geniculate nucleus (LGN) and visual cortex, which belong to the cortical and subcortical pathways for visual fear processing, we investigated the temporal relationship between these regions in visual processing in rats. A quick flash-evoked potential (FEP) component was identified in the AMY. This emerged as early as in the LGN and was approximately 25 ms prior to the earliest component recorded in the SC, which was assumed to be an important area in visual fear. This quick P1 component in the AMY was not affected by restraint stress or corticosterone injection, but was diminished by RU38486, a glucocorticoid receptor blocker. By injecting a monosynaptic retrograde AAV tracer into the AMY, we found that it received a direct projection from the retina. These results confirm the existence of a direct connection from the retina to the AMY, that the latency in the AMY to flashes is equivalent to that in the sensory thalamus, and that the response is modulated by glucocorticoids.

✉ Jingkuan Wei
weijk@lpbr.cn

[1] Department of Basic Medicine, Medical School, Kunming University of Science and Technology, Kunming 650550, China

[2] State Key Laboratory of Primate Biomedical Research, Institute of Primate Translational Medicine, Kunming University of Science and Technology, Kunming 650500, China

Keywords Subcortical visual pathway · Amygdala · Superior colliculus · Corticosterone · Flash-evoked potential

Introduction

The neural network for visual processing in most mammals has evolved into a sophisticated neural system to perceive visual signals including colors, shapes, and textures [1]. Visual information is also crucial for detecting potential threats, because rapidly identifying and responding to danger is critical for survival. In rodents and primates, threatening visual stimulus-processing is highly conserved and innate [2, 3]. It requires not only the visual system but also some evolutionarily-conserved nuclei, such as the amygdala (AMY) [4, 5]. However, the details about how the visual system interacts with the AMY to process threating visual stimuli in such an efficient and high-speed manner remains to be elucidated. In addition, it is unknown whether the processing of threatening visual signals in this circuit are affected by other systems, such as hormones.

It has been speculated that the AMY receives information about visual fear from two parallel routes: a slower route from the thalamus through the sensory cortex to the AMY, which allows cortical analysis (for a review, see [6]), and a faster subcortical route that unconsciously processes emotional stimuli; this is composed of a series of subcortical structures, including the superior colliculus [7] (SC), the visual pulvinar [8, 9], and the AMY [10–12]. Recently, a fast route from the medial region of the SC *via* the lateral posterior nucleus of the thalamus (LP) to the lateral amygdala has been reported, and a population of glutamatergic neurons in the AMY has been found to respond to and mediate fear-related behavior in mice [13]. However, whether there exist some more concise pathways

still needs to be explored, as indirect neuronal relays before the AMY might not be the most evolutionary efficient way to prepare an animal very rapidly for an incoming danger.

Some morphological studies have shown that retinal ganglion cells innervate the peri-amygdaloid area and the medial AMY, suggesting a direct retina-AMY projection [14–17]. However, the function of this projection and the relationship between the AMY and the classic visual processing pathway is still unknown. In laboratory animals, event-related potentials (ERPs) can be easily recorded from both cortical and subcortical sites. Because of the high temporal resolution with millisecond precision, the ERP provides a useful method to investigate early information processing and the subsequent transitions to higher-level cognitive operations [18]. We postulated that a flash-evoked potential (FEP) [19] study that explores the detailed temporal relationship between the relevant nuclei when responding to visual stimuli would provide insights about this projection.

In the present study, we used retrograde neuronal tracing to examine the projection from the retina to the AMY. Then, FEPs were simultaneously recorded from the SC, AMY, LP, lateral geniculate nucleus (LGN), and visual cortex (V1) in freely-moving rats to measure the relative latencies across these areas. Glucocorticoids (cortisol in humans and corticosterone in rodents) are released from the adrenal cortex in response to stressful situations [20, 21], and they modulate emotional [22, 23] and cognitive processing [24, 25] . Thus, we also tested FEPs in these areas after stress and/or treatment with the glucocorticoid receptor antagonist RU38486. The response latency and amplitude of the main components in FEPs from individual brain regions were compared to understand signal processing in these areas.

Materials and Methods

Animals

Male adult (8–10 weeks of age) Sprague–Dawley rats (purchased from the Experimental Animal Institute of Sichuan Academy of Medical Science) were used. The rats were housed under standard conditions (12-h light/dark cycle with lights on from 07:00 to 19:00). Food and water were available *ad libitum* and the rats were familiarized with the experimenter and laboratory conditions for at least 1 week before experiments started. The experiments were carried out during the light phase of the cycle. All experiments were conducted in accordance with the guidelines for National Care and Use of Animals approved by the National Animal Research Authority. Protocols were approved by the Medical Animal Care & Welfare Committee of Kunming University of Science and Technology (No. 2014010).

Virus-Mediated Retrograde Tracing

Rats were anesthetized with pentobarbital sodium salt (60 mg/kg, Merck) and atropine sulfate (0.4 mg/kg), and then placed in a stereotactic apparatus (RWD Life Science). 200 nL retrograde AAV (AAV-CMV bGI-EGFP-WPRE-pA, Shanghai Taitool Bioscience Co., Ltd) was injected into the right AMY (2.8 mm posterior, 4.8 mm lateral, 8.5 mm ventral to bregma; see Fig. 1A). Two weeks later, the rats were sacrificed and perfused with 200 mL of 0.9% saline followed by 200 mL of 4% paraformaldehyde. Subsequently, the brains and eyes were removed and post-fixed in 4% paraformaldehyde and then 30% sucrose. The eyes were processed, embedded in paraffin, and sectioned at 3 μm. After that, the sections were stained with DAPI and then observed for AAV labelling. For the brain, frozen sections (40-μm thick) were cut on a microtome, and the AAV injection sites were confirmed.

Electrode Implantation

The recording electrodes were pair of twisted Teflon-coated stainless-steel wires (50 μm diameter, Stainl. Steel (HH), 790600, A–M Systems Co.). The electrodes were inserted into target areas at the following coordinates (in mm relative to bregma). SC: 5.4 posterior, 0.4 lateral, 4.2 ventral; LP: 4.8 posterior, 2.5 lateral, 4.4 ventral; AMY: 2.8 posterior, 4.8 lateral, 8.5 ventral; LGN: 4.8 posterior, 3.8 lateral, 5 ventral; V1: 7 posterior, 2.5 lateral, 2 ventral. Two stainless-steel screws (one served as a ground electrode, and the other as an anchor) were inserted into the skull through drilled holes without piercing the dura. The whole assembly was sealed and fixed to the skull using dental acrylic. All rats were then housed individually for at least one week of recovery. The location of injection site was determined using Nissl staining. Off-target recording locations were excluded from further analysis.

Animal Treatments Before Recording

FEPs were recorded simultaneously from electrodes in the SC, LP, AMY, LGN, and V1. The rats were given 2 days of familiarization to the testing procedures, followed by 2–3 days of rest before actual data collection. Tests were conducted from 10:00 to 18:00, which ensured a relatively stable physiological state. During testing, the rats were awake and moving freely. FEPs were recorded from all rats in the following situations: (1) Control; (2) 30 min after restraint stress (RS); (3) 30 min after injection of RU38486 (20 mg/kg, i.p.); (4) 30 min after RU38486 plus RS; and (5)

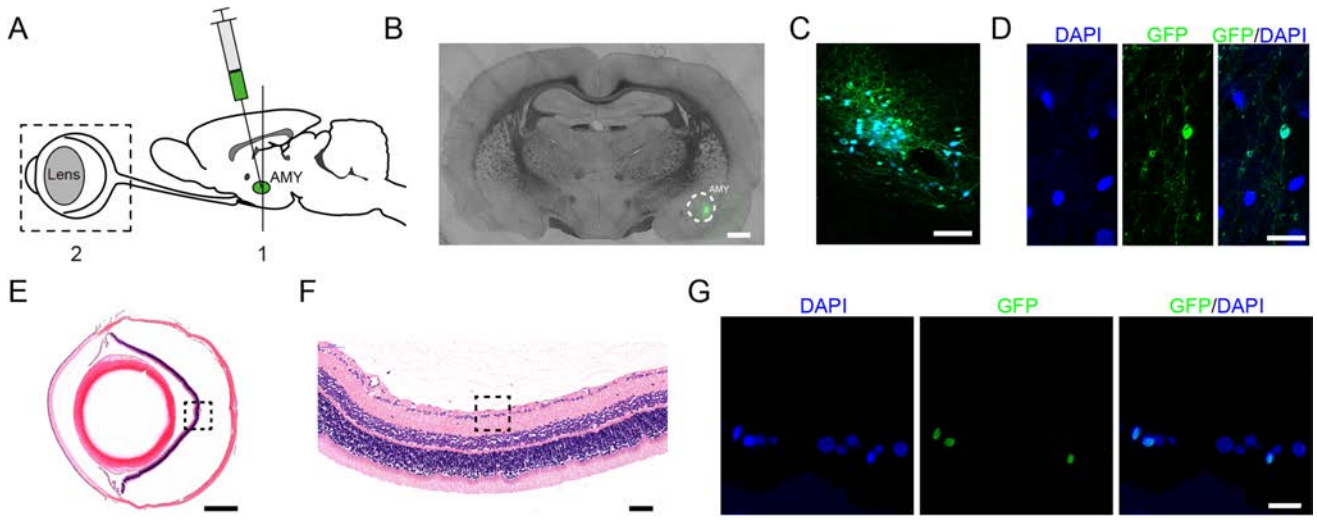

Fig. 1 Retrograde tracing of neuronal projection between retina and amygdala. **A** Schematic of the AAV retrograde tracer with EGFP injection into the AMY (1, coronal sections; 2, sagittal sections). **B** Merged fluorescence micrograph showing the location of EGFP-accumulating cells (dashed line, AMY; scale bar, 1 mm). **C** Magnified image of the labeled area as in **B** (from another section) (blue, DAPI; green, EGFP; scale bar, 50 μm). **D** Axon of an EGFP-accumulating cell (blue, DAPI; green, EGFP; scale bar, 10 μm). **E** Eyeball stained with hematoxylin and eosin (HE; scale bar, 0.5 mm). **F** Magnified image of the rectangle on the retina in **E** (scale bar, 50 μm). **G** EGFP-positive neural cells in the inner layer in an area of the retina as in **F** (from another section) (blue, DAPI; green, EGFP; scale bar, 20 μm).

30 min after injection of corticosterone (10 mg/kg, i.p.). This approach considerably reduced the number of animals required and facilitated within-subject comparisons across tests. In treatment #4, rats were first injected with 20 mg/kg RU38486 and 15 min later they were exposed to RS. RS was induced by putting the rat into a plastic tube (6 cm in diameter and 20 cm long) which prevented forward and backward movement and limited side-to-side mobility but did not discomfort the animal in any other way. Holes in the neck and sides of the tube ensured that the rats were able to breathe. Each rat was restrained in the tube for 20 min.

Flash-evoked Potential (FEP) Procedure and Data Analyses

FEP recordings were made in a shielded recording room with dim background illumination (<3 lux). The animals were freely-moving in a white Plexiglas testing box (45 cm × 40 cm × 25 cm, length × width × height). The top of the box was a photic stimulation display. A self-made cable connector was used to connect electrodes in the head of a rat and the signal amplifier, which reduced artifacts associated with cable movements.

Flash stimuli were generated by Psychophysics Toolbox version 3 (PTB-3, MatLab, R2013a) and presented on a computer monitor (1600 × 900 at 120 Hz, LCD, Dell, China) suitably linearized by gamma correction. For FEP recording, a train of 800 flash stimuli were generated. Each stimulus lasted 100 ms, with a photic intensity of 133 lux (DR-1600 Photometer, Gamma Scientific, Hong Kong). The inter-trial interval of flashes was 1 s to 5 s (0.2–1 Hz, random). The background noise of the recording room was 45 dB, and no sound was generated when displaying the flash stimulus (Digital Sound Level Meter AR814, Smart Sensor, Hong Kong).

Evoked potentials were amplified by UEA-BZ preamplifiers (SYMTOP, Beijing, China) with a 2.5-kHz sample rate, band-pass filtered at 0.1–150 Hz. Data were processed using EegLab 13.4 (MatLab toolbox). LFPs recorded in each brain area were filtered with a digital finite impulse response filter (band-pass 2–60 Hz). Waveforms were averaged in 500 ms epochs, 100 ms before and 400 ms after the onset of a flash (time zero).

We used a photodiode placed at the top-left of the display to synchronize the stimulus flash onset on the display to the data collection. The electrical signal of the photodiode was collected on one channel of the EEG amplifier. The screen luminance as recorded by the photodiode increased in a non-linear manner reaching its peak within 6–8 ms. Here, we marked the zero-point by detecting the maximum of the differential value of the photodiode signal, which indicated the fastest signal change.

FEP Component Identification and Statistical Analysis

Averaged FEP waveforms for each of the five brain areas are shown in Fig. 2 (components designated by their

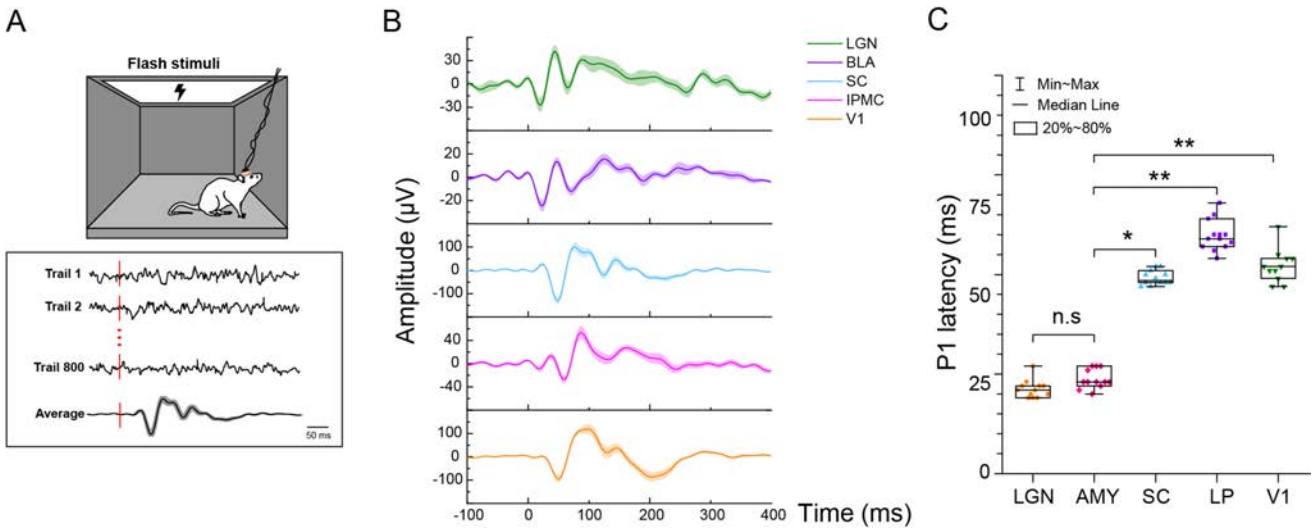

Fig. 2 Group averaged flash-evoked potential (FEP) waveforms for the control. **A** Upper panel, schematic of FEP recording in freely-moving rats in response to flashes in a dim environment. Lower panel, waveform of FEPs averaged from 800 trials (vertical lines, flash onset). **B** FEP waveforms recorded in the LGN, AMY, SC, LP, and V1. **C** Boxplots showing the P1 latencies of the main FEP components in the five brain areas (n = 12 in LGN, AMY, and SC, n = 13 in LP, n = 11 in V1; data are presented as the mean ± SEM).

polarity and by their sequence from the onset of the light flash are identified in the traces). Peak latencies and amplitudes were measured from the waveforms of each of the five brain regions (Fig. 2). We measured the highest amplitude value of peaks and valleys of the FEP waveform during baseline (100 ms before stimulation), then we compared this value with that after the flash. If there was a significant difference between these two values, the components of evoked potential were identified and named in order. The first positive component in the FEP waveform was named P1, and the first negative component was named N1. Peak latencies were measured from the onset of the stimulus. The peak-to-peak (P1/N1, N1/P2) amplitudes between two adjacent wave troughs and crests were used as a measure of wave amplitude in each FEP. We named the late components of the FEPs P130, N280, and N300, based on their latency and amplitude (positive or negative). The amplitude and latency of each late component was measured. Data are presented as the mean ± standard error of the mean (SEM). The effects of stress and/or a glucocorticoid receptor antagonist on the FEP were analyzed by comparing the differences of latency and amplitude between each treatment by two-way ANOVA. Between-group factors were the RS treatment and the RU38486 treatment. Within-group factors were P1 latency, P1 amplitude, peak-to peak amplitude, and late FEP components when analyzing different data.

Statistics

The statistical analyses were performed using SPSS 20.0 (SPSS, Chicago, IL, USA), and figures were plotted and constructed using Prism 6 (GraphPad Software, Inc., San Diego, CA, USA) or SPSS. Normality was tested using the Kolmogorov-Smirnov test and F-tests were used to assess equality of variance. Data from FEP test were analyzed using either two-tailed Student's t-tests (normal distribution), Mann-Whitney U tests (non-normal distribution), or one-way ANOVA with Tukey's *post hoc* test. P levels are indicated as ns $P > 0.05$, $*P < 0.05$, $**P < 0.01$, or $***P < 0.001$, except where indicated, when criteria could be defined more stringently.

Results

Amygdala Receives Direct Innervation from Retina

To determine whether there is a direct projection from the retina to the AMY, the retrograde tracer, adeno-associated virus (AAV) carrying enhanced green fluorescent protein (EGFP) with the CMV promoter was injected into the AMY (Fig. 1A). Two weeks later, the animals were sacrificed, and the eyeballs and brain were then prepared for histological observation. In the AMY sections, a number of EGFP-accumulating cells displayed green fluorescence under the fluorescence microscope at the AAV injection site (Fig. 1B), which indicated that the retrograde tracer (AAV with EGFP) was taken up by local neural cells. Some of these EGFP-positive cell had long axons (Fig. 1C, D). In the eyeball sections, the retinal ganglion cells were located in inner layer of the retina (Fig. 1E, F), and some of the EGFP labeled cells with green fluorescence were observed in the ganglion cell layer.

Because AAV cannot be transmitted across synapses, these results suggested that there are some direct projections from the retina to the AMY.

Flash-evoked Potentials in SC, LP, AMY, LGN, and V1

In the current study, we recorded FEPs in brain areas associated with visual information processing (AMY, LP, SC, LGN, and V1) in freely-moving rats (Fig. 2A). The FEP waveforms in each area showed different patterns (Fig. 2B). An early P1 component was recorded in the AMY, with a latency of 23.75 ± 0.70 ms, which was as fast as that in the LGN (21.25 ± 0.65 ms; $P > 0.05$, one-way ANOVA with Tukey's multiple comparison test), and significantly shorter than that in the SC (49.17 ± 0.52 ms), LP (60 ± 1.14 ms), and V1 (52.18 ± 1.27 ms).

Effects of Stress and/or RU38486 on FEPs in Visual Pathway

Stress has been reported to modulate visual processing and visual behavioral outcome in animals [26]. Glucocorticoid receptors are widely expressed in the AMY [27]. To test whether the rapid detection of a flash in the AMY and other areas are affected by stress, we recorded FEPs simultaneously in the five brain regions after the following treatments: (1) RS; (2) corticosterone antagonist (RU38486) injection; and (3) RS plus RU38486 injection.

Effects in the Amygdala

The highest positive amplitude in the AMY under baseline conditions was lower than that of the P1 component (baseline: 5.21 ± 1.55 μV, P1: 26.70 ± 5.06 μV; $n = 6$, paired t-test, $t_{(5)} = 3.53$, $P = 0.017$). We then measured the latency and amplitude of FEP components after saline or after stress or RU38486 treatment (Fig. 3A). The latency and amplitude of the P1 component after RS did not differ from that after saline. After RU38486 injection, the P1 component was diminished and was only discriminated in 4 of the 7 tested rats. Therefore, the latency of P1 did not differ significantly between control and the three treatment groups (Fig. 3B). In order to explore the differences in amplitude, in the 3 rats that P1 component cannot be discriminated, P1 amplitude was valued as the mean amplitude during the earliest and latest latencies among the 4 rats. We found a significant effect of RU38486 on P1 amplitude (main effect of RU38486: $F_{(1,24)} = 18.77$, $P < 0.001$). The P1 amplitude was decreased by RU38486 and RU38486 plus RS compared with controls ($F_{(3,33)} = 10.15$, $P < 0.001$; Tukey's multiple comparisons test:

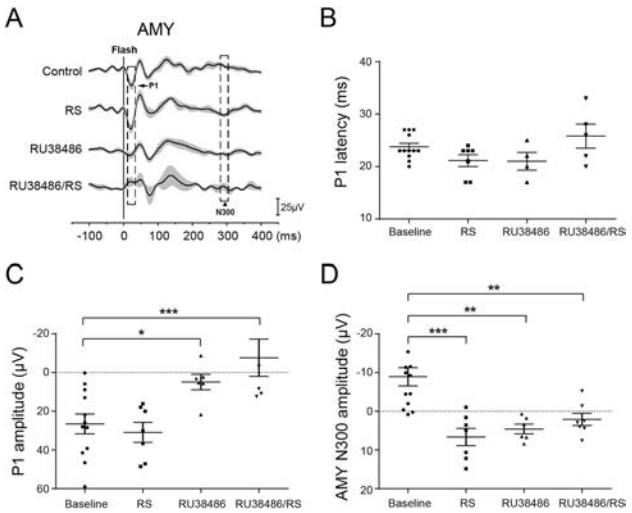

Fig. 3 Effects of stress and/or RU38486 on FEPs in the AMY. **A** Group averaged FEP waveforms in the AMY in control and under restraint stress (RS) and/or RU38486 treatment (solid vertical line, flash onset; dashed boxes, P1 and N300 components. **B** P1 latencies after each treatment (Control, 23.75 ± 0.70 ms; RS, 21.14 ± 1.12 ms; RU38486, 21.00 ± 1.68 ms; RU38486+RS, 25.80 ± 2.29 ms). **C** P1 amplitude after each treatment (Control, –26.53 ± 5.13 μV; RS, 30.95 ± 5.16 μV; RU38486, 4.89 ± 4.00 μV; RU38486+RS, –7.66 ±9.62 μV). **D** Effects of stress and/or RU38486 on a later FEP component (N300) in the AMY (Control, –8.94 ±2.36 μV; RS, 6.65 ± 2.24 μV; RU38486, 4.58 ± 1.26 μV; RU38486+RS, 2.10 ± 1.58 μV). Data are presented as the mean ± SEM (*$P < 0.05$, ***$P < 0.001$ *vs* Control).

Control *vs* RU38486: $P = 0.045$; Control *vs* RU38486 + RS: $P = 0.001$; Fig 3C).

Besides, the amplitude of N300, a later component in the AMY, was significantly decreased by stress (main effect of stress: $F_{(1,24)} = 5.80$, $P = 0.024$) and RU38486 treatment. One-way ANOVA comparisons showed that the N300 amplitude was decreased after all three treatments compared with control ($F_{(3,29)} = 11.64$, $P < 0.001$, *post hoc* Tukey: control *vs* stress: $P < 0.001$; control *vs* stress: $P = 0.001$; control *vs* stress: $P = 0.006$).

These results suggested that the P1 component in the AMY was not affected by RS, but was diminished by the glucocorticoid receptor antagonist, indicating that glucocorticoid receptors are necessary for this early component. In addition, we found that the later FEP component in the AMY was affected by both RU38486 and stress.

Effects in the LGN

In the LGN, the P1 component was also not changed by stress, but was modulated by RU38486 (main effect of RU38486: ($F_{(1,23)} = 16.001$, $P = 0.001$). As shown in Fig. 4A, the P1 component in the LGN was diminished after RU38486 injection. 30 min after RU38486 injection, the latency of the P1 component in the LGN was longer than control ($F_{(3,23)} = 5.517$, $P = 0.005$, Tukey's multiple

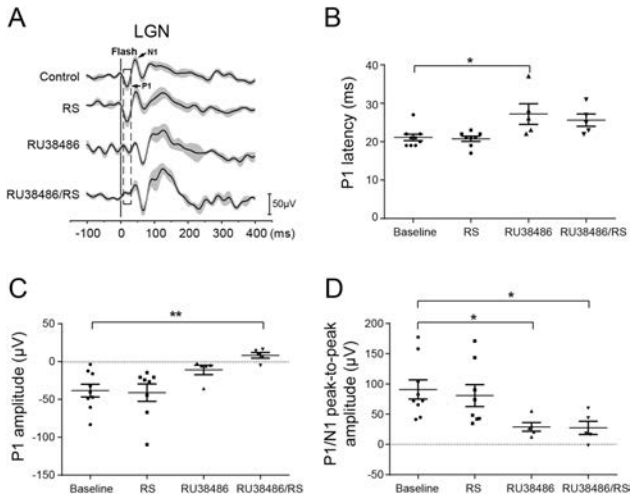

Fig. 4 Effects of stress and/or RU38486 on FEPs in the LGN. **A** Group averaged FEP waveforms in control and under restraint stress (RS) and/or RU38486 treatment (black vertical line, flash onset; dashed box, P1 component). **B** P1 latencies after each treatment (Control, 21.11 ± 0.84 ms; RS, 20.75 ± 0.67 ms; RU38486, 27.20 ± 2.67 ms; RU38486+RS, 25.60 ± 1.6 ms). **C** P1 amplitude after each treatment (Control, 38.30 ± 8.42 μV; RS, 41.04 ± 11.53 μV; RU38486, 10.97 ± 6.22 μV; RU38486+RS, –8.30 ± 3.75 μV). **D** Effects of stress and/or RU38486 on P1/N1 peak-to peak amplitude (Control, 90.82 ± 15.89 μV; RS, 80.76 ± 18.09 μV; RU38486, 28.96 ± 7.21 μV; RU38486+RS, 27.41 ± 10.91 μV). Data are presented as the mean ± SEM (*P <0.05, **P <0.01 *vs* Control).

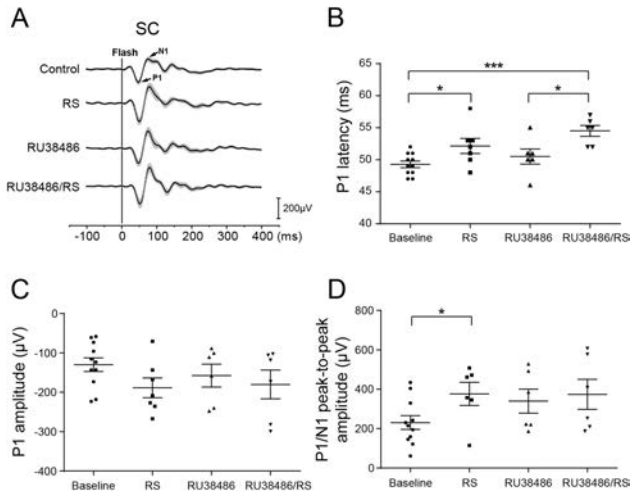

Fig. 5 Effects of stress and/or RU38486 on FEPs in the SC. **A** Group averaged FEP waveforms in control and under restraint stress (RS) and/or RU38486 treatment (black vertical line, flash onset; dashed box, P1 component). **B** P1 latencies after each treatment (Control, 49.27± 0.51 ms; RS, 52.14 ± 1.18 ms; RU38486, 50.50 ± 1.18 ms; RU38486+RS, 54.50 ±0.85 ms). **C** P1 amplitude after each treatment (Control: 129.73 ± 17.39 μV; RS: 188.53 ± 25.20 μV; RU38486, 157.56 ± 28.90 μV; RU38486+RS, 180.06 ± 36.47 μV). **D** Effects of stress and or RU38486 on P1/N1 peak-to peak amplitude (Control, 230.62 ± 35.17 μV; RS, 376.30 ± 58.70 μV; RU38486, 339.41 ± 61.16 μV; RU38486+RS, 373.94 ± 76.13 μV). Data are presented as the mean ± SEM (*P <0.05, **P <0.01 *vs* Control).

comparison test: control *vs* RU38486: $P = 0.020$, Fig. 4B), and the amplitude of the P1 component in RU38486 plus RS group was decreased compared with control ($F_{(3,23)} = 5.739$, $P = 0.004$, Tukey's multiple comparison test: Control *vs* RU38486 + RS: p = 0.011, Fig. 4C). In addition, the P1/N1 peak-to-peak amplitude decreased after RU38486 and/or stress ($F_{(3,23)} = 4.137$, $P = 0.017$, Control *vs* RU38486: $P = 0.014$, Control *vs* RU38486 + RS: $P = 0.012$, Tukey's multiple comparison test, Fig. 4D).

These results indicated that, just as in the AMY, the P1 component in the LGN was not changed by RS, but was diminished by the glucocorticoid receptor antagonist RU38486.

Effects in the SC

The latency of the P1 component in the SC was increased by RS (main effect of stress: $F_{(1,26)} = 14.42$, $P = 0.001$). As shown in Fig. 5B, 30 min after RS treatment, the P1 latency was significantly longer than control ($t_{(16)} = 2.545$, $P = 0.022$, dependent samples t-test, two-tailed). The P1 latency in rats receiving RS plus RU38486 was also longer than that in rats receiving RU38486 alone ($t_{(10)} = 2.76$, $P = 0.02$, dependent samples *t*-test, two-tailed) and the control ($t_{(15)} = 5.659$, P <0.001, dependent samples *t*-test, two-tailed). However, there was no effect of stress or RU38486 on P1 amplitude (Fig. 5C). We then analyzed the P1/N1 peak-peak amplitude of the SC FEP, and found that two-way ANOVA showed no effects of stress or RU38486, but one-way ANOVA with *post hoc* Tukey's test indicated that the P1/N1 peak-peak amplitude in rats undergoing restraint was increased compared with control ($F_{(3,31)} = 2.30$, $P = 0.045$; Control *vs* RS: P <0.05).

These results suggested that RS modulates the early component in the SC by increasing the P1 latency and P1/N1 peak-to peak amplitude, but RS has no effects on the late component of FEPs in the SC. As to the glucocorticoid receptor antagonist, RU38486 did not change any of the FEP components recorded in the SC.

Effects in the LP

In the LP, the latency of the P1 component was increased by stress (main effect of stress: $F_{(1,26)} = 7.132$, $P = 0.003$). After RS, the P1 latency was approximately 6 ms longer than the control (Control: 59.08 ± 0.90 ms; RS: 66 ± 1.03 ms, $F_{(3,26)} = 3.245$, $P = 0.038$; control *vs* stress: P <0.05, Tukey's multiple comparisons test, Fig. 6B). But stress did not alter the P1 amplitude or the P1/N1 peak-to peak amplitude. After RU38486 or RU38486 plus RS, neither the latency nor the amplitude of the P1 component differed from the control (Fig. 6C).

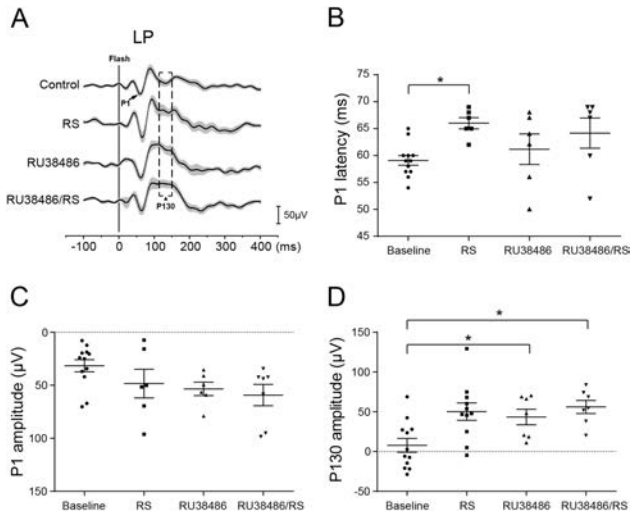

Fig. 6 Effects of stress and/or RU38486 on FEPs in the LP. **A** Group averaged FEP waveforms in control and under restraint stress (RS) and/or RU38486 treatment (black vertical line, flash onset; dashed box, P1 component). **B** P1 latencies after each treatment (Control, 59.08 ± 0.90 ms; RS, 66.00 ± 1.03 ms; RU38486, 61.17 ± 2.83 ms; RU38486+RS, 64.17 ± 2.80 ms). **C** P1 amplitude after each treatment (Control, 31.52 ± 5.76 μV; RS, 48.37 ± 13.54 μV; RU38486, 53.41 ± 6.31 μV; RU38486+RS, 59.26 ± 10.07 μV). **D** Effects of stress and or RU38486 on P130 amplitude (Control, 7.80 ± 8.69 μV; RS, 38.12 ± 12.83 μV; RU38486, 43.41 ± 9.88 μV; RU38486+RS, 56.01 ± 8.29 μV). Data are presented as the mean ± SEM (**P* <0.05, ***P* <0.01 *vs* Control).

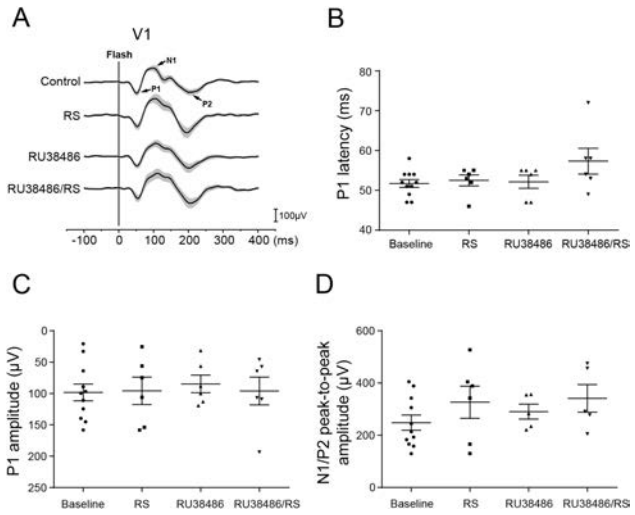

Fig. 7 Effects of stress and/or RU38486 on FEPs in V1. **A** Group averaged FEP waveforms under control or restraint stress (RS) and/or RU38486 treatment (black vertical line, flash onset; dashed box, P1 component). **B** P1 latencies after each treatment (Control, 51.73 ± 0.99 ms; RS, 52.50 ± 1.38 ms; RU38486, 52.17 ± 1.64 ms; RU38486+RS, 57.33 ± 3.24 ms). **C** P1 amplitude after each treatment (Control, 98.29 ± 13.45 μV; RS, 95.73 ± 21.87 μV; RU38486, 84.75 ± 13.98 μV; RU38486+RS, 96.03 ± 22.21 μV). **D** Effects of stress and or RU38486 on N1/P2 peak-to peak amplitude (Control, 248.23 ± 29.19 μV; RS, 326.58 ± 61.83 μV; RU38486, 290.26 ± 28.74 μV; RU38486+RS, 341.33 ± 53.00 μV). Data are presented as the mean ± SEM (**P* <0.05, ***P* <0.01 *vs* Control).

As shown in Fig. 6A, there was a late FEP component in the LP that changes after stress and RU38486 (main effect of stress: $F_{(1,28)}$ = 4.402, P = 0.045; main effect of RU38486: $F_{(1,28)}$ = 6.84, P = 0.014, two-way ANOVA). In the control, the amplitude of this component declined between 130 ms and 150 ms after the flash onset, but RU38486-treated rats did not show a significant decline and demonstrated a plateau around this P130 component. One-way ANOVA indicated that the P130 amplitude increased after RU38486 and RU38486 + RS when compared with control ($F_{(3,28)}$ = 5.448, P = 0.004; Control *vs* RU38486: P <0.05; Control *vs* RU38486 + RS: P <0.01, Tukey's multiple comparisons test; Fig. 6D).

These results showed that RS modulated the early component by increasing the P1 latency, while the glucocorticoid receptor antagonist RU38486 changed the late component of the FEP in the LP.

Effects in the V1

As shown in Fig. 7, the P1 component of the FEPs in the visual cortex was not affected by stress or RU38486, neither the latency nor the amplitude changed after the treatment (Fig. 7B, C). We then analyzed the effects of RS and/or RU38486 on the P2 latency and amplitude, as well as the N1/P2 peak-to-peak amplitude, and the data showed no differences from controls. These results indicated that the FEPs in the visual cortex were not modulated by either RS or a glucocorticoid receptor antagonist.

Effects of Corticosterone on FEPs in Visual Pathway

Corticosterone, the adrenal steroid hormone, is known to be secreted during stressful situations in rats and has been reported to enhance visual behavioral outcomes [28]. To further confirm the effects of stress on flash processing, we recorded FEPs 30 min after corticosterone injection (10 mg/kg, i.p.). No change of P1 latency or amplitude in the AMY, LGN, and V1 were found, just as after RS. There were also some changes of P1 component in the SC: the P1/N1 peak-to-peak amplitude was increased by corticosterone administration ($t_{(5)}$ = 2.942, P = 0.032), and the P1 amplitude in the LP was increased by corticosterone ($t_{(4)}$ = 4.81, P = 0.009). As for the late FEP components, stress decreased N300 in the AMY ($t_{(5)}$ = 3.651, P = 0.015) and N280 in the LGN ($t_{(6)}$ = 6.868, P = 0.001), and increased P130 in the LP ($t_{(4)}$ = 4.77, P = 0.009) and the N1/P2 peak-to-peak amplitude in V1 ($t_{(9)}$ = 2.31, P = 0.046), but no changes in the late components were seen in the SC (Table 1).

All these results indicated that corticosterone and RS have similar effects on FEPs in the AMY, LP, SC, LGN,

Table 1 Effects of stress and/or RU38486 administration on early and late components of FEPs recorded in the AMY, LGN, SC, LP, and V1.

	AMY			LGN			SC			LP			V1		
	P1 Lat.	P1 Amp.	LC Amp.	P1 Lat.	P1 Amp.	LC Amp.	P1 Lat.	P1 Amp.	LC Amp.	P1 Lat.	P1 Amp.	LC Amp.	P1 Lat.	P1 Amp.	LC Amp.
Restraint Stress	–	–	↓	–	–	–	↑	–	–	↑	–	–	–	–	–
RU38486	N/A	↓	↓	↑	–	↓	–	–	–	–	–	↑	–	–	–
RU38486/ Stress	N/A	↓	↓	–	↓	↓	↑	–	–	–	–	↑	–	–	–

'–' no change from control; '↑ increased than control; '↓' decreased than control; $P < 0.05$. Lat., latency; Amp., amplitude; LC, late component; N/A, not applicable.

and V1. Early components of FEPs in the AMY, LGN, and V1 were not affected by stress, but stress modulated the early components in the SC and LP. Stress modulated certain late component in most of the five areas except for the SC.

Discussion

In the present study, we recorded flash-induced potentials in the AMY, SC, LP, LGN, and V1, which are components of the sub-cortical and cortical pathways in visual processing. We found a rapid FEP component in the AMY that was as quick as in the LGN and much quicker than that in the SC. This component was not changed by RS or corticosterone treatment, but diminished after injection of RU38486, a glucocorticoid receptor blocker. Along with our neuronal tracing experiment, which showed a direct projection from retina to AMY, we postulated that the AMY receives direct innervation from the retina, and this pathway might play roles in the rapid processing of visual information.

Rapid detection of threat in the environment is critical for survival. The AMY is one of the most extensively studied subcortical nuclei responsible for the defensive responses to a wide range of threats. However, it remains unknown how visual information gains access to the AMY. It was known that a large number of retinal ganglion cells target the SC (also known as the optic tectum) in vertebrates. The SC, distinct from the dLGN [29, 30], is a subcortical center that mediates early sensorimotor integration and transformation. In primates, the SC sends projections to the pulvinar [31, 32], which subsequently project to high-order visual cortical areas [8, 33]. In rodents, the SC sends projections to the LP, which serves as a pulvinar- like structure [34]. Recently, it has been confirmed that the pathway through the SC and pulvinar to the AMY play important roles in fear detection, enabling quick information processing without being consciously perceived [35, 36]. However, evaluation and comparison of the processing speed in cortical and subcortical structures is still an open issue owing to current methodological limitations.

In the present study, we recorded FEPs simultaneously in the SC, LP, AMY, LGN, and V1. FEPs are electrical potentials obtained by averaging hundreds of EEG epochs after visual flash stimuli. The waveform of an FEP represents the summation of functional activity of large numbers of neuronal elements acting in synchrony during information processing and is time-locked to the stimulus [37, 38]. By comparing the latencies to the first main component of FEPs in different brain areas, we clarified the temporal course of these brain regions. As shown in Fig. 2, a quick FEP component emerged at approximately 21 ms after the flash in LGN, at approximately 49 ms in the SC, 60 ms in the LP, and 52 ms in V1. Different from the postulated sequence from the SC, through the LP to the AMY, we found a quick FEP component in the AMY at approximately 23 ms after the flash onset and as quickly as in the LGN. The LGN is the primary relay for visual signals from retina to cortex. But why did the AMY respond to the flash as quickly as the LGN? Which pathway leads to this response?

We then injected rAAV2-retro into the right AMY in rats. Two weeks later, GFP expression was found in the retina of the right eye, which suggesting direct retinal inputs to the AMY. These results are consistent with recent studies showing that the intrinsically photosensitive retinal ganglion cells (ipRGCs) in the retina project their axons directly to the medial and the central AMY [16]. Thus, besides the recognized sub-cortical pathway from the SC through LP to the lateral AMY [39], which quickly processes visual fear, there is a direct pathway from retina to AMY. The P1 component in the AMY might occur *via* this direct pathway, and the P2 component in AMY is more likely to represent signal processing from the SC through the LP to the lateral AMY because it occurs after the early component in the LP. However, further studies to identify

which kind of RGCs in retina are labelled by retro-AAV in the AMY are needed in order to understand more about the AMY-projecting neurons in the retina.

The amplitude of P1 in the AMY was smaller than that in other regions, such as the SC or V1. A possible reason might be that only some portion of neurons in the AMY respond to visual stimuli, because it is not a specific visual center. In addition, it is possible that the early response in the AMY is not sufficient for detection, especially for weak visual stimuli. It is still the SC-pulvinar connection that sends the actual information that the AMY then uses to inform the threat response. The AMY is more likely to functionally modulate rapid visual detection than to process rapid detection independently. Further studies using optogenetic methods might clarify the role of this direct projection in visual processing.

The homeostasis of hormones in the brain is important for cognitive and emotional behaviors. Acute stress has been shown to alter the way emotional and cognitive systems process information. Stress causes the secretion of corticotropin-releasing hormone (CRH) from the periventricular nucleus of the hypothalamus, which then causes the release of adrenocorticotropic hormone from the pituitary, resulting in the secretion of glucocorticoids from the adrenal cortex. Glucocorticoid receptors are widely expressed throughout the brain, such as the prefrontal cortex, hippocampus, and AMY, which may modulate emotional arousal and memory consolidation, as well as visual signal processing [40]. Glucocorticoid receptor mRNA has also been detected in the human primary visual cortex [41]. In the SC, it has been found that the serotonergic system, operating at some level of glucocorticoid function, is involved in the integration of appetitive and consummatory grooming behaviors in the cat [42]. Thus, it is reasonable to suggest that stress would modulate FEPs recorded in brain areas expressing glucocorticoid receptors or receiving projections from these brain areas.

Stress is one of the triggering factors that causes mental disorders, such as anxiety and depression. Acute RS is a widely used and convenient method to induce both psychological and physical stress. Restraint is painless and does not cause physical harm to the animals, but does activate the HPA-axis and increases the production of glucocorticoids, initiating the deleterious effects of stress [43]. After RS, rats always show increased restricted mobility, aggression, and fecal pellet output. In this study, stress did not change the P1 component in FEPs recorded in the AMY, LGN, and V1, but increased P1 latency and P1/N1 peak-to peak amplitude in the SC, and increased P1 latency in the LP. It is known that early FEP components (peak latency less than $\sim$100 ms) are involved in sensory processing. Although there is one recent study showing that intracerebroventricular infusions of corticotropin releasing factor increase the magnitude of dLGN neuronal responses to threshold level light stimuli and increase the speed of transmission of these signals through the thalamic visual circuitry [44], we did not found any changes in the P1 component in the LGN, and there was also no change in the P1 component in the AMY and V1. In nocturnal animals such as rodents, a strong white flash in a dim background can be seen as a threatening stimulus, like looming visual stimuli [45, 46]. Thus, the randomly generated flash in our FEP study might be a stress to rats and the effect of RS on FEPs might meet a ceiling effect such that RS had no further effect. We then recorded FEPs in the five brain regions 30 min after 10 mg/kg corticosterone injection (Fig. 8). Similar to the results after RS, corticosterone-treated rats also showed no changes in the P1 component in the AMY, LGN, and V1, but increased P1 amplitude in the LP, and increased P1/N1 peak-to-peak amplitude in the SC. Thus, the flash stimuli used in this study might lead to stress in rats, and the fearful visual signal leads to a quick P1 component in the AMY, confirming the role of the AMY in rapid visual processing in rats.

Interestingly, the P1 amplitude in both the AMY and LGN was diminished by the glucocorticoid receptor

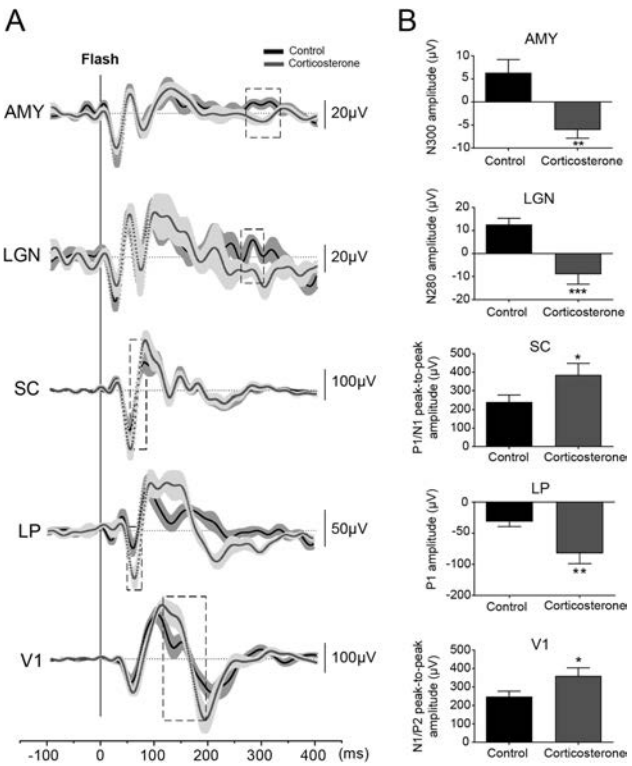

Fig. 8 Effects of corticosterone treatment on FEPs in the AMY, LGN, SC, LP, and V1. **A** Averaged FEP waveforms from different brain regions. **B** Histograms showing significant changes in FEP components after corticosterone administration compared with control. Data are presented as the mean ± SEM (*P <0.05, **P <0.01 *vs* Control).

antagonist RU38486 compared with control. These results indicated that the normal function of glucocorticoids is critical for the early processing of visual stimuli in the AMY and LGN. As visual signals are important for arousal, and the AMY is associated with arousal modulation, the direct retinal pathway might be associated with the regulation of arousal in rats, and this deserves further research. However, RU38486 did not change the early and late FEP components in the SC or V1. As stress or corticosterone increased the P1 latency in the SC, these results suggested that stress can modulate the function of the SC and V1, but the activity of glucocorticoid receptors is not necessary for the function of these two areas.

As to the late components, we found that they were modulated by stress in the AMY, LGN, and LP, but not in V1 and the SC. The later components of the FEP reflect higher cognitive processing, which requires the normal functions of many brain areas. Thus, the change of the late component caused by stress might be a result of changes in early visual processing through the SC, LP, or other related regions, as the P1 component in the SC and LP was significantly changed by stress. Interestingly, the P300 amplitude in the AMY was also decreased by RU38486, suggesting that both glucocorticoid receptor agonists and antagonists modulate the later processing of visual stimuli in the AMY. As the FEP in the LGN was significantly changed by RU38486, the changes of P300 in the AMY might also a result from the changes in the previous stage of signal processing. In V1, although there were no changes in the late component after RS or RU38486 treatment, the N1/P2 peak-to-peak amplitude in rats injected with corticosterone significantly increased after exposure to stress, thus, the function in V1 might also be changed by stress.

To our knowledge, this is the first study to record FEP simultaneously in the AMY, LP, SC, LGN, and V1 in freely-moving rats. FEPs recorded in V1 and SC have been described in many studies [38, 47, 48], the results of which are similar to ours, indicating valid recording and data analysis in this study. However, the P1 latencies in our study were longer than that reported in previous studies [38, 48]. We postulate that the zero-point of the flash marked by our photodiode may be earlier than the peak of the stimulus luminance that maximally drove the retinal ganglion cells, lengthening our overall latency estimate. In addition, the shape of FEP waveforms can be affected by the bandpass filter parameters, which could cause the P1 latency to differ from that reported by others.

There have been no reports of FEPs recorded in the AMY, LP, and LGN. There are only some studies showing auditory-evoked potentials (AEPs) in the lateral AMY. It was found that the N150 component of the AEP recorded from the lateral AMY undergoes a profound amplitude increase in fear conditioning [49], and this enhancement is specific for learning experiences that are accompanied by autonomic arousal [50]. Although the waveform of the AEP has some similarity with the FEP recorded in this study, these studies did not pay attention to the earliest P1 component as this component represents early signal processing which is not affected by higher cognitive processing such as learning and memory. The LP is a critical relay structure that conveys threat-related visual information through the subcortical visual circuit [51], which receives projections from the SC. Both early and late components of FEP in LP were changed by stress. Stress decreased the latency and increased the amplitude of P1 in rats, and the amplitude of the late P130 component also increased after stress treatment. These results suggested that visual processing in the LP is sensitive to stress. Many LGN, V1, and SC neurons are visually selective, and do not respond optimally to full-field flashes. Many of these neurons have antagonistic surrounds and therefore respond to contrast, not luminance. Thus, visually selective cells may not be well driven by a full-field flash. In FEP recordings, the averaged waveforms are the summation of local field potentials recorded from each brain area. The FEP measures do not allow us to infer whether their changes are due to excitatory or inhibitory effect on neuronal responses.

In conclusion, we recorded FEPs in the SC, LP, AMY, LGN, and V1, which serve as the subcortical and cortical pathways of emotional visual processing. By comparing the latency of the first main component of these FEPs, we found a quick component in the AMY, which emerged as quickly as in the LGN and even quicker than that in the SC. Along with the neuronal tracing finding of a direct neuronal projection from retina to AMY, we postulate that there is a direct retina-to-AMY pathway for quick detection of visual stimuli in rats. We also found that this quick detection of a flash requires normal glucocorticoid receptor function or arousal in rats.

Acknowledgements This work was supported by the National Key Research and Development Program of China (2018YFA0108503), the National Natural Science Foundation of China (81760251 and 81560234), and the Yunnan Provincial Natural Science Foundation (2018FB118 and KKSY201626001).

Conflict of interest The authors declare no competing financial interests.

References

1. Cant JS, Large ME, McCall L, Goodale MA. Independent processing of form, colour, and texture in object perception. Perception 2008, 37: 57–78.

2. Blanchard RJ, Mast M, Blanchard DC. Stimulus control of defensive reactions in the albino rat. J Comp Physiol Psychol 1975, 88: 81–88.
3. Wiener SG, Levine S. Behavioral and physiological responses of mother and infant squirrel monkeys to fearful stimuli. Dev Psychobiol 1992, 25: 127–136.
4. McFadyen J. Investigating the subcortical route to the amygdala across species and in disordered fear responses. J Exp Neurosci 2019, 13: 1179069519846445.
5. Janak PH, Tye KM. From circuits to behaviour in the amygdala. Nature 2015, 517: 284–292.
6. Tamietto M, de Gelder B. Neural bases of the non-conscious perception of emotional signals. Nat Rev Neurosci 2010, 11: 697–709.
7. Hadjikhani N, Asberg Johnels J, Zurcher NR, Lassalle A, Guillon Q, Hippolyte L. Look me in the eyes: constraining gaze in the eye-region provokes abnormally high subcortical activation in autism. Sci Rep 2017, 7: 3163.
8. Zhou N, Masterson SP, Damron JK, Guido W, Bickford ME. The mouse pulvinar nucleus links the lateral extrastriate cortex, striatum, and amygdala. J Neurosci 2018, 38: 347–362.
9. Hakamata Y, Sato E, Komi S, Moriguchi Y, Izawa S, Murayama N, *et al.* The functional activity and effective connectivity of pulvinar are modulated by individual differences in threat-related attentional bias. Sci Rep 2016, 6: 34777.
10. Morris JS, Ohman A, Dolan RJ. A subcortical pathway to the right amygdala mediating "unseen" fear. Proc Natl Acad Sci USA 1999, 96: 1680–1685.
11. Tamietto M, Pullens P, de Gelder B, Weiskrantz L, Goebel R. Subcortical connections to human amygdala and changes following destruction of the visual cortex. Curr Biol 2012, 22: 1449–1455.
12. Pessoa L, Adolphs R. Emotion processing and the amygdala: from a "low road" to "many roads" of evaluating biological significance. Nat Rev Neurosci 2010, 11: 773–783.
13. Wei P, Liu N, Zhang Z, Liu X, Tang Y, He X, *et al.* Processing of visually evoked innate fear by a non-canonical thalamic pathway. Nat Commun 2015, 6: 6756.
14. Cooper HM, Parvopassu F, Herbin M, Magnin M. Neuroanatomical pathways linking vision and olfaction in mammals. Psychoneuroendocrinology 1994, 19: 623–639.
15. Hattar S, Kumar M, Park A, Tong P, Tung J, Yau KW, *et al.* Central projections of melanopsin-expressing retinal ganglion cells in the mouse. J Comp Neurol 2006, 497: 326–349.
16. Luan L, Ren C, Wang W, Nan Y, Gao J, Pu M. Morphological properties of medial amygdala-projecting retinal ganglion cells in the Mongolian gerbil. Sci China Life Sci 2018, 61: 644–650.
17. Elliott AS, Weiss ML, Nunez AA. Direct retinal communication with the peri-amygdaloid area. Neuroreport 1995, 6: 806–808.
18. Porjesz B, Rangaswamy M, Kamarajan C, Jones KA, Padmanabhapillai A, Begleiter H. The utility of neurophysiological markers in the study of alcoholism. Clin Neurophysiol 2005, 116: 993–1018.
19. Matteucci MJ, Wisner DH, Gunther RA, Woolley DE. Effects of hypertonic and isotonic fluid infusion on the flash evoked potential in rats: hemorrhage, resuscitation, and hypernatremia. J Trauma 1993, 34: 1–7.
20. Simoens VL, Istok E, Hyttinen S, Hirvonen A, Naatanen R, Tervaniemi M. Psychosocial stress attenuates general sound processing and duration change detection. Psychophysiology 2007, 44: 30–38.
21. Watanabe Y, Gould E, Cameron HA, Daniels DC, McEwen BS. Phenytoin prevents stress- and corticosterone-induced atrophy of CA3 pyramidal neurons. Hippocampus 1992, 2: 431–435.
22. Xu L, Anwyl R, Rowan MJ. Behavioural stress facilitates the induction of long-term depression in the hippocampus. Nature 1997, 387: 497–500.
23. Mitra R, Sapolsky RM. Acute corticosterone treatment is sufficient to induce anxiety and amygdaloid dendritic hypertrophy. Proc Natl Acad Sci U S A 2008, 105: 5573–5578.
24. Hui GK, Figueroa IR, Poytress BS, Roozendaal B, McGaugh JL, Weinberger NM. Memory enhancement of classical fear conditioning by post-training injections of corticosterone in rats. Neurobiol Learn Mem 2004, 81: 67–74.
25. Phillips RG, LeDoux JE. Lesions of the dorsal hippocampal formation interfere with background but not foreground contextual fear conditioning. Learn Mem 1994, 1: 34–44.
26. Shackman AJ, Maxwell JS, McMenamin BW, Greischar LL, Davidson RJ. Stress potentiates early and attenuates late stages of visual processing. J Neurosci 2011, 31: 1156–1161.
27. Gray TS, Bingaman EW. The amygdala: corticotropin-releasing factor, steroids, and stress. Crit Rev Neurobiol 1996, 10: 155–168.
28. Roozendaal B. Stress and memory: opposing effects of glucocorticoids on memory consolidation and memory retrieval. Neurobiol Learn Mem 2002, 78: 578–595.
29. Vaney DI, Peichl L, Wässle H, Illing RB. Almost all ganglion cells in the rabbit retina project to the superior colliculus. Brain Research 1981, 212: 447–453.
30. Beckstead RM, Frankfurter A. A direct projection from the retina to the intermediate gray layer of the superior colliculus demonstrated by anterograde transport of horseradish peroxidase in monkey, cat and rat. Exp Brain Res 1983, 52: 261–268.
31. Stepniewska I, Qi HX, Kaas JH. Do superior colliculus projection zones in the inferior pulvinar project to MT in primates?. Eur J Neurosci 1999, 11: 469–480.
32. Berman RA, Wurtz RH. Functional identification of a pulvinar path from superior colliculus to cortical area MT. J Neurosci 2010, 30: 6342–6354.
33. Frank DW, Sabatinelli D. Human thalamic and amygdala modulation in emotional scene perception. Brain Res 2014, 1587: 69–76.
34. Krout KE, Loewy AD, Westby GW, Redgrave P. Superior colliculus projections to midline and intralaminar thalamic nuclei of the rat. J Comp Neurol 2001, 431: 198–216.
35. Almeida I, Soares SC, Castelo-Branco M. The distinct role of the amygdala, superior colliculus and pulvinar in processing of central and peripheral snakes. PLoS One 2015, 10: e0129949.
36. Koller K, Rafal RD, Platt A, Mitchell ND. Orienting toward threat: contributions of a subcortical pathway transmitting retinal afferents to the amygdala *via* the superior colliculus and pulvinar. Neuropsychologia 2019, 128: 78–86.
37. Odom JV, Bach M, Brigell M, Holder GE, McCulloch DL, Mizota A, *et al.* ISCEV standard for clinical visual evoked potentials: (2016 update). Doc Ophthalmol 2016, 133: 1–9.
38. Jansen BH, Zouridakis G, Brandt ME. A neurophysiologically-based mathematical model of flash visual evoked potentials. Biol Cybern 1993, 68: 275–283.
39. Levine JD, Weiss ML, Rosenwasser AM, Miselis RR. Retinohypothalamic tract in the female albino rat: a study using horseradish peroxidase conjugated to cholera toxin. J Comp Neurol 1991, 306: 344–360.
40. Reul JM, de Kloet ER. Two receptor systems for corticosterone in rat brain: microdistribution and differential occupation. Endocrinology 1985, 117: 2505–2511.
41. Perlman WR, Webster MJ, Herman MM, Kleinman JE, Weickert CS. Age-related differences in glucocorticoid receptor mRNA levels in the human brain. Neurobiology of Aging 2007, 28: 447–458.

42. Trulson ME. Biological bases for the integration of appetitive and consummatory grooming behaviors in the cat: a review. Pharmacol Biochem Behav 1976, 4: 329–334.
43. Harris RB, Gu H, Mitchell TD, Endale L, Russo M, Ryan DH. Increased glucocorticoid response to a novel stress in rats that have been restrained. Physiol Behav 2004, 81: 557–568.
44. Zitnik GA, Clark BD, Waterhouse BD. Effects of intracerebroventricular corticotropin releasing factor on sensory-evoked responses in the rat visual thalamus. Brain Res 2014, 1561: 35–47.
45. Vagnoni E, Lourenco SF, Longo MR. Threat modulates perception of looming visual stimuli. Curr Biol 2012, 22: R826-827.
46. Yilmaz M, Meister M. Rapid innate defensive responses of mice to looming visual stimuli. Curr Biol 2013, 23: 2011–2015.
47. Cambiaghi M, Teneud L, Velikova S, Gonzalez-Rosa J J, Cursi M, Comi G, et al. Flash visual evoked potentials in mice can be modulated by transcranial direct current stimulation. Neuroscience 2011, 185: 161–165.
48. Hetzler Bruce E, McLester-Davis Lauren WY, Tenpas Sadie E. Methylphenidate and alcohol effects on flash-evoked potentials, body temperature, and behavior in Long-Evans rats. Alcohol 2019, 77: 79–89.
49. Knippenberg JM, Maes JH, Coenen AM, van Luijtelaar GL. Influence of emotional arousal on the N150 of the auditory evoked potential from the rat amygdala. Acta Neurobiol Exp (Wars) 2009, 69: 109–118.
50. Knippenberg JM, Maes JH, Coenen AM, van Luijtelaar G. Effect of appetitive pavlovian conditioning on the N150 of the amygdalar auditory evoked potential in the rat. Brain Res 2009, 1267: 57–64.
51. Bertini C, Pietrelli M, Braghittoni D, Ladavas E. Pulvinar lesions disrupt fear-related implicit visual processing in hemianopic patients. Front Psychol 2018, 9: 2329.

Neurosci. Bull. August, 2021, 37(8):1119–1134
https://doi.org/10.1007/s12264-021-00687-8

www.neurosci.cn
www.springer.com/12264

ORIGINAL ARTICLE

Single Exposure to Cocaine Impairs Reinforcement Learning by Potentiating the Activity of Neurons in the Direct Striatal Pathway in Mice

Zhijun Diao[1] · Yuanyuan Di[1] · Meilin Wu[1] · Chenyang Zhai[2] · Mengsi Kang[2] · Yongfeng Li[1] · Yingxun Liu[1] · Chunling Wei[1] · Qiaohua Zheng[1] · Jing Han[1] · Zhiqiang Liu[1] · Yingfang Tian[2] · Wei Ren[1]

Received: 12 November 2020 / Accepted: 22 January 2021 / Published online: 27 April 2021

Abstract Plasticity in the glutamatergic synapses on striatal medium spiny neurons (MSNs) is not only essential for behavioral adaptation but also extremely vulnerable to drugs of abuse. Modulation on these synapses by even a single exposure to an addictive drug may interfere with the plasticity required by behavioral learning and thus produce impairment. In the present work, we found that the negative reinforcement learning, escaping mild foot-shocks by correct nose-poking, was impaired by a single *in vivo* exposure to 20 mg/kg cocaine 24 h before the learning in mice. Either a single exposure to cocaine or reinforcement learning potentiates the glutamatergic synapses on MSNs expressing the striatal dopamine 1 (D1) receptor (D1-MSNs). However, 24 h after the cocaine exposure, the potentiation required for reinforcement learning was disrupted. Specific manipulation of the activity of striatal D1-MSNs in D1-cre mice demonstrated that activation of these MSNs impaired reinforcement learning in normal D1-cre mice, but inhibition of these neurons reversed the reinforcement learning impairment induced by cocaine. The results suggest that cocaine potentiates the activity of direct pathway neurons in the dorsomedial striatum and this potentiation might disrupt the potentiation produced during and required for reinforcement learning.

Keywords Cocaine · Reinforcement learning · Striatum · Medium spiny neurons · Long-term potentiation

Introduction

It is well acknowledged that chronic cocaine abuse is a devastating neuropsychiatric disorder causing a wide range of emotional and cognitive deficits [1–4]. In contrast, the prolonged deleterious effects of occasional or recreational use of cocaine is still in debate [5–7]. Recent studies found that recreational users are less able to inhibit overt manual and covert attentional responses, and show more switching costs and perseverative errors [8, 9]. It has also been found that a single injection or exposure of mice to cocaine affects excitatory synapses, although this dosage of cocaine is not sufficient to make mice addicted [10–12]. Such deficits also impair a series of adaptive behaviors, including reinforcement learning [13, 14], which relies on the proper functioning of the basal ganglia-thalamo-cortical loop [15, 16]. In addition, synapses in this loop are the primary targets of many addictive drugs, including cocaine [17–19]. However, the neuropathological changes in the basal ganglia circuits induced by acute cocaine exposure and the relationship between these changes and the impairment of reinforcement learning are still unclear.

Basal ganglia circuits are essential for action selection and the encoding of action-outcome relations. Lesions or disorders affecting different nodes of these circuits lead to a variety of deficits in action initiation and goal-directed movement [17–21]. These same circuits are able to

Supplementary Information The online version contains supplementary material available at https://doi.org/10.1007/s12264-021-00687-8.

✉ Yingfang Tian
yingfang_tian@snnu.edu.cn

✉ Wei Ren
renwei@snnu.edu.cn

[1] Key Laboratory of Modern Teaching Technology, Ministry of Education, Shaanxi Normal University, Xi'an 710062, China

[2] College of Life Sciences, Shaanxi Normal University, Xi'an 710119, China

undergo plastic changes, ranging from plasticity in synaptic strength and excitability to the remodeling of microcircuits, in response to environmental challenges [22, 23]. Therefore, the basal ganglia circuits are not only important for the initiation and performance of actions, but also necessary for reinforcement learning and behavior remodeling. It has been reported that the dorsomedial striatum (DMS) is heavily involved in reinforcement learning, while the dorsolateral striatum is closely associated with the execution of habituated behaviors [20, 24]. Two major pathways constitute the cortico-striatal-basal ganglia loops: the direct pathway, a monosynaptic gabaergic projection from medium-sized spiny neurons expressing dopamine 1 (D1) receptors (D1-MSNs) to the substantia nigra pars reticulata, and the indirect pathway, a polysynaptic projection from MSNs expressing dopamine 2 (D2) receptors (D2-MSNs) to the substantia nigra pars reticulata through the external globus pallidus and subthalamic nucleus [20]. Striatal D1-MSNs and D2-MSNs are differentially modulated by dopamine and work in an antagonistic manner to facilitate or suppress movement, respectively [20]. A large body of experimentation has demonstrated that long-term plastic changes of the excitatory synapses on striatal D1-MSNs facilitate movement, positive reinforcement, and reward, while long-term plastic changes of the excitatory synapses on striatal D2-MSNs mediate inhibition of motion, negative reinforcement, and punishment [13, 14, 16], showing the fundamental roles of striatal plasticity in behavioral adaptations, including reinforcement learning [16, 25].

Single administration of cocaine has been frequently used in animal experiments to study the acute effects of the drug on the plastic changes in neurotransmission in different brain regions [12, 26, 27]. It has been demonstrated that cocaine binds with the dopamine transporter and inhibits the re-uptake of dopamine into dopaminergic terminals, therefore increasing the extracellular dopamine concentration, which in turn results in the potentiation of dopaminergic neurotransmission and an exaggerated effect of dopamine on postsynaptic neurons. The persistent neuroadaptive effects left by such an acute action mediate the emotional and behavioral changes of single cocaine exposure [28, 29]. Previous studies have found that acute exposure to cocaine exerts significant effects on the glutamatergic transmission onto D1-MSNs and/or the D2-MSNs in the nucleus accumbens and the dopaminergic neurons in the ventral tegmental area [12, 30, 31].

A few studies also indicate that both the effects of acute cocaine and the completion of reinforcement learning rely on plastic changes in the glutamatergic transmission on striatal MSNs [21, 24, 32]. Therefore, the plastic changes induced by acute exposure to cocaine may disturb the formation of the neural plasticity required for reinforcement learning, causing impairments in the learning. Negative reinforcement learning is essential to animals for behavioral adaptation, it has been widely used as a standardized experimental behavioral paradigm, and substance dependence or even single injection of cocaine affects negative reinforcement learning (NRL) [33–35], but the mechanisms are still unclear. The present work aimed to study the effects of a single *in vivo* exposure to cocaine on NRL in mice. To reach this goal, the changes in the glutamatergic transmission on DMS D1-MSNs and D2-MSNs induced by cocaine, reinforcement learning, and reinforcement learning at 24 h after exposure to cocaine were recorded. Since both the exposure to cocaine and the experience of reinforcement learning facilitated striatal glutamatergic transmission on DMS D1-MSNs, the sufficiency and necessity of the facilitation induced by cocaine in the learning impairment was also investigated by manipulation of the activity of DMS D1-MSNs.

Materials and Methods

Animals

Male C57BL/6J mice between 7 to 8 weeks old (from the Model Animal Research Center of Nanjing University, China) were used to record the effects of cocaine on reinforcement learning and excitatory neurotransmission on striatal MSNs. In the chemogenetic activation or inhibition of D1-MSNs, heterozygotic male progeny of dopamine 1 receptor (D1R)-Cre (Drd1-Cre, 262, Gensat) mice (gifts from the laboratory of Professor. Fuqiang Xu) were used and produced by mating transgenic male mice with C57BL/6J females. Mice were housed in a pathogen-free facility maintained at a constant temperature and on a 12-h light/dark cycle (light on from 08:00 to 20:00). Water and food were available *ad libitum*. Intraperitoneal injection of 20 mg/kg cocaine (Qinghai Pharmaceutical Factory, China) or 0.9% saline was given to the mice 24 h before experiments. All procedures were approved by the Medicine Animal Care and Use Committee of Shaanxi Normal University and conformed to the Guide for the National Institutional Animal Care.

Behavioral Tests

Open Field Test (OFT)

Each mouse was gently placed in a corner of an illuminated (10 lux) square box ($50 \times 50 \times 35$ cm^3), facing the opaque walls. Its movements were automatically recorded for 10 min with a video camera above the box and analyzed with EthoVision software (Version 1.9, Noldus Information Technology, USA). The locomotor activity was evaluated

as the total distance travelled, and anxiety-like behavior was evaluated by measuring the time spent and total number of entries in the center area.

Negative Reinforcement Learning to Escape Foot-Shocks (NRL)

NRL was performed as described previously [36]. All learning experiments were conducted in operant chambers ($30 \times 24 \times 30$ cm^3; MED Associates, USA), which were positioned in sound-attenuating boxes, equipped with a ventilation fan, a house light, an observation window, and two nose-pokers located 2 cm above the metal grid floor. Briefly, a day before the reinforcement learning experiment, each mouse was placed in an operant chamber and allowed to explore the chamber freely for 100 min for adaption to the environment, during which no shock was delivered. On the day of reinforcement training, foot-shocks were delivered through the metal grid floor. A very mild intensity (0.15 mA) was used. One of the two nose-pokers was designated randomly as "active" and was illuminated by a light-emitting diode (LED, 20 lux) during the shock period and its activation triggered shock termination. Shock and the light began simultaneously and terminated whenever the learning mouse poked the active nose-poker, signaled by a 1.5-s tone (2.9 kHz, 65 dB) and turning off the LED; this was followed by a pseudorandom timeout period ranging from 30 s to 60 s. The learning procedure consisted of 50 trials, amounting to a total session duration of approximately 100 min. We defined one successful session as consisting of eight consecutive correct responses, similar to previous studies [37]. The trials continued until each mouse completed 50 trials. The total number of right or wrong (poking the inactive nose-poker) responses, and the escape latency were recorded.

Electrophysiological Recording

Brain Slice Preparation

Acute brain slices for analyzing synaptic function were prepared as previously described [38, 39]. Briefly, each mouse was anesthetized with isoflurane and decapitated. The brain was then rapidly removed and glued to a cutting stage immersed in artificial cerebrospinal fluid (ACSF) containing (in mmol/L): 125 NaCl, 2.5 KCl, 25 glucose, 25 $NaHCO_3$, 1.25 NaH_2PO_4, 2 $CaCl_2$, and 1 $MgCl_2$, gassed with 5% CO_2/95% O_2. Sagittal slices (300 μm) through the striatum were cut with a microslicer (VT 1200S, Leica, Germany) at an advance speed of 0.06 mm/s. The slices were then transferred to a holding chamber filled with oxygenated ACSF at 34 °C and allowed to recover for at least 0.5 h before use.

Electrophysiology

Individual slices were transferred to a recording chamber and continuously perfused with ACSF for the duration of the experiment. The DMS area in each slice was visually identified according to The Mouse Brain in Stereotaxic Coordinates (second edition). DMS MSNs were visualized under an upright microscope (DM LFSA, Leica, Germany). The recording pipettes had 3–8 MΩ resistance when filled with the RNase-free intracellular solution (in mmol/L): 140 $CsCH_3SO_3$, 10 HEPES, 2 QX-314, 2 $MgCl_2$, 0.2 EGTA, 4 MgATP, 0.3 Na_2GTP, 10 Na_2-phosphocreatine (pH 7.2–7.4 with CsOH). All experiments were carried out in the presence of 100 μmol/L picrotoxin (PTX, Sigma, USA). Series and input resistances were determined with each afferent stimulus and were monitored for stability throughout each experiment. Recordings were obtained using a Multiclamp 700B amplifier and a Digidata 1550 (Molecular Devices, USA). Data were filtered at 2 kHz and digitized at 10 kHz. After recording, D1-MSNs and D2-MSNs were identified by single-cell PCR as described in the methods for single-cell PCR. A patch pipette filled with RNase-free intracellular solution positioned close to the tissue in the recording chamber was used as the negative control.

For miniature excitatory postsynaptic current (mEPSC) recording, the cell membrane potential was clamped at −80 mV in the presence of 1 μmol/L TTX (Hebei Fishery Science and Technology Development Co., China).

For AMPAR/NMDAR (α-amino-3-hydroxy-5-methyl-4-isoxazolepropionic acid receptor/N-methyl-D-aspartate receptor) ratio calculation, a stainless-steel bipolar microelectrode was located on the white matter between the cortex and the DMS close to the recording electrode and stimulated at a baseline frequency of 0.1 Hz. The AMPAR- and NMDAR-mediated current ratio was recorded in the presence of 100 μmol/L PTX at a holding membrane potential of −80 mV and +40 mV, respectively. The AMPAR/NMDAR ratio was calculated as the ratio of the average peak EPSC amplitude at −80 mV to the average EPSC amplitude recorded at +40 mV (averaged at 50 ms after afferent stimulation). All EPSCs used for analysis were averaged from 10 consecutive traces.

Long-term potentiation (LTP) was induced in the DMS in the slices by using the following high-frequency stimulation (HFS) protocol: 4 trains of 100 Hz paired with postsynaptic depolarization at 0 mV. Data were excluded when the series resistance changed by >20%. In this experiment, $MgCl_2$ was omitted from the ACSF.

In the pharmacological modulation study, current-clamp recording was used to measure evoked action potentials in Clozapine N-oxide (CNO; BrainVTA, China) activation or inhibition experiments. After applying currents in 25-pA steps, ranging from –100 pA to 300 pA and 1000 ms in duration, neurons were allowed to recover for 5 min before the slices were perfused with ACSF containing 10 μmol/L CNO. The same current-clamp procedure was performed 15 min after CNO perfusion. All recording sessions were recorded and analyzed using Clampfit 10.5 software (Molecular Devices, USA).

Single-Cell PCR

Single-cell PCR was performed as previously reported with minor modification [40, 41]. Briefly, after recording, the solution containing an ejected cell was transferred into a PCR tube containing 3 μL of RNase-free water and 0.5 μL of 40 U/μL RNasin (Promega, USA).

Single-strand cDNA was synthesized in PCR tubes containing 2 μL mixed dNTPs (2.5 mmol/L each), 0.5 μL oligo(dT) primer (50 μmol/L), and 0.5 μL random primer (100 μmol/L) (all from Takara, Japan). The mixture was heated to 65 °C for 5 min and then cooled on ice for 1 min, then 2.5 μL 5× RT Buffer and 0.75 μL Maxima Reverse Transcriptase (200 U/μL; Thermo Scientific, USA) were added and held at 25 °C for 10 min; 50 °C for 30 min; and 85 °C for 5 min; then kept at 4 °C.

A multiplex single-cell nested-PCR was carried out for detection of dopamine receptors (*Drd1*, *Drd2*) and glutamic acid decarboxylase 67 (*GAD67*). Primers and amplicons are listed in Table 1. The first-round PCR was started after adding 2× PCR Master Mix, ddH_2O, and primer 1 (4 μmol/L each) to the RT product (final volume 20 μL). Forty cycles were performed (denaturation at 94 °C, 3 min; annealing at 59 °C, 1 min; extension at 72 °C, 1 min; final elongation at 72 °C, 10 min). An aliquot (2 μL) of the first-round PCR product was used as a template for the second-round PCR (35 cycles; annealing at 58 °C, 30 s; extension at 72 °C, 30 s). The PCR reaction mix profiles were the same as in the first-round except that primer 1 was substituted by primer 2. The second-round PCR products were identified by 2% agarose gel electrophoresis. All PCR reagents were from Takara (Japan).

Stereotaxic Surgery and Viral Injections

Surgery was performed under anesthesia using isoflurane (4% for induction and 1% for maintenance). Each animal was then mounted in a stereotaxic frame with non-puncturing ear bars (RWD Life Science Inc., China). The viruses AAV-hSyn-DIO-hM3Dq(Gq)-mCherry (5.63×10^{12} GC/mL, BrainVTA) or AAV-hSyn-DIO-hM4Di(Gi)-mCherry (4.72×10^{12} GC/mL, BrainVTA) or AAV-hSyn-DIO-mCherry (5.96×10^{12} GC/ml, BrainVTA) were bilaterally injected into the DMS through borosilicate glass pipettes connected to a 10-μL microsyringe (Gaoge, China) at the coordinates AP: 0.6 mm; ML: ± 1.5 mm; DV: 2.7 and 2.9 mm; AP: 1.0 mm; ML: ± 1.2 mm; DV: 2.6 and 2.8 mm. A total volume of 90 nL was injected at each desired depth at 30 nL per min, and the needle was held at the site for an additional 10 min. After surgery, mice were allowed to recover for 3 weeks before behavioral tests.

Statistical Analysis

All data were transferred to GraphPad Prism for analysis and graphing. Behavioral and electrophysiological data are presented as the mean ± standard error of the mean (SEM). Data were analyzed using a two-tailed unpaired *t* test,

Table 1 Oligonucleotide primers used for single-cell PCR.

Gene	GeneBank accession no.	Primer name	Primer sequence	Product length (bp)
Gad67	XM_011239023	Gad67-F1	TGTTCCTTTCCTGGTGAGTGC	296
		Gad67-R1	GGTAGGAAGCATGCATCTGGT	
		Gad67-F2	CTTGGCTGTAGCTGACATCTG	207
		Gad67-R2	TGCATCAGTCCCTCCTCTCTA	
Drd1	NM_010076	Drd1-F1	TCCGATAGTTGGGCTCATCG	372
		Drd1-R1	CTGTTGCAATACCCCCACCC	
		Drd1-F2	ATAGTTGGGCTCATCGCTGG	222
		Drd1-R2	ACCGGGAAGGGGTTCTTCTA	
Drd2	NM_010077	Drd2-F1	AACACACGCTACAGCTCCAA	325
		Drd2-R1	TCATGTCCTCAGGGTGGGTA	
		Drd2-F2	CCCACTGCTCTTTGGACTCA	152
		Drd2-R2	GCTTGCGGAGAACGATGTAG	

F, forward; R, reverse; 1, primers for first-round PCR; 2, primers for second-round PCR.

paired *t* test, or two-way or three-way repeated-measures ANOVA followed by Tukey's multiple comparisons test. A $P < 0.05$ was considered significant and all data used a confidence level of 95%.

Results

Single Exposure to Cocaine Impairs Reinforcement Learning in Mice

Two groups of mice were used in this behavioral experiment: one was subjected to the behavioral tests 24 h after a single exposure to 20 mg/kg cocaine (Cocaine+NRL) and the other was subjected to the tests 24 h after saline injection (Saline+NRL). Since repeated cocaine administration induces neural adaptation in the dopamine system and causes a progressive increase in locomotor activity [42, 43], before subjecting the animals to the reinforcement learning, the effects of cocaine on the locomotor activity was first evaluated in the OFT (Fig. 1A). The total distance moved in the Cocaine+NRL group did not differ from that in the Saline+NRL group (Fig. 1C, $t_{18} = 1.636$, $P = 0.1192$), suggesting that the cocaine exposure did not produce behavioral sensitization 24 h after administration. Then, 30 min after the OFT, the two groups were subjected to reinforcement training (Fig. 1A, B). The escape latency for the 50 training trials in the Cocaine+NRL group was significantly longer than that in the Saline+NRL group, resulting in a significant difference between the learning curves of the two groups (Fig. 1D, interaction $F_{49,\ 900} = 2.638$, $P < 0.0001$; Trials $F_{49,\ 900} = 7.390$, $P < 0.0001$; Treatment $F_{1,\ 900} = 445.7$, $P < 0.0001$). Consistently, both the mean escape latency (Fig. 1E, $t_{18} = 8.109$, $P < 0.0001$) and the total number of mistakes (Fig. 1F, $t_{18} = 2.989$, $P = 0.0079$) in the Cocaine+NRL group were larger than those in the Saline+NRL group. With the success of learning defined as the completion of eight consecutive correct responses [37], the time to reach the first successful learning session by the Cocaine+NRL group was also longer than that by the Saline+NRL group (Fig. 1G, $t_{18} = 6.437$, $P < 0.0001$). To exclude other possible cocaine-induced deficits in reinforcement learning, the effects on anxiety-like behaviors and pain sensitivity were evaluated. To assess anxiety-like behaviors, the time spent in the center zone and total number of entries in the OFT were analyzed first, and there were no significant differences in the Cocaine group before and 24 h after the single injection (Fig. S1A, B, Time in the center zone (Fig. S1A): interaction $F_{1,\ 36} = 0.0283$, $P = 0.8675$; Treatment $F_{1,\ 36} = 0.3395$, $P = 0.5637$; Pre & Post $F_{1,\ 36} = 0.1271$, $P = 0.7235$; Total number of entries (Fig. S1B): interaction $F_{1,\ 36} = 0.2639$, $P = 0.6106$; Treatment $F_{1,\ 36} = 0.9214$, $P = 0.3435$; Pre & Post $F_{1,\ 36} = 0.1757$, $P = 0.6776$). In addition, in the elevated plus maze test, there were no significant differences between two groups in the time spent in the open arms (Fig. S1C, interaction $F_{1,\ 36} = 0.7687$, $P = 0.3864$; Treatment $F_{1,\ 36} = 0.1199$, $P = 0.7312$; Pre & Post $F_{1,\ 36} = 0.1125$, $P = 0.7392$) and the percentage of entries before and 24 h after the single injection (Fig. S1D, interaction $F_{1,\ 36} = 3.124$, $P = 0.0856$; Treatment $F_{1,\ 36} = 0.0143$, $P = 0.9054$; Pre & Post $F_{1,\ 36} = 0.2800$, $P = 0.6000$). To test if the cocaine-treated animals were less sensitive to the electric shock, which might lead to the prolonged escape latency, we compared the sensitivity to thermal and mechanical stimuli before and 24 h after the single injection of cocaine; the results showed that the responses to thermal and mechanical stimuli did not differ between the groups (Figs. S2A–B, Thermal withdrawal latency (Fig. S2A): interaction $F_{1,\ 36} = 0.2108$, $P = 0.6489$; Treatment $F_{1,\ 36} = 0.0030$, $P = 0.9566$; Pre & Post $F_{1,\ 36} = 1.244$, $P = 0.2721$; Mechanical withdrawal threshold (Fig. S2B): interaction $F_{1,\ 36} = 0.5991$, $P = 0.4440$; Treatment $F_{1,\ 36} = 2.317$, $P = 0.1367$; Pre & Post $F_{1,\ 36} = 3.226$, $P = 0.0809$). Based on the above results, effects of anxiety-like behaviors and pain sensitivity on the Cocaine group could be excluded. During the habituation period, there was no significant difference between the total number of spontaneous nose-pokes on the active and inactive nose-pokers in the Saline+NRL and Cocaine+NRL groups, showing no preference for either of the nose-pokers (Fig. 1H, interaction $F_{1,\ 36} = 0.0002$, $P > 0.9999$; Nosepoke $F_{1,\ 36} = 0.1086$, $P = 0.7436$; Treatment $F_{1,\ 36} = 0.8473$, $P = 0.3634$). In contrast, the total numbers on the active nose-pokers in the two groups were significantly larger than those on the inactive nose-pokers, showing the preference for the active nose-poker induced by the mild aversive foot-shocks. In addition, the total number of active nose-pokes in the Cocaine+NRL group was significantly lower than that in the Saline+NRL group, indicating that the Cocaine+NRL group had fewer correct responses than the Saline+NRL group (Fig. 1I, interaction $F_{1,\ 36} = 11.42$, $P = 0.0018$; Nose-poke $F_{1,\ 36} = 111.0$, $P < 0.0001$; Treatment $F_{1,\ 36} = 18.99$, $P = 0.0001$; followed by Tukey's *post hoc* test: Saline+NRL *vs* Cocaine+NRL, active nose-pokes $P < 0.0001$). The above results clearly showed that the reinforcement learning was markedly impaired by a single dose of cocaine administered 24 h before the learning. The possible mechanism underlying the impairment was then studied by using electrophysiological recordings in brain slices 30 min after the learning (Fig. 1A).

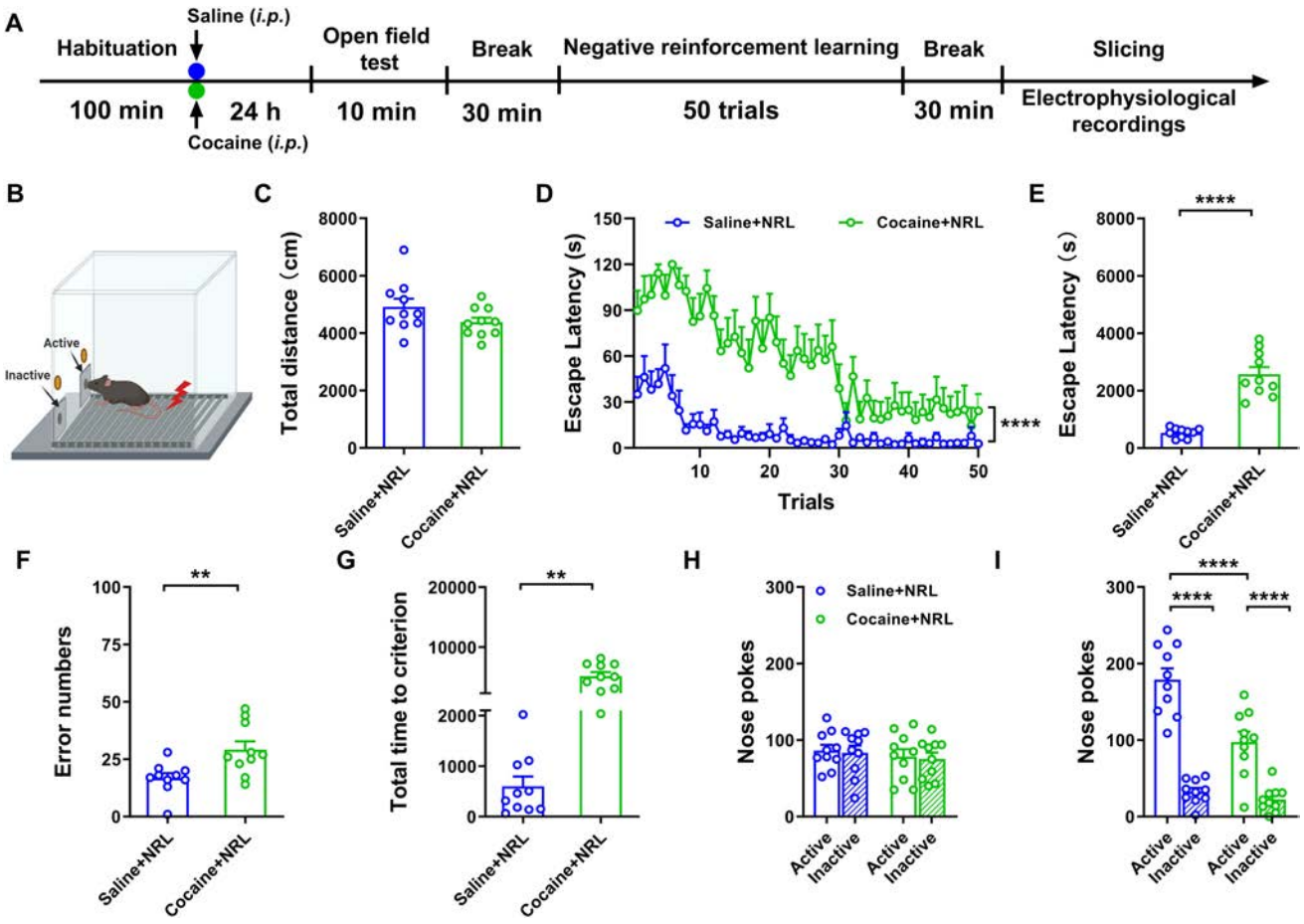

Fig. 1 Single cocaine injection-induced impairment in reinforcement learning in mice. **A** Experimental schedule for cocaine administration and behavioral tests. **B** The operant chamber. **C** Open field test (OFT): there is no difference in total distance between the Saline+NRL and Cocaine+NRL groups. **D** During the 50 trials of reinforcement learning, the escape latency curve is significantly increased by a single dose of cocaine administered 24 h before the learning. **E**–**G** Mean escape latency (**E**), total numbers of errors (**F**), and total time to criterion (**G**) are significantly greater in the Cocaine+NRL group than in the Saline+NRL group. **H** There is no preference between the active and the inactive nose-pokers in the Saline+NRL and Cocaine+NRL groups during the habituation period. **I** The number of active nose-pokes are significantly larger than that of the inactive nose-poker in both groups, while the number of active nose-pokes is larger in the Saline+NRL group than in the Cocaine+NRL group during the learning period (Saline+NRL, n = 10 mice; Cocaine+NRL, n = 10 mice). Data represent the mean ± SEM (*P <0.05, **P <0.01, ***P < 0.001; two-tailed unpaired t test in **C**, **E**, **F**, **G** and two-way RM ANOVA in **D**, **H** and **I**).

Single Exposure to Cocaine Enhances Striatal Glutamatergic Transmission and Prevents the Plastic Changes Produced by Reinforcement Learning

The basal glutamatergic transmission on DMS D1-MSNs and D2-MSNs in the DMS slices was evaluated by whole-cell voltage clamp recording of mEPSCs in the following groups: Saline, Cocaine, Saline+NRL, and Cocaine+NRL. In addition to the Saline+NRL and Cocaine+NRL groups used in the behavioral tests described above, slices were also prepared from the Saline and the 20 mg/kg Cocaine groups, prepared in the same way as the NRL groups before slicing but without NRL. D1-MSNs and D2-MNSs were identified *post hoc* by single-cell PCR using cytoplasm collected immediately after recording (Fig. 2A, D, and G).

The frequency of mEPSCs in the Saline+NRL group was significantly greater than that in the Saline and the Cocaine groups (Fig. 2B, interaction $F_{1,\ 82}$ = 7.347, P = 0.0082; NRL $F_{1,\ 82}$ = 14.48, P = 0.0003; Treatment $F_{1,\ 82}$ = 9.263, P = 0.0031 in D1-MSNs: followed by Tukey's *post hoc* test, P = 0.00004 *vs* Saline; P = 0.000008 *vs* Cocaine), showing that the experience of reinforcement learning enhanced the excitatory transmission on D1-MSNs by increasing the presynaptic release of glutamate. There was no significant difference between the frequency of mEPSCs in the Cocaine group and that in the Saline group (P = 0.9952), suggesting that the presynaptic release of glutamate was not enhanced by exposure to cocaine.

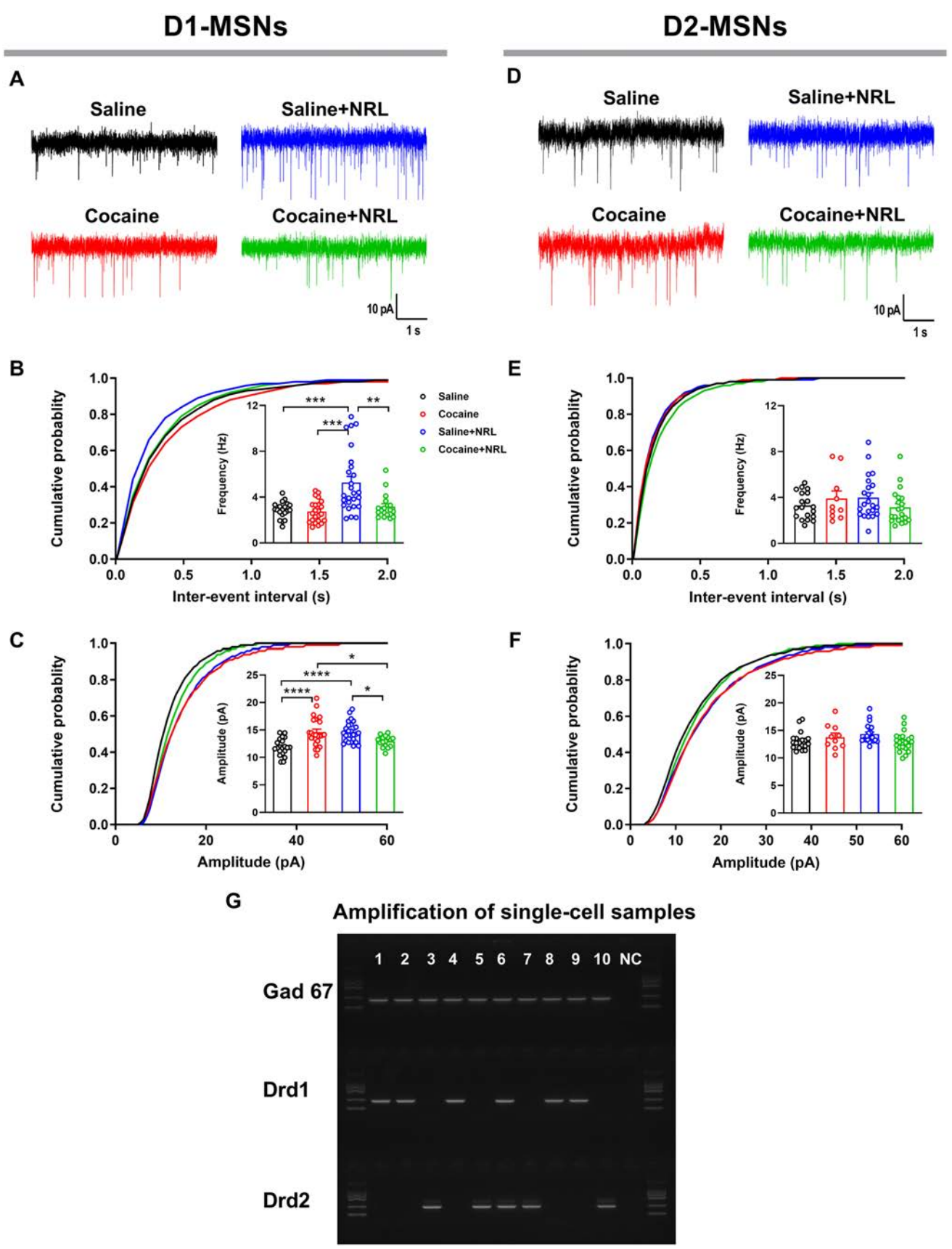
D1-MSNs
D2-MSNs
A
Saline
Saline+NRL
Cocaine
Cocaine+NRL
10 pA
1 s
D
Saline
Saline+NRL
Cocaine
Cocaine+NRL
10 pA
1 s
B
Cumulative probablity
Inter-event interval (s)
Frequency (Hz)
Saline
Cocaine
Saline+NRL
Cocaine+NRL
E
Cumulative probablity
Inter-event interval (s)
Frequency (Hz)
C
Cumulative probablity
Amplitude (pA)
Amplitude (pA)
F
Cumulative probablity
Amplitude (pA)
Amplitude (pA)
G
Amplification of single-cell samples
1 2 3 4 5 6 7 8 9 10 NC
Gad 67
Drd1
Drd2

◀**Fig. 2** Single exposure to cocaine inhibits the potentiation of glutamatergic transmission on D1-MSNs produced during reinforcement learning. **A, D** Representative recordings of mEPSCs from D1-MSNs (**A**) and D2-MSNs (**D**) in the groups with saline, cocaine, reinforcement learning after saline (Saline+NRL), and reinforcement learning after cocaine (Cocaine+NRL). **B, E** Summary data for mEPSC frequency with cumulative probability plots of inter-event intervals in D1-MSNs (**B**) and D2-MSNs (**E**). **C, F** Summary of mEPSC amplitude with cumulative probability plots in D1-MSNs (**C**) and D2-MSNs (**F**). **G** Representative image of the agarose gel electrophoresis of single-cell PCR with nested primers applied to single GABAergic MSNs with Dopamine type 1 receptor (*Drd1*) and Dopamine type 2 receptor (*Drd2*) (NC: Negative control). Double-expressing cells in single-cell PCR were not counted. D1-MSNs: Saline, $n = 20$ cells from 10 mice; Cocaine, $n = 23$ cells from 10 mice; Saline+NRL, $n = 26$ cells from 10 mice; Cocaine+NRL, $n = 17$ cells from 10 mice. D2-MSNs: Saline, $n = 19$ cells from 11 mice; Cocaine, $n = 10$ cells from 6 mice; Saline+NRL, $n = 22$ cells from 10 mice; Cocaine+NRL, $n = 21$ cells from 10 mice. $^{*}P < 0.05$, $^{**}P < 0.01$, $^{***}P < 0.001$, two-way RM ANOVA.

Surprisingly, the increase in the frequency of mEPSCs in D1-MSNs in the Saline+NRL group was absent from the Cocaine+NRL group ($P = 0.0007$), suggesting that exposure to cocaine prevented the increase of the presynaptic release of glutamate produced during reinforcement learning.

The average mEPSC amplitude in the Saline+NRL group was significantly larger than that in the Saline and Cocaine+NRL groups (Fig. 2C, interaction $F_{1, 82} = 27.87$, $P < 0.0001$, NRL $F_{1, 82} = 1.627$, $P = 0.2057$, Treatment $F_{1, 82} = 1.629$, $P = 0.2054$; followed by Tukey's *post hoc* test, *vs* Saline, $P < 0.0001$; *vs* Cocaine+NRL, $P = 0.0315$), showing that reinforcement learning enhanced the excitatory transmission on D1-MSNs by increasing the amplitude of the postsynaptic current. The average mEPSC amplitude in the Cocaine group was also larger than that in the Saline ($P < 0.0001$) and Cocaine+NRL groups ($p = 0.0377$) (Fig. 2C), indicating that exposure to cocaine also enhanced the excitatory transmission on D1-MSNs by increasing the postsynaptic current. There was no significant difference between the average mEPSC amplitude in the Cocaine+NRL group and that in the Saline group (Fig. 2C, $P = 0.3358$), showing that the enhancement of postsynaptic current induced by reinforcement learning was also prevented by administration of cocaine 24 h before learning.

The above results showed that a single exposure to cocaine enhanced the postsynaptic current of glutamatergic synapses on DMS D1-MSNs and this enhancement may prevent the formation of the increase in both the presynaptic glutamate release and the postsynaptic current that were produced during reinforcement learning (Fig. 1).

On the other hand, no significant differences were found among the values of frequency and average amplitude of mEPSCs in D2-MSNs among the Saline, Saline+NRL, Cocaine, and the Cocaine+NRL groups, which suggests that the excitatory transmission on D2-MSNs might not be involved in the impairment of reinforcement learning induced by exposure to cocaine (Fig. 2E, F; Frequency: interaction $F_{1, 68} = 3.249$, $P = 0.0759$; NRL $F_{1, 68} = 0.0091$, $P = 0.9245$; Treatment $F_{1, 68} = 0.0893$, $P = 0.7660$; Amplitude: interaction $F_{1, 68} = 5.487$, $P = 0.0221$; NRL $F_{1, 68} = 0.2401$, $P = 0.6257$; Treatment $F_{1, 68} = 0.5894$, $P = 0.4453$).

To further confirm the above changes in the average amplitude of mEPSCs, the ratio of the amplitudes of evoked AMPAR- and NMDAR-EPSCs (A/N ratio) in D1-MSNs and D2-MSNs was recorded in DMS slices (Fig. 3A, C). In D1-MSNs, the A/N ratio in the Saline+NRL group was significantly larger than those in the Saline and the Cocaine+NRL groups (Fig. 3B; interaction $F_{1, 70} = 32.90$, $P < 0.0001$; NRL $F_{1, 70} = 0.2215$, $P = 0.6393$; Treatment $F_{1, 70} = 2.177$, $P = 0.1446$, followed by Tukey's *post hoc* test: *vs* Saline, $P = 0.0039$; *vs* Cocaine+NRL, $P < 0.0001$), further suggesting that reinforcement learning enhanced the excitatory transmission on D1-MSNs by increasing the AMPAR-mediated postsynaptic current. The A/N ratio in D1-MSNs in the Cocaine group was also significantly larger than those in the Saline and the Cocaine+NRL groups (Fig. 3B; *vs* Saline, $P = 0.0345$; *vs* Cocaine+NRL, $P < 0.0001$), confirming that exposure to cocaine also enhanced the excitatory transmission on D1-MSNs by increasing the AMPAR-mediated postsynaptic current. There was no significant difference between the A/N ratio in D1-MSNs in the Cocaine+NRL group and that in the Saline group (Fig. 3B; $P = 0.5528$).

Consistent with the findings for the average amplitude of mEPSCs, in D2-MSNs, there were also no significant differences in the A/N ratio of the postsynaptic current among the Saline, Cocaine, Saline+NRL, and Cocaine+NRL groups (Fig. 3D; interaction $F_{1, 68} = 3.701$, $P = 0.0586$; NRL $F_{1, 68} = 4.135$, $P = 0.0459$; Treatment $F_{1, 68} = 0.6395$, $P = 0.4267$), suggesting that the excitatory transmission on D2-MSNs might not play a key role in the impairment of reinforcement learning after exposure to cocaine.

Alterations of synaptic AMPAR and NMDAR subunits on the postsynaptic membrane contribute to the expression of long-term changes in synaptic strength, as in LTP and LTD [28]. To further explore whether the history of synaptic activation caused by single-dose cocaine interferes with the induction of potentiation by NRL, we examined HFS LTP induction in D1-MSNs *in vitro* after single-dose cocaine exposure. We found that the HFS protocol (4 trains of 100 Hz given at 10-s intervals paired with depolarization of the neuron to 0 mV) failed to elicit LTP in D1-MSNs approximately 24 h after cocaine

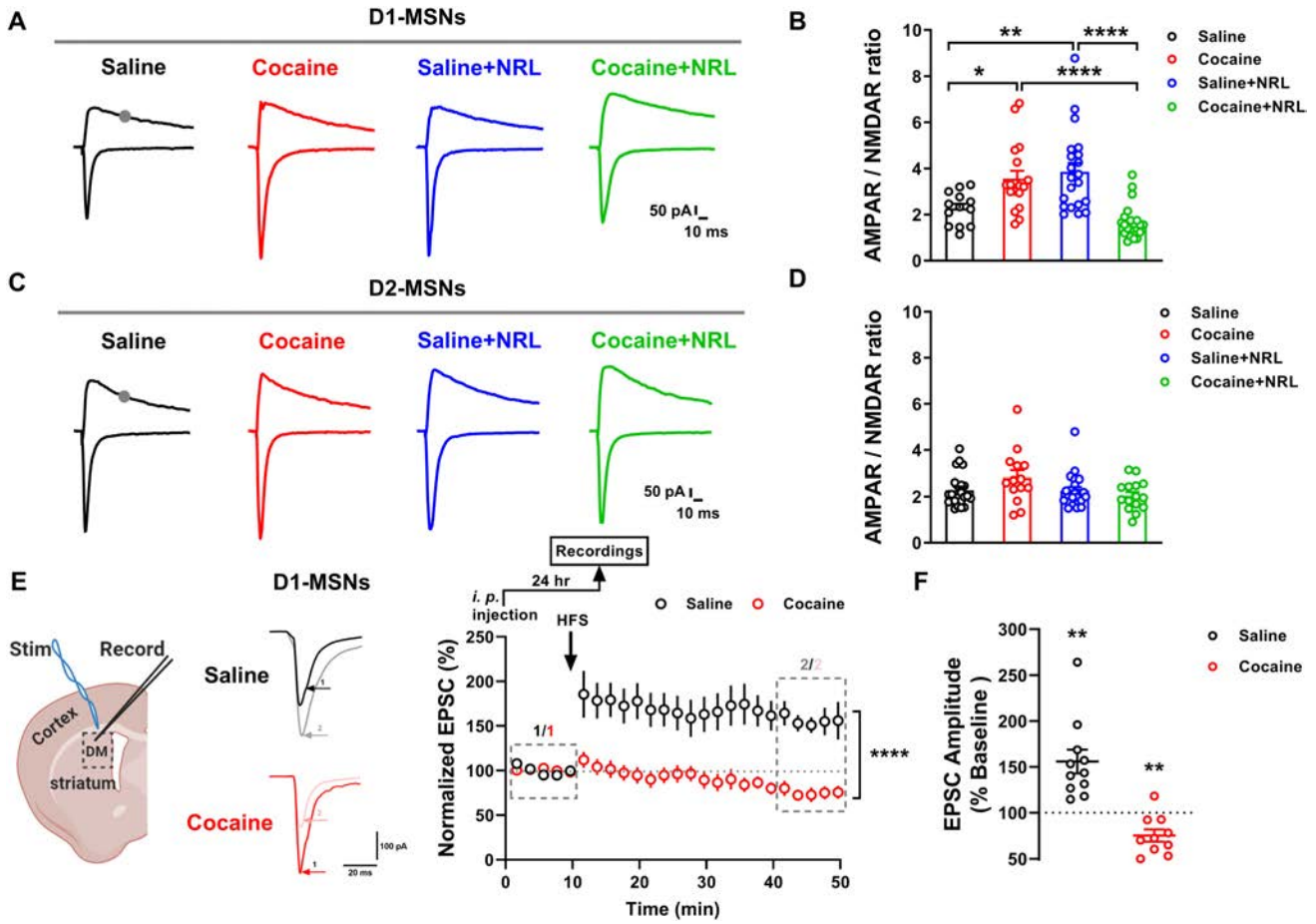

Fig. 3 Single exposure to cocaine enhances the AMPAR- and NMDAR-EPSCs ratio, resulting in disruption of HFS-induced LTP in D1-MSNs, then inhibits the potentiation of the ratio by reinforcement learning. **A, C** Representative traces of NMDAR EPSCs at +40 mV (upper traces) and AMPAR EPSCs at –80 mV (lower traces) in D1-MSNs **(A)** and D2-MSNs **(C)** from the Saline, Cocaine, Saline+NRL, and Cocaine+NRL groups. **B**, **D** Statistics of the ratio of AMPAR to NMDAR EPSCs in D1-MSNs (**B**) and D2-MSNs, (**D**) corresponding to **A** and **C**, respectively (D1-MSNs: Saline, $n = 13$ cells from 7 mice; Cocaine, $n = 18$ cells from 7 mice; Saline+NRL, $n = 21$ cells from 9 mice; Cocaine+NRL, $n = 22$ cells from 9 mice. D2-MSNs: Saline, $n = 22$ cells from 8 mice; Cocaine, $n = 14$ cells from 7 mice; Saline+NRL, $n = 21$ cells from 10 mice; Cocaine+NRL, $n = 15$ cells from 9 mice). **E** HFS induces LTP in DMS D1-MSNs in single-dose saline- or cocaine-treated mice. Left: schematic of a striatal slice with the stimulating electrode (Stim) and recording electrode (Record) in the dorsomedial subregion (DMS); right: dark traces represent the baseline EPSC average from 0 to 10 min (labeled "1"), and light traces represent the average EPSC from the last 10 min after LTP induction (labeled "2"). **F** Summary of the magnitude of HFS-LTP induction in the Saline and Cocaine groups (comparison between baseline and the last 10 min of recording). (D1-MSNs, Saline, $n = 11$ cells from 5 mice; Cocaine, $n = 10$ cells from 5 mice; $^{*}P < 0.05$, $^{**}P < 0.01$, $^{***}P < 0.001$, two-way RM ANOVA for **B**, **D**, **E**, paired t test for **F**).

exposure; instead, this protocol tended to produce LTD (Fig. 3E–F, eEPSC amplitude in the last 10 min relative to baseline, Saline: 155.9 ± 4.20%, $t_{10} = 4.337$, $P = 0.0015$; Cocaine: 75.25 ± 2. 32%, $t_9 = 3.725$, $P = 0.0047$; Saline *vs* Cocaine 40–50 min $t_{19} = 5.375$, $P < 0.0001$). The results showed that exposure to cocaine enhanced the excitatory transmission in DMS D1-MSNs and thereby prevented further synaptic potentiation in the same population. In addition, this potentiated state elicited by cocaine may leave an enduring trace that affects the subsequent induction of plasticity, such as the response to the HFS protocol or activity-dependent paradigms (NRL as in Fig. 1). If cocaine-evoked potentiation is causally involved in the impairment of NRL behavior, then potentiating these synapses may artificially simulate the role of cocaine in the learning behavior deficits, while de-potentiating these synapses may reverse the behavioral change.

Activation of D1-MSNs is Sufficient for the Impairment of Reinforcement Learning

The results presented above strongly suggest that a single exposure to cocaine enhances the excitatory transmission on DMS D1-MSNs and impairs reinforcement learning in mice. As both LTP and LTD are depolarization-dependent, which might arise from alterations in the activity of

postsynaptic neurons, both synaptic transmission and the postsynaptic neuronal activity jointly contribute to the activity level changes of the striatal direct pathway. To comprehensively assess the role of activity in neurons of the direct striatal pathway (D1-MSNs) in the impairment of NRL by cocaine, we used the designer receptors exclusively activated by designer drugs (DREADD) approach (Fig. 4A). We first tested whether the activation of D1-MSNs, mimicking the effects of cocaine, produces an impairment of reinforcement learning similar to that induced by cocaine. AAV viral vectors expressing the Gq-coupled human M3 muscarinic receptor (hM3Dq) or AAV-hSyn-DIO-mCherry were injected bilaterally into the DMS in D1-Cre mice [44, 45], targeting the D1-MSNs (Fig. 4B). Three weeks after virus injection, the spiking response to current stimulation in the hM3Dq-expressing D1-MSNs was significantly increased in brain slices by bath application of CNO (10 μmol/L), while that in the control mCherry-expressing D1-MSNs was unaffected (Fig. 4C). The rheobase of spike generation in the hM3Dq-expressing D1-MSNs was reduced by CNO (Fig. 4D; t_9 = 7.584, P <0.0001), while that in the

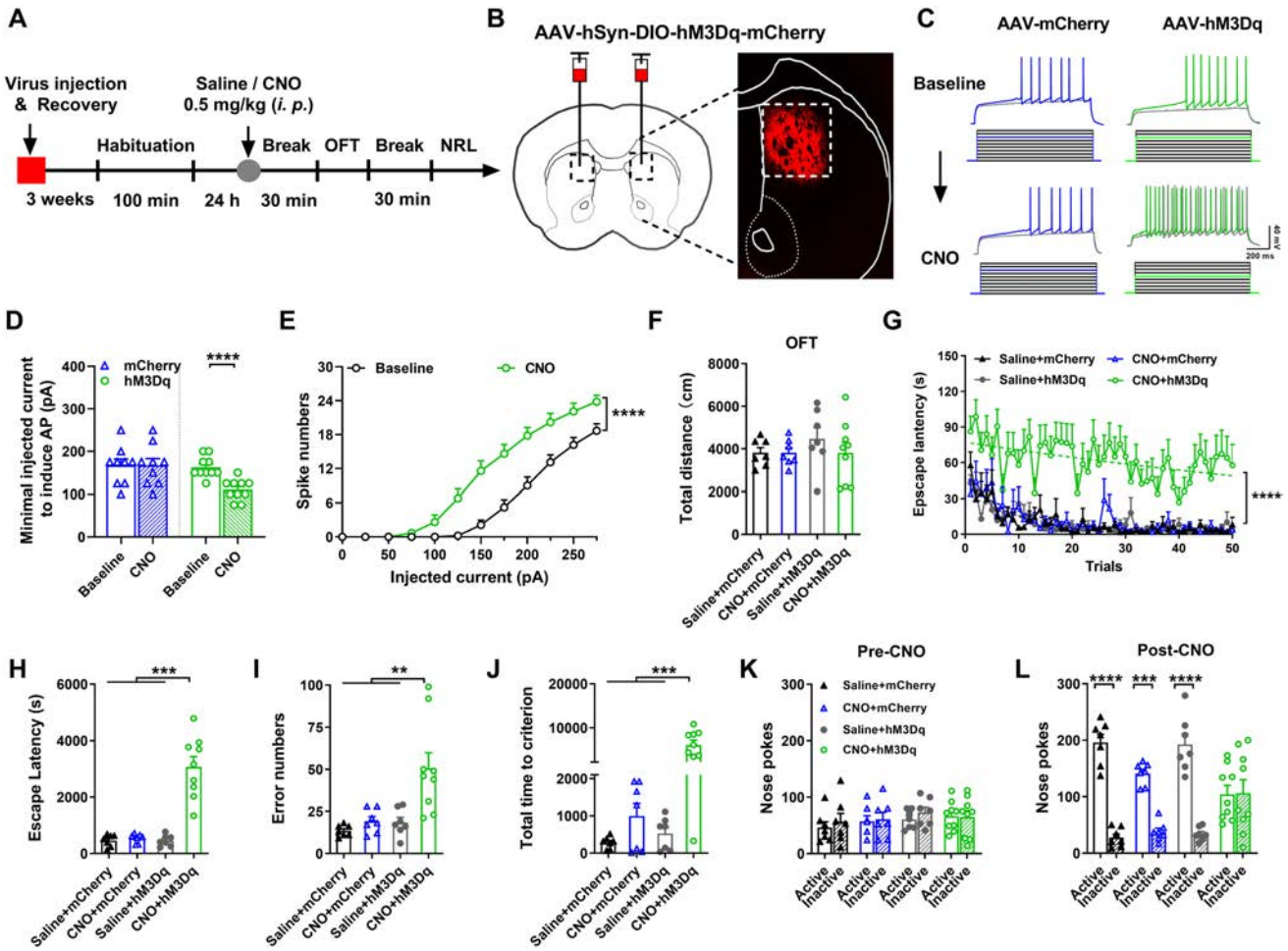

Fig. 4 Activating D1-MSNs with DREADD-hM3Dq impairs reinforcement learning in D1-Cre mice. **A** Experimental paradigm. **B** Injection site of AAV-DIO-hM3Dq-mCherry virus in the DMS. **C** Current-voltage relationship of representative D1-MSNs recorded before and after 10 μmol/L CNO perfusion. **D** The minimal injected current to induce action potentials (Aps) is decreased by CNO. **E** Number of Aps induced at different current steps (mCherry, n = 9 cells from 3 mice; hM3Dq, n = 10 cells from 3 mice). **F** Open field test: there is no difference in total distance traveled among the groups. **G** Escape latency is significantly increased in mice expressing hM3Dq after injection of CNO. **H**–**J** Mean escape latency (**H**), error numbers (**I**), and total time to the first successful session (**J**) in hM3Dq-expressing mice with CNO are significantly larger than those in the other three groups. **K** There is no preference between the active and inactive nose-poker in the mCherry and hM3Dq groups without saline or CNO during the habituation period of 100 min. **L** The number of active nose-pokes is significantly greater than that of inactive nose-pokes in the mCherry-expressing group and hM3Dq-expressing mice treated with saline, but the number of active nose-pokes in the hM3Dq-expressing group treated with CNO did not differ from that of inactive nose-pokes (Saline-mCherry, CNO-mCherry, Saline-hM3Dq n = 7 mice; CNO-hM3Dq n = 9 mice). Data represent the mean ± SEM (*P <0.05; **P <0.01; ***P <0.001, paired t test for **D**, two-way RM ANOVA for **E**, **F**, **H**, **I**, and **J**, and three-way RM ANOVA for **G**, **K**, and **L**.

mCherry-expressing D1-MSNs was unaffected ($t_8 = 0.000$, $P > 0.9999$). The excitability of the hM3Dq-expressing D1-MSNs was significantly enhanced by CNO, showing that the application of CNO activated the hM3Dq-expressing D1-MSNs, compared to the pre-CNO baseline (Fig. 4E; $F_{1,\ 216} = 110.4$, $P < 0.0001$).

Then, *in vivo* injection of CNO into mice expressing hM3Dq or mCherry was used to assess the effects of D1-MSN activation on reinforcement learning. In the OFT carried out 30 min after CNO injection (0.5 mg/kg) [46], there was no significant difference in the total distance traveled by mice expressing hM3Dq or mCherry with or without CNO (Fig. 4F; interaction $F_{1,\ 26} = 0.6300$, $P = 0.4345$; Treatment $F_{1,\ 26} = 0.6295$, $P = 0.4347$; Groups $F_{1,\ 26} = 0.6109$, $P = 0.4415$). Interestingly, during the 50 training trials, the escape latency in the hM3Dq-expressing mice with CNO was significantly longer than in those expressing Cherry or hM3Dq with saline, resulting in marked differences among the four learning curves (Fig. 4G; Trials × Treatment × Groups $F_{49,\ 1274} = 0.7306$, $P = 0.9175$; Treatment × Groups $F_{1,\ 26} = 31.07$, $P < 0.0001$; Treatment $F_{1,\ 26} = 30.68$, $P < 0.0001$; Groups $F_{1,\ 26} = 35.30$, $P < 0.0001$). In addition, in the hM3Dq-expressing mice, the mean escape latency (Fig. 4H; interaction $F_{1,\ 26} = 30.87$, $P < 0.0001$; Treatment $F_{1,\ 26} = 34.92$, $P < 0.0001$; Groups $F_{1,\ 26} = 30.66$, $P < 0.0001$), the total error numbers (Fig. 4I; interaction $F_{1,\ 26} = 4.872$, $P = 0.0363$; Treatment $F_{1,\ 26} = 10.00$, $P = 0.0040$; Groups $F_{1,\ 26} = 9.259$, $P = 0.0053$), and the time to the first successful session (Fig; 4J, interaction $F_{1,\ 26} = 11.68$, $P = 0.0021$; Treatment $F_{1,\ 26} = 19.63$, $P = 0.0002$; Groups $F_{1,\ 26} = 14.15$, $P = 0.0009$) were all significantly larger than those in those expressing Cherry or hM3Dq with saline. During the habituation period, no mice showed a preference for either the active or the inactive nose-poker (Fig. 4K; Nosepoke × Treatment × Groups $F_{1,\ 26} = 0.0786$, $P = 0.7815$; Nosepoke × Treatment $F_{1,\ 26} = 0.0210$, $P = 0.8859$; Nosepoke × Groups $F_{1,\ 26} = 0.7586$, $P = 0.3917$). However, during reinforcement learning, the number of active nose-pokes was still significantly higher than that of inactive nose-pokes in the mice expressing mCherry or hM3Dq with saline (Fig. 4L**,** Nosepoke × Treatment × Groups $F_{1,\ 26} = 12.53$, $P = 0.0015$; Nosepoke × Treatment $F_{1,\ 26} = 70.76$, $P < 0.0001$; Nosepoke × Groups $F_{1,\ 26} = 18.26$, $P = 0.0002$; followed by Tukey's *post-hoc* test, mCherry with Saline $P < 0.0001$, with CNO $P < 0.0001$; hM3Dq with Saline $P < 0.0001$), but exhibited no difference in the hM3Dq-expressing mice treated with CNO ($P > 0.9999$). These results indicate that selective activation of D1-MSNs in the DMS impairs reinforcement learning, similar to the effects of a single exposure to cocaine (Fig. 1).

Inhibiting D1-MSNs Reverses the Impairment of Reinforcement Learning Induced by Cocaine

In order to verify the necessity of the enhancement of D1-MSN activation in the impairment of reinforcement learning induced by exposure to cocaine, AAV viral vectors expressing the Gi/o-coupled human M4 muscarinic receptor (hM4Di) or AAV-hSyn-DIO-mCherry was bilaterally injected into the DMS [44, 45] in D1-Cre mice (Fig. 5A, B). Three weeks after the virus injection, the spiking response to current injection in D1-MSNs expressing hM4Di in brain slices was inhibited by bath application of CNO (10 μmol/L), while that in mCherry-expressing D1-MSNs was unaffected (Fig. 5C). The rheobase of spike generation in the hM4Di-expressing D1-MSNs was significantly increased by CNO (Fig. 5D, $t_9 = 4.707$, $P = 0.0011$), while that in the mCherry-expressing D1-MSNs was unaffected ($t_7 = 1.000$, $P = 0.3506$). The excitability of D1-MSNs expressing hM4Di was significantly reduced by CNO (Fig. 5E, F1, 216 = 10.00, $P = 0.0018$), showing that application of CNO inhibits the activity of hM4Di-expressing neurons.

We next investigated the effects of D1-MSN suppression on cocaine-induced reinforcement learning impairment through *in vivo* injection of CNO into mice expressing hM4Di or mCherry. Twenty-four hours after cocaine exposure and 30 mins after CNO injection, the total distance moved by the mice in the CNO+hM4Di group in the OFT was significantly shorter than that by the mice in the other three groups (Fig. 5F, interaction $F_{1,\ 26} = 14.78$, $P = 0.0007$; Treatment $F_{1,\ 26} = 12.23$, $P = 0.0017$; Groups $F_{1,\ 26} = 11.53$, $P = 0.0022$). This suggests that inhibition of D1-MSNs by CNO at 0.5 mg/kg significantly reduces the locomotor activity of hM4Di-expressing mice. In reinforcement training following the OFT, as shown in Fig 5G, the escape latency in all 50 training trials in the hM4Di-expressing mice treated with CNO was significantly shorter than that of the other three groups. This resulted in marked differences among the four learning curves (Trials × Treatment × Groups $F_{49,\ 1274} = 0.7471$, $P = 0.9013$; Treatment × Groups $F_{1,\ 26} = 11.59$, $P = 0.0022$; Treatment $F_{1,\ 26} = 5.304$, $P = 0.0295$; Groups $F_{1,\ 26} = 4.918$, $P = 0.0355$). Furthermore, in the hM4Di-expressing mice with CNO, the mean escape latency (Fig. 5H; interaction $F_{1,\ 26} = 7.374$, $P = 0.0116$; Treatment $F_{1,\ 26} = 6.380$, $P = 0.0180$; Groups $F_{1,\ 26} = 2.610$, $P = 0.1183$), the total error numbers (Fig. 5I; interaction $F_{1,\ 26} = 4.571$, $P = 0.0421$; Treatment $F_{1,\ 26} = 2.972$, $P = 0.0966$; Groups $F_{1,\ 26} = 9.770$, $P = 0.0043$), and the time to the first successful session (Fig. 5J; interaction $F_{1,\ 26} = 6.486$, $P = 0.0171$; Treatment $F_{1,\ 26} = 4.844$, $P = 0.0368$; Groups $F_{1,\ 26} = 3.292$, $P = 0.0812$) were all significantly lower than those in the mice expressing mCherry with saline or CNO, and

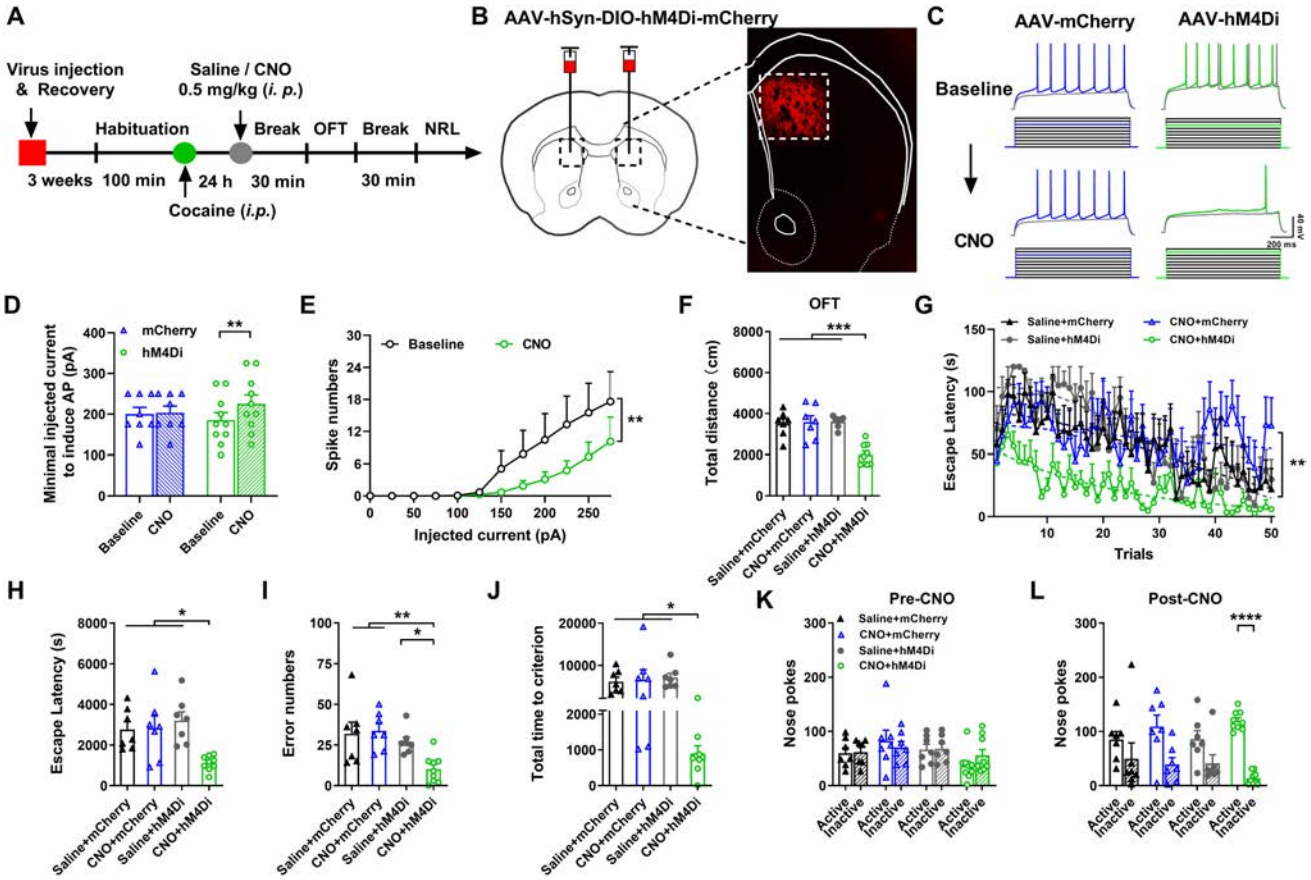

Fig. 5 Inhibiting the activity of D1-MSNs with the DREADD hM4Di reverses the impairment in reinforcement learning induced by exposure to cocaine. **A** The experimental paradigm. **B** Injection site of AAV-DIO-hM4Di-mCherry virus in the DMS. **C** Current-voltage relationship of representative D1-MSNs recorded before, and after 10 μmol/L CNO perfusion. **D** The minimal injected current to induce action potentials (Aps) is increased by CNO. **E** Number of induced Aps at different current steps (mCherry, n = 8 cells from 3 mice; hM4Di, n = 10 cells from 3 mice). **F** Open field test: the total distance traveled significantly decreases after CNO perfusion in the hM4Di group *vs* other groups. **G** Escape latency is reversed by CNO in hM4Di-expressing mice, but not in other groups. **H**–**J** Mean escape latency (**H**), error numbers (**I**), and total time to the first successful session (**J**) in the CNO+hM4Di group are significant smaller than those in the other three groups. **K** There is no preference between the active and inactive nose-pokers in the mCherry and hM4Di groups without saline or CNO during the habituation period of 100 min. **L** The number of active nose-pokes is significantly greater than that of inactive nose-pokes in the CNO+hM4Di group (Saline-mCherry, CNO-mCherry, Saline-hM4Di n = 7 mice; CNO-hM4Di n = 9 mice). Data represent the mean ± SEM (*P <0.05, **P <0.01, ***P <0.001, paired t test for **D**, two-way RM ANOVA for **E**, **F**, **H**, **I**, and **J**, and three-way RM ANOVA for **G**, **K**, and **L**).

mice expressing hM4Di with saline. During the habituation period, no mice showed a preference for either the active or the inactive nose-poker (Fig. 5K; Nosepoke × Treatment × Groups $F_{1,\ 26}$ = 1.710, P = 0.2025; Nosepoke × Treatment $F_{1,\ 26}$ = 0.0244, P = 0.8770; Nosepoke × Groups $F_{1,\ 26}$ = 1.648, P = 0.2105). However, during reinforcement training, the number of active nose-pokes was significantly higher than that of inactive nose-pokes in the hM4Di-expressing mice treated with CNO. To evaluate whether the effect of CNO on reinforcement learning in hM4Di-expressing mice was related to the reduction of locomotor activity, the total numbers of the nose-pokes were checked, and there were no significant differences in all four groups after CNO injection (Fig 5L). These results indicated that the effect on reinforcement learning by DREADD inhibition was not associated with decreased locomotor activity in this study (Fig. 5L; Nosepoke × Treatment × Groups $F_{1,\ 26}$ = 0.2791, P = 0.6018; Nosepoke × Treatment $F_{1,\ 26}$ = 3.566, P = 0.0702; Nosepoke × Groups $F_{1,\ 26}$ = 0.7986, P = 0.3797; followed by *post hoc* Tukey's test, mCherry with Saline P = 0.8712, with CNO P = 0.1765; hM4Di with Saline P = 0.6847; hM4Di with CNO P = 0.0022). The above results showed that in mice whose DMS D1-MSNs expressed mCherry or hM4Di without CNO injection, the impairment of reinforcement learning by cocaine was preserved, while in mice whose DMS D1-MSNs expressed hM4Di and were inhibited by CNO, the impairment was reversed (Fig. 1). These results indicate that enhancement of DMS D1-MSN activity is required for

the impairment in reinforcement learning induced by a single exposure to cocaine.

Discussion

Reward-based or aversion-induced reinforcement of certain behaviors is essential for survival in a changing environment. Such behavioral adaptation relies on feedback modulation by the outcomes of immediately previous actions. The basal ganglia circuit plays a key role in linking the outcomes produced by previous actions to the selection and adjustment of future actions, thus enabling the organism to approach profitable and avoid harmful environmental events [20, 47, 48]. Neurotransmission in the striatum, the input nuclei of the basal ganglia circuit, is sensitive to the feedback information conveyed by midbrain dopamine signals. This sensitivity guarantees the flexibility of behavioral remodeling [21]. Unfortunately, the same sensitivity to modulation at this node also endows the basal ganglia circuit with vulnerability to addictive drugs. For example, even a single exposure to cocaine produces prolonged impairments in adaptive behaviors by inducing plastic changes in brain regions mediating reinforcement learning [1, 6, 9, 10, 33, 34]. In present study, using a classic instrumental learning paradigm in mice, we provide further novel evidence showing that a single exposure to cocaine remarkably impairs reinforcement learning even 24 h after administration of the drug (Fig. 1). Previous studies have reported that peak cocaine values occur approximately 5–15 min after drug administration, and cocaine half-life ranges from 16 to 72 min depending on species, drug dose, and experimental conditions [49]. Although cocaine is metabolized rapidly, its metabolites including benzoylecgonine and ecgonine methyl ester are still detectable 24 h after the first cocaine exposure in humans [50]. These results indicate that a single exposure to cocaine, either occasionally taken or used for recreational purposes, causes significant deficits in behavioral learning even after the drug is metabolized. The persistent traces left by the drug exist in the brain and can still strongly interfere in the normal functioning of neural circuits mediating adaptive behavioral learning.

Previous studies have reported that potentiation in excitatory synapses on striatal D1-MSNs mediate the positive, reward-induced, reinforcement learning [13, 20]. In the present study, we further found that potentiation of both the frequency and amplitude of mEPSCs in glutamatergic synapses on DMS D1-MSNs, but not on D2-MSNs, was produced during NRL. The postsynaptic A/N ratio in D1-MSNs was also enhanced. The results showed that potentiation of excitatory transmission in direct striatal pathway neurons is essential for the completion of both positive and NRL (Figs. 2, 3). We also found a significant enhancement in the amplitude of mEPSCs in D1-MSNs, but not in D2-MSNs, was produced by a single exposure to cocaine. This result is similar to previous reports on ventral tegmental area dopamine neurons and locus coeruleus norepinephrine neurons, in which a single exposure to cocaine was found to enhance the AMPAR-mediated postsynaptic current, but did not affect the presynaptic glutamate release probability [12, 28]. Most importantly, previous studies indicated that acute cocaine exposure is sufficient to alter the AMPAR subunit composition in D1-MSNs in ventral striatum that may contribute to the synaptic potentiation [51, 52].

Interestingly, when mice were subjected to reinforcement learning 24 h after exposure to cocaine, the learning was significantly impaired. In electrophysiological recordings immediately after the reinforcement learning, enhancement in the frequency and amplitude of mEPSCs in DMS D1-MSNs was found in mice pre-exposed to saline but was absent in those pre-exposed to cocaine. These results suggest that enhancement of the AMPAR-mediated postsynaptic current induced by cocaine interferes with or inhibits the presynaptic and postsynaptic potentiation produced during reinforcement learning, and this disruption might be an important reason for the impairment of reinforcement learning induced by exposure to cocaine. The mechanisms underlying this inhibition remain to be elucidated.

Ample evidence has shown that the efficiency of synaptic transmission in the central nervous system is dynamically modulated in many physiological and pathophysiological processes [13, 14, 24, 53, 54]. Previous studies have demonstrated that de-potentiation from potentiated synaptic strength is involved in a series of normal and abnormal states. For example, when the glutamatergic transmission in the hippocampus is enhanced to a potentiated level, experience or a stimulation protocol normally resulting in LTP can only induce further de-potentiation, reversing the established potentiation to the previous baseline transmission level. Such de-potentiation mechanisms have been strongly implicated in erasing hippocampal-dependent fear memories [55, 56]. Consistent with the mechanism responsible for this deficiency of LTP reported by previous studies, our results confirmed that a single cocaine injection was sufficient to drive the inhibition of subsequent LTP in D1-MSNs (Fig. 3E, F). We hypothesize that single-dose cocaine, as a priming signal, contributes to the neuronal activity, persistently altering the response to a subsequent plasticity-inducing event, such as NRL. This synaptic plasticity might be the reason why mice pretreated with cocaine perform poorly during NRL. To test this hypothesis, we used DREADD systems that could selectively activate or depress D1-MSNs in the DMS. First,

the impairment of reinforcement learning by selective activation of D1-MSNs expressing hM3Dq (Fig. 4) might result from a mechanism similar to the reported de-potentiation. After enhancement of the D1-MSN activity, the experience of reinforcement learning normally resulting in potentiation in the glutamatergic synaptic transmission on those D1-MSNs might be reversed to de-potentiate those synapses and thus interfere with the dynamic modulation of synaptic plasticity during the learning process, leading to an impairment of learning. It is well established that cocaine strengthens the action of dopamine on D1-MSNs through occupying dopamine transporters and increasing the extracellular concentration of dopamine. Activation of dopamine D1 receptors then potentiates glutamatergic transmission on the D1-MSNs by increasing the calcium concentration in the postsynaptic cytoplasm and up-regulating the AMPAR-mediated postsynaptic current [25, 30, 57]. In such a potentiated condition induced by cocaine, the experience of reinforcement learning producing potentiation of glutamatergic transmission on D1-MSNs might be reversed to induce de-potentiation of the established potentiation state. Although this assumption is supported by the present results showing that the inhibition of hM4Di-expressing D1-MSNs successfully reversed the impairment of reinforcement learning by cocaine (Fig. 5), it still needs to be verified with cellular and molecular evidence in future. Previous studies found that the administration of CNO at 0.7 mg/kg is a commonly used dose in mice, which significantly reduces their locomotor activity [46]. In our results, administration of CNO at 0.5 mg/kg also caused inhibition of locomotor activity in hM4Di-expressing mice, but not in hM3Dq-expressing mice. On the other hand, we found the dose of 0.5 mg/kg CNO combined with D1R significantly improved the behavior of mice in NRL. And the total number of the nose-pokes were not affected in the CNO-treated hM4Di-expressing mice (Fig. 5L), indicating that the nose-poke-related behaviors were not reduced. These results indicated that the inhibition of locomotor activity in the CNO-treated hM4Di-expressing mice was not the reason for the improvement in NRL. However, further studies are needed to answer this question.

In a number of previous studies, an artificial bacterial chromosome (BAC) was introduced into mice to label D1-MSNs or D2-MSNs with GFP [58, 59]. Some of those studies also suggested that there could be behavioral abnormalities in the BAC transgenic mice [60, 61]. In order to study the neural plasticity in D1-MSNs and D2-MSNs using mice with an identical wild-type genotype, the present work collected the cytoplasm content immediately after the patch-clamp recording and assessed the transcription levels of dopamine D1 and D2 receptors (Fig. 2). This strategy successfully identified the two types of neurons, with ratios of the two subpopulations (data not shown) very similar to previous reports [17, 62]. In the present study, intraperitoneal delivery of cocaine at 20 mg/kg was chosen through a set of preliminary experiments to assess the effects on reinforcement learning. This dose is also consistent with those used in a number of animal studies [63, 64]. The effects of exposure to cocaine on reinforcement learning in the present study is also comparable with a series of previous human studies, which reported the impairment in various instrumental and go-directed behavior patterns [34, 65]. However, the present study provided electrophysiological evidence indicating that dynamic modulation of the excitatory transmission on direct striatal pathway neurons may underpin the effects of cocaine. By specifically manipulating the activity of D1-MSNs, we also demonstrated that activation of those neurons is sufficient to impair reinforcement learning, while their suppression reverses the effects of cocaine, showing that the enhancement of direct striatal pathway activity is required for the effects of cocaine.

Acknowledgments We thank Dr. Fuqiang Xu for sharing the D1-Cre transgenic mice. This work was supported by he National Natural Science Foundation of China (81971285, 11727813), and the Fundamental Research Funds for the Central Universities (GK202005001), Shaanxi Normal University.

Conflict of interest The authors declare no conflicts of interest.

References

1. Verdejo-García A, Bechara A, Recknor EC, Pérez-García M. Executive dysfunction in substance dependent individuals during drug use and abstinence: An examination of the behavioral, cognitive and emotional correlates of addiction. J Int Neuropsychol Soc 2006, 12: 405–415.
2. Verdejo-García A, Pérez-García M. Profile of executive deficits in cocaine and heroin polysubstance users: Common and differential effects on separate executive components. Psychopharmacology (Berl) 2007, 190: 517–530.
3. Franken IHA, van Strien JW, Franzek EJ, van de Wetering BJ. Error-processing deficits in patients with cocaine dependence. Biol Psychol 2007, 75: 45–51.
4. Monterosso J, Ehrman R, Napier KL, O'Brien CP, Childress AR. Three decision-making tasks in cocaine-dependent patients: do they measure the same construct?. Addiction 2001, 96: 1825–1837.
5. Soar K, Mason C, Potton A, Dawkins L. Neuropsychological effects associated with recreational cocaine use. Psychopharmacology (Berl) 2012, 222(4): 633–643.
6. Bolla KI, Rothman R, Cadet JL. Dose-related neurobehavioral effects of chronic cocaine use. J Neuropsychiatry Clin Neurosci 1999, 11: 361–369.
7. Hoff AL, Riordan H, Morris L, Cestaro V, Wieneke M, Alpert R. Effects of crack cocaine on neurocognitive function. Psychiatry Res 1996, 60: 167–176.

8. Colzato LS, van den Wildenberg WPM, Hommel B. Impaired inhibitory control in recreational cocaine users. PLoS One 2007, 2: e1143.
9. Colzato LS, Hommel B. Recreational use of cocaine eliminates inhibition of return. Neuropsychology 2009, 23: 125–129.
10. Lüscher C. Cocaine-evoked synaptic plasticity of excitatory transmission in the ventral tegmental area. Cold Spring Harb Perspect Med 2013, 3: a012013.
11. Kasanetz F, Gamonet VD, Berson N, Balado E, Lafourcade M, Manzoni O, *et al.* Transition to addiction is associated with a persistent impairment in synaptic plasticity. Science 2010, 328: 1709–1712.
12. Ungless MA, Whistler JL, Malenka RC, Bonci A. Single cocaine exposure *in vivo* induces long-term potentiation in dopamine neurons. Nature 2001, 411: 583–587.
13. Jin X, Tecuapetla F, Costa RM. Basal ganglia subcircuits distinctively encode the parsing and concatenation of action sequences. Nat Neurosci 2014, 17(3): 423–430.
14. Tecuapetla F, Jin X, Lima SQ, Costa RM. Complementary contributions of striatal projection pathways to action initiation and execution. Cell 2016, 166: 703–715.
15. Zhang CC, Ni PY, Liu YK, Tian Y, Wei JX, Xiang N, *et al.* GABAergic abnormalities associated with aensorimotor cortico-striatal community structural deficits in ErbB4 knockout mice and first-episode treatment-naïve patients with schizophrenia. Neurosci Bull 2020, 36: 97–109.
16. Hikida T, Kimura K, Wada N, Funabiki K, Nakanishi S. Distinct roles of synaptic transmission in direct and indirect striatal pathways to reward and aversive behavior. Neuron 2010, 66: 896–907.
17. Bertran-Gonzalez J, Bosch C, Maroteaux M, Matamales M, Hervé D, Valjent E, *et al.* Opposing patterns of signaling activation in dopamine D1 and D2 receptor-expressing striatal neurons in response to cocaine and haloperidol. J Neurosci 2008, 28: 5671–5685.
18. Beurrier C, Malenka RC. Enhanced inhibition of synaptic transmission by dopamine in the nucleus accumbens during behavioral sensitization to cocaine. J Neurosci 2002, 22: 5817–5822.
19. Calipari ES, Bagot RC, Purushothaman I, Davidson TJ, Yorgason IT, Pena CJ, *et al. In vivo* imaging identifies temporal signature of D1 and D2 medium spiny neurons in cocaine reward. Proc Natl Acad Sci USA 2016, 113: 2726–2731.
20. Kravitz AV, Tye LD, Kreitzer AC. Distinct roles for direct and indirect pathway striatal neurons in reinforcement. Nat Neurosci 2012, 15: 816–818.
21. Costa RM. Plastic corticostriatal circuits for action learning: What's dopamine got to do with it?. Ann N Y Acad Sci 2007, 1104: 172–191.
22. Costa RM, Cohen D, Nicolelis MAL. Differential corticostriatal plasticity during fast and slow motor skill learning in mice. Curr Biol 2004, 14: 1124–1134.
23. Barnes TD, Kubota Y, Hu D, Jin DZ, Graybiel AM. Activity of striatal neurons reflects dynamic encoding and recoding of procedural memories. Nature 2005, 437: 1158–1161.
24. Yin HH, Mulcare SP, Hilário MRF, Clouse E, Hollowa T, Davis MI, *et al.* Dynamic reorganization of striatal circuits during the acquisition and consolidation of a skill. Nat Neurosci 2009, 12: 333–341.
25. Shan Q, Ge M, Christie MJ, Balleine BW. The acquisition of goal-directed actions generates opposing plasticity in direct and indirect pathways in dorsomedial striatum. J Neurosci 2014, 34: 9196–9201.
26. Kim JA, Pollak KA, Hjelmstad GO, Fields HL. A single cocaine exposure enhances both opioid reward and aversion through a ventral tegmental area-dependent mechanism. Proc Natl Acad Sci 2004, 101: 5664–5669.
27. Arbuthnott GW, Wickens J. Space, time and dopamine. Trends Neurosci 2007, 30: 62–69.
28. Zhu F, Wu Q, Li J, Grycel K, Liu B, Sun X, *et al.* A single dose of cocaine potentiates glutamatergic synaptic transmission onto locus coeruleus neurons. Cell Calcium 2017, 67: 11–20.
29. Volkow N, Li T. Science and society: drug addiction: the neurobiology of behaviour gone awry. Nat Rev Neurosci 2004, 5(12): 963–970.
30. Ferrario CR, Li X, Wolf ME. Effects of acute cocaine or dopamine receptor agonists on AMPA receptor distribution in the rat nucleus accumbens. Synapse 2011, 65: 54–63.
31. Schroeder JA, McCafferty MR, Unterwald EM. Regulation of dynamin 2 and G protein-coupled receptor kinase 2 in rat nucleus accumbens during acute and repeated cocaine administration. Synapse 2009, 63: 863–870.
32. Hyman SE, Malenka RC, Nestler EJ. Neural mechanisms of addiction: The role of reward-related learning and memory. Annu Rev Neurosci 2006, 29: 565–598.
33. Laetitia L, Thompson ED, Claus SK, Mikulich G, Marie TB, Thomas C, *et al.* Negative reinforcement learning is affected in substance dependence. Drug Alcohol Depend 2012, 123: 84–90.
34. Colzato LS, Huizinga M, Hommel B. Recreational cocaine polydrug use impairs cognitive flexibility but not working memory. Psychopharmacology 2009, 207: 225–234.
35. Colzato LS, van den Wildenberg WPM, Hommel B. Reduced spontaneous eye blink rates in recreational cocaine users: Evidence for dopaminergic hypoactivity. PLoS One 2008, 3: 1–4.
36. Yao L, Li YF, Qian ZQ, Wu ML, Yang HF, Chen NJ, *et al.* Loss of control over mild aversive events produces significant helplessness in mice. Behav Brain Res 2019, 376: 112173.
37. Wang X, Qiao Y, Dai Z, Sui N, Shen F, Zhang J, *et al.* Medium spiny neurons of the anterior dorsomedial striatum mediate reversal learning in a cell-type-dependent manner. Brain Struct Funct 2019, 224: 419–434.
38. Ting JT, Daigle TL, Chen Q, Feng G. Acute brain slice methods for adult and aging animals: application of targeted patch clamp analysis and optogenetics. Methods Mol Biol 2014, 1183: 221–242.
39. Huang S, Uusisaari MY. Elevated temperature during slicing enhances acute slice preparation quality. Front Cell Neurosci 2013, 7: 1–8.
40. Cadwell CR, Palasantza A, Jiang X, Berens P, Deng Q, Yilmaz M, *et al.* Electrophysiological, transcriptomic and morphologic profiling of single neurons using Patch-seq. Nat Biotechnol 2016, 34: 199–203.
41. Cadwell CR, Scala F, Li S, Livrizzi G, Shen S, Sandberg R, *et al.* Multimodal profiling of single-cell morphology, electrophysiology, and gene expression using Patch-seq. Nat Protoc 2017, 12: 2531–2553.
42. Kalivas PW, Stewart J. Dopamine transmission in the initiation and expression of drug- and stress-induced sensitization of motor activity. Brain Res Rev 1991, 16: 223–244.
43. Hikida T, Kaneko S, Isobe T, Kitabatake Y, Watanabe D, Pastan I, *et al.* Increased sensitivity to cocaine by cholinergic cell ablation in nucleus accumbens. Proc Natl Acad Sci 2001, 98: 13351–13354.
44. Liu L, Xu HF, Wang J, Li J, Tian YY, Zheng JQ, *et al.* Cell type-differential modulation of prefrontal cortical GABAergic interneurons on low gamma rhythm and social interaction. Sci Adv 2020, 6: 1–14.
45. Chen P, Lou SH, Huang ZH, Wang ZN, Shan QH, Wang Y, *et al.* Prefrontal cortex corticotropin-releasing factor neurons control behavioral style selection under challenging situations. Neuron 2020, 106: 301–315.

46. Wang WT, Li CC, Chen Q, Goes MS, Hawrot J, Yao AY, *et al.* Striatopallidal dysfunction underlies repetitive behavior in Shank3-deficient model of autism. J Clin Invest 2017, 127: 1978–1990.
47. Jin X, Costa RM. Shaping action sequences in basal ganglia circuits. Curr Opin Neurobiol 2015, 33: 188–196.
48. Santos FJ, Oliveira RF, Jin X, Costa RM. Corticostriatal dynamics encode the refinement of specific behavioral variability during skill learning. Elife 2015, 4: 1–19.
49. Sanders A, McDougall MG, Apodoca AMY, Adrian D, Mendez CG, Katz AT, *et al.* Ontogeny of cocaine-induced behaviors and cocaine pharmacokinetics in male and female neonatal, preweanling, and adult rats. Psychopharmacology (Berl) 2018, 235: 1967–1980.
50. Walsh SL, William W, Stoops DE. Moody SN, Lin GEB. Repeated dosing with oral cocaine in humans: assessment of direct effects, withdrawal and pharmacokinetics. Exp Clin Psychopharmacol 2009, 17: 205–216.
51. Terrier J, Lüscher C, Pascoli V. Cell-type specific insertion of GluA2-lacking AMPARs with cocaine exposure leading to sensitization, cue-induced seeking, and incubation of craving. Neuropsychopharmacology 2016, 41: 1779–1789.
52. Pascoli V, Turiault M, Lüscher C. Reversal of cocaine-evoked synaptic potentiation resets drug-induced adaptive behaviour. Nature 2011, 481: 71–76.
53. Willingham DB, Koroshetz WJ. Evidence for dissociable motor skills in Huntington's disease patients. Psychobiology 1993, 21: 173–182.
54. Wichmann T, Delong MR. Functional neuroanatomy of the basal ganglia in Parkinson's disease. Adv Neurol 2003, 91: 9–18.
55. Schimanski LA, Nguyen PV. Impaired fear memories are correlated with subregion-specific deficits in hippocampal and amygdalar LTP. Behav Neurosci 2005, 119: 38–54.
56. Shors TJ, Seib TB, Levine S, Thompson RF. Inescapable versus escapable shock modulates long-term potentiation in the rat hippocampus. Science 1989, 244: 224–226.
57. Brown MT, Bellone C, Mameli M, Labouèbe G, Bocklisch C, Balland B, *et al.* Drug-driven AMPA receptor redistribution mimicked by selective dopamine neuron stimulation. PLoS One 2010, 5.
58. Gong S, Zheng C, Doughty ML, Losos K, Didkovsky N, Schambra UB, *et al.* A gene expression atlas of the central nervous system based on bacterial artificial chromosomes. Nature 2003, 425: 917–925.
59. Heintz N. BAC to the future: The use of BAC transgenic mice for neuroscience research. Nat Rev Neurosci 2001, 2: 861–870.
60. Kramer PF, Christensen CH, Hazelwood LA, Dobi A, Alvarez VA. Dopamine D2 receptor overexpression alters behavior and physiology in Drd2-EGFP mice. J Neurosci 2011, 31: 126–132.
61. Ade KK, Wan Y, Chen M, Gloss B, Calakos N. An improved BAC transgenic fluorescent reporter line for sensitive and specific identification of striatonigral medium spiny neurons. Front Syst Neurosci 2011, 5: 1–9.
62. Matamales M, Bertran-Gonzalez J, Salomon L, Degos B, Deniau JM, Valjent E, *et al.* Striatal medium-sized spiny neurons: Identification by nuclear staining and study of neuronal subpopulations in BAC transgenic mice. PLoS One 2009, 4.
63. Hammad AM, Sari Y. Effects of cocaine exposure on astrocytic glutamate transporters and relapse-like ethanol-drinking behavior in male alcohol-preferring rats. Alcohol Alcohol 2020, 55: 254–263.
64. Buffalari DM, Rinaman L. Cocaine self-administration and extinction alter medullary noradrenergic and limbic forebrain cFos responses to acute, noncontingent cocaine injections in adult rats. Neuroscience 2014, 281: 241–250.
65. Lim TV, Cardinal RN, Savulich G, Jones PS, Moustafa AA, Robbins TW, *et al.* Impairments in reinforcement learning do not explain enhanced habit formation in cocaine use disorder. Psychopharmacology 2019, 236: 2359–2371.

Neurosci. Bull. August, 2021, 37(8):1135–1146
https://doi.org/10.1007/s12264-021-00705-9

www.neurosci.cn
www.springer.com/12264

ORIGINAL ARTICLE

Dicer Deletion in Astrocytes Inhibits Oligodendroglial Differentiation and Myelination

Kun Liu[1,2] · Bin Yu[1,2] · Jing-Fei Chen[1] · Rui-Xue Li[1] · Lin Chen[1] · Shu-Yu Ren[1] · Fei Wang[1] · Feng Mei[1] · Lan Xiao[1,2]

Received: 11 November 2020 / Accepted: 13 February 2021 / Published online: 9 June 2021

Abstract Increasing evidence has shown that astrocytes are implicated in regulating oligodendrocyte myelination, but the underlying mechanisms remain largely unknown. To understand whether microRNAs in astrocytes function in regulating oligodendroglial differentiation and myelination in the developing and adult CNS, we generated inducible astrocyte-specific Dicer conditional knockout mice (hGFAP-CreERT; Dicer fl/fl). By using a reporter mouse line (mT/mG), we confirmed that hGFAP-CreERT drives an efficient and astrocyte-specific recombination in the developing CNS, upon tamoxifen treatment from postnatal day 3 (P3) to P7. The Dicer deletion in astrocytes resulted in inhibited oligodendroglial differentiation and myelination in the developing CNS of Dicer cKO mice at P10 and P14, and did not alter the densities of neurons or axons, indicating that Dicer in astrocytes is required for oligodendrocyte myelination. Consequently, the Dicer deletion in astrocytes at P3 resulted in impaired spatial memory and motor coordination at the age of 9 weeks. To understand whether Dicer in astrocytes is also required for remyelination, we induced Dicer deletion in 3-month-old mice and then injected lysolecithin into the corpus callosum to induce demyelination. The Dicer deletion in astrocytes blocked remyelination in the corpus callosum 14 days after induced demyelination. Together, our results indicate that Dicer in astrocytes is required for oligodendroglia myelination in both the developing and adult CNS.

Keywords White matter · Myelination · MicroRNA · GFAP · MT/mG · Microglia · Oligodendrocyte · Demyelination · Remyelination

Introduction

Astrocytes are a type of glial cell that are widely distributed in the central nervous system (CNS) [1]. It has been well established that astrocytes play important roles in CNS development and injuries, such as providing nutrients to neurons [2–4] and responding to injury and inflammation [5, 6]. Oligodendrocytes (OLs) wrap axons and form myelin sheaths that ensure fast and efficient transmission of action potentials in the CNS [7, 8]. The OL differentiation and myelination are initiated by axon-OL recognition, and this process is also guided by interacting with other cell types [9, 10]. Indeed, astrocytes are closely associated with OLs by communicating through gap junctions and secretory factors [11, 12]. *In vitro* evidence has shown that astrocytes can influence the differentiation, proliferation and migration of OL precursor cells (OPCs) [13]. For example, astrocytes secret growth factors that can promote OPC proliferation and survival in cultures [14]. Elimination of astrocyte in the developing CNS causes OL death and disrupts myelination in the developing CNS, indicating that astrocytes are functionally required for OL

Kun Liu and Bin Yu have contributed equally to this work.

✉ Feng Mei
meif@tmmu.edu.cn

✉ Lan Xiao
xiaolan35@hotmail.com

[1] Department of Histology and Embryology, Chongqing Key Laboratory of Neurobiology, Brain and Intelligence Research Key Laboratory of Chongqing Education Commission, Third Military Medical University (Army Medical University), Chongqing 400038, China

[2] Department of Neurosurgery, 2nd affiliated Hospital, Third Military Medical University (Army Medical University), Chongqing 400038, China

survival [15]. However, *in vivo* mechanisms of astrocytes that regulate OL myelination remain largely unknown during CNS development and injuries.

Dicer is a key enzyme that is responsible for generating functional noncoding micro-RNAs (miRNAs), that bind to and degrade target message RNAs. The functional importance of Dicer in OLs and neurons has been extensively investigated. Conditional deletion of Dicer driven by mGFAP-Cre or hGFAP-Cre in the developing CNS results in premature death of the knockout mice and disrupted synaptogenesis in developing brains [16, 17]. It is noticeable that the mGFAP-Cre and hGFAP-Cre lines induce non-selective recombination in neurons, OLs, and astrocytes [18], due to the GFAP expression in embryonic neural stem cells [19]. Since myelination occurs in the CNS postnatally and continues throughout life in mice, it is still unknown whether the expression of Dicer in astrocytes is required for OL differentiation and myelination.

In this study, we used the hGFAP-CreERT mouse line to induce recombination in astrocytes from postnatal days 3–7. The recombination occurred efficiently and specifically in astrocytes. By crossing the hGFAP-CreERT mouse to the Dicer floxed (Dicer fl/fl) mouse, the induction of Dicer deletion in astrocytes resulted in delayed OL differentiation and myelination, and subsequently caused spatial memory and motor coordination deficits at the age of 9 weeks. To understand whether Dicer is required for remyelinaiton, we induced Dicer ablation in astrocyte at the age of 3 months and then demyelination by injecting lysolecithin into the corpus callosum. Consistently, the remyelination was also inhibited in the corpus callosum of Dicer cKO mice compared to wild-type controls 14 days after lesion. Together, our results indicate that Dicer in astrocytes is required for OL differentiation and myelination and astrocyte may play an important role in regulating OL myelination.

Materials and Methods

Animals

Mice used in this study were handled according to the protocols approved by the Laboratory Animal Welfare and Ethics Committee of the Army Medical University (Third Military Medical University). The hGFAP-CreERT mice were a generous gift from Dr. Christian Giaume (MGI:4418665) and were described previously [20]. To generate astrocyte-specific Dicer cKO mice, the hGFAP-CreERT2 mice were bred with the Dicer fl/fl line (The Jackson Laboratory, Catalog # 006366) to obtain hGFAP-CreERT; Dicer fl/fl mice. The reporter gene mice mT/mG were purchased from The Jackson Laboratory (Catalog # 007676) and crossed with the hGFAP-CreERT line. Genomic DNA was extracted from mouse tails and genotypes of all mice were analyzed by PCR with the according primers. Dicer fl/fl mice or hGFAP-CreERT; mT/mG littermates were used as controls.

Administration of Tamoxifen

To induce Cre recombination in mice, Tamoxifen (Sigma-Aldrich, St. Louis, MO) was dissolved in sunflower oil to a final concentration of 10 mg/mL. Newborn pups and adult mice were administered tamoxifen at 50 mg/kg per day for five consecutive days by oral gavage.

Immunofluorescence Staining

Immunofluorescence staining was carried out as described previously [21]. Briefly, floating tissue sections (20 μm) were prepared from 4% paraformaldehyde perfused brains and were blocked with 5% bovine serum albumin (BSA) containing 0.4% Triton-X 100 for 1 h at room temperature. Then tissues were incubated with primary antibodies to rabbit anti-NG2 (Millipore,1:200), rabbit anti-BLBP (Abcam, 1:1000), rabbit anti-Olig2 (Millipore, 1:200), rabbit anti-NeuN (Abcam, 1:500), rabbit anti-NF200 (Sigma-Aldrich 1:1000), rat anti-MBP (Millipore 1:200), mouse anti-CC1 (Calbiochem 1:200), rabbit anti-Iba1 (Wako 1:500), or goat anti-GFAP (Abcam, 1:500) overnight at 4°C. After thorough washing, appropriate secondary antibody (Alexa Fluor 647 donkey anti-mouse IgG, Alexa Fluor 647 donkey anti-rabbit IgG, Alexa Fluor 647 donkey anti-goat IgG, or Alexa Fluor 647 goat anti-rat IgG; Molecular Probes, Invitrogen) was applied at 1:1000. Nuclei were counterstained with 4', 6-diamino-2-phenylindole (DAPI, Invitrogen).

Morris Water Maze (MWM)

The water maze is a behavioral test designed to assess the spatial learning skill [22]. The test apparatus consists of a circular water tank filled with opaque water and a hidden platform submerged a few centimeters under the water surface in one quadrant of the tank. In the training trials, mice were place into the water at different quadrants to find the hidden platform at a fixed position. All mice were tested four times a day for 3–5 consecutive days. In the test trials, the platform was removed and distance moved in platform quadrant, time spent in the platform quadrant, or times crossing the platform area was measured to assess long-term spatial memory. Investigators were blinded for the genotype information and mice were handled gently to avoid stress in the experiment.

Beam Walking Test

This test was applied to measure hind limb motor coordination. A 0.5 cm wide beam was placed 50 cm over the floor in a dark room, the starting side was lightened by a lamp and the other side was in a box (non-transparent, 20 cm × 10 cm × 20 cm). Padding material from cages was placed on the bottom of the box to attract the mice to walk through. Each mouse was put on the beam in a sequence of 30-cm, 50-cm, and 70-cm from the end during the training day. And this kind of training was repeated two times per day for 3 consecutive days before testing. On the testing day, videos were recorded from both sides of the beam. The frequency of hind limb slippage was measured as the index of the beam walking test when the mice walked along the 90-cm long beam [23].

Open Field Test

The open field test was used to measure motor capacity by using an open field activity system (Biowill, Shanghai, China). Mice were placed in the center of the uncovered box (50 cm × 50 cm × 50 cm), and their movements were recorded for 10 min as they moved around and explored the environment. After the experiment was completed, the distance traveled was measured by a computer tracking programs.

Image Acquisition and Quantification

Fluorescent images were obtained with an Axio Imager M2 fluorescence microscope (Zeiss, Oberkochen, Germany) and a confocal laser-scanning microscope (Olympus, FV 3000, Shinjuku, Tokyo) at appropriate excitation wavelengths. For statistical analysis, at least three representative images (20×) from comparable locations were acquired for each sample. Quantification was analyzed using Image-Pro Plus 6.0 software (Media Cybernetics, Silver Spring, MD, USA).

Lysolecithin Demyelination Model

Three-month-old mice (Dicer cKO or control) were anesthetized with isoflurane, and the skull was fixed horizontally during injection. A steel needle (30 GA, Hamilton) was attached to a 10 μL Hamilton syringe by a microtube segment, and installed on a stereotaxic micromanipulator (RWD). 1.5 μL of 1% lysolecithin (Sigma-Aldrich) solution was injected unilaterally into the corpus callosum (1.00 mm posterior to bregma, 1.04 mm lateral to bregma,1.58 mm deep) to induce focal demyelination. The needle was kept in place for 5 min to reduce reflux along the needle track. 2 weeks later, mice were sacrificed and their demyelination and remyelination were assessed [24].

Electron Microscopy

Electron microscopy (EM) was performed as previously described [25]. Briefly, animals were anesthetized with 1% pentobarbital and perfused with 1.25% glutaraldehyde/2% paraformaldehyde in 0.1 mol/L PB, pH 7.4. Tissues were postfixed with 1% OsO_4, incubated with uranyl acetate, dehydrated through a graded acetone series and embedded in epoxy resin 618. Ultrathin sections (60 nm) were cut by an ultramicrotome (LKB-V, LKB Produkter AB, Bromma) and observed under a transmission electron microscope (TECNAI10, Philips). High-resolution images were taken with an AMT XR-60 CCD Digital Camera System and analyzed with Image-Pro Plus 6 (Media Cybernetics, Silver Spring, MD, USA). The lateral horn white matter of the spinal cord at cervical levels 2–5 was collected for semithin sections. The g-ratios of the myelinated fibers were calculated as the ratio of the diameter of the axon to the diameter of the myelin sheath wrapping the axon.

Statistical Analysis

The statistical significance of differences between groups was determined using GraphPad Prism 7 software (La Jolla, CA [https://www.graphpad.com/]). All values are expressed as the mean ± SEM. Data from the acquisition phase in the Morris water maze were analyzed by separate repeated measures two-way ANOVA. For other data, statistical analysis was performed using the two-tailed unpaired *t*-test. Each experiment included at least three samples. *P*-values less than 0.05 were considered statistically significant. Significance was reported as $*P < 0.05$, $**P < 0.01$, or $***P < 0.001$.

Results

Astrocyte-Specific Recombination Driven by hGFAP-CreERT

To understand the role of astrocytes during CNS development, we used the hGFAP-CreERT mouse line to induce recombination in the developing CNS (Fig. 1). To examine the recombination specificity and efficiency driven by hGFAP-CreERT, we crossed this line to the mT(omato)/mG(FP) reporter line and mice were treated with tamoxifen at postnatal day 3 (P3) and sacrificed at P14 (Fig. 1A). The membrane-bound GFP (mGFP) expression was initiated upon recombination, and the mGFP positive cells were widely distributed throughout the brain (Fig. 1A). To verify

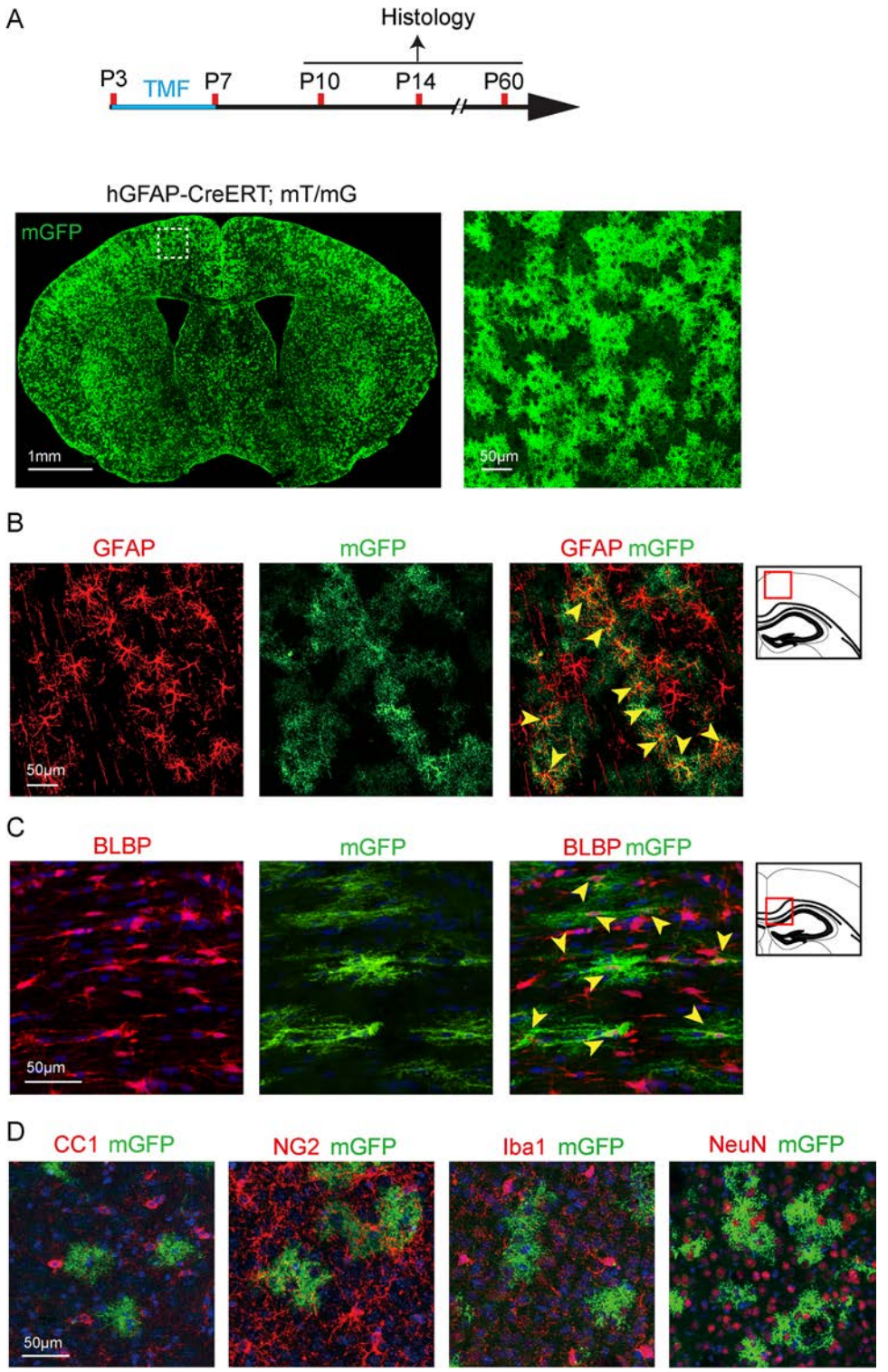

Fig. 1. Recombination in hGFAP-CreERT; mT/mG brains. **A** Schematic diagram displaying the time course of tamoxifen (TMF) treatment and histology. Representative image of mGFP-positive cells in the brain at P14 (left), and magnified mGFP-positive cells in the cortex (right image corresponding to the dotted area in the left panel); **B**, **C** Counter-immunostaining for GFAP (yellow arrowheads indicating astrocytes in **B**), BLBP (yellow arrowheads indicating astrocytes in **C**); **D** CC1 (mature oligodendrocytes), NG2 (OPCs), Iba1 (Microglia), and NeuN (Neurons) positive cells in hGFAP-CreERT; mT/mG brains. Scale bar, 1 mm (Left panel of **A**) and 50 μm (Right panel of **A**, **B**, **C**, and **D**).

if the hGFAP-CreERT line can induce astrocyte-specific recombination in the postnatal CNS, we carried out immunostaining for GFAP, brain lipid-binding protein (BLBP, astrocytes), NeuN (neurons), CC1 (OLs), Iba1 (microglia), and NG2 (OPCs) on the hGFAP-CreERT; mT/mG brain sections (Fig. 1B–D). Our results showed that mGFP-positive cells were exclusively co-localized with astroglial markers, GFAP or BLBP, and did not overlap with CC1, Iba1, NeuN, or NG2 expression (Fig. 1B, C). It was noticeable that approximately 85% of GFAP- and 60% of BLBP-positive cells expressed mGFP in the cortex and corpus callosum respectively, indicating that the hGFAP-CreERT line was reliable in inducing astrocyte-specific recombination in the gray and white matter of the developing CNS (Fig. 1).

Dicer Deletion in Astrocytes Inhibits Oligodendrocyte Myelination

Then we decided to assess whether Dicer deletion in astrocytes can change myelination in the developing CNS, since the mGFP-positive astrocytes seems to be closely associated with MBP-positive myelin sheaths in the 3D-reconstructed Z-stack images (Fig. 2A). We examined myelination by using transmission electronic microscopy (TEM), and the myelinated axon density was greatly decreased in the P7 spinal cord white matter of Dicer-cKO mice, manifested as higher *g*-ratios (Fig. 2B, C), suggesting Dicer deletion in astrocytes inhibits myelination in the developing CNS. In support of this notion, the area of MBP-positive myelin and the number of CC1-positive mature OLs were greatly decreased in the spinal cords of the P10 Dicer-cKO mice compared to wild-type controls (Fig. 2D). Consistently, MBP expression and CC1-positive cells were also significantly decreased in the P10 Dicer-cKO brains (Fig. 3A–D) without altering NG2-positive OPCs (Fig. 3E). The Olig2-positive OL density was also decreased in the Dicer-cKO brains at P10 (Fig. 3F), suggesting that Dicer deletion in astrocytes inhibits OL differentiation. The densities of NeuN-positive neurons and NF200-positive axons were not changed in the P10 Dicer-cKO cortex, indicating that Dicer deletion in astrocytes is unlikely to cause neuronal death or axonal degeneration (Fig. 3G, H). In addition, hypomyelination was still evident in the corpus callosum and hippocampus in the P14 Dicer-cKO brains revealed by MBP and CC1 immunostaining as compared to wild-type controls (Fig. 4A–C). We next examined the change of astrocytes upon Dicer deletion from P3 by immunostaining for GFAP. Our results showed increased numbers of GFAP-positive astrocytes and 3D reconstruction manifested an amplified shape of GFAP-positive cells with branched processes in the Dicer-cKO brains at P14 (Fig. 4D), suggesting that Dicer ablation in astrocytes may cause astrogliosis and activation. It is notable that the hypomyelination was persistently present at P60, as revealed by decreased MBP expression in the cortex and hippocampus of Dicer-cKO mice as compared to wild-type controls (Fig. 4E, F), while NF200 axon density was not altered (Fig. 4G). These findings indicate that Dicer expression in astrocytes is required for OL differentiation and myelination in the developing CNS.

Dicer Deletion in Astrocytes Causes Prolonged Functional Deficits in Adulthood

To investigate whether the Dicer deletion in astrocytes could affect neurofunction development, we examined the behavioral changes in adulthood at P60 with the induction of recombination at P3 (Fig. 5A). The Dicer-cKO mice were viable without showing visible abnormalities, and had a lifespan similar to that of littermate controls. It was interesting that the Dicer-cKO mice displayed impaired spatial memory in the Morris water maze test, with prolonged latency in the training process and lower frequency of passing the target sector (Fig. 5B). In addition, the beam-walking test displayed that motor coordination was impaired in the Dicer-cKO mice, showing a higher frequency of foot-slip than wild-type controls (Fig. 5C). To examine whether motor function was altered in the Dicer-cKO mice, the mice were subjected to the open field test, and the travel distance was not significantly different between the Dicer-cKO and littermate control mice (Fig. 5D). The results indicated that the Dicer deletion in astrocytes during CNS development caused neuronal dysfunctions in spatial memory and motor coordination in adulthood (Fig. 5). To further examine if the functional deficits were due to Dicer deletion during development or adulthood, we induced recombination in adulthood at the age of 60 days (Fig. 5E–G). One month after recombination, we challenged the Dicer-cKO and control mice with the same set of behavioral tests. The Dicer-cKO mice did not manifest significant changes in the water maze (Fig. 5F), beam-walking (Fig. 5G), or open field test (Fig. 5H), suggesting that Dicer deletion in astrocytes during adulthood may not cause instant functional deficits.

Dicer Deletion in Astrocytes Delays Remyelination After Lysolecithin-Induced Demyelination

To confirm the recombination efficiency in astrocytes driven by hGFAP-CreERT in adulthood, we examined the mGFP expression rate by immunostaining for GFAP in the hGFAP-CreERT; mT/mG mouse at P90, 30 days after induction from P60 (Fig. 6A). Our results showed that mGFP expression was exclusively co-localized with GFAP-positive cells, and approximately 75% of GFAP-

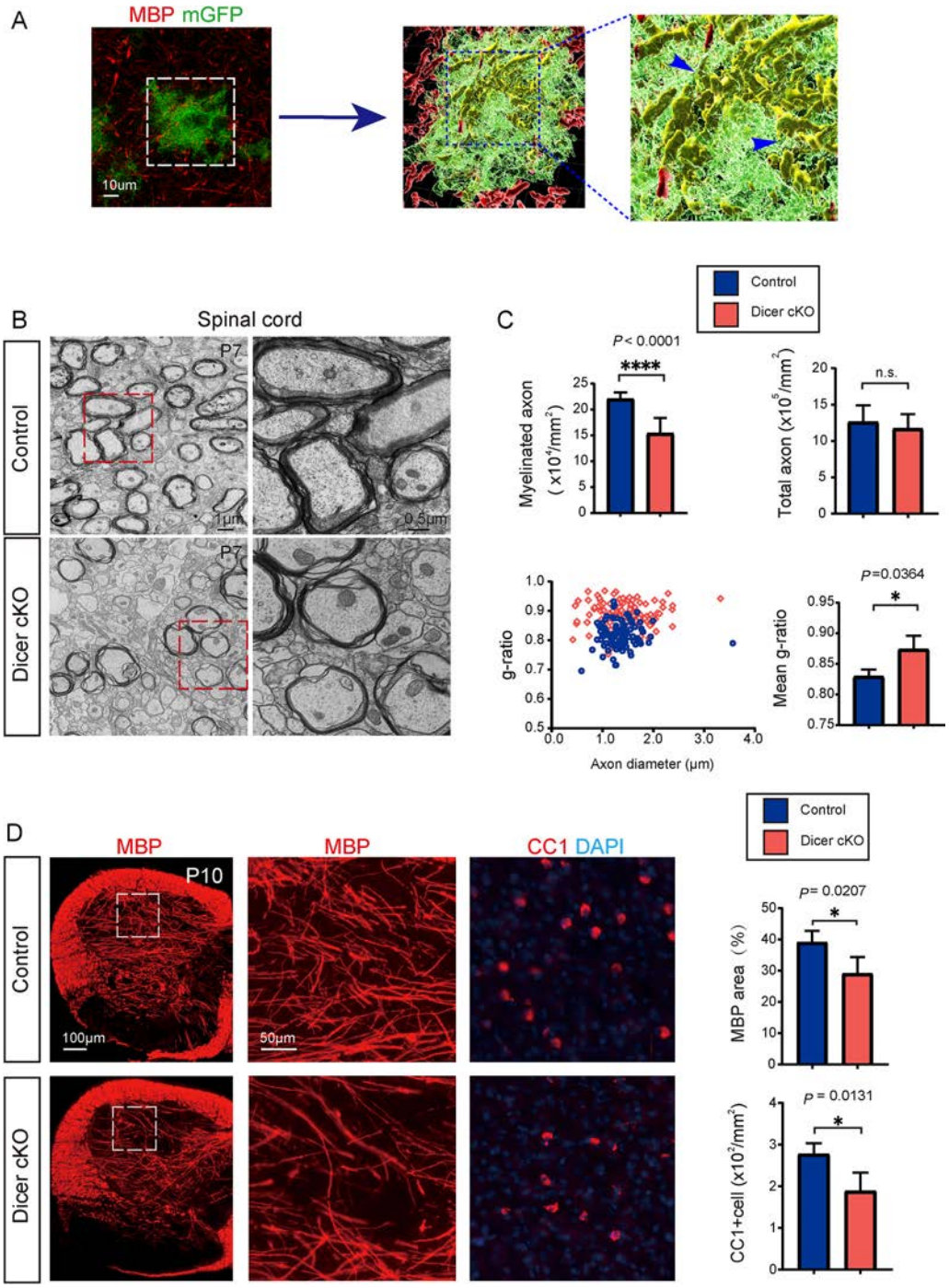

Fig. 2. Dicer deletion in astrocytes inhibits myelination in the developing spinal cord. **A** 3D reconstruction of mGFP-positive astrocytes, MBP-positive myelin sheaths, and arrows indicating the myelin sheaths engulfed by an mGFP-positive astrocyte; **B** Representative TEM images showing spinal cord white matter in the Dicer-cKO mice and littermates (left panels) and magnified images (right panels). Scale bars, 1 μm (left panels) and 0.5 μm (right panels). **C** Quantification of myelinated axons and total axons, myelin sheath thickness, and scatterplot of g-ratios of individual axons as a function of axonal diameter. **D** Representative images and quantification of MBP expression and CC1-positive cells in the spinal cords of Dicer-cKO and control mice. Scale bars, 100 μm (left panels) and 50 μm (middle and right panels). Error bars represent mean ± SEM. $^{*}P < 0.05$ or $^{****}P < 0.0001$, Student's *t*-test, Dicer-cKO *vs* control, $n = 4$ for all experiments.

positive cells expressed mGFP at P90, indicating astroglia-specific and efficient recombination in the adult CNS (Fig. 6B). To investigate if Dicer deletion in astrocytes could change myelin regeneration in lesions, we induced recombination at the age of 90 days and injected lysolecithin into the corpus callosum 7 days after the

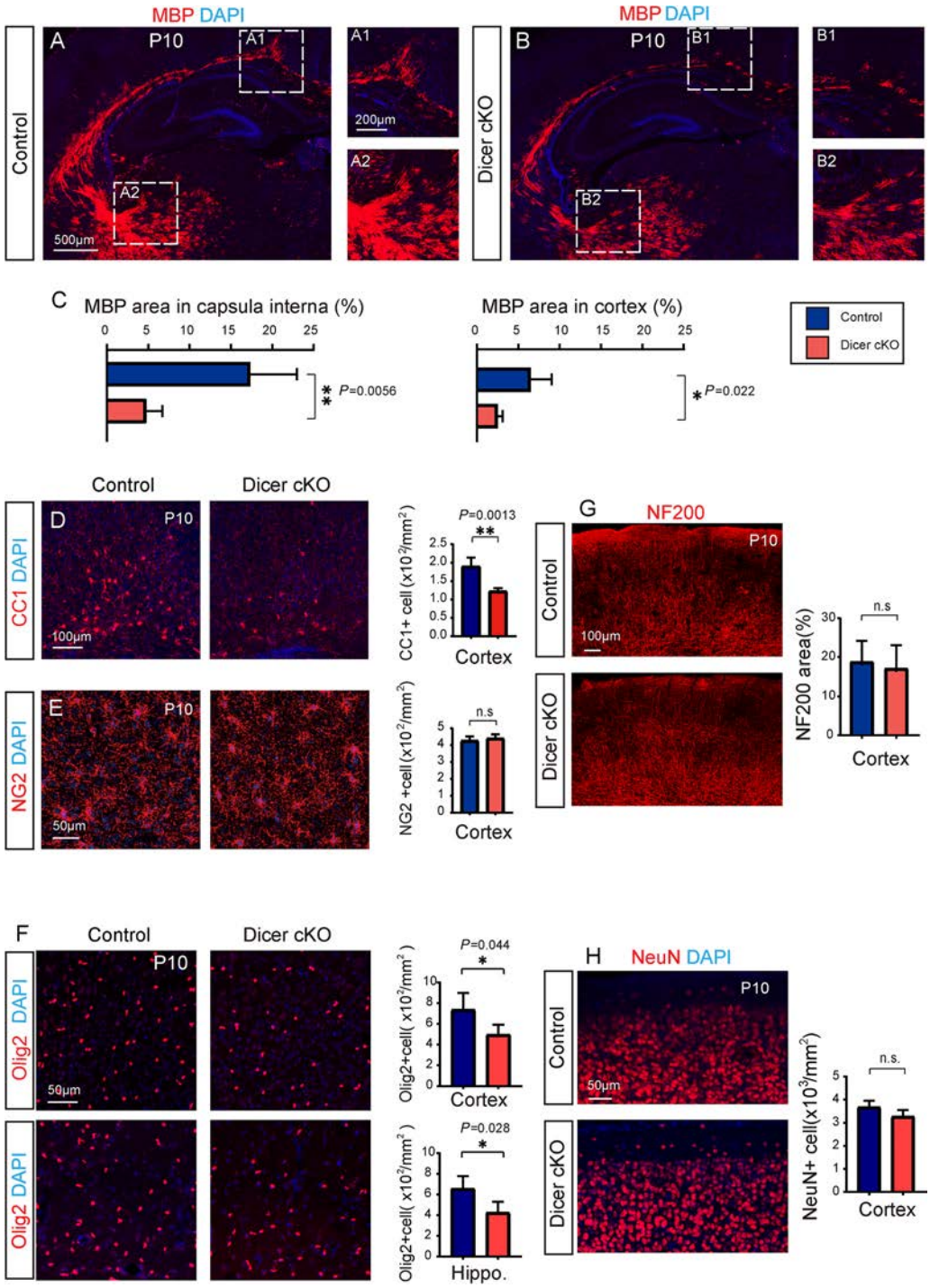

Fig. 3. Dicer deletion in astrocytes inhibits myelination in the brain. **A, B** Representative images showing MBP-positive areas in the brains of Dicer-cKO (**A**) mice and littermates (**B**) at P10 and magnified images showing MBP expression in the cortex (**A1, B1**) and capsula interna (**A2, B2**). Scale bars, 500 μm (**A**, **B**) and 200 μm (**A1, A2, B1, B2**). **C** Quantification of MBP expression in the cortex and capsula interna. **D–H** Representative images and quantification of CC1-positive cells (**D**, **F**), NG2-positive cells (**E**, **F**), NF200 axons (**G**), and NeuN-positive neurons (**H**) in the cortex of Dicer-cKO mice and littermates at P10. Scale bars,100 μm (**D**, **G**) and 50 μm (**E**, **F**, and **H**). Error bars represent the mean ± SEM. $^{**}P < 0.01$, Student's t-test, Dicer-cKO *vs* control, $n = 3$–4 for all experiments.

recombination (Fig. 6C). Demyelination induced by lysolecithin injection triggers an automatic myelin reparative process in the CNS, that allows for measuring remyelination kinetics in the lesions. The MBP immunostaining results indicated that remyelination in the corpus callosum was greatly decreased 14 days post-injury,

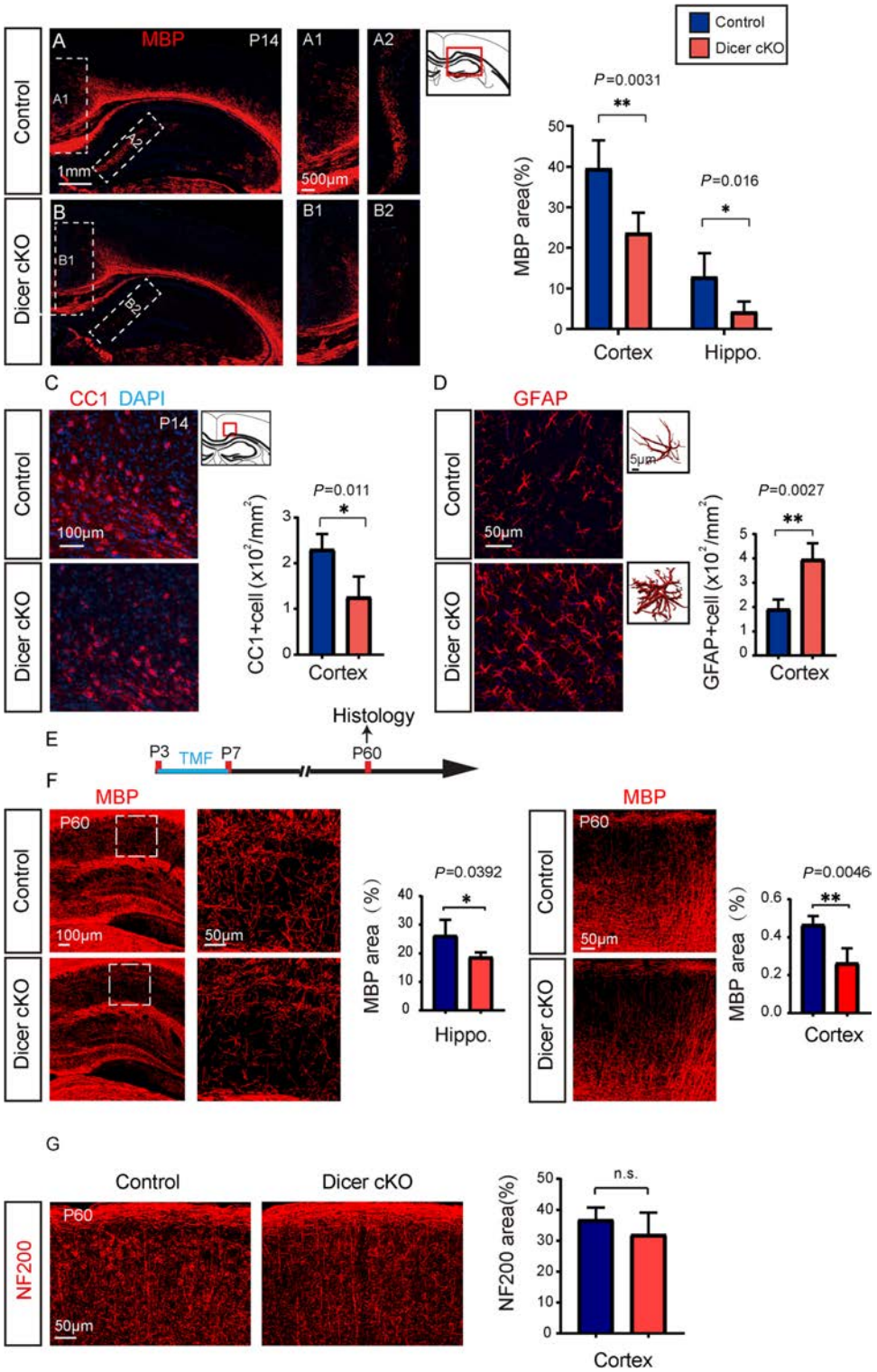

Fig. 4. Persistent hypomyelination in the Dicer-cKO brain. **A, B** Representative images showing MBP-positive areas in the brains of Dicer-cKO (**A**) mice and littermates (**B**) at P14 and magnified images showing MBP expression in the corpus callosum (**A1, B1**) and hippocampus (**A2, B2**). Scale bars, 1 mm (**A, B**) and 500 μm (**A1, A2, B1, B2**). **C, D** Representative images and quantification of CC1- (**C**) and GFAP-(**D**) positive cells in the cortex of Dicer-cKO mice and littermates at P14. Scale bars, 100 μm (**C**), 50 μm (**D**). **E** Schematic diagram of the time course of tamoxifen (TMF) treatment and histology; **F** Representative images showing MBP-positive areas in the brains of Dicer-cKO mice and littermates at P60 and magnified images showing MBP expression in the hippocampus and cortex. Scale bars, 100 μm (left panel) and 50 μm (middle and right panels). **G** Images showing NF200-positive areas in the brains of Dicer-cKO mice and littermates. Error bars represent the mean ± SEM. $^{**}P < 0.01$, Student's *t*-test, Dicer-cKO *vs* control, $n = 4$–5 for all experiments.

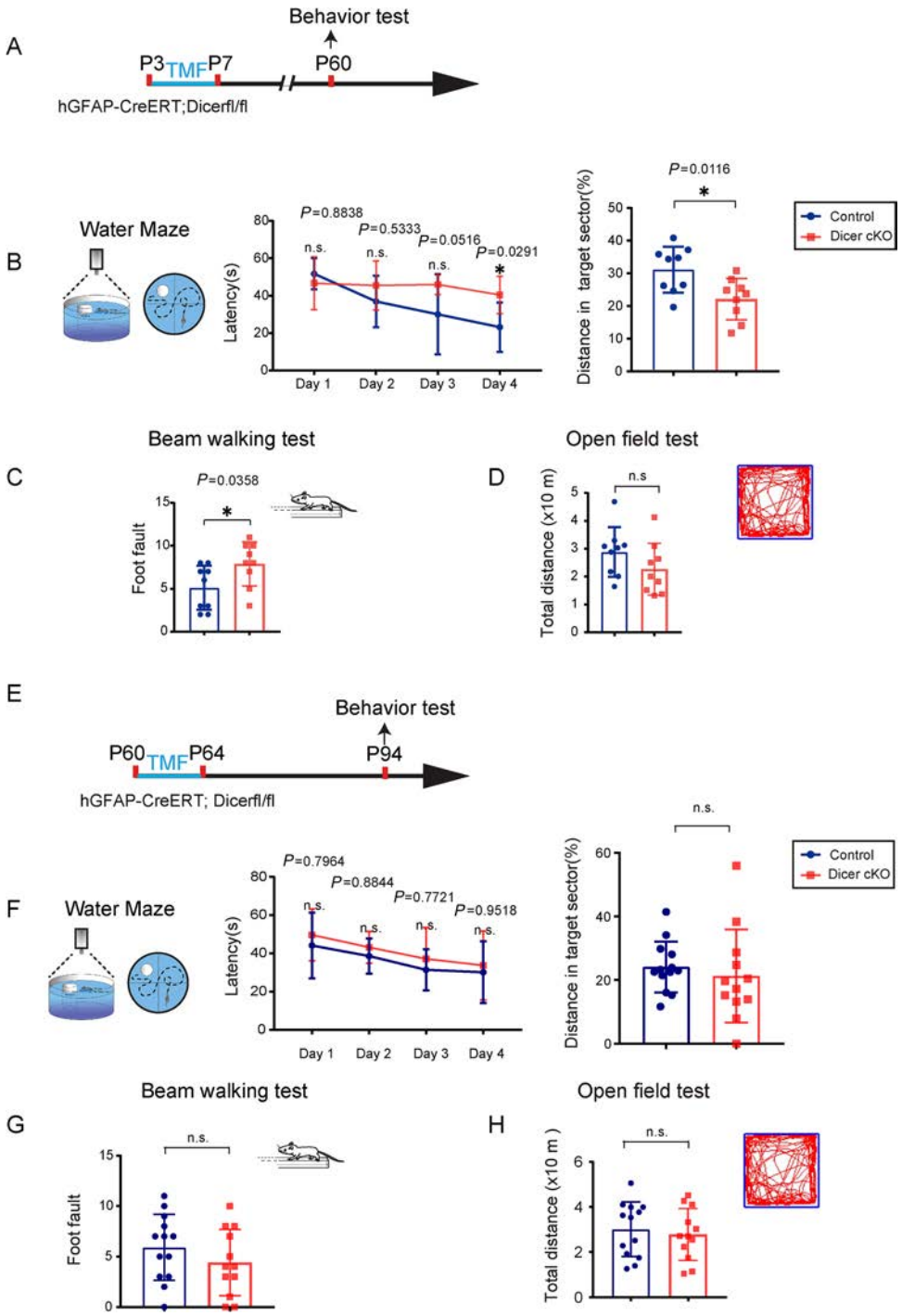

Fig. 5. Dicer deletion in astrocytes causes memory and motor deficits. **A, E** Schematic diagram showing the time course of tamoxifen (TMF) treatment in P3 or P60 mice and behavioral tests; **B, F** The Morris water maze test reveals the latency to platform in the acquisition phase and distance spent in the target quadrant in the 60-day-old (**B**) or 94-day-old (**F**) Dicer-cKO and littermate control mice. Error bars represent the mean ± SEM. *P <0.05, unpaired t test and two-sided unpaired Mann-Whitney test were used for latency to platform and distance in the target sector. (**C, G**) Mean numbers of foot slips of Dicer-cKO and control mice in the beam-walking test at P60 (**C**) or P94 (**G**). Error bars represent the mean ± SEM. *$P < 0.05$, non-parametric Mann-Whitney test, Dicer-cKO *vs* control mice; **D, H** Total distance in the open field test at P60 (**D**) or P94 (**H**). n = 9 Dicer-cKO mice and n = 9 control mice at P60 (**B, C**), and n = 13 Dicer-cKO mice and n = 12 control mice at P94 (**D, F**); non-parametric Mann-Whitney test.

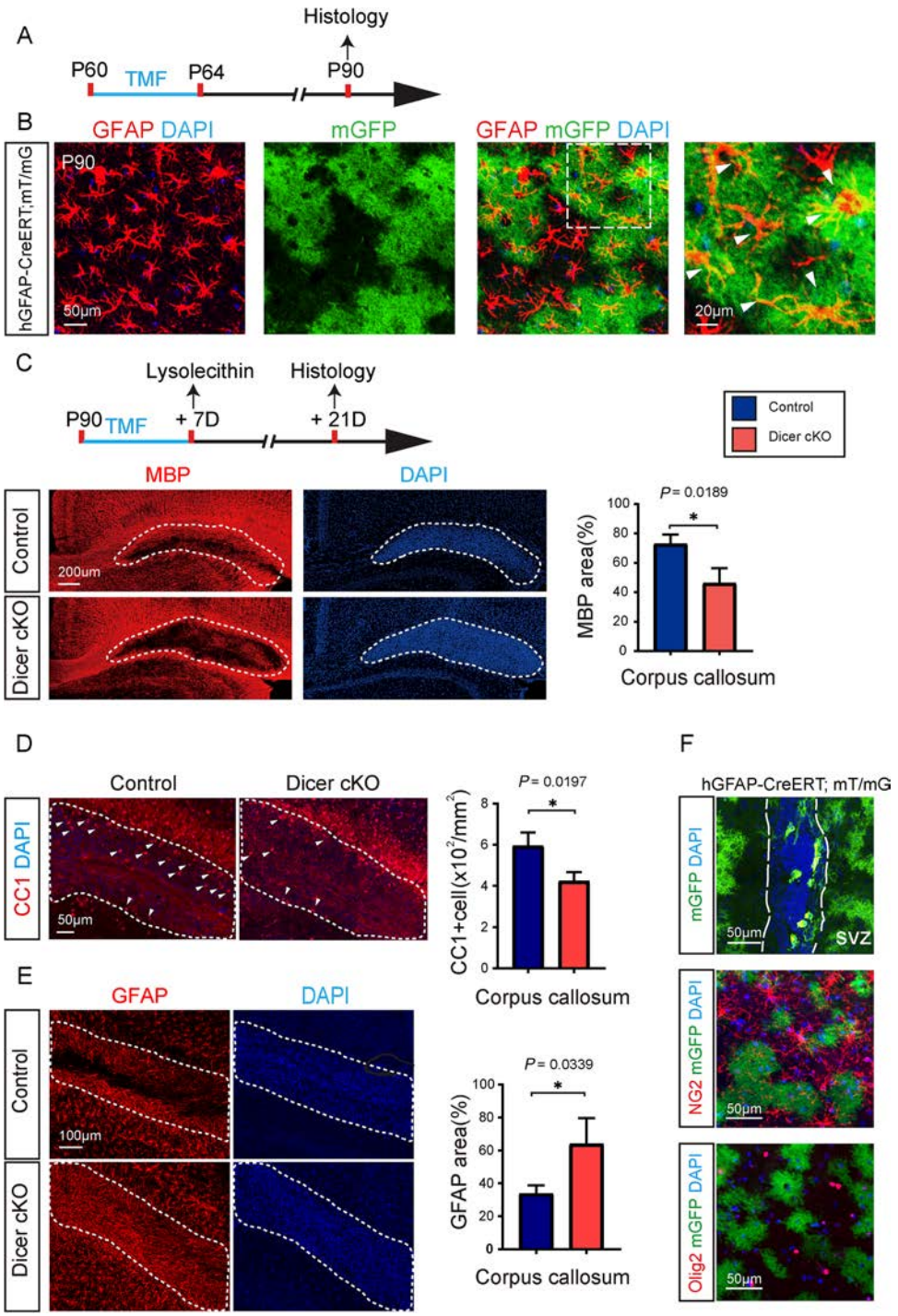

Fig. 6. Dicer deletion in astrocytes inhibits remyelination after lysolecithin-induced demyelination. **A** Schematic diagram of the time course of tamoxifen (TMF) treatment and histology; **B** Counter-immunostaining for GFAP (white arrowheads indicating astrocytes in **B**). Scale bars, 50 μm (middle and left panels) and 20 μm (right panels); **C** Schematic diagram showing the time course of tamoxifen (TMF) treatment, lysolecithin injection, and histology. Representative images and quantification of MBP expression in the lesion (dotted areas) reveal cumulative nuclei (DAPI). Scale bar, 200 μm. **D, E** Representative images and quantification of CC1- and GFAP-positive cells in the lesion (dotted areas). Scale bars, 50 μm (**D**), 100 μm (**E**). **F** mGFP in the SVZ and counter-immunostaining for NG2 (OPCs) and Olig2 (OLs) in the hGFAP-CreERT; mT/mG brain. Scale bar, 50 μm. Error bars represent the mean ± SEM. *$P < 0.05$, Student's t-test, Dicer-cKO vs control, n = 3–4 for all experiments.

suggesting that Dicer deletion in astrocytes also inhibits remyelination after lysolecithin lesions. In support of this finding, the CC1-positive cell density was also significantly lower in the Dicer-cKO lesions than in the wild-type controls (Fig. 6D). Immunostaining for GFAP revealed increased astroglial area of the Dicer-cKO lesion, implying astrogliosis induced by Dicer deletion (Fig. 6E). It was notable that hGFAP-CreERT also induced recombination in the SVZ progenitors, and approximately 10% of SVZ cells expressed mGFP. Since SVZ neural progenitors can migrate to the lesions and differentiate into OPCs, contributing to remyelination, we next examined if any OLs in the lesions were derived from mGFP-positive cells (Fig. 6F). Immunostaining for NG2 or Olig2 did not show any mGFP-positive cells co-expressing NG2 or Olig2 (Fig. 6F), indicating that the SVZ progenitors were unlikely to differentiate into OLs and contribute to remyelination after lysolecithin-induced demyelination in this case. Therefore, our results indicated that Dicer deletion in astrocytes during adulthood caused astrogliosis and inhibited OL differentiation after lysolecithin-induced demyelination.

Discussion

Astrocytes play an important role in governing CNS development [26, 27]. The functional importance of Dicer in OLs [28], microglia, and neurons has been extensively investigated [29, 30]. Here, we used the hGFAP-CreERT line to induce recombination in the developing and adult CNS. Revealed by the mT/mG reporter line, hGFAP-CreERT can drive an efficient and astrocyte-specific recombination without leaking into other cell types in the postnatal CNS. Previous reports have shown that the conditional Dicer deletion driven by hGFAP-Cre or mGFAP-Cre results in severe functional deficits, such as ataxia and seizures, and premature deaths of the mutant mice [16], while the Dicer deletion in the developing CNS causes memory and motor coordination deficits in adulthood without severe dysfunctions. The differences were probably due to the non-specific Dicer deletion in astrocytes, neurons and OLs by hGFAP-Cre and mGFAP-Cre [19, 31]. It remains largely unknown how Dicer deletion in astrocytes impairs neurofunctions in this case. Given that hypomyelination may disrupt synaptogenesis and cause long-term functional deficits [32] and we demonstrated that Dicer deletion in astrocytes causes hypomyelination in the developing CNS, it is possible that the hypomyelination may also contribute, at least partially, to functional abnormalities in the Dicer-cKO mice. Regarding the functional importance of astrocytes in supporting neurons and regulating neuronal synaptogenesis, it also highly probable that Dicer deletion in astrocytes could directly affect neuronal functions and be involved in the functional deficits in the Dicer-cKO mice [16, 17]. It is notable that Dicer deletion in astrocytes during adulthood seems unlikely to cause instant functional deficits, suggesting that Dicer deletion in adult astrocytes may not impart acute and severe damage to neuronal function.

Evidence has shown that astrocytes and OLs are closely associated during CNS development. Elimination of astrocytes in developing CNS causes OL death and disrupts myelination in the developing CNS, indicating that astrocytes are functionally required for OL survival [15]. Astrocytes can support myelination through both cell-to-cell communication and secretory mechanisms. Previously, we and others have shown that astrocytes can provide nutrients to OPCs by gap junctions, and deletion of Connexin 43 in astrocytes inhibits astrogliosis and promotes remyelination [33–35]. Further, astrocytes can also produce a number of growth factors, like CNTF and PDGF, to support OL proliferation and myelination [36, 37]. Thus, it is also possible that the Dicer deletion in astrocytes might diminish the support for OL differentiation and myelination. Since Dicer deletion can cause astrogliosis and overactivation in the developing and adult CNS, it is plausible that the aberrant astroglial changes may disrupt the supporting functions for OL differentiation and myelination. Together, this study has demonstrated that Dicer in astrocytes is required for OL myelination and neurofunction development.

Acknowledgements We thank Mrs. Yu Sun for her kind assistance in preparing specimens for electron microscopy and Dr. Christian Giaume for his providing of hGFAP-CreERT mice. This work was supported by the Chongqing Education Commission Fund (CXQT19009) and Chongqing Outstanding Young Investigator Fund Project (cstc2019jcyjjqx0001), the Open Project Program of the Brain and Intelligence Research Key Laboratory of Chongqing Education Commission of China (BIR2019002), the Chongqing Scientific and Technical Innovation Foundation of China (CSTCKJCXLJRC07), and the National Natural Science Foundation of China (31970921).

Conflict of interest The authors have no competing financial interests to declare.

References

1. Sofroniew MV, Vinters HV. Astrocytes: biology and pathology. Acta Neuropathol 2010, 119: 7–35.
2. Suzuki A, Stern SA, Bozdagi O, Huntley GW, Walker RH, Magistretti PJ. Astrocyte-neuron lactate transport is required for long-term memory formation. Cell 2011, 144: 810–823.
3. Bélanger M, Allaman I, Magistretti PJ. Brain energy metabolism: Focus on astrocyte-neuron metabolic cooperation. Cell Metab 2011, 14: 724–738.
4. Falkowska A, Gutowska I, Goschorska M, Nowacki P, Chlubek D, Baranowska-Bosiacka I. Energy metabolism of the brain, including the cooperation between astrocytes and neurons, especially in the context of glycogen metabolism. Int J Mol Sci 2015, 16: 25959–25981.
5. Colangelo AM, Alberghina L, Papa M. Astrogliosis as a therapeutic target for neurodegenerative diseases. Neurosci Lett 2014, 565: 59–64.
6. Glass CK, Saijo K, Winner B, Marchetto MC, Gage FH. Mechanisms underlying inflammation in neurodegeneration. Cell 2010, 140: 918–934.
7. Sherman DL, Brophy PJ. Mechanisms of axon ensheathment and myelin growth. Nat Rev Neurosci 2005, 6: 683–690.
8. Hartline DK, Colman DR. Rapid conduction and the evolution of giant axons and myelinated fibers. Curr Biol 2007, 17: R29–R35.
9. Miron VE. Microglia-driven regulation of oligodendrocyte lineage cells, myelination, and remyelination. J Leukoc Biol 2017, 101: 1103–1108.
10. Lundgaard I, Osório MJ, Kress BT, Sanggaard S, Nedergaard M. White matter astrocytes in health and disease. Neuroscience 2014, 276: 161–173.
11. Orthmann-Murphy JL, Abrams CK, Scherer SS. Gap junctions couple astrocytes and oligodendrocytes. J Mol Neurosci 2008, 35: 101–116.
12. Padovani-Claudio DA, Liu L, Ransohoff RM, Miller RH. Alterations in the oligodendrocyte lineage, myelin, and white matter in adult mice lacking the chemokine receptor CXCR2. Glia 2006, 54: 471–483.
13. Jiang P, Chen C, Liu XB, Pleasure DE, Liu Y, Deng W. Human iPSC-derived immature astroglia promote oligodendrogenesis by increasing TIMP-1 secretion. Cell Rep 2016, 15: 1303–1315.
14. Meyer-Franke A, Shen S, Barres BA. Astrocytes induce oligodendrocyte processes to align with and adhere to axons. Mol Cell Neurosci 1999, 14: 385–397.
15. Tognatta R, Karl MT, Fyffe-Maricich SL, Popratiloff A, Garrison ED, Schenck JK, *et al.* Astrocytes are required for oligodendrocyte survival and maintenance of myelin compaction and integrity. Front Cell Neurosci 2020, 14: 74.
16. Howng SY, Huang Y, Ptáček L, Fu YH. Understanding the role of dicer in astrocyte development. PLoS One 2015, 10: e0126667.
17. Sun C, Zhu L, Ma R, Ren J, Wang J, Gao S, *et al.* Astrocytic miR-324-5p is essential for synaptic formation by suppressing the secretion of CCL5 from astrocytes. Cell Death Dis 2019, 10: 141.
18. Felts PA, Woolston AM, Fernando HB, Asquith S, Gregson NA, Mizzi OJ, *et al.* Inflammation and primary demyelination induced by the intraspinal injection of lipopolysaccharide. Brain 2005, 128: 1649–1666.
19. Hong P, Jiang M, Li H. Functional requirement of dicer1 and miR-17-5p in reactive astrocyte proliferation after spinal cord injury in the mouse. Glia 2014, 62: 2044–2060.
20. Hirrlinger PG, Scheller A, Braun C, Hirrlinger J, Kirchhoff F. Temporal control of gene recombination in astrocytes by transgenic expression of the tamoxifen-inducible DNA recombinase variant CreERT2. Glia 2006, 54: 11–20.
21. Wang F, Ren SY, Chen JF, Liu K, Li RX, Li ZF, *et al.* Myelin degeneration and diminished myelin renewal contribute to age-related deficits in memory. Nat Neurosci 2020, 23: 481–486.
22. Vorhees CV, Williams MT. Morris water maze: Procedures for assessing spatial and related forms of learning and memory. Nat Protoc 2006, 1: 848–858.
23. Brooks SP, Dunnett SB. Tests to assess motor phenotype in mice: A user's guide. Nat Rev Neurosci 2009, 10: 519–529.
24. Mei F, Mayoral SR, Nobuta H, Wang F, Desponts C, Lorrain DS, *et al.* Identification of the kappa-opioid receptor as a therapeutic target for oligodendrocyte remyelination. J Neurosci 2016, 36: 7925–7935.
25. Mei F, Wang H, Liu S, Niu J, Wang L, He Y, *et al.* Stage-specific deletion of Olig2 conveys opposing functions on differentiation and maturation of oligodendrocytes. J Neurosci 2013, 33: 8454–8462.
26. Molofsky AV, Krencik R, Ullian EM, Tsai HH, Deneen B, Richardson WD, *et al.* Astrocytes and disease: A neurodevelopmental perspective. Genes Dev 2012, 26: 891–907.
27. Liu JH, Li ZL, Liu YS, Chu HD, Hu NY, Wu DY, *et al.* Astrocytic GABAB receptors in mouse *Hippocampus* control responses to behavioral challenges through astrocytic BDNF. Neurosci Bull 2020, 36: 705–718.
28. Li T, Wang J, Wang H, Yang Y, Wang S, Huang N, *et al.* The deletion of dicer in mature myelinating glial cells causes progressive axonal degeneration but not overt demyelination in adult mice. Glia 2018, 66: 1960–1971.
29. Varol D, Mildner A, Blank T, Shemer A, Barashi N, Yona S, *et al.* Dicer deficiency differentially impacts microglia of the developing and adult brain. Immunity 2017, 46: 1030-1044.e8.
30. Chmielarz P, Konovalova J, Najam SS, Alter H, Piepponen TP, Erfle H, *et al.* Dicer and microRNAs protect adult dopamine neurons. Cell Death Dis 2017, 8: e2813.
31. Chen X, Wang F, Gan J, Zhang Z, Liang X, Li T, *et al.* Myelin deficits caused by Olig2 deficiency lead to cognitive dysfunction and increase vulnerability to social withdrawal in adult mice. Neurosci Bull 2020, 36: 419–426.
32. Wang F, Yang YJ, Yang N, Chen XJ, Huang NX, Zhang J, *et al.* Enhancing oligodendrocyte myelination rescues synaptic loss and improves functional recovery after chronic hypoxia. Neuron 2018, 99: 689-701.e5.
33. Li T, Niu J, Yu G, Ezan P, Yi C, Wang X, *et al.* Connexin 43 deletion in astrocytes promotes CNS remyelination by modulating local inflammation. Glia 2020, 68: 1201–1212.
34. Rash JE, Yasumura T, Dudek FE, Nagy JI. Cell-specific expression of connexins and evidence of restricted gap junctional coupling between glial cells and between neurons. J Neurosci 2001, 21: 1983–2000.
35. Niu JQ, Li T, Yi CJ, Huang NX, Koulakoff A, Weng CH, *et al.* Connexin-based channels contribute to metabolic pathways in the oligodendroglial lineage. J Cell Sci 2016, 129: 1902–1914.
36. Stankoff B, Aigrot MS, Noël F, Wattilliaux A, Zalc B, Lubetzki C. Ciliary neurotrophic factor (CNTF) enhances myelin formation: A novel role for CNTF and CNTF-related molecules. J Neurosci 2002, 22: 9221–9227.
37. Modi KK, Sendtner M, Pahan K. Up-regulation of ciliary neurotrophic factor in astrocytes by aspirin: Implications for remyelination in multiple sclerosis. J Biol Chem 2013, 288: 18533–18545.

Neurosci. Bull. August, 2021, 37(8):1147–1159
https://doi.org/10.1007/s12264-021-00700-0

www.neurosci.cn
www.springer.com/12264

ORIGINAL ARTICLE

Hippocampal Interneurons are Required for Trace Eyeblink Conditioning in Mice

Wei-Wei Zhang[1] · Rong-Rong Li[1] · Jie Zhang[1] · Jie Yan[1] · Qian-Hui Zhang[2] · Zhi-An Hu[1] · Bo Hu[1,3] · Zhong-Xiang Yao[1] · Hao Chen[4]

Received: 12 October 2020 / Accepted: 22 December 2020 / Published online: 15 May 2021

Abstract While the hippocampus has been implicated in supporting the association among time-separated events, the underlying cellular mechanisms have not been fully clarified. Here, we combined *in vivo* multi-channel recording and optogenetics to investigate the activity of hippocampal interneurons in freely-moving mice performing a trace eyeblink conditioning (tEBC) task. We found that the hippocampal interneurons exhibited conditioned stimulus (CS)-evoked sustained activity, which predicted the performance of conditioned eyeblink responses (CRs) in the early acquisition of the tEBC. Consistent with this, greater proportions of hippocampal pyramidal cells showed CS-evoked decreased activity in the early acquisition of the tEBC. Moreover, optogenetic suppression of the sustained activity in hippocampal interneurons severely impaired acquisition of the tEBC. In contrast, suppression of the sustained activity of hippocampal interneurons had no effect on the performance of well-learned CRs. Our findings highlight the role of hippocampal interneurons in the tEBC, and point to a potential cellular mechanism subserving associative learning.

Keywords Hippocampus · Interneuron · Trace eyeblink conditioning · Sustained activity · Associative learning

Introduction

Learning to associate two events that occur separately in time is critical for animals to produce behavioral responses with appropriate timing and strength [1, 2]. Research has identified the neural mechanisms underlying associative learning [3, 4], but how this time-linked memory is acquired is not yet fully understood.

Evidence has accumulated that the hippocampus is one of the brain areas critically involved in associative learning. For instance, lesions of the dorsal hippocampus before training prevents subsequent associative learning [5–9]. Likewise, blockade of NMDA receptors in the dorsal hippocampus severely impairs the learning of associations between time-separated stimuli [10, 11]. Consistent with these lesion and inactivation studies, *in vivo* electrophysiological recordings show that a group of hippocampal pyramidal cells exhibits elevated activity and encodes information about discontiguous sets of stimuli [12]. Therefore, it has been hypothesized that the hippocampus functions to form associations between time-separated events, thereby supporting associative learning [2, 13].

Supplementary Information The online version contains supplementary material available at https://doi.org/10.1007/s12264-021-00700-0.

✉ Bo Hu
bohu@tmmu.edu.cn

✉ Zhong-Xiang Yao
yaozhx@yahoo.com

✉ Hao Chen
haochen@tmmu.edu.cn

[1] Department of Physiology, College of Basic Medical Sciences, Army Medical University, Chongqing 400038, China

[2] Department of Foreign Language, College of Basic Medical Sciences, Army Medical University, Chongqing 400038, China

[3] Brain and Intelligence Research Key Laboratory of Chongqing Education Commission, Army Medical University, Chongqing 400038, China

[4] Experimental Center of Basic Medicine, College of Basic Medical Sciences, Army Medical University, Chongqing 400038, China

Nevertheless, the contribution of distinct neuronal subtypes to associative learning remains unknown. The hippocampus contains a large number of GABAergic interneurons [14–16]. They play key roles in modulating the integration of synaptic inputs [17–19] and shaping the outputs of pyramidal cells [20], thus giving rise to oscillatory activity at different frequency bands [21–24]. These forms of network oscillatory activity are strongly correlated with associative learning performance [25, 26]. The above findings support the idea that the hippocampal interneurons participate in associative learning. However, there is still a lack of direct evidence illustrating whether and how the hippocampal interneurons are involved in associative learning.

To address this issue, we combined multiple-unit recordings and optogenetic techniques to measure and manipulate the firing activity of hippocampal interneurons while the freely-moving mice performed a hippocampus-dependent trace eyeblink conditioning (tEBC) task [7]. This type of conditioning is an ideal model in which to study the neural mechanisms of associative learning, because of its convenience in precisely controlling the delivery of a conditioned stimulus (CS; e.g., a light flash or a pure tone) and a reinforcing unconditioned stimulus (US; e.g., a corneal air-puff or a cutaneous electrical shock to the eyelid) [13]. Our results revealed the dynamic changes of CS-evoked sustained activity in hippocampal interneurons across distinct stages of tEBC acquisition. Moreover, we establish the causal relationship between the sustained activity of hippocampal interneurons and tEBC acquisition, verifying a pivotal role of hippocampal interneurons in this process. These findings thus extend the current knowledge of the cellular mechanisms underlying hippocampal involvement in associative learning.

Materials and Methods

Subjects

All experimental procedures were approved by the Animal Care Committee of Army Medical University. Wild-type C57/BL6 mice (n = 23, 3–6 months old, 20–25 g, both genders) were used as the subjects. In addition, optogenetic experiments were performed in GAD2-Cre mice (Stock no. 028867, Jackson Laboratory, USA, n = 20, 3–6 months old, 20–25 g, both genders) injected with either AAV2-CAG-FLEX-ArchT-GFP or AAV2-EF1α-DIO-GFP. Before the experiments and between the recording sessions, the mice were individually housed under a 12-h light-dark cycle with free access to food and water. All experiments were conducted between 8:00 and 20:00.

Multiple Units Recording

The mice were anesthetized with isoflurane (0.6%–1.0% by volume in O_2). The tungsten tetrodes (bare diameter, 20 μm; insulated diameter, 25 μm; California Fine Wire, USA) were implanted targeting the CA1 area of the left dorsal hippocampus (AP: − 1.9 mm, ML: − 1.65 mm, DV: 0.7 mm−0.8 mm from bregma). During 5–7 days of postoperative recovery, the tetrodes were moved (approximately 70 μm/day) until they reached the pyramidal cell layer characterized by a large-amplitude sharp wave-ripple (SWR). *In vivo* electrophysiological signals were continuously recorded at 20 kHz using a RHD2000 interface board (Intan Technology, C3334) and stored for offline analysis [27]. The local field potential in the dorsal hippocampus was sampled at 1250 Hz. All of the electrophysiological data were visualized using NeuroScope software (http://neurosuite.sourceforge.net) [28]. After each experiment, the brain was extracted for histological analysis.

Behavioral Procedure

Following postoperative recovery, the mice were adapted to a containing box (45 cm × 25 cm × 20 cm) and the preamplifier plug-in and plug-out procedures, ensuring they behaved naturally during training and recording. The habituated mice were given daily behavioral training. For trace eyeblink conditioning (tEBC) training, the CSs were LED pulses of blue light flashes (150-ms in duration), while the USs were 100-ms air-puffs directed to the left cornea. The CS offset was separated from the US onset by a 250-ms trace interval. Daily tEBC training consisted of 100 CS–US paired presentation trials. The inter-trial interval (ITI) varied from 18 to 28 s with a mean value of 23 s. Pseudo-conditioned mice received 100 CSs and 100 USs per training day (mean ITI = 11.5 s), but the two stimuli were explicitly unpaired. All mice were trained for 4 consecutive days.

Virus Injection and Diode-tetrode Assembly Implantation

Either AAV2-CAG-FLEX-ArchT-GFP or AAV2-EF1α-DIO-GFP (OBiO, China) was injected bilaterally into the hippocampus of GAD2-Cre mice (AP: − 1.9 mm, ML: ± 1.25, 1.50, and 1.75 mm, DV: 1.10 mm; 150 nL per site) using a microinjector (Nanoject II, Drummond Scientific). After the injection, the craniotomy was covered by low-viscosity silicone (Kwik-Cast^{TM}, WPI) and the skin was sutured. After 4 weeks of post-injection viral expression, diode-tetrode assemblies were implanted bilaterally into the dorsal hippocampus of GAD2-cre mice (AP: − 1.9

mm, ML: ± 1.6 mm, DV: 1.0 mm). Fabrication of the diode-tetrode assembly has been previously described in detail [29]. Briefly, a 200-μm optic fiber (0.37 NA, FT200EMT, Thorlabs, Germany) was combined with the tetrode array. The light power was measured with an optical power meter (PM100D, Thorlabs). After the surgery, the mice were individually housed and allowed to recover for 5–7 days.

Optogenetic Manipulation

During tEBC training, laser stimulation was delivered through the optical fibers. Laser diodes were activated by a driver (LDC–205C, Thorlabs) under the control of a pulse generator (Pulse Pal, Sanworks) [30]. The green laser (520 nm in wavelength; 15 mW/mm^2–25 mW/mm^2 at the fiber tip) was triggered by the CS and lasted for 400-ms in each trial to cover the periods of both the CS and trace interval.

Data Analysis

EMG Analysis

The electromyography (EMG) signal from the left upper orbicularis oculi muscle was used to detect eyelid movement [31]. The eyeblink response was defined based on an algorithm as follows: (1) EMG data were collected, rectified and integrated with a time constant of 1-ms; (2) 300-ms EMG amplitude values before the CS onset were averaged cross 100 trials in each session to quantify the daily baseline and standard deviation (SD); (3) an invalid trial was identified when the 300-ms EMG amplitude values were at least 4 SDs above the daily baseline, otherwise a valid trial was identified; (4) significant eyeblink responses were detected in the valid trails in which the EMG amplitude exceeded the baseline by 4 SDs for at least 25-ms; and (5) an eyeblink response detected during 51-ms–400-ms after the CS onset was counted as a conditioned eyeblink response (CR).

Spike Sorting

The spikes were sorted using the procedures introduced in our recent report [32]. In brief, the spikes were extracted from high-pass filtered signals off-line, and their waveforms projected onto a common basis obtained by principal component analysis of the filtered data. Single-unit spikes were isolated off-line using both semi-automatic clustering with KlustaKwik software (http://klustakwik.sourceforge.net/) and manual clustering with Klusters software (http://neurosuite.sourceforge.net/). The accuracy of unit clustering was further verified by confirming the presence of a 2-ms refractory period devoid of spikes in the autocorrelogram of a putative single unit [28].

Unit Classification

Single units were classified into either putative pyramidal cells (Pyrs) or interneurons (INs) based on their firing rate and waveform (i.e., the trough-to-peak duration and spike width). Units with an average firing rate <6 Hz and a peak-to-trough duration >0.35-ms were classified as putative Pyrs, while units with an average firing rate ≥6 Hz and a peak-to-trough duration ≤0.35-ms were classified as putative INs [29, 33]. The spikes recorded during each valid trial were assigned to 50-ms time bins, beginning 1000-ms before and extending 1000-ms after the CS onset. The firing rate (FR) for each bin across all valid trials was calculated. The mean FR for the 20 bins before the CS onset was used as the baseline, and their SDs were computed. The firing rate of each bin was normalized by using the Z score as follows (#bin refers to an arbitrary time bin):

$$Z = \left(FR_{\#\text{bin}} - \text{mean } FR_{\text{baseline}}\right) / \text{SD } (FR_{\text{baseline}}).$$

Histology

Electrolytic lesions (30-μA for 10 s, DC current) were made following the electrophysiology experiments to confirm the recording site of the tetrode assembly. 48 h later, the mice were transcardially perfused with 4% paraformaldehyde (PFA; prepared in 0.1 mol/L phosphate buffer, pH 7.4). After post-fixation with 4% PFA for 8 h followed by dehydration with 30% sucrose PBS for 48 h, each brain was cut into 50-μm coronal sections (CM1900, Leica) and immune-stained with DAPI to visualize nuclei.

GAD2-Cre mice were transcardially perfused immediately following the optogenetic experiments to confirm the viral expression and optical fiber position. 50-μm coronal sections were cut using the above procedure. The sections were prepared for 1-h permeabilization with 0.5% TritonX-100 in PBS followed by 1 h blocking with 5% BSA. Afterwards, the sections were incubated overnight with rabbit antibody to GABA (1:800, A2052, Stock no. A2052, Sigma, USA) at 4 °C followed by 2 h incubation with Alexa Fluor 568-conjugated donkey antibody to rabbit (1:800, Stock no. A10042, Thermo Scientific, USA) at room temperature. The sections were incubated with DAPI and mounted in Fluoromount (stock no. 0100-01, Southern Biotech). All sections were imaged using a fluorescence microscope (BX53, Olympus, Japan).

Statistics

Data are expressed as the mean ± SEM unless otherwise noted. We first tested the normality of each dataset using Shapiro-Wilk test. Parametric tests were used if the dataset passed the normality test. Otherwise, the Wilcoxon rank sum test was used. The statistical significance for behavioral analysis was determined by one-way or two-way ANOVAs with repeated measures. Difference in firing activity between two groups (paired *vs* unpaired) was determined by the independent *t* test (2-tailed). Paired *t* tests were used to determine the significance of differences in firing activity between two states (CR *vs* no-CR) and the effect of optogenetic manipulation on the performance of well-learned CRs. A value of $P < 0.05$ was considered to be significant for all tests. Significance levels of data are denoted as $^{*}P < 0.05$, $^{**}P < 0.01$, and $^{***}P < 0.001$. $P > 0.05$ was considered to be not-significant and is denoted as *n.s*.

Results

Behavioral Performance

To examine tEBC task-related interneuron activity in the dorsal hippocampus, we trained the freely-moving mice to acquire tEBC, in which a 250-ms trace interval was inserted between the light CS and the air-puff US (Fig. 1A). We found that the mice receiving CS-US paired presentations learned this task and exhibited adaptive CRs to the light CSs (Fig. 1A). This was further supported by the statistical results that the mice with CS-US paired training showed significant increases in the CR incidence and peak amplitude across 4 training days (paired group, $n = 12$ mice, CR incidence: $F_{3,\ 33} = 7.678$, $P = 0.001$; CR peak amplitude: $F_{3,\ 33} = 3.785$, $P = 0.019$, one-way ANOVAs with repeated measures, Fig. 1B, C). On average, the CR incidence increased from 44.1% ± 4.9% on day1 to 64.1% ± 5.8% on day 4. In contrast, the mice with unpaired training showed no sign of learning, as evidenced by the decreased CR levels across 4 training days (unpaired group, $n = 11$ mice, CR incidence: $F_{3,\ 30} = 4.893$, $P = 0.007$; peak amplitude: $F_{3,\ 30} = 2.831$, $P = 0.055$, one-way ANOVAs with repeated measures). Moreover, our statistical analysis revealed that the mice with paired training exhibited higher CR levels than those with unpaired training (main effects, CR incidence: $F_{1,\ 21} = 26.794$, $P < 0.001$; CR peak amplitude: $F_{1,\ 21} = 6.367$, $P = 0.020$; Interaction, CR incidence: $F_{3,\ 63} = 2.057$, $P = 0.115$; CR peak amplitude: $F_{3,\ 63} = 1.954$, $P = 0.222$, two-way ANOVAs with repeated measures, Fig. 1B, C). These results indicated that tEBC was acquired in the CS-US mice with paired training across 4 training days. It should be noted that the higher CR level was unlikely to result from better learning in the mice with paired training because they showed CR scores similar to those of the mice with unpaired training at the beginning of training on day 1 (Fig. S1).

In vivo Electrophysiological Identification of Putative Interneurons

We identified the recorded hippocampal units as either putative interneurons (INs) or putative pyramidal cells (Pyrs) by discharge rates and the spike waveform. Recording in the dorsal hippocampus was determined by both *post hoc* histological examination (Fig. 2A) and the large amplitude of sharp wave-ripples (Fig. S2). Hippocampal INs have been reported to exhibit high discharge rates (>6 Hz) and narrow spike width (valley-to-peak width ≤0.35-ms) [29, 33]. By using these criteria, 104 putative INs were identified in the mice with CS-US paired presentation (across 12 mice, average 8.7 units per mouse, Fig. 2B), and 63 putative INs were identified in the mice with unpaired training (across 11 mice, average 5.7 units per mouse, Fig. 2B). There were no significant differences in either average firing rate or spike width of putative INs between the mice with paired and unpaired training (average firing rate, paired group: 16.5 ± 1.4 Hz, unpaired group: 15.8 ± 1.2 Hz, $t_{21} = 0.397$, $P = 0.695$, Fig. 2C; spike width, paired group: 0.257 ± 0.008-ms, unpaired group: 0.258 ± 0.012 ms, $t_{21} = -0.051$, $P = 0.960$, independent *t* tests, Fig. 2D). It should be noted that, in the current study, 997 putative Pyrs were identified in the mice with CS-US paired training (across 12 mice, average 83.1 units per mouse, Fig. 2B), and 725 putative Pyrs were identified in the unpaired mice (across 11 mice, average 65.9 units per mouse, Fig. 2B).

Hippocampal Interneurons Show Sustained Activity During tEBC

We examined the characteristics of hippocampal IN activity during tEBC training. Strong CS-evoked firing activity was recorded in the INs (Fig. 3A), and it did not cease until the trace interval period (Fig. 3B). On the first 2 days, there were no significant differences in the baseline activity of INs between the mice with paired and unpaired training (day 1: $t_{42} = 1.137$, $P = 0.262$; day 2: $t_{43} = 0.349$, $P = 0.729$; independent *t* tests, Fig. 3D). However, the CS-evoked sustained activity of INs in mice with paired-training was greater than in those with unpaired training (average *Z* score, day 1: $t_{42} = 2.070$, $P = 0.045$; day 2: $t_{43} = 2.128$, $P = 0.039$; maximum *Z* score, day 1: $t_{42} = 2.039$, $P = 0.048$; day 2: $t_{43} = 2.364$, $P = 0.023$; independent *t* tests, Fig. 3C–E). Moreover, on the first 2 days, we found a

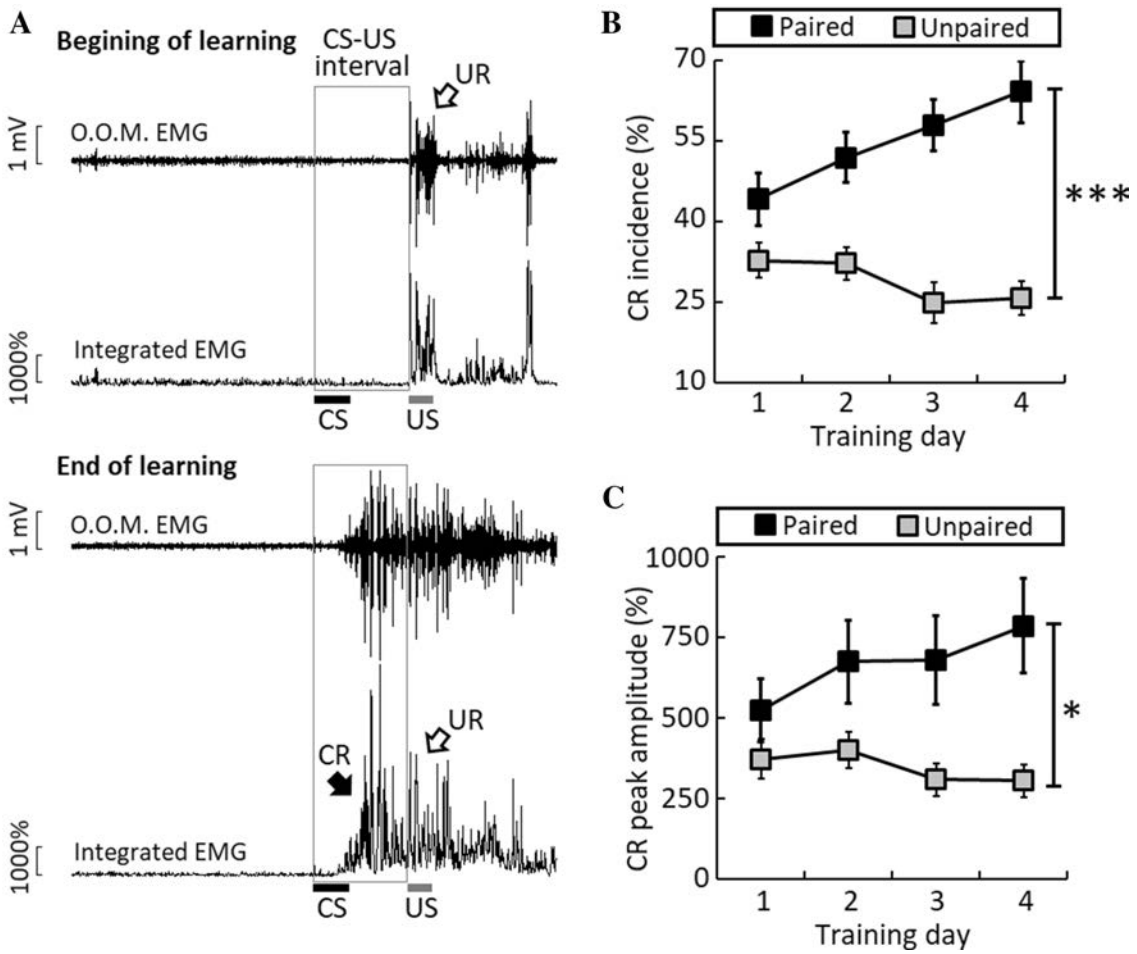

Fig. 1 Acquisition of trace eyeblink conditioning in freely-moving mice. **A** Example of eyelid responses from a mouse before (upper) and after learning (lower). The CS was a 150-ms LED light, while the US was a 100-ms air-puff to the cornea. The interval between the CS offset and the US onset was 250-ms. The top trace of each panel shows the raw orbicularis oculi muscle (O.O.M.) EMG, while the bottom trace shows the integrated EMG. **B**, **C** CR incidence (**B**) and CR peak amplitude (**C**) from the paired (n = 12, black squares) and unpaired (n = 11, grey squares) trained mice across 4 training days. Data are expressed as the mean ± SEM (*P <0.05, ***P <0.001, two-way ANOVAs with repeated measures).

greater proportion of sustained active INs in the paired-training mice than in the unpaired-training mice (paired group: 96.2% (51 of 53 units) *vs* unpaired group: 61.1% (22 of 36 units), $\chi^2 = 17.927$, $df = 1$, $P < 0.001$, Pearson χ^2 test, Fig. 3C). These results suggest that hippocampal INs manifest strong CS-evoked sustained activity during the early acquisition of tEBC.

On days 3 and 4, however, the CS-evoked sustained activity of hippocampal interneurons in paired-training mice tended to diminish (Fig. 3C). This activity on day 4 was lower than on day 1 (average Z score, day 1 *vs* day 4: $t_{47} = 2.408$, $P = 0.020$; maximum Z score, day1 *vs* day 4: $t_{47} = 1.567$, $P = 0.124$; independent t tests, Fig. 3C–E). Moreover, no significant differences in the CS-evoked sustained activity of INs were found between the paired and unpaired training mice (average Z score, day 3: $t_{42} = 0.384$, $P = 0.703$; day 4: $t_{32} = -0.547$, $P = 0.194$; maximum Z score, day 3: $t_{42} = 1.872$, $P = 0.075$; day 4: $t_{32} = 1.326$, $P = 0.194$; independent t tests, Fig. 3C–E). Likewise, comparable proportions of sustained active INs were found between the paired and unpaired training mice (paired group: 82.4% (42 of 51 units) *vs* unpaired group: 66.7% (18 of 27 units), $\chi^2 = 2.447$, $df = 1$, $P = 0.118$, Pearson χ^2 test, Fig. 3C). These results suggest that stronger CS-evoked sustained activity of hippocampal INs only occurs during the early, rather than the late acquisition of tEBC.

In parallel with greater sustained activity of hippocampal INs during the early acquisition of tEBC, we also recorded decreased CS-evoked firing in putative hippocampal Pyrs. Putative Pyrs in the mice with paired training showed decreased firing activity at 138.0 ± 6.7-ms after the CS onset, and showed a greater decrement in firing than the mice with unpaired training (days 1–2, paired group:

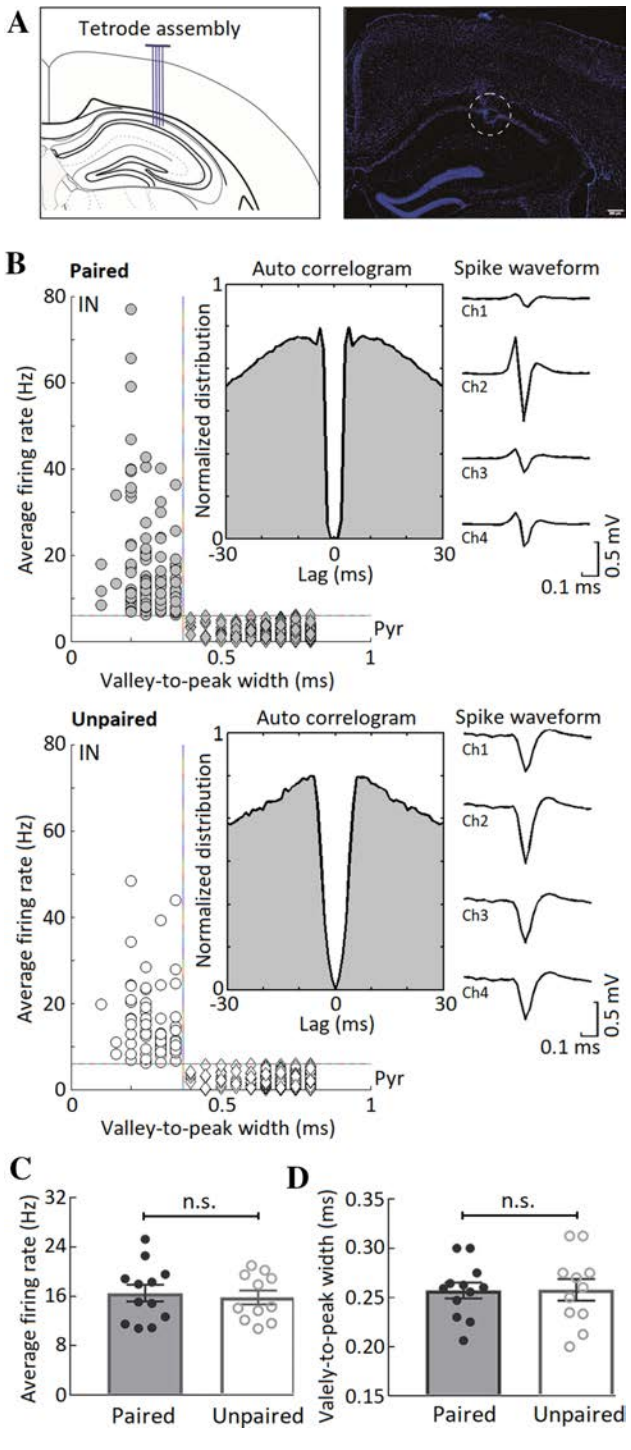

◀**Fig. 2** Classification of hippocampal units into putative interneurons and pyramidal cells. **A** Location of recording sites in the dorsal hippocampus. Left, schematic of tetrode recording in the dorsal hippocampus; right: a DAPI-stained coronal section illustrating a representative recording site in the dorsal hippocampus (dashed circle; scale bar, 200-μm). **B** Scatter plots of valley-to-peak width of spike waveforms *vs* average firing rates for 1101 and 788 hippocampal units isolated from mice with paired (upper, $n = 12$ mice, across 4 sessions) and unpaired training (lower, $n = 11$ mice, across 4 sessions). Representative spike train autocorrelations and spike waveforms of the representative INs from mice with paired and unpaired training. **C** There are no significant differences in the average firing rates of putative INs between the paired ($n = 104$, across 12 mice in 4 sessions) and unpaired trained mice ($n = 63$, across 11 mice in 4 sessions). **D** There are no significant differences in the valley-to-peak widths of putative INs between the paired ($n = 104$, across 12 mice in 4 sessions) and unpaired trained mice ($n = 63$, across 11 mice in 4 sessions). Data are expressed as the mean ± SEM (n.s., not significant, two-tailed independent *t* test).

$n = 68$ units, unpaired group: $n = 51$ units, $t_{117} = -3.197$, $P = 0.002$, independent *t* test, Fig. 4A–C). Again, such a difference in firing activity did not occur in the late acquisition of tEBC (days 3–4, paired group: $n = 98$ units, unpaired group: $n = 68$ units, $t_{164} = -1.224$, $P = 0.223$, independent *t* test, Fig. 4D–F). These results provide further evidence for the stronger inhibition of hippocampal network activity during the early, rather than the late acquisition of tEBC.

Sustained Activity of Hippocampal Interneurons Bias between CR and no-CR States

In the mice with paired training, the hippocampal INs increased their firing activity at 131.0 ± 7.5 ms after the CS onset (Fig. 5A, B), and this was in parallel with the occurrence of the CR. Therefore, we hypothesized that these INs contributed to the CR acquisition. To test this hypothesis, we first compared the sustained activity of the INs between the CR and no-CR states. This showed that, on days 1 and 2, sustained activity of INs in the CR trials was significantly higher than that in the no-CR trials ($n = 53$, average Z score: $t_{52} = 5.368$, $P < 0.001$; maximum Z score: $t_{52} = 5.660$, $P < 0.001$, paired *t* test, Fig. 5B), indicating that sustained IN activity was biased between the CR and no-CR states. In contrast, no significant bias was found in the sustained activity of INs between the CR and no-CR states on days 3 and 4 ($n = 51$, average Z score: $t_{50} = 1.772$, $P = 0.083$; maximum Z score: $t_{50} = 2.695$, $P = 0.0097$, paired *t* test, Fig. 5C). Together, these results suggest that the sustained activity of hippocampal INs is strongly correlated with the CR occurrence during the early stage of tEBC acquisition.

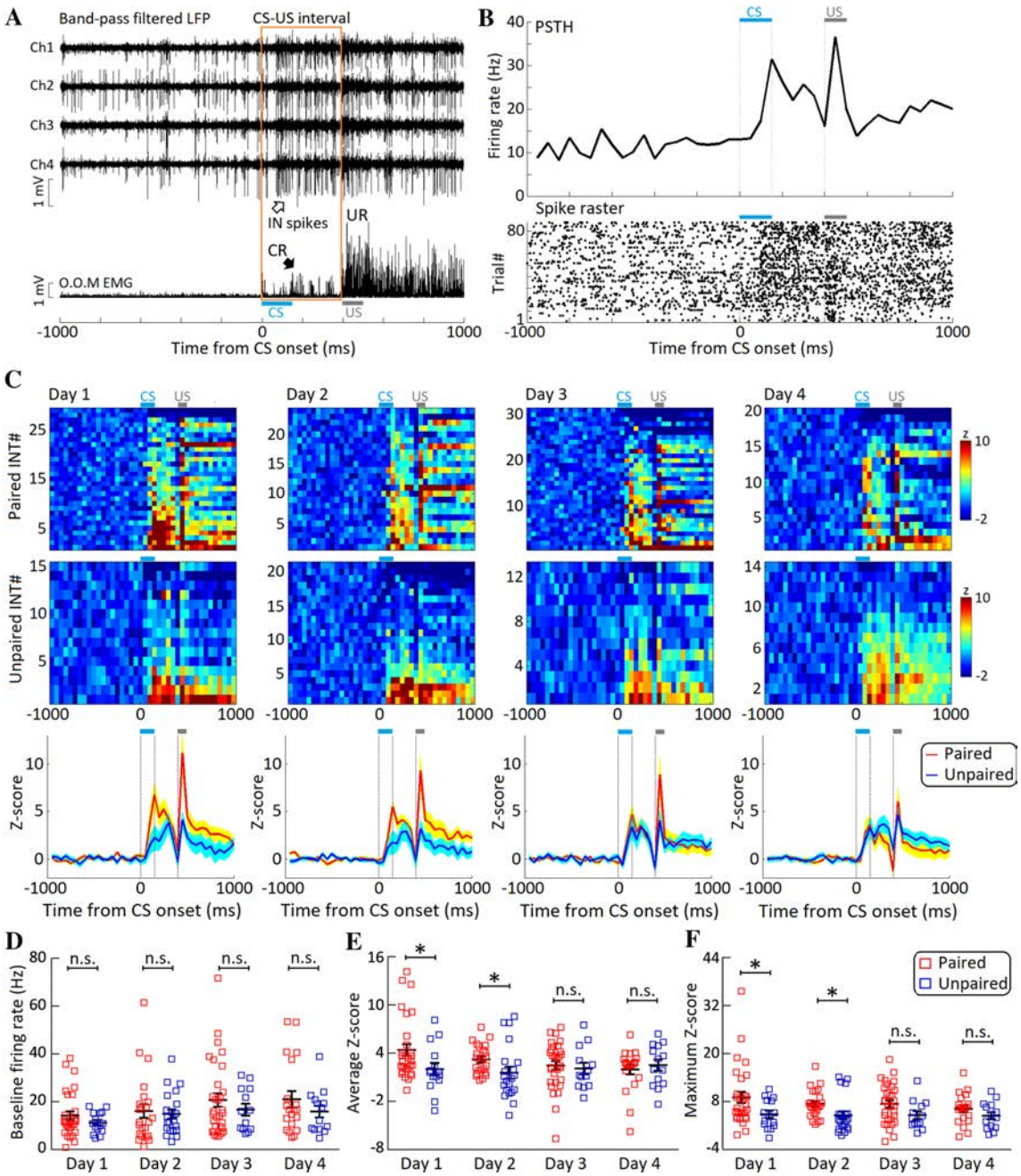

Fig. 3 CS-evoked sustained activity of hippocampal interneurons (INs) during tEBC. **A** Upper, tetrode recording of CS-evoked sustained activity in a representative IN during tEBC training; lower, orbicularis oculi muscle (O.O.M.) EMG trace peristimulus. **B** Peristimulus time histogram (PSTH, upper) and raster plot (lower) of the spiking responses of a representative IN to light CSs. **C** CS-evoked sustained activity of INs in mice with paired and unpaired training across 4 training days. Upper, rows, heatmaps of Z-score-transformed average PSTHs for individual INs; columns, time bins relative to CS onset (50-ms bin-width); lower, plots of the average Z score responses for INs in mice with paired (red) and unpaired (blue) training across 4 training days. **D** Average baseline firing rates of INs in mice with paired (red squares) and unpaired (blue squares) training. **E, F** CS-evoked sustained activity of INs in mice with paired training (red squares) was significantly stronger than that in mice with unpaired training (blue squares) on days 1 and 2. In contrast, CS-evoked sustained activity in INs in mice with paired training (red squares) were comparable to those in mice with unpaired training (blue squares) on days 3 and 4. Data are expressed as the mean ± SEM (*P <0.05, n.s., not significant; two-tailed independent t test).

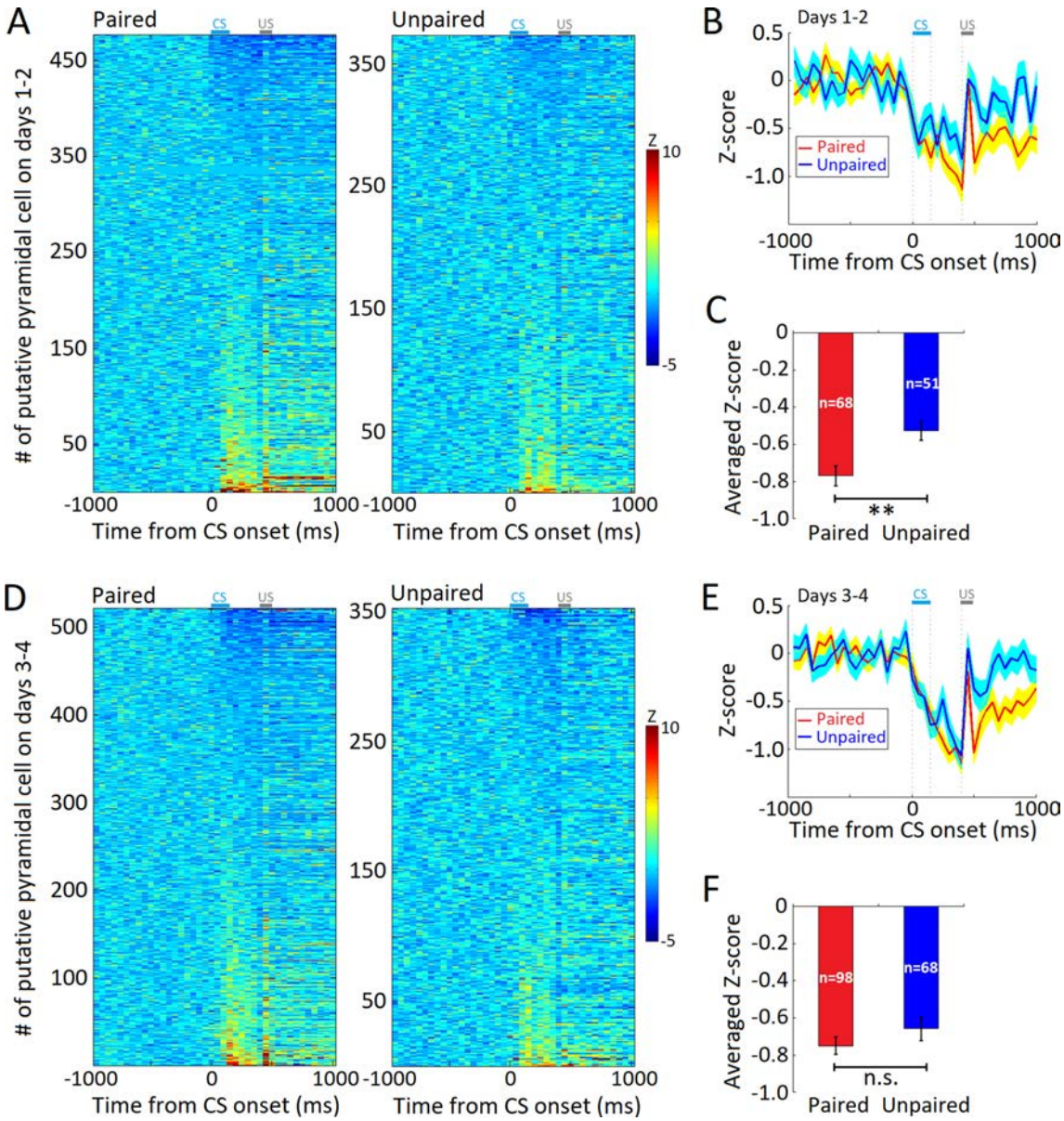

Fig. 4 CS-evoked firing activity of putative pyramidal cells (Pyrs) during tEBC training. **A** Pseudo-colored, baseline normalized peri-CS histograms of all classified Pyrs during the early acquisition of tEBC in mice with paired (left, n = 476) and unpaired training (right, n = 373). Lighter shades represent increases in firing activity. Cells are sorted according to the magnitude of the change in CS-evoked firing activity. **B** Average peri-event responses of CS-evoked decreased firing in Pyrs in the early-learning stage. **C** CS-evoked decrement in firing of Pyrs in mice with paired training is greater than that in mice with unpaired training (days 1–2; paired, n = 68 units; unpaired, n = 51 units, $t_{117} = -3.197$, P = 0.002, independent t test). **D** Pseudo colored, baseline normalized peri-CS histograms of all classified Pyrs during the late acquisition of tEBC in the mice with paired (left, n = 521) and unpaired training (right, n = 352). Lighter shades represent increases in firing activity. Cells are sorted according to the magnitude of the change in CS-evoked firing activity. **E** Average peri-event responses of Pyrs with CS-evoked decreased firing in the late-learning stage. **F** The CS-evoked decrement in firing of Pyrs in mice with paired training is comparable to that in those with unpaired training (days 3–4; paired, n = 98 units, unpaired, n = 68 units, $t_{164} = -1.224$, P = 0.223, independent t test). Data are expressed as the mean ± SEM (**P <0.01, n.s., not significant).

Optogenetic Suppression of Hippocampal Interneurons Impairs the Acquisition of tEBC

The sustained activity of hippocampal INs was correlated with behavioral outcome in terms of CR and no-CR states, indicating that this activity contributes to the acquisition of tEBC. Consequently, we further quantified this contribution by acutely suppressing the firing response. For this purpose, we tested another group of mice, in which the inhibitory opsin ArchT was virally expressed in hippocampal INs (Fig. 6A, B). We found that presentation of 400-ms green laser light after the CS onset suppressed the sustained

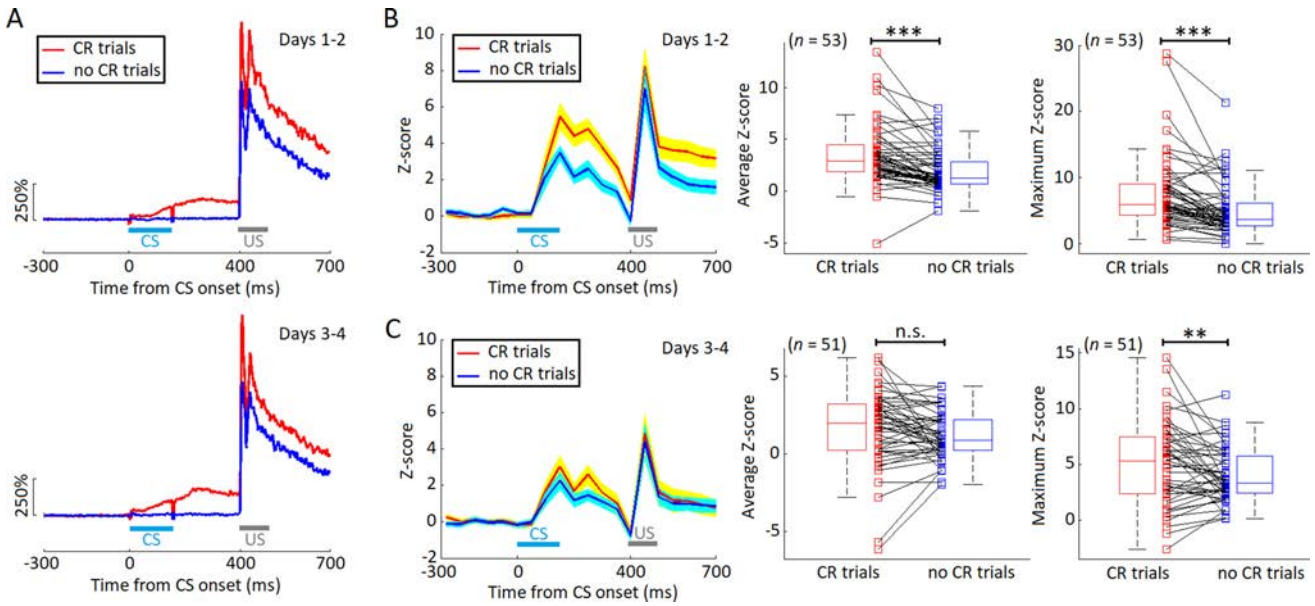

Fig. 5 Hippocampal interneuron (IN) activity in CR *vs* no-CR trials. **A** Average CR (red) and no-CR trials (blue) across mice with CS-US paired training (n = 12) during the early (days 1–2, upper) and late (days 3–4, lower) stages of tEBC acquisition. **B** On days 1 and 2, the sustained activity of INs in the CR trials (red) is significantly stronger than that in the no-CR trials (blue). **C** On days 3 and 4, the sustained activity of INs in the CR trials (red) is comparable to those in the no-CR trials (blue) (***P <0.001, **P <0.01, n.s., not significant, paired t test.

activity of INs (Fig. 6C, D), and suppression of the INs disinhibited (increased) the firing activity of putative Pyrs (Fig. S3). Importantly, suppressing sustained IN activity resulted in a marked impairment of CR acquisition (main effects: CR incidence: $F_{1,\ 12}$ = 14.143, P = 0.003; CR peak amplitude: $F_{1,\ 21}$ = 4.789, P = 0.049; interaction: CR incidence: $F_{1,\ 12}$ = 0.786, P = 0.393; CR magnitude: $F_{1,\ 12}$ = 0.455, P = 0.513, two-way ANOVAs with repeated measures, Fig. 6E–G). These results suggest that sustained activity of hippocampal INs, rather than increased firing activity of Pyrs, is required for the acquisition of tEBC.

Optogenetic Suppression of Hippocampal Interneurons Fails to Impact the Performance of Well-learned CRs

If the sustained activity of hippocampal INs only participates in the early acquisition of tEBC, one would expect that acutely blocking this activity would have minimal effects on the performance of well-learned CRs. We therefore tested another group of GAD2-cre mice that had established a well-learned CR. Since the inhibitory opsin ArchT was virally expressed in dorsal hippocampal INs, we could optogenetically inhibit their sustained activity during the interval between the CS and the US. We found that inhibition of the sustained activity of the INs caused no significant change in the incidence of well-learned CRs (CR incidence: laser on: 67.4 ± 8.2% *vs* laser off: 67.1 ± 6.4%, t_5 = − 0.047, P = 0.965, paired t test, n = 6 mice, Fig. 7), suggesting that the sustained activity of hippocampal INs is not required for the performance of well-learned CRs.

Discussion

In this study, we combined multiple-unit recording and optogenetics to investigate the role of hippocampal INs in a hippocampus-dependent tEBC task. We found that, during the acquisition of tEBC, the INs exhibited CS-evoked firing activity sustained during the time interval between the CS and the US. This activity was correlated with CR performance in a learning stage-specific manner. Moreover, optogenetic suppression of the sustained activity in the INs severely impaired the acquisition of tEBC. In contrast, suppression of this sustained activity had no effect on the performance of well-learned CRs. Our results provide direct evidence that hippocampal INs participate in associative learning *via* CS-evoked sustained activity.

Although the hippocampus is thought to support the association among time-separated events [2, 34–36], the underlying cellular mechanisms are not fully understood. It has been suggested that transgenic mice with altered IN function display impaired associative learning in hippocampus-dependent tasks [37], and the excitability and activity of hippocampal INs are increased with associative learning [38, 39]. We report here associative learning-induced sustained activity in hippocampal INs. The CS-

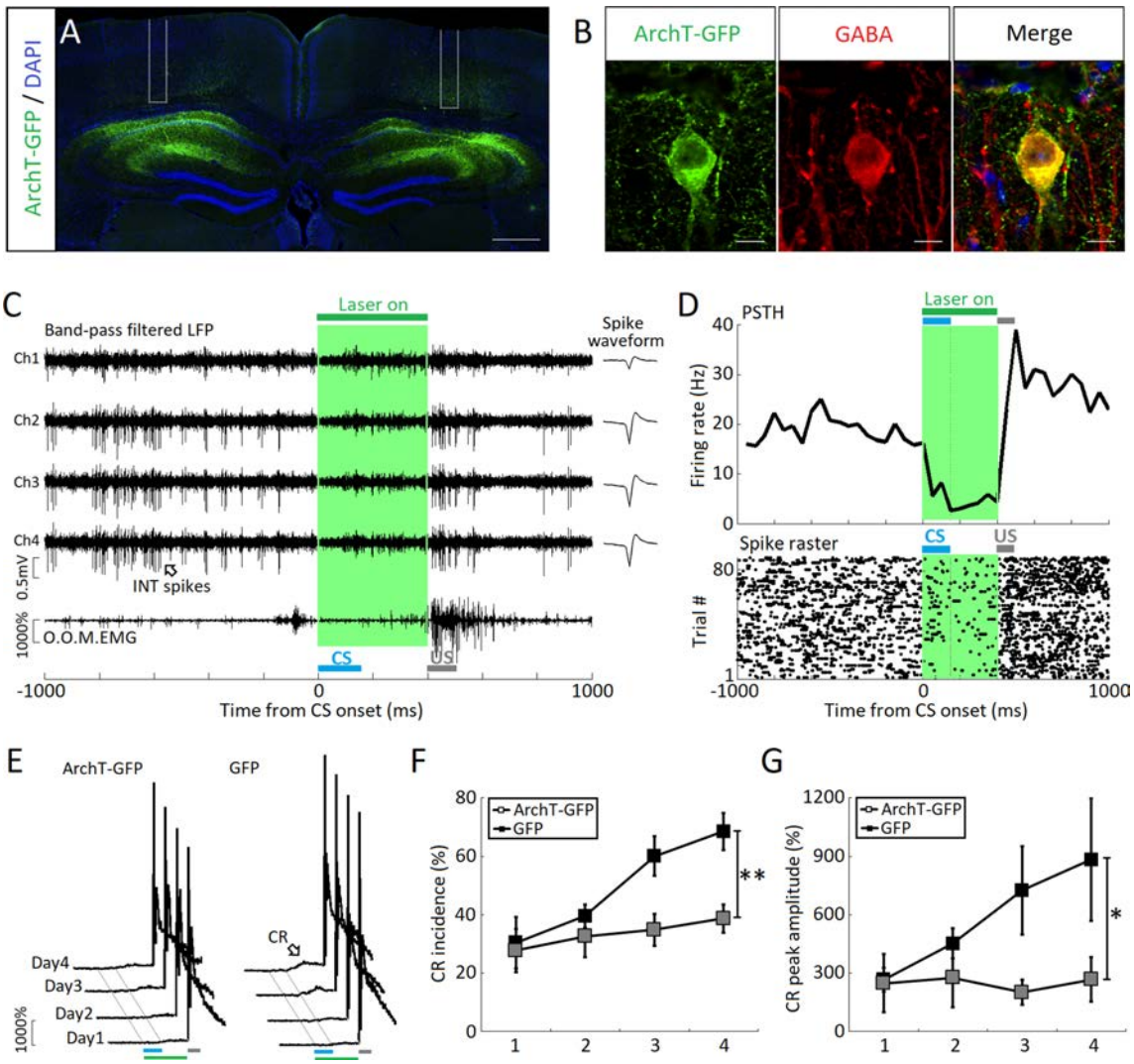

Fig. 6 Optogenetic suppression of sustained activity in hippocampal interneurons (INs) impairs the acquisition of tEBC. **A** Coronal section of a GAD2-Cre mouse brain showing ArchT-GFP expression (green) stained with DAPI (blue) in the dorsal hippocampus. **B** Magnified images showing overlap of ArchT-GFP (green) expression and GABA immunoreactivity (red) in the hippocampal CA1 area of a GAD2-cre mouse (scale bars, 50-μm). **C** Upper, tetrode recording showing the optogenetic suppression of sustained activity in a representative IN; lower, orbicularis oculi muscle (O.O.M.) EMG during peri-optogenetic stimulation. **D** PSTH (upper) and raster plot (lower) illustrating the spiking responses of the representative IN in **C** to 400-ms green light stimulation. **E** Average eyelid responses of valid trials across 4 training days for GAD2-Cre mice with viral injection of AAV-CAG-ArchT-GFP (n = 7, left) and GAD2-Cre mice with viral injection of AAV-DIO-GFP (n = 7, right). **F, G** CR incidence (**F**) and CR peak amplitude (**G**) measured in the ArchT-GFP (n = 7, filled squares) and GFP (n = 7, open squares) groups across 4 training days. Data are expressed as the mean ± SEM (**P <0.01, *P <0.05, two-way ANOVAs with repeated measures).

evoked sustained activity was recorded in 89.4% (93 of 104 units) hippocampal neurons during tEBC, indicating that it is a homogeneous feature of hippocampal INs in this process. Notably, optogenetic suppression of the sustained activity impaired the acquisition of tEBC. Therefore, our results not only provide direct evidence that hippocampal INs are critically involved in the acquisition of tEBC, but also suggest that their sustained activity is one of the cellular mechanisms required for successful associative learning.

The hippocampus is thought to play a time-limited role in the acquisition of tEBC [40–42]. Consistent with this, we found that greater sustained activity in hippocampal INs was correlated with CR occurrence in the early acquisition of tEBC, suggesting that CS-evoked sustained activity of these INs is possibly involved in the initial learning that requires short-term memory, for which CS-evoked activity is sustained up to the onset of US. At the late learning stage, however, the magnitude of this sustained activity began to decline. Therefore, it is reasonable to propose that the sustained activity of the INs no longer differs from that

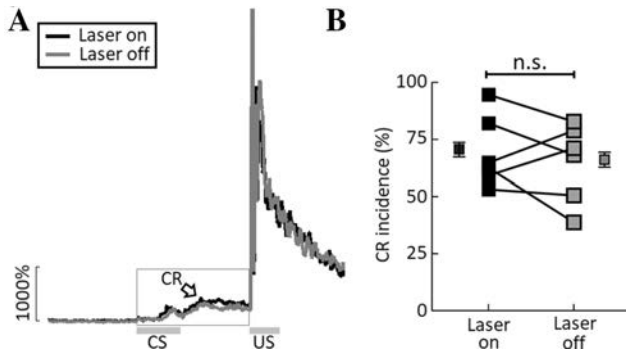

Fig. 7 Optogenetic suppression of hippocampal interneurons (INs) fails to impair the performance of well-learned CRs. **A** Average eyelid movement traces illustrating the effect of optogenetic suppression of INs on the performance of well-learned CRs ($n = 6$ mice; arrow, CRs; open rectangle, delivery of green laser light in the CS–US period). **B** Optogenetic suppression of INs during the CS-US period has no effect on the CR incidence when the CRs are well-learned ($n = 6$ mice). Data are expressed as the mean ± SEM; n.s., not significant, paired t test).

with unpaired training on days 3–4 because long-term memory is established. In support of this, suppression of the sustained activity in the INs had no evident effect on the performance of well-learned CRs. Our findings thus indicate that dynamic change in the sustained activity of hippocampal INs is a candidate cellular process reflecting the differential involvement of the hippocampus in various stages of tEBC acquisition.

But how does the sustained activity of hippocampal interneurons participate in tEBC acquisition? Many studies have demonstrated that tEBC is mediated by cerebellar learning in response to forebrain-driven mossy fiber inputs that persist beyond CS offset to overlap with the US [43–47]. Among the forebrain areas, the hippocampus has been implicated because of the CS-evoked theta synchronization between the hippocampus and the cerebellum during tEBC [48, 49]. Electrophysiological studies have demonstrated that, at the population level, the activity of hippocampal Pyrs increases during the CS–US period [12]. This Pyr activity has been hypothesized to support the associations between time-separated events [2, 13]. Similar to the previous electrophysiological reports [12], we recorded ~40.1% (400/997) of the recorded Pyrs exhibited CS-evoked increased firing activity. Meanwhile, ~16.6% (166/997) of the recorded Pyrs showed CS-evoked decreased firing. The latency of the CS-evoked decreased firing in Pyrs was similar to that of the sustained activity in INs, implying these two responses might be correlated. Indeed, it has been suggested that the inhibitory IN inputs to excitatory principal cells can increase signal-to-noise in the brain [50, 51]. We thus speculated that the sustained IN activity might result in augmenting the signal-to-noise of hippocampal Pyr encoding during the CS–US period, and helps to shape and propagate the hippocampal outputs involved in tEBC acquisition [52].

It should be noted that more hippocampal Pyrs showed increased firing than that showed a decreased firing (Fig. 4A). This result seemed to contradict the fact of overall increased IN activity in the hippocampus. Indeed, it has been demonstrated that lateral inhibition allows a first assembly of Pyrs to suppress the activity of another assembly of Pyrs through the excitation of inhibitory INs [53]. Therefore, one possible explanation for our current findings is that the increased firing of Pyrs interacts with the sustained IN firing *via* collaterals, and this interaction in turn contributes to the lateral inhibition of neighboring Pyrs in the hippocampus [52–54].

Establishing an association between the CS and the US is a prerequisite for the acquisition of tEBC [7, 9, 11]. In this study, we found that both INs and Pyrs showed increased firing activity after the US onset. Previous studies suggested that the US-evoked firing activity is important because the CS-evoked activity would sharply decrease if no USs were further presented [55]. In most INs and some Pyrs we recorded, the CS-evoked firing activity was sustained up to the US-evoked activity period. Consequently, it is reasonable to hypothesize that, at the cellular level, such a firing pattern is a candidate mechanism bridging the time gap between two stimuli to mediate associative learning [53].

The results reported here add to our understanding of the role of inhibitory INs in the hippocampus during associative learning. However, considering the diversity of GABAergic INs in the hippocampus [14–16], the question arises as to the contribution of different subsets of hippocampal INs to associative learning. Consequently, future experiments combing fiber photometry with optogenetics to precisely record and control the activity of different subsets of hippocampal INs [17, 56, 57], are necessary to determine which type of IN(s) is essential for successful associative learning. In addition, a feature of the sustained activity was elevated spiking during the interval between the CS and US that was required for sustained maintenance [58, 59]. Therefore, future experiments can be done to vary the time interval between the CS and the US to better uncover the feature of sustained hippocampal activity.

In conclusion, previous studies have focused on the activity of hippocampal Pyrs, providing progress in research on the brain areas critically involved in associative learning. However, the activity and function of hippocampal INs in this process were neglected. Our current findings provide a mechanistic understanding of the properties of hippocampal IN activity that supports successful associative learning. Nevertheless, further experiments are needed to unravel how the sustained activity of hippocampal INs

sculpts the activity of the Pyr network, so as to shape the outputs of the hippocampus and support the communication between the hippocampus and extra-hippocampal areas.

Acknowledgements This work was supported by the National Natural Science Foundation of China (32071014), the Open Project Program of Brain and Intelligence Research Key Laboratory of Chongqing Education Commission (BIR2019001), and the Foundation for Innovative Research Groups of the National Natural Science Foundation of China (31921003).

Conflict of interest The authors declare no competing interests.

References

1. Raybuck JD, Lattal KM. Bridging the interval: theory and neurobiology of trace conditioning. Behav Processes 2014, 101: 103–111.
2. Pilkiw M, Takehara-Nishiuchi K. Neural representations of time-linked memory. Neurobiol Learn Mem 2018, 153: 57–70.
3. Weiss C, Disterhoft JF. Exploring prefrontal cortical memory mechanisms with eyeblink conditioning. Behav Neurosci 2011, 125: 318–326.
4. Takehara-Nishiuchi K. The anatomy and physiology of eyeblink classical conditioning. Curr Top Behav Neurosci 2018, 37: 297–323.
5. Weiss C, Bouwmeester H, Power JM, Disterhoft JF. Hippocampal lesions prevent trace eyeblink conditioning in the freely moving rat. Behav Brain Res 1999, 99: 123–132.
6. McEchron MD, Tseng W, Disterhoft JF. Neurotoxic lesions of the dorsal hippocampus disrupt auditory-cued trace heart rate (fear) conditioning in rabbits. Hippocampus 2000, 10: 739–751.
7. Tseng W, Guan R, Disterhoft JF, Weiss C. Trace eyeblink conditioning is hippocampally dependent in mice. Hippocampus 2004, 14: 58–65.
8. Burman MA, Gewirtz JC. Hippocampal activity, but not plasticity, is required for early consolidation of fear conditioning with a short trace interval. Eur J Neurosci 2007, 25: 2483–2490.
9. Walker AG, Steinmetz JE. Hippocampal lesions in rats differentially affect long- and short-trace eyeblink conditioning. Physiol Behav 2008, 93: 570–578.
10. Misane I, Tovote P, Meyer M, Spiess J, Ogren SO, Stiedl O. Time-dependent involvement of the dorsal hippocampus in trace fear conditioning in mice. Hippocampus 2005, 15: 418–426.
11. Sakamoto T, Takatsuki K, Kawahara S, Kirino Y, Niki H, Mishina M. Role of hippocampal NMDA receptors in trace eyeblink conditioning. Brain Res 2005, 1039: 130–136.
12. McEchron MD, Disterhoft JF. Sequence of single neuron changes in CA1 hippocampus of rabbits during acquisition of trace eyeblink conditioned responses. J Neurophysiol 1997, 78: 1030–1044.
13. Woodruff-Pak DS, Disterhoft JF. Where is the trace in trace conditioning? Trends Neurosci 2008, 31: 105–112.
14. Freund TF, Buzsáki G. Interneurons of the hippocampus. Hippocampus 1996, 6: 347–470.
15. Parra P, Gulyás AI, Miles R. How many subtypes of inhibitory cells in the hippocampus? Neuron 1998, 20: 983–993.
16. Pelkey KA, Chittajallu R, Craig MT, Tricoire L, Wester JC, McBain CJ. Hippocampal GABAergic inhibitory interneurons. Physiol Rev, 2017. 97: 1619–1747.
17. Leão RN, Mikulovic S, Leão KE, Munguba H, Gezelius H, Enjin A, *et al.* OLM interneurons differentially modulate CA3 and entorhinal inputs to hippocampal CA1 neurons. Nat Neurosci 2012, 15: 1524–1530.
18. Lovett-Barron M, Kaifosh P, Kheirbek MA, Danielson N, Zaremba JD, Reardon TR, *et al.* Dendritic inhibition in the hippocampus supports fear learning. Science 2014, 343: 857–863.
19. Bloss EB, Cembrowski MS, Karsh B, Colonell J, Fetter RD, Spruston N. Structured dendritic inhibition supports branch-selective integration in CA1 pyramidal cells. Neuron 2016, 89: 1016–1030.
20. Grienberger C, Milstein AD, Bittner KC, Romani S, Magee JC. Inhibitory suppression of heterogeneously tuned excitation enhances spatial coding in CA1 place cells. Nat Neurosci 2017, 20: 417–426.
21. Amilhon B, Huh CY, Manseau F, Ducharme G, Nichol H, Adamantidis A, *et al.* Parvalbumin interneurons of hippocampus tune population activity at theta frequency. Neuron 2015, 86: 1277–1289.
22. Lasztóczi B, Klausberger T. Layer-specific GABAergic control of distinct gamma oscillations in the CA1 hippocampus. Neuron 2014, 81: 1126–1139.
23. Stark E, Roux L, Eichler R, Senzai Y, Royer S, Buzsáki G. Pyramidal cell-interneuron interactions underlie hippocampal ripple oscillations. Neuron 2014, 83: 467–480.
24. Xu Y, Shen FY, Liu YZ, Wang L, Wang YW, Wang Z. Dependence of generation of hippocampal CA1 slow oscillations on electrical synapses. Neurosci Bull, 2020, 36:39–48.
25. Seager MA, Johnson LD, Chabot ES, Asaka Y, Berry SD. Oscillatory brain states and learning: Impact of hippocampal theta-contingent training. Proc Natl Acad Sci U S A. 2002, 99: 1616–1620.
26. Nokia MS, Penttonen M, Wikgren J. Hippocampal ripple-contingent training accelerates trace eyeblink conditioning and retards extinction in rabbits. J Neurosci 2010, 30: 11486–11492.
27. Zhang LB, Zhang J, Sun MJ, Chen H, Yan J, Luo FL, *et al.* Neuronal activity in the cerebellum during the sleep-wakefulness transition in mice. Neurosci Bull 2020, 36: 919–931.
28. Hazan L, Zugaro M, Buzsaki G. Klusters, NeuroScope, NDManager: a free software suite for neurophysiological data processing and visualization. J Neurosci Methods 2006, 155: 207–216.
29. Zhang J, Zhang KY, Zhang LB, Zhang WW, Feng H, Yao ZX, *et al.* A method for combining multiple-units readout of optogenetic control with natural stimulation-evoked eyeblink conditioning in freely-moving mice. Sci Rep 2019, 9: 1857.
30. Sanders J, Kepecs A. A low-cost programmable pulse generator for physiology and behavior. Front Neuroeng 2014, 7:43.
31. Knuttinen MG, Parrish TB, Weiss C, LaBar KS, Gitelman DR, Power JM, *et al.* Electromyography as a recording system for

eyeblink conditioning with functional magnetic resonance imaging. Neuroimage 2002, 17: 977–987.
32. Qin H, Fu L, Hu B, Liao X, Lu J, He WJ, *et al.* A visual-cue-dependent memory circuit for place navigation. Neuron 2018, 99: 47–55.
33. Witton J, Staniaszek LE, Bartsch U, Randall AD, Jones MW, Brown JT. Disrupted hippocampal sharp-wave ripple-associated spike dynamics in a transgenic mouse model of dementia. J Physiol 2016, 594: 4615–4630.
34. Wallenstein GV, Eichenbaum H, Hasselmo ME. The hippocampus as an associator of discontiguous events. Trends Neurosci 1998, 21: 317–323.
35. Kitamura T, Macdonald CJ, Tonegawa S. Entorhinal-hippocampal neuronal circuits bridge temporally discontiguous events. Learn Mem 2015, 22: 438–443.
36. Li Y, Xu J, Liu Y, Zhu J, Liu N, Zeng W, *et al.* A distinct entorhinal cortex to hippocampal CA1 direct circuit for olfactory associative learning. Nat Neurosci 2017 20: 559–570.
37. Fuchs EC, Zivkovic AR, Cunningham MO, Middleton S, Lebeau FE, Bannerman DM, et al. Recruitment of parvalbumin-positive interneurons determines hippocampal function and associated behavior. Neuron 2007, 53: 591–604.
38. McKay BM, Oh MM, Disterhoft JF. Learning increases intrinsic excitability of hippocampal interneurons. J Neurosci 2013, 33: 5499–5506.
39. Spurny B, Seiger R, Moser P, Vanicek T, Reed MB, Heckova E, *et al.* Hippocampal GABA levels correlate with retrieval performance in an associative learning paradigm. Neuroimage 2020, 204: 116244.
40. Kim JJ, Clark RE, Thompson RF. Hippocampectomy impairs the memory of recently, but not remotely, acquired trace eyeblink conditioned responses. Behav Neurosci 1995, 109: 195–203.
41. Takehara K, Kawahara S, Takatsuki K, Kirino Y. Time-limited role of the hippocampus in the memory for trace eyeblink conditioning in mice. Brain Res 2002, 951: 183–190.
42. Takehara K, Kawahara S, Kirino Y. Time-dependent reorganization of the brain components underlying memory retention in trace eyeblink conditioning. J Neurosci 2003, 23: 9897–9905.
43. Kalmbach BE, Ohyama T, Mauk MD. Temporal patterns of inputs to cerebellum necessary and sufficient for trace eyelid conditioning. J Neurophysiol 2010, 104: 627–640.
44. Kalmbach BE, Ohyama T, Kreider JC, Riusech F, Mauk MD. Interactions between prefrontal cortex and cerebellum revealed by trace eyelid conditioning. Learn Mem 2009, 16: 86–95.
45. Siegel JJ, Kalmbach B, Chitwood RA, Mauk MD. Persistent activity in a cortical-to-subcortical circuit: bridging the temporal gap in trace eyelid conditioning. J Neurophysiol 2012, 107: 50–64.
46. Siegel JJ, Mauk MD. Persistent activity in prefrontal cortex during trace eyelid conditioning: dissociating responses that reflect cerebellar output from those that do not. J Neurosci 2013, 33: 15272–15284.
47. Chen H, Wang YJ, Yang L, Sui JF, Hu ZA, Hu B. Theta synchronization between medial prefrontal cortex and cerebellum is associated with adaptive performance of associative learning behavior. Sci Rep 2016, 6: 20960.
48. Hoffmann LC, Berry SD. Cerebellar theta oscillations are synchronized during hippocampal theta-contingent trace conditioning. Proc Natl Acad Sci U S A 2009, 106: 21371–21376.
49. Wikgren J, Nokia MS, Penttonen M. Hippocampo-cerebellar theta band phase synchrony in rabbits. Neuroscience 2010, 165:1538–1545.
50. Courtin J, Chaudun F, Rozeske RR, Karalis N, Gonzalez-Campo C, Wurtz H, *et al.* Prefrontal parvalbumin interneurons shape neuronal activity to drive fear expression. Nature 2014, 505: 92–96.
51. Lee K, Holley SM, Shobe JL, Chong NC, Cepeda C, Levine MS, *et al.* Parvalbumin interneurons modulate striatal output and enhance performance during associative learning. Neuron 2017, 93: 1451–1463.
52. McKenzie S. Inhibition shapes the organization of hippocampal representations. Hippocampus 2018, 28: 659–671.
53. Roux L, Buzsáki G. Tasks for inhibitory interneurons in intact brain circuits. Neuropharmacology 2015, 88: 10–23.
54. Crandall SR, Connors BW. Diverse ensembles of inhibitory interneurons. Neuron 2016, 90: 4–6.
55. Wang H, Sun MJ, Chen H, Zhang J, Zhang LB, Zhang WW, *et al.* Spontaneous recovery of conditioned eyeblink responses is associated with transiently decreased cerebellar theta activity in guinea pigs. Behav Brain Res 2019, 359: 457–466.
56. Xia F, Richards BA, Tran MM, Josselyn SA, Takehara-Nishiuchi K. Parvalbumin-positive interneurons mediate neocortical-hippocampal interactions that are necessary for memory consolidation. Elife 2017, 6: e27868.
57. Udakis M, Pedrosa V, Chamberlain SEL, Clopath C, Mellor JR. Interneuron-specific plasticity at parvalbumin and somatostatin inhibitory synapses onto CA1 pyramidal neurons shapes hippocampal output. Nat Commun 2020, 11: 4395.
58. Kamiński J, Sullivan S, Chung JM, Ross IB, Mamelak AN, Rutishauser U. Persistently active neurons in human medial frontal and medial temporal lobe support working memory. Nat Neurosci 2017, 20: 590–601.
59. Kamiński J, Brzezicka A, Mamelak AN, Rutishauser U. Combined phase-rate coding by persistently active neurons as a mechanism for maintaining multiple items in working memory in humans. Neuron 2020, 106: 256–264.

Neurosci. Bull. August, 2021, 37(8):1160–1175
https://doi.org/10.1007/s12264-021-00681-0

www.neurosci.cn
www.springer.com/12264

ORIGINAL ARTICLE

Acrolein Induces Systemic Coagulopathy *via* Autophagy-dependent Secretion of von Willebrand Factor in Mice after Traumatic Brain Injury

Wenxing Cui[1] · Xun Wu[1] · Dayun Feng[1] · Jianing Luo[1] · Yingwu Shi[1] · Wei Guo[1] · Haixiao Liu[1] · Qiang Wang[1] · Liang Wang[1] · Shunnan Ge[1] · Yan Qu[1]

Received: 11 September 2020 / Accepted: 5 December 2020 / Published online: 3 May 2021

Abstract Traumatic brain injury (TBI)-induced coagulopathy has increasingly been recognized as a significant risk factor for poor outcomes, but the pathogenesis remains poorly understood. In this study, we aimed to investigate the causal role of acrolein, a typical lipid peroxidation product, in TBI-induced coagulopathy, and further explore the underlying molecular mechanisms. We found that the level of plasma acrolein in TBI patients suffering from coagulopathy was higher than that in those without coagulopathy. Using a controlled cortical impact mouse model, we demonstrated that the acrolein scavenger phenelzine prevented TBI-induced coagulopathy and recombinant ADAMTS-13 prevented acrolein-induced coagulopathy by cleaving von Willebrand factor (VWF). Our results showed that acrolein may contribute to an early hypercoagulable state after TBI by regulating VWF secretion. mRNA sequencing (mRNA-seq) and transcriptome analysis indicated that acrolein over-activated autophagy, and subsequent experiments revealed that acrolein activated autophagy partly by regulating the Akt/mTOR pathway. In addition, we demonstrated that acrolein was produced in the perilesional cortex, affected endothelial cell integrity, and disrupted the blood-brain barrier. In conclusion, in this study we uncovered a novel pro-coagulant effect of acrolein that may contribute to TBI-induced coagulopathy and vascular leakage, providing an alternative therapeutic target.

Keywords Traumatic brain injury · Coagulopathy · Autophagy · Acrolein · Von Willebrand factor

Introduction

Traumatic brain injury (TBI) constitutes a significant proportion of global injuries, and remains one of the major causes of traumatic death and disability [1]. Despite advances in the treatment of TBI, a high risk of poor outcomes still exists in these patients. There are areas regarding our comprehension of the pathogenesis and optimal treatment strategies of TBI that need improvement. Coagulopathy is a common secondary injury in TBI patients, occurring in 33% to 66% of cases, due to the different detection methods and definitions [2, 3]. TBI-induced coagulopathy is consistently associated with poor outcomes [4, 5], and these patients tend to suffer from progressive intracranial hemorrhage and microvascular thrombosis [6, 7].

TBI-induced coagulopathy follows a distinct pathogenic pathway. First, the incidence of coagulopathy after TBI is higher than that after traumatic injuries of other organs. Second, isolated TBI can also induce early and systemic coagulopathy, even without substantial blood loss and hemodilution because of fluid resuscitation [8]. Previous studies have shown that TBI-induced coagulopathy manifests as a hypercoagulable state induced by pro-coagulant molecules (such as tissue factors, phosphatidylserine, and

Wenxing Cui, Xun Wu, and Dayun Feng contributed equally to this work.

Supplementary Information The online version contains supplementary material available at https://doi.org/10.1007/s12264-021-00681-0.

✉ Shunnan Ge
gesn8561@fmmu.edu.cn

✉ Yan Qu
yanqu0123@fmmu.edu.cn

[1] Department of Neurosurgery, Tangdu Hospital, Fourth Military Medical University, Xi'an 710038, China

cardiolipin) released from injured brain tissue; this then develops into a late consumptive hypocoagulable state [5, 8–10]. However, the removal of these pro-coagulant molecules does not completely correct the coagulation dysfunction [11], which suggests that there may be other molecules involved in TBI-induced coagulopathy.

It is widely known that the brain is the most lipid-rich organ (approximately 50% of the brain dry weight) [12]. Oxidative stress is a crucial contributor to secondary insult following TBI [13], and the role of lipid peroxidation in the course of this pathology is gradually being recognized [14]. However, whether lipid peroxidation products affect coagulation in the early stage of TBI is unclear. Acrolein, a highly active unsaturated aldehyde [15], is abundantly produced during the acute phase of TBI [16], and the strong covalent bonds to cellular and mitochondrial proteins can impair the structural and functional integrity in cells [17–19]. Other evidence also shows that acrolein is closely associated with the occurrence of thrombotic diseases [20], which indicates its role in stimulation of the coagulation cascade. Here, we hypothesized that acrolein promotes TBI-induced coagulopathy in the early stage. In the current study, we first identified a potential relationship between plasma acrolein levels in TBI patients and coagulopathy. Next, *in vitro* and *in vivo* studies were performed to explore the novel role of acrolein in contributing to secondary coagulopathy after TBI in mice. Then, we performed transcriptome sequencing to explore the possible mechanism of acrolein-induced coagulopathy and validated the findings. Finally, we verified that phenelzine, an acrolein scavenger, has great therapeutic potential.

Materials and Methods

Animals and Ethics

All experimental procedures strictly followed the guidelines of the National Institutes of Health Guide for the Care and Use of Laboratory Animals and were approved by the Ethics Committee of the Fourth Military Medical University. Eight- to twelve-week-old healthy adult male C57BL/6J mice weighing 20 g–25 g (wild type) were purchased from the Animal Center of the Fourth Military Medical University. All mice were kept at a constant humidity (60%), temperature (18°C–22°C), with a regular 12-h light/dark cycle and free access to food and water in a specific pathogen-free animal room. This study was approved by the Ethics Committee of Tangdu Hospital, Fourth Military Medical University (201907-03), and was registered on clinicaltrials.gov (NCT04274777).

TBI Procedure and Drug Administration

A controlled cortical impact (CCI) model for TBI was established as previously described [21]. Briefly, each mouse was anesthetized with 2% pentobarbital sodium, and underwent TBI surgery with the CCI device (68099 Precision Strike, RWD, Shenzhen, Guangzhou, China). Each mouse was fixed on a stereotactic device, and the skull was exposed. A bone window 2 mm in diameter was drilled with a grinder at 1.5 mm behind the bregma and 1.5 mm on the right side, while the integrity of the dura was maintained. The round metal tip perpendicularly struck the exposed cortical surface at a velocity of 3 m/s and remained for 0.2 s, leading to a depth of 1.5 mm. Then, tissue adhesive was used to cover the damaged cortex. Mice in the sham injury underwent the same procedure without the use of the CCI device. Phenelzine (MedChemExpress, HY-B1018A) was dissolved in 0.9% saline. Mice in the phenelzine treatment group were intraperitoneally injected with 10 mg/kg phenelzine immediately after TBI [22]. Mice in the recombinant human ADAMTS-13 (rhADAMTS-13, R&D, 4245-AD-020) treatment group were intraperitoneally injected with 200 μg/Kg rhADAMTS-13 immediately after TBI [23]. Mice in the positive control group were injected with acrolein through the tail vein [24], while mice in the vehicle group were injected with saline through the tail vein.

Western Blot Analysis

Western blot analysis was performed as previously described [25]. The selected tissue samples were homogenized in lysis buffer containing 1% protease inhibitor. Protein concentrations were measured using a BCA protein assay kit (Thermo Scientific; UA276918). Proteins were separated on SDS-PAGE gels, and transferred onto PVDF membranes (Millipore, Billerica, MA), which were then incubated with primary antibodies at 4°C overnight. After 3 × 5-min washes in TBST, the membranes were probed with the appropriate horseradish peroxidase-conjugated anti-rabbit or anti-mouse secondary antibodies (1:5000, 27°C, 2 h). Protein signals were exposed with a BioRad imaging system (Bio-Rad, Hercules, CA). Images were analyzed using ImageJ. The primary antibodies used were as follows: anti-acrolein (1:1000, ab240918, Abcam), anti-Atg5 (1:1000, 12994S, Cell Signaling), anti-Atg7 (1:1000, 8558S, Cell Signaling), anti-Beclin 1 (1:1000, 3738S, Cell Signaling), anti-LC3 (1:1000,2775S, Cell Signaling), anti-Akt (1:1000, 4691S, Cell Signaling), anti-p Akt (1:1000, 4060S, Cell Signaling), anti-mTOR (1:1000, 2983S, Cell Signaling), anti-p mTOR (1:1000,2971S, Cell Signaling), anti-Occludin (1:1000, 27260-1-AP, Proteintech), anti-ZO-

1 (1:200, ab96587, Abcam), and anti-β-actin (1:3000, wh096194, Wanleibio).

ELISA

The levels of acrolein in the plasma of TBI patients and mice were measured using ELISA kits (MBS7213206, Biocompare; JL47824, Jianglai, respectively). The levels of VWF and D-dimer in mouse plasma were determined using an Elisa kit (E-EL-M1247c, Elabscience; JL20160, Jianglai, respectively). Whole blood from patients or mice was centrifuged at 1500 g for 15 min to obtain plasma, and then stored at − 80°C. The levels of VWF in human endothelial cell medium were determined using a VWF ELISA kit (ab108918, Abcam). The ELISA procedures were carried out in strict accordance with the instructions.

Immunofluorescence Staining

Immunofluorescence staining was performed as previously described [25]. Briefly, mice were sacrificed 24 h after TBI and perfused with 4% paraformaldehyde. The brain was removed and fixed with 4% paraformaldehyde at 4°C overnight, and then dehydrated in 10%, 20%, and 30% sucrose. Next, the brain was cut into 15–25 μm sections, and incubated in 0.1% Triton X-100 for 30 min, followed by incubation in 10% donkey serum for 2 h. The sections were incubated with the mouse anti-acrolein (1:200, ab48501, Abcam), anti-glial fibrillary acidic protein (GFAP; 1:200; Invitrogen, USA), and anti-CD31 (1:200, ab222783, Abcam) at 4°C overnight. All sections were analyzed under a fluorescence microscope (A1 Si, Nikon) in a blinded manner. Representative images were from three independent experiments using six mice.

Clotting Time

Careful collection of blood is vital for analyzing coagulation. We collected blood as previously described [26]. Briefly, the mice were anesthetized using 2% pentobarbital sodium. Then, they were placed in dorsal recumbency, and the thorax exposed by cutting the skin around the rib cage. Next, we carefully and quickly inserted a needle into the right ventricle to draw the blood. Immediately, we transferred the blood from the syringe into the Century Clot blood coagulation and platelet function analyzer (Shijiyikang, Tianjin). This device uses a sensitive mechanical sensing system to detect viscoelasticity, and continuously monitors the coagulation process of blood samples *in vitro* in real time, allowing the accurate determination of clotting time.

Quantitative Real-time PCR (qRT-PCR)

qRT-PCR was performed as previously described [27]. Total RNA was isolated from cells using TRIzol reagent (Invitrogen). Reverse transcription was conducted to obtain cDNAs using HiScript II Q RT SuperMix for qRT-PCR (+gDNA wiper) (Vazyme, USA). qRT-PCR was conducted using an iQTM 5 Optical Module Real-Time PCR Detection System (Bio-Rad, USA). Gene expression was normalized to β-actin and calculated using the $2^{-\Delta\Delta Ct}$ method. The primer sequences are listed in Table S1.

Cell Culture and CCK8 Cell Viability Assay

Human umbilical vein endothelial cells (HUVECs) were cultured in endothelial cell medium (1001, Science Cell), containing endothelial cell growth supplement (Cat. No. 1052), in a humidified incubator with 5% CO_2 at 37°C. The CCK8 cell viability assay was performed as previously described [28]. After exposing the cells to acrolein for 6 h, CCK8 reagent was added to each well. After incubation for 2 h at 37°C, we measured the absorbance at 450 nm using a plate reader. The survival rate of the untreated cells was set at 100%.

Transwell Assay

A transwell assay was used to measure endothelial permeability as previously described [23]. HUVECs were seeded onto inserts coated with collagen. After reaching confluence, the cells were incubated with a concentration gradient of acrolein (25, 50, and 100 μmol/L) at 37°C for 6 h. Next, the cells were incubated with 1 mg/mL FITC-dextran at 37°C for 1 h. Then, the insert was removed, and 100 μL of liquid in the bottom receiving plate was collected to measure the fluorescence intensity in a plate reader.

Quantification of Lesion Volume and Edema

The lesion volume was measured as previously described [29]. Briefly, 24 h after TBI, the brains were collected and sections were prepared as above. Then, the sections were stained with Cresyl violet (for Nissl bodies). The lesion area was measured using ImageJ software.

Brain water content was quantified by the wet/dry method one day after TBI and calculated as a percentage using the following equation: brain water content = (wet weight − dry weight)/wet weight × 100% [29].

Evans Blue Extravasation Analysis

Evans blue extravasation was used to assess blood-brain barrier (BBB) integrity as previously described [30]. Briefly, at 24 h post-TBI, Evans blue was intravenously injected and allowed to circulate for 1 h. Then, the mice were sacrificed and perfused with PBS. Afterward, the brains were isolated and homogenized with trichloroacetic acid solution. Next, the homogenates were centrifuged at 12,000×g for 30 min, and the OD of the supernatant was measured at 610 nm using a microplate reader.

Modified Neurological Severity Score

The modified neurological severity score (mNSS) was used to assess neurological functional impairment as previously described [31]. The mNSS, including motor, sensory, reflex, and balance tests, ranged from 0 to 18 (0: normal score; 18: maximal deficit score). The scoring was conducted at 6 h and 1, 3, 5, and 7 days after TBI by two observers who were blinded to the groups.

Patients and Ethical Considerations

This prospective study was conducted from September 2019 to March 2020 and approved by the Ethics Committee of Tangdu Hospital, Fourth Military Medical University, and was registered on clinicaltrials.gov. Two milliliters of venous blood were collected from TBI patients after admission. The clinical data of the patients were collected and included age, gender, admission Glasgow Coma Scale, pupil reaction at admission, medical history, and biochemical tests [activated partial thromboplastin time (aPTT), international normalized ratio (INR), platelet count, RBC, HCT, GLU, AST, and ALT]. Traumatic coagulopathy was defined as aPTT >36 s and/or INR >1.2 and/or platelet count $<100 \times 10^9$ per liter, based on a previous study [32]. The main inclusion criteria were patients with mild, moderate, or severe TBI. The exclusion criteria were as follows: (1) age <16 years or >80 years; (2) interval from injury to admission >24 h; (3) severe systemic diseases including uremia, cirrhosis, and malignant tumors; (4) ischemic or hemorrhagic vascular disease occurring within half a year; and (5) a medical history of taking anticoagulants or antiplatelet drugs and a history of smoking.

Statistical Analysis

Statistical analysis was performed using IBM SPSS Statistics 20.0 software (IBM, New York, NY). Continuous variables are presented as the mean ± SEM. Categorical data are presented as the frequency (percentages). Univariate analysis was performed to find significant variables, which were entered into the multivariate logistic regression to identify the independent risk factors for coagulopathy. The levels of plasma acrolein were classified by applying ROC curve analysis based on coagulopathy. Two independent groups were compared using unpaired two-tailed Student's *t* test, while multiple groups were analyzed using one-way analysis of variance, followed by the Tukey *post hoc* test. Neurobehavioral data were analyzed using the Kruskal–Wallis one-way analysis of variance on ranks followed by the Student–Newman–Keuls test. A value of $P < 0.05$ was defined as statistically significant.

Results

The Plasma Acrolein Level in TBI Patients is Correlated with Coagulopathy

A total of 55 TBI patients were enrolled in this prospective clinical study. First, we found that the plasma acrolein level in TBI patients was higher than that in normal individuals ($P < 0.01$; Fig. 1A). Further, plasma acrolein levels were higher in patients with coagulopathy than those without coagulopathy ($P < 0.01$; Fig. 1B). ROC curve analysis was used to test the discriminative ability of plasma acrolein levels for coagulopathy (Fig. 1C). An optimal cutoff value of acrolein concentration (18.4 nmol/mL) was chosen, which discriminated TBI patients at risk of coagulopathy with 80.0% sensitivity and 82.5% specificity with an area under the curve of 0.830. According to the univariate analysis, older age ($P = 0.005$), reduced Glasgow coma score ($P = 0.047$), abnormal pupil reaction ($P = 0.037$), abnormal RBC ($P = 0.014$), abnormal HCT ($P = 0.008$), abnormal AST ($P = 0.013$), abnormal ALT ($P = 0.004$), and increased plasma acrolein level ($P < 0.001$) were associated with coagulopathy (Table 1). An increased plasma acrolein level (OR = 1.260, 95% CI 1.098–1.447, $P = 0.001$; Table 1) remained an independent risk factor for coagulopathy. These clinical results strongly suggested that there is a positive correlation between the plasma acrolein level and TBI-induced coagulopathy.

Upregulation of Acrolein in Peripheral Blood After TBI in Mice and the Association with an Early Hypercoagulable State

First, ELISA was used to assess the alterations in acrolein with time after TBI with or without the administration of the acrolein scavenger phenelzine. The acrolein level in peripheral blood increased significantly at 6 h, and was cleared by phenelzine (Fig. 2A). To explore the effects of

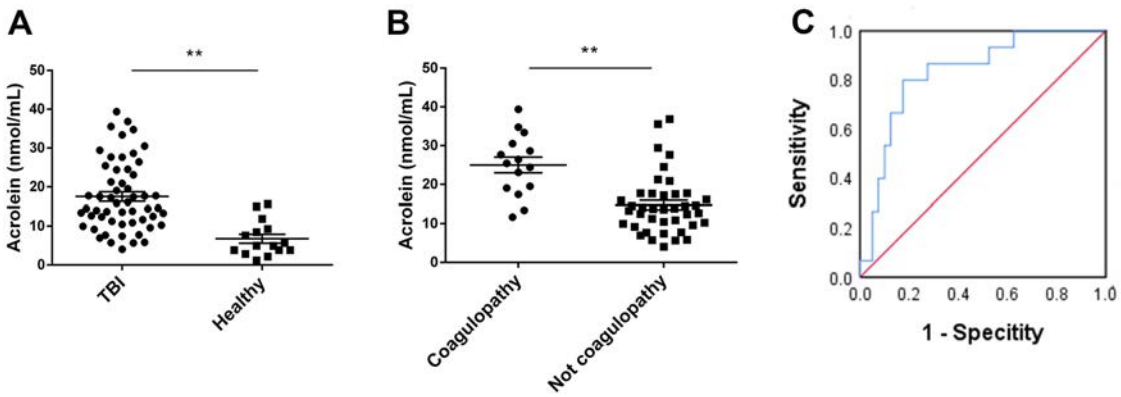

Fig. 1 Plasma acrolein levels in TBI patients and their ability to discriminate coagulopathy. **A** Plasma acrolein concentrations in healthy controls and TBI patients ($n = 60$, $^{**}P < 0.01$). **B** Plasma acrolein concentrations in TBI patients suffering from coagulopathy at admission and those without coagulopathy ($n = 55$, $^{**}P < 0.01$). **C** Analysis of the discriminative ability of plasma acrolein concentrations for patients at risk of coagulopathy after TBI using the receiver operating characteristic curve.

Table 1 Characteristics of the study population.

	Study population ($n = 55$)	Coagulopathy ($n = 15$)	No coagulopathy ($n = 40$)	P value	Adjusted P value	Adjusted OR (95% CI)
Demographics						
Age, years (SD)	54.5 (12.0)	61.5 (9.5)	51.9 (11.8)	0.005	0.023	1.151 (1.019, 1.299)
Male, *n* (%)	40 (72.7)	12 (80.0)	28 (70.0)	0.458		
GCS (SD)	10.0 (3.5)	8.3 (3.8)	10.6 (3.2)	0.047		
Abnormal pupil reaction, *n* (%)	24 (43.6)	10 (66.7)	14 (35.0)	0.037		
Medical history						
Hypertension, *n* (%)	9 (16.4)	2 (13.3)	7 (17.5)	0.71		
Diabetes, *n* (%)	1 (1.8)	1 (6.7)	0 (0)	0.537		
Coronary artery disease, *n* (%)	2 (3.6)	1 (6.7)	1 (2.5)	0.462		
Mechanism of injury						
Motor vehicle, *n* (%)	26 (47.3)	9 (60.0)	17 (42.5)	0.247		
Fall, *n* (%)	27 (49.1)	6 (40.0)	21 (52.5)	0.409		
Assault, *n* (%)	1 (1.8)	0 (0)	1 (2.5)	0.537		
Laboratory biochemical examinations						
Abnormal RBC, *n* (%)	13 (23.6)	7 (46.7%)	6 (15.0)	0.014		
Abnormal HCT, *n* (%)	15 (27.3)	8 (53.3)	7 (17.5)	0.008	0.024	11.304 (1.380, 92.581)
Abnormal GLU, *n* (%)	14 (25.5)	6 (40.0)	8 (20.0)	0.129		
Abnormal AST, *n* (%)	29 (52.7)	12 (80.0)	17 (42.5)	0.013		
Abnormal ALT, *n* (%)	17 (30.9)	9 (60.0)	8 (20.0)	0.004		
Acrolein (ng/mL) (SD)	17.5 (8.9)	25.0 (7.9)	14.7 (7.6)	< 0.001	0.001	1.260 (1.098, 1.447)

increasing acrolein on the clotting system, we selected two representative time points (6 h and 24 h) to measure the commonly used indicators of coagulation including clotting time and d-dimers, based on previous studies [11]. In mice, we found that the clotting time was shortened in the early stage (6 h) of trauma and prolonged in the later stage (24 h) (Fig. 2B). These changes were partly reversed by the administration of phenelzine after TBI (Fig. 2B). The level of plasma D-dimer increased significantly after TBI, and this abnormal elevation was mitigated by treatment with phenelzine (Fig. 2C). To further validate the role of acrolein in coagulation, uninjured mice were injected

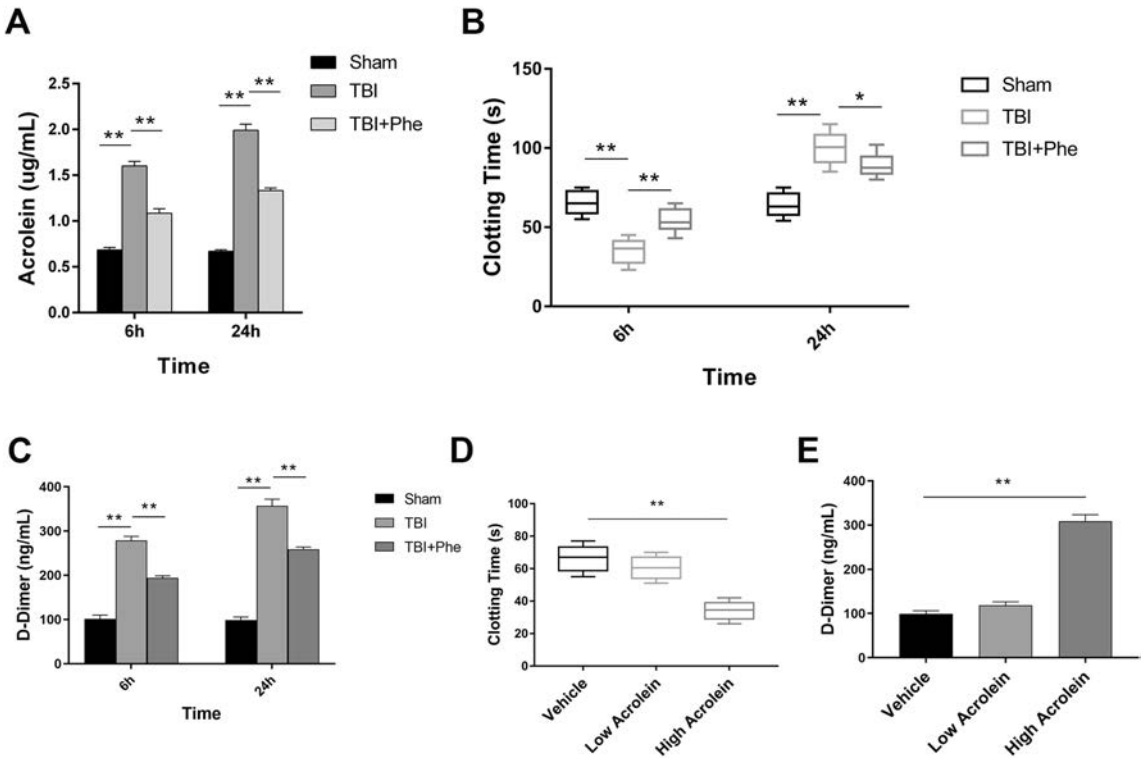

Fig. 2 Upregulation of acrolein in peripheral blood after TBI in mice contributes to an early hypercoagulable state. **A** ELISA results showing the acrolein levels in peripheral blood at 6 h and 24 h in each group (Sham; TBI; TBI+Phe). **B** Clotting time at 6 h and 24 h in each group. **C** Plasma levels of D-dimer at 6 h in each group. **D** Clotting time at 6 h in each group (vehicle; low acrolein: 3 nmol; high acrolein: 30 nmol). **E** Plasma levels of D-dimer at 6 h in each group. Values are presented as the mean ± SEM, $n = 6$ per group, $^{**}P < 0.01$.

through the tail vein with different doses of acrolein (low dose: 3 nmol; high dose: 30 nmol). The selection of doses was based on the level of acrolein in peripheral blood after TBI, as measured by ELISA. Low-dose acrolein (3 nmol) and saline had no significant effect on clotting time or the level of plasma D-dimer 6 h after injection, while high-dose acrolein (30 nmol) significantly shortened the clotting time and increased the level of D-dimer (Fig. 2D, E). These results revealed that acrolein, a pro-coagulant, is produced at an early stage after TBI and induces an early hypercoagulable state, which in turn causes a consumptive hypocoagulable state.

Acrolein Induces Coagulopathy Partly by Regulating VWF Secretion

VWF is an adhesion molecule released and stored by endothelial cells, and is regarded as a marker of endothelial cell activation [33]. VWF is considered to be involved in coagulopathy and thromboembolic disease associated with trauma [23, 34, 35]. Therefore, we hypothesized that TBI-induced high-level plasma acrolein promotes coagulopathy *via* the release of VWF. First, the levels of circulating VWF were significantly increased at 6 h post-TBI, and this was partly reversed by phenelzine (Fig. 3A). Low-dose acrolein had no significant effects on circulating VWF levels, while high-dose acrolein significantly increased them (Fig. 3B). Next, the administration of rhADAMTS-13, an enzyme that cleaves VWF [36], significantly reduced circulating VWF levels after TBI. Similarly, rhADAMTS-13 reduced the increase in VWF induced by acrolein (Fig. 3C). Then, we explored whether rhADAMTS-13 reversed the coagulopathy induced by TBI or acrolein. We also found that rhADAMTS-13 partly reversed the abnormal clotting time and D-dimer level at 6 h post-TBI or acrolein injection (Fig. 3D, E). These results suggest that acrolein causes TBI-induced coagulopathy partly by promoting VWF secretion.

Acrolein Activates the Autophagy Pathway in HUVECs as shown by mRNA-Seq Analysis

To elucidate the effect of acrolein on HUVECs and VWF secretion, we first examined the toxicity of acrolein by CCK8 assays and found that the LD_{50} for acrolein was approximately 50 μmol/L after 6 h of treatment (Fig. S1A). Next, to investigate how acrolein activates HUVECs, we determined the profiles of transcriptomics changes in the

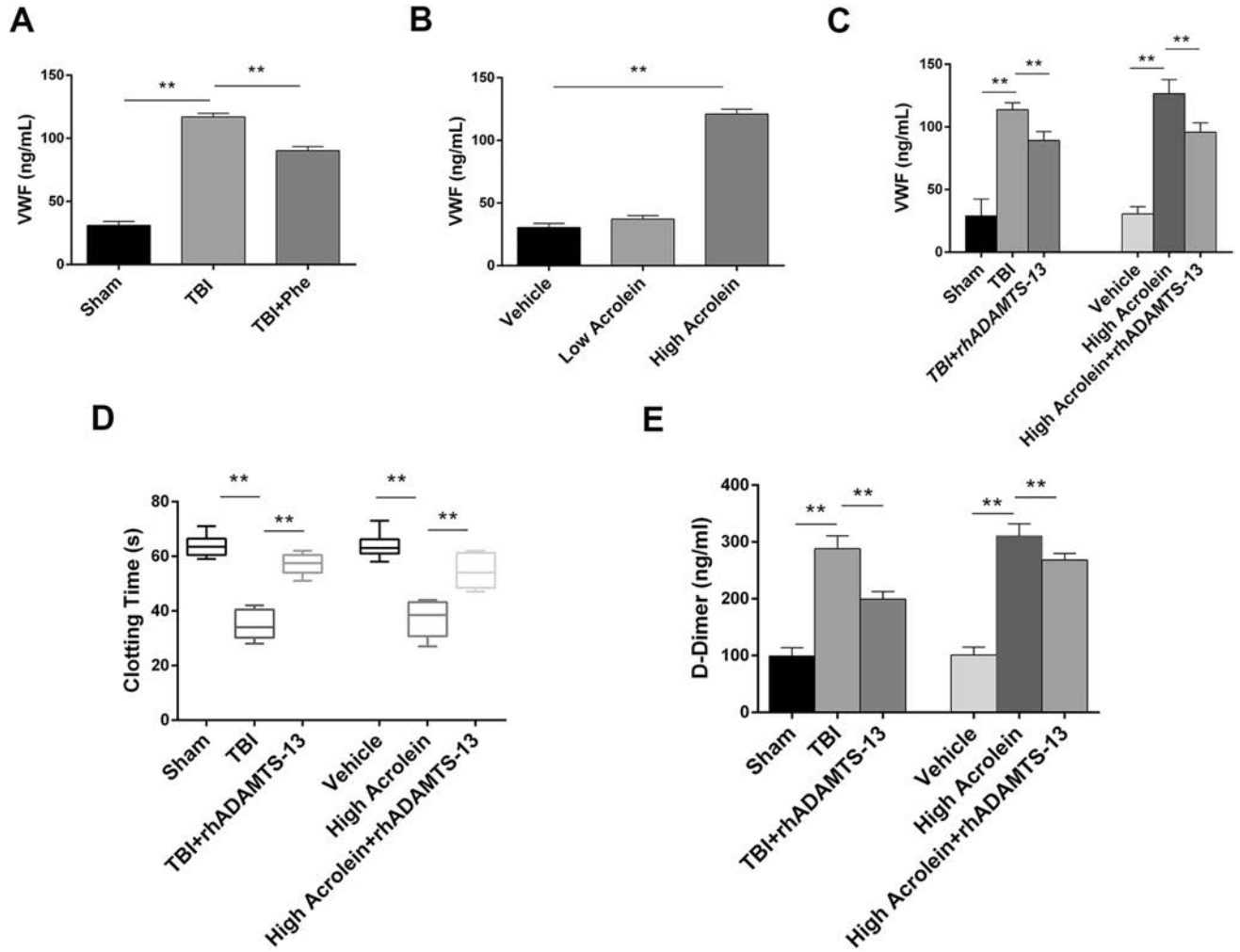

Fig. 3 Acrolein induces coagulopathy partly by regulating VWF secretion. **A** VWF levels in mice treated with or without phenelzine after TBI and in sham mice. **B** VWF levels in mice infused with acrolein or PBS. **C** VWF levels in mice treated with rhADAMTS-13 after TBI or acrolein infusion. **D** Clotting times in the above treatment groups. **E** Plasma levels of D-dimer from mice in the above treatment groups. Values are presented as the mean ± SEM, $n = 6$ per group, $^{**}P < 0.01$.

control and acrolein treatment groups using RNA-seq analysis. Volcano plots and heatmaps of the two groups show the total upregulated and downregulated genes (Fig. 4A, B). We used GO (Gene Ontology) terms for biological process, cellular components, and molecular function to determine the functional enrichment of the differentially-expressed genes (Fig. 4C). Autophagy was most enriched in biological process and cellular components, and enzyme binding was most enriched in molecular function (Fig. S1B–D). Kyoto Encyclopedia of Genes Genomes (KEGG) enrichment analysis identified that autophagy was the most enriched pathway after acrolein treatment (Fig. 4D). Then, a heat map showing autophagy-related gene expression was generated to analyze the expression changes of each gene (Fig. 4E), and the trends in these typical genes was verified by qPCR (Fig. S4E). The mRNA-Seq analysis suggested that acrolein significantly activates the autophagy pathway.

Acrolein Promotes the Release of VWF by Activating Autophagy

Previous studies have shown that autophagy regulates endothelial VWF secretion [37], so we hypothesized that acrolein promotes the release of VWF by activating autophagy, thereby leading to coagulopathy. HUVECs were treated with different concentrations of acrolein (0, 25, 50, and 100 μmol/L) for 6 h. First, Western blotting was used to assess changes in the levels of autophagy-related molecules. The results revealed that acrolein upregulated the levels of Atg5, Atg7, and Beclin-1 and promoted the conversion of LC3-I to LC3-II in a dose-dependent manner (Fig. 5A, B). Using an ELISA-based approach on the culture medium, we found a significant increase in VWF secretion after treatment with acrolein, and this was also dose-dependent (Fig. 5C). Incubation of HUVECs with 3- Methyladenine (5 mmol/L) inhibited

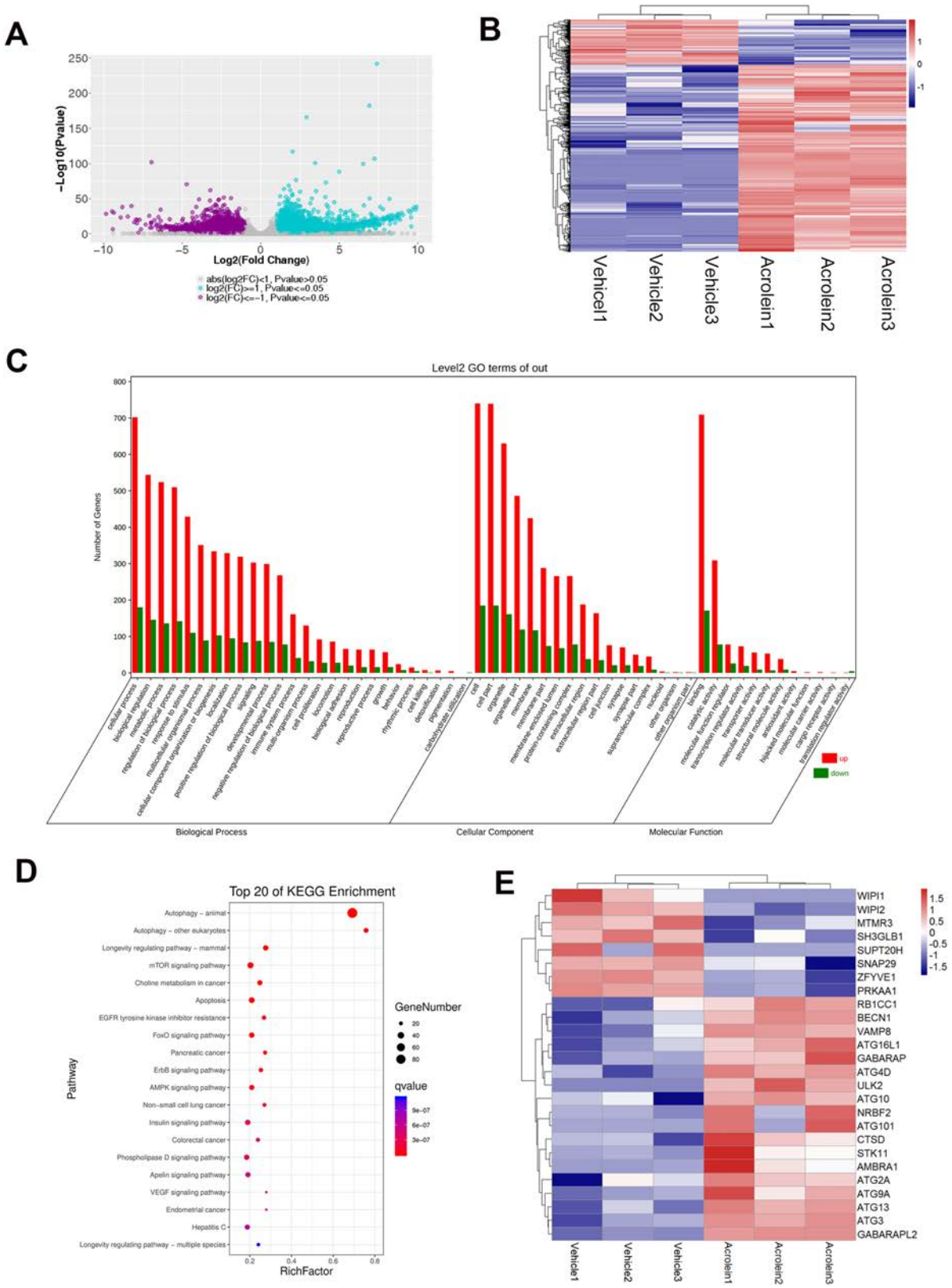

Fig. 4 mRNA-Seq analysis showing that acrolein activates the autophagy pathway in HUVECs. **A, B** Volcano plot (**A**) and heatmap (**B**) of the control and acrolein treatment groups showing the total up-regulated and down-regulated genes. **C** GO terms for biological process, cellular components, and molecular function. **D** Top 20 from KEGG Enrichment. **E** Heat map showing autophagy-related gene expression.

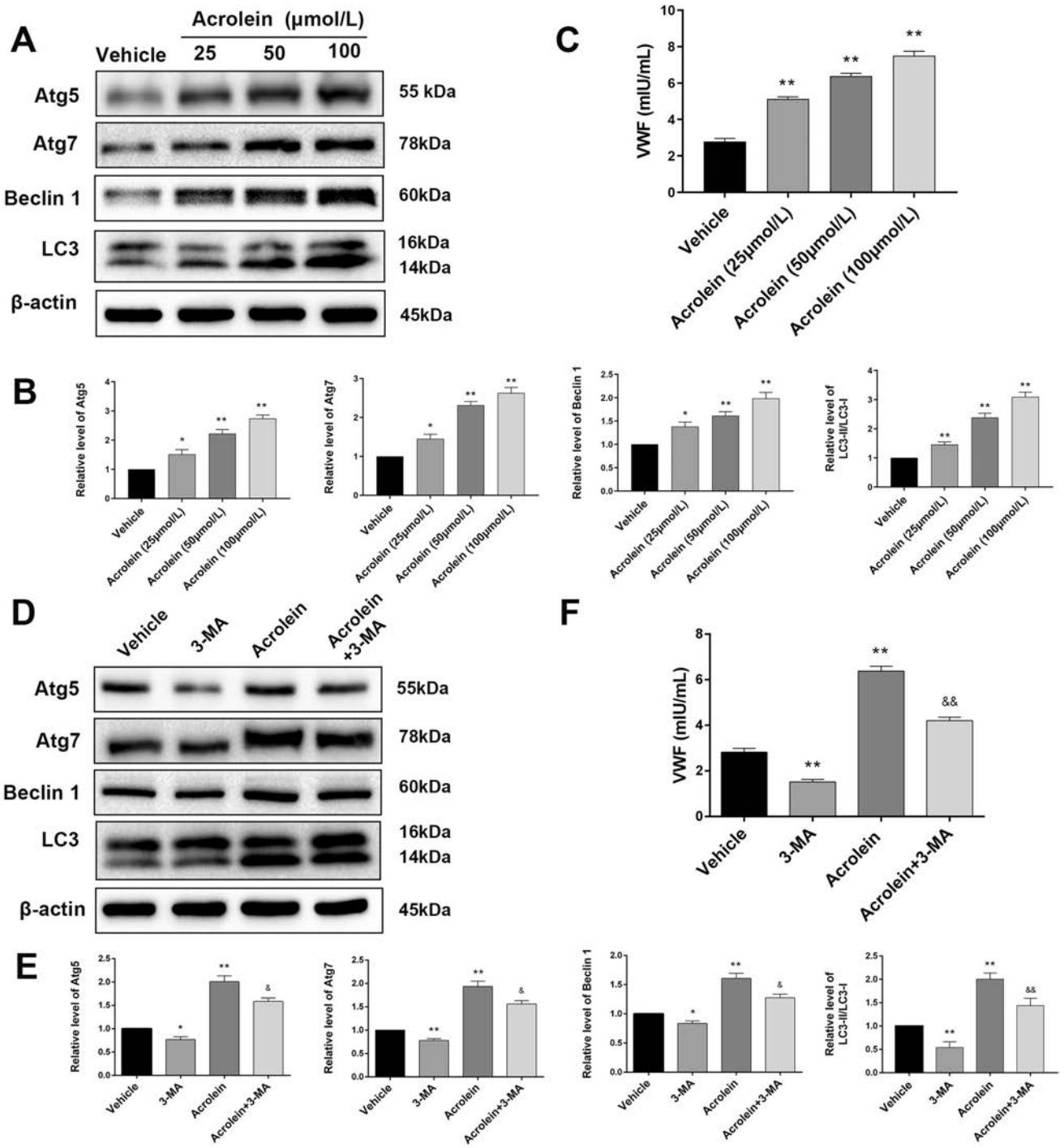

Fig. 5 Acrolein regulates the secretion of VWF by activating autophagy. **A** Western blots of Atg5, Atg7, Becline1, and LC3 in HUVECs treated with different concentrations of acrolein (25, 50, and 100 μmol/L) and vehicle for 6 h. **B** Relative levels of these proteins expressed as percentages of β-actin. **C** Effects of acrolein on VWF secretion in the above groups. **D** Western blots of Atg5, Atg7, Beclin-1, and LC3 in HUVECs pretreated with or without 5 mmol/L 3-MA for 2 h, followed by treatment with acrolein (50 μmol/L) for 6 h. **E** Relative levels of these proteins expressed as percentages of β-actin. **F** Effects of 3-MA (5 mmol/L) on acrolein-induced VWF secretion in the above groups. Values are presented as the mean ± SEM, $n = 3$ per group, $^{*}P < 0.1$, $^{**}P < 0.01$.

acrolein-induced autophagy (Fig. 5D, E), and acrolein-stimulated VWF secretion (Fig. 5F). The above results revealed that acrolein induces the release of VWF by activating autophagy.

Acrolein Activates Autophagy *via* the Akt/mTOR Pathway

We next explored the possible mechanism by which acrolein activates autophagy. First, GO and KEGG enrichment analyses indicated that the mTOR signaling pathway was one of the most enriched pathways (Fig. 4F). The Akt/mTOR axis is a classic autophagy signaling pathway [38]. Therefore, we hypothesized that acrolein activates autophagy by regulating the Akt/mTOR pathway. After treatment with acrolein (50 μmol/L), the p-Akt/Akt and p-mTOR/mTOR ratios were significantly downregulated (Fig. 6A, B). Then, an Akt activator (SC79) and an mTOR activator (MHY1485) were added after treatment with acrolein. SC79 (5 μg/mL) or MHY1485 (10 μmol/L) abrogated the acrolein-induced reduction in the p-mTOR/mTOR ratio. Accordingly, the expression of Atg5, Atg7,

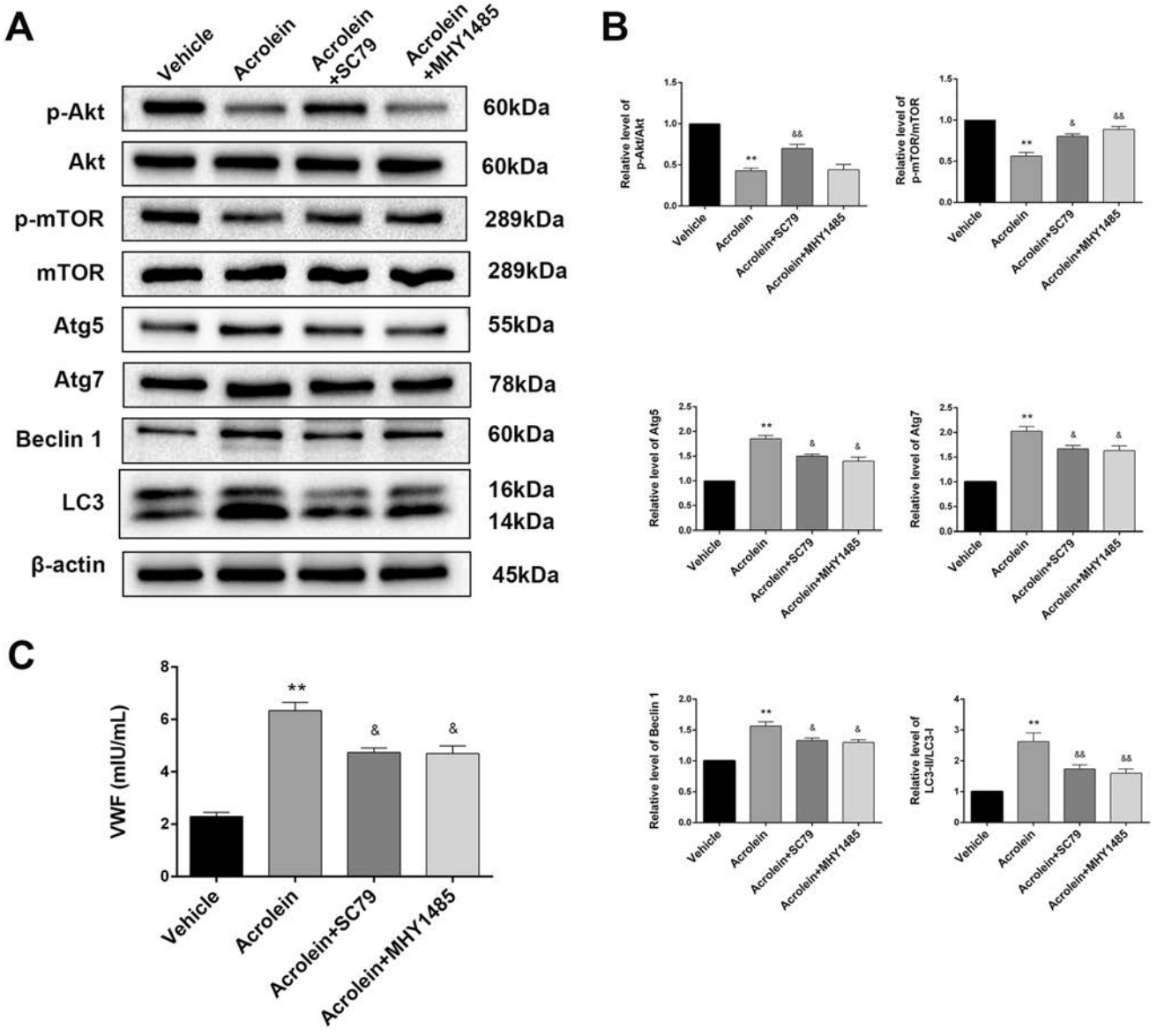

Fig. 6 Acrolein activates autophagy *via* the AKT/mTOR pathway. **A** Western blots of p-Akt, Akt, p-mTOR, mTOR, Atg5, Atg7, Beclin 1, and LC3 in each group. **B** Relative levels of these proteins expressed as percentages of β-actin. **C** Effects of SC79 or MHY1485 on acrolein-induced VWF secretion in each group. Values are presented as the mean ± SEM, $n = 3$ per group, $^{*}P < 0.05$, $^{**}P < 0.01$ *vs* vehicle group. $^{\&}P < 0.05$, $^{\&\&}P < 0.01$ *vs* acrolein group.

Beclin1, and LC3-II/LC3-I decreased in the SC79+acrolein and MHY1485+acrolein groups compared with the acrolein group (Fig. 6A, B). Furthermore, we measured the level of VWF release in each group. The secretion of VWF was significantly reduced after co-treatment with acrolein and SC79 or MHY1485 (Fig. 6C). These results indicated that the Akt/mTOR-mediated autophagy pathway is involved in the regulation of acrolein-mediated VWF release.

Acrolein is Upregulated in the Perilesional Cortex, Disrupts the Blood-brain Barrier, and Affects Endothelial Cell Integrity

First, Western blot and immunofluorescence staining were used to assess the alterations in acrolein over time post-TBI in the perilesional cortex of mice with or without phenelzine. The results showed that acrolein was increased in a time-dependent manner in the perilesional cortex, and was cleared by phenelzine (Fig. 7A–C). As described in previous studies, destruction of the BBB plays an important role in TBI secondary coagulopathy [8], so we next explored whether acrolein is involved in the destruction of the BBB. First, we found that acrolein was co-localized with endothelial cells in the cortex (Fig. S2). Then, the administration of phenelzine after TBI abrogated the downregulation of Occludin and ZO-1 (Fig. 7D, E). Next, acrolein treatment of HUVECs reduced the expression of Occludin and ZO-1 in a concentration- and time-dependent manner (Fig. 7D, E). Compared to that of sham mice, TBI significantly increased Evans blue extravasation. Treatment of the mice with phenelzine after TBI significantly mitigated BBB disruption (Figs. 7F and S3). Using a transwell cell migration assay, we found that acrolein contributed to FITC-dextran leakage through the endothelial cell barrier (Fig. 7G). These results revealed that acrolein is significantly upregulated in the perilesional cortex, and contributes to the disruption of the BBB and endothelial cell integrity.

Phenelzine as a Therapeutic

The clearance of acrolein by phenelzine during the acute phase of TBI strongly indicated the therapeutic potential of phenelzine in preventing TBI-induced coagulopathy. We found that a single administration of phenelzine 30 min after TBI reduced circulating acrolein (Fig. 2A) and reversed the trauma-induced hypercoagulable state (Fig. 2B, C). Nissl staining at 24 h after TBI showed that the lesion volume was 15.1% smaller in mice treated with phenelzine than in those treated with vehicle (Fig. 8A, B). Phenelzine also mitigated brain injury and brain edema after TBI (Fig. 8C). By preventing coagulopathy, cerebral edema, and reducing lesion volume, the 7-day mortality was decreased by 28.6% in mice treated with phenelzine, compared to those treated with vehicle (Fig. 8D). Mice treated with phenelzine after TBI had lower neurologic deficit scores than mice in the vehicle-treated group at both time points during the 7-day monitoring period (Fig. 8E). These results indicate the therapeutic and protective effects of phenelzine.

Discussion

Coagulopathy is a common clinical complication after severe TBI, and is closely associated with intracranial hemorrhage [39] and progressive hemorrhagic injury [40]. Coagulopathy has a detrimental effect on the outcome and overall prognosis of TBI patients [41, 42], leading to an increased risk of mortality and more unfavorable outcomes than in those without coagulopathy [43, 44]. However, the pathophysiological mechanism of TBI-induced coagulopathy remains unclear, resulting in limited measures for prevention and treatment. In an effort to deepen our insight into the molecular mechanisms underlying coagulopathy disease and identify novel therapeutic targets, we investigated the role of lipid-related molecules in TBI. Acrolein, a typical lipid peroxidation product, can lead to thrombosis [20]. Considering its important role in stimulation of the coagulation cascade, we showed for the first time that acrolein is involved in TBI-induced coagulopathy using samples from TBI patients, animal models, and HUVECs.

In the present work, we demonstrated for the first time that acrolein induces systemic coagulopathy after TBI *via* autophagy-dependent secretion of VWF and that acrolein is an interesting potential therapeutic target. Several experimental findings substantiate our conclusions: (1) the plasma acrolein level is increased in TBI patients, and a high plasma acrolein level is associated with the incidence of coagulopathy; (2) acrolein is significantly upregulated in peripheral blood after TBI in mice and contributes to an early hypercoagulable state; (3) acrolein induces coagulopathy by regulating VWF secretion; (4) mRNA-Seq analysis and follow-up experiments demonstrate that acrolein over-activates autophagy by regulating the Akt/mTOR pathway, through which acrolein induces VWF secretion; and (5) acrolein is upregulated in the perilesional cortex, affects endothelial cell integrity, and disrupts the BBB.

To determine the role of acrolein in TBI, we first evaluated its plasma levels in TBI patients and healthy controls, and found that it was higher in TBI patients. We also provided evidence that high plasma acrolein is associated with coagulopathy. Moreover, logistic regression analysis indicated that acrolein is an independent risk

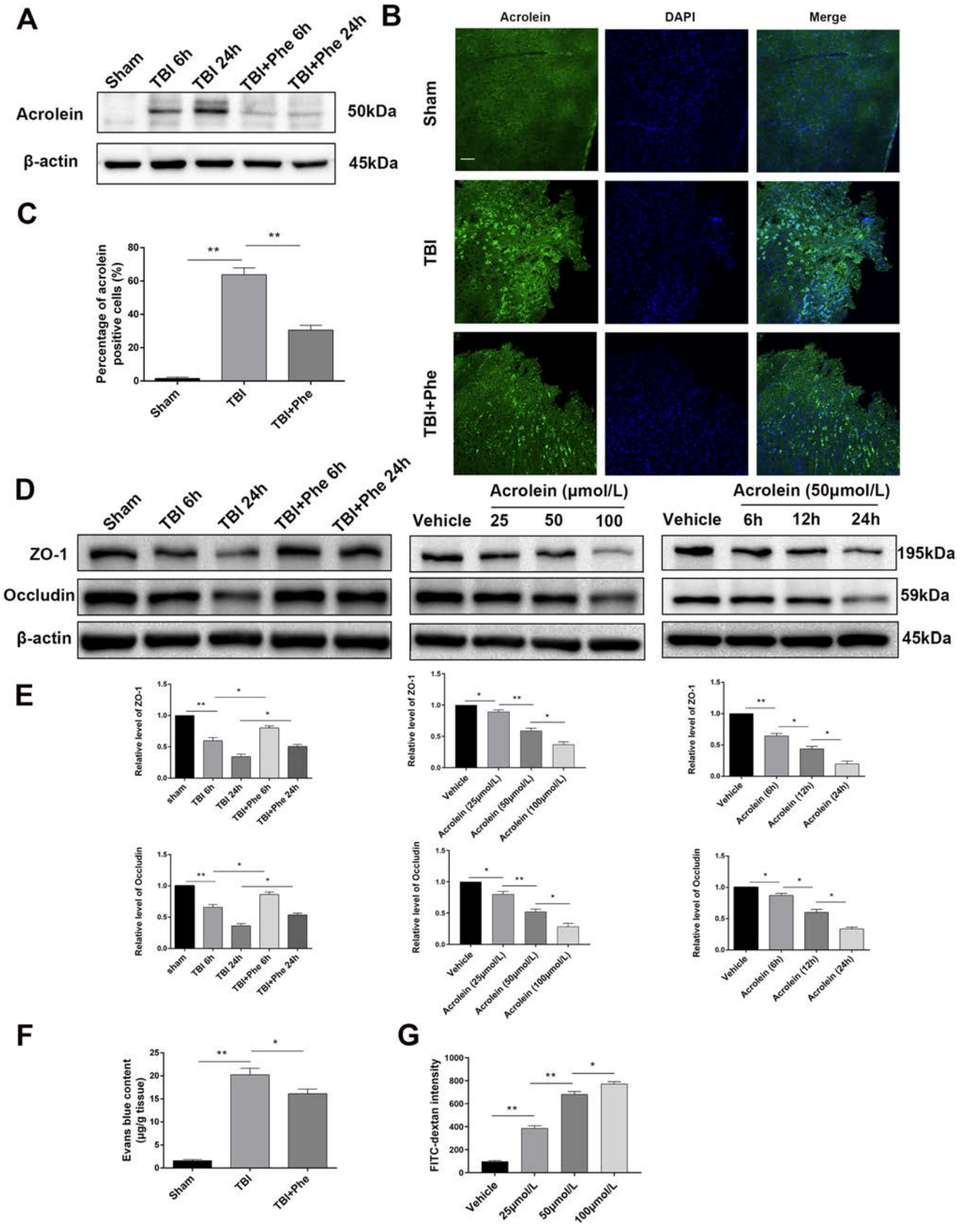
A
Sham
TBI 6h
TBI 24h
TBI+Phe 6h
TBI+Phe 24h
Acrolein
50kDa
β-actin
45kDa
B
Acrolein
DAPI
Merge
Sham
TBI
TBI+Phe
C
Percentage of acrolein positive cells (%)
Sham
TBI
TBI+Phe
D
Acrolein (μmol/L)
Acrolein (50μmol/L)
Vehicle
25
50
100
6h
12h
24h
ZO-1
Occludin
β-actin
195kDa
59kDa
45kDa
E
Relative level of ZO-1
Relative level of Occludin
sham
TBI 6h
TBI 24h
TBI+Phe 6h
TBI+Phe 24h
Vehicle
Acrolein (25μmol/L)
Acrolein (50μmol/L)
Acrolein (100μmol/L)
Acrolein (6h)
Acrolein (12h)
Acrolein (24h)
F
Evans blue content (μg/g tissue)
Sham
TBI
TBI+Phe
G
FITC-dextan intensity
Vehicle
25μmol/L
50μmol/L
100μmol/L

◀**Fig. 7** Acrolein is upregulated in the perilesional cortex, disrupts the blood-brain barrier, and affects endothelial cell integrity. **A** Western blots of acrolein in the perilesional cortex of mice at 6 h and 24 h after TBI with or without phenelzine. **B** Representative images of immunofluorescence staining for acrolein (green) in the perilesional cortex 24 h after TBI with or without phenelzine (scale bar, 50 μm). **C** Percentages of acrolein-positive cells. **D, E** Western blots (**D**) and analysis (**E**) of Occludin and ZO-1 expression in each group. **F** Evans blue levels in the brain. **G** Dextran staining intensity in confluent HUVECs in Transwells stimulated with different concentrations of acrolein (25, 50, and 100 μmol/L) and vehicle for 6 h and then incubated with FITC-dextran for 30 min. Values are presented as the mean ± SEM, $n = 6$ per group, $^{*}P < 0.05$, $^{**}P < 0.01$.

factor for coagulopathy. Many studies have explored potential molecules to predict acute traumatic coagulopathy. For example, plasma copeptin levels independently predict acute traumatic coagulopathy and progressive hemorrhagic injury after TBI [45]. Plasma galectin-3 concentrations after TBI are closely related to trauma severity, inflammation, and acute traumatic coagulopathy [46]. The pro-coagulant activity of brain-derived microparticles after TBI has been increasingly studied [24]. It is well established that the brain is rich in lipids [47]; however, the predictive ability and related mechanism of lipid peroxidation products produced after TBI in coagulopathy have not been investigated. The role of acrolein in TBI-induced coagulopathy was indicated in our study. Our clinical evidence supported the notion that high levels of plasma acrolein is an important and powerful predictor of coagulopathy and might play a potential role in the mechanism of coagulopathy. In view of the important role of acrolein in coagulopathy, the clinical importance of acrolein deserves further study.

In a mouse model of TBI, the mice rapidly develop a hypercoagulable state at 6 h, followed by a hypocoagulable state later (at approximately 24 h) [9, 11], consistent with our findings. Our study mainly focused on the time point associated with hypercoagulability, with the goal of preventing and correcting it after TBI. We also evaluated the expression of acrolein in other organs (heart, liver, kidney, intestine, skeletal muscle, and lung) after trauma and found that these organs produced very little (Fig. S4A). We hypothesized that the acrolein produced by the perilesional cortex is an important source of the increased acrolein in peripheral blood. We found that the administration of an acrolein scavenger after TBI improved coagulopathy, and we injected healthy mice with different concentrations of acrolein through the tail vein to simulate

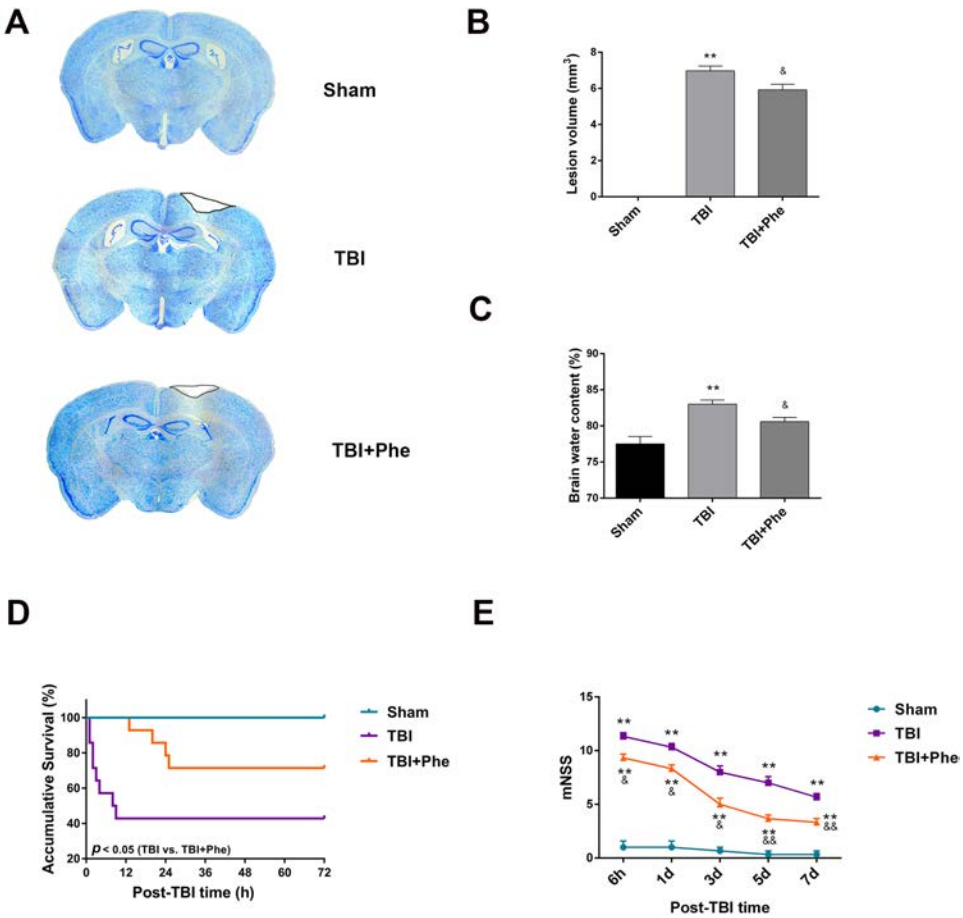

Fig. 8 Effects of phenelzine (acrolein scavenger) on lesion volume, brain water content, survival, and neurological function scores in mice after intracranial hemorrhage. **A** Representative images of brains serially sliced and subjected to Nissl staining ($n = 6$ per group). **B** Quantification of lesion volume ($n = 6$ per group). **C** Quantification of brain water content ($n = 6$ per group). **D** Kaplan-Meier survival plots of mice treated with or without phenelzine after TBI and sham mice ($n = 14$ per group). **E** Neurological recovery determined by mNSS at 6 h and 1, 3, 5, and 7 days post-TBI ($n = 6$ per group). Values are presented as the mean ± SEM, $^{*}P < 0.05$, $^{**}P < 0.01$ *vs* sham group, $^{\&}P < 0.05$, $^{\&\&}P < 0.01$ *vs* TBI group.

elevated acrolein in the circulatory system. Acrolein-induced coagulopathy was concentration-dependent, consistent with our clinical findings.

VWF is a large multimeric glycoprotein that is critical in regulating the balance between bleeding and clotting [48]. It is synthesized only in vascular endothelial cells and megakaryocytes [49]. Although a portion of VWF undergoes basal secretion into the plasma, the majority is stored in the Weibel-Palade bodies (WPBs) in endothelial cells and in the alpha granules of platelets. VWF in the plasma mainly comes from endothelial cells [50]. Its secretion endothelial cells is associated with hypercoagulability and the risk of thrombosis [51]. However, the original initiator of VWF in TBI is unclear. In our study, VWF was increased in the plasma in the acute phase after TBI, and the administration of phenelzine reduced this increase. Similarly, tail vein injection of acrolein caused an increase in VWF in plasma. ADAMTS13 (a disintegrin and metalloproteinase with a thrombospondin type 1 motif, member 13) is mainly synthesized in the liver [52] and is associated with the degradation of thrombogenic VWF multimers [52, 53]. In our study, the administration of rhADAMTS-13 improved the hypercoagulability after tail vein injection of acrolein. Our results suggested that acrolein induces hypercoagulability partly through the secretion of VWF. However, the specific mechanism by which acrolein promotes the secretion of VWF is unclear.

To clarify the specific mechanism by which acrolein promotes VWF release, we determined the transcriptomics changes in HUVECs after acrolein treatment. KEGG analysis indicated that acrolein treatment over-activated autophagy in HUVECs. Interestingly, Takehiro *et al.* demonstrated that WPBs and autophagosomes directly interact and that VWF and WPB remnants are found within autophagosomes. Knockdown or deletion of the essential autophagy genes *Atg5* or *Atg7* impairs the secretion of VWF *in vitro* and *in vivo*, and pharmacological inhibition of autophagic flux leads to a significant prolongation of bleeding time [37]. Proteomic analysis of these secreted endothelial autophagic vacuoles showed that they contain VWF [54]. In our results, we demonstrated that acrolein activated autophagy, and induced the formation of autophagic lysosomes and the release of VWF. The secretion of VWF significantly decreased after acrolein treatment when HUVECs were incubated with autophagy inhibitors. Our results indicated that acrolein regulates the secretion of VWF partly through the autophagy pathway. Furthermore, we explored how acrolein activated autophagy and KEGG analysis showed that the mTOR signaling pathway was one of the most enriched pathways. mTOR plays an important role in regulating autophagy [55], and emerging evidence suggests that Akt is crucial for mTOR phosphorylation and autophagy inhibition [56, 57]. In the present study, treatment with acrolein significantly reduced the phosphorylation of Akt and mTOR. However, co-treatment with acrolein and the AKT activator SC79 or mTOR activator MHY1485 induced a significant increase in the phosphorylation of mTOR. Our studies suggested that acrolein induces autophagy *via* the Akt/mTOR signaling pathway.

We also explored some other possible mechanisms by which acrolein could cause coagulopathy. BBB disruption could contribute to TBI-induced coagulopathy by allowing the release of brain-derived pro-coagulant substances (such as tissue factors, phosphatidylserine, and cardiolipin) into the circulation to induce systemic coagulopathy [8, 9, 24]. Interestingly, in our study the KEGG analysis indicated that acrolein could affect endothelial cell integrity. Here, we demonstrated that acrolein was abundantly produced in the perilesional cortex, disrupted the BBB, and affected endothelial cell integrity. Further disruption of the BBB allowed more acrolein to be released into the circulatory system. In addition, we provided evidence that acrolein is present in blood vessels in the perilesional cortex (Figs S2 and S4B), suggesting that acrolein acts on endothelial cells to some extent. Moreover, acrolein was found in blood vessels in the ipsilateral non-perilesional cortex (Fig. S4C), indicating that acrolein produced at the site of injury can be released into the circulation.

Some limitations should be noted when interpreting the experimental data. First, our study demonstrated that acrolein promotes the secretion of VWF. However, we have not explored whether acrolein affects the synthesis of VWF. Second, our results suggested that acrolein promotes the release of VWF by activating autophagy *via* the AKT/mTOR pathway *in vitro*. In future studies, the use of animals with endothelial cell-specific knockout of autophagy-related genes (such as *Atg5* or *Atg7*) could provide more convincing evidence. Finally, the role of other lipid peroxidation products in TBI-induced coagulopathy deserves further study.

In conclusion, this study showed that acrolein exacerbates systemic coagulopathy in TBI by promoting the secretion of VWF from endothelial cells. At the molecular level, acrolein might regulate VWF release by activating autophagy *via* the AKT/mTOR pathway. Overall, data from our study deserve further investigation to validate acrolein as a promising novel therapeutic target for TBI-induced coagulopathy.

Acknowledgements This work was supported by the National Natural Science Foundation of China (81630027).

Conflict of interest The authors declare no conflicts of interest.

References

1. Global, regional, and national burden of traumatic brain injury and spinal cord injury, 1990–2016: a systematic analysis for the Global Burden of Disease Study 2016. Lancet Neurol 2019, 18: 56–87.
2. Franschman G, Greuters S, Jansen WH, Posthuma LM, Peerdeman SM, Wattjes MP. Haemostatic and cranial computed tomography characteristics in patients with acute and delayed coagulopathy after isolated traumatic brain injury. Brain Inj 2012, 26: 1464–1471.
3. de Oliveira Manoel AL, Neto AC, Veigas PV, Rizoli S. Traumatic brain injury associated coagulopathy. Neurocrit Care 2015, 22: 34–44.
4. Sun Y, Wang J, Wu X, Xi C, Gai Y, Liu H, *et al.* Validating the incidence of coagulopathy and disseminated intravascular coagulation in patients with traumatic brain injury–analysis of 242 cases. Br J Neurosurg 2011, 25: 363–368.
5. Maegele M, Schöchl H, Menovsky T, Maréchal H, Marklund N, Buki A, *et al.* Coagulopathy and haemorrhagic progression in traumatic brain injury: advances in mechanisms, diagnosis, and management. Lancet Neurol 2017, 16: 630–647.
6. Stein SC, Spettell C, Young G, Ross SE. Delayed and progressive brain injury in closed-head trauma: radiological demonstration. Neurosurgery 1993, 32: 25–30; discussion 30–21.
7. Kumar MA, Cao W, Pham HP, Raju D, Nawalinski K, Maloney-Wilensky E, *et al.* Relative deficiency of plasma a disintegrin and metalloprotease with thrombospondin Type 1 repeats 13 activity and elevation of human neutrophil peptides in patients with traumatic brain injury. J Neurotrauma 2019, 36: 222–229.
8. Zhang J, Zhang F, Dong JF. Coagulopathy induced by traumatic brain injury: systemic manifestation of a localized injury. Blood 2018, 131: 2001–2006.
9. Zhao Z, Wang M, Tian Y, Hilton T, Salsbery B, Zhou EZ, *et al.* Cardiolipin-mediated procoagulant activity of mitochondria contributes to traumatic brain injury-associated coagulopathy in mice. Blood 2016, 127: 2763–2772.
10. Zhao Z, Zhou Y, Li M, Zhang J, Dong JF. Extracellular mitochondria in traumatic brain injury induced coagulopathy. Semin Thromb Hemost 2020, 46: 167–175.
11. Zhou Y, Cai W, Zhao Z, Hilton T, Wang M, Yeon J, *et al.* Lactadherin promotes microvesicle clearance to prevent coagulopathy and improves survival of severe TBI mice. Blood 2018, 131: 563–572.
12. Hsu MC, Huang YS, Ouyang WC. Beneficial effects of omega-3 fatty acid supplementation in schizophrenia: possible mechanisms. Lipids Health Dis 2020, 19: 159.
13. Khatri N, Thakur M, Pareek V, Kumar S, Sharma S, Datusalia AK. Oxidative stress: Major threat in traumatic brain injury. CNS Neurol Disord Drug Targets 2018, 17: 689–695.
14. Anthonymuthu TS, Kenny EM, Lamade AM, Kagan VE, Bayır H. Oxidized phospholipid signaling in traumatic brain injury. Free Radic Biol Med 2018, 124: 493–503.
15. Esterbauer H, Schaur RJ, Zollner H. Chemistry and biochemistry of 4-hydroxynonenal, malonaldehyde and related aldehydes. Free Radic Biol Med 1991, 11: 81–128.
16. Hill RL, Singh IN, Wang JA, Hall ED. Time courses of post-injury mitochondrial oxidative damage and respiratory dysfunction and neuronal cytoskeletal degradation in a rat model of focal traumatic brain injury. Neurochem Int 2017, 111: 45–56.
17. Pocernich CB, Butterfield DA. Acrolein inhibits NADH-linked mitochondrial enzyme activity: implications for Alzheimer's disease. Neurotox Res 2003, 5: 515–520.
18. Stevens JF, Maier CS. Acrolein: sources, metabolism, and biomolecular interactions relevant to human health and disease. Mol Nutr Food Res 2008, 52: 7–25.
19. Wu X, Cui W, Guo W, Liu H, Luo J, Zhao L, *et al.* Acrolein aggravates secondary brain injury after intracerebral hemorrhage through Drp1-mediated mitochondrial oxidative damage in mice. Neurosci Bull 2020, 36: 1158–1170.
20. Zirak MR, Mehri S, Karimani A, Zeinali M, Hayes AW, Karimi G. Mechanisms behind the atherothrombotic effects of acrolein, a review. Food Chem Toxicol 2019, 129: 38–53.
21. Siebold L, Obenaus A, Goyal R. Criteria to define mild, moderate, and severe traumatic brain injury in the mouse controlled cortical impact model. Exp Neurol 2018, 310: 48–57.
22. Cebak JE, Singh IN, Hill RL, Wang JA, Hall ED. Phenelzine protects brain mitochondrial function *in vitro* and *in vivo* following traumatic brain injury by scavenging the reactive carbonyls 4-hydroxynonenal and acrolein leading to cortical histological neuroprotection. J Neurotrauma 2017, 34: 1302–1317.
23. Wu Y, Liu W, Zhou Y, Hilton T, Zhao Z, Liu W, *et al.* von Willebrand factor enhances microvesicle-induced vascular leakage and coagulopathy in mice with traumatic brain injury. Blood 2018, 132: 1075–1084.
24. Tian Y, Salsbery B, Wang M, Yuan H, Yang J, Zhao Z, *et al.* Brain-derived microparticles induce systemic coagulation in a murine model of traumatic brain injury. Blood 2015, 125: 2151–2159.
25. Liu AH, Chu M, Wang YP. Up-regulation of Trem2 inhibits hippocampal neuronal apoptosis and alleviates oxidative stress in epilepsy *via* the PI3K/Akt pathway in mice. Neurosci Bull 2019, 35: 471–485.
26. Brake MA, Ivanciu L, Maroney SA, Martinez ND, Mast AE, Westrick RJ. Assessing blood clotting and coagulation factors in mice. Curr Protoc Mouse Biol 2019, 9: e61.
27. Wu X, Luo J, Liu H, Cui W, Guo K, Zhao L, *et al.* Recombinant adiponectin peptide ameliorates brain injury following intracerebral hemorrhage by suppressing astrocyte-derived inflammation *via* the inhibition of Drp1-mediated mitochondrial fission. Transl Stroke Res 2020.
28. Zhou Z, Shao T, Qin M, Miao X, Chang Y, Sheng W, *et al.* The effects of autophagy on vascular endothelial cells induced by airborne PM2.5. J Environ Sci (China) 2018, 66: 182–187.
29. Wang J, Jiang C, Zhang K, Lan X, Chen X, Zang W, *et al.* Melatonin receptor activation provides cerebral protection after traumatic brain injury by mitigating oxidative stress and inflammation *via* the Nrf2 signaling pathway. Free Radic Biol Med 2019, 131: 345–355.
30. Hu HM, Li B, Wang XD, Guo YS, Hui H, Zhang HP, *et al.* Fluoxetine is neuroprotective in early brain injury *via* its anti-inflammatory and anti-apoptotic effects in a rat experimental subarachnoid hemorrhage model. Neurosci Bull 2018, 34: 951–962.

31. Jing Y, Yang DX, Wang W, Yuan F, Chen H, Ding J, *et al.* Aloin protects against blood-brain barrier damage after traumatic brain injury in mice. Neurosci Bull 2020, 36: 625–638.
32. Lustenberger T, Talving P, Kobayashi L, Barmparas G, Inaba K, Lam L, *et al.* Early coagulopathy after isolated severe traumatic brain injury: relationship with hypoperfusion challenged. J Trauma 2010, 69: 1410–1414.
33. Sporn LA, Marder VJ, Wagner DD. Inducible secretion of large, biologically potent von Willebrand factor multimers. Cell 1986, 46: 185–190.
34. Johansson PI, Sørensen AM, Perner A, Welling KL, Wanscher M, Larsen CF, *et al.* Disseminated intravascular coagulation or acute coagulopathy of trauma shock early after trauma? An observational study. Crit Care 2011, 15: R272.
35. Russell RT, McDaniel JK, Cao W, Shroyer M, Wagener BM, Zheng XL, *et al.* Low plasma ADAMTS13 activity is associated with coagulopathy, endothelial cell damage and mortality after severe paediatric trauma. Thromb Haemost 2018, 118: 676–687.
36. Plautz WE, Raval JS, Dyer MR, Rollins-Raval MA, Zuckerbraun BS, Neal MD. ADAMTS13: origins, applications, and prospects. Transfusion 2018, 58: 2453–2462.
37. Torisu T, Torisu K, Lee IH, Liu J, Malide D, Combs CA, *et al.* Autophagy regulates endothelial cell processing, maturation and secretion of von Willebrand factor. Nat Med 2013, 19: 1281–1287.
38. Wang HC, Zhang T, Kuerban B, Jin YL, Le W, Hara H, *et al.* Autophagy is involved in oral rAAV/Aβ vaccine-induced Aβ clearance in APP/PS1 transgenic mice. Neurosci Bull 2015, 31: 491–504.
39. Zhang D, Gong S, Jin H, Wang J, Sheng P, Zou W, *et al.* Coagulation parameters and risk of progressive hemorrhagic injury after traumatic brain injury: A systematic review and meta-analysis. Biomed Res Int 2015, 2015: 261825.
40. Yuan Q, Sun YR, Wu X, Yu J, Li ZQ, Du ZY, *et al.* Coagulopathy in traumatic brain injury and its correlation with progressive hemorrhagic injury: A systematic review and meta-analysis. J Neurotrauma 2016, 33: 1279–1291.
41. Epstein DS, Mitra B, O'Reilly G, Rosenfeld JV, Cameron PA. Acute traumatic coagulopathy in the setting of isolated traumatic brain injury: A systematic review and meta-analysis. Injury 2014, 45: 819–824.
42. Greuters S, van den Berg A, Franschman G, Viersen VA, Beishuizen A, Peerdeman SM, *et al.* Acute and delayed mild coagulopathy are related to outcome in patients with isolated traumatic brain injury. Crit Care 2011, 15: R2.
43. Harhangi BS, Kompanje EJ, Leebeek FW, Maas AI. Coagulation disorders after traumatic brain injury. Acta Neurochir (Wien) 2008, 150: 165–175; discussion 175.
44. Talving P, Benfield R, Hadjizacharia P, Inaba K, Chan LS, Demetriades D. Coagulopathy in severe traumatic brain injury: A prospective study. J Trauma 2009, 66: 55-61; discussion 61–52.
45. Yang DB, Yu WH, Dong XQ, Du Q, Shen YF, Zhang ZY, *et al.* Plasma copeptin level predicts acute traumatic coagulopathy and progressive hemorrhagic injury after traumatic brain injury. Peptides 2014, 58: 26–29.
46. Shen YF, Yu WH, Dong XQ, Du Q, Yang DB, Wu GQ, *et al.* The change of plasma galectin-3 concentrations after traumatic brain injury. Clin Chim Acta 2016, 456: 75–80.
47. Singh A, Kukreti R, Saso L, Kukreti S. Oxidative stress: A key modulator in neurodegenerative diseases. Molecules 2019, 24
48. Xiang Y, Hwa J. Regulation of VWF expression, and secretion in health and disease. Curr Opin Hematol 2016, 23: 288–293.
49. Sadler JE. Biochemistry and genetics of von Willebrand factor. Annu Rev Biochem 1998, 67: 395–424.
50. Chen J, Chung DW. Inflammation, von Willebrand factor, and ADAMTS13. Blood 2018, 132: 141–147.
51. Dmitrieva NI, Burg MB. Secretion of von Willebrand factor by endothelial cells links sodium to hypercoagulability and thrombosis. Proc Natl Acad Sci U S A 2014, 111: 6485–6490.
52. Zheng X, Chung D, Takayama TK, Majerus EM, Sadler JE, Fujikawa K. Structure of von Willebrand factor-cleaving protease (ADAMTS13), a metalloprotease involved in thrombotic thrombocytopenic purpura. J Biol Chem 2001, 276: 41059–41063.
53. Crawley JT, de Groot R, Xiang Y, Luken BM, Lane DA. Unraveling the scissile bond: how ADAMTS13 recognizes and cleaves von Willebrand factor. Blood 2011, 118: 3212–3221.
54. Pallet N, Sirois I, Bell C, Hanafi LA, Hamelin K, Dieudé M, *et al.* A comprehensive characterization of membrane vesicles released by autophagic human endothelial cells. Proteomics 2013, 13: 1108–1120.
55. Rubinsztein DC, Gestwicki JE, Murphy LO, Klionsky DJ. Potential therapeutic applications of autophagy. Nat Rev Drug Discov 2007, 6: 304–312.
56. Liang Q, Luo Z, Zeng J, Chen W, Foo SS, Lee SA, *et al.* Zika virus NS4A and NS4B proteins deregulate Akt-mTOR signaling in human fetal neural stem cells to inhibit neurogenesis and induce autophagy. Cell Stem Cell 2016, 19: 663–671.
57. Kim JH, Choi TG, Park S, Yun HR, Nguyen NNY, Jo YH, *et al.* Mitochondrial ROS-derived PTEN oxidation activates PI3K pathway for mTOR-induced myogenic autophagy. Cell Death Differ 2018, 25: 1921–1937.

Neurosci. Bull. August, 2021, 37(8):1176–1187
https://doi.org/10.1007/s12264-021-00689-6

www.neurosci.cn
www.springer.com/12264

REVIEW

Hypothalamic-Pituitary-End-Organ Axes: Hormone Function in Female Patients with Major Depressive Disorder

Yuncheng Zhu[1,2] · Xiaohui Wu[2] · Rubai Zhou[2] · Oliver Sie[3] · Zhiang Niu[2] · Fang Wang[4] · Yiru Fang[2,5,6]

Received: 6 August 2020 / Accepted: 27 November 2020 / Published online: 28 April 2021

Abstract Classic hypothalamic-pituitary-end-organ feedback loops – the hypothalamic-pituitary-adrenal axis (HPAA), hypothalamic-pituitary-thyroidal axis (HPTA), and hypothalamic-pituitary-gonadal axis (HPGA) – are associated with the neuroendocrine and immune systems in major depressive disorder (MDD). Female patients with MDD present with evident neuroendocrine and immunological changes. Glucocorticoid, thyroid hormone, and reproductive steroid levels fluctuate with menstrual cycles, which might lead to glucocorticoid receptor resistance, impairment of triiodothyronine conversion, and sex hormone secretion disorders. In this review, we summarize the independent and interactive functions of these three axes in female MDD patients. The similar molecular structure of steroids implies an interrelationship between the hypothalamic-pituitary-end-organ axes and the competitive inhibitory effects at the receptor level, especially when considering the HPAA and HPGA.

Keywords Major depressive disorder · Neurosecretory systems · Sex steroid hormones

Yuncheng Zhu and Xiaohui Wu contributed equally to this work.

✉ Fang Wang
wangfangpsychiatry@163.com

✉ Yiru Fang
yirufang@aliyun.com

[1] Division of Mood Disorders, Shanghai Hongkou Mental Health Center, Shanghai 200083, China

[2] Clinical Research Center, Shanghai Mental Health Center, Shanghai Jiao Tong University School of Medicine, Shanghai 200030, China

[3] Shanghai Medical College, Fudan University, Shanghai 200032, China

[4] Shanghai Yangpu Mental Health Center, Shanghai 200093, China

[5] CAS Center for Excellence in Brain Science and Intelligence Technology, Shanghai 200031, China

[6] Shanghai Key Laboratory of Psychotic Disorders, Shanghai 201108, China

Introduction

Although the monoamine hypothesis of MDD is well-accepted, precisely how antidepressants come into effect remains unclear [1]. There is increasing evidence that chronic stress derives from abnormalities in the biological processes of the human internal environment (especially the endocrine and immune systems) [2], which might raise the morbidity of MDD [3]. Postmortem and animal studies have revealed neuropathological changes in depressed patients and animals, such as monoaminergic system down-regulation, neurogenesis impairment, abnormal activity of the central nervous system (CNS), and synaptic dysfunction [4].

Proinflammatory cytokines can impair neurogenesis by affecting monoaminergic systems. Regional abnormalities found in the CNS, as well as neurodegeneration, have been reproduced in cell and animal models of depression [5]. In addition, strong evidence supports the hypothesis that inflammation and depression are closely related [6], and that it also affects the role of glucocorticoids in depression [7]. Under endogenous and exogenous stress, cytokines (such as nuclear factor-kappa and protein kinase A), can result in glucocorticoid receptor (GR) resistance [8] (impairing function of the HPAA and its reactivity to cortisol) and the induction of MDD *via* the neuroendocrine pathway [8, 9]. Fig. 1 shows a schematic diagram of these

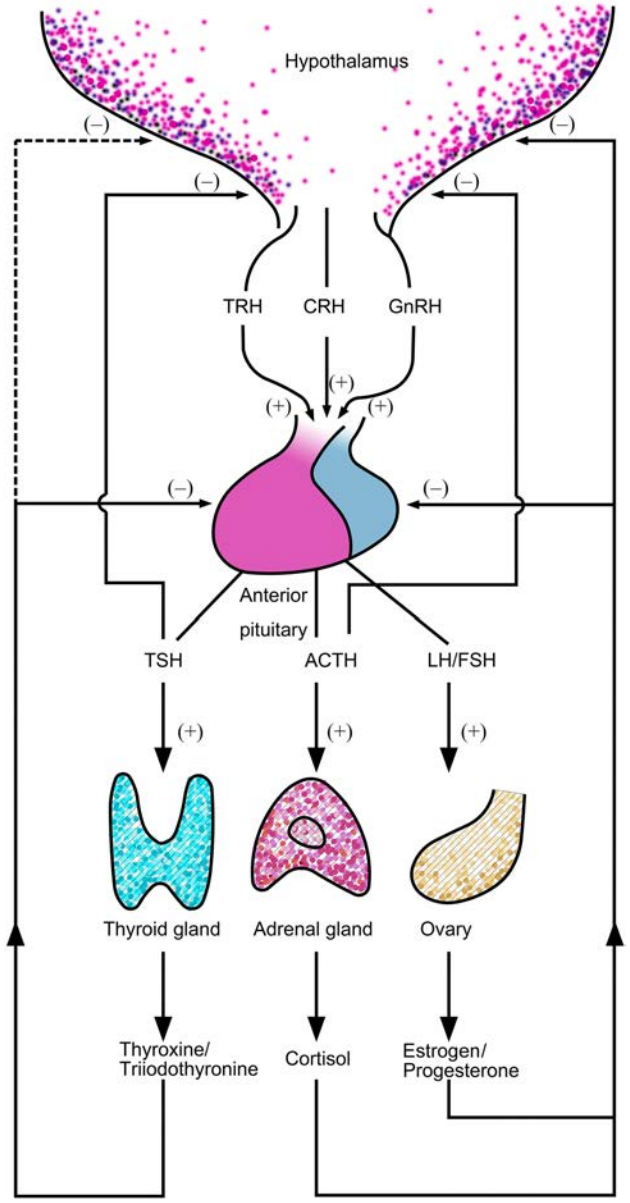

Fig. 1 Schematic of three functional hypothalamic-pituitary-end-organ axes of females, generating the interactive mechanism among inflammatory cytokines and these axes. The dashed line represents an uncertain feedback mechanism. A special case, estrogen has a positive feedback effect on the pituitary gland during the follicular phase and a negative feedback effect during the luteal phase. TRH, thyrotropin-releasing hormone; CRH, corticotropin-releasing hormone; GnRH, gonadotrophin-releasing hormone; TSH, thyroid stimulating hormone; ACTH, adrenocorticotropic hormone; LH, luteinizing hormone; FSH, follicle-stimulating hormone.

three classic feedback loops (HPAA, HPTA, and HPGA) in the human neuroendocrine and neuroimmune systems [10]. It is worth noting that the most common diseases of these neuroendocrine systems present with obvious sex differences [11–13] (Table 1). Clinical evidence has demonstrated that MDD is almost twice as common in females, with a first peak in prevalence in the second and third decades of life, with a second peak in the fifth decade [14]. The two onset peaks of female MDD are around the ages when neuroendocrine levels fluctuate greatly [15, 16].

Table 1 Gender ratios in common hypothalamic-pituitary-glandular axis disorders and depressive disorders

Disease	Gender ratio (male:female)
Hyperthyroidism	1:(4–6)
Hypothyroidism	1:4
Cushing disease	1:3
Addison's disease	1:(2–3)
Depressive disorders	1:2

Hypothalamic-Pituitary-Adrenal Axis and MDD

HPAA, Chronic Stress, and MDD

The HPAA participates in a wide range of biological functions, primarily those related to the stress response. Cortisol, produced by the adrenal cortex, has a potent effect on carbohydrate metabolism. The human body shows physical and psychological adaptive reactions to potential threats *via* cortisol activation [17]. In MDD patients, chronic stress may result in abnormalities of HPAA homeostasis and cause relevant effects [18]. MDD individuals present with increased volumes of pituitary and adrenal glands, as well as an up-regulation of cortisol function [19]. Long-term psychological stress could give rise to the suppression of cortisol, resulting in diminished sensitivity of the stress response [20].

In addition to increasing hormone concentrations, inhibition of GR function has also been found to accompany chronic stress in MDD patients [21]. GRs are widely distributed in the hippocampus; they respond to intracellular signaling by second messengers, and regulate HPAA feedback. The most widely accepted theory is that in MDD patients, glucocorticoid resistance leads to impairments in HPAA function. Dexamethasone inhibition and corticotropin-releasing hormone inhibition tests have shown that negative feedback is more likely to be inhibited [22]. GR resistance is seen as an inadequate *in vivo* response of glucocorticoid target genes to dexamethasone. In chronic stress states, the quantity of GRs and the affinity of glucocorticoids to them are changeable [23]; consequently, glucocorticoid resistance can arise. Similar to like insulin and insulin resistance, it has long been debated which comes first: increases in cortisol levels or GR resistance?

Neurogenesis, in which synaptic function plays an important role, can be decreased by long-term systemic cortisol exposure in MDD [24]. Relevant studies support the glucocorticoid theory of MDD, in which chronic stress states induce HPAA hyperactivity and excessive secretion of cortisol. This would aggravate the neuropathological process of MDD [18]. This hypothesis provides a new theoretical basis to explore MDD pharmacotherapy; perhaps there is potential in glucocorticoid agonists and antagonists as new antidepressants targeting GR function and cortisol levels. Furthermore, this could also point to studying HPAA dysfunctions as new biomarkers of MDD.

HPAA, Immune Inflammation, and MDD

Inflammatory cytokines can increase the levels of cortisol by both direct and indirect pathways [25]. This results in dysregulation of the HPAA by increasing the release of corticotropin-releasing hormone and adrenocorticotropic hormone (ACTH). In addition, inflammatory cytokines regulate GR sensitivity to cortisol indirectly. From another perspective, the HPAA can, in return, influence the immune system [26]; this may inhibit the secretion and release of pro-inflammatory factors *via* blocking of transcription factor activity [27]. However, physiologically overdemanding use of glucocorticoids in the clinic inhibits the release of cytokines, thereby exerting anti-inflammatory and immunosuppressant effects. Increases in glucocorticoid-generating signals allow for activation of the neuroendocrine and sympathetic nervous systems, while chronic stress may lead to glucocorticoid resistance. On the other hand, opposite views suggest that glucocorticoids promote inflammation in certain circumstances, depending on environmental and temporal factors. In addition, that cortisol has a negative correlation with both pro-inflammatory factors [interleukin-1β (IL-1β) and tumor necrosis factor α], and anti-inflammatory factors (IL-4, IL-5, IL-10, and IL-13) simultaneously [28] is worth discussing.

The association between stress and immune enhancement is regulated by glucocorticoid resistance. Stressed individuals present with higher glucocorticoid resistance than non-stressed individuals. Glucocorticoid resistance is strongly linked to pro-inflammatory cytokines; enhanced inflammatory responses occur most in glucocorticoid-resistant individuals, second only to in those exposed to acute stressors, and both are linked to chronic stress and MDD [9]. According to the glucocorticoid resistance hypothesis, high concentrations of pro-inflammatory cytokines and cortisol only occur in glucocorticoid-resistant MDD patients. It has been reported that increases in glucocorticoid resistance and pro-inflammatory cytokines are more common than an increase in cortisol alone, and 85% of cases that have increases in inflammation also present with glucocorticoid resistance [10]. In a meta-analysis, glucocorticoid resistance and inflammation levels had a positive correlation, with effect size 0.38 ($P = 0.06$; 95% CI, 0.14–0.62) [10]. Therefore, we should perhaps focus on glucocorticoids and their signaling rather than on cortisol levels alone. The glucocorticoid resistance hypothesis provides a reasonable explanation for synchronized elevations in cortisol and pro-inflammatory cytokines.

Another hypothesis is that glucocorticoids do not only have anti-inflammatory effects in MDD. Whether they are pro-inflammatory or anti-inflammatory mainly depends on the exact environment of individuals; a pro-inflammatory response requires special settings, such as large-dose glucocorticoid therapy [29]. The reaction time of glucocorticoids depends on the severity of inflammatory injury, which is also in line with evolution. When faced with a threatening event, it is necessary to utilize immunosuppressive and glucocorticoid-elevating effects to energize for either facing an attack or escape (fight or flight). However, recovery from trauma takes time. While glucocorticoid levels normalize, immune function needs to be enhanced [29]. Therefore, stress responses and the resulting elevated glucocorticoid levels are warning signs of central and peripheral inflammation. The microglia are important CNS cells that work against neuroendocrine warning signals; they react strongly to immune stimulation by generating pro-inflammatory cytokines and down-regulating glucocorticoid inhibition. Increases in this activity can result from an increased density of microglia in the hippocampus as a result of chronic stress, inducing immune-promoting states and impairing glucocorticoid inhibition [30]. Microglia inhibitors are able to reduce hypothalamic IL-1β levels during stress responses, which contribute to pro-inflammatory effects [31].

Due to MDD-related factors, glucocorticoids have some indirect interactions with inflammation. For example, in states of chronic stress, glucocorticoids can affect the sympathetic nervous system [32], which can influence the immune response [33]. Such an interaction would be another bridge that connects the HPAA and the immune system. Clinical use of adrenergic receptor inhibitors such as propranolol reduces the unstable psychological symptoms caused by stress [33]. Therefore, it is difficult to dispute the role of glucocorticoids in the development of MDD, and more research is needed in this area. Besides, mineralocorticoids (MRs), secreted by the adrenal glomerular zone, maintain the balance of water and electrolytes in the human body. The renin-angiotensin-aldosterone system mainly regulates blood pressure, causing vascular smooth muscle contraction as well as the retention of water and sodium [34]. Previous studies have suggested that MRs are also important stress modulators, which influence stress-induced HPAA up-regulation, the

appraisal of stress, and fearful memories [35]. Evidence has demonstrated that genetic variations in GRs and MRs are able to predict cognitive function in MDD, where GR genetic variation is associated with changes in attention and work-related memory, and MR genetic variation with changes in verbal memory [36].

As noted above, up-regulated levels of glucocorticoid play a driving role in inflammation, and over-activation of HPAA may be a key factor. Despite these increases in cortisol levels, the critical issue remains the decrease of glucocorticoid signaling. This hypothesis may explain some complex and perhaps more debated results of MDD treatment, including the efficacy of glucocorticoid antagonist treatment. Furthermore, GR resistance has been shown to be more predictive of depressive outcomes than hypercortisolemia [37]. Notwithstanding, it remains a challenge to study the effects of hypercortisolemia and GR resistance separately [38].

HPAA, Sex Differences and MDD

There are sex differences related to HPAA in MDD patients [39]. Young *et al.* have reported that depressed women manifest more disorderly secretion of ACTH. This study indicated that hormonal rhythm abnormalities do occur in depressed female patients and are associated with accentuated ACTH feedforward drive [40]. A recent study found that, after *in vivo* glucocorticoid stimulation, the higher GR sensitivity of healthy women was absent in depressed female patients. This suggested that sex-related differences in the regulation of HPAA may contribute to the vulnerability of females to the development of depression [41]. In the acute phase of stress, females appear to have a stronger positive correlation between cortisol levels and cognitive representation than males [42]. Serum cortisol levels are significantly higher in female patients [39]. Moreover, in first-episode MDD patients, the cortisol levels of women are higher than those in relapsed patients and healthy controls [43]. A study of chronic stress and the HPAA found that individuals who had suffered maltreatment in childhood also presented with sex differences in HPAA function: the cortisol activation response in females was significantly slower than in males [44].

Hypothalamic-Pituitary-Thyroid Axis and MDD

Thyroid Hormones and MDD

Thyroid hormones are important for metabolism and the growth and development of the nervous system. Lack of thyroid hormone in childhood may cause permanent brain damage, and can affect brain function in adulthood as well. Much clinical evidence has demonstrated that aberrant levels of thyroid hormone are associated with cognitive and emotional dysfunction. There are clearly overlapping symptoms between hypothyroidism and depression, such as fatigue, weight change, and depressive mood [45]. After release into the blood, thyrotropin (thyroid stimulating hormone, TSH) binds to the TSH receptor in the thyroid gland, resulting in the secretion of triiodothyronine (T3) and thyroxine (T4). Negative feedback in the HPTA results in elevated thyroid hormones, which inhibit pituitary gland release of TSH.

Several studies have endeavored to associate MDD with subclinical hypothyroidism, and attempts to use thyroid hormones as antidepressants have achieved clinical efficacy [46]. Moreover, it has been shown that T3 shortens the time to onset of tricyclic antidepressants [47]; a review of the guidelines of the British Association of Psychopharmacology found that MDD patients who had no response to first-line antidepressants could achieve treatment efficacy after the addition of highly bioactive T3 as a potentiator. The antidepressant effect of T3 augmentation of selective serotonin reuptake inhibitors is correlated with significant changes in the bioenergetic metabolism of the brain [48]. Similarly, T4 (with a relatively lower bioactivity) also has a potential synergistic effect on treatment-resistant MDD [49]. In a large-sample MDD treatment study with 1,410 MDD patients and 204 thyroid dysfunction patients, 60.64% of patients received combination therapy or synergistic therapy. Among all the risk factors, the regression coefficient of thyroid dysfunction and MDD was 0.74 (*odd ratio* = 2.1) [50]. A relationship has been reported between hypothyroidism and hyperlipidemia and other cardiovascular risk factors [51], as well as the aggravation of depression and anxiety, but there are also studies presenting no correlation between them [52, 53]. TSH showed a delayed response to thyrotropin-releasing hormone (TRH) only in several MDD patients who were in a depressive episode [52]. Furthermore, some studies have demonstrated that age and TSH are not factors associated with MDD, but that MDD severity might only be related to stress from life events [54]. Elucidation of the exact relationship between MDD and the HPTA requires further studies with larger sample sizes.

HPTA, Sex Differences, and MDD

From another perspective, thyroid-related diseases in women have an incidence 5–20 times greater than in men [55]. At certain physiological periods such as pregnancy, HPTA function becomes altered. The increase of estrogen during this period results in increases in thyroxine-binding globulin (TBG) as high as 150% [56]. TBG concentration may be a sensitive indicator of estrogen level, and

emotional instability in postpartum MDD is also likely to be associated with gonadal and thyroid hormone concentrations [57]. Recent studies have established models in pregnant and non-pregnant women, suggesting that pregnancy factors result in decreases in TSH and free T4 (FT4) levels. However, a negative correlation between TSH and FT4 induced by the negative feedback of the physiological axis could not be established in the third trimester of pregnancy [58, 59], which is considered to be precisely the highest-risk period for female MDD. As such, decreases in T4 and FT4 levels are associated with perinatal depression [60]. Significant physiological fluctuations of thyroid hormones in prenatal and postpartum subjects provide new perspectives to study the neuroendocrine aspects of MDD.

The perimenopausal period is also significant, in which the HPTA also presents changes [55]. Morbidity of thyroid-related diseases often increases with age, including that from autoimmune thyroiditis, hypothyroidism, nodular goiter, and thyroid tumors. They are more common in older women, presenting with symptoms such as anxiety, palpitations, sweating, sudden changes in weight, and insomnia. Both thyroid and ovarian dysfunctions are able to cause these symptoms.

Hypothalamic-Pituitary-Gonadal Axis and MDD

HPGA and Reproductive Depression

Correlation studies of female sexual dysfunction and the HPGA in MDD are very limited due to the complexity involved, and females often have significant physiological fluctuations of hormone levels during the menstrual cycle. Previous studies have shown that a sudden decrease of reproductive hormones may result in an abnormal state of mood [61]. This axis is also called the hypothalamic-pituitary-ovarian axis (HPOA) in women. Sexual dysfunction can have adverse effects on the quality of life, including psychological, biological, and sociological [62]. Some factors of sexual dysfunction have been identified, such as age, metabolic syndromes, diabetes, drug effects, mental health, behavioral disorders, intrauterine devices, and the adrenal and thyroid diseases described above, among others [63–67].

The prevalence of MDD in women is almost double that in men [68]. It is undetermined if this phenomenon results from environmental, social, or hormonal factors [69]. The impact of immune exposure on depression can be assessed by decreases in gonadal hormones during specific situations [68], such as in premenstrual syndrome (PMS), premenstrual dysphoric disorder (PMDD), and postpartum depression (PPD). The menopausal transition in perimenopausal depression (PMD) is associated with profound changes in reproductive hormones [70].

Before menstruation, many women may experience irritability or other psychological and behavioral changes, and these symptoms may remit suddenly after menstruation. PMS includes a series of mental and physical symptoms that occur in the premenstrual period in women of childbearing age, and symptoms generally cease with or after menstruation. About 50–80% of females experience mild PMS, while 20% of them require pharmacological therapy [71, 72]. The clinical definition of PMS is that 7–14 days before menstruation, patients experience mental symptoms including irritability, mental lethargy, inattention, and stress, as well as symptoms of physical discomfort such as insomnia, headache, fatigue, weakness, breast pain, diarrhea, edema, and paresthesia during the luteal phase. Some of these severe symptoms are analogous to that found in the International Classification of Diseases (10th revision) criteria of MDD with the characteristic of periodic episodes. PMS is commonly found in women 30 to 40 years old; the typical course begins at the start of the luteal phase (around 1 week before menstruation) when symptoms gradually worsen and become most severe 2–3 days before menstruation, then suddenly disappear with menstruation.

There are numerous theories attempting to explain the high prevalence of MDD in women, particularly from psychosocial and biological aspects. Among the biological factors, gonadal hormones play an important role. It has been found that estrogen and progesterone can affect the circadian rhythm [73], neurotransmission, and neuroendocrine function in mood disorders. Certain states can bring about dramatic fluctuations in gonadal hormone levels, which influence the HPGA feedback loop in PPD [74] and PMD [75].

These subtypes of depression have been categorized under reproductive depression, being derived from fluctuations in endocrine hormones rather than by primary classification under antidepressant treatment response; reproductive depression includes cyclic depression, PPD, and PMD. Interestingly, severe PMDD cases occurring before pregnancy in patients with reproductive depression is rare, but with age, perinatal period depression gradually increases and recurs frequently weeks or months after delivery; such outcomes often evolve into premenstrual depression [76]. In cases of ineffective MDD treatment, recurrence of MDD in female patients is characterized by treatment resistance to multiple antidepressants. A retrospective study found that in refractory female MDD patients, symptoms disappear several years before the last pregnancy [77]. Reproductive depression can be alleviated or cease following the end of menopause. Estrogen has no therapeutic effect on senile MDD patients with or without

adjunctive progestogen [78], however it can improve vasomotor symptoms, sleep quality, and pain and dryness during sexual intercourse caused by vaginal atrophy. The pathological basis of reproductive depression is unclear; it is presumably related to neurotransmitters, neuroendocrine function, genetic factors, psychosocial factors, and the interactions between them.

Sex differences also play a role in the lifetime prevalence of MDD. Due to accelerated gonadal differentiation and development after puberty, females with MDD may suffer more changeable symptoms following the menstrual cycle. The clinical manifestations and signs of MDD in females differ from those in males of the same age, including irritability, anxiety, and physical complaints [79]. Atypical MDD symptoms, such as excessive appetite, weight gain, hypersomnia, and atypical reactions to drugs, are also more common in women [80]. A recent study has summarized evidence supporting the importance of sex in modulating responses to rapid-acting antidepressant treatment [81].

Therefore, hormones play a vital role in the emotional symptoms of women. Use of hormonal contraception is associated with subsequent use of antidepressants and a first diagnosis of depression, suggesting that depression is a potential adverse effect of hormonal contraceptive use [82]. Female bipolar disorder patients have a high risk of postpartum depression [83]. Reproductive depression is characterized by periodicity, thus it is commonly misdiagnosed as bipolar disorder [83]; these misdiagnosed patients might receive mood stabilizers, antidepressants, or modified electroconvulsive therapy [84]. According to preliminary statistics, 67% of female patients with bipolar disorder develop PPD [85]; associations might include family history, genetic susceptibility, and other precipitating factors. Another viewpoint is that, with profound reproductive hormonal up-regulation during pregnancy and lactation, long-time cyclic depression can result from the rapid withdrawal of gonadal steroids, not remitting until the new menstrual cycle is established. Sex hormones interact with the neurotransmission of serotonin and gamma-aminobutyric acid (GABA) [86], both of which have close connections with mood disorders.

Reliable evidence that supports the theory of sex-related depression has been summarized as the following [84]: (1) cyclic depression; (2) premenstrual symptoms that have already occurred in puberty; (3) a stable mental state before pregnancy; (4) depressive syndrome within the postpartum period; (5) significant mood relief during intervals between episodes of depression; (6) several years of recurrent depression without manic episodes; (7) coexistence of periodic physical complaints with depressive symptoms such as breast pain, bloating and headache; and (8) emotional symptoms associated with oral contraceptives.

Treatment of MDD with Sex Hormones

It is worth discussing whether these symptoms are induced by abnormalities of hormone levels or by abnormal responses to normal levels. This has also caused controversy in the fields of psychiatry and endocrinology as to whether such changes mean individual or intergroup differences. It is noteworthy that the US FDA approved the first drug for treatment of PPD in 2019 [87]. Allopregnanolone (also named tetrahydroprogesterone, THP) is a derivative of progesterone, which is the most potent of the progesterone metabolites. The potential role of allopregnanolone is that it could act as a safe and effective antidepressant therapy by its function of modulating $GABA_A$ function, which can correct postpartum dysregulation of the $GABA_A$ receptor and rebalance the activity of the $GABA_A$ and N-methyl-D-aspartate receptors [88]. Besides, progesterone modulates the concentration of tryptophan hydroxylase through the expression of 5α-reductase and 3α-hydroxysteroid dehydrogenase. It also contributes to suppression of neuronal excitability, providing neuroprotection, and promoting neurogenesis and neural restoration. However, there are negative effects such as anxiety, and aggression. Such contradictory results have dose-symptom curve dependence on THP, and also takes on individual differences. THP have biphasic effects, in that low concentrations increase an adverse, anxiogenic effect whereas higher concentrations decrease this effect and show beneficial, calming properties [89]. In gonadal steroid-withdrawn postpartum female rats, inescapable stress leads to a loss of hippocampal spine synapses, which is associated with poor escape performance [90]. THP can also increase the concentration of brain-derived neurotrophic factor, promoting hippocampal neuronal regeneration and improving depressive symptoms [91].

Correlations Between Female Hypothalamic-Pituitary-Glandular Axis (HPTA, HPAA, HPGA) Hormone Levels

Indeed, it is still hard to study the effects of hormones on MDD separately, especially when the gender variable is considered, so analyzing the correlation between hormones in these axes of females is needed.

In MDD, corticosteroids may interact with T3 and T4, and depressed mood is often correlated with hypothyroidism. Although the thyroid function of patients with MDD might show no abnormality, a relative hypothyroidism can exist in the CNS. At the downstream glandular level, T4 can be converted into T3 *via* type II 5'-deiodinase. In patients with MDD, cortisol may inhibit this enzyme, but conversely enhance the process of reverse

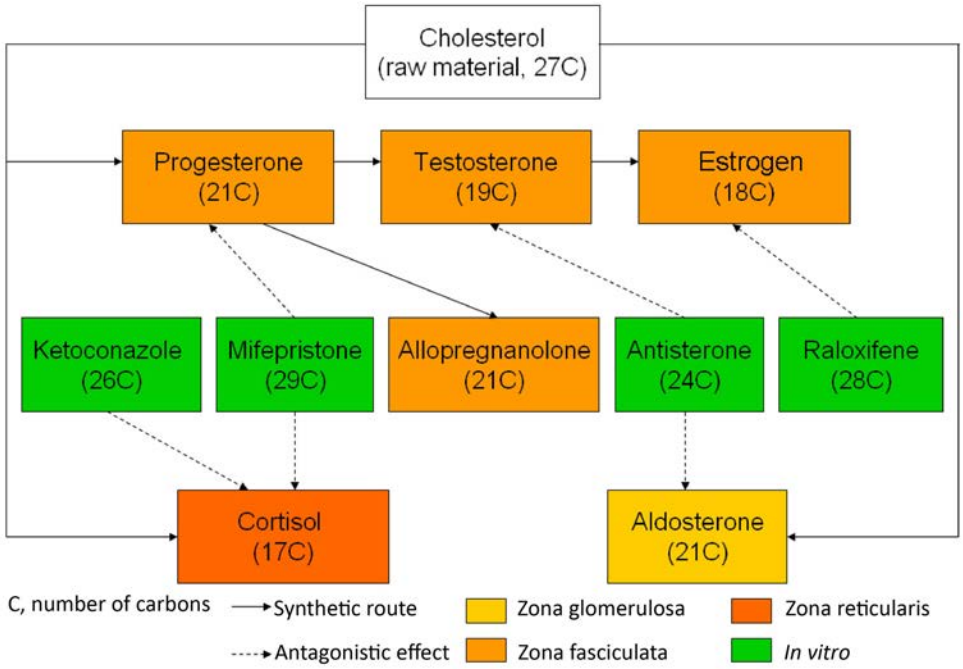

Fig. 2 Steroid hormones: number of carbon atoms, locations and pathways of synthesis, and antagonistic interactions (including some produced *in vitro*).

T3 production [92]. At the midstream pituitary level, HPAA activation is accompanied by chronic elevation of cortisol which impairs the release of TSH by TRH, resulting in declining thyroid function as well [93].

After binding to the intracellular progesterone receptor (PR), progesterone changes its configuration and form a dimer with then released heat shock protein (HSP), subsequently binding to the relevant hormone response factor in DNA. After the downstream transcription activator factor is activated, proteins are synthesized *via* mRNA and later on generate hormone-related biological effects. Mifepristone has a higher PR affinity than progesterone, and the mifepristone-receptor-HSP complex is more stable and shows a stronger affinity for nuclear proteins; however, mifepristone cannot act on DNA. It can competitively block the biological activity of progesterone, achieving its anti-progesterone effect. This drug also possesses another characteristic, which is its competitive action on GRs. Hence, mifepristone is a dual antagonist of the GR and PR. Such a similarity demonstrates possible associations between the HPG and HPA axes. The antidepressant effects of allopregnanolone are not only brought about by positively modulating the $GABA_A$ receptor, but also negatively modulating HPAA activity. Chronic stress in MDD down-regulates the expression of the rate-limiting enzyme 5α-reductase in the synthesis of THP. The decrease in THP levels results in decreased regulation of the HPAA, causing an increased level of cortisol and weakening nerve regeneration [94]. In addition, spironolactone, an aldosterone antagonist, has diuretic and antihypertensive effects. However, its side-effects include male breast development, which suggests that it may have anti-androgenic effects, leading to an imbalance between estrogen and androgens. This phenomenon might be due to the similar structural chemistry of steroid hormones (Fig. 2).

Hypercortisolism resulting from HPAA imbalance is closely connected to affective disorders. Recent studies have found that mood disorders can be treated effectively with GR antagonists, among which mifepristone is the most commonly used. It is able to treat psychotic depression by GR antagonism [95]. The efficacy of mifepristone indicates that an imbalance in glucocorticoid homeostasis may exist in MDD patients. Effective antidepressant treatment can restore normal glucocorticoid levels. The finding of relationships between antidepressant action and HPAA regulation leads to the conclusion that the disruption of HPAA may be a contributing factor to depression, rather than other biological abnormalities [96]. At present, mifepristone is another potential new antidepressant drug undergoing clinical trials. Early in 2006, the efficacy of mifepristone in patients with depression was reported, especially in those with psychotic symptoms [97]. Previous studies also indicated that mifepristone could alleviate the stress response in depressed patients by inhibiting the excessive activation of GR, thereby improving cognitive function and alleviating MDD symptoms [98].

Studies have reported a therapeutic effect of estrogen on postpartum and menopausal depression, and sequential hormonal therapy with estrogen and progesterone can improve nervousness, irritability, and depressive

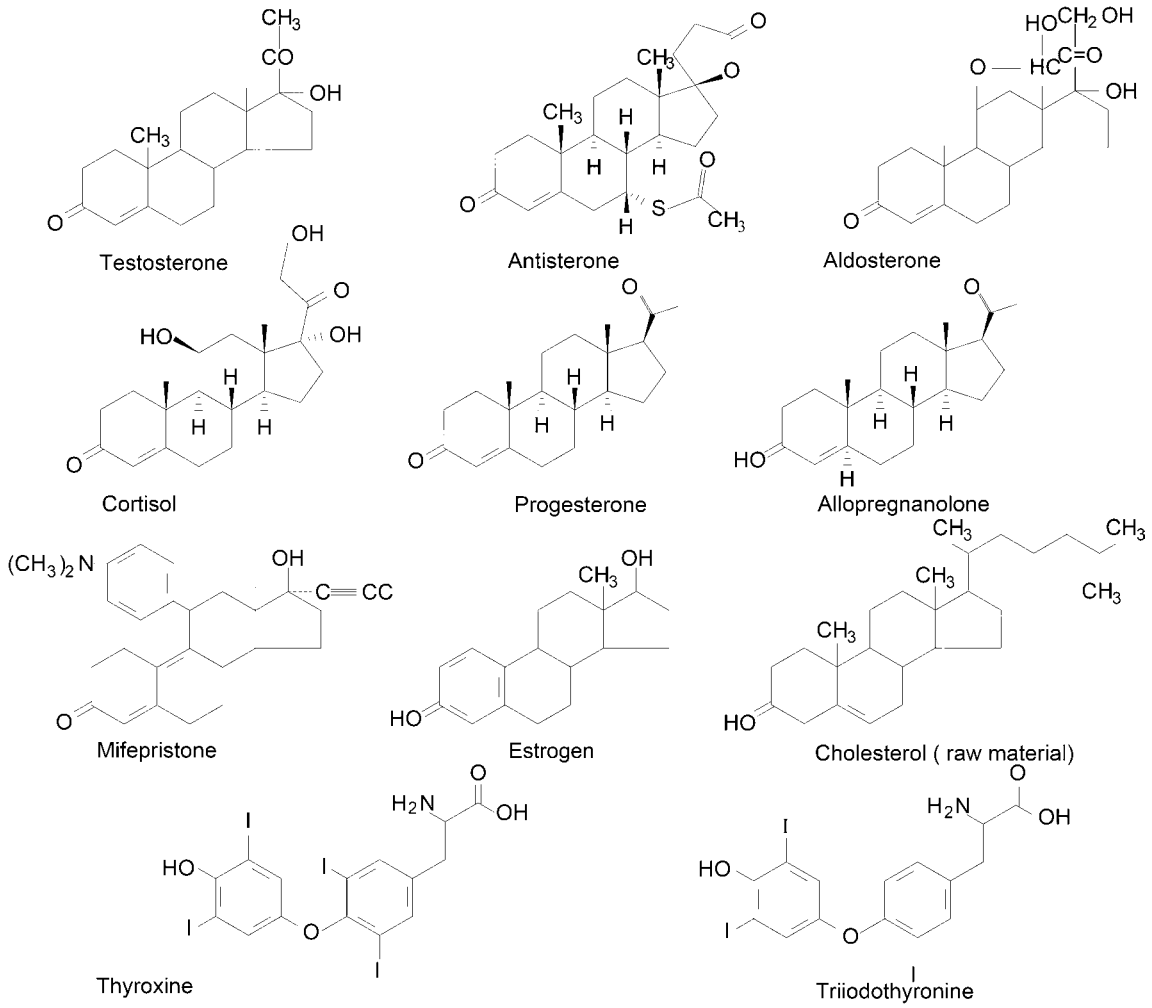

Fig. 3 Downstream hormones of the HPA, HPG, and HPT axes and the similarity of cholesterol to its derivatives in the HPAA and HPGA. HPA, hypothalamic-pituitary-adrenal; HPG, hypothalamic-pituitary-gonadal; HPT, hypothalamic-pituitary-thyroidal.

symptoms, especially with low doses of estrogen [99]. In clinical practice, it is difficult to acknowledge a link between the improvement of symptoms and changing levels of estrogen and progesterone, because progesterone cannot carry out its biological role in the absence of estrogen, similar to the permissive action of glucocorticoids. Nonetheless, observations made during single estrogen replacement therapy in PMD patients suggest that estrogen does not show correlated effects [78], while the estrogen receptor antagonist raloxifene does not seem to cause any depressive adverse reactions [100]. All the evidence suggests that hormones and mood are not simply linearly correlated, but have a more extensive and complicated relationship.

An imbalance in the HPAA may be caused by the accumulation of menstrual cycle-related disorders. When adapting to pressure, critical stressors correlated to menstrual cycles constitute a series of repeated stimuli. If these stimuli persist, repeated injury to the psychological coping mechanism can occur, inducing HPAA dysregulation. The cortisol synthesis inhibitor ketoconazole promotes hippocampal function in MDD patients; it was unexpectedly found that this drug improves the prognosis of MDD [98]. No studies have shown a significant correlation between cortisol levels and the menstrual cycle [101, 102]. There is also a lack of evidence for differences in cortisol dysregulation between patients with PMS and PMDD, and healthy controls [103]; the reason might be that various points were not elaborated systematically. In current models, the relationship between female periodic depressive symptoms and HPAA function may depend on particular critical stressors and the extent of disease prognosis. This connection might have been established during sensitive periods of human development. Long-term data on the stability of recurrence is required.

Perspectives

With respect to molecular structure, sex hormones and glucocorticoids both belong to the neurosteroid class, in that they are more similar in structure than with thyroid hormones. Their differences include the number of carbon atoms, benzene ring stability, and mirror image isomerism (Fig. 3). Affected by the concentration of these hormones, non-specific receptors may produce different biological effects; these effects could be more closely related than previously thought, and this may better explain the high morbidity of neuroendocrine diseases in women. Through the perspective of new drug developments based on the hormone levels and hormonal changes of these three axes, individual differences in female MDD patients become obvious. Phenotypic differences among individuals might be determined by genetic factors, but the main factors are supposed to consist of the relevant hormone receptors and environment-related epigenetic factors. The molecular structure of hormones is consistent across individuals, but differences can arise in receptors and hormone-receptor-protein complexes, leading to incongruence among biological factors of depression. Different responses to these hormones should be the core element of pathological theory and research.

Acknowledgements We thank Yueyin Pan for image processing. This review was supported by the National Key Research and Development Program of China (2016YFC1307100, 2016YFC1307105), the National Natural Science Foundation of China (81771465, 81930033), the National Key Technologies R&D Program of China (2012BAI01B04), Shanghai Key Project of Science and Technology (2018SHZDZX05), the Sanming Project of Medicine in Shenzheng (SZSM201612006), Shanghai Key Medicine Specialties Program (ZK2019A06), Shanghai Clinical Research Center for Mental Health (SCRC-MH, 19MC1911100), the Special Project for Clinical Research in Health Industry of Shanghai Municipal Health Commission (20204Y0025), the Innovative Research Team of High-level Local Universities in Shanghai, and the National Health System "Good Doctor" Construction Project of Yangpu District of Shanghai Municipality (2020–2023).

Conflict of interest The authors declare that they have no conflicts of interest.

References

1. Lee EH, Han PL. Reciprocal interactions across and within multiple levels of monoamine and cortico-limbic systems in stress-induced depression: A systematic review. Neurosci Biobehav Rev 2019, 101: 13–31.
2. Liang X, Zhu Y, Fang Y. COVID-19 and post-traumatic stress disorder: A vicious circle involving immunosuppression. CNS Neurosci Ther 2020, 26: 876–878.
3. Cohen S, Janicki-Deverts D, Miller GE. Psychological stress and disease. JAMA 2007, 298: 1685–1687.
4. Miller AH, Maletic V, Raison CL. Inflammation and its discontents: the role of cytokines in the pathophysiology of major depression. Biol Psychiatry 2009, 65: 732–741.
5. Zunszain PA, Hepgul N, Pariante CM. Inflammation and depression. Curr Top Behav Neurosci 2013, 14: 135–151.
6. Wang F, Jin J, Wang J, He R, Li K, Hu X. Association between olfactory function and inhibition of emotional competing distractors in major depressive disorder. Sci Rep 2020, 10: 6322.
7. Dantzer R, O'Connor JC, Freund GG, Johnson RW, Kelley KW. From inflammation to sickness and depression: when the immune system subjugates the brain. Nat Rev Neurosci 2008, 9: 46–56.
8. Pace TW, Miller AH. Cytokines and glucocorticoid receptor signaling. Relevance to major depression. Ann N Y Acad Sci 2009, 1179: 86–105.
9. Jeon SW, Kim YK. The role of neuroinflammation and neurovascular dysfunction in major depressive disorder. J Inflamm Res 2018, 11: 179–192.
10. Horowitz MA, Zunszain PA. Neuroimmune and neuroendocrine abnormalities in depression: two sides of the same coin. Ann N Y Acad Sci 2015, 1351: 68–79.
11. Bale TL. Neuroendocrine and immune influences on the CNS: it's a matter of sex. Neuron 2009, 64: 13–16.
12. Zhu Y, Ji H, Tao L, Cai Q, Wang F, Ji W, *et al.* Functional status of hypothalamic–pituitary–thyroid and hypothalamic–pituitary–adrenal axes in hospitalized schizophrenics in Shanghai. Front Psychiatry 2020, 11: 65.
13. Han Y, Ji H, Liu L, Zhu Y, Jiang X. The relationship of functional status of cortisol, testosterone, and parameters of metabolic syndrome in male schizophrenics. Biomed Res Int 2020, 2020: 9124520.
14. Malhi GS, Mann JJ. Depression. Lancet 2018, 392: 2299–2312.
15. Chen X, Zheng X, Ding Z, Su Y, Wang S, Cui B, *et al.* Relationship of gender and age on thyroid hormone parameters in a large Chinese population. Arch Endocrinol Metab 2020, 64: 52–58.
16. Honour JW. Biochemistry of the menopause. Ann Clin Biochem 2018, 55: 18–33.
17. Kudielka BM, Buske-Kirschbaum A, Hellhammer DH, Kirschbaum C. HPA axis responses to laboratory psychosocial stress in healthy elderly adults, younger adults, and children: impact of age and gender. Psychoneuroendocrinology 2004, 29: 83–98.
18. Pariante CM, Lightman SL. The HPA axis in major depression: classical theories and new developments. Trends Neurosci 2008, 31: 464–468.
19. Pariante CM. Risk factors for development of depression and psychosis. Glucocorticoid receptors and pituitary implications for treatment with antidepressant and glucocorticoids. Ann N Y Acad Sci 2009, 1179: 144–152.
20. Burke HM, Davis MC, Otte C, Mohr DC. Depression and cortisol responses to psychological stress: a meta-analysis. Psychoneuroendocrinology 2005, 30: 846–856.
21. Wang SS, Mu RH, Li CF, Dong SQ, Geng D, Liu Q, *et al.* microRNA-124 targets glucocorticoid receptor and is involved in depression-like behaviors. Prog Neuropsychopharmacol Biol Psychiatry 2017, 79: 417–425.
22. Pariante CM, Miller AH. Glucocorticoid receptors in major depression: relevance to pathophysiology and treatment. Biol Psychiatry 2001, 49: 391–404.
23. Bekhbat M, Rowson SA, Neigh GN. Checks and balances: The glucocorticoid receptor and NFkB in good times and bad. Front Neuroendocrinol 2017, 46: 15–31.
24. Lee DY, Kim E, Choi MH. Technical and clinical aspects of cortisol as a biochemical marker of chronic stress. Bmb Reports 2015, 48: 209–216.

25. Makhija K, Karunakaran S. The role of inflammatory cytokines on the aetiopathogenesis of depression. Aust N Z J Psychiatry 2013, 47: 828–839.
26. Niu Z, Yang L, Wu X, Zhu Y, Chen J, Fang Y. The relationship between neuroimmunity and bipolar disorder: Mechanism and translational application. Neurosci Bull 2019, 35: 595–607.
27. Silverman MN, Sternberg EM. Glucocorticoid regulation of inflammation and its functional correlates: from HPA axis to glucocorticoid receptor dysfunction. Ann N Y Acad Sci 2012, 1261: 55–63.
28. Shelton MM, Schminkey DL, Groer MW. Relationships among prenatal depression, plasma cortisol, and inflammatory cytokines. Biol Res Nurs 2015, 17: 295–302.
29. Frank MG, Watkins LR, Maier SF. Stress-induced glucocorticoids as a neuroendocrine alarm signal of danger. Brain Behav Immun 2013, 33: 1–6.
30. Tynan RJ, Naicker S, Hinwood M, Nalivaiko E, Buller KM, Pow DV, *et al.* Chronic stress alters the density and morphology of microglia in a subset of stress-responsive brain regions. Brain Behav Immun 2010, 24: 1058–1068.
31. Blandino P Jr, Barnum CJ, Deak T. The involvement of norepinephrine and microglia in hypothalamic and splenic IL-1beta responses to stress. J Neuroimmunol 2006, 173: 87–95.
32. Ulrich-Lai YM, Herman JP. Neural regulation of endocrine and autonomic stress responses. Nat Rev Neurosci 2009, 10: 397–409.
33. Walker FR, Nilsson M, Jones K. Acute and chronic stress-induced disturbances of microglial plasticity, phenotype and function. Curr Drug Targets 2013, 14: 1262–1276.
34. Alt SR, Turner JD, Klok MD, Meijer OC, Lakke EA, Derijk RH, *et al.* Differential expression of glucocorticoid receptor transcripts in major depressive disorder is not epigenetically programmed. Psychoneuroendocrinology 2010, 35: 544–556.
35. ter Heegde F, De Rijk RH, Vinkers CH. The brain mineralocorticoid receptor and stress resilience. Psychoneuroendocrinology 2015, 52: 92–110.
36. Keller J, Gomez R, Williams G, Lembke A, Lazzeroni L, Murphy GM Jr, *et al.* HPA axis in major depression: cortisol, clinical symptomatology and genetic variation predict cognition. Mol Psychiatry 2017, 22: 527–536.
37. Raison CL, Miller AH. When not enough is too much: the role of insufficient glucocorticoid signaling in the pathophysiology of stress-related disorders. Am J Psychiatry 2003, 160: 1554–1565.
38. Anacker C, Zunszain PA, Carvalho LA, Pariante CM. The glucocorticoid receptor: pivot of depression and of antidepressant treatment?. Psychoneuroendocrinology 2011, 36: 415–425.
39. Pochigaeva K, Druzhkova T, Yakovlev A, Onufriev M, Grishkina M, Chepelev A, *et al.* Hair cortisol as a marker of hypothalamic-pituitary-adrenal axis activity in female patients with major depressive disorder. Metab Brain Dis 2017, 32: 577–583.
40. Young EA, Veldhuis JD. Disordered adrenocorticotropin secretion in women with major depression. J Clin Endocrinol Metab 2006, 91: 1924–1928.
41. Rampp C, Eichelkraut A, Best J, Czamara D, Rex-Haffner M, Uhr M, *et al.* Sex-related differential response to dexamethasone in endocrine and immune measures in depressed in-patients and healthy controls. J Psychiatr Res 2018, 98: 107–115.
42. Roos LE, Beauchamp KG, Giuliano R, Zalewski M, Kim HK, Fisher PA. Children's biological responsivity to acute stress predicts concurrent cognitive performance. Stress 2018, 21: 347–354.
43. Wei J, Sun G, Zhao L, Yang X, Liu X, Lin D, *et al.* Analysis of hair cortisol level in first-episodic and recurrent female patients with depression compared to healthy controls. J Affect Disord 2015, 175: 299–302.
44. Kaess M, Whittle S, O'Brien-Simpson L, Allen NB, Simmons JG. Childhood maltreatment, pituitary volume and adolescent hypothalamic-pituitary-adrenal axis - Evidence for a maltreatment-related attenuation. Psychoneuroendocrinology 2018, 98: 39–45.
45. Zhu Y, Wu Z, Sie O, Cai Y, Huang J, Liu H, *et al.* Causes of drug discontinuation in patients with major depressive disorder in China. Prog Neuropsychopharmacol Biol Psychiatry 2020, 96: 109755.
46. Fischer S, Ehlert U. Hypothalamic-pituitary-thyroid (HPT) axis functioning in anxiety disorders. A systematic review. Depress Anxiety 2018, 35: 98–110.
47. Cleare A, Pariante CM, Young AH, Anderson IM, Christmas D, Cowen PJ, *et al.* Evidence-based guidelines for treating depressive disorders with antidepressants: A revision of the 2008 British Association for Psychopharmacology guidelines. J Psychopharmacol 2015, 29: 459–525.
48. Iosifescu DV, Bolo NR, Nierenberg AA, Jensen JE, Fava M, Renshaw PF. Brain bioenergetics and response to triiodothyronine augmentation in major depressive disorder. Biol Psychiatry 2008, 63: 1127–1134.
49. Tundo A, de Filippis R, Proietti L. Pharmacologic approaches to treatment resistant depression: Evidences and personal experience. World J Psychiatry 2015, 5: 330–341.
50. Dold M, Bartova L, Mendlewicz J, Souery D, Serretti A, Porcelli S, *et al.* Clinical correlates of augmentation/combination treatment strategies in major depressive disorder. Acta Psychiatr Scand 2018, 137: 401–412.
51. Martin SS, Daya N, Lutsey PL, Matsushita K, Fretz A, McEvoy JW, *et al.* Thyroid function, cardiovascular risk factors, and incident atherosclerotic cardiovascular disease: The atherosclerosis risk in communities (ARIC) study. J Clin Endocrinol Metab 2017, 102: 3306–3315.
52. Hage MP, Azar ST. The link between thyroid function and depression. J Thyroid Res 2012, 2012: 590648.
53. Giynas Ayhan M, Uguz F, Askin R, Gonen MS. The prevalence of depression and anxiety disorders in patients with euthyroid Hashimoto's thyroiditis: a comparative study. Gen Hosp Psychiatry 2014, 36: 95–98.
54. Saidi S, Iliani Jaafar SN, Daud A, Musa R, Nik Ahmad NNF. Relationship between levels of thyroid stimulating hormone, age, and gender, with symptoms of depression among patients with thyroid disorders as measured by the Depression Anxiety Stress Scale 21 (DASS-21). Enferm Clin 2018, 28(Suppl 1): 180–183.
55. Gietka-Czernel M. The thyroid gland in postmenopausal women: physiology and diseases. Prz Menopauzalny 2017, 16: 33–37.
56. Gaberscek S, Zaletel K. Thyroid physiology and autoimmunity in pregnancy and after delivery. Expert Rev Clin Immunol 2011, 7: 697–706; quiz 707.
57. Pedersen C, Leserman J, Garcia N, Stansbury M, Meltzer-Brody S, Johnson J. Late pregnancy thyroid-binding globulin predicts perinatal depression. Psychoneuroendocrinology 2016, 65: 84–93.
58. Kurioka H, Takahashi K, Miyazaki K. Maternal thyroid function during pregnancy and puerperal period. Endocr J 2005, 52: 587–591.
59. Jonklaas J, Kahric-Janicic N, Soldin OP, Soldin SJ. Correlations of free thyroid hormones measured by tandem mass spectrometry and immunoassay with thyroid-stimulating hormone across 4 patient populations. Clin Chem 2009, 55: 1380–1388.

60. Pedersen CA, Johnson JL, Silva S, Bunevicius R, Meltzer-Brody S, Hamer RM, *et al.* Antenatal thyroid correlates of postpartum depression. Psychoneuroendocrinology 2007, 32: 235–245.
61. Rubinow DR, Schmidt PJ. Sex differences and the neurobiology of affective disorders. Neuropsychopharmacology 2019, 44: 111–128.
62. Barut MU, Coksuer H, Sak S, Bozkurt M, Agacayak E, Hamurcu U, *et al.* Evaluation of sexual function in women with hypogonadotropic hypogonadism using the female sexual function index (FSFI) and the beck depression inventory (BDI). Med Sci Monit 2018, 24: 5610–5618.
63. Sakinci M, Ercan CM, Olgan S, Coksuer H, Karasahin KE, Kuru O. Comparative analysis of copper intrauterine device impact on female sexual dysfunction subtypes. Taiwan J Obstet Gynecol 2016, 55: 460–461.
64. Basson R, Rees P, Wang R, Montejo AL, Incrocci L. Sexual function in chronic illness. J Sex Med 2010, 7: 374–388.
65. Berman JR, Bassuk J. Physiology and pathophysiology of female sexual function and dysfunction. World J Urol 2002, 20: 111–118.
66. Atis G, Dalkilinc A, Altuntas Y, Atis A, Caskurlu T, Ergenekon E. Sexual dysfunction in women with clinical hypothyroidism and subclinical hypothyroidism. J Sex Med 2010, 7: 2583–2590.
67. Bhasin S, Enzlin P, Coviello A, Basson R. Sexual dysfunction in men and women with endocrine disorders. Lancet 2007, 369: 597–611.
68. Goldstein JM, Hale T, Foster SL, Tobet SA, Handa RJ. Sex differences in major depression and comorbidity of cardiometabolic disorders: impact of prenatal stress and immune exposures. Neuropsychopharmacology 2019, 44: 59–70.
69. Studd J. Personal view: Hormones and depression in women. Climacteric 2015, 18: 3–5.
70. Santoro N. Perimenopause: From research to practice. J Womens Health (Larchmt) 2016, 25: 332–339.
71. Naheed B, Kuiper JH, Uthman OA, O'Mahony F, O'Brien PM. Non-contraceptive oestrogen-containing preparations for controlling symptoms of premenstrual syndrome. Cochrane Database Syst Rev 2017, 3: CD010503.
72. Biggs WS, Demuth RH. Premenstrual syndrome and premenstrual dysphoric disorder. Am Fam Physician 2011, 84: 918–924.
73. Carrier J, Semba K, Deurveilher S, Drogos L, Cyr-Cronier J, Lord C, *et al.* Sex differences in age-related changes in the sleep-wake cycle. Front Neuroendocrinol 2017, 47: 66–85.
74. Schiller CE, Meltzer-Brody S, Rubinow DR. The role of reproductive hormones in postpartum depression. CNS Spectr 2015, 20: 48–59.
75. Gordon JL, Girdler SS, Meltzer-Brody SE, Stika CS, Thurston RC, Clark CT, *et al.* Ovarian hormone fluctuation, neurosteroids, and HPA axis dysregulation in perimenopausal depression: a novel heuristic model. Am J Psychiatry 2015, 172: 227–236.
76. Studd J, Nappi RE. Reproductive depression. Gynecol Endocrinol 2012, 28(Suppl 1): 42–45.
77. Studd JW. A guide to the treatment of depression in women by estrogens. Climacteric 2011, 14: 637–642.
78. Whedon JM, KizhakkeVeettil A, Rugo NA, Kieffer KA. Bioidentical estrogen for menopausal depressive symptoms: A systematic review and meta-analysis. J Womens Health (Larchmt) 2017, 26: 18–28.
79. Wang F, Wu X, Gao J, Li Y, Zhu Y, Fang Y. The relationship of olfactory function and clinical traits in major depressive disorder. Behav Brain Res 2020, 386: 112594.
80. Rodgers S, Vandeleur CL, Ajdacic-Gross V, Aleksandrowicz AA, Strippoli MF, Castelao E, *et al.* Tracing the associations between sex, the atypical and the combined atypical-melancholic depression subtypes: A path analysis. J Affect Disord 2016, 190: 807–818.
81. Herzog DP, Wegener G, Lieb K, Muller MB, Treccani G. Decoding the mechanism of action of rapid-acting antidepressant treatment strategies: Does gender matter?. Int J Mol Sci 2019, 20: 949.
82. Skovlund CW, Morch LS, Kessing LV, Lidegaard O. Association of hormonal contraception with depression. JAMA Psychiatry 2016, 73: 1154–1162.
83. Sharma V, Al-Farayedhi M, Doobay M, Baczynski C. Should all women with postpartum depression be screened for bipolar disorder?. Med Hypotheses 2018, 118: 26–28.
84. Studd J. Spotlight on severe premenstrual syndrome and bipolar disorder: a frequent tragic confusion. Climacteric 2011, 14: 602.
85. Sharma V, Burt VK, Ritchie HL. Assessment and treatment of bipolar II postpartum depression: a review. J Affect Disord 2010, 125: 18–26.
86. Barth C, Villringer A, Sacher J. Sex hormones affect neurotransmitters and shape the adult female brain during hormonal transition periods. Front Neurosci 2015, 9: 37.
87. Frieder A, Fersh M, Hainline R, Deligiannidis KM. Pharmacotherapy of postpartum depression: Current approaches and novel drug development. CNS Drugs 2019, 33: 265–282.
88. Patte-Mensah C, Meyer L, Taleb O, Mensah-Nyagan AG. Potential role of allopregnanolone for a safe and effective therapy of neuropathic pain. Prog Neurobiol 2014, 113: 70–78.
89. Andreen L, Nyberg S, Turkmen S, van Wingen G, Fernandez G, Backstrom T. Sex steroid induced negative mood may be explained by the paradoxical effect mediated by GABAA modulators. Psychoneuroendocrinology 2009, 34: 1121–1132.
90. Baka J, Csakvari E, Huzian O, Dobos N, Siklos L, Leranth C, *et al.* Stress induces equivalent remodeling of hippocampal spine synapses in a simulated postpartum environment and in a female rat model of major depression. Neuroscience 2017, 343: 384–397.
91. Schule C, Eser D, Baghai TC, Nothdurfter C, Kessler JS, Rupprecht R. Neuroactive steroids in affective disorders: target for novel antidepressant or anxiolytic drugs?. Neuroscience 2011, 191: 55–77.
92. Brown SB, MacLatchy DL, Hara TJ, Eales JG. Effects of cortisol on aspects of 3,5,3'-triiodo-L-thyronine metabolism in rainbow trout (Oncorhynchus mykiss). Gen Comp Endocrinol 1991, 81: 207–216.
93. Sahoo M, Subho C. Cortisol hypersecretion in unipolar major depression with melancholic and psychotic features: dopaminergic, noradrenergic and thyroid correlates. Psychoneuroendocrinology 2007, 32: 210; author reply 211–212.
94. Evans J, Sun Y, McGregor A, Connor B. Allopregnanolone regulates neurogenesis and depressive/anxiety-like behaviour in a social isolation rodent model of chronic stress. Neuropharmacology 2012, 63: 1315–1326.
95. Block T, Petrides G, Kushner H, Kalin N, Belanoff J, Schatzberg A. Mifepristone plasma level and glucocorticoid receptor antagonism associated with response in patients with psychotic depression. J Clin Psychopharmacol 2017, 37: 505–511.
96. Mason BL, Pariante CM. The effects of antidepressants on the hypothalamic-pituitary-adrenal axis. Drug News Perspect 2006, 19: 603–608.
97. DeBattista C, Belanoff J, Glass S, Khan A, Horne RL, Blasey C, *et al.* Mifepristone versus placebo in the treatment of psychosis in patients with psychotic major depression. Biol Psychiatry 2006, 60: 1343–1349.
98. Soria V, Gonzalez-Rodriguez A, Huerta-Ramos E, Usall J, Cobo J, Bioque M, *et al.* Targeting hypothalamic-pituitary-adrenal axis hormones and sex steroids for improving cognition in major

mood disorders and schizophrenia: a systematic review and narrative synthesis. Psychoneuroendocrinology 2018, 93: 8–19.
99. Bjorn I, Sundstrom-Poromaa I, Bixo M, Nyberg S, Backstrom G, Backstrom T. Increase of estrogen dose deteriorates mood during progestin phase in sequential hormonal therapy. J Clin Endocrinol Metab 2003, 88: 2026–2030.
100. Khorsand I, Kashef R, Ghazanfarpour M, Mansouri E, Dashti S, Khadivzadeh T. The beneficial and adverse effects of raloxifene in menopausal women: A mini review. J Menopausal Med 2018, 24: 183–187.
101. Hoyer J, Burmann I, Kieseler ML, Vollrath F, Hellrung L, Arelin K, *et al.* Menstrual cycle phase modulates emotional conflict processing in women with and without premenstrual syndrome (PMS) - a pilot study. Plos One 2013, 8: e59780.
102. Wolfram M, Bellingrath S, Kudielka BM. The cortisol awakening response (CAR) across the female menstrual cycle. Psychoneuroendocrinology 2011, 36: 905–912.
103. Kiesner J, Granger DA. A lack of consistent evidence for cortisol dysregulation in premenstrual syndrome/premenstrual dysphoric disorder. Psychoneuroendocrinology 2016, 65: 149–164.

Neurosci. Bull. August, 2021, 37(8):1188–1202
https://doi.org/10.1007/s12264-021-00683-y

www.neurosci.cn
www.springer.com/12264

REVIEW

Emerging Role of PD-1 in the Central Nervous System and Brain Diseases

Junli Zhao[1] · Alexus Roberts[1,2] · Zilong Wang[1] · Justin Savage[3] · Ru-Rong Ji[1,3,4]

Received: 13 October 2020 / Accepted: 19 December 2020 / Published online: 20 April 2021

Abstract Programmed cell death protein 1 (PD-1) is an immune checkpoint modulator and a major target of immunotherapy as anti-PD-1 monoclonal antibodies have demonstrated remarkable efficacy in cancer treatment. Accumulating evidence suggests an important role of PD-1 in the central nervous system (CNS). PD-1 has been implicated in CNS disorders such as brain tumors, Alzheimer's disease, ischemic stroke, spinal cord injury, multiple sclerosis, cognitive function, and pain. PD-1 signaling suppresses the CNS immune response *via* resident microglia and infiltrating peripheral immune cells. Notably, PD-1 is also widely expressed in neurons and suppresses neuronal activity *via* downstream Src homology 2 domain-containing protein tyrosine phosphatase 1 and modulation of ion channel function. An improved understanding of PD-1 signaling in the cross-talk between glial cells, neurons, and peripheral immune cells in the CNS will shed light on immunomodulation, neuromodulation, and novel strategies for treating brain diseases.

✉ Junli Zhao
junli.zhao@duke.edu

✉ Ru-Rong Ji
ru-rong.ji@duke.edu

[1] Department of Anesthesiology, Duke University Medical Center, Durham 27710, USA

[2] Department of Biology, Duke University Medical Center, Durham 27710, USA

[3] Department of Neurobiology, Duke University Medical Center, Durham 27710, USA

[4] Department of Cell Biology, Duke University Medical Center, Durham 27710, USA

Keywords PD-1 · Central nervous system · Immune checkpoint · Immunotherapy · Neurotherapy

Introduction

Programmed cell death protein 1 (PD-1, also known as PDCD1 and CD279) is a cell surface receptor which contains 288 amino-acids and is widely expressed in immune cells (T cells, B cells, natural killer cells, dendritic cells, and macrophages) and other cell types (microglia and neurons) (Table 1). In 1992, PD-1 was initially found by the Honjo group at Kyoto University during screening for genes involved in apoptosis [1]. Over the ensuing decades, it has become clear that PD-1 is a negative regulator of immune responses [2, 3] (Fig. 1). PD-1 binds two ligands, PD-L1 (B7-H1) and PD-L2 (B7-DC) [4–7]. PD-L1 is expressed on a variety of hematopoietic and non-hematopoietic cells [8–11]. PD-L2 is mainly restricted to antigen presenting cells (APCs) [8, 12]. Binding to either of these ligands, PD-1 signaling regulates the immune response by down-regulating the immune system and promotes self-tolerance by suppressing T cell inflammatory activity. This inhibitory signaling through the PD-1 pathway is an important mechanism underlying many physiological and pathological conditions. Physiologically, the PD-1 signaling pathway regulates T cell activation, T cell tolerance, and immune hemostasis [13]. Perturbation of the PD-1 pathway can profoundly impact host physiology [14, 15]. Pathologically, PD-1 and its ligands are strongly expressed during many chronic diseases, especially in cancer [16, 17]. In 2002, Minato *et al.* found that *Pdcd1* gene deletion inhibited tumor growth in mice. In 2010, the first clinical trial of anti-PD-1 antibody (BMS-936558/ONO-4538) was launched in Japan for cancer

Table 1 Expression of PD-1 in various tissues and cells

Tissue or cell with PD-1 expression	Level of expression	Function of expression	References (methods)
B-cells	Low expression in peripheral blood under normal conditions	Inhibits B-cell activation, proliferation, and differentiation	[100] (FC, IF), [101], [102] (FC, RT-PCR)
Dendritic cells	Low expression under normal conditions	Restricts T-cell activation and lowers innate immunity	[103] (FC), [104] (FC, RT-PCR)
DRG sensory neurons	Expressed in DRG sensory neurons as well as in axons	Interacts with PD-L1 to modulate pain and lower sensitivity	[19] (IF, ISH, WB), [95, 105] (ISH, IF, PLA, co-IP)
Hippocampal neurons	Expressed in hippocampal CA1 and CA3 neurons, low expression in DG neurons	Regulates neuronal excitability, synaptic transmission, plasticity, and memory	[92] (IF, ISH)
Macrophages	Low expression under normal conditions	Functions as a control mechanism for systemic immune responses through redirection or delays	[31] (FC, IF), [106] (FC, RT-PCR), [107] (FC)
Microglia	Low expression under normal conditions	Regulates the inflammatory reaction after injury or infection	[23] (RT-PCR, IF)
NK cells	Low expression under normal conditions	Prevents NK cell activation and cytotoxicity in specific situations	[108] (FC), [109] (FC, IHC)
Retinal ganglion cells	Expressed in almost all adult retinal ganglion cells	Promotes apoptosis, which is necessary for proper maturation	[110] (IF, IHC, WB, RT-PCR), [111] (IF, WB, RT-PCR)
Spinal cord	Expressed in spinal neurons, primary afferent terminals, and microglia	Regulates pain, opioid analgesia and tolerance, GABAergic neurotransmission	[95] (IF), [24, 95] (ISH)
T-cells	Highly expressed in activated T-cells	Functions as an immune checkpoint receptor	[13, 27, 112] (FC), [113] (IF, FC), [114] (FC, PCR)

Abbreviations FC, flow cytometry; IHC, immunohistochemical analysis; IF, immunofluorescence; ISH, *in situ* hybridization; PCR, polymerase chain reaction; RT-PCR, reverse-transcription-polymerase chain reaction; WB, Western blotting; PLA, proximity ligation assay; co-IP, co-immunoprecipitation; DRG, dorsal root ganglion; NK cells, natural killer cells.

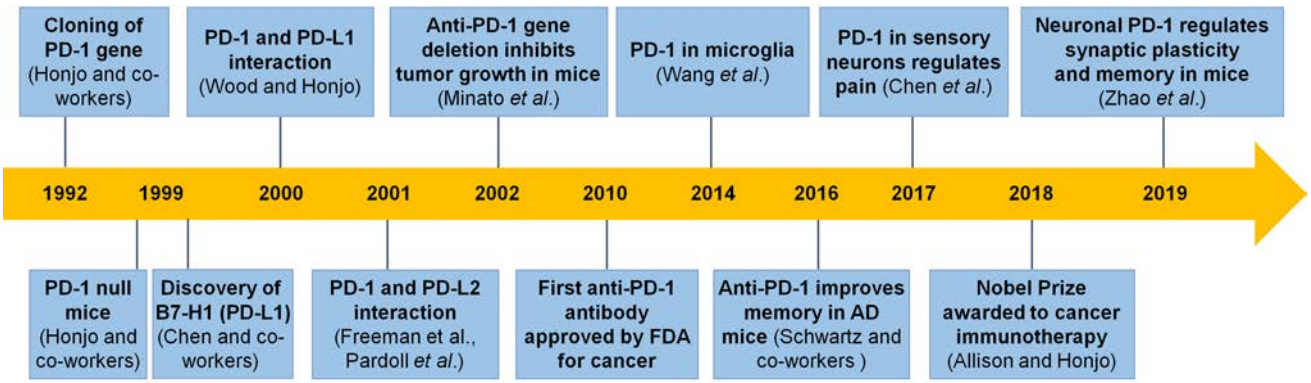

Fig. 1 Timeline for major events leading to the development of PD-1 functions and PD-1-based immunotherapy.

treatment (Fig. 1). Since 2014, several anti-PD-1 monoclonal antibodies such as Nivolumab (Opdivo), Pembrolizumab (Keytruda), and Cemiplimab-rwlc (Libtayo) have been approved by the FDA. Given the success of the emerging immunotherapy with anti-PD-1 and anti-CTLA4 (cytotoxic T-lymphocyte-associated protein 4) monoclonal antibodies in cancer treatment, the 2018 Nobel Prize in Physiology or Medicine was awarded to James P. Allison and Tasuku Honjo for their discovery of cancer therapy by inhibition of negative immune regulation (Fig. 1).

In addition to the prominent role of PD-1 in the immune system, accumulating evidence also suggests an activating

role of PD-1 signaling in both the central nervous system (CNS) and the peripheral nervous system (PNS) (Figs. 2–5). PD-1 reduces neuroinflammatory responses and may also regulate neuronal activity in several CNS diseases, such as brain tumors, Alzheimer's disease, stroke, chronic pain, multiple sclerosis, and cognitive deficits [18, 19]. The mechanisms underlying the actions of PD-1 in these disease conditions are multifaceted. First, the recent progress in demonstrating peripheral immune cell recruitment to the CNS under pathological conditions challenges the historical view of CNS immune privilege. Functional lymphatic vessels in the meninges have recently been discovered that provided a direct drainage pathway for PD-1^+ immune cells from the cervical lymph nodes into the brain [20, 21]. Thus, PD-1^+ immune cells such as T cells may play a role in the CNS similar to that in the peripheral immune system. Second, PD-1 is expressed by macrophages as well as microglia in the spinal cord and brain [22, 23]. Under CNS disease conditions such as brain trauma and spinal cord injury, brain resident PD-1^+ microglia are activated in the spinal cord and brain and PD-1^+ macrophages are also recruited to the CNS, where these microglia and macrophages undergo substantial phenotypic changes to regulate neuroinflammation and disease progression [23]. Finally, accumulating evidence demonstrates that PD-1 is also expressed by CNS neurons and that PD-1 signaling in neurons regulates neuronal excitability, synaptic transmission, and plasticity *via* PD-1/

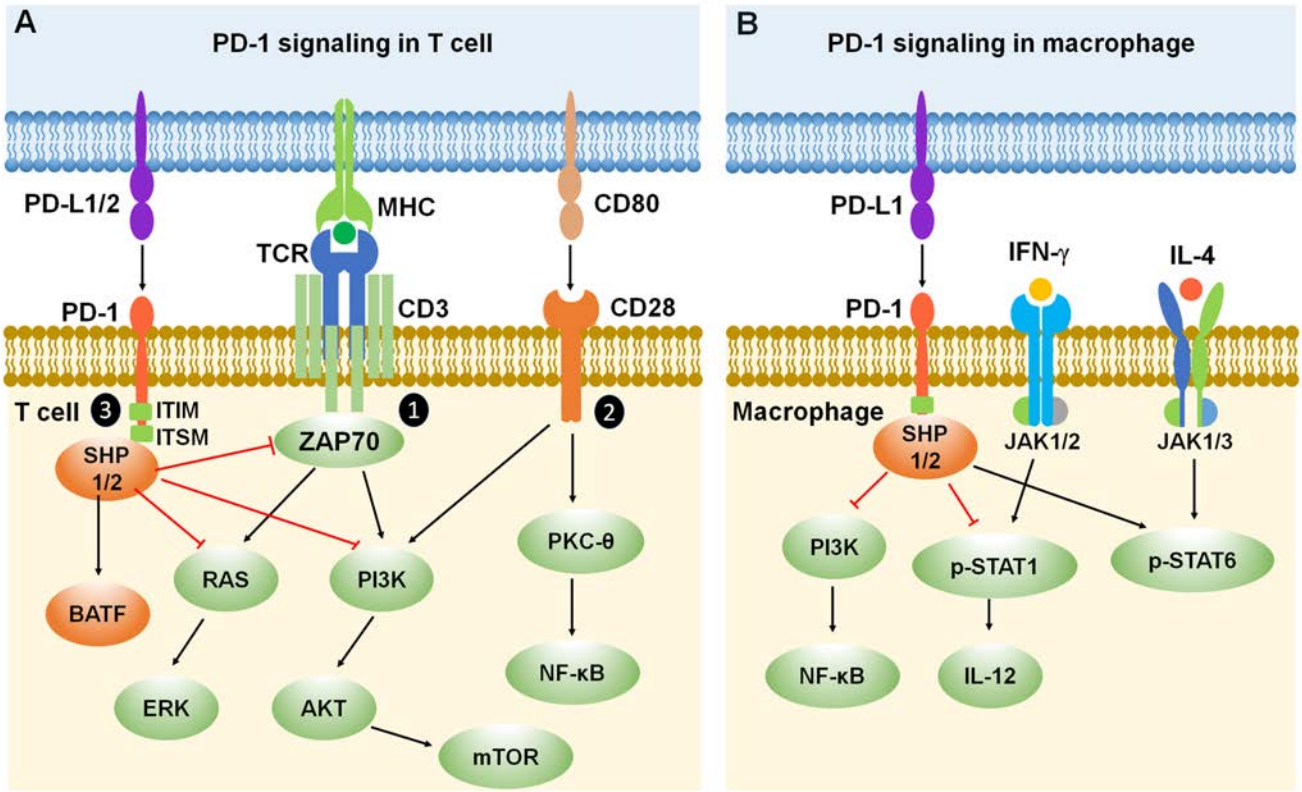

Fig. 2 PD-1 signaling in T cells and macrophages. **A** Mechanisms of PD-1 signaling in T cells. PD-1 inhibits T cell function by recruiting phosphatases SHP-1/SHP-2 to the ITIM/ITSM domain in the PD-1 tail and increasing the expression of transcription factor BATF. In addition, PD-1 inhibitory signaling antagonizes positive T cell signaling events triggered by (1) TCR interacting with MHC and (2) CD28 interacting with CD80. (3) PD-1 signaling inhibits ZAP70 and the RAS-ERK and PI3K-AKT-mTOR signaling pathways. **B** Mechanisms of PD-1 signaling in macrophages. PD-1 inhibits macrophage function by recruiting phosphatases SHP-1/SHP-2 to the ITIM/ITSM domain in the PD-1 tail, leading to inhibition of the PI3K-NF-κB signaling pathway. Moreover, PD-1 signaling suppresses IFN-γ-activated M1 macrophage polarization by reducing the phosphorylation of STAT1 and the secretion of IL-12, while promoting IL-4-activated M2 macrophage polarization by increasing STAT6 phosphorylation. Red lines ending in a bar represent inhibitory signaling, and black arrows indicate positive signaling. Abbreviations: PD-1, programmed cell death protein 1; PD-L1/2, PD-1 ligands, PD-L1 (B7-H1) and PD-L2 (B7-DC); ITIM, immunoreceptor tyrosine-based inhibitory motif; ITSM, immunoreceptor tyrosine-based switch motif; SHP, Src homology 2 domain-containing protein tyrosine phosphatase; BATF, basic leucine zipper ATF-like transcription factor; MHC, major histocompatibility complex; TCR, T cell receptor; CD, cluster of differentiation; ZAP70, zeta-chain-associated protein kinase 70; RAS, a small GTPase encoding *RAS* (retrovirus-associated DNA sequences); ERK, extracellular signal-regulated kinase; PI3K, type I phosphatidylinositol 3-kinase; AKT, serine/threonine-specific protein kinase; mTOR, mammalian target of rapamycin; PKC-θ, protein kinase C theta; NF-κB, nuclear factor kappa B; p-STAT1/6, phosphorylated signal transducer and activator of transcription 1/6; IL, interleukin; IFN-γ, interferon gamma; JAK, Janus kinase.

SHP-1 signaling and downstream modulation of ion channels [19, 24].

The role of the PD-1 pathway in the immune system has been elegantly discussed in a number of reviews [25, 26]. In this review, we focus on the diverse roles of PD-1 signaling in the context of the CNS, including in physiological cognitive function as well as pathological conditions such as brain tumors, Alzheimer's disease, stroke, spinal cord injury, multiple sclerosis, and pain (Table 2). We further discuss how this knowledge can be applied to understanding how the PD-1 pathway can modulate the treatment of CNS diseases. And finally, we consider the challenges and opportunities for utilizing the PD-1 signaling pathway for immunotherapies and neurotherapies in CNS disease conditions.

Immune Modulation of CNS Disorders by PD-1

PD-1 Signaling in Immune T Cells, Macrophages, and Microglia

PD-1 is widely expressed by immune cells and its signaling pathway is best characterized in activated T cells [27]. Activated T cells receive three signals from APCs during cytokine production, proliferation, differentiation, apoptosis, and survival (Fig. 2A). Signal one consists of TCR-CD3 (T cell receptor and cluster of differentiation 3) and its co-receptor (CD4 or CD8) binding to the major histocompatibility complex (MHC), and subsequently activating the co-receptor associated lymphocyte-specific protein tyrosine kinase (LCK). LCK phosphorylates the intracellular portions of the CD3 complex and creates a docking site for zeta-chain-associated protein kinase 70 (ZAP70), which is expressed near the surface membrane of T cells and plays a crucial role in T-cell signaling. ZAP70 starts multiple signaling events through activation of the RAS-ERK (extracellular signal-regulated kinase) and PI3K-AKT (type I phosphatidylinositol 3-kinase to serine/threonine-specific protein kinase) pathways. Signal two is composed of CD80-CD28 interactions between APCs and T cells. LCK phosphorylates the CD28 intracellular domain, providing a docking site for the PI3K complex. PI3K then generates phosphatidylinositol-(3,4,5)-trisphosphate, activating downstream kinases including AKT, which enhances proliferation and survival through the mammalian/mechanistic target of rapamycin (mTOR) pathway. CD28 activation further activates protein kinase C theta (PKC-θ) and subsequent activation of the nuclear factor kappa B (NF-κB) pathway. Signal three is a result of PD-1 signaling which serves as an antagonist of the two activated pathways noted above. PD-1 has two tyrosine-

Table 2 Brain diseases and other conditions influenced by PD-1 signaling

Disease or condition	Resources	Role of PD-1	References
Alzheimer's disease	Human patients	Decreased PD-1 expression decreases amyloid plaques in some studies but not others	[64, 65, 67, 115]
	Mice		
Glioblastoma	Human patients	Tumor cells interact with PD-1 through the PD-l/PD-L1 axis to increase PD-1 expression, which then decreases T-cell production	[116–119]
	Mice		
Melanoma	Human patients	Metastatic tumor cells interact with PD-1 through the PD-l/PD-L1 axis to increase PD-1 expression, which then decreases T-cell production	[120–123]
	Mice		
Multiple sclerosis	Human patients	Increased PD-1 expression correlated with disease remission due to the PD-1/PD-L1 pathway limiting the immune response	[84, 85, 124, 125]
	Mice		
Memory	Mice	PD-1 deficiency or blockade in brain improves learning and memory	[92]
Pain	Human patients	The PD-1/PD-L1 axis has an analgesic effect by suppressing peripheral neuronal excitability and spinal synaptic transmission, thereby reducing pain	[19, 95, 98, 126–128]
	Mice		
Spinal cord injury	Mice	PD-1 is highly expressed after spinal injury to restrict the inflammatory response	[23, 81]
Stroke	Human patients	Increased PD-1 expression linked to reduced post-stroke inflammation, but the PD-1 ligands PD-L1 and PD-L2 play distinct roles in stroke	[22, 71–74]
	Mice		

based signaling motifs in its cytoplasmic domain: an immunoreceptor tyrosine-based inhibitory motif (ITIM) and an immunoreceptor tyrosine-based switch motif (ITSM), both of which are essential for PD-1 function. When engaged with PD-L1, PD-1 counteracts TCR-CD3 signal transduction and terminates ZAP70 and PI3K phosphorylation by recruiting SHP-1 or/and SHP-2 phosphatases to its tyrosine phosphorylated ITIM and ITSM motifs, affecting downstream signaling pathways including those involving PI3K-AKT and RAS-ERK [28]. In addition, PD-1 inhibits T cell functions by increasing the expression of transcription factors such as basic leucine zipper ATF-like transcription factor (BATF), which further counters effector transcriptional programs [29]. The functional outcome of these effects is decreased T cell activation, proliferation, survival, and cytokine production as well as altered metabolism.

Subsequent studies have shown that, in addition to T cells, PD-1 is also expressed by macrophages and microglia (Figs. 2B and 3A), especially under pathological conditions [30, 31]. Macrophages and microglia have different phenotypes such as M1 and M2, which show nearly opposite functionality in the immune system and CNS. M1 macrophages and microglia are highly pro-inflammatory and effective killer cells. M2 macrophages and microglia, on the other hand, are induced by a variety of stimuli, including interleukin-4 (IL-4) [32]. In addition to M1 and M2 phenotypes, macrophages and microglia must have additional phenotypes for maintaining homeostasis and promoting resolution [33–35]. PD-1^+ macrophages play the main role in the peripheral immune system, and brain-resident PD-1^+ microglia may serve an analogous function in the CNS. In cancer, there is a higher proportion of M2 macrophages among PD-1^+ tumor-associated macrophages *versus* M1 macrophages [31]. Anti-PD-1 therapy stimulates macrophage infiltration into tumors and increases the proportion of M1 over M2 macrophages in tumors. Thus, PD-1 signaling alters the function of macrophages and microglia by affecting the M1/M2 phenotypes during pathological conditions.

The canonical interferon (IFN) regulatory factor/STAT (signal transducer and activator of transcription) signaling pathways activated by IFN-γ promote the formation of M1 macrophages *via* STAT1 activation. In contrast, IL-4 promotes the M2 phenotype *via* STAT6 activation [36]. PD-1 activation induces M2 polarization of macrophages and microglia through decreased STAT1 phosphorylation and increased STAT6 phosphorylation, as well as the down-regulation of crucial downstream NF-κB signaling, which otherwise could be activated by PI3K (Figs. 2B and 3A). Activation of PD-1 also reduces the production of cytokine IL-12 by macrophages and microglia, which further regulates the function of immune cells and affects pathological conditions [37] (Figs. 2B and 3A). In addition, microglial ERK activation is a critical regulator of pro-inflammatory immune responses in many pathological conditions including neuropathic pain, and PD-1 signaling may regulate the microglial ERK signaling pathway in these conditions [38–41] (Fig. 3A). Finally, PD-1 signaling in neurons shares similarities with that in immune cells and glial cells but also shows clear differences by functional interactions with ion channels (Fig. 3B).

Anti-PD-1 Immunotherapy for Brain Tumors and Brain Metastases

Anti-PD-1 immunotherapies have been used as clinical treatments for brain tumors [42–44]. Anti-PD-1 blocking antibodies have been shown by various studies to cause an increase of T cells in the brain and anti-tumor immunity by mobilizing the immune system (Fig. 4A). Although PD-1 blockade has shown positive effects for treating brain tumors and metastases in cancer patients, the clinical efficacy of PD-1 blockades has shown certain limitations and unpredictability. The characteristics of certain brain tumors can make effective treatment difficult. Glioblastoma (GBM) is the most common and aggressive brain tumor diagnosed in adults but <10% of GBM patients show a long-term response to anti-PD-1 treatment [45]. One of the limiting factors is the blood-brain barrier (BBB), which makes it difficult for anti-PD1 antibodies such as nivolumab to access the tumor. Combining anti-PD-1 antibodies with BBB peptide shuttles enhances delivery of the drug to the brain and efficiently eliminates brain tumor cells [46]. Another limitation of PD-1 blockade to treat brain tumors and metastases is the low immunogenic response and immunosuppressive microenvironment in brain tumors [47]. Immunosuppression mediated by the CNS-native myeloid cells in the tumor microenvironment has been linked to poor outcomes in cancer and a reduced response to immunotherapies. A recent study showed that loss of Cx3cr1 (C-X3-C motif chemokine receptor 1) in CNS-myeloid triggers a Cxcl10 (C-X3-C motif chemokine receptor 10)-mediated vicious cycle, promoting brain metastases and immunosuppression [48]. TREM2 (triggering receptor expressed on myeloid cells 2)-positive myeloid cells have also been shown to mediate immunosuppression in the tumor microenvironment, and TREM2 deficiency or administration of a TREM2 antibody increases the efficacy of anti-PD-1 immunotherapy [49, 50]. Thus, it will be necessary to identify potential biomarkers in patients who could obtain the greatest benefit from anti-PD-1 treatment. A recent study in GBM patients treated with anti-PD-1 immunotherapy showed a significant enrichment of PTEN (phosphatase and tensin homolog deleted on chromosome ten) mutations associated with

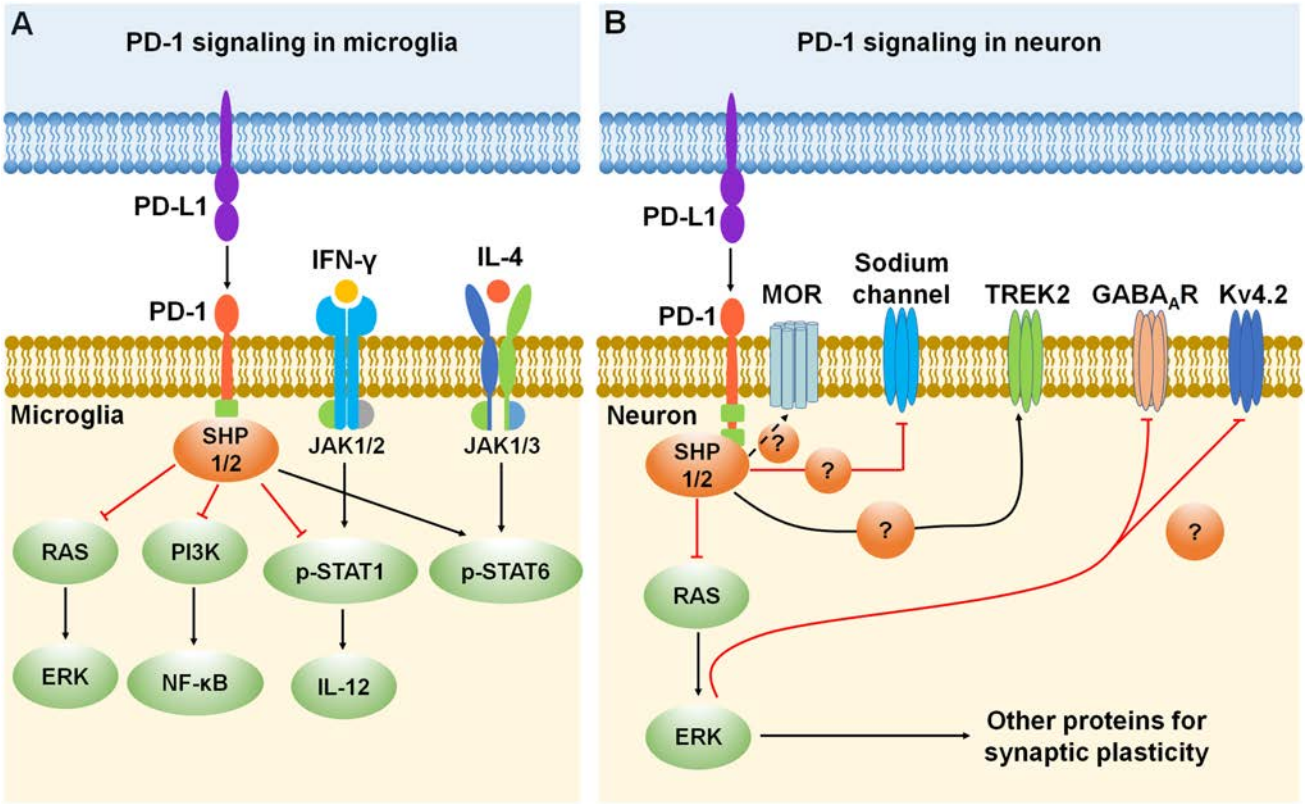

Fig. 3 PD-1 signaling and expression in microglia and neurons. **A** Mechanisms of PD-1 signaling in microglia. PD-1 inhibits microglial function by recruiting phosphatases SHP-1/SHP-2 to the ITIM/ITSM domain in the PD-1 tail and then inhibiting the RAS-ERK and PI3K-NF-κB signaling pathways. Moreover, PD-1 signaling suppresses IFN-γ-activated M1 microglia polarization by reducing the phosphorylation of STAT1 and the secretion of IL-12, while promoting IL-4-activated M2 microglia polarization by increasing STAT6 phosphorylation. **B** Mechanisms of PD-1 signaling in neurons. Activation of the PD-1 pathway dampens neuronal excitation *via* activation of the phosphatase SHP-1/2 and resulting in the downstream modulation of sodium and potassium channels (TREK2 and Kv4.2), as well as $GABA_A$ receptors. Moreover, PD-1 signaling regulates mu-opioid receptor (MOR) function through activation of the phosphatase SHP-1. Red lines ending in a bar represent inhibitory signaling, and black arrows indicate positive signaling. Abbreviations: PD-1, programmed cell death protein 1; PD-L1, PD-1 ligand; SHP, Src homology 2 domain-containing protein tyrosine phosphatase; RAS, a small GTPase encoding *RAS* (retrovirus-associated DNA sequences); ERK, extracellular signal-regulated kinase; PI3K, type I phosphatidylinositol 3-kinase; NF-κB, nuclear factor kappa B; p-STAT 1/6, phosphorylated signal transducer and activator of transcription 1/6; IL, interleukin; IFN-γ, interferon gamma; JAK, Janus kinase; MOR, mu-opioid receptor; TREK2, TWIK-related K^+ channel-2; $GABA_A$R, gamma-aminobutyric acid A receptor; Kv4.2, potassium voltage-gated channel subfamily D member 2.

immunosuppressive expression signatures in non-responders and an enrichment of mitogen-activated protein kinase pathway alterations (PTPN11 and BRAF) in responders [51]. Notably, anti-PD-1 immunotherapy aims to induce a pro-inflammatory environment characterized by increased immune infiltrates into tumors. When this immune checkpoint inhibitor is targeted to treat peripheral tumors, the systemic immune activation may cause central neuroinflammation and associated behavioral and cognitive side-effects. Early clinical studies described some behavioral and cognitive outcomes following anti-PD-1 immunotherapy, including headache, cerebellar ataxia, and transient cognitive dysfunction [52–56]. However, there remains a gap in how these therapies modulate behavioral and cognitive changes. Therefore, pharmacological strategies to cross the BBB and elucidating the mechanisms underlying the immunosuppressive microenvironment, combined with measurement of potential biomarkers that favor anti-PD-1 treatment will improve the efficacy of immunotherapy for clinical brain tumors and metastases, and furthermore, predict adverse CNS events in the treatment of peripheral tumors.

Anti-PD-1 Immunotherapy in Alzheimer's Disease

Alzheimer's disease (AD) is an age-related neurodegenerative disease and the most common cause of dementia [57]. The pathological hallmarks of AD are the extracellular accumulation of β-amyloid (Aβ) plaques which leads to chronic neuroinflammation in the brain [58]. Expression of PD-1 on T cells and PD-L1 on monocytes and macrophages significantly decreases in AD patients and in

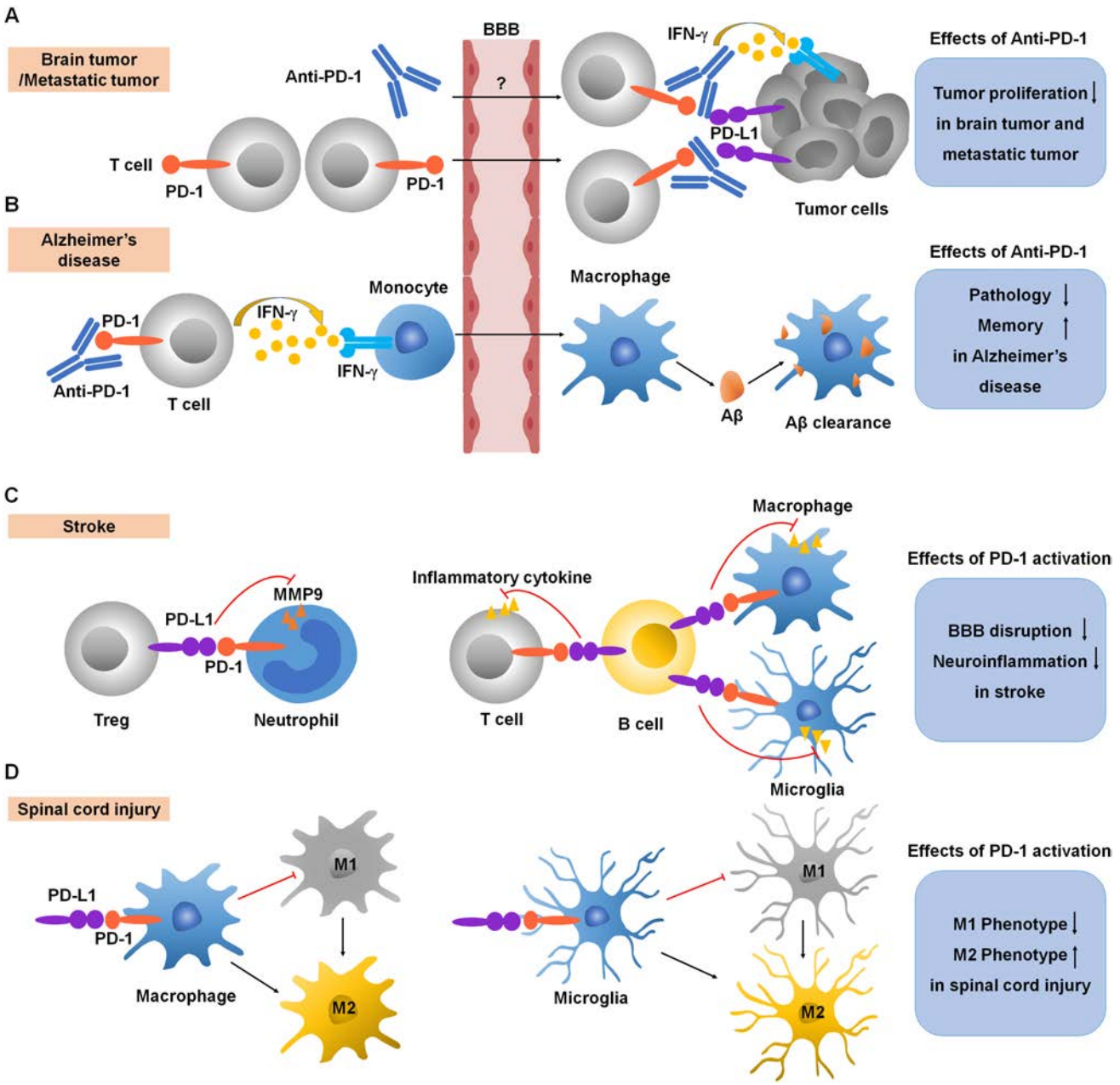

Fig. 4 Immunomodulation by PD-1 in CNS diseases. **A** Anti-PD-1 antibody treatment induces IFN-γ–dependent activity and promotes T cell recruitment to the brain for anti-tumor immunotherapy. **B** Anti-PD-1 antibody treatment evokes a systemic IFN-γ–dependent immune response that enables the mobilization of monocyte-derived macrophages to the brain, thereby reducing pathology and improving memory in Alzheimer's disease. **C** Activation of PD-1 signaling suppresses (1) the release of MMPs from neutrophils, protecting the BBB and (2) the release of inflammatory cytokines from T cell and microglia and macrophages, reducing neuroinflammation in stroke. **D** Activation of PD-1 signaling suppresses microglia and macrophage M1 polarization and promotes M2 polarization in spinal cord injury. Red lines ending in a bar represent inhibitory signaling, and black arrows indicate positive signaling. Abbreviations: PD-1, programmed cell death protein 1; PD-L1, PD-1 ligand; IFN-γ, interferon gamma; BBB, blood-brain barrier; Aβ, β-amyloid; MMP, matrix metallopeptidases.

patients with mild cognitive impairment compared with age- and sex-matched healthy controls, underscoring the importance of PD-1 signaling in AD [59]. Decreased cytokine IL-10 production has been reported in AD patients [60]. Impairment in PD-1 signaling is associated with inhibition of IL-10 production, suggesting that positive PD-1 signaling boosts IL-10 production. IL-10, in turn, has been shown to limit inflammatory responses and ameliorate AD pathology in animal models [61, 62]. Therefore, activation of PD-1 signaling-related

immunoregulatory mechanisms during the progression of AD may help re-establish immune homeostasis. In contrast, in mouse models of AD, the trafficking of blood-borne myeloid cells (monocyte-derived macrophages) to the CNS has also been shown to be neuroprotective. PD-1 blockade evokes a systemic IFN-γ-dependent immune response that enables the mobilization of monocyte-derived macrophages to the brain [63]. In additional studies in rodent AD models, PD-1 blockade reduced cerebral Aβ plaque loads and repeated anti-PD-1 treatment confers long-lasting beneficial effects on AD pathology [64, 65] (Fig. 4b). However, follow-up studies from other groups have shown that inhibition of PD-1 signaling is not sufficient to reduce amyloid pathology in a variety of transgenic AD models [66, 67]. These studies suggest that anti-PD-1 treatments may improve dementia *via* different mechanisms.

PD-1 Signaling in Stroke

Stroke is a devastating CNS condition in which a sudden interruption of blood flow to the brain results in cell death and clinical symptoms such as trouble understanding speech or speaking, paralysis or numbness of the face, arm, or leg, blurred vision, headache, and loss of coordination [68]. Stroke is associated with strong and persistent neuroinflammation. In stroke, the damaged areas of the brain have massive increases in inflammatory factors, activated local microglia, and disruptions of the BBB. There is also major infiltration into the brain of peripheral immune cells, including macrophages, T-cells, and B-cells. PD-1 signaling in T cells and B cells, as well as microphages and microglia, is involved in post-stroke neuroinflammation [69, 70].

Animal models of stroke have shown increased PD-1 expression in activated microglia and macrophages, and that PD-1 deficiency leads to larger brain infarcts and exacerbated neurological deficits. Thus, activation of the PD-1 inhibitory pathway in microglia and macrophages provides a protective effect after stroke (Fig. 4C) [22, 35]. PD-1 expression on B cells leads to inhibition of inflammatory responses in other immune effector cells, and B cells also produce IL-10 and increase the PD-1 expression by T cells, providing neuroprotection against stroke [22, 69, 70].

Another study showed that T regulatory cells mediate the inhibition of neutrophils through PD-1/PD-L1 signaling, and this interaction protects against BBB disruption by suppressing the expression of matrix metalloproteinase-9 (MMP-9) (Fig. 4C) [71]. However, the particular role of PD-L1 in stroke remains controversial. Some studies have shown that PD-L1 exacerbates inflammation in stroke, and treatment with anti-PD-L1 antibodies can control CNS inflammation. Conversely, other studies have demonstrated that PD-L1 significantly attenuates neurological deficits and provides neuroprotection in stroke [72–74]. These opposing results indicate a dual effect of PD-L1/PD-1 signaling in CNS inflammatory conditions. Notably, MMP-9 inhibition is beneficial in the early phase of stroke but detrimental in the late phase of stroke [75]. Time-dependent modulation of neuroinflammation by different MMPs has also been shown in neuropathic pain after nerve injury [76]. Thus, PD-L1/PD-1 signaling in stroke may lead to positive or negative outcomes depending on the different phases and stages of stroke.

PD-1 Signaling in Spinal Cord Injury

Spinal cord injury is a severe CNS condition in which damage to the spinal cord results in paradoxical loss-of-function (e.g., mobility) and gain-of-function (e.g., neuropathic pain) [77–79]. The inflammatory response plays an important role in its pathogenesis and excessive neuroinflammation aggravates the neurological damage after such injury [79, 80]. PD-1 signaling in T cells as well as macrophages and microglia are involved in neuroinflammation after spinal cord injury. One study has shown that the injury impairs T cell cytokine production, and this T cell dysfunction is a result of increased expression of PD-1. Thus, blocking PD-1 signaling can rescue the T cell functionality in spinal cord injury [81]. In addition, PD-1 signaling modulates macrophage and microglial phenotypes after injury. Specifically, PD-1 signaling has been shown to suppress the M1 polarization/phenotype and promote the M2 polarization/phenotype, thereby mitigating neuroinflammation from microglia and macrophages after spinal cord injury (Fig. 4D) [23, 82]. However, the particular molecular mechanism that connects PD-1 signaling to the M1/M2 phenotypic change needs to be further investigated.

PD-1 Signaling in Multiple Sclerosis

Multiple sclerosis is a chronic inflammatory disorder of the brain and spinal cord characterized by focal lymphocytic infiltration leading to the damage of myelin and axons [83]. Expression of PD-1 on T cells and PD-L1 on APCs is increased in multiple sclerosis patients and an impairment of PD-1 inhibitory signaling on T cells as a result of a PD-1 polymorphism is associated with progression of the disease [84, 85]. Preclinical studies of experimental autoimmune encephalomyelitis, an animal model of multiple sclerosis, also showed that genetic deletion of *Pdcd1* or pharmacological blockade of PD-1 enhances the activation and expansion of T-cells and aggravates the pathology in the CNS [86, 87]. Mechanistically, IFN-β has been used to

alleviate multiple sclerosis through up-regulation of PD-L1 and inhibition of CNS neuroinflammation [88]. PD-L1/PD-1 signaling regulates cytokine expression in T cells (IFN-γ and IL-17) and B cells (IL-10) [89, 90]. In addition, IL-12, which is mainly produced by APCs, has also been shown to suppress the development of multiple sclerosis through stimulating IFN-γ production in APCs and enhancing downstream PD-1 signaling [91]. Thus, enhancement of PD-L1/PD-1 inhibitory signaling holds promise as a therapeutic strategy for patients suffering from multiple sclerosis.

Neuromodulation by PD-1 in the PNS and CNS

PD-1 has been studied extensively thus far in non-neuronal cells, and now, PD-1 signaling in neurons is gaining increasing attention. Recent studies have shown that PD-1 is expressed in various neuronal populations including dorsal root ganglion (DRG) sensory neurons, spinal cord neurons, and neurons in specific brain regions, such as the hippocampus [19, 24, 92]. In neurons, PD-1 acts as an inhibitor as it does in immune cells. More specifically, PD-1 expression in neurons affects neuronal excitability, synaptic transmission, and synaptic plasticity (Fig. 5).

Intriguingly, PD-1 is involved in diverse neuronal signaling pathways, four of which are further detailed in this section (Figs. 3B and 5). (1) Activation of PD-1 signaling dampens the excitation of neurons, which occurs *via* the activation of phosphatase SHP-1 and downstream modulation of sodium and potassium channels. PD-1 also affects the characteristics of the neuronal membrane through TWIK-related K^+ channel-2 (TREK2), which is a potassium channel involved in the regulation of the resting membrane potential of sensory neurons [19] (Fig. 5A). SHP-1 has also been shown to dephosphorylate transient receptor potential subtype V1 (TRPV1) in DRG neurons and alleviate inflammatory pain in rats [93]. Furthermore, a recent study has shown that conditioned deletion of SHP-1 in $Na_V1.8^+$ neurons facilitates bone cancer pain [94]. These studies strongly suggest that the phosphatase SHP-1 in nociceptors acts as a pain suppressant. (2) The co-localization of PD-1 with the mu-opioid receptor (MOR) in DRG neurons regulates opioid antinociception [95] (Fig. 5A). (3) PD-1 regulates GABAergic neurotransmission and GABA-mediated analgesia and anesthesia [24] (Fig. 5B). (4) PD-1 in hippocampal CA1 neurons regulates neuronal excitability and synaptic plasticity [92] (Fig. 5C). Due to the important role of PD-1 in neuronal regulation, PD-1 inhibitors may have both beneficial effects (e.g., learning and memory) and detrimental effects (e.g., pain) under different pathological conditions.

PD-1 is broadly expressed by DRG sensory neurons, as well as spinal cord dorsal horn and ventral horn neurons. PD-1 in mouse and human DRG neurons is further transported by axons to their peripheral and central terminals in the skin and spinal cord, respectively [19]. PD-L1 has an analgesic effect that is mediated by PD-1 in naïve mice, as well as in mouse models of inflammatory, neuropathic, and cancer pain [19, 94, 96]. Activation of the PD-L1/PD-1 pathway suppresses action potentials in mouse and human DRG sensory neurons through the modulation of sodium and potassium channels. Furthermore, the TREK2 potassium channel, which regulates the resting membrane potential in C-fiber nociceptors [97], is potentiated by PD-1/PD-L1 signaling in DRG neurons. These modifications of sodium channels and TREK2 potassium channels are regulated by SHP-1, which is activated by PD-L1 in DRG nociceptive neurons *via* phosphorylation (Fig. 5A) [19]. PD-L1 also activates SHP-1 to down-regulate TRPV1 in DRG neurons and delay the development of bone cancer pain in mice [94]. While the PD-L1/PD-1 axis produces acute antinociception through neuromodulation, the delayed effects of this pathway may also depend on immunomodulation. In a mouse model of bone cancer pain, anti-PD-1 treatment with Nivolumab initially increased bone cancer pain through neuronal modulation [98]. In contrast, Nivolumab reduced bone cancer pain in the late phase through modulation of osteoclasts and protection against bone destruction. Thus, anti-PD-1 treatment initially increases cancer pain before reducing it at later time points as a result of both neuromodulation and immunomodulation [98].

PD-1 is co-localized with MOR in DRG sensory neurons and their axons in mouse and human (Fig. 5A). Through interaction with MOR, PD-1 regulates the function of opioid receptors in sensory neurons and plays a crucial role in MOR signaling. PD-1 deficiency or blockade impairs morphine-mediated analgesia in mice and nonhuman primates [95]. Morphine produces antinociception *via* suppression of calcium currents in DRG neurons, inhibition of excitatory synaptic transmission in spinal cord neurons, and induction of outward currents in spinal neurons. But all of these antinociceptive mechanisms are impaired after loss of PD-1 function in *Pd1* (or *Pdcd1*) knockout mice. In addition, loss of PD-1 signaling enhances opioid-induced hyperalgesia and tolerance and potentiates opioid-induced long-term potentiation in the spinal cord [95]. Future studies are warranted to determine how PD-1 interacts with MOR at the molecular level.

Apart from spinal cord neurons, *Pd1* mRNA and PD-1 protein are also widely expressed in neurons of many brain regions, including cortical, thalamic, hypothalamic, and hippocampal neurons. Despite low expression levels, PD-1 in CNS neurons is fully functional. Interestingly, PD-1 is

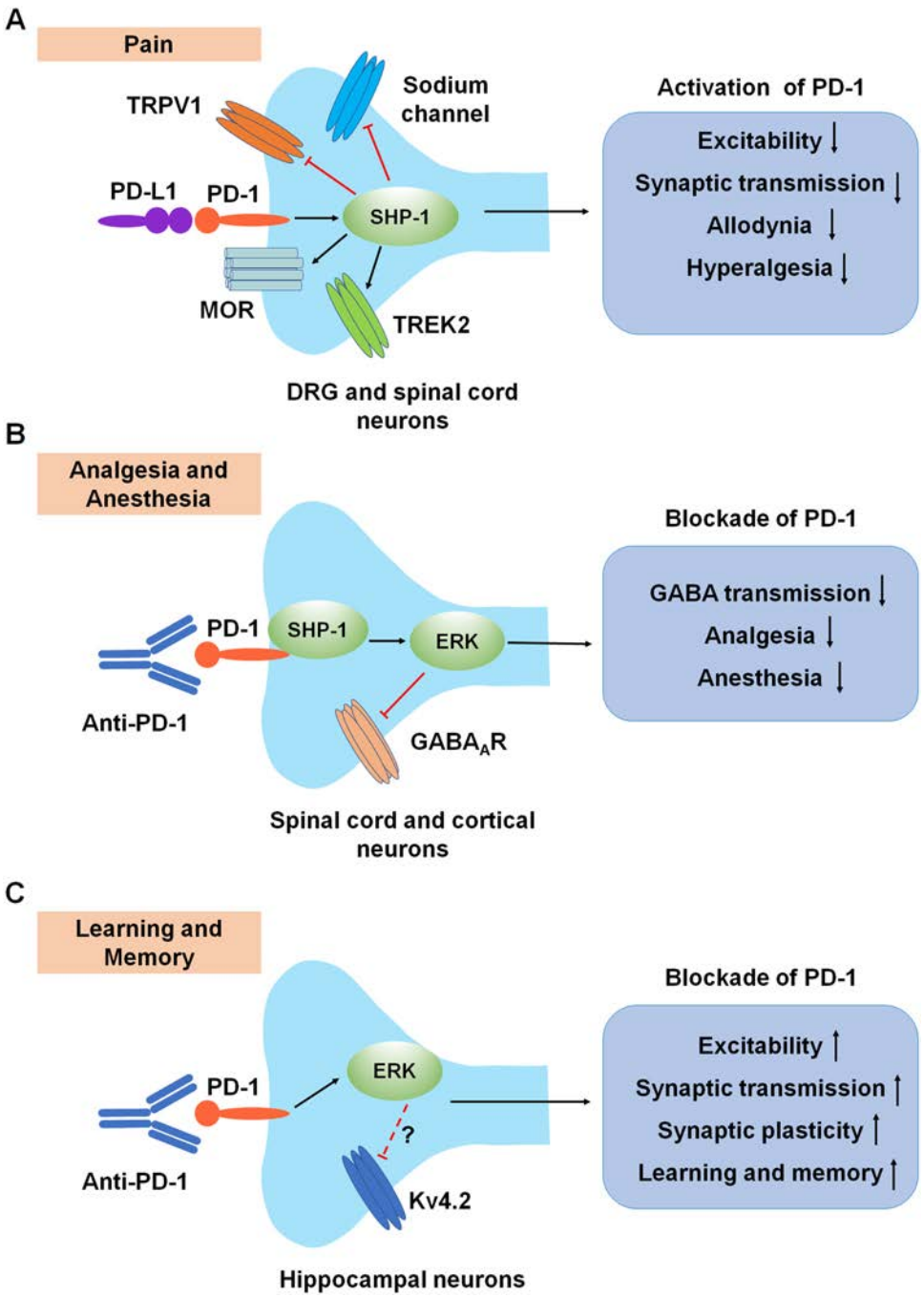

Fig. 5 Neuromodulation by PD-1 in the PNS and CNS. **A** Modulation of pain in primary sensory neurons and spinal dorsal horn neurons. Activation of PD-1 signaling in DRG neurons decreases neuronal excitability and synaptic transmission and inhibits physiological pain and pathological pain (allodynia and hyperalgesia) through modulation of ion channels. **B** Modulation of GABA-mediated analgesia and anesthesia in CNS neurons. **C** Modulation of learning and memory in hippocampal neurons. Anti-PD-1 antibody treatment increases hippocampal neuronal excitability, synaptic transmission, and synaptic plasticity, thereby enhancing learning and memory. Red lines ending in a bar represent inhibitory signaling, and black arrows indicate positive signaling. Abbreviations: PD-1, programmed cell death protein 1; PD-L1, PD-1 ligand; TRPV1, transient receptor potential subtype V1; MOR, mu-opioid receptor; TREK2, TWIK-related K^+ channel-2; DRG, dorsal root ganglion; SHP-1, Src homology 2 domain-containing protein tyrosine phosphatase 1; ERK, extracellular signal-regulated kinase; $GABA_AR$, gamma-aminobutyric acid A receptor; Kv4.2, potassium voltage-gated channel subfamily D member 2.

required for GABAergic neurotransmission, especially the actions of $GABA_ARs$ (Fig. 5B). PD-1 blockade with Nivolumab causes a profound reduction (50%) of GABA-currents across the CNS, including lamina IIo and lamina I in the spinal dorsal horn, S1 sensory cortex, the ventral posterior medial and ventral lateral nuclei of the thalamus, hypothalamus, and the hippocampus. GABAergic neurotransmission is known to mediate analgesia and anesthesia, but strikingly, GABA-mediated analgesia and anesthesia are compromised in $Pd1^{-/-}$ mice [24]. Thus, in CNS neurons, PD-1 is coupled to two inhibitory signaling pathways, mediated by opioid receptors and GABA receptors. Strikingly, PD-1 deficiency or blockade leads to enhanced hippocampal learning and memory [92]. Patch-clamp recording has demonstrated that loss of PD-1 increases neuronal excitability, excitatory synaptic transmission, and synaptic plasticity in hippocampal neurons. Because PD-1 suppresses ERK activation, and ERK phosphorylates the Kv4.2 potassium channel to suppress its activity in hippocampal neurons [99], we postulate that PD-1 signaling

plays an important role as a neuronal inhibitor in learning and memory by regulating the ERK pathway and Kv4.2 potassium channel activity (Fig. 5C). Anti-PD-1 antibodies may potentially serve as a neurotherapy to improve memory function and counteract cognitive decline.

Conclusions and Future Directions

The expression of PD-1 in immune cells, glial cells, and neurons allows for multiple tiers of immunomodulation and neuromodulation in the CNS. PD-1 acts as an inhibitory receptor in various types of cells. Increasing evidence suggests a critical role of PD-1 signaling in CNS resident microglia and peripherally recruited immune cells, as well as neurons under physiological and pathological conditions. Because PD-1 not only regulates immune responses but also neuronal function, PD-1 modulation can exert a range of neuroimmune effects. Thus, the function of PD-1 signaling in the cross-talk between immune cells, glial cells, and neurons in the CNS needs to be further investigated.

To guide rational PD-1-based immunotherapy and neurotherapy in the CNS, several key issues need to be addressed. (1) PD-1-based therapies used for CNS conditions must overcome the obstacles of the BBB. What is the ideal carrier to deliver anti-PD-1 drugs into the brain? (2) The role of PD-1 signaling in restricting local neuroinflammation in the CNS has not been examined. It will be important to determine whether modulation of the PD-1 signaling pathway during CNS injury or neurodegeneration influences the balance between debris clearance, brain repair, and inflammatory damage. (3) PD-1 ligands (e.g., PD-L1 and PD-L2) are expressed by various cell types. What are the specific contributions of these ligands to glial and neuronal functions in CNS disease conditions? (4) Intracellular signaling of neuronal PD-1 must be distinct from that of immune and glial PD-1 due to unique coupling to ion channels. What are the precise molecular mechanisms underlying PD-1 signaling in microglia and neurons in different CNS disease conditions? It is also important to know how PD-1 is coupled to neuron-specific ion channels. (5) To uncover the precise role of PD-1 signaling in immune cells, glial cells, and neurons, conditional-knockout mice will need to be generated to enable specific PD-1 deletions in different cell types and subtypes (e.g., excitatory *versus* inhibitory neurons).

Finally, it is important to point out that PD-1 signaling in the CNS can act like a double-edged sword, producing both beneficial and detrimental effects. A temporary PD-1 signaling blockade, for instance, may cause excitatory effects in microglia and neurons providing beneficial effects under physiological conditions, while a more persistent PD-1 signaling blockade may lead to adverse over-excitatory effects. Thus, the challenge for developing new strategies in using PD-1 signaling therapeutically, will be determining which precise neuronal circuits and cell types need to be tuned for different CNS conditions.

Acknowledgements The work related to this review was partially supported by Duke University Fund.

Conflict of interest The authors claim that there are no conflicts of interest.

References

1. Ishida Y, Agata Y, Shibahara K, Honjo T. Induced expression of PD-1, a novel member of the immunoglobulin gene superfamily, upon programmed cell death. EMBO J 1992, 11: 3887–3895.
2. Agata Y, Kawasaki A, Nishimura H, Ishida Y, Tsubata T, Yagita H. Expression of the PD-1 antigen on the surface of stimulated mouse T and B lymphocytes. Int Immunol 1996, 8: 765–772.
3. Bardhan K, Anagnostou T, Boussiotis VA. The PD1:PD-L1/2 pathway from discovery to clinical implementation. Front Immunol 2016, 7: 550.
4. Dong HD, Zhu GF, Tamada K, Chen LP. B7–H1, a third member of the B7 family, co-stimulates T-cell proliferation and interleukin-10 secretion. Nat Med 1999, 5: 1365–1369.
5. Freeman GJ, Long AJ, Iwai Y, Latchman Y, Bourque K, Brown JA, *et al.* Engagement of the PD-1 immunoinhibitory receptor by a novel B7-family member leads to negative regulation of lymphocyte activation. Blood 2000, 96: 810a–811a.
6. Latchman Y, Wood C, Chemova T, Iwai Y, Malenkovich N, Long A, *et al.* PD-L2, a novel B7 homologue, is a second ligand for PD-1 and inhibits T cell activation. FASEB J 2001, 15: A345–A345.
7. Tseng SY, Otsuji M, Gorski K, Huang X, Slansky JE, Pai SI, *et al.* B7-DC, a new dendritic cell molecule with potent costimulatory properties for T cells. J Exp Med 2001, 193: 839–845.
8. Yamazaki T, Akiba H, Iwai H, Matsuda H, Aoki M, Tanno Y, *et al.* Expression of programmed death 1 ligands by murine T cells and APC. J Immunol 2002, 169: 5538–5545.
9. Sugita S, Usui Y, Horie S, Futagami Y, Aburatani H, Okazaki T, *et al.* T-cell suppression by programmed cell death 1 ligand 1 on retinal pigment epithelium during inflammatory conditions. Invest Ophthalmol Vis Sci 2009, 50: 2862–2870.
10. Liang SC, Latchman YE, Buhlmann JE, Tomczak MF, Horwitz BH, Freeman GJ, *et al.* Regulation of PD-1, PD-L1, and PD-L2 expression during normal and autoimmune responses. Eur J Immunol 2003, 33: 2706–2716.
11. Hu J, He H, Yang Z, Zhu G, Kang L, Jing X, *et al.* Programmed death ligand-1 on microglia regulates Th1 differentiation via nitric oxide in experimental autoimmune encephalomyelitis. Neurosci Bull 2016, 32: 70–82.
12. Loke P, Allison JP. PD-L1 and PD-L2 are differentially regulated by Th1 and Th2 cells. Proc Natl Acad Sci U S A 2003, 100: 5336–5341.
13. Keir ME, Francisco LM, Sharpe AH. PD-1 and its ligands in T-cell immunity. Curr Opin Immunol 2007, 19: 309–314.
14. Nishimura H, Nose M, Hiai H, Minato N, Honjo T. Development of lupus-like autoimmune diseases by disruption of the PD-1 gene encoding an ITIM motif-carrying immunoreceptor. Immunity 1999, 11: 141–151.

15. Nishimura H, Okazaki T, Tanaka Y, Nakatani K, Hara M, Matsumori A, *et al.* Autoimmune dilated cardiomyopathy in PD-1 receptor-deficient mice. Science 2001, 291: 319–322.
16. Dong HD, Strome SE, Salomao DR, Tamura H, Hirano F, Flies DB, *et al.* Tumor-associated B7–H1 promotes T-cell apoptosis: A potential mechanism of immune evasion. Nat Med 2002, 8: 793–800.
17. Thompson RH, Gillett MD, Cheville JC, Lohse CM, Dong HD, Webster WS, *et al.* Costimulatory B7–H1 in renal cell carcinoma patients: Indicator of tumor aggressiveness and potential therapeutic target. J Urol 2005, 173: 169–169.
18. Zhao S, Li F, Leak RK, Chen J, Hu X. Regulation of neuroinflammation through programed death-1/programed death ligand signaling in neurological disorders. Front Cell Neurosci 2014, 8: 271.
19. Chen G, Kim YH, Li H, Luo H, Liu DL, Zhang ZJ, *et al.* PD-L1 inhibits acute and chronic pain by suppressing nociceptive neuron activity via PD-1. Nat Neurosci 2017, 20: 917–926.
20. Louveau A, Smirnov I, Keyes TJ, Eccles JD, Rouhani SJ, Peske JD, *et al.* Structural and functional features of central nervous system lymphatic vessels. Nature 2015, 523: 337–341.
21. Alves de Lima K, Rustenhoven J, Kipnis J. Meningeal immunity and its function in maintenance of the central nervous system in health and disease. Annu Rev Immunol 2020, 38: 597–620.
22. Ren X, Akiyoshi K, Vandenbark AA, Hurn PD, Offner H. Programmed death-1 pathway limits central nervous system inflammation and neurologic deficits in murine experimental stroke. Stroke 2011, 42: 2578–2583.
23. Yao A, Liu F, Chen K, Tang L, Liu L, Zhang K, *et al.* Programmed death 1 deficiency induces the polarization of macrophages/microglia to the M1 phenotype after spinal cord injury in mice. Neurotherapeutics 2014, 11: 636–650.
24. Jiang C, Wang Z, Donnelly CR, Wang K, Andriessen AS, Tao X, *et al.* PD-1 regulates GABAergic neurotransmission and GABA-mediated analgesia and anesthesia. iScience 2020, 23: 101570.
25. Francisco LM, Sage PT, Sharpe AH. The PD-1 pathway in tolerance and autoimmunity. Immunol Rev 2010, 236: 219–242.
26. Topalian SL, Drake CG, Pardoll DM. Targeting the PD-1/B7-H1(PD-L1) pathway to activate anti-tumor immunity. Curr Opin Immunol 2012, 24: 207–212.
27. Riley JL. PD-1 signaling in primary T cells. Immunol Rev 2009, 229: 114–125.
28. Chemnitz JM, Parry RV, Nichols KE, June CH, Riley JL. SHP-1 and SHP-2 associate with immunoreceptor tyrosine-based switch motif of programmed death 1 upon primary human T cell stimulation, but only receptor ligation prevents T cell activation. J Immunol 2004, 173: 945–954.
29. Quigley M, Pereyra F, Nilsson B, Porichis F, Fonseca C, Eichbaum Q, *et al.* Transcriptional analysis of HIV-specific $CD8^+$ T cells shows that PD-1 inhibits T cell function by upregulating BATF. Nat Med 2010, 16: 1147–1151.
30. Lu D, Ni Z, Liu X, Feng S, Dong X, Shi X, *et al.* Beyond T Cells: understanding the role of PD-1/PD-L1 in tumor-associated macrophages. J Immunol Res 2019, 2019: 1919082.
31. Gordon SR, Maute RL, Dulken BW, Hutter G, George BM, McCracken MN, *et al.* PD-1 expression by tumour-associated macrophages inhibits phagocytosis and tumour immunity. Nature 2017, 545: 495–499.
32. Kigerl KA, Gensel JC, Ankeny DP, Alexander JK, Donnelly DJ, Popovich PG. Identification of two distinct macrophage subsets with divergent effects causing either neurotoxicity or regeneration in the injured mouse spinal cord. J Neurosci 2009, 29: 13435–13444.
33. Ransohoff RM. A polarizing question: do M1 and M2 microglia exist?. Nat Neurosci 2016, 19: 987–991.
34. Chen G, Zhang YQ, Qadri YJ, Serhan CN, Ji RR. Microglia in pain: detrimental and protective roles in pathogenesis and resolution of pain. Neuron 2018, 100: 1292–1311.
35. Qin C, Zhou LQ, Ma XT, Hu ZW, Yang S, Chen M, *et al.* Dual functions of microglia in ischemic stroke. Neurosci Bull 2019, 35: 921–933.
36. Ohmori Y, Hamilton TA. IL-4-induced STAT6 suppresses IFN-gamma-stimulated STAT1-dependent transcription in mouse macrophages. J Immunol 1997, 159: 5474–5482.
37. Zhang Y, Ma CJ, Ni L, Zhang CL, Wu XY, Kumaraguru U, *et al.* Cross-talk between programmed death-1 and suppressor of cytokine signaling-1 in inhibition of IL-12 production by monocytes/macrophages in hepatitis C virus infection. J Immunol 2011, 186: 3093–3103.
38. Zhuang ZY, Gerner P, Woolf CJ, Ji RR. ERK is sequentially activated in neurons, microglia, and astrocytes by spinal nerve ligation and contributes to mechanical allodynia in this neuropathic pain model. Pain 2005, 114: 149–159.
39. Katsura H, Obata K, Mizushima T, Sakurai J, Kobayashi K, Yamanaka H, *et al.* Activation of Src-family kinases in spinal microglia contributes to mechanical hypersensitivity after nerve injury. J Neurosci 2006, 26: 8680–8690.
40. Chen G, Luo X, Qadri MY, Berta T, Ji RR. Sex-dependent glial signaling in pathological pain: distinct roles of spinal microglia and astrocytes. Neurosci Bull 2018, 34: 98–108.
41. Chen Q, Xu LX, Du TJ, Hou YX, Fan WJ, Wu QL, *et al.* Enhanced expression of PD-L1 on microglia after surgical brain injury exerts self-protection from inflammation and promotes neurological repair. Neurochem Res 2019, 44: 2470–2481.
42. Wang X, Guo G, Guan H, Yu Y, Lu J, Yu J. Challenges and potential of PD-1/PD-L1 checkpoint blockade immunotherapy for glioblastoma. J Exp Clin Cancer Res 2019, 38: 87.
43. Xue S, Hu M, Iyer V, Yu J. Blocking the PD-1/PD-L1 pathway in glioma: a potential new treatment strategy. J Hematol Oncol 2017, 10: 81.
44. Johanns T, Waqar SN, Morgensztern D. Immune checkpoint inhibition in patients with brain metastases. Ann Transl Med 2016, 4: S9.
45. Filley AC, Henriquez M, Dey M. Recurrent glioma clinical trial, CheckMate-143: the game is not over yet. Oncotarget 2017, 8: 91779–91794.
46. Cavaco M, Gaspar D, Arb Castanho M, Neves V. Antibodies for the treatment of brain metastases, a dream or a reality? Pharmaceutics 2020, 12.
47. Sampson JH, Gunn MD, Fecci PE, Ashley DM. Brain immunology and immunotherapy in brain tumours. Nat Rev Cancer 2020, 20: 12–25.
48. Guldner IH, Wang Q, Yang L, Golomb SM, Zhao Z, Lopez JA, *et al.* CNS-native myeloid cells drive immune suppression in the brain metastatic niche through Cxcl10. Cell 2020, 183: 1234–1248. e25.
49. Molgora M, Esaulova E, Vermi W, Hou J, Chen Y, Luo J, *et al.* TREM2 modulation remodels the tumor myeloid landscape enhancing anti-PD-1 immunotherapy. Cell 2020, 182: 886–900. e17.
50. Katzenelenbogen Y, Sheban F, Yalin A, Yofe I, Svetlichnyy D, Jaitin DA, *et al.* Coupled scRNA-Seq and intracellular protein activity reveal an immunosuppressive role of TREM2 in cancer. Cell 2020, 182: 872–885. e19.
51. Zhao, Chen AX, Gartrell RD, Silverman AM, Aparicio L, Chu T, *et al.* Immune and genomic correlates of response to anti-PD-1 immunotherapy in glioblastoma. Nat Med 2019, 25: 462–469.
52. Goldberg SB, Gettinger SN, Mahajan A, Chiang AC, Herbst RS, Sznol M, *et al.* Pembrolizumab for patients with melanoma or non-small-cell lung cancer and untreated brain metastases: early

analysis of a non-randomised, open-label, phase 2 trial. Lancet Oncol 2016, 17: 976–983.
53. Feng S, Coward J, McCaffrey E, Coucher J, Kalokerinos P, O'Byrne K. Pembrolizumab-Induced encephalopathy: a review of neurological toxicities with immune checkpoint inhibitors. J Thorac Oncol 2017, 12: 1626–1635.
54. Kao JC, Liao B, Markovic SN, Klein CJ, Naddaf E, Staff NP, *et al.* Neurological complications associated with anti-programmed death 1 (PD-1) antibodies. JAMA Neurol 2017, 74: 1216–1222.
55. McGinnis GJ, Raber J. CNS side effects of immune checkpoint inhibitors: preclinical models, genetics and multimodality therapy. Immunotherapy 2017, 9: 929–941.
56. Mirabile A, Brioschi E, Ducceschi M, Piva S, Lazzari C, Bulotta A, *et al.* PD-1 inhibitors-related neurological toxicities in patients with non-small-cell lung cancer: a literature review. Cancers (Basel) 2019, 11.
57. Fan DY, Wang YJ. Early intervention in Alzheimer's disease: how early is early enough? Neurosci Bull 2020, 36: 195–197.
58. Bharadwaj PR, Dubey AK, Masters CL, Martins RN, Macreadie IG. Abeta aggregation and possible implications in Alzheimer's disease pathogenesis. J Cell Mol Med 2009, 13: 412–421.
59. Saresella M, Calabrese E, Marventano I, Piancone F, Gatti A, Farina E, *et al.* A potential role for the PD1/PD-L1 pathway in the neuroinflammation of Alzheimer's disease. Neurobiol Aging 2012, 33: e611-622.
60. Torres KC, Araujo Pereira P, Lima GS, Bozzi IC, Rezende VB, Bicalho MA, *et al.* Increased frequency of T cells expressing IL-10 in Alzheimer disease but not in late-onset depression patients. Prog Neuropsychopharmacol Biol Psychiatry 2013, 47: 40–45.
61. Guillot-Sestier MV, Doty KR, Gate D, Rodriguez J Jr, Leung BP, Rezai-Zadeh K, *et al.* Il10 deficiency rebalances innate immunity to mitigate Alzheimer-like pathology. Neuron 2015, 85: 534–548.
62. Koronyo-Hamaoui M, Ko MHK, Koronyo Y, Azoulay D, Seksenyan A, Kunis G, *et al.* Attenuation of AD-like neuropathology by harnessing peripheral immune cells: local elevation of IL-10 and MMP-9. J Neurochem 2009, 111: 1409–1424.
63. Kunis G, Baruch K, Rosenzweig N, Kertser A, Miller O, Berkutzki T, *et al.* IFN-gamma-dependent activation of the brain's choroid plexus for CNS immune surveillance and repair. Brain 2013, 136: 3427–3440.
64. Rosenzweig N, Dvir-Szternfeld R, Tsitsou-Kampeli A, Keren-Shaul H, Ben-Yehuda H, Weill-Raynal P, *et al.* PD-1/PD-L1 checkpoint blockade harnesses monocyte-derived macrophages to combat cognitive impairment in a tauopathy mouse model. Nat Commun 2019, 10: 465.
65. Baruch K, Deczkowska A, Rosenzweig N, Tsitsou-Kampeli A, Sharif AM, Matcovitch-Natan O, *et al.* PD-1 immune checkpoint blockade reduces pathology and improves memory in mouse models of Alzheimer's disease. Nat Med 2016, 22: 135–137.
66. Lin Y, Rajamohamedsait HB, Sandusky-Beltran LA, Gamallo-Lana B, Mar A, Sigurdsson EM. Chronic PD-1 checkpoint blockade does not affect cognition or promote tau clearance in a tauopathy mouse model. Front Aging Neurosci 2019, 11: 377.
67. Latta-Mahieu M, Elmer B, Bretteville A, Wang YM, Lopez-Grancha M, Goniot P, *et al.* Systemic immune-checkpoint blockade with anti-PD1 antibodies does not alter cerebral amyloid-beta burden in several amyloid transgenic mouse models. Glia 2018, 66: 492–504.
68. Dirnagl U, Iadecola C, Moskowitz MA. Pathobiology of ischaemic stroke: an integrated view. Trends Neurosci 1999, 22: 391–397.
69. Bodhankar S, Chen YX, Vandenbark AA, Murphy SJ, Offner H. IL-10-producing B-cells limit CNS inflammation and infarct volume in experimental stroke. Metab Brain Dis 2013, 28: 375–386.
70. Ren XF, Akiyoshi K, Dziennis S, Vandenbark AA, Herson PS, Hurn PD, *et al.* Regulatory B cells limit CNS inflammation and neurologic deficits in murine experimental stroke. J Neurosci 2011, 31: 8556–8563.
71. Li PY, Mao LL, Liu XR, Gan Y, Zheng J, Thomson AW, *et al.* Essential role of program death 1-ligand 1 in regulatory T-cell-afforded protection against blood-brain barrier damage after stroke. Stroke 2014, 45: 857–864.
72. Bodhankar S, Chen YX, Lapato A, Dotson AL, Wang JM, Vandenbark AA, *et al.* PD-L1 monoclonal antibody treats ischemic stroke by controlling central nervous system inflammation. Stroke 2015, 46: 2926–2934.
73. Bodhankar S, Chen Y, Vandenbark AA, Murphy SJ, Offner H. PD-L1 enhances CNS inflammation and infarct volume following experimental stroke in mice in opposition to PD-1. J Neuroinflammation 2013, 10: 111.
74. Han R, Luo J, Shi Y, Yao Y, Hao J. PD-L1 (programmed death ligand 1) protects against experimental intracerebral hemorrhage-induced brain injury. Stroke 2017, 48: 2255–2262.
75. Zhao BQ, Wang S, Kim HY, Storrie H, Rosen BR, Mooney DJ, *et al.* Role of matrix metalloproteinases in delayed cortical responses after stroke. Nat Med 2006, 12: 441–445.
76. Kawasaki Y, Xu ZZ, Wang X, Park JY, Zhuang ZY, Tan PH, *et al.* Distinct roles of matrix metalloproteases in the early- and late-phase development of neuropathic pain. Nat Med 2008, 14: 331–336.
77. Li G, Fan ZK, Gu GF, Jia ZQ, Zhang QQ, Dai JY, *et al.* Epidural spinal cord stimulation promotes motor functional recovery by enhancing oligodendrocyte survival and differentiation and by protecting myelin after spinal cord injury in rats. Neurosci Bull 2020, 36: 372–384.
78. Huang Q, Duan W, Sivanesan E, Liu S, Yang F, Chen Z, *et al.* Spinal cord stimulation for pain treatment after spinal cord injury. Neurosci Bull 2019, 35: 527–539.
79. Hulsebosch CE, Hains BC, Crown ED, Carlton SM. Mechanisms of chronic central neuropathic pain after spinal cord injury. Brain Res Rev 2009, 60: 202–213.
80. Donnelly DJ, Popovich PG. Inflammation and its role in neuroprotection, axonal regeneration and functional recovery after spinal cord injury. Exp Neurol 2008, 209: 378–388.
81. Zha J, Smith A, Andreansky S, Bracchi-Ricard V, Bethea JR. Chronic thoracic spinal cord injury impairs $CD8^+$ T-cell function by up-regulating programmed cell death-1 expression. J Neuroinflammation 2014, 11: 65.
82. He HF, Zhou YY, Zhou YL, Zhuang JY, He X, Wang SY, *et al.* Dexmedetomidine mitigates microglia-mediated neuroinflammation through upregulation of programmed cell death protein 1 in a rat spinal cord injury model. J Neurotrauma 2018, 35: 2591–2603.
83. Compston A, Coles A. Multiple sclerosis. Lancet 2008, 372: 1502–1517.
84. Trabattoni D, Saresella M, Pacei M, Marventano I, Mendozzi L, Rovaris M, *et al.* Costimulatory pathways in multiple sclerosis: distinctive expression of PD-1 and PD-L1 in patients with different patterns of disease. J Immunol 2009, 183: 4984–4993.
85. Kroner A, Mehling M, Hemmer B, Rieckmann P, Toyka KV, Maurer M, *et al.* A PD-1 polymorphism is associated with disease progression in multiple sclerosis. Ann Neurol 2005, 58: 50–57.
86. Ortler S, Leder C, Mittelbronn M, Zozulya AL, Knolle PA, Chen L, *et al.* B7–H1 restricts neuroantigen-specific T cell responses and confines inflammatory CNS damage: implications

for the lesion pathogenesis of multiple sclerosis. Eur J Immunol 2008, 38: 1734–1744.
87. Salama AD, Chitnis T, Imitola J, Ansari MJ, Akiba H, Tushima F, *et al.* Critical role of the programmed death-1 (PD-1) pathway in regulation of experimental autoimmune encephalomyelitis. J Exp Med 2003, 198: 71–78.
88. Harari D, Kuhn N, Abramovich R, Sasson K, Zozulya AL, Smith P, *et al.* Enhanced in vivo efficacy of a type I interferon superagonist with extended plasma half-life in a mouse model of multiple sclerosis. J Biol Chem 2014, 289: 29014–29029.
89. Carter LL, Leach MW, Azoitei ML, Cui J, Pelker JW, Jussif J, *et al.* PD-1/PD-L1, but not PD-1/PD-L2, interactions regulate the severity of experimental autoimmune encephalomyelitis. J Neuroimmunol 2007, 182: 124–134.
90. Bodhankar S, Wang C, Vandenbark AA, Offner H. Estrogen-induced protection against experimental autoimmune encephalomyelitis is abrogated in the absence of B cells. Eur J Immunol 2011, 41: 1165–1175.
91. Cheng X, Zhao Z, Ventura E, Gran B, Shindler KS, Rostami A. The PD-1/PD-L pathway is up-regulated during IL-12-induced suppression of EAE mediated by IFN-gamma. J Neuroimmunol 2007, 185: 75–86.
92. Zhao J, Ji RR. Anti-PD-1 treatment as a neurotherapy to enhance neuronal excitability, synaptic plasticity and memory. BioRxiv 2019, https://doi.org/10.1101/870600
93. Xiao X, Zhao XT, Xu LC, Yue LP, Liu FY, Cai J, *et al.* Shp-1 dephosphorylates TRPV1 in dorsal root ganglion neurons and alleviates CFA-induced inflammatory pain in rats. Pain 2015, 156: 597–608.
94. Liu BL, Cao QL, Zhao X, Liu HZ, Zhang YQ. Inhibition of TRPV1 by SHP-1 in nociceptive primary sensory neurons is critical in PD-L1 analgesia. JCI Insight 2020, 5.
95. Wang Z, Jiang C, He Q, Matsuda M, Han Q, Wang K, *et al.* Anti-PD-1 treatment impairs opioid antinociception in rodents and nonhuman primates. Sci Transl Med 2020, 12.
96. Sheng HY, Zhang YQ. Emerging molecular targets for the management of cancer pain. Neurosci Bull 2020, 36: 1225–1228.
97. Acosta C, Djouhri L, Watkins R, Berry C, Bromage K, Lawson SN. TREK2 expressed selectively in IB4-binding C-fiber nociceptors hyperpolarizes their membrane potentials and limits spontaneous pain. J Neurosci 2014, 34: 1494–1509.
98. Wang K, Gu Y, Liao Y, Bang S, Donnelly CR, Chen O, *et al.* PD-1 blockade inhibits osteoclast formation and murine bone cancer pain. J Clin Invest 2020, 130: 3603–3620.
99. Yuan LL, Adams JP, Swank M, Sweatt JD, Johnston D. Protein kinase modulation of dendritic K^+ channels in hippocampus involves a mitogen-activated protein kinase pathway. J Neurosci 2002, 22: 4860–4868.
100. Thibult ML, Mamessier E, Gertner-Dardenne J, Pastor S, Just-Landi S, Xerri L, *et al.* PD-1 is a novel regulator of human B-cell activation. Int Immunol 2013, 25: 129–137.
101. Goodman A, Patel SP, Kurzrock R. PD-1-PD-L1 immune-checkpoint blockade in B-cell lymphomas. Nat Rev Clin Oncol 2017, 14: 203–220.
102. Wang X, Wang G, Wang Z, Liu B, Han N, Li J, *et al.* PD-1-expressing B cells suppress $CD4^+$ and $CD8^+$ T cells via PD-1/PD-L1-dependent pathway. Mol Immunol 2019, 109: 20–26.
103. Lim TS, Chew V, Sieow JL, Goh S, Yeong JP, Soon AL, *et al.* PD-1 expression on dendritic cells suppresses $CD8^+$ T cell function and antitumor immunity. Oncoimmunology 2016, 5: e1085146.
104. Yao S, Wang S, Zhu Y, Luo L, Zhu G, Flies S, *et al.* PD-1 on dendritic cells impedes innate immunity against bacterial infection. Blood 2009, 113: 5811–5818.
105. Qin W, Hu L, Zhang X, Jiang S, Li J, Zhang Z, *et al.* The diverse function of PD-1/PD-L pathway beyond cancer. Front Immunol 2019, 10: 2298.
106. Bally AP, Lu P, Tang Y, Austin JW, Scharer CD, Ahmed R, *et al.* NF-κB regulates PD-1 expression in macrophages. J Immunol 2015, 194: 4545–4554.
107. Huang X, Venet F, Wang YL, Lepape A, Yuan Z, Chen Y, *et al.* PD-1 expression by macrophages plays a pathologic role in altering microbial clearance and the innate inflammatory response to sepsis. Proc Natl Acad Sci U S A 2009, 106: 6303–6308.
108. Norris S, Coleman A, Kuri-Cervantes L, Bower M, Nelson M, Goodier MR. PD-1 expression on natural killer cells and $CD8^+$ T cells during chronic HIV-1 infection. Viral Immunol 2012, 25: 329–332.
109. Concha-Benavente F, Kansy B, Moskovitz J, Moy J, Chandran U, Ferris RL. PD-L1 mediates dysfunction in activated $PD\text{-}1^+$ NK cells in head and neck cancer patients. Cancer Immunol Res 2018, 6: 1548–1560.
110. Chen L, Sham CW, Chan AM, Francisco LM, Wu Y, Mareninov S, *et al.* Role of the immune modulator programmed cell death-1 during development and apoptosis of mouse retinal ganglion cells. Invest Ophthalmol Vis Sci 2009, 50: 4941–4948.
111. Wang W, Chan A, Qin Y, Kwong JMK, Caprioli J, Levinson R, *et al.* Programmed cell death-1 is expressed in large retinal ganglion cells and is upregulated after optic nerve crush. Exp Eye Res 2015, 140: 1–9.
112. Fourcade J, Sun ZJ, Benallaoua M, Guillaume P, Luescher IF, Sander C, *et al.* Upregulation of Tim-3 and PD-1 expression is associated with tumor antigen-specific $CD8^+$ T cell dysfunction in melanoma patients. J Exp Med 2010, 207: 2175–2186.
113. Badoual C, Hans S, Merillon N, Van Ryswick C, Ravel P, Benhamouda N, *et al.* PD-1-expressing tumor-infiltrating T cells are a favorable prognostic biomarker in HPV-associated head and neck cancer. Cancer Res 2013, 73: 128–138.
114. Mizuno R, Sugiura D, Shimizu K, Maruhashi T, Watada M, Okazaki IM, *et al.* PD-1 primarily targets TCR signal in the inhibition of functional T cell activation. Front Immunol 2019, 10: 630.
115. Schwartz M, Arad M, Ben-Yehuda H. Potential immunotherapy for Alzheimer disease and age-related dementia. Dialogues Clin Neurosci 2019, 21: 21–25.
116. Cloughesy TF, Mochizuki AY, Orpilla JR, Hugo W, Lee AH, Davidson TB, *et al.* Neoadjuvant anti-PD-1 immunotherapy promotes a survival benefit with intratumoral and systemic immune responses in recurrent glioblastoma. Nat Med 2019, 25: 477–486.
117. Caccese M, Indraccolo S, Zagonel V, Lombardi G. PD-1/PD-L1 immune-checkpoint inhibitors in glioblastoma: A concise review. Crit Rev Oncol Hematol 2019, 135: 128–134.
118. Litak J, Mazurek M, Grochowski C, Kamieniak P, Rolinski J. PD-L1/PD-1 axis in glioblastoma multiforme. Int J Mol Sci 2019, 20.
119. Hardcastle J, Mills L, Malo CS, Jin F, Kurokawa C, Geekiyanage H, *et al.* Immunovirotherapy with measles virus strains in combination with anti-PD-1 antibody blockade enhances antitumor activity in glioblastoma treatment. Neuro-Oncol 2017, 19: 493–502.
120. Hugo W, Zaretsky JM, Sun L, Song CY, Moreno BH, Hu-Lieskovan S, *et al.* Genomic and transcriptomic features of response to anti-PD-1 therapy in metastatic melanoma. Cell 2016, 165: 35–44.
121. Kleffel S, Posch C, Barthel SR, Mueller H, Schlapbach C, Guenova E, *et al.* Melanoma cell-intrinsic PD-1 receptor functions promote tumor growth. Cell 2015, 162: 1242–1256.
122. Gopalakrishnan V, Spencer CN, Nezi L, Reuben A, Andrews MC, Karpinets TV, *et al.* Gut microbiome modulates response to anti-PD-1 immunotherapy in melanoma patients. Science 2018, 359: 97–103.

123. Matson V, Fessler J, Bao R, Chongsuwat T, Zha YY, Alegre ML, *et al.* The commensal microbiome is associated with anti-PD-1 efficacy in metastatic melanoma patients. Science 2018, 359: 104–108.
124. Pittet CL, Newcombe J, Prat A, Arbour N. Human brain endothelial cells endeavor to immunoregulate CD8 T cells via PD-1 ligand expression in multiple sclerosis. J Neuroinflammation 2011, 8: 155.
125. Javan MR, Aslani S, Zamani MR, Rostamnejad J, Asadi M, Farhoodi M, *et al.* Downregulation of immunosuppressive molecules, PD-1 and PD-L1 but not PD-L2, in the patients with multiple sclerosis. Iran J Allergy Asthma Immunol 2016, 15: 296–302.
126. Shi S, Han Y, Wang D, Guo P, Wang J, Ren T, *et al.* PD-L1 and PD-1 expressed in trigeminal ganglia may inhibit pain in an acute migraine model. Cephalalgia 2020, 40: 288–298.
127. Hirth M, Gandla J, Kuner R. A checkpoint to pain. Nat Neurosci 2017, 20: 897–899.
128. Zhang J, Zhang H, Luo Y. Association between activation of the programmed cell death-1 (PD-1)/programmed death-ligand 1 (PD-L1) pathway and pain in patients with cancer. Med Sci Monit 2019, 25: 1275–1282.

Neurosci. Bull. August, 2021, 37(8):1203–1217
https://doi.org/10.1007/s12264-021-00716-6

www.neurosci.cn
www.springer.com/12264

REVIEW

Illuminating Neural Circuits in Alzheimer's Disease

Yang Ying[1] · Jian-Zhi Wang[1]

Received: 30 November 2020 / Accepted: 6 March 2021 / Published online: 5 June 2021

Abstract Alzheimer's disease (AD) is the most common neurodegenerative disorder and there is currently no cure. Neural circuit dysfunction is the fundamental mechanism underlying the learning and memory deficits in patients with AD. Therefore, it is important to understand the structural features and mechanisms underlying the deregulated circuits during AD progression, by which new tools for intervention can be developed. Here, we briefly summarize the most recently established cutting-edge experimental approaches and key techniques that enable neural circuit tracing and manipulation of their activity. We also discuss the advantages and limitations of these approaches. Finally, we review the applications of these techniques in the discovery of circuit mechanisms underlying β-amyloid and tau pathologies during AD progression, and as well as the strategies for targeted AD treatments.

Keywords Neural circuit · Alzheimer's disease · Single cell RNA sequencing · Neural circuit tracing · Optogenetics · Chemogenetics

✉ Yang Ying
yingyang@hust.edu.cn

✉ Jian-Zhi Wang
wangjz@mail.hust.edu.cn

[1] Department of Pathophysiology, School of Basic Medicine, Ministry of Education Key Laboratory for Neurological Disorders, Hubei Key Laboratory for Neurological Disorders, Tongji Medical College, Huazhong University of Science and Technology, Wuhan 430030, China

Introduction

Alzheimer's disease (AD) is the most common neurodegenerative disorder in the elderly. The characteristic clinical symptom is progressive memory loss [1]. Several key neuropathological hallmarks of AD have been revealed, including extracellular neuritic plaques composed of β-amyloid (Aβ) and intracellular neurofibrillary tangles (NFTs) composed of hyperphosphorylated tau protein [2]. Both Aβ plaques and NFTs impair synaptic function and neural circuit networks. Using functional MRI, electrophysiological techniques, and biochemical data, researchers have found aberrant neural activities in patients with AD and mouse models [3, 4]. These abnormal activities trigger a disorganized brain network and interfere with the intricate processes underlying learning, memory, and other cognitive functions. Pharmacological therapies targeting either Aβ or tau have shown limited efficacy in the treatment of AD. This has motivated novel approaches designed not only to specifically rescue the cognitive impairments in AD but also avoid drug-induced side-effects or pharmacoresistant symptoms.

Different types of brain cells orchestrate to modulate cognitive function. Heterogeneous brain cells show distinct alterations during AD development. Given the advantages of neuron type-specificity and manipulation accuracy, single-cell RNA sequencing, optogenetics, and chemogenetics are increasingly used in the study of AD to investigate molecular and circuit mechanisms. Novel findings from AD studies that use these cutting-edge techniques may help us better understand the AD memory dysfunction induced by Aβ and tau proteins. They may also provide novel therapeutic strategies for AD treatment in the future. In this review, we briefly describe the most

advanced tools currently available for neural circuit research relating to AD.

Single-Cell RNA Sequencing

There are billions of highly differentiated and interconnected cells within the brain. Distinct neurons communicate with each other and form intricate neural networks to control physical and mental functions. Traditional research at the bulk-tissue level of resolution may mask the complexity of changes across brain cells and within cell groups [5]. For example, using bulk RNA-sequencing, it may be difficult to differentiate whether low-abundance transcripts are expressed at low levels in common cell types or at high levels in rare cell types. Moreover, in diseases, the low abundance transcriptional changes in a rare cell type may be undetectable when a bulk RNA-sequencing approach is employed. As such, the newly developed single-cell RNA sequencing (scRNA-seq) techniques have the potential to overcome these limitations. In addition to providing a comprehensive landscape of brain cell-type diversity based on transcriptional profiles, the scRNA-seq method may be useful in mapping the mammalian connectome and exploring the mechanisms of brain-related disorders, such as AD, at the single-cell level.

Individual cells can be physically separated. The isolation methods vary in the number of isolated cells (high-throughput or low-throughput) and the means of cell selection (biased or unbiased) [6]. By whole-cell patch clamping, cellular content from a sucked single cell can be used to acquire RNA for quantitative RT-PCR or microarray analysis [7, 8]. Moreover, this method provides additional information, such as location, electrophysiological properties, and morphology of the examined cell. However, it is not quantitative enough, nor does it provide an unbiased assessment of global gene expression patterns. Moving from pipetting and manual selection, several automated single-cell compartmentalization methods have been developed, such as fluorescence-activated cell sorting and the fluidigm C1 system. Although they have been combined with scRNA-seq techniques, including SMART-seq and CEL-seq, to explore the brain at the single-cell level [9–11], there are two limitations: (1) the total number of captured cells is not quantitative enough for the high-throughput format; and (2) they do not maintain the native heterogeneity of brain constituents [12, 13]. Currently, droplet-based technologies to randomly capture single cells with barcoded beads are commonly used as a high-throughput and unbiased solution [14]. The three most widely used platforms are Droplet sequencing (Drop-seq) [15], indexing droplets RNA sequencing (inDrop) [16], and GemCode/Chromium 10× (widely known as 10× Genomics) [17, 18]. They use microfluidics to tag individual cells with single beads containing a unique barcode. Each mRNA transcript is also linked with a unique molecular identifier (UMI). By comparison, 10× Genomics is the most sensitive for detecting the greatest number of transcripts, while inDrop is ideal for detecting weakly-expressed genes (DEGs) [17].

scRNA-seq techniques require freshly-harvested, viable, and intact cells. Moreover, most of the single-cell isolation methods may impair neurons and cause some cell types to be under- or over-represented in the final datasets. Since nuclei are more resistant to mechanical and physical stress, single nuclei RNA sequencing (snRNA-seq) is an alternative approach to scRNA-seq and has been used in the study of the cellular composition in the brain [19–22]. Compared with whole-cell transcriptomes, there is no difference in snRNA-seq data in terms of the number of detected genes and resolved cell types [23].

Full-length and tag-based approaches are used to generate single-cell sequencing libraries [24]. Since reads are derived from across the entire length of genes, full-length methods greatly improve the overall sensitivity. It is worth noting that full-length library preparation shows a bias for longer genes rather than shorter genes because counts are often missed for the latter [25]. In tag-based methods, the incorporated UMIs allow the identification and quantification of individual transcripts.

A generalized single-cell transcriptomic experiment includes single cell isolation, barcoding, cDNA amplification, library construction, sequencing, and analysis. For each experiment, the technical performance of the scRNA-seq data should be evaluated from the sensitivity, accuracy and precision aspects [24, 26, 27]. Sensitivity measurement is highly dependent on the depth of sequencing [24, 26]. Accuracy can be influenced by factors specific to the protocol being used [24, 26]. Precision is inversely proportional to the technical noise in the RNA-seq measurements [24, 26].

A major disadvantage of the scRNA-seq method is the lack of spatial information [28–30]. By fluorescence *in situ* hybridization (FISH), the spatial locations of genes identified in scRNA-seq can be clearly visualized. For example, in single-molecule FISH (smFISH), multiple fluorescent probes are used to characterize distinct cell groups [31]. However, the number of colors that can be visualized at once is very limited in this technique. In contrast, sequential FISH (seqFISH) can sequentially label tissue for different RNA markers [32, 33]. After each round of labeling, fluorescence is washed out and cell populations are binarily labeled for the presence or absence of a particular gene. As such, seqFISH is more efficient and robust in cell population identification than smFISH.

Cutting-Edge Experimental Approaches for Visualizing Neural Circuits

To understand the complex brain functions carried out by neural circuits, it is necessary to dissect their structural organization. To date, several viral tracers have become available to delineate the structural connectivity between distinct neurons or different brain regions

Anterograde Trans-Synaptic Tracing

Herpes simplex virus (HSV) and vesicular stomatitis virus (VSV) have been commonly used in anterograde trans-synaptic tracing. Both viruses invade and replicate in first-order infected starter neurons and then spread into synaptically connected neurons.

HSV

The HSV type 1 strain H129 has been widely used in anterograde multi-synaptic tracing [34–36]. Tyrosine kinase (TK) is required for HSV replication and is necessary for its anterograde spread in non-mitotic cells. Recently, HSV has been genetically modified to achieve monosynaptic tracing. In this system, TK is deleted and then trans-complementation of TK restores the ability of H129-ΔTK to replicate and spread into directly projected targets. If the expression cassette of the *TK* gene is in a Cre-recombinase-dependent strategy, the starter cell type can be greatly restricted.

H129 mainly transmits anterogradely, but it can also infect upstream neurons through axon terminal uptake [37]. More importantly, the main drawback of the H129 strain is its high toxicity. It can also cause cell death and animal death. With current trans-multisynaptic H129 tracer systems, experimental animals die within 3 to 5 days after injection of H129 [38], which greatly restricts the sampling time to within 3 days. Although toxicity can be reduced by engineering viral genomes, such as TK-null H129 [39], this problem has not been resolved completely. *TK*-deficient recombinant viruses show milder cytotoxicity without damage to their infectivity and viral gene expression. However, trans-monosynaptic H129 tracer systems remain insufficient for electrophysiological recordings from brain slices. Thus, to support functional studies, more efforts are needed to reduce the cytotoxicity of trans-synaptic HSV in the future.

VSV

VSV is an arthropod-borne virus. It leads to vesiculation and ulceration around the mouth, teats, and hoofs after infection. These symptoms usually resolve within a few weeks without fatality [40]. Compared to HSV, VSV is less virulent to humans [41].

The glycoprotein (VSV-G) is necessary for VSV binding to target cells [42]. When VSV-G binds to phosphatidylserine on the cell surface membrane [41], VSV can enter cells and start to replicate rapidly. The first progeny of viruses are generated and released within 1.5 h [43]. It has been found that the direction of VSV transmission greatly depends on the glycoprotein. The intrinsic glycoprotein endows its characteristic of anterograde transmission [44]. However, G protein from either lymphocytic choriomeningitis virus or Rabies virus can change the transmission from anterograde to retrograde [44]. Toxicity and inefficiency are the main shortcomings of VSVs. Thus, the modification of virulence and efficiency of spread will enable the wider applications of VSV in circuit structure dissection and functional studies.

A recent study showed that adenovirus associated virus 1 (AAV1) and AAV9 can be used as monosynaptic anterograde tracers [45]. They exhibit anterograde trans-synaptic spread properties with relatively low efficiency. Therefore, the viral spread is restricted to direct postsynaptic targets of the infected cells, and the labelling of postsynaptic cells relies on reporter expression activated by a recombinase-expressing virus. Such a strategy can be used to perform afferent-dependent tagging of postsynaptic neurons and support functional manipulations with Cre-dependent tool genes. However, care should be taken when using it to map connections between reciprocally connected regions because retrograde trans-synaptic spread can also occur, especially at high titers [46].

Retrograde Trans-Synaptic Tracing

Rabies Virus (RV) is a neurotropic virus. It retrogradely transmits from the infected peripheral site to the central nervous system, leading to lethal zoonotic disease. Unlike HSV, the RV spreads exclusively in the retrograde direction. High neuronal specificity without causing glial cell infection makes RV an ideal tool for neural circuit tracing.

RV envelope protein G is necessary for neuronal infection and trans-synaptic transmission of the RV. SAD-B19, an attenuated vaccine strain of RV, was developed for the monosynaptic trans-synaptic system [47, 48]. In this system, the *RVG* gene is replaced by EGFP and pseudotyped with envelope glycoprotein (EnvA) from avian sarcoma-leukosis virus (ASLV-A). TVA is the cognate receptor of EnvA and does not exist in mammals. Thus, the recombinant RV [SADDG-EGFP(EnvA)] cannot infect mammalian neurons unless they are exogenously supplied with TVA. RV-DG(EnvA), a mutant rabies virus

with glycoprotein G gene deletion and a helper virus (AAV) that expresses TVA and RVG in a Cre-dependent manner are both injected into the desired region, where RV can only invade cells with Cre expression and then retrogradely spread to their direct upstream neurons, but cannot spread any further. Therefore, in such cases, only monosynaptic connections to starter cells are marked [49].

Recently, Schwarz *et al*. developed a method termed TRIO (for tracing the relationship between input and output) and cell-type-specific TRIO (cTRIO) [50]. In this system, canine adenovirus type 2 (CAV2) is used to provide the recombinase (Cre or Flp). Although CAV2 is not a trans-synaptic tracer, it can transduce neurons through their axonal terminals and efficiently transport back to the soma. In the TRIO system, after the injection of CAV-Cre into one of the output regions, Cre is specifically expressed in neurons that project to the CAV2-injected region. Then, by injecting RVDG(EnvA) and Cre-dependent AAV helper virus that expresses TVA and RVG into the targeted area, RV can only infect neurons in the targeted area which directly project to the CAV2-injected regions. It then transports to monosynaptic upstream neurons. In contrast to TRIO, cTRIO has the advantage of being neuron type-specific. CAV2 is used to express Flp and AAV is used to express TVA. RVG is only in neurons with both Cre and Flp. With the help of these two viruses, RV can infect Cre-expressing neurons in the targeted area that innervate neurons within the CAV-injected region (Fig. 1). Thus, cTRIO enables monosynaptic tracing from a specific type of cell projecting to a specific brain area.

Cytotoxicity is the main limitation of the above RV tracing system (first generation). Chatterjee *et al*. recently introduced a new class of double-deletion-mutant rabies viral vectors, which show low toxicity in transduced cells [51]. They deleted a second gene known as 'large protein' gene (NCBI symbol: RABVgp5). This gene encodes the viral polymerase, which is required for the transcription of viral genes and replication of the viral genome [52]. Compared to first-generation viruses, these new ('second-generation' or 'Δ GL') viral vectors can also retrogradely infect projection neurons. The target neurons remain alive and healthy in terms of both electrophysiology and morphology up to a year after the virus injection. Thus, this system is promising for long-term tracing, functional detection, and optogenetic manipulation.

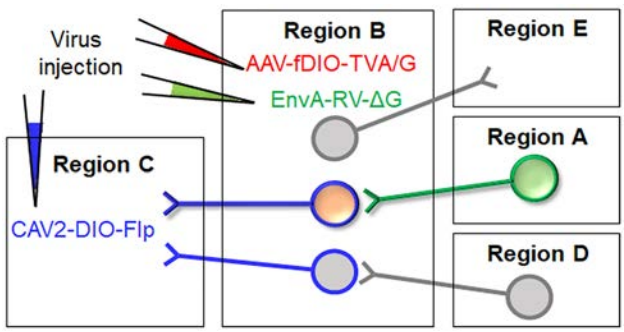

Fig. 1 Schematic of cTRIO for neural circuit tracing. In X-Cre mice, CAV2-DIO-Flp is injected into region C, while AAV-fDIO-TVA/G and EnvA-RV-ΔG are injected into region B. Only the presynaptic inputs to neurons that are located in region B, project to region C, and express geneX (orange cell in region B) will be retrogradely labelled by RV (green cell in region A) (A → B^{X+} → C). However, presynaptic inputs to region B neurons that innervate region C but do not express gene X (grey cell in region D) (D → B^{X-} → C), or region B cells that do not project to region C (B → E) will not be labeled.

Cutting-Edge Experimental Approaches for Manipulating Neural Circuits

Optogenetics

Optogenetics could be an invaluable tool in neuroscience research. It encompasses the knowledge of optics, microbial biology, virology, and biochemistry [53, 54]. About 50 years ago, light-activated proteins were first discovered. Bacteriorhodopsin was discovered in 1971 [54], halorhodopsin in 1977 [55], and channelrhodopsin in 2002 [56]. Upon light exposure, these opsins act as channels or pumps to directly induce electrochemical signaling in cells. This feature is distinct from rhodopsin, which indirectly transduces electrical current *via* G-proteins. In 2005, a microbial opsin gene was first introduced into neurons and it precisely controlled neuronal spiking upon light exposure [57]. In 2007, the fiber-optic interface and single-component control of freely-moving mammals were described [58, 59]. A series of Cre recombinase-dependent opsin-expressing viruses have been developed and widely used in mouse lines that selectively express Cre recombinase in defined cell types. Thus, researchers can use these latest optogenetic controls to investigate the functions of defined cells in specific brain regions under physiological conditions and their alterations in diseases.

Channelrhodopsins, derived from *Chlamydomonas reinhardtii*, are one kind of light-driven proteins. Channelrhodopsin 2 (ChR2) is composed of seven transmembrane helices, and a retinal component is embedded within the helices [60]. Upon illumination, the retinal component absorbs light and quickly causes a conformational change, which opens the pore and allows the movement of cations down their electrochemical gradient on ChR2-expressing neurons. These inward currents drive fast membrane depolarization and robustly excite neurons [61, 62] (Fig. 2A). H134R, a gain-of-function mutant of ChR2, causes larger stationary photocurrents than wild-type ChR2 [63]. However, the recovery from inactivation of both

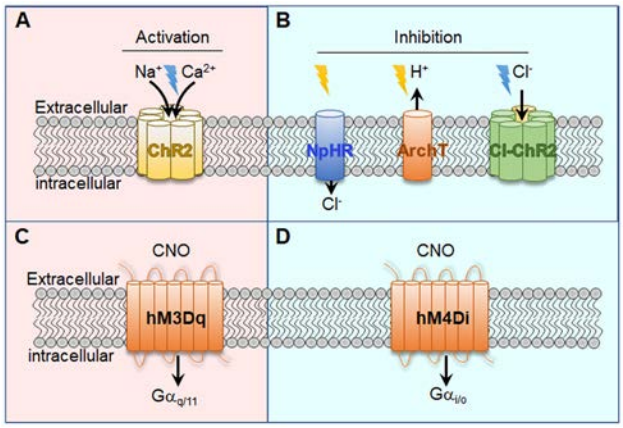

Fig. 2 Schematics of neural manipulation by optogenetics and chemogenetics. **A**, **B** Upon light stimulation, Na^+ and Ca^{2+} move down their electrochemical gradients on the ChR2-expressing neurons and depolarize the membrane, resulting in neuron excitation. While hyperpolarizing current on NpHR-, Arch- or mutated ChR2-expressing neurons leads to neuron inhibition. **C**, **D** In the presence of CNO, hM3Dq-expressing neurons are activated, while hM4Di-expressing neurons are inhibited *via* changing the concentration of second messengers.

wild-type ChR2 and H134R is slow, which limits the precision in the optogenetic control of neurons, especially at stimulating frequencies above the γ range [57, 64]. Gunaydin *et al*. designed point mutations in the ChR2 sequence and developed ChETA, which accelerates channel closing and rapid repolarization of neurons following light stimulation [65]. Recently, many variants have been developed, such as red-shifted (VChR1 [66], ReaChR [67]) and blue-shifted (CheRiff) variants [68].

In addition to depolarizing cells, some microbial opsins can hyperpolarize cells upon illumination. NpHR isolated from *Natronomonas pharaonis* is sensitive to yellow-green light. Light activation of NpHR produces an inward Cl^- (hyperpolarizing current), which inhibits the action potential firing of NpHR-expressing neurons (Fig. 2B). Arch is a light-activated proton pump bacteriorhodopsin [69]. By pumping H^+ out, Arch also hyperpolarizes cells when exposed to light (Fig. 2B). Furthermore, ChR2 can also be used to inhibit neurons upon light stimulation when its permeability is changed to Cl^- instead of cations after mutation in its pore structure [70] (Fig. 2B).

Chemogenetics

Recently, chemogenetics has been widely employed in neuroscience research to regulate the activities of specific neurons or neural circuits. Chemogenetics refers to the use of genetically-engineered receptors that interact with specific synthetic ligands or molecules to alter cellular signal transduction [71]. Since the receptors (e.g. G protein-coupled receptors and ligand-gated ion channels) are modified through random or site-directed mutagenesis, they are no longer responsive to their natural ligands, but can be specifically activated by synthetic chemicals [71].

Designer receptors exclusively activated by designer drugs (DREADDs) [72] are engineered G protein-coupled receptors (GPCRs) that can precisely control GPCR signaling pathways (for example, Gq, Gs, and Gi). Currently, hM3Dq and hM4Di are the most commonly-used DREADDs [73, 74]. Due to their mutations, both hM3Dq and hM4Di can only be activated in the presence of clozapine N-oxide (CNO), a compound modified from clozapine (Fig. 2C, D). CNO only activates these "designer receptors" without changing the functions of endogenous receptors. However, this specificity can be changed at a high dose of CNO. It has been reported that intracranial injections of CNO at micromolar concentrations (10 μmol/L) competitively inhibit binding at several receptors, including muscarinic M1, M3, M4, histamine H1, 5-HT2A, and dopamine D1 and D2 [75]. Thus, these off-target effects at endogenous receptors may significantly confound the agonistic effects of CNO.

Compared to optogenetics, chemogenetics has an incomparable advantage in that the stimulus can be administered *via* less- or non-invasive routes, such as intraperitoneal injection and oral administration [73, 76, 77]. Although chemogenetics cannot achieve precise temporal control, they can provide prolonged manipulation of neurons and their circuit activities [77].

Neural Circuit Defect in AD Brains and Strategies for Targeted Manipulations

The hippocampus is vulnerable in patients with AD [78–80], and its dysfunction is closely associated with cognitive impairment during AD progression [80, 81]. Next, we focus on the hippocampus and briefly introduce some recent studies on hippocampus-associated neural circuits in AD.

Application of Single Cell Transcriptomics in AD

In addition to cell-type classification under physiological conditions, snRNA-seq has recently been used in AD to understand the vulnerability of different cell types [19, 82]. 80,660 droplet-based single-nucleus transcriptomes from prefrontal cortex in human subjects with varying degrees of AD pathology were profiled and analyzed [19]. Differentially-expressed genes between AD-pathology and no-pathology groups were downregulated in excitatory (Ex) and inhibitory (In) neurons, while they were upregulated in oligodendrocytes (Olis), astrocytes (Asts), and microglia (Mic), indicating a heterogeneous response to AD

pathologies among cell types [19]. In cellular subpopulations, many subclusters of Ex and In neurons, Asts, Mic, Olis, and oligodendrocyte progenitor cells (Opcs), have been identified. Among them, some cellular subpopulations were associated with cells isolated from subjects with AD pathology traits, while some were associated with cells from subjects with no pathology [19]. Furthermore, genes associated with protein folding and stability, neuronal and necrotic death, T-cell activation, and immunity were identified in some subpopulations of AD pathology-associated In neurons, Opcs, and Mic, indicating cell-type-specific responses in AD [19]. Moreover, male and female individuals showed differential transcriptional responses to AD pathology, especially in neurons and oligodendrocyte cells [19]. Thus, this single-cell view of transcriptional alterations associated with AD pathologies highlights the complexity of AD mechanisms from the perspective of cellular heterogeneity. Also, an understanding of neuronal vulnerability may expedite the study of circuit mechanisms in AD and provide molecular targets for circuit-specific interventions.

Glutamatergic Circuits

Dysfunction of Glutamatergic Neurons in the Hippocampus During AD

In AD, Aβ can induce neuronal hyperactivation and hypoactivation. Aβ-dependent neuronal hyperactivation may contribute to preclinical hippocampal hyperexcitability [83–85]. Mechanistically, Aβ inhibits the glutamate uptake capacity of astrocytes to produce excess glutamate accumulation, leading to the neurotoxic effects in AD [86, 87]. On the other hand, oligomeric Aβ acts on α-amino-3-hydroxy-5-methyl-4-isoxazolepropionic acid receptors (AMPARs) [88] and extrasynaptic N-methyl-D-aspartate receptors (NMDARs) to elicit excitotoxic effects [89, 90]. In turn, neuronal hyperactivity promotes the activity-dependent production of Aβ, eventually forming a positive feedback and leading to synapse loss, arbor shrinkage, and hypoexcitability in the late stages of AD [91–93]. In postmortem AD brains, Aβ is co-localized in glutamatergic boutons. Aβ accumulation causes loss of dendritic spines and severe neuropil damage [94–97]. Functionally, excess Aβ gains toxicity by inhibiting synaptic transmission [94, 98, 99], and impairing synaptic plasticity [94, 96, 100–103].

Tau pathology is another causal factor leading to the impairment of glutamatergic synapses. In our previous study, we found that overexpression of wild-type human tau (htau) in hippocampal CA3 decreases spontaneous excitatory postsynaptic currents with unchanged spontaneous inhibitory postsynaptic currents. These results indicate that glutamatergic synapses in hippocampal CA3 are more vulnerable to tau pathology [104]. Mechanistically, calcineurin-mediated inactivation of nuclear CaMKIV/CREB signaling is responsible for the glutamatergic impairments and memory deficits induced by htau accumulation[104]. When tau accumulates in the hippocampus, it inhibits NMDAR expression by upregulating STAT1, a transcription factor [105]. It also inhibits CREB/GluN1 phosphorylation by suppressing PKA [106]. In addition to accumulation, tau is mis-localized from the axon to the dendrites during AD progression. Then, the mis-localized tau interacts with fyn and triggers fyn to move to the dendritic spines to phosphorylate the GluN2B subunit of NMDAR, thereby enhancing excitotoxicity [107]. In AD, tau undergoes aberrant post-translational modifications, such as hyperphosphorylation, sumoylation, acetylation, glycosylation, andproteolytic cleavages, which promote tau accumulation and hippocampal propagation, causing memory deficits [108–111]. In cultured hippocampal neurons, expression of mutated tau, which mimics the phosphorylation of 14 residues, significantly reduces the number of AMPARs at synapses [112]. When expressing htau with mutations to mimic the acetylation of K274 and K281, mice have deficits in spatial and pattern separation memory with impairment in AMPAR trafficking during LTP [113]. Blocking the caspase-2 cleavage of human P301L tau by mutating the Asp314 residue on tau restores AMPAR-mediated synaptic transmission in neurons and memory deficits in mice [114]. Although P301L tau has been found to reduce the excitability of hippocampal CA1 neurons by shifting the axon initial segment (AIS) [115], Sohn *et al*. found that the V337M tau mutation in human neurons leads to hyperexcitability of neuronal networks by impacting the AIS cytoskeleton [116].

Recently, an *in vivo* neural dynamic recording system has been developed to detect cell-specific neuronal activity while monitoring the behaviors of freely-moving subjects. For example, calcium-based fiber photometry is one such system that measures calcium fluorescence signals and directly reflects neuronal spiking activity *in vivo*. In APP/PS1 mice, a genetically encoded calcium indicator, GCaMP6 [117], was expressed in basolateral amygdala (BLA) neurons. During the elevated plus maze test, disorganized firing patterns of BLA neurons were clearly detectable in response to BLA Aβ pathology and correlated with the anxious state of APP/PS1 mice [34]. Thus, in addition to hyperactivation and hypoactivation, AD pathologies produce abnormal neuronal firing patterns, which may result in dysfunction of information encoding and contribute to AD phenotypes.

It is worth noting that the fiber photometry system can only record population calcium. A fluorescence microscope (miniscope) system has recently been applied in

neuroscience research to visualize neural activity from deep brain regions in freely-behaving animals [118]. The advantage of this calcium imaging is that the recording of neural activity from a specific population of neurons can occur longitudinally at the single-cell level of resolution. It is expected that the combination of a fluorescence microscope system and behavioral tests will provide more detailed information on neuronal dysfunction and cognitive impairment in AD.

Targeting Glutamatergic Neurons to Rescue AD-Like Memory Disorder

Whether and how targeting abnormal glutamatergic neurons could restore memory deficits remain unclear. Previous studies have suggested that episodic memory deficits in patients with AD may be due to information encoding failure [119]. However, Roy *et al*. employed optogenetics combined with behavioral testing and found significant disruption of memory retrieval in the early stages of AD [120]. They used immediate-early gene-dependent tools [121] to label memory engram cells (i.e., neurons holding traces of a specific memory) in APP/PS1 mice (an AD mouse model) and reported a close correlation between the progressive reduction in spine density of the hippocampal dentate gyrus (DG) engram cells and age-dependent amnesia [120]. Direct photoactivation of hippocampal DG memory engram cells with ChR2 was sufficient to induce memory recall in AD mice, indicating a deficit of memory retrieval during early AD-related memory loss [120]. Further, optogenetic induction of LTP at perforant path synapses of hippocampal DG engram cells significantly restored both spine density and memory in AD mice [120]. This study highlights the contribution of memory retrieval failure during early AD-related memory loss. Moreover, it identifies a causal role of entorhinal cortex-DG glutamatergic circuit dysfunction in memory retrieval disruption in AD.

Glutamatergic neurons in the hippocampus also receive innervation from the amygdala and their connections undergo robust degeneration during AD. Under physiological conditions, researchers combined retrograde (RV [122]) and anterograde (HSV [34]) tracing systems to delineate a novel connection between the posterior BLA (pBLA) and ventral hippocampal CA1 (vCA1), that is, the pBLA-vCA1 circuit. Using optogenetics and electrophysiological recordings, they demonstrated that vCA1 Calbindin 1 ($vCA1^{Calb1}$) neurons are downstream of pBLA glutamatergic neurons [34]. However, in AD mice, the pBLA-$vCA1^{Calb1}$ circuit is significantly inhibited in response to Aβ accumulation and results in AD-like anxiety. Photostimulation of the pBLA-$vCA1^{Calb1}$ circuit efficiently attenuates AD-like anxiety. Simultaneously, targeting the pBLA-$vCA1^{Calb1}$ circuit by optogenetics during memory retrieval significantly restores memory disorders in AD mice [34]. This novel circuit links emotions to memory. It may also provide a promising intervention target for AD patients with anxiety and cognitive impairment.

Previous work has revealed that elevated neuronal activity accelerates the progression of pathological Aβ and tau [123] and in turn continuously destroys circuit functions, forming a vicious cycle. In EC-Tau/hAPP mice, hM4Di was virally delivered and expressed in the EC, then, CNO was intraperitoneally injected. Using these chemogenetic tools, neuronal activity in the entorhinal cortex was significantly attenuated, and its beneficial effects on reducing Aβ accumulation and tau spreading into the hippocampus along the cortex-hippocampal (EC-HP) circuit were detected [77]. Thus, inhibition of hyperactivated circuits in response to Aβ and tau may be a novel strategy to prevent the progression of AD along the neural networks and break the vicious cycle between AD pathologies and memory-associated circuit dysfunction.

GABAergic Circuits

Dysfunction of GABAergic Neurons in the Hippocampus During AD

The GABA is the main inhibitory neurotransmitter in the brain. Early studies in postmortem human brains and animal models revealed that GABAergic neurons are less vulnerable than glutamatergic neurons to AD pathology. However, this idea has been challenged. There is accumulating evidence that GABAergic neurotransmission undergoes enormous changes in AD, causing excitatory/inhibitory (E/I) imbalance during AD progression.

In brain sections from patients with AD and APP/PS1 mice, perisomatic GABAergic terminals are significantly decreased, especially on the cortical neurons adjacent to amyloid plaques, suggesting an association between GABAergic neuronal impairments and Aβ [124, 125]. In addition to loss, GABAergic presynaptic terminals are elevated at an early stage in tgCRND8 and APP/PS1 mice [126, 127], indicating complicated alterations of GABAergic function in response to Aβ pathologies. During AD progression, GABAergic neuronal subpopulations are also lost. Both somatostatin -expressing neurons (conferring distal dendritic inhibition of pyramidal cells) and parvalbumin (PV)-expressing neurons (providing perisomatic inhibition of pyramidal cells) are notably decreased in the brains of patients with AD and transgenic mice with Aβ pathologies [128–130].

There is a reciprocity between tau hyperphosphorylation and GABAergic synaptic dysfunction. On one hand,

GABAergic signaling regulates tau hyperphosphorylation. Several $GABA_A$ receptor modulators have been found to increase the interaction between tau and Peptidyl-prolyl cis-trans isomerase 1 (Pin 1), by which more protein phosphatase 2A (PP2A) is recruited to the cell surface to dephosphorylate $GABA_A$ receptor β3 subunit and simultaneously reduces the availability of PP2A for tau dephosphorylation [131]. In line with this mechanism, the activation of $GABA_A$ receptors robustly induces tau hyperphosphorylation at the AT8 epitope in cultured cortical neurons [131]. On the other hand, tau pathologies modify GABA release. In P301L mice, GABAergic interneurons are hyperactivated, resulting in higher GABA levels in the brain [132]. Thus, there may be a vicious cycle by which activation of $GABA_A$ receptors promote tau hyperphosphorylation by reducing the association of PP2A with tau, then, the hyperphosphorylated tau enhances GABAergic neurotransmission in turn during AD progression.

Dysfunction of GABAergic transmission produces E/I imbalance in local circuits. In 14-month-old APdE9 mice, hyperexcitability was detected in the hippocampal DG and this was associated with the silencing of local inhibitory neurons [133]. Recently, we reported a prominent accumulation of hyperphosphorylated tau in a DG subset in AD patients and mice, including mature excitatory neurons, immature granular neurons, and GABAergic interneurons. However, only interneuron-specific overexpression of full-length wild-type htau to mimic AD-like tau accumulation in the mouse DG induced adult hippocampal neurogenesis deficits and increased neural stem cell-derived astrogliosis. Using calcium-based fiber photometry, hyperactivated neighboring excitatory neurons were detected *in vivo* after interneuron-specific overexpression of htau. Chemogenetic inhibition of excitatory neurons or pharmacologically strengthening GABAergic efficiently rescue the human tau-induced deficits in adult hippocampal neurogenesis with improved contextual cognition [134]. This work demonstrated a causal role of tau accumulation in GABAergic impairments and linked local circuit disinhibition with disruption of hippocampal neurogenesis in AD.

In addition to local microcircuits, GABAergic neurons in CA1 are also innervated by pyramidal neurons in the entorhinal cortex layer II (ECIIPN) [135]. Using a retrograde monosynaptic tracing system, researchers have identified direct connections between ECIIPN and parvalbumin-positive CA1 (CA1PV, one type of GABAergic neuron) under physiological conditions. Their functional connection (ECIIPN → CA1PV) was significantly decreased according to optogenetic and electrophysiological examinations. Further, *in vivo* electrophysiological recording revealed a disruption of E/I balance and dispersed place-associated firings in CA1 during ECIIPN → CA1PV degeneration in AD mice. No change in ECIIPN → CA1PN (pyramidal neurons in CA1) was observed. These data highlight the vulnerability of the ECIIPN → CA1PV circuit and its role in encoding the impairment of place information in AD.

In addition, there are some long-range inhibitory circuits from other brain regions, such as the amygdala [136] and medial septum [137], to the hippocampus. However, the details of these connections, such as the neuron type, the innervation pattern, and their transcriptome characteristics, remain elusive. More importantly, whether and how their structure and function change during AD progression also deserve further investigation.

Targeting GABAergic Neurons to Rescue AD-Like Memory Disorders

Dysfunctions in GABAergic transmission can lead to theta and gamma oscillation impairments which are important for synaptic plasticity and spatial memory. Theta oscillations (6–10 Hz) have been linked to exploratory behavior-related activities, reflecting internally-generated dynamics [138] and goal-related behaviors [139]. In rTg4510 mice (a model of tauopathy), theta and place cell (i.e. cells firing at a specific location in an environment) sequences are both significantly impaired. Principal cell firing is independent of the environmental context,, indicating the inability of mice to form new spatial memories. A reduced firing rate of the recorded interneurons may contribute to this rigid firing sequence [140]. GABAergic cell loss can decrease theta power, which is associated with cognitive dysfunction in a rat amyloid model [141]. Impaired gamma oscillation integrity has also been reported in the AD model [142, 143] and patients [144], contributing to the inefficient execution of spatial working memory [145].

However, there are distinct subtypes of interneurons in the hippocampus. Whether and how targeting different hippocampal interneurons rescues the abnormal oscillations in AD and restores memory loss remains unclear. Somatostatin-positive (SST) interneurons preferentially modulate theta oscillations [146], while parvalbumin-positive (PV) interneurons modulate gamma oscillations [147, 148]. A reduction in behaviorally-driven gamma oscillations is detectable before the onset of plaque formation or cognitive decline in a mouse model of AD. Using a Cre-dependent strategy, optoactivation of PV interneurons at gamma (40 Hz) but not at other frequencies significantly reduces Aβ levels [147]. In the J20 AD mouse model, optostimulation of PV neurons in the medial septum specifically at 40 Hz during memory retrieval restores the hippocampal slow gamma oscillation (30-60 Hz) [149]. In Aβ-injected SST-Cre or PV-Cre mice, optogenetic activation of ChR2-expressing SST and PV interneurons

increases theta power and gamma oscillations, respectively, with resynchronized CA1 pyramidal cell (PC) spikes. Photoactivation of SST and PV interneurons resynchronizes SST and PV interneuron spike phases relative to theta and gamma oscillations [150], while simultaneously selectively enhancing spontaneous inhibitory postsynaptic currents onto CA1 PCs at theta and gamma frequencies, respectively [150]. Given the degeneration of the ECIIPN–CA1PV pathway in AD, optogenetic activation of ECIIPN–CA1PV synapses with a theta burst stimulation paradigm once per day for 35 consecutive days effectively enhanced theta oscillations in the hippocampal CA1 of AD mice and interrupted the progression of ECIIPN–CA1PV synaptic decays [135]. Targeting the ECIIPN–CA1PV pathway also improved the representation and precise spatial firing of CA1 place cells in AD mice, simultaneously rescuing their spatial memory deficits [135]. Together, targeting distinct interneurons may be a potential therapeutic strategy for restoring disorganized hippocampal networks and synaptic plasticity impairments in AD.

Others

The hippocampus also receives cholinergic innervation [151]. Choline acetyltransferase (ChAT) is responsible for acetylcholine synthesis and is viewed as a reliable marker of cholinergic integrity [151]. In AD brains, cortical ChAT activity is significantly decreased, and this is closely correlated with the severity of dementia [152]. In the AD hippocampus, ChAT immunopositivity is also robustly decreased [153]. Thus, degeneration of cholinergic neurons in the basal forebrain may lead to a reduction in cholinergic input to the AD hippocampus. α-Secretase-cleaved APP has been found to accumulate in cholinergic dystrophic neurites during AD progression [154]. Overexpression of Aβ decreases cholinergic spontaneous and miniature excitatory postsynaptic currents [155]. When anti-murine-p75-SAP (conjugation of saporin to a rat monoclonal antibody against the mouse p75 nerve growth factor receptor) was intracerebroventricularly injected, ChAT activity in the hippocampus and neocortex was selectively inhibited in a dose-dependent manner. These anti-murine-p75-SAP-lesioned mice showed significant spatial memory deficits in the Morris water maze test therapies remain critical in the management of patients with AD [156], the precise structural connections between cholinergic neurons in the basal forebrain and hippocampal neurons, as well as their alterations during AD progression, remain unclear.

In AD, rates of cognitive deficits are also correlated with impairment of the serotonergic system [157, 158]. Serotonergic cells are lost in the brainstem of patients with AD [159]. Selective serotonin reuptake inhibitors improve cognitive function and reduce AD-associated behavioral disorders [159, 160]. Anatomically, serotonergic neurons consist mainly of dorsal and median raphe nuclei, which send dense serotonergic projections to the hippocampus [160, 161]. It has been found that serotonin inhibits the ventral hippocampus, and its inhibition is responsible for sustained goal-directed behavior [162]. Photostimulation of 5-HT neurons expressing ChR2 in the median raphe nucleus significantly increases 5-HT concentration in the dorsal hippocampus (dHC) and produce anxiety-like behavior [163]. Further, optoactivation of 5-HT terminals in the dHC also promote anxiety [163]. Within the hippocampus, optoactivation of serotonergic terminals in CA1 enhances excitatory transmission at CA3-to-CA1 synapses and promotes spatial memory in ChR2-expressing mice [164]. Optogenetic inhibition of CA1 5-HT terminals *via* Arch inhibits spatial memory [164]. However, how changes occur in the hippocampus-associated serotonergic circuits in AD remain elusive.

Perspective

The study of neural circuitry is of great significance for understanding the mechanisms linking brain pathologies and cognitive symptoms in AD. Here, we have summarized the major experimental approaches for neural circuit tracing and their functional manipulations. Furthermore, the introduction of aberrant neural circuits identified in AD mouse models or patients may provide novel therapeutic strategies for AD treatment in the clinic (Fig. 3). However, some key questions need to be addressed.

The application of viral approaches greatly facilitates research on AD neural circuit dissection. In addition to applications, we should pay more attention to their advantages and shortcomings, as noted earlier in this review. To date, there is no perfect viral vector that suits all needs. H129-ΔTK in anterograde trans-synaptic tracing cannot be used to trace local outputs because non-TK-expressing cells can also be infected at the injection site. Due to its virulence, HSV is not suitable for long-term tracing. Retrograde viral tracers, RV, also require further optimization to reduce their toxicity and meet the needs for electrophysiological recording. Furthermore, the infection and tracing efficiency of viral tracers may vary in different brain regions and cell types. Thus, cross-validating tracing results among multiple tracers is highly recommended for the dissection of AD-associated neural circuits.

Optogenetics and chemogenetics have enormous advantages in the functional studies of neural circuits. Combined with electrophysiology and tracers, we can identify functional connections between distinct neurons and evaluate their functional alterations in AD models. Together with

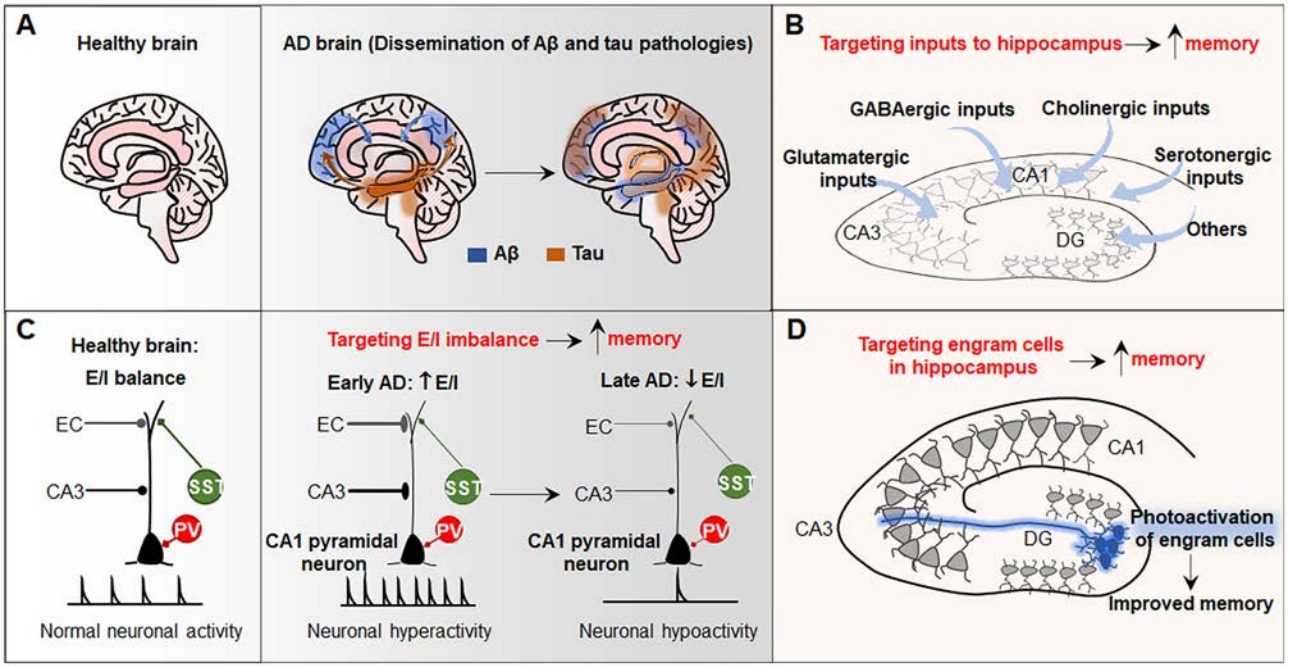

Fig. 3 Hippocampal circuits involved in AD and strategies for targeted manipulations. **A** Topographical dissemination of Aβ and tau pathologies in AD. Tau aggregates develop in the locus coeruleus (LC), and last in broad areas of the neocortex (NC). In contrast to tau pathology, amyloid-β deposits in AD are first observed in the NC and then in basal ganglia structures and the brainstem. **B** During AD progression, projections from other brain regions to the hippocampus undergo distinct alterations. Targeting those inputs may rescue spatial memory deficits in AD. **C** Schematic showing gradual changes of different synaptic inputs onto a CA1 pyramidal neuron across different stages of AD. Entorhinal cortex (EC) and CA3 are two major excitatory inputs, while PV and SST are two main inhibitory inputs to the CA1 pyramidal neuron. Compared with healthy brain, CA1 pyramidal neurons may become hyperactive due to a combination of decreased inhibition as well as an increase in excitation (↑E/I) during the early stages of AD. Then, during the later stages, aggressive Aβ and tau pathologies may affect synapses globally, resulting in hypoactivity (↓E/I). Targeting E/I imbalance may rescue spatial memory deficits in AD. **D** Stimulating engram cells in the hippocampus may improve memory retrieval in AD.

behavioral tests, we can find specific neural circuits involved in different stages of the memory process and identify which circuit is responsible for AD-like cognitive dysfunction in various AD animal models. Optogenetics and chemogenetics have not only helped us understand the pathogenesis of AD but have also opened the door to using these tools for providing treatment. However, there are at least four major obstacles to the application of optogenetics and chemogenetics in patients with AD: (1) autoimmune reactions in patients because of the direct introduction of foreign objects into the brain, (2) the methodology of opsin and DREADD expression in specifically targeted neurons without invasion, (3) the evaluation of opsin and DREADD expression levels in specifically targeted neurons, and (4) tissue damage due to overheating from light stimulation.

Due to space constraints in this review, we introduced only some of the recent studies on hippocampal glutamatergic and GABAergic neural circuits in AD. Other glutamatergic and GABAergic neural circuits outside the hippocampal regions and neural circuits of other neuron types, such as cholinergic and serotonergic neurons, also deserve further investigation.

Acknowledgements This review was supported by Grants from the Natural Science Foundation of China (31730035, 82071219, 91632305, and 91949205), the Ministry of Science and Technology of China (2016YFC1305800), and the Guangdong Provincial Key S&T Program (2018B030336001).

References

1. Qiu C, Kivipelto M, von Strauss E. Epidemiology of Alzheimer's disease: Occurrence, determinants, and strategies toward intervention. Dialogues Clin Neurosci 2009, 11: 111–128.
2. Kumar A, Singh A, Ekavali. A review on Alzheimer's disease pathophysiology and its management: An update. Pharmacol Rep 2015, 67: 195–203.
3. Gu XM, Jiang ZF, Huang HC. Magnetic resonance imaging of Alzheimer's disease: From diagnosis to therapeutic evaluation. Chin J Integr Med 2010, 16: 276–282.
4. Harrison TM, Maass A, Adams JN, Du R, Baker SL, Jagust WJ. Tau deposition is associated with functional isolation of the *Hippocampus* in aging. Nat Commun 2019, 10: 4900.
5. De Strooper B, Karran E. The cellular phase of Alzheimer's disease. Cell 2016, 164: 603–615.
6. Svensson V, Vento-Tormo R, Teichmann SA. Exponential scaling of single-cell RNA-seq in the past decade. Nat Protoc 2018, 13: 599–604.

7. Rossier J, Bernard A, Cabungcal JH, Perrenoud Q, Savoye A, Gallopin T. Cortical fast-spiking parvalbumin interneurons enwrapped in the perineuronal net express the metallopeptidases Adamts8, Adamts15 and Neprilysin. Mol Psychiatry 2015, 20: 154–161.
8. Subkhankulova T, Yano K, Robinson HP, Livesey FJ. Grouping and classifying electrophysiologically-defined classes of neocortical neurons by single cell, whole-genome expression profiling. Front Mol Neurosci 2010, 3: 10.
9. Hashimshony T, Senderovich N, Avital G, Klochendler A, de Leeuw Y, Anavy L, *et al.* CEL-Seq2: Sensitive highly-multiplexed single-cell RNA-Seq. Genome Biol 2016, 17: 77.
10. Zeisel A, Muñoz-Manchado AB, Codeluppi S, Lönnerberg P, La Manno G, Juréus A, *et al.* Brain structure Cell types in the mouse cortex and Hippocampus revealed by single-cell RNA-seq. Science 2015, 347: 1138–1142.
11. Usoskin D, Furlan A, Islam S, Abdo H, Lönnerberg P, Lou DH, *et al.* Unbiased classification of sensory neuron types by large-scale single-cell RNA sequencing. Nat Neurosci 2015, 18: 145–153.
12. Wu AR, Neff NF, Kalisky T, Dalerba P, Treutlein B, Rothenberg ME, *et al.* Quantitative assessment of single-cell RNA-sequencing methods. Nat Methods 2014, 11: 41–46.
13. Pollen AA, Nowakowski TJ, Shuga J, Wang XH, Leyrat AA, Lui JH, *et al.* Low-coverage single-cell mRNA sequencing reveals cellular heterogeneity and activated signaling pathways in developing cerebral cortex. Nat Biotechnol 2014, 32: 1053–1058.
14. Prakadan SM, Shalek AK, Weitz DA. Scaling by shrinking: Empowering single-cell 'omics' with microfluidic devices. Nat Rev Genet 2017, 18: 345–361.
15. Macosko EZ, Basu A, Satija R, Nemesh J, Shekhar K, Goldman M, *et al.* Highly parallel genome-wide expression profiling of individual cells using nanoliter droplets. Cell 2015, 161: 1202–1214.
16. Klein AM, Mazutis L, Akartuna I, Tallapragada N, Veres A, Li V, *et al.* Droplet barcoding for single-cell transcriptomics applied to embryonic stem cells. Cell 2015, 161: 1187–1201.
17. Zhang XN, Li TQ, Liu F, Chen YQ, Yao JC, Li ZY, *et al.* Comparative analysis of droplet-based ultra-high-throughput single-cell RNA-seq systems. Mol Cell 2019, 73: 130-142.e5.
18. Zheng GX, Terry JM, Belgrader P, Ryvkin P, Bent ZW, Wilson R, *et al.* Massively parallel digital transcriptional profiling of single cells. Nat Commun 2017, 8: 14049.
19. Mathys H, Davila-Velderrain J, Peng ZY, Gao F, Mohammadi S, Young JZ, *et al.* Author Correction: Single-cell transcriptomic analysis of Alzheimer's disease. Nature 2019, 571: E1. https://doi.org/10.1038/s41586-019-1329-6.
20. Lake BB, Ai R, Kaeser GE, Salathia NS, Yung YC, Liu R, *et al.* Neuronal subtypes and diversity revealed by single-nucleus RNA sequencing of the human brain. Science 2016, 352: 1586–1590.
21. Krishnaswami SR, Grindberg RV, Novotny M, Venepally P, Lacar B, Bhutani K, *et al.* Using single nuclei for RNA-seq to capture the transcriptome of postmortem neurons. Nat Protoc 2016, 11: 499–524.
22. Lake BB, Chen S, Sos BC, Fan J, Kaeser GE, Yung YC, *et al.* Integrative single-cell analysis of transcriptional and epigenetic states in the human adult brain. Nat Biotechnol 2018, 36: 70–80.
23. Lake BB, Codeluppi S, Yung YC, Gao D, Chun J, Kharchenko PV, *et al.* A comparative strategy for single-nucleus and single-cell transcriptomes confirms accuracy in predicted cell-type expression from nuclear RNA. Sci Rep 2017, 7: 6031.
24. Ziegenhain C, Vieth B, Parekh S, Reinius B, Guillaumet-Adkins A, Smets M, *et al.* Comparative analysis of single-cell RNA sequencing methods. Mol Cell 2017, 65: 631-643.e4.
25. Phipson B, Zappia L, Oshlack A. Gene length and detection bias in single cell RNA sequencing protocols. F1000Res 2017, 6: 595.
26. Wu AR, Wang JB, Streets AM, Huang YY. Single-cell transcriptional analysis. Annu Rev Anal Chem (Palo Alto Calif) 2017, 10: 439–462.
27. Saliba AE, Westermann AJ, Gorski SA, Vogel J. Single-cell RNA-seq: Advances and future challenges. Nucleic Acids Res 2014, 42: 8845–8860.
28. Crosetto N, Bienko M, van Oudenaarden A. Spatially resolved transcriptomics and beyond. Nat Rev Genet 2015, 16: 57–66.
29. Zeng HK, Sanes JR. Neuronal cell-type classification: Challenges, opportunities and the path forward. Nat Rev Neurosci 2017, 18: 530–546.
30. Lein E, Borm LE, Linnarsson S. The promise of spatial transcriptomics for neuroscience in the era of molecular cell typing. Science 2017, 358: 64–69.
31. Raj A, van den Bogaard P, Rifkin SA, van Oudenaarden A, Tyagi S. Imaging individual mRNA molecules using multiple singly labeled probes. Nat Methods 2008, 5: 877–879.
32. Shah S, Lubeck E, Zhou W, Cai L. *In situ* transcription profiling of single cells reveals spatial organization of cells in the mouse *Hippocampus*. Neuron 2016, 92: 342–357.
33. Lubeck E, Coskun AF, Zhiyentayev T, Ahmad M, Cai L. Single-cell *in situ* RNA profiling by sequential hybridization. Nat Methods 2014, 11: 360–361.
34. Pi GL, Gao D, Wu DQ, Wang YL, Lei HY, Zeng WB, *et al.* Posterior basolateral amygdala to ventral hippocampal CA1 drives approach behaviour to exert an anxiolytic effect. Nat Commun 2020, 11: 183.
35. Dum RP, Levinthal DJ, Strick PL. The spinothalamic system targets motor and sensory areas in the cerebral cortex of monkeys. J Neurosci 2009, 29: 14223–14235.
36. McGovern AE, Davis-Poynter N, Farrell MJ, Mazzone SB. Transneuronal tracing of airways-related sensory circuitry using *Herpes simplex* virus 1, strain H129. Neuroscience 2012, 207: 148–166.
37. Su P, Wang HD, Xia JJ, Zhong X, Hu L, Li YL, *et al.* Evaluation of retrograde labeling profiles of HSV_1 H129 anterograde tracer. J Chem Neuroanat 2019, 100: 101662.
38. Wojaczynski GJ, Engel EA, Steren KE, Enquist LW, Patrick Card J. The neuroinvasive profiles of H129 (*Herpes simplex* virus type 1) recombinants with putative anterograde-only transneuronal spread properties. Brain Struct Funct 2015, 220: 1395–1420.
39. Kit S, Kit M, Pirtle EC. Attenuated properties of thymidine kinase-negative deletion mutant of pseudorabies virus. Am J Vet Res 1985, 46: 1359–1367.
40. Roberts A, Buonocore L, Price R, Forman J, Rose JK. Attenuated vesicular stomatitis viruses as vaccine vectors. J Virol 1999, 73: 3723–3732.
41. Lichty BD, Power AT, Stojdl DF, Bell JC. Vesicular stomatitis virus: Re-inventing the bullet. Trends Mol Med 2004, 10: 210–216.
42. Hastie E, Cataldi M, Marriott I, Grdzelishvili VZ. Understanding and altering cell tropism of vesicular stomatitis virus. Virus Res 2013, 176: 16–32.
43. van den Pol AN, Ozduman K, Wollmann G, Ho WS, Simon I, Yao Y, *et al.* Viral strategies for studying the brain, including a replication-restricted self-amplifying delta-G vesicular stomatis virus that rapidly expresses transgenes in brain and can generate a multicolor Golgi-like expression. J Comp Neurol 2009, 516: 456–481.
44. Beier KT, Saunders A, Oldenburg IA, Miyamichi K, Akhtar N, Luo L, *et al.* Anterograde or retrograde transsynaptic labeling of

CNS neurons with vesicular stomatitis virus vectors. PNAS 2011, 108: 15414–15419.
45. Zingg B, Chou XL, Zhang ZG, Mesik L, Liang FX, Tao HW, *et al.* AAV-mediated anterograde transsynaptic tagging: Mapping corticocollicular input-defined neural pathways for defense behaviors. Neuron 2017, 93: 33–47.
46. Hollis Ii ER, Kadoya K, Hirsch M, Samulski RJ, Tuszynski MH. Efficient retrograde neuronal transduction utilizing self-complementary AAV1. Mol Ther 2008, 16: 296–301.
47. Wickersham IR, Lyon DC, Barnard RJ, Mori T, Finke S, Conzelmann KK, *et al.* Monosynaptic restriction of transsynaptic tracing from single, genetically targeted neurons. Neuron 2007, 53: 639–647.
48. Wall NR, Wickersham IR, Cetin A, De La Parra M, Callaway EM. Monosynaptic circuit tracing *in vivo* through Cre-dependent targeting and complementation of modified rabies virus. Proc Natl Acad Sci USA 2010, 107: 21848–21853.
49. Wickersham IR, Finke S, Conzelmann KK, Callaway EM. Retrograde neuronal tracing with a deletion-mutant rabies virus. Nat Methods 2007, 4: 47–49.
50. Schwarz LA, Miyamichi K, Gao XJ, Beier KT, Weissbourd B, DeLoach KE, *et al.* Viral-genetic tracing of the input-output organization of a central noradrenaline circuit. Nature 2015, 524: 88–92.
51. Chatterjee S, Sullivan HA, MacLennan BJ, Xu R, Hou YY, Lavin TK, *et al.* Nontoxic, double-deletion-mutant rabies viral vectors for retrograde targeting of projection neurons. Nat Neurosci 2018, 21: 638–646.
52. Albertini AA, Ruigrok RW, Blondel D. Rabies virus transcription and replication. Adv Virus Res 2011, 79: 1–22.
53. Boyden ES. A history of optogenetics: The development of tools for controlling brain circuits with light. F1000 Biol Rep 2011, 3: 11.
54. Deisseroth K. Optogenetics. Nat Methods 2011, 8: 26–29.
55. Matsuno-Yagi A, Mukohata Y. Two possible roles of bacteriorhodopsin; a comparative study of strains of *Halobacterium halobium* differing in pigmentation. Biochem Biophys Res Commun 1977, 78: 237–243.
56. Nagel G, Ollig D, Fuhrmann M, Kateriya S, Musti AM, Bamberg E, *et al.* Channelrhodopsin-1: a light-gated proton channel in green algae. Science 2002, 296: 2395–2398.
57. Boyden ES, Zhang F, Bamberg E, Nagel G, Deisseroth K. Millisecond-timescale, genetically targeted optical control of neural activity. Nat Neurosci 2005, 8: 1263–1268.
58. Aravanis AM, Wang LP, Zhang F, Meltzer LA, Mogri MZ, Schneider MB, *et al.* An optical neural interface: *In vivo* control of rodent motor cortex with integrated fiberoptic and optogenetic technology. J Neural Eng 2007, 4: S143–S156.
59. Adamantidis AR, Zhang F, Aravanis AM, Deisseroth K, de Lecea L. Neural substrates of awakening probed with optogenetic control of hypocretin neurons. Nature 2007, 450: 420–424.
60. Kato HE, Zhang F, Yizhar O, Ramakrishnan C, Nishizawa T, Hirata K, *et al.* Crystal structure of the channelrhodopsin light-gated cation channel. Nature 2012, 482: 369–374.
61. Deisseroth K. Optogenetics: 10 years of microbial opsins in neuroscience. Nat Neurosci 2015, 18: 1213–1225.
62. Schneider F, Grimm C, Hegemann P. Biophysics of channelrhodopsin. Annu Rev Biophys 2015, 44: 167–186.
63. Nagel G, Brauner M, Liewald JF, Adeishvili N, Bamberg E, Gottschalk A. Light activation of channelrhodopsin-2 in excitable cells of *Caenorhabditis elegans* triggers rapid behavioral responses. Curr Biol 2005, 15: 2279–2284.
64. Lin JY, Lin MZ, Steinbach P, Tsien RY. Characterization of engineered channelrhodopsin variants with improved properties and kinetics. Biophys J 2009, 96: 1803–1814.
65. Gunaydin LA, Yizhar O, Berndt A, Sohal VS, Deisseroth K, Hegemann P. Ultrafast optogenetic control. Nat Neurosci 2010, 13: 387–392.
66. Zhang F, Prigge M, Beyrière F, Tsunoda SP, Mattis J, Yizhar O, *et al.* Red-shifted optogenetic excitation: A tool for fast neural control derived from *Volvox carteri*. Nat Neurosci 2008, 11: 631–633.
67. Lin JY, Knutsen PM, Muller A, Kleinfeld D, Tsien RY. ReaChR: a red-shifted variant of channelrhodopsin enables deep transcranial optogenetic excitation. Nat Neurosci 2013, 16: 1499–1508.
68. Hochbaum DR, Zhao YX, Farhi SL, Klapoetke N, Werley CA, Kapoor V, *et al.* All-optical electrophysiology in mammalian neurons using engineered microbial rhodopsins. Nat Methods 2014, 11: 825–833.
69. Chow BY, Han X, Dobry AS, Qian XF, Chuong AS, Li MJ, *et al.* High-performance genetically targetable optical neural silencing by light-driven proton pumps. Nature 2010, 463: 98–102.
70. Wietek J, Wiegert JS, Adeishvili N, Schneider F, Watanabe H, Tsunoda SP, *et al.* Conversion of channelrhodopsin into a light-gated chloride channel. Science 2014, 344: 409–412.
71. Atasoy D, Sternson SM. Chemogenetic tools for causal cellular and neuronal biology. Physiol Rev 2018, 98: 391–418.
72. Conklin BR, Hsiao EC, Claeysen S, Dumuis A, Srinivasan S, Forsayeth JR, *et al.* Engineering GPCR signaling pathways with RASSLs. Nat Methods 2008, 5: 673–678.
73. Alexander GM, Rogan SC, Abbas AI, Armbruster BN, Pei Y, Allen JA, *et al.* Remote control of neuronal activity in transgenic mice expressing evolved G protein-coupled receptors. Neuron 2009, 63: 27–39.
74. Stachniak TJ, Ghosh A, Sternson SM. Chemogenetic synaptic silencing of neural circuits localizes a hypothalamus→midbrain pathway for feeding behavior. Neuron 2014, 82: 797–808.
75. Gomez JL, Bonaventura J, Lesniak W, Mathews WB, Sysa-Shah P, Rodriguez LA, *et al.* Chemogenetics revealed: DREADD occupancy and activation via converted clozapine. Science 2017, 357: 503–507.
76. Todd WD, Fenselau H, Wang JL, Zhang R, Machado NL, Venner A, *et al.* A hypothalamic circuit for the circadian control of aggression. Nat Neurosci 2018, 21: 717–724.
77. Rodriguez GA, Barrett GM, Duff KE, Hussaini SA. Chemogenetic attenuation of neuronal activity in the entorhinal cortex reduces Aβ and tau pathology in the *Hippocampus*. PLoS Biol 2020, 18: e3000851. https://doi.org/10.1371/journal.pbio.3000851.
78. Braak H, Braak E. Neuropathological stageing of Alzheimer-related changes. Acta Neuropathol 1991, 82: 239–259.
79. Serrano-Pozo A, Frosch MP, Masliah E, Hyman BT. Neuropathological alterations in Alzheimer disease. Cold Spring Harb Perspect Med 2011, 1: a006189.
80. Devanand DP, Pradhaban G, Liu X, Khandji A, De Santi S, Segal S, *et al.* Hippocampal and entorhinal atrophy in mild cognitive impairment: Prediction of Alzheimer disease. Neurology 2007, 68: 828–836.
81. Busche MA, Hyman BT. Synergy between amyloid-β and tau in Alzheimer's disease. Nat Neurosci 2020, 23: 1183–1193.
82. Zhou YY, Song WM, Andhey PS, Swain A, Levy T, Miller KR, *et al.* Author Correction: Human and mouse single-nucleus transcriptomics reveal TREM2-dependent and TREM2-independent cellular responses in Alzheimer's disease. Nat Med 2020, 26: 981.
83. Huijbers W, Mormino EC, Schultz AP, Wigman S, Ward AM, Larvie M, *et al.* Amyloid-β deposition in mild cognitive impairment is associated with increased hippocampal activity, atrophy and clinical progression. Brain 2015, 138: 1023–1035.

84. Busche MA, Eichhoff G, Adelsberger H, Abramowski D, Wiederhold KH, Haass C, *et al.* Clusters of hyperactive neurons near amyloid plaques in a mouse model of Alzheimer's disease. Science 2008, 321: 1686–1689.
85. Zott B, Simon MM, Hong W, Unger F, Chen-Engerer HJ, Frosch MP, *et al.* A vicious cycle of β amyloid-dependent neuronal hyperactivation. Science 2019, 365: 559–565.
86. Matos M, Augusto E, Machado NJ, dos Santos-Rodrigues A, Cunha RA, Agostinho P. Astrocytic adenosine A2A receptors control the amyloid-β peptide-induced decrease of glutamate uptake. J Alzheimers Dis 2012, 31: 555–567.
87. Canas PM, Porciúncula LO, Cunha GM, Silva CG, Machado NJ, Oliveira JM, *et al.* Adenosine A2A receptor blockade prevents synaptotoxicity and memory dysfunction caused by beta-amyloid peptides via p38 mitogen-activated protein kinase pathway. J Neurosci 2009, 29: 14741–14751.
88. Wang DY, Govindaiah G, Liu RJ, De Arcangelis V, Cox CL, Xiang YK. Binding of amyloid beta peptide to beta2 adrenergic receptor induces PKA-dependent AMPA receptor hyperactivity. FASEB J 2010, 24: 3511–3521.
89. Huang Y, Shen W, Su J, Cheng B, Li D, Liu G, *et al.* Modulating the balance of synaptic and extrasynaptic NMDA receptors shows positive effects against amyloid-β-induced neurotoxicity. J Alzheimers Dis 2017, 57: 885–897.
90. Hardingham GE, Fukunaga Y, Bading H. Extrasynaptic NMDARs oppose synaptic NMDARs by triggering CREB shut-off and cell death pathways. Nat Neurosci 2002, 5: 405–414.
91. Abramov E, Dolev I, Fogel H, Ciccotosto GD, Ruff E, Slutsky I. Amyloid-beta as a positive endogenous regulator of release probability at hippocampal synapses. Nat Neurosci 2009, 12: 1567–1576.
92. He Y, Wei MD, Wu Y, Qin HP, Li WN, Ma XL, *et al.* Amyloid β oligomers suppress excitatory transmitter release via presynaptic depletion of phosphatidylinositol-4, 5-bisphosphate. Nat Commun 2019, 10: 1193.
93. Talantova M, Sanz-Blasco S, Zhang XF, Xia P, Akhtar MW, Okamoto S, *et al.* Aβ induces astrocytic glutamate release, extrasynaptic NMDA receptor activation, and synaptic loss. Proc Natl Acad Sci USA 2013, 110: E2518–E2527.
94. Shankar GM, Li SM, Mehta TH, Garcia-Munoz A, Shepardson NE, Smith I, *et al.* Amyloid-beta protein dimers isolated directly from Alzheimer's brains impair synaptic plasticity and memory. Nat Med 2008, 14: 837–842.
95. Leshchyns'ka I, Liew HT, Shepherd C, Halliday GM, Stevens CH, Ke YD, *et al.* Aβ-dependent reduction of NCAM2-mediated synaptic adhesion contributes to synapse loss in Alzheimer's disease. Nat Commun 2015, 6: 8836.
96. Hsieh H, Boehm J, Sato C, Iwatsubo T, Tomita T, Sisodia S, *et al.* AMPAR removal underlies Abeta-induced synaptic depression and dendritic spine loss. Neuron 2006, 52: 831–843.
97. Hrynchak MV, Rierola M, Golovyashkina N, Penazzi L, Pump WC, David B, *et al.* Chronic presence of oligomeric aβ differentially modulates spine parameters in the *Hippocampus* and cortex of mice with low APP transgene expression. Front Synaptic Neurosci 2020, 12: 16.
98. Ting JT, Kelley BG, Lambert TJ, Cook DG, Sullivan JM. Amyloid precursor protein overexpression depresses excitatory transmission through both presynaptic and postsynaptic mechanisms. Proc Natl Acad Sci USA 2007, 104: 353–358.
99. Lin L, Liu AY, Li HQ, Feng J, Yan Z. Inhibition of histone methyltransferases EHMT1/2 reverses amyloid-β-induced loss of AMPAR currents in human stem cell-derived cortical neurons. J Alzheimers Dis 2019, 70: 1175–1185.
100. Du YH, Fu M, Huang ZL, Tian X, Li JJ, Pang YY, *et al.* $TRPV_1$ activation alleviates cognitive and synaptic plasticity impairments through inhibiting AMPAR endocytosis in APP23/PS45 mouse model of Alzheimer's disease. Aging Cell 2020, 19: e13113. https://doi.org/10.1111/acel.13113.
101. Rodrigues EM, Scudder SL, Goo MS, Patrick GN. Aβ-induced synaptic alterations require the E3 ubiquitin ligase Nedd4-1. J Neurosci 2016, 36: 1590–1595.
102. Snyder EM, Nong Y, Almeida CG, Paul S, Moran T, Choi EY, *et al.* Regulation of NMDA receptor trafficking by amyloid-beta. Nat Neurosci 2005, 8: 1051–1058.
103. Hsu WL, Ma YL, Hsieh DY, Liu YC, Lee EH. STAT1 negatively regulates spatial memory formation and mediates the memory-impairing effect of Aβ. Neuropsychopharmacology 2014, 39: 746–758.
104. Yin YL, Gao D, Wang YL, Wang ZH, Wang X, Ye JW, *et al.* Tau accumulation induces synaptic impairment and memory deficit by calcineurin-mediated inactivation of nuclear CaMKIV/CREB signaling. Proc Natl Acad Sci USA 2016, 113: E3773–E3781.
105. Li XG, Hong XY, Wang YL, Zhang SJ, Zhang JF, Li XC, *et al.* Tau accumulation triggers STAT1-dependent memory deficits by suppressing NMDA receptor expression. EMBO Rep 2019, 20: e47202.
106. Ye JW, Yin YL, Liu HH, Fang L, Tao XQ, Wei LY, *et al.* Tau inhibits PKA by nuclear proteasome-dependent PKAR2α elevation with suppressed CREB/GluA1 phosphorylation. Aging Cell 2020, 19: e13055. https://doi.org/10.1111/acel.13055.
107. Ittner LM, Ke YD, Delerue F, Bi M, Gladbach A, van Eersel J, *et al.* Dendritic function of tau mediates amyloid-beta toxicity in Alzheimer's disease mouse models. Cell 2010, 142: 387–397.
108. Luo HB, Xia YY, Shu XJ, Liu ZC, Feng Y, Liu XH, *et al.* SUMOylation at K340 inhibits tau degradation through deregulating its phosphorylation and ubiquitination. Proc Natl Acad Sci USA 2014, 111: 16586–16591.
109. Feng Q, Luo Y, Zhang XN, Yang XF, Hong XY, Sun DS, *et al.* MAPT/Tau accumulation represses autophagy flux by disrupting IST1-regulated ESCRT-III complex formation: A vicious cycle in Alzheimer neurodegeneration. Autophagy 2020, 16: 641–658.
110. Wang X, Liu EJ, Liu Q, Li SH, Li T, Zhou QZ, *et al.* Tau acetylation in entorhinal cortex induces its chronic hippocampal propagation and cognitive deficits in mice. J Alzheimers Dis 2020, 77: 241–255.
111. Ye JW, Yin Y, Yin YL, Zhang HQ, Wan HL, Wang L, *et al.* Tau-induced upregulation of C/EBPβ-$TRPC_1$-SOCE signaling aggravates tauopathies: A vicious cycle in Alzheimer neurodegeneration. Aging Cell 2020, 19: e13209. https://doi.org/10.1111/acel.13209.
112. Hoover BR, Reed MN, Su JJ, Penrod RD, Kotilinek LA, Grant MK, *et al.* Tau mislocalization to dendritic spines mediates synaptic dysfunction independently of neurodegeneration. Neuron 2010, 68: 1067–1081.
113. Tracy TE, Sohn PD, Minami SS, Wang C, Min SW, Li YQ, *et al.* Acetylated tau obstructs KIBRA-mediated signaling in synaptic plasticity and promotes tauopathy-related memory loss. Neuron 2016, 90: 245–260.
114. Zhao XH, Kotilinek LA, Smith B, Hlynialuk C, Zahs K, Ramsden M, *et al.* Caspase-2 cleavage of tau reversibly impairs memory. Nat Med 2016, 22: 1268–1276.
115. Hatch RJ, Wei Y, Xia D, Götz J. Hyperphosphorylated tau causes reduced hippocampal CA1 excitability by relocating the axon initial segment. Acta Neuropathol 2017, 133: 717–730.
116. Sohn PD, Huang CT, Yan R, Fan L, Tracy TE, Camargo CM, *et al.* Pathogenic tau impairs axon initial segment plasticity and excitability homeostasis. Neuron 2019, 104: 458-470.e5.
117. Chen TW, Wardill TJ, Sun Y, Pulver SR, Renninger SL, Baohan A, *et al.* Ultrasensitive fluorescent proteins for imaging neuronal activity. Nature 2013, 499: 295–300.

118. Jimenez JC, Su K, Goldberg AR, Luna VM, Biane JS, Ordek G, *et al.* Anxiety cells in a hippocampal-hypothalamic circuit. Neuron 2018, 97: 670-683.e6.
119. Granholm E, Butters N. Associative encoding and retrieval in Alzheimer's and Huntington's disease. Brain Cogn 1988, 7: 335–347.
120. Roy DS, Arons A, Mitchell TI, Pignatelli M, Ryan TJ, Tonegawa S. Memory retrieval by activating engram cells in mouse models of early Alzheimer's disease. Nature 2016, 531: 508–512.
121. He QY, Wang JH, Hu HL. Illuminating the activated brain: Emerging activity-dependent tools to capture and control functional neural circuits. Neurosci Bull 2019, 35: 369–377.
122. Yang Y, Wang ZH, Jin S, Gao D, Liu N, Chen SP, *et al.* Opposite monosynaptic scaling of BLP-vCA1 inputs governs hopefulness- and helplessness-modulated spatial learning and memory. Nat Commun 2016, 7: 11935.
123. Wu JW, Hussaini SA, Bastille IM, Rodriguez GA, Mrejeru A, Rilett K, *et al.* Neuronal activity enhances tau propagation and tau pathology *in vivo*. Nat Neurosci 2016, 19: 1085–1092.
124. Garcia-Marin V, Blazquez-Llorca L, Rodriguez JR, Boluda S, Muntane G, Ferrer I, *et al.* Diminished perisomatic GABAergic terminals on cortical neurons adjacent to amyloid plaques. Front Neuroanat 2009, 3: 28.
125. Ramos-Miguel A, Hercher C, Beasley CL, Barr AM, Bayer TA, Falkai P, *et al.* Loss of Munc18-1 long splice variant in GABAergic terminals is associated with cognitive decline and increased risk of dementia in a community sample. Mol Neurodegener 2015, 10: 65.
126. Bell KF, de Kort GJ, Steggerda S, Shigemoto R, Ribeiro-da-Silva A, Cuello AC. Structural involvement of the glutamatergic presynaptic boutons in a transgenic mouse model expressing early onset amyloid pathology. Neurosci Lett 2003, 353: 143–147.
127. Bell KF, Ducatenzeiler A, Ribeiro-da-Silva A, Duff K, Bennett DA, Cuello AC. The amyloid pathology progresses in a neurotransmitter-specific manner. Neurobiol Aging 2006, 27: 1644–1657.
128. Sanchez-Mejias E, Nuñez-Diaz C, Sanchez-Varo R, Gomez-Arboledas A, Garcia-Leon JA, Fernandez-Valenzuela JJ, *et al.* Distinct disease-sensitive GABAergic neurons in the perirhinal cortex of Alzheimer's mice and patients. Brain Pathol 2020, 30: 345–363.
129. Ramos B, Baglietto-Vargas D, del Rio JC, Moreno-Gonzalez I, Santa-Maria C, Jimenez S, *et al.* Early neuropathology of somatostatin/NPY GABAergic cells in the *Hippocampus* of a PS1xAPP transgenic model of Alzheimer's disease. Neurobiol Aging 2006, 27: 1658–1672.
130. Zallo F, Gardenal E, Verkhratsky A, Rodríguez JJ. Loss of calretinin and parvalbumin positive interneurones in the hippocampal CA1 of aged Alzheimer's disease mice. Neurosci Lett 2018, 681: 19–25.
131. Nykänen NP, Kysenius K, Sakha P, Tammela P, Huttunen HJ. Γ-Aminobutyric acid type A (GABAA) receptor activation modulates tau phosphorylation. J Biol Chem 2012, 287: 6743–6752.
132. Nilsen LH, Rae C, Ittner LM, Götz J, Sonnewald U. Glutamate metabolism is impaired in transgenic mice with tau hyperphosphorylation. J Cereb Blood Flow Metab 2013, 33: 684–691.
133. Hazra A, Gu F, Aulakh A, Berridge C, Eriksen JL, Ziburkus J. Inhibitory neuron and hippocampal circuit dysfunction in an aged mouse model of Alzheimer's disease. PLoS ONE 2013, 8: e64318. https://doi.org/10.1371/journal.pone.0064318.
134. Zheng J, Li HL, Tian N, Liu F, Wang L, Yin YL, *et al.* Interneuron accumulation of phosphorylated tau impairs adult hippocampal neurogenesis by suppressing GABAergic transmission. Cell Stem Cell 2020, 26: 462–466.
135. Yang X, Yao C, Tian T, Li X, Yan H, Wu J, *et al.* A novel mechanism of memory loss in Alzheimer's disease mice via the degeneration of entorhinal-CA1 synapses. Mol Psychiatry 2018, 23: 199–210.
136. Bienvenu TC, Busti D, Magill PJ, Ferraguti F, Capogna M. Cell-type-specific recruitment of amygdala interneurons to hippocampal *Theta* rhythm and noxious stimuli *in vivo*. Neuron 2012, 74: 1059–1074.
137. Loreth D, Ozmen L, Revel FG, Knoflach F, Wetzel P, Frotscher M, *et al.* Selective degeneration of septal and hippocampal GABAergic neurons in a mouse model of amyloidosis and tauopathy. Neurobiol Dis 2012, 47: 1–12.
138. Wang Y, Romani S, Lustig B, Leonardo A, Pastalkova E. *Theta* sequences are essential for internally generated hippocampal firing fields. Nat Neurosci 2015, 18: 282–288.
139. Wikenheiser AM, Redish AD. Hippocampal *Theta* sequences reflect current goals. Nat Neurosci 2015, 18: 289–294.
140. Cheng JH, Ji DY. Rigid firing sequences undermine spatial memory codes in a neurodegenerative mouse model. Elife 2013, 2: e00647. https://doi.org/10.7554/eLife.00647.
141. Villette V, Poindessous-Jazat F, Simon A, Léna C, Roullot E, Bellessort B, *et al.* Decreased rhythmic GABAergic septal activity and memory-associated *Theta* oscillations after hippocampal amyloid-beta pathology in the rat. J Neurosci 2010, 30: 10991–11003.
142. Martorell AJ, Paulson AL, Suk HJ, Abdurrob F, Drummond GT, Guan W, *et al.* Multi-sensory gamma stimulation ameliorates Alzheimer's-associated pathology and improves cognition. Cell 2019, 177: 256-271.e22.
143. Jun H, Bramian A, Soma S, Saito T, Saido TC, Igarashi KM. Disrupted place cell remapping and impaired grid cells in a knockin model of Alzheimer's disease. Neuron 2020, 107: 1095-1112.e6.
144. Herrmann CS, Demiralp T. Human EEG gamma oscillations in neuropsychiatric disorders. Clin Neurophysiol 2005, 116: 2719–2733.
145. Yamamoto J, Suh J, Takeuchi D, Tonegawa S. Successful execution of working memory linked to synchronized high-frequency gamma oscillations. Cell 2014, 157: 845–857.
146. Mikulovic S, Restrepo CE, Siwani S, Bauer P, Pupe S, Tort ABL, *et al.* Ventral hippocampal OLM cells control type 2 *Theta* oscillations and response to predator odor. Nat Commun 2018, 9: 3638.
147. Iaccarino HF, Singer AC, Martorell AJ, Rudenko A, Gao F, Gillingham TZ, *et al.* Author Correction: Gamma frequency entrainment attenuates amyloid load and modifies microglia. Nature 2018, 562: E1. https://doi.org/10.1038/s41586-018-0351-4.
148. Huh CY, Amilhon B, Ferguson KA, Manseau F, Torres-Platas SG, Peach JP, *et al.* Excitatory inputs determine phase-locking strength and spike-timing of CA1 stratum *Oriens/Alveus* parvalbumin and somatostatin interneurons during intrinsically generated hippocampal *Theta* rhythm. J Neurosci 2016, 36: 6605–6622.
149. Etter G, van der Veldt S, Manseau F, Zarrinkoub I, Trillaud-Doppia E, Williams S. Optogenetic gamma stimulation rescues memory impairments in an Alzheimer's disease mouse model. Nat Commun 2019, 10: 5322.
150. Chung H, Park K, Jang HJ, Kohl MM, Kwag J. Dissociation of somatostatin and parvalbumin interneurons circuit dysfunctions underlying hippocampal *Theta* and gamma oscillations impaired by amyloid β oligomers *in vivo*. Brain Struct Funct 2020, 225: 935–954.

151. Mesulam MM. The cholinergic innervation of the human cerebral cortex. Prog Brain Res 2004, 145: 67–78.
152. Wilcock GK, Esiri MM, Bowen DM, Smith CC. Alzheimer's disease. Correlation of cortical choline acetyltransferase activity with the severity of dementia and histological abnormalities. J Neurol Sci 1990, 57: 407–417.
153. Kooi EJ, Prins M, Bajic N, Beliën JA, Gerritsen WH, van Horssen J, *et al.* Cholinergic imbalance in the multiple sclerosis *Hippocampus*. Acta Neuropathol 2011, 122: 313–322.
154. Yoon SY, Choi JU, Cho MH, Yang KM, Ha H, Chung IJ, *et al.* A-secretase cleaved amyloid precursor protein (APP) accumulates in cholinergic dystrophic neurites in normal, aged *Hippocampus*. Neuropathol Appl Neurobiol 2013, 39: 800–816.
155. Fang LQ, Duan JJ, Ran DZ, Fan ZH, Yan Y, Huang NY, *et al.* Amyloid-β depresses excitatory cholinergic synaptic transmission in *Drosophila*. Neurosci Bull 2012, 28: 585–594.
156. Berger-Sweeney J, Stearns NA, Murg SL, Floerke-Nashner LR, Lappi DA, Baxter MG. Selective immunolesions of cholinergic neurons in mice: Effects on neuroanatomy, neurochemistry, and behavior. J Neurosci 2001, 21: 8164–8173.
157. Lai MK, Tsang SW, Alder JT, Keene J, Hope T, Esiri MM, *et al.* Loss of serotonin 5-HT2A receptors in the postmortem temporal cortex correlates with rate of cognitive decline in Alzheimer's disease. Psychopharmacology (Berl) 2005, 179: 673–677.
158. Lai MK, Tsang SW, Francis PT, Keene J, Hope T, Esiri MM, *et al.* Postmortem serotoninergic correlates of cognitive decline in Alzheimer's disease. Neuroreport 2002, 13: 1175–1178.
159. Yamamoto T, Hirano A. Nucleus raphe dorsalis in Alzheimer's disease: Neurofibrillary tangles and loss of large neurons. Ann Neurol 1985, 17: 573–577.
160. Mowla A, Mosavinasab M, Haghshenas H, Borhani Haghighi A. Does serotonin augmentation have any effect on cognition and activities of daily living in Alzheimer's dementia? A double-blind, placebo-controlled clinical trial. J Clin Psychopharmacol 2007, 27: 484–487.
161. Mokler DJ, Lariviere D, Johnson DW, Theriault NL, Bronzino JD, Dixon M, *et al.* Serotonin neuronal release from dorsal *Hippocampus* following electrical stimulation of the dorsal and Median raphé nuclei in conscious rats. Hippocampus 1998, 8: 262–273.
162. Yoshida K, Drew MR, Mimura M, Tanaka KF. Serotonin-mediated inhibition of ventral *Hippocampus* is required for sustained goal-directed behavior. Nat Neurosci 2019, 22: 770–777.
163. Abela AR, Browne CJ, Sargin D, Prevot TD, Ji XD, Li Z, *et al.* Median raphe serotonin neurons promote anxiety-like behavior via inputs to the dorsal *Hippocampus*. Neuropharmacology 2020, 168: 107985.
164. Teixeira CM, Rosen ZB, Suri D, Sun Q, Hersh M, Sargin D, *et al.* Hippocampal 5-HT input regulates memory formation and schaffer collateral excitation. Neuron 2018, 98: 992-1004.e4.

Neurosci. Bull. August, 2021, 37(8):1218–1233
https://doi.org/10.1007/s12264-021-00706-8

www.neurosci.cn
www.springer.com/12264

REVIEW

Evolving Models and Tools for Microglial Studies in the Central Nervous System

Yang Zhang[1,2] · Donghong Cui[1,2]

Received: 13 October 2020 / Accepted: 27 December 2020 / Published online: 9 June 2021

Abstract Microglia play multiple roles in such processes as brain development, homeostasis, and pathology. Due to their diverse mechanisms of functions, the complex subclassifications, and the large differences between different species, especially compared with humans, very different or even opposite conclusions can be drawn from studies with different research models. The choice of appropriate research models and the associated tools are thus key ingredients of studies on microglia. Mice are the most commonly used animal models. In this review, we summarize *in vitro* and *in vivo* models of mouse and human-derived microglial research models, including microglial cell lines, primary microglia, induced microglia-like cells, transgenic mice, human-mouse chimeric models, and microglial replacement models. We also summarize recent developments in novel single-cell and *in vivo* imaging technologies. We hope our review can serve as an efficient reference for the future study of microglia.

Keywords Microglial cell lines · Primary microglia · Induced microglia-like cells · Transgenic mice · Human-mouse chimeric models · Microglial replacement · Single-cell technology · *In vivo* imaging

✉ Donghong Cui
manyucc@126.com

[1] Shanghai Mental Health Center, Shanghai Jiao Tong University School of Medicine, Shanghai 200030, China

[2] Shanghai Key Laboratory of Psychotic Disorders, Shanghai 201108, China

Introduction

Microglia are tissue-resident macrophages in the brain parenchyma, accounting for more than 5% of all glial cells in the human brain [1]. The proportion of microglia in the normal adult mouse brain varies from 5% to 12% depending on the region [2]. Unlike other neurons and glial cells in the brain that develop from the ectoderm, microglia are derived from the yolk sac [3]. Taking mice as an example, their microglia originate from the erythro-myeloid progenitors of the yolk sac around embryonic day 7.25 (E7.25), earlier than the appearance of other glial cells, and have the potential for primitive erythropoiesis [4]. They migrate into the central nervous system (CNS) when neural progenitor cells begin to divide and form neurons, just before definitive hematopoiesis begins [5, 6]. Mononuclear cells derived from blood do not enter the brain through the blood-brain barrier (BBB) under normal physiological conditions. Under neuroinflammatory and neurodegenerative pathological conditions, peripheral myeloid cells can invade the brain through the BBB [7].

Microglial activation plays a major role in the brain's immune response and is an important indicator of immune activation and neuroinflammation [8]. In addition to participating in immune regulation, microglia contribute largely to brain development during embryonic and perinatal periods. They are pioneers in the developing brain and regulate the establishment of neural circuits. Microglia can regulate the growth and development of dopaminergic axons and the migration of interneurons (especially parvalbumin-positive (PV+) interneurons) [9]. The absence or dysfunction of microglia can lead to an imbalance of the neural distribution at birth and postnatal inhibition/excitation balance disorder. Microglia regulate neurogenesis by actively promoting neuronal cell death and

eliminating neural precursor cells (NPCs) in the developing CNS [10–12]. Microglia also support the proliferation of NPCs and promote neuronal survival by releasing trophic factors [8, 13]. Besides, microglia play a key role in synaptic density and homeostasis regulation by engulfing synapses, which can mediate synapse elimination [14]. Furthermore, microglia are vital in the pathological processes of neuropsychiatric disorders such as depression, schizophrenia, neurodevelopment disorders such as autism spectrum disorders, neurodegenerative diseases such as Alzheimer's disease (AD), and also stroke [15–19]. In short, microglia are involved in the development of the brain and the processes of various CNS diseases. The study on the role and mechanism of microglia has received a lot of attention recently.

However, there are still many unresolved questions and obstacles in the field of microglial research. There are many controversies and uncertainties about the conclusions of existing research in this field, such as the development and classification of microglia, the mechanisms of microglial action in different physiological processes, the determinants of CNS-associated macrophages (CAMs) differentiating from microglia in the development, function, and dynamics. The differences between microglia of different species also bring uncertainty to the research results. Although microglia of different species do share some basic similarities, research using animal models sometimes do not encompass the complexity of the human condition [20]. So, choosing the appropriate research program and model is the key to studying microglia. Our review comprehensively introduces the current models and tools used in microglial research, from traditional 2D culture to 3D culture and then to *in vivo* models, from single-cell technology to *in vivo* imaging technology. The applicability and advantages and disadvantages of these tools are discussed. The combination of these emerging technologies provides the possibility to explore the spatiotemporal characteristics of microglia and their heterogeneity in different physiological and pathological conditions at the single-cell level. Our discussion may inspire readers to develop new research approaches to microglia and answer those key questions.

In Vitro Microglial Models

Microglial Cell Lines

The characterization of human cells has been limited due to the restricted availability of primary sources of human microglia. So human immortalized microglial cell lines are important tools for studying the characteristics of microglia. The human microglia clone 3 cell line (HMC3 or HMC-3), also under the name of CHME-3, CHME-5, or C13-NJ among different laboratories, was established through SV40-dependent immortalization of a human fetal brain-derived primary microglial cell culture [21]. HMC3 cells retain most of the original antigenic properties and express many specific microglial markers. They strongly express the microglia/macrophage marker IBA1 (ionized calcium binding adapter molecule 1) at rest, and MHC II (major histocompatibility complex class II), CD68, CD11b, and other markers after being activated. Other commonly used human-derived microglial cell lines include HMO6 and HM1900. These cells also retain a similar antigenic profile and similar functional properties. They are capable of responding to a pattern of chemokines and inflammatory stimuli, regulating the expression of typical activation markers of microglia. Mouse immortalized microglial cell lines have also been established. The SIM-A9 cell line is a spontaneously immortalized cell line derived from mouse primary microglial cell cultures [22]. It expresses microglial markers such as CD68 and IBA1 and exhibits phagocytic activity under inflammatory stimulation. Other mouse immortalized microglial cell lines include BV-2, N9, and C8-B4. Using immortalized microglial cell lines for research can shorten the experimental period and cost of microglial cell cultures, and the cell uniformity is high. However, microglial cell lines are *in vitro* models. And after conversion to immortalization, their characteristics also change somewhat compared with *in vivo* microglia.

Primary Microglial Cells

Primary mouse microglia are widely used in microglia-associated studies. The current acquisition of primary mouse microglia is based on the cultivation of mixed glial cells [23]. After isolating the target brain region and digesting it into a single-cell suspension, cells are cultured in the glial culture medium and gradually adhere to the wall and fuse. The mixed glial cells are cultured for about 14 days, and the upper microglia are harvested by gentle trypsin digestion or shaking on a shaker. This method has strict requirements on the time window. Usually, newborn mice at postnatal 1–4 days are taken. But microglia are not fully mature at this time; they behave differently from adult microglia. A second method has been optimized with the addition of immuno-magnetic cell sorting steps [24], which select microglia by specific antibodies to recognize microglia-specific surface antigens such as CD11b. This second method can also be used for the screening and subsequent cultivation of adult mouse microglia. Another method for isolating and culturing primary microglia of adult mice is purifying the digested mixed brain cells by density gradient centrifugation and adding GM-CSF [granulocyte-macrophage colony-stimulating factor, or colony

stimulating factor 2 (CSF2)] to the culture medium [25]. The purity of primary microglia obtained by these methods is generally 95%–99%. Caution should be taken that there are other subsets of macrophages residing in the brain: CNS border-associated macrophages, which are also called CAMs, in the meninges, choroid plexus, and perivascular spaces [26]. These cells share several myeloid lineage-related properties in the CNS, and may be mixed into the microglia during the experimental manipulation and affect the research results. The serum is also an important factor affecting the culture of microglia because serum cannot penetrate the BBB and serum has drastic effects on cell morphology and function, leaving microglia in an activated state of inflammation. So, serum-free medium is recommended in microglial cell culture to mimic the *in vivo* state. Primary microglial cell culture has been used for decades to study their function. However, cultured primary microglia is only a poor model to investigate ramified microglia. Various electrophysiological and genetic studies have provided evidence that primary microglia lose many of their functions compared to cells *in vivo* and are more closely related to activated peripheral macrophages [27].

Human brain tissue is usually derived from elderly and diseased autopsy brains when such material is available. Immunohistochemical staining for certain microglial markers (like Iba1 and Ki-M1P) on autopsy brain tissue, can detect changes in the number and activity of microglia and help to characterize the pathogenic role of microglia in these diseases [28]. Alternative sources to autopsy include surgically excised and fetal brain tissues [29–31], but these tissues are more difficult to obtain due to ethical issues. Isolating microglia from human brain tissue through a rapid autopsy program can be used in primary culture and subsequent research [32]. After enzymatic digestion, using density gradient centrifugation to separate the cell layer containing microglia, and then pure microglia can be obtained by their characteristic strong and rapid attachment to plastic culture surfaces while the other cell types require coating matrices to attach. These isolated microglia can be phenotypically heterogeneous, so experiments using cells from different preparation procedures and brain regions may produce discordant results. When there are enough cases, using the same cell acquisition procedure from the same brain regions, one can still study the impact of age, disease, and treatment on the morphology and function of microglia.

Induced Microglia-like Cells

Since the technology of human induced-pluripotent stem cells (iPSCs) came out in 2007 [33, 34], they have been widely used in disease modeling, drug screening, and disease treatment. iPSCs possess multiple differentiation potentials and their expansion can be scaled up easily *in vitro*. But it was not until the last few years that human induced microglia-like cell (iMGL), also named pluripotent stem cell-derived microglia-like cell (pMGL) technology was realized (Fig. 1A).

One technique is based on the belief that only when iPSCs are differentiated into hematopoietic progenitor cells (iHPCs) first and then differentiated into microglia, they can recapitulate the true ontogeny of microglia [35]. This two-step protocol effectively generates iMGLs from iPSCs in more than 5 weeks. First of all, iPSCs are grown in defined conditions with several hematopoietic growth factors under certain oxygen concentrations (5% for 4 days and 20% for 6 days). This yields primitive $CD43^+$/$CD235a^+$/$CD41^+$ iHPCs by 10 days with a $> 90\%$ purity. These iHPCs represent the early primitive hematopoietic cells derived from the yolk sac that give rise to microglia. Secondly, $CD43^+$ iHPCs are cultured in serum-free differentiation medium containing CSF-1, IL-34, and TGFβ1. On day 14, induced cells present an early commitment to the fate of microglia and are similar to the developing microglial progenitor cells found *in vivo*. On day 38, iMGLs seem to resemble human microglia rather than monocytes or macrophages by cytospin/Giemsa staining. As iMGLs mature, they also become more branched. Transcriptome analysis shows that the iMGLs induced by this method are highly similar to primary human microglia. In contrast to their respective iPSCs, genomic integrity is also maintained during differentiation. This approach outlines the ontogenesis of microglia and can be easily scaled up for high-content screening. Another two-stage protocol also first differentiates iPSCs into iHPCs, then into microglia-like cells by co-culture with astrocytes [36]. The cells induced in this way also have phenotypic, transcriptional, and *in vitro* functional characteristics of brain-derived microglia. Compared with the previous method, this method does not require specific changes in oxygen concentration during the induction process of iHPCs, which is more feasible for most laboratories.

The second scheme is to induce iPSCs to differentiate into embryoid bodies (EBs) first, and then continue to culture and isolate iMGLs [37]. Uniform clumps of iPSCs are transferred in ultra-low attachment plates and cultured in a fully defined serum-free neuroglial differentiation (NGD) medium. The components and concentrations of this medium match human cerebrospinal fluid and extra IL-34 and CSF1 are added. Formed EBs have two types of structure. One is composed of compact phase-bright neuralized spheroids, and the other is composed of large, expanding cystic bodies. The second type of EB is positive for VE-cadherin, c-kit CD41, and CD235a, which have been identified as markers of early yolk sac myelogenesis

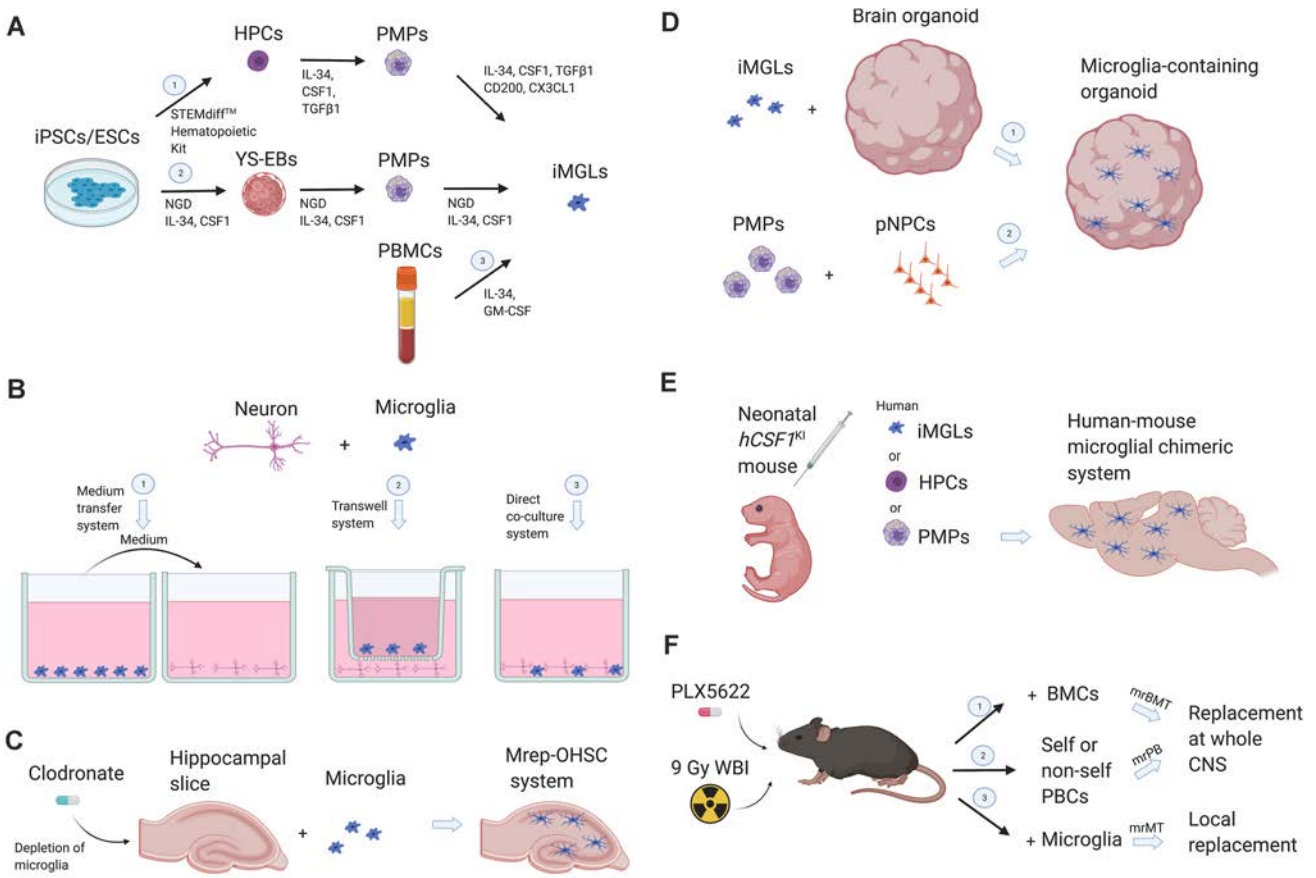

Fig. 1 Toolkits for studying microglial cells. **A** Strategies for developing human induced microglia-like cells: iPSCs/ESCs are differentiated into HPCs (top) or YS-EBs (middle) first to recapitulate the true ontogeny of microglia. Or, iMGLs are directly generated from PBMCs (bottom). **B** 2D co-culture systems of microglia and neurons have three different levels of cell-to-cell communication: Left, a conditioned medium transfer system in which no cell-to-cell contact or communication is possible; Center, a transwell system that allows cell-contact-independent communication through diffusible soluble factors; and Right, a co-culture system that permits direct contact of microglia and neurons. **C** Refilling the ramified microglia isolated from adult mouse brains into OHSC with microglia depleted, creates the Mrep-OHSC system. This system provides a situation that is very close to *in vivo*. Replenished microglia can integrate into the tissue and exhibit characteristics like their counterparts in the mouse brain. **D** Microglia-containing brain organoid system. Mature iMGLs are integrated into brain organoids that have been cultured for a long time. Or, pNPCs and PMPs are co-cultured to undergo differentiation and maturation together. In this 3D system, induced microglia-like cells extend varying degrees of ramified processes that resemble microglia *in vivo*. **E** The human-mouse chimeric microglial system provides a tool to study the role of human microglia *in vivo*. **F** Three efficient strategies for microglial replacement: microglial replacement by bone marrow transplantation (mrBMT), microglial replacement by peripheral blood (mrPB), and microglial replacement by microglial transplantation (mrMT). Abbreviations: NGD, serum-free neuroglial differentiation medium; YS-EBs, yolk sac embryoid bodies; PMPs, primitive macrophage progenitors or microglial precursors; pNPCs, primitive neural progenitor cells; iMGLs, human induced microglia-like cells; OHSCs, organotypic hippocampal slice cultures; Mrep-OHSCs, microglia-replenished OHSCs; iPSCs, induced pluripotent stem cells; ESCs, embryonic stem cells; PBMCs, peripheral blood mononuclear cells; BMCs, bone marrow cells; PBCs, peripheral blood cells; PLX5622, a CSF1R inhibitor; WBI, whole-body irradiation. The figure was created with BioRender.com.

in mice. Therefore, these EBs are referred to as yolk sac EBs (YS-EBs). Large domains of the YS-EBs are positive for myeloid transcription factor PU.1, which is necessary for microglial differentiation and maintenance. Every 5 days, the YS-EBs are triturated gently and cells of interest are selected for further culture. Attached cells are monitored for morphological characteristics of microglial precursors. iMGLs generated by this method are believed to faithfully recapitulate the expected ontogeny and characteristics of their *in vivo* counterparts, and they highly resemble primary human microglia. But the yield of this scheme is low.

There is also an alternative approach which directly induces iMGLs from peripheral blood mononuclear cells (PBMCs) simply by supplementing IL-34 and GM-CSF into PBMC culture medium [18, 38]. Cells can be harvested or used for functional assays in 10 days. This approach does not aim at representing the ontogeny of microglia. Cluster analysis shows that the iMGLs generated by this method are the closest to the gene expression

of human fetal primary microglia. This approach is simple and easy to operate, and does not need to repeat the complicated development process.

There are other reports on how to induce microglia-like cells [39–43]. For a further overview of methods for generating induced microglia-like cells, see Table 1. But actually, there is no gold standard for successful generation of induced microglia yet and no iMGLs can recapitulate all aspects of microglial characteristics. iMGL models based on patient-derived iPSCs can better reflect the patient's genetic background, but they can still not reflect the epigenetic or environmental factors' contribution to the pathophysiology of diseases. This is a rapidly developing field, and as single-cell sequencing provides more detailed information, researchers can determine the most accurate models that resemble a certain state of interest. But human iPSC-derived microglia under 2D culture condition are immature, and can best represent embryonic microglia. That is the rational microglia-containing brain organoid, and human-mouse microglial chimeric models are needed.

Co-culture of Microglial Cells and Other Cells/ Tissues

The co-culture model of microglia and neurons can be used in studying the interaction between microglia and neurons. Microglia and neurons can be co-cultured with three experimental systems involving different levels of cell-to-cell communication [44, 45]: (1) a conditioned medium transfer system in which no cell-to-cell contact or communication is possible, (2) a transwell system that allows cell-contact-independent communication only through diffusible soluble factors, and (3) a co-culture system that permits direct contact of microglia and neurons (Fig. 1B). These strategies can be used in investigating the roles of soluble and/or cell-associated chemokines in neuron-microglia interactions.

The *ex vivo* brain slice can retain important cell-to-cell interactions and is an important model for studying the activation and migration of parenchymal microglia [46]. However, the preparation of *ex vivo* brain slices causes trauma, especially damage of neuronal axons, resulting in microglia in brain slices having many of the same pathological damages that occur with serum exposure. Organotypic hippocampal slice culture (OHSC) is a well-accepted model in which to study different neurobiological aspects very close to the *in vivo* situation [47]. The Masuch team refilled the ramified microglia isolated from adult mouse brains into OHSC with microglia depleted, creating microglia-replenished OHSC (Mrep-OHSC) (Fig. 1C). Replenished microglia can integrate into the tissue, and the degree of ramification is no different from their counterparts in the mouse brain. Studies suggest that these replenished microglia maintain their original functions and properties as *in vivo*. This model is a unique tool for constructing chimeric brain slices allowing study of the function of different phenotypes of *in vivo*-like microglia in a tissue culture environment.

As noted in the last section, iPSC technologies are constantly evolving. And then, a new class of *in vitro* system—the 3D culture of brain organoids—has been improved [48]. This brain organoid can contain a variety of randomly distributed structures similar to different regions of the brain, or it can be directionally differentiated into the structure of a specific brain region. They can reproduce the process of the early development of the human brain. These models have been quickly applied to the study of human brain development and related diseases, and have achieved many results. Generally, iPSCs *in vitro* are stimulated to develop EBs. EBs are then subjected to neural induction in a minimal medium that only supports the development of neuroectoderm. The neuroectodermal tissues then gradually develop into mature brain organoids by enormous self-organizing capacity. This process determines that the brain organoid models do not contain microglia derived from the yolk sac. Therefore, researchers attempt to fuse brain organoids and microglia from various sources to build models for studying the role of microglia in human brain development, neurodegenerative diseases, and neuropsychiatric diseases (Fig. 1D). Abud *et al.* transplanted iMGLs into 3D human brain organoids to resemble microglia in the brain environment [35]. The limitation of their model is that integration of mature microglia and the organoid at a stage when neurons have already developed, which may not reflect the early embryonic development when microglial progenitors and neural progenitor cells (NPCs) interact with each other and undergo differentiation and maturation together. There is also a report that microglia can innately develop within a brain organoid model and display certain microglial characteristics [49]. However, due to the absence of SMAD (small mothers against decapentaplegic signaling) inhibition, the heterogeneity of cell types in these organoids is high and uncontrollable. Recently, Xu *et al.* generated developmentally appropriate and brain region-specific microglia-containing brain organoids by co-culturing hPSC-derived primitive macrophage progenitors (PMPs) and primitive neural progenitor cells (pNPCs) [50]. This model better mimics early neurodevelopmental processes observed in *in vivo* brain development and the ratio of microglia can be adjusted by controlling the starting number of pNPCs and PMPs. At present, the relevant technology threshold still is relatively high. And due to the problem of high heterogeneity of brain organoids, such technology needs to be further improved.

Table 1 Strategies for establishing human induced microglia-like cells

Name (reference)	Process of induction	Characteristics (including strength and weakness)	Additional information
pMGLs (Muffat *et al*. 2016 [37])	1. Form YS-EBs from iPSCs/ESCs 2. Microglial differentiation and maintenance	• Resemble primary human fetal microglia • Resemble yolk sac ontogeny • Can embed in neuronal co-culture environment • The organotypic 3D culture system cannot resemble *in vivo* environment	Cited in tMGs established by Claes *et al*. 2019 [43] (the last row in this table)
iMGLs (Abud *et al*. 2017 [35])	1. Differentiate iPSCs to iHPCs 2. Differentiate iHPCs to iMGLs	• Resemble primary human microglia • Resemble hematopoietic ontogeny • Need hypoxic conditions (5%) • Can integrate within 3D brain organoids • Can engraft into MITRG mice and act as microglia in the development	Associated kits are commercially available from STEMCELL Technologies Inc.; Improved into iPS-microglia 2.0 by McQuade *et al*. 2018 [42] (row 6 in this table, from the same lab); Cited in tMGs established by Claes *et al*. 2019 [43] (the last row in this table)
iPS-MG (Pandya *et al*. 2017 [36])	1. Differentiate iPSCs to iPS-HPCs 2. Co-culture with astrocytes and differentiate to iPS-MG	• Resemble primary human fetal microglia • Resemble hematopoiesis ontogeny • Need co-culture with astrocytes to induce final differentiation • 2D culture system cannot resemble *in vivo* environment	
iPSC-MG (Douvaras *et al*. 2017 [39])	1. Differentiate ESCs/iPSCs to myeloid progenitors 2. Continue to differentiate into ramified microglia	• Resemble primary human microglia • Resemble primitive hematopoiesis ontogeny • monoculture system cannot resemble *in vivo* environment	Cited in human-mouse microglial chimeras established by Svoboda *et al*. 2019 [86]
co-pMG (Haenseler *et al*. 2017 [40])	1. Form defined-size EBs from iPSCs 2. pMacpre differentiate from EBs 3. Differentiate iPSCs to pNeurons 4. Co-culture pMacpre with pNeurons	• Resemble primary human fetal microglia • Resemble yolk sac ontogeny • Need co-culture with neurons • 2D culture system cannot resemble *in vivo* environment	Cited in human-mouse microglial chimeras established by Xu *et al*. 2020 [85]; Cited in microglia-containing brain organoids established by Xu *et al*. 2020 [50]
iPS-microglia 2.0 (McQuade *et al*. 2018 [42])	1. Simplified differentiation of iPSCs/ESCs to HPCs 2. Updated differentiation of HPCs to iPS-microglia 2.0	• Equivalent to previously developed iPSC-microglia (Abud *et al*. 2017 [35]) • Do not need hypoxia or cell sorting • Can engraft into MITRG mice and enable *in vivo* study of human microglia	Cited in human-mouse microglial chimeras established by Hasselmann *et al*. 2019 [82] (from the same lab)
oMG (Ormel *et al*. 2018 [49])	1. iPSC generation 2. Microglia-containing organoid differentiation	• Resemble primary human adult microglia • Innately developing within cerebral organoids can mimic the CNS microenvironment • Heterogeneity is high and uncontrollable	
hiMG (Sellgren *et al*. 2017 [38])	1. Preparation of PBMCs from whole blood 2. Generation of hiMG from PBMCs	• Resemble primary human fetal microglia • Do not represent the ontogeny of microglia • The method is quick and convenient • 2D culture system cannot resemble *in vivo* environment	

Table 1 continued

Name (reference)	Process of induction	Characteristics (including strength and weakness)	Additional information
tMGs (Claes *et al*. 2019 [43])	1. Differentiate hPSCs to monocytes 2. Transdifferentiate monocytes to tMGs	• Resemble primary human microglia • Do not represent the ontogeny of microglia	Cited in human-mouse microglial chimeras established by Mancuso *et al*. 2019 [84] (from the same lab)

Abbreviations: ESCs, embryonic stem cells; pMGLs, pluripotent stem cell-derived microglia-like cells; iHPCs, iPSC-derived human hematopoietic progenitor cells; iMGLs, human microglia-like cells; iPS-HPCs, induced pluripotent stem cell-derived hematopoietic progenitor-like cells; iPS-MG, induced pluripotent stem cell-derived microglia-like cells; iPSC-MG, induced pluripotent stem cell-derived microglia; hiMG, human induced microglia-like cells; co-pMG, co-culture PSC microglia; pMacpre, PSC-derived macrophage precursors; pNeurons, PSC-derived cortical neurons; oMG, organoid-grown microglia; EBs, embryoid bodies; YS-EBs, yolk sac embryoid bodies; PBMCs, peripheral blood mononuclear cells; tMGs, transdifferentiated microglia-like cells.

In Vivo Microglial Models

Labeling of Microglia

Visualization is an important way to study microglia *in vivo*. Iba1 is a specific marker for microglia. *Iba1-EGFP* transgenic mice use an *Iba1* promoter fragment to control the expression of fluorescent reporter genes, which can effectively mark *in vivo* microglia [51]. The expression of EGFP can be detected from embryonic day 10.5 (E10.5) onwards, and strong EGFP signals appear in the yolk sac and the CNS ~E11.5. In recent years, *Cx3cr1*$^{+/GFP}$ transgenic mice have also been widely used to investigate the functions of microglia and other myeloid cells in the CNS [52]. CX3CR1 is the receptor of fractalkine and has been shown to be of great importance for the development of the CNS. The *Cx3cr1*$^{+/GFP}$ mouse line knocks the *EGFP* gene into the gene locus of *Cx3cr1* and can strongly label microglia. The colony-stimulating factor 1 receptor (CSF1R), also known as macrophage colony-stimulating factor receptor (MCSFR) and cluster of differentiation 115 (CD115), is a cell-surface protein encoded by the *Csf1r* gene and plays a vital role in the development and maintenance of macrophages. The "MacGreen" (*Csf1r-EGFP*) mouse line, which uses the *Csf1r* gene promoter element to control EGFP expression [53], as well as the "MacBlue" (*Csf1r-Gal4VP16/UAS-ECFP*) mouse line [54], both can be used to label microglia *in vivo*. However, whether it is IBA1, CX3CR1, or CSF1R, they are not expressed exclusively in microglia. That means fluorescent reporter genes are not only expressed in microglia but also in other cells of the monophagocytic system [55]. TMEM119 is a newly identified microglia-specific marker in both mice and humans [56]. It has better specificity to target microglia. The *Tmem119-EGFP* mouse line was generated and was shown to completely and faithfully label parenchymal microglia rather than other brain macrophages [57], and *Tmem119* mRNA is expressed throughout microglial development. The *Tmem119-EGFP* line can be used for early developmental studies of microglia.

Depletion of Microglia

The depletion of microglia is an effective model in which to study the regulatory function and activity of microglia in neurodevelopment. A model for knocking out microglia *in vivo* is CSF1R-deficient (*Csf1r*$^{-/-}$) mice [58]. microglia of this mouse line are practically completely knocked out during development, and these mice develop a disturbed brain architecture during the post-natal period. But these mice die a few weeks after birth. Surprisingly, it has been reported that CSF1R is also expressed in some neurons and has a protective effect on excitotoxic injury [59]. Therefore, *Csf1r*$^{-/-}$ mice may not only be devoid of microglia, but some neurons are also directly affected. The *CD11b-HSVTK* transgenic mouse is another model for ablating microglia [60]. CD11b is also known as ITGAM, αM integrin, or complement receptor 3 (CR3), and is specifically expressed in myeloid cells such as macrophages. This model uses the *CD11b* promoter to control the expression of herpes simplex virus thymidine kinase (HSVTK) so that HSVTK is exclusively expressed by microglia in the brain. Thymidine kinase can convert ganciclovir (GCV) into a cytotoxic kinase that can cause cell suicide. This means that ganciclovir exposure can induce the suicide of HSVTK-expressing microglia in *CD11b-HSVTK* transgenic mice. However, CD11b is also expressed in the circulatory system. Systemic ganciclovir administration can cause hematopoietic toxicity and lead to fatal aplastic anemia, which should be prevented by transplanting bone marrow cells from wild-type mice. However, this bone marrow chimeric mouse needs to receive whole-body radiation before transplantation, which causes damage to the BBB [61], so this model may not reflect the normal physiological state. One alternative method of ganciclovir administration is by intraventricular

injection to achieve partial removal of microglia in the cortex [62]. However, it should be noted that, as an antiviral drug, ganciclovir itself has an effect on the immune response. It has been shown to significantly inhibit the proliferation and activity of microglia in certain diseases, which may have an impact on microglial research [63]. Another method of selectively depleting microglia involves the use of *DTR* transgenic mice in which the human diphtheria toxin receptor (DTR) is expressed under the control of the *CD11b* promoter [64]. Localized injection of diphtheria toxin into the mice selectively ablates the microglia expressing human DTR. The number of microglia decreases significantly 12–24 h after diphtheria toxin treatment, but then gradually increases and returns to control levels at 36 h. Besides, transgenic mice targeting CD11c and PU.1 may be potential models for *in vivo* microglial study [65, 66]. However, due to their limitations, these models have not been widely used in the study of microglia.

There are also methods of using drugs to knock out microglia. Clodronate is such a drug which mediates apoptosis, but itself cannot penetrate cell membranes. It can be encapsulated in liposomes and then be engulfed by phagocytes. Once engulfed, the liposomes degrade and clodronate is released. This method was first used to selectively delete macrophages [67] but has now been used to deplete microglia. Clodronate liposomes are injected directly into the lateral ventricle of late embryonic rats, or clodronate liposomes are added to the culture medium of brain slices *in vitro* [10, 68]. The knock-out rate of microglia can reach 90% and 95%, respectively. CSF1R inhibitors are novel choices which can effectively deplete microglia in the CNS. PLX3397 is a small molecule CSF1R inhibitor. By oral gavage for consecutive 21 days, it can cross the mouse BBB and deplete $\sim$90% of $CD11b^{+}CD45^{int}$ microglia without significantly altering the number of monocytes or macrophages [69]. PLX5622 is another CSF1R inhibitor. It can achieve acute and near-complete microglial depletion within 3 days [70]. These pharmacological approaches to specifically deplete microglia have been used more commonly. It is worth noting that, since CSF1R is also expressed by myeloid cells including monocytes and macrophages, as CSF1R inhibitors, PLX5622 and PLX3397, have off-target effects, not only targeted on microglia.

Altering Gene Expression of Microglia

Alteration of gene expression in microglia *in vivo* is usually achieved through the *Cre-loxP* recombinase system. Using *CD11b-Cre* transgenic mice to hybridize with mice whose target gene is marked by *loxP* sites, can specifically knock out the target gene in cells expressing CD11b [71, 72]. Also, *CD11c-Cre*, *Csf1r-iCre*, *Csf1r-Mer-iCre-Mer*, $Cx3cr1^{Cre}$, and other transgenic mice may become potential research models for altering microglial gene expression [73–75]. This technique of altering microglial gene expression has the same problem as microglial labeling and knockout, that is, it is not specific to microglia. Besides, approaches of genetic targeting, including the approaches noted above, contain hidden risks. The integration process of inserting or deleting sequences can cause unpredictable consequences like mutations in coding regions and altering the expression of other genes, affecting non-coding genomic elements [76]. A 2016 paper identified the $Sall1^{CreER}$ line as another specific genetic mouse line for microglia-specific manipulation [77]. Sall1 was reported to be critical in maintaining the microglial core signature. In this mouse line, the Cre recombinase is under the control of the *Sall1* promoter and is expressed under tamoxifen induction. It should be noted that although *Sall1* is expressed largely by microglia but not peripheral myeloid cells or other adult CNS-resident cells, its expression can be detected in liver, kidney, and neuronal and glial progenitors in the CNS during embryogenesis. The *Tmem119-CreERT2* line was also established to control gene expression in both adult and early postnatal microglia [57]. This line has better specificity but the Cre activity of this mouse line is still not 100% specific in microglia. There is low Cre activity in the choroid plexus and blood monocytes. Researchers have newly identified hexosaminidase subunit beta (*Hexb*) as a core gene stably expressed by microglia both during homeostasis and disease [78]. They applied CRISPR/Cas9 genome editing to develop new transgenic mouse models for visualizing and altering the gene expression of microglia under the control of the *Hexb* promoter. These models can discriminate microglia from CAMs at the genetic level and stably monitor microglial behavior *in vivo*.

Recombinant viruses are important tools for manipulating gene expression in *in vivo* models and can achieve cell type-specific gene expression regulation in a short time. In neuroscience, viral targeting strategies have been successful in neurons, astrocytes, and oligodendrocytes. Although microglia are refractile to viruses, there have also been numerous attempts to achieve the viral transduction of microglia. Lentiviruses and adeno-associated viruses (AAVs) are preferentially selected because they have low immunogenicity. One study demonstrated that a capsid-modified rAAV6 expresses the transgene under the control of microglia-specific promoters (F4/80 or CD68) [79]. This rAAV6 capsid variant has triple mutations (Y731F/Y705F/T492V) which prevent proteasomal degradation when AAV escapes the endosomal compartment and has high tropism for monocytes. Researchers report a high transduction efficiency in primary microglia, but low specificity

when injected into the mouse brain. One approach for enhancing viral selectivity toward a specific type of cell is by posttranscriptional regulation. *Via* inserting complementary miRNA target sites into the transgene cassette, transgene messenger RNA degrades specifically in cells expressing the miRNA. It has been reported that murine microglia lack microRNA-9 (miR-9) activity, whereas most other cells with a neuroectodermal origin in the brain express miR-9. Injection of miR-9-regulated lentivirus vectors into the striatum of adult rats induces expression of the GFP reporter gene mainly in ramified microglia [80], 75% of GFP-expressing cells co-label with the microglial marker IBA1. In general, it is still difficult to achieve high efficiency and high specificity for microglial transduction *in vivo* and available approaches are very limited. As a type of immune cell, the resistance to virus infection of microglia may be due to their functions of detecting, engulfing, and destroying pathogens similar to macrophages [81]. Better viral vectors need to be designed so that can be used efficiently in microglial transduction.

Human-Mouse Chimeric Model

For a long time, there has been no experimental platform for systematic research and analysis of human microglia *in vivo*. The human-mouse microglial chimeric model emerged and has become an alternative solution (Fig. 1E). In 2019, Mathew Blurton-Jones's lab improved a chimeric method to study human microglia based on their previous study [82]. They used MITRG humanized immunodeficient mice to establish this chimeric model. This mouse line was constructed by knocking the genes of humanized *M-CSFh*, *IL-3/GM-CSFh*, and *TPOh* into BRG (Balb/c $Rag2^{-/-}$-$Il2rg^{-/-}$) immunodeficient mice through homologous recombination technology [83]. Since the survival of microglia is CSF1R signal-dependent, xenotransplantation of iPSC-derived iHPCs into the early postnatal brain of this MITRG mouse can cause their environment-dependent differentiation into microglia. They showed that the expression of hCSF2 (hGM-CSF) and hTPO are not necessary for xenotransplanted microglia (xMG); hCSF1 is both necessary and sufficient to enable long-term survival of xMG in the mouse brain. These xMGs have the transcriptome characteristics of human microglia *in vivo* and are responsive to both acute and chronic injuries. But a small population of the transplanted iHPCs was found to differentiate into other CNS macrophages. At a similar time, Bart De Strooper's lab also reported a chimeric model established by using other types of human cells and mouse lines [84]. hESCs were differentiated into microglia first before being transplanted. And the recipient $Rag2^{-/-}Il2r\gamma^{-/-}hCSF1^{KI}$ mice ($hCSF1^{KI}$) were pretreated with the CSF1R inhibitor BLZ945 to remove nearly half of the host microglia. Although most transplanted cells of this chimeric model mimic primary human microglia at the transcriptome level, some cells also showed a CAM expression profile. The hPSC-derived microglial chimeric mouse brain model developed by Peng Jiang's lab is also based on the human *CSF1* knock-in mouse line [85]. The transplanted cells are hPSC-derived primitive macrophage progenitors (PMPs). They tracked these engrafted cells for a longer time of 6 months. The vast majority of hPSC-derived PMPs differentiated into microglia and a relatively small population developed into CAMs or remained as progenitors. hPSC-derived microglia showed gradual maturation in a spatiotemporal manner. Rudolf Jaenisch's lab used NSG mice (NOD scid gamma mice), NSG-T mice (NSG mice carrying the humanized *IL3*, *SCF*, and *GM-CSF* genes; NSG-triples), and NSG-Q mice (NSG-T mice also carrying the humanized *CSF1* gene; NSG-quads) as recipients of their chimeric model [86]. And they also confirmed that human CSF1 is crucial for the survival and integration of transplanted human cells. The donor cells they used were hiPSC-derived iMPs (induced microglial precursors) or iMGs (induced microglia-like cells) which carry a GFP reporter for tracking. They found that iMPs more efficiently integrate into the mouse brain than iMGs. They explored the maturation process of transplanted iMPs. But they did not mention whether transplanted iMPs differentiated into other CNS macrophages. In summary, human-mouse chimeric models are new and potential tools for detecting the *in vivo* function of patient-derived or specific genetically modified microglia.

Replacement of Microglia

As shown above, the genetic manipulation of microglia has great limitations. Some scholars believe that exogenous microglial replacement may be an effective solution to this problem and a potential clinical treatment strategy. Varvel *et al*. established an irradiation-independent microglial replacement system *via* intracerebroventricular GCV treatment for 2 weeks in *CD11b-HSVTK* transgenic mice and assessed the peripheral origin of engrafted cells [87]. But in their further study, this model failed in AD therapy [88]. This raised the problem that whether myeloid-derived microglial replacement is not an effective therapeutic approach or whether those replaced microglia are exclusively from the bloodstream. Parabiosis is a surgical union of two organisms allowing sharing of the blood circulation [89]. Ajami *et al*. established a mouse blood-chimeric model by joining GFP-expressing transgenic mice and C57BL/6 wild-type mice in parabiosis [90]. They showed that the replacement of microglia by circulating precursors cannot be induced under physiological conditions. Huang *et al*. further validated that BBB disruption is not a

sufficient prerequisite for blood cells differentiating into microglia and repopulated microglia are derived from residual microglia by using the symbiotic mouse model [91]. Another method of microglial replacement is through bone marrow transplantation (BMT). Derecki *et al*. transplanted wild-type bone marrow into a lethally irradiated mouse model of Rett syndrome that resulted in engraftment of bone-marrow-derived microglia-like myeloid cells into brain parenchyma and helped to keep the disease from developing [92]. But a validation study does not support BMT-derived microglial replacement as therapy for Rett syndrome [93]. Although attempts to replace microglia are less successful in the treatment of diseases, researchers are still trying. Recently, Xu *et al*. developed three improved strategies and named them microglial replacement by bone marrow transplantation (mrBMT), microglial replacement by peripheral blood (mrPB), and microglial replacement by microglial transplantation (mrMT), which can effectively increase the replacement rate of microglia [94] (Fig. 1F). The prerequisite for the successful replacement of microglia is to make a microglia-free niche. The strategies in this study were to utilize the CSF1R inhibitor PLX5622 before giving 9 Gy whole-body irradiation (WBI) treatment. Because CSF1R is essential for microglial survival, two-week administration of PLX5622 can fully deplete CNS-resident microglia. mrBMT and mrPB can replace microglia-like cells at the CNS-wide scale, and the replacement rate can reach 92% and 80%, respectively. However, transcriptome analysis showed that the microglia-like cells derived from these two methods exhibited characteristics closer to those of macrophages. mrMT can replace endogenous microglia with exogenous microglia in specific brain regions of interest, with a local replacement rate of >50%. Transcriptome analysis shows that mrMT cells retain microglia-like characteristics. The researchers tested replacement cells of these 3 strategies by intraperitoneal injection of lipopolysaccharide and confirmed that these cells retain the environmental surveillance function as CNS-resident immune cells. But no other functions of microglia were tested. And the researchers did not test the therapeutic potentials on diseases. The clinical application of microglial replacement may still have a long way to go.

Tools for Microglial Studies

Single-Cell Techniques

Microglia participate in a wide range of physiological and pathological processes in the brain. From development to aging, from homeostasis to disease, microglia are highly heterogeneous. It is thought that different subpopulations of microglia may play a role in different events, and the expression profile of microglia also changes in different responses. However, in the past, the classification of microglia was relatively simple, mainly based on their morphology, density, surface marker expression, and electrophysiological characteristics. Single-cell RNA sequencing (scRNA-seq) is a technology that has developed rapidly in recent years. It can analyze the complex heterogeneity of cell populations by accurately identifying single cells and labeling them. This method prevents the biologically relevant signals of a single cell from being obscured by the average measurement data of a large number of cells. Single-cell transcriptome sequencing of brain tissues from different regions, different developmental stages, and different physiological and pathological characteristics can obtain spatio-temporal specific and disease-related expression profiles of microglia, helping to describe the development, migration, and response processes of microglia, and may discover new subtypes of microglia [95]. The discovery of new biomarkers, such as the *Hexb* gene noted above, also benefited from the use of massively parallel single-cell sequencing technology [78]. Single-cell sequencing can be used not only for transcriptome analysis but also for studying epigenetic modifications and protein-protein interactions. The problem with this technique is that a single cell suspension is needed first. For tissue cells, the cell state and acute expression may change due to environmental changes and cell damage caused by the process of cell dissociation. And fresh human brain tissue is difficult to obtain. Single-nucleus RNA sequencing (snRNA-seq) is an alternative to scRNA-seq as it allows transcriptomic profiling of frozen human brain tissue. Studies have used snRNA-seq to assess changes in expression in multiple cell lineages from frozen post-mortem brain tissue of multiple sclerosis (MS) and AD and found transcriptomic changes in the microglia in these diseases [96, 97]. Gerrits *et al*. compared cellular *versus* nuclear transcriptomes from fresh and frozen human brain samples and demonstrated that microglial nuclear RNAs obtained from CNS tissue are a reliable proxy for microglial gene expression [98]. But Thrupp *et al*. put forward that snRNA-seq is not suitable for the detection of microglial activation genes in human frozen biopsy tissues [99]. They demonstrated that although there are only a small set of genes (1.1% of the gene population) is depleted in nuclei relative to cells in human microglia by using snRNA and scRNA sequencing, this population is enriched for microglial activation genes. Further improvements in snRNA-seq library preparation may possibly acquire better sensitivity and resolution of the nuclear transcriptome.

Another emerging single-cell technology is cytometry by time-of-flight mass spectrometry (CyTOF) [100]. This is a revolutionary technology merging conventional flow cytometry and mass spectrometry with more than 50

different surface markers, which can deeply profile the immune phenotype of small samples at the single-cell level. Böttcher *et al*. used this method to simultaneously measure multiple samples from different donors and brain regions, and compare them with cells from other compartments at the same time to study the heterogeneity of microglia [101]. This single-cell technique can help establish a more comprehensive molecular view of microglia, making it possible to identify novel markers, pathways, and regulators that are critical to their development, health, and disease. Moreover, by a combination of scRNA-seq with CyTOF, Sankowski *et al*. identified diverse functional states of human microglia and demonstrated microglial spatial diversity during homeostasis and disease [102].

While scRNA-seq and CyTOF give a comprehensive molecular characterization of a population of cells, they do not provide the *in situ* spatial information of the brain during homeostasis and disease progression. Both changes in molecular profiling and morphological transformations serve as a read-out of microglial functional changes. Salamanca *et al*. developed an automated pipeline named Microglia and Immune Cells Morphologies Analyser and Classifier (MIC-MAC) [103]. It specializes in accurately reconstructing and classifying 3D microglial morphologies at the single-cell level in more complex human postmortem samples. In the future, by combining this unbiased high-throughput imaging technology with other single-cell technologies, the spatial information of heterogenous microglia in health and disease can be more enriched.

In Vivo Imaging Techniques

Live imaging can help to elucidate the precise functions and responses of cells *in vivo*. Transcranial two-photon imaging of GFP-labeled microglia reveals their rapid dynamics and response to traumatic injuries in the mouse brain [104]. Wu's lab has further revealed that the mechanism of microglia-neuron communication depends on neuronal NMDA receptors and microglial P2Y12 receptors through two-photon time-lapse imaging techniques [105]. They also documented a daily rearrangement of the microglial landscape using chronic *in vivo* two-photon imaging and show that the microglial landscape can be modulated by various pathological states [106]. A recent study identified an interaction site between microglial processes and neuronal cell bodies by *in vivo* two-photon imaging [107]. Combined with STORM super-resolution microscopy, high-resolution electron tomography, and other techniques, they further discovered that microglia-neuron junctions have a specialized nanoarchitecture optimized for purinergic signaling. Three-photon imaging is a revolutionary non-invasive method for investigating deep brain structures in live and behaving animals [108]. It can be a potential tool for *in vivo* imaging of subcortical microglia within an intact mouse brain.

Calcium imaging is an method based on calcium shifts operated by different intracellular and extracellular mechanisms [109]. It has been widely used in studies in various brain cells. However, the knowledge about *in vivo* calcium signaling in microglia has been lacking since microglia largely resist attempts of *in vivo* labeling that are routinely used for *in vivo* calcium imaging of other cell types [110]. Tvrdik *et al*. used a Cre-dependent conditional mouse reporter of calcium, which facilitates the deployment of genetically encoded calcium indicators, to cross with the *Iba1(Aif1)-IRES-Cre* mouse line [111]. Microglial calcium signals have been recorded through high-speed intravital two-photon laser scanning microscopy. This method effectively reflects changes in the intracellular free calcium concentration in large microglial cell populations.

Studies on human *in vivo* microglia have mainly been carried out by *in vivo* imaging. Activated microglia express a series of pro-inflammatory cytokines and certain receptors on their surface, including the 18 kDa translocator protein (TSPO), which has been identified as the peripheral-type benzodiazepine receptor (PBR). In mammalian brains, the expression of TSPO turns out to be very low. However, under conditions of local inflammatory responses caused by brain injuries, neoplasms, or infections, the expression of TSPO appears to be upregulated. This makes TSPO a potentially ideal and sensitive biomarker of brain injury. Therefore, translocator protein positron emission tomography (TSPO-PET) imaging has been developed and widely used to track microglial activation. Positive signals can be found in the early stages in patients with AD and other psychoses [112]. However, translocator protein is not expressed in microglia exclusively but also in reactive astrocytes and other proliferating cells. This has led to the development of numerous second-generation TSPO ligands such as the radioligand [^{11}C]PBR28 [113]. The total gray matter [^{11}C]PBR28 binding ratio is used as a marker of microglial activity. [^{11}C]PBR28 combined with PET imaging technology shows improved affinity and nonspecific binding properties.

Outlook

There are many classic and emerging research tools and technologies in the field of microglial research. In addition to rodents, animal models used to study microglia include non-human primates, other mammals, zebrafish, chickens, and *Drosophila* [114–117]. Human microglia have some basic similarities to their animal counterparts. For instance, they have some similar protein expression, such as IBA-1,

transcription factor PU.1, adaptor protein DAP12, and M-CSF receptor. But microglia of these animal models, including rodent models, have some properties of their own, and human microglia differ from these animals in many ways. For example, *in vitro* cultures of primary mouse microglia do not adhere to the wall but on the upper layer of astrocytes, while human primary microglia directly adhere to the surface of the culture dish [25, 32]. The proliferation of rodent microglia cultured *in vitro* is also inconsistent compared to humans, and evaluating the proliferation of human microglia *in vivo* is more complicated [20]. Due to biochemical differences, microglia in rodents and humans have different responses to drugs. In certain cases, the effects of drugs may even be in opposite directions. Taking valproic acid (VPA), a neuroactive drug clinically used to treat bipolar disorder and epilepsy, as an example, rodent studies have found that VPA selectively kills microglia through a caspase-3-dependent mechanism, while primary microglia in humans fail to activate caspase 3 or induce apoptosis. VPA can also increase the phagocytosis of rodent microglia, but it inhibits the phagocytic capacity of human primary microglia [118, 119]. A cross-species single-cell analysis revealed that human microglia exhibit significant heterogeneity compared to all other mammals, including primates [117]. The origin of microglia in different species is not unique as well. In mice, microglia are derived from primitive macrophages emanating from the embryonic yolk sac during development and sustain the microglial population locally by self-renewal [8, 120]. Zebrafish embryonic microglia initiate from the rostral blood island, which is similar to the yolk sac, while adult microglia in zebrafish arise from the ventral wall of the dorsal aorta [121]. Human hematopoiesis also starts in the yolk sac [122]. And human microglia originate similar to their rodent counterparts [123]. Therefore, it is very important and challenging to choose appropriate research tools and to improve the existing animal models. Only then the research results in alternative models can be translated into humans and even applied to clinical practice.

The patient-derived iMGL is an emerging tool with great potential to study the pathogenesis and therapeutic targets of microglia-related CNS diseases. Microglial markers and morphological identification, phagocytosis assay, migration assay, and cytokine and chemokine profile analysis are traditional experiments for microglial identification. But these methods are not precise enough at the transcriptome level and mainly target the inflammatory response function of microglia. Transcriptomic analysis, especially single-cell techniques, can better identify and analyze the microglia in different states. The iMGL models have been used to study mental illnesses such as schizophrenia and AD. It has been found that the abnormal engulfment and increased inflammatory responses of brain microglia may be the cause of various mental illnesses [18, 35]. But patient-derived iMGLs under traditional 2D culture are immature and can only represent embryonic microglia. The microglia-containing brain organoid and human-mouse microglial chimeric models can partially solve this problem by providing an environment that complex cell-to-cell or cell-matrix interactions exist. The 3D and *in vivo* models are becoming superior tools to study microglia in human CNS diseases [35, 50, 82, 84–86].

To study the origin and development of microglia, the role and mechanism of microglia in normal physiology and disease, the ultimate target is to carry out microglia-related drug development and clinical treatment. Eliminating the genetically defective microglia and transplanting genetically modified microglia is a possible direction for the treatment of microglia-related CNS diseases. Efficient microglial replacement has been achieved in mouse models though there is still a long way to go before it can be applied to humans. Metachromatic leukodystrophy (MLD) is a neurodegenerative lysosomal storage disease (LSD). A phase I/II clinical trial for MLD patients has shown that after transplantation of the genetically modified hematopoietic stem cells into the patients' CNS, these HSCs differentiate into microglia and then delay disease progress [124]. Microglial replacement has also been exploited to deliver therapeutics to X-linked adrenoleukodystrophy (X-ALD) and mucopolysaccharidosis (MPS) [125]. Transdifferentiation is another possible option. The approaches of converting glial cells like astrocytes into neurons of different subtypes *in vivo* have been achieved and have become a potential treatment option for some neurodegenerative diseases [126, 127]. When nerve injury occurs, innate microglia can rapidly multiply and recruit to the injury site. Based on these properties of microglia, if transdifferentiation of microglia into functional neurons *in vivo* could be realized, it would be a potential direction for the treatment of neurological damage and neurodegenerative diseases in the future.

Auxiliary tools for microglial research include mitochondrial energy metabolism analysis, genomic, proteomic, expression profile analysis, chemogenetic and optogenetic tools, electrophysiological recording, and behavioral analysis. Electrophysiological behaviors of microglia have been described both in cultured primary microglia and *in situ* microglia in acutely isolated brain slices [128, 129]. The ramified *in situ* microglia are distinct from their cultured counterparts. Even in the same acute cerebral slices from an AD mouse model, microglia show plaque-associated electrophysiological heterogeneity [130]. Chemogenetic and optogenetic tools are highly prevalent in neuronal studies. But these techniques have not been widely applied to microglia, perhaps due to

microglial resistance to viral vectors. Recently, Yi *et al*. used transgenic mice to enable selective expression of inhibitory Designer Receptors Exclusively Activated by Designer Drugs (Gi DREADD) in microglia [131]. This chemogenetic approach in microglia can inhibit neuroinflammation and neuropathic pain in mice. In the future, with the development of effective targeting strategies for microglia, opto/chemogenetic tools could be broadly used in microglial research. Combination of RNAseq profiling, *in situ* hybridization, or mass cytometry together with high-throughput imaging technologies can help to enrich the spatial information of heterogenous microglia at the single-cell level. Studies of microglia can also benefit from various interdisciplinary approaches, like physics, mathematics, chemistry, information science, and artificial intelligence, to help develop new technologies, models, and tools. We expect significant progress and breakthroughs will be made in the field of microglial research in the near future.

Acknowledgments This review was supported by grants from the National Key Research and Development Program of China (2017YFC0909200), the National Natural Science Foundation of China (81671336), Shanghai Key Laboratory of Psychotic Disorders (YG2016ZD06), and the Shanghai Mental Health Center (2019-YJ06).

Conflict of interest All authors claim that there is no conflict of interest.

References

1. Pelvig DP, Pakkenberg H, Stark AK, Pakkenberg B. Neocortical glial cell numbers in human brains. Neurobiol Aging 2008, 29: 1754–1762.
2. Lawson LJ, Perry VH, Dri P, Gordon S. Heterogeneity in the distribution and morphology of microglia in the normal adult mouse brain. Neuroscience 1990, 39: 151–170.
3. Tay TL, Savage JC, Hui CW, Bisht K, Tremblay MÈ. Microglia across the lifespan: From origin to function in brain development, plasticity and cognition. J Physiol 2017, 595: 1929–1945.
4. Ginhoux F, Greter M, Leboeuf M, Nandi S, See P, Gokhan S. Fate mapping analysis reveals that adult microglia derive from primitive macrophages. Science 2010, 330: 841–845.
5. Hirbec H, Déglon N, Foo LC, Goshen I, Grutzendler J, Hangen E, *et al.* Emerging technologies to study glial cells. Glia 2020, 68: 1692–1728.
6. Prinz M, Jung S, Priller J. Microglia biology: One century of evolving concepts. Cell 2019, 179: 292–311.
7. Cronk JC, Filiano AJ, Louveau A, Marin I, Marsh R, Ji E, *et al.* Peripherally derived macrophages can engraft the brain independent of irradiation and maintain an identity distinct from microglia. J Exp Med 2018, 215: 1627–1647.
8. Nayak D, Roth TL, McGavern DB. Microglia development and function. Annu Rev Immunol 2014, 32: 367–402.
9. Squarzoni P, Oller G, Hoeffel G, Pont-Lezica L, Rostaing P, Low D, *et al.* Microglia modulate wiring of the embryonic forebrain. Cell Rep 2014, 8: 1271–1279.
10. Cunningham CL, Martínez-Cerdeño V, Noctor SC. Microglia regulate the number of neural precursor cells in the developing cerebral cortex. J Neurosci 2013, 33: 4216–4233.
11. Mallat M, Marín-Teva JL, Chéret C. Phagocytosis in the developing CNS: More than clearing the corpses. Curr Opin Neurobiol 2005, 15: 101–107.
12. Marín-Teva JL, Cuadros MA, Martín-Oliva D, Navascués J. Microglia and neuronal cell death. Neuron Glia Biol 2011, 7: 25–40.
13. Chounchay S, Noctor SC, Chutabhakdikul N. Microglia enhances proliferation of neural progenitor cells in an *in vitro* model of hypoxic-ischemic injury. EXCLI J 2020, 19: 950–961.
14. Schafer DP, Lehrman EK, Kautzman AG, Koyama R, Mardinly AR, Yamasaki R, *et al.* Microglia sculpt postnatal neural circuits in an activity and complement-dependent manner. Neuron 2012, 74: 691–705.
15. Hong S, Beja-Glasser VF, Nfonoyim BM, Frouin A, Li S, Ramakrishnan S, *et al.* Complement and microglia mediate early synapse loss in Alzheimer mouse models. Science 2016, 352: 712–716.
16. Kim HJ, Cho MH, Shim WH, Kim JK, Jeon EY, Kim DH, *et al.* Deficient autophagy in microglia impairs synaptic pruning and causes social behavioral defects. Mol Psychiatry 2017, 22: 1576–1584.
17. Brites D, Fernandes A. Neuroinflammation and depression: Microglia activation, extracellular microvesicles and microRNA dysregulation. Front Cell Neurosci 2015, 9: 476.
18. Sellgren CM, Gracias J, Watmuff B, Biag JD, Thanos JM, Whittredge PB, *et al.* Increased synapse elimination by microglia in schizophrenia patient-derived models of synaptic pruning. Nat Neurosci 2019, 22: 374–385.
19. Qin C, Zhou LQ, Ma XT, Hu ZW, Yang S, Chen M, *et al.* Dual functions of microglia in ischemic stroke. Neurosci Bull 2019, 35: 921–933.
20. Smith AM, Dragunow M. The human side of microglia. Trends Neurosci 2014, 37: 125–135.
21. Dello Russo C, Cappoli N, Coletta I, Mezzogori D, Paciello F, Pozzoli G, *et al.* The human microglial HMC3 cell line: Where do we stand? A systematic literature review. J Neuroinflammation 2018, 15: 259.
22. Nagamoto-Combs K, Kulas J, Combs CK. A novel cell line from spontaneously immortalized murine microglia. J Neurosci Methods 2014, 233: 187–198.
23. Floden AM, Combs CK. Microglia repetitively isolated from *in vitro* mixed glial cultures retain their initial phenotype. J Neurosci Methods 2007, 164: 218–224.
24. Gordon R, Hogan CE, Neal ML, Anantharam V, Kanthasamy AG, Kanthasamy A. A simple magnetic separation method for high-yield isolation of pure primary microglia. J Neurosci Methods 2011, 194: 287–296.
25. Moussaud S, Draheim HJ. A new method to isolate microglia from adult mice and culture them for an extended period of time. J Neurosci Methods 2010, 187: 243–253.
26. Utz SG, See P, Mildenberger W, Thion MS, Silvin A, Lutz M, *et al.* Early fate defines microglia and non-parenchymal brain macrophage development. Cell 2020, 181: 557–573.e18.
27. Biber K, Owens T, Boddeke E. What is microglia neurotoxicity (Not)? Glia 2014, 62: 841–854.
28. Bergner CG, van der Meer F, Winkler A, Wrzos C, Türkmen M, Valizada E, *et al.* Microglia damage precedes major myelin breakdown in X-linked adrenoleukodystrophy and metachromatic leukodystrophy. Glia 2019, 67: 1196–1209.
29. Nagai A, Mishima S, Ishida Y, Ishikura H, Harada T, Kobayashi S, *et al.* Immortalized human microglial cell line: Phenotypic expression. J Neurosci Res 2005, 81: 342–348.

30. Williams K, Bar-Or A, Ulvestad E, Olivier A, Antel JP, Yong VW. Biology of adult human microglia in culture: Comparisons with peripheral blood monocytes and astrocytes. J Neuropathol Exp Neurol 1992, 51: 538–549.
31. McLarnon JG, Helm J, Goghari V, Franciosi S, Choi HB, Nagai A, *et al.* Anion channels modulate store-operated calcium influx in human microglia. Cell Calcium 2000, 28: 261–268.
32. Lue LF, Beach TG, Walker DG. Alzheimer's disease research using human microglia. Cells 2019, 8: 838.
33. Takahashi K, Tanabe K, Ohnuki M, Narita M, Ichisaka T, Tomoda K, *et al.* Induction of pluripotent stem cells from adult human fibroblasts by defined factors. Cell 2007, 131: 861–872.
34. Yu J, Vodyanik MA, Smuga-Otto K, Antosiewicz-Bourget J, Frane JL, Tian S, *et al.* Induced pluripotent stem cell lines derived from human somatic cells. Science 2007, 318: 1917–1920.
35. Abud EM, Ramirez RN, Martinez ES, Healy LM, Nguyen CHH, Newman SA, *et al.* iPSC-derived human microglia-like cells to study neurological diseases. Neuron 2017, 94: 278–293.e9.
36. Pandya H, Shen MJ, Ichikawa DM, Sedlock AB, Choi Y, Johnson KR, *et al.* Differentiation of human and murine induced pluripotent stem cells to microglia-like cells. Nat Neurosci 2017, 20: 753–759.
37. Muffat J, Li Y, Yuan B, Mitalipova M, Omer A, Corcoran S, *et al.* Efficient derivation of microglia-like cells from human pluripotent stem cells. Nat Med 2016, 22: 1358–1367.
38. Sellgren CM, Sheridan SD, Gracias J, Xuan D, Fu T, Perlis RH. Patient-specific models of microglia-mediated engulfment of synapses and neural progenitors. Mol Psychiatry 2017, 22: 170–177.
39. Douvaras P, Sun B, Wang M, Kruglikov I, Lallos G, Zimmer M, *et al.* Directed differentiation of human pluripotent stem cells to microglia. Stem Cell Reports 2017, 8: 1516–1524.
40. Haenseler W, Sansom SN, Buchrieser J, Newey SE, Moore CS, Nicholls FJ, *et al.* A highly efficient human pluripotent stem cell microglia model displays a neuronal-co-culture-specific expression profile and inflammatory response. Stem Cell Reports 2017, 8: 1727–1742.
41. Beutner C, Roy K, Linnartz B, Napoli I, Neumann H. Generation of microglial cells from mouse embryonic stem cells. Nat Protoc 2010, 5: 1481–1494.
42. McQuade A, Coburn M, Tu CH, Hasselmann J, Davtyan H, Blurton-Jones M. Development and validation of a simplified method to generate human microglia from pluripotent stem cells. Mol Neurodegener 2018, 13: 67.
43. Claes C, Van Den Daele J, Boon R, Schouteden S, Colombo A, Monasor LS, *et al.* Human stem cell-derived monocytes and microglia-like cells reveal impaired amyloid plaque clearance upon heterozygous or homozygous loss of TREM2. Alzheimers Dement 2019, 15: 453–464.
44. Zujovic V, Taupin V. Use of cocultured cell systems to elucidate chemokine-dependent neuronal/microglial interactions: Control of microglial activation. Methods 2003, 29: 345–350.
45. Roqué PJ, Costa LG. Co-culture of neurons and microglia. Curr Protoc Toxicol 2017, 74: 11.24.1–11.24.17.
46. Petersen MA, Dailey ME. Diverse microglial motility behaviors during clearance of dead cells in hippocampal slices. Glia 2004, 46: 195–206.
47. Masuch A, van der Pijl R, Füner L, Wolf Y, Eggen B, Boddeke E, *et al.* Microglia replenished OHSC: A culture system to study *in vivo* like adult microglia. Glia 2016, 64: 1285–1297.
48. Lancaster MA, Knoblich JA. Generation of cerebral organoids from human pluripotent stem cells. Nat Protoc 2014, 9: 2329–2340.
49. Ormel PR, Vieira de Sá R, van Bodegraven EJ, Karst H, Harschnitz O, Sneeboer MAM, *et al.* Microglia innately develop within cerebral organoids. Nat Commun 2018, 9: 4167.
50. Xu R, Boreland AJ, Li X, Erickson C, Jin M, Atkins C, *et al.* Developing human pluripotent stem cell-based cerebral organoids with a controllable microglia ratio for modeling brain development and pathology. bioRxiv 2020. https://doi.org/10.1101/2020.10.09.331710.
51. Hirasawa T, Ohsawa K, Imai Y, Ondo Y, Akazawa C, Uchino S, *et al.* Visualization of microglia in living tissues using Iba1-EGFP transgenic mice. J Neurosci Res 2005, 81: 357–362.
52. Jung S, Aliberti J, Graemmel P, Sunshine MJ, Kreutzberg GW, Sher A, *et al.* Analysis of fractalkine receptor CX_3CR1 function by targeted deletion and green fluorescent protein reporter gene insertion. Mol Cell Biol 2000, 20: 4106–4114.
53. Sasmono RT, Oceandy D, Pollard JW, Tong W, Pavli P, Wainwright BJ, *et al.* A macrophage colony-stimulating factor receptor-green fluorescent protein transgene is expressed throughout the mononuclear phagocyte system of the mouse. Blood 2003, 101: 1155–1163.
54. Ovchinnikov DA, van Zuylen WJ, DeBats CE, Alexander KA, Kellie S, Hume DA. Expression of Gal4-dependent transgenes in cells of the mononuclear phagocyte system labeled with enhanced cyan fluorescent protein using Csf1r-Gal4VP16/UAS-ECFP double-transgenic mice. J Leukoc Biol 2008, 83: 430–433.
55. Wieghofer P, Prinz M. Genetic manipulation of microglia during brain development and disease. Biochim Biophys Acta 2016, 1862: 299–309.
56. Bennett ML, Bennett FC, Liddelow SA, Ajami B, Zamanian JL, Fernhoff NB, *et al.* New tools for studying microglia in the mouse and human CNS. Proc Natl Acad Sci U S A 2016, 113: E1738–E1746.
57. Kaiser T, Feng G. Tmem119-EGFP and Tmem119-CreERT2 transgenic mice for labeling and manipulating microglia. eNeuro 2019, 6. https://doi.org/10.1523/eneuro.0448-18.2019.
58. Erblich B, Zhu L, Etgen AM, Dobrenis K, Pollard JW. Absence of colony stimulation factor-1 receptor results in loss of microglia, disrupted brain development and olfactory deficits. PLoS One 2011, 6: e26317.
59. Luo J, Elwood F, Britschgi M, Villeda S, Zhang H, Ding Z, *et al.* Colony-stimulating factor 1 receptor (CSF1R) signaling in injured neurons facilitates protection and survival. J Exp Med 2013, 210: 157–172.
60. Heppner FL, Greter M, Marino D, Falsig J, Raivich G, Hövelmeyer N, *et al.* Experimental autoimmune encephalomyelitis repressed by microglial paralysis. Nat Med 2005, 11: 146–152.
61. Mildner A, Schmidt H, Nitsche M, Merkler D, Hanisch UK, Mack M, *et al.* Microglia in the adult brain arise from Ly-6ChiCCR2+ monocytes only under defined host conditions. Nat Neurosci 2007, 10: 1544–1553.
62. Simard AR, Soulet D, Gowing G, Julien JP, Rivest S. Bone marrow-derived microglia play a critical role in restricting senile plaque formation in Alzheimer's disease. Neuron 2006, 49: 489–502.
63. Ding Z, Mathur V, Ho PP, James ML, Lucin KM, Hoehne A, *et al.* Antiviral drug ganciclovir is a potent inhibitor of microglial proliferation and neuroinflammation. J Exp Med 2014, 211: 189–198.
64. Ueno M, Fujita Y, Tanaka T, Nakamura Y, Kikuta J, Ishii M, *et al.* Layer V cortical neurons require microglial support for survival during postnatal development. Nat Neurosci 2013, 16: 543–551.
65. Goldmann T, Wieghofer P, Müller PF, Wolf Y, Varol D, Yona S, *et al.* A new type of microglia gene targeting shows TAK1 to

be pivotal in CNS autoimmune inflammation. Nat Neurosci 2013, 16: 1618–1626.
66. McKercher SR, Torbett BE, Anderson KL, Henkel GW, Vestal DJ, Baribault H, et al. Targeted disruption of the PU.1 gene results in multiple hematopoietic abnormalities. EMBO J 1996, 15: 5647–5658.
67. van Rooijen N, van Nieuwmegen R. Elimination of phagocytic cells in the spleen after intravenous injection of liposome-encapsulated dichloromethylene diphosphonate. An enzyme-histochemical study. Cell Tissue Res 1984, 238: 355–358.
68. Faustino JV, Wang X, Johnson CE, Klibanov A, Derugin N, Wendland MF, *et al.* Microglial cells contribute to endogenous brain defenses after acute neonatal focal stroke. J Neurosci 2011, 31: 12992–13001.
69. Li MS, Li ZG, Ren HL, Jin WN, Wood K, Liu Q, *et al.* Colony stimulating factor 1 receptor inhibition eliminates microglia and attenuates brain injury after intracerebral hemorrhage. J Cereb Blood Flow Metab 2017, 37: 2383–2395.
70. Acharya MM, Green KN, Allen BD, Najafi AR, Syage A, Minasyan H, *et al.* Elimination of microglia improves cognitive function following cranial irradiation. Sci Rep 2016, 6: 31545.
71. Ferron M, Vacher J. Targeted expression of Cre recombinase in macrophages and osteoclasts in transgenic mice. Genesis 2005, 41: 138–145.
72. Boillée S, Yamanaka K, Lobsiger CS, Copeland NG, Jenkins NA, Kassiotis G, *et al.* Onset and progression in inherited ALS determined by motor neurons and microglia. Science 2006, 312: 1389–1392.
73. Caton ML, Smith-Raska MR, Reizis B. Notch-RBP-J signaling controls the homeostasis of CD8- dendritic cells in the spleen. J Exp Med 2007, 204: 1653–1664.
74. Deng L, Zhou JF, Sellers RS, Li JF, Nguyen AV, Wang Y, *et al.* A novel mouse model of inflammatory bowel disease links mammalian target of rapamycin-dependent hyperproliferation of colonic epithelium to inflammation-associated tumorigenesis. Am J Pathol 2010, 176: 952–967.
75. Qian BZ, Li JF, Zhang H, Kitamura T, Zhang JH, Campion LR, *et al.* CCL2 recruits inflammatory monocytes to facilitate breast-tumour metastasis. Nature 2011, 475: 222–225.
76. Wieghofer P, Knobeloch KP, Prinz M. Genetic targeting of microglia. Glia 2015, 63: 1–22.
77. Buttgereit A, Lelios I, Yu X, Vrohlings M, Krakoski NR, Gautier EL, *et al.* Sall1 is a transcriptional regulator defining microglia identity and function. Nat Immunol 2016, 17: 1397–1406.
78. Masuda T, Amann L, Sankowski R, Staszewski O, Lenz M, D Errico P, et al. Novel Hexb-based tools for studying microglia in the CNS. Nat Immunol 2020, 21: 802–815.
79. Rosario AM, Cruz PE, Ceballos-Diaz C, Strickland MR, Siemienski Z, Pardo M, *et al.* Microglia-specific targeting by novel capsid-modified AAV6 vectors. Mol Ther Methods Clin Dev 2016, 3: 16026.
80. Åkerblom M, Sachdeva R, Quintino L, Wettergren EE, Chapman KZ, Manfre G, *et al.* Visualization and genetic modification of resident brain microglia using lentiviral vectors regulated by microRNA-9. Nat Commun 2013, 4: 1770.
81. Maes ME, Colombo G, Schulz R, Siegert S. Targeting microglia with lentivirus and AAV: Recent advances and remaining challenges. Neurosci Lett 2019, 707: 134310.
82. Hasselmann J, Coburn MA, England W, Figueroa Velez DX, Kiani Shabestari S, Tu CH, *et al.* Development of a chimeric model to study and manipulate human microglia *in vivo*. Neuron 2019, 103: 1016–1033.e10.
83. Rongvaux A, Willinger T, Martinek J, Strowig T, Gearty SV, Teichmann LL, *et al.* Development and function of human innate immune cells in a humanized mouse model. Nat Biotechnol 2014, 32: 364–372.
84. Mancuso R, Van Den Daele J, Fattorelli N, Wolfs L, Balusu S, Burton O, *et al.* Stem-cell-derived human microglia transplanted in mouse brain to study human disease. Nat Neurosci 2019, 22: 2111–2116.
85. Xu RJ, Li XX, Boreland AJ, Posyton A, Kwan K, Hart RP, *et al.* Human iPSC-derived mature microglia retain their identity and functionally integrate in the chimeric mouse brain. Nat Commun 2020, 11: 1577.
86. Svoboda DS, Barrasa MI, Shu J, Rietjens R, Zhang S, Mitalipova M, *et al.* Human iPSC-derived microglia assume a primary microglia-like state after transplantation into the neonatal mouse brain. Proc Natl Acad Sci U S A 2019, 116: 25293–25303.
87. Varvel NH, Grathwohl SA, Baumann F, Liebig C, Bosch A, Brawek B, *et al.* Microglial repopulation model reveals a robust homeostatic process for replacing CNS myeloid cells. Proc Natl Acad Sci U S A 2012, 109: 18150–18155.
88. Varvel NH, Grathwohl SA, Degenhardt K, Resch C, Bosch A, Jucker M, *et al.* Replacement of brain-resident myeloid cells does not alter cerebral amyloid-β deposition in mouse models of Alzheimer's disease. J Exp Med 2015, 212: 1803–1809.
89. Kamran P, Sereti KI, Zhao P, Ali SR, Weissman IL, Ardehali R. Parabiosis in mice: A detailed protocol. J Vis Exp 2013, https://doi.org/10.3791/50556
90. Ajami B, Bennett JL, Krieger C, Tetzlaff W, Rossi FM. Local self-renewal can sustain CNS microglia maintenance and function throughout adult life. Nat Neurosci 2007, 10: 1538–1543.
91. Huang Y, Xu Z, Xiong S, Sun F, Qin G, Hu G, *et al.* Repopulated microglia are solely derived from the proliferation of residual microglia after acute depletion. Nat Neurosci 2018, 21: 530–540.
92. Derecki NC, Cronk JC, Lu Z, Xu E, Abbott SB, Guyenet PG, *et al.* Wild-type microglia arrest pathology in a mouse model of Rett syndrome. Nature 2012, 484: 105–109.
93. Wang J, Wegener JE, Huang TW, Sripathy S, De Jesus-Cortes H, Xu P, *et al.* Wild-type microglia do not reverse pathology in mouse models of Rett syndrome. Nature 2015, 521: E1–E4.
94. Xu Z, Rao Y, Huang Y, Zhou T, Feng R, Xiong S, *et al.* Efficient strategies for microglia replacement in the central nervous system. Cell Rep 2020, 32: 108041.
95. Li Q, Cheng Z, Zhou L, Darmanis S, Neff NF, Okamoto J, *et al.* Developmental heterogeneity of microglia and brain myeloid cells revealed by deep single-cell RNA sequencing. Neuron 2019, 101: 207–223.e10.
96. Schirmer L, Velmeshev D, Holmqvist S, Kaufmann M, Werneburg S, Jung D, *et al.* Neuronal vulnerability and multilineage diversity in multiple sclerosis. Nature 2019, 573: 75–82.
97. Mathys H, Davila-Velderrain J, Peng Z, Gao F, Mohammadi S, Young JZ, *et al.* Single-cell transcriptomic analysis of Alzheimer's disease. Nature 2019, 570: 332–337.
98. Gerrits E, Heng Y, Boddeke EWGM, Eggen BJL. Transcriptional profiling of microglia; current state of the art and future perspectives. Glia 2020, 68: 740–755.
99. Thrupp N, Sala Frigerio C, Wolfs L, Skene NG, Fattorelli N, Poovathingal S, et al. Single-nucleus RNA-seq is not suitable for detection of microglial activation genes in humans. *Cell Rep* 2020, 32: 108189.
100. Masuda T, Sankowski R, Staszewski O, Prinz M. Microglia heterogeneity in the single-cell era. Cell Rep 2020, 30: 1271–1281.
101. Böttcher C, Schlickeiser S, Sneeboer MAM, Kunkel D, Knop A, Paza E, *et al.* Human microglia regional heterogeneity and

phenotypes determined by multiplexed single-cell mass cytometry. Nat Neurosci 2019, 22: 78–90.
102. Sankowski R, Böttcher C, Masuda T, Geirsdottir L, Sagar, Sindram E, et al. Mapping microglia states in the human brain through the integration of high-dimensional techniques. Nat Neurosci 2019, 22: 2098–2110.
103. Salamanca L, Mechawar N, Murai KK, Balling R, Bouvier DS, Skupin A. MIC-MAC: An automated pipeline for high-throughput characterization and classification of three-dimensional microglia morphologies in mouse and human postmortem brain samples. Glia 2019, 67: 1496–1509.
104. Davalos D, Grutzendler J, Yang G, Kim JV, Zuo Y, Jung S, *et al.* ATP mediates rapid microglial response to local brain injury *in vivo*. Nat Neurosci 2005, 8: 752–758.
105. Eyo UB, Peng J, Swiatkowski P, Mukherjee A, Bispo A, *et al.* Neuronal hyperactivity recruits microglial processes via neuronal NMDA receptors and microglial P2Y12 receptors after status epilepticus. J Neurosci 2014, 34: 10528–10540.
106. Eyo UB, Mo M, Yi MH, Murugan M, Liu J, Yarlagadda R, *et al.* P2Y12R-dependent translocation mechanisms gate the changing microglial landscape. Cell Rep 2018, 23: 959–966.
107. Cserép C, Pósfai B, Lénárt N, Fekete R, László ZI, Lele Z, *et al.* Microglia monitor and protect neuronal function through specialized somatic purinergic junctions. Science 2020, 367: 528–537.
108. Horton NG, Wang K, Kobat D, Clark CG, Wise FW, Schaffer CB, *et al. In vivo* three-photon microscopy of subcortical structures within an intact mouse brain. Nat Photonics 2013, 7: 205–209.
109. de Melo Reis RA, Freitas HR, de Mello FG. Cell calcium imaging as a reliable method to study neuron-glial circuits. Front Neurosci 2020, 14: 569361.
110. Brawek B, Garaschuk O. Microglial calcium signaling in the adult, aged and diseased brain. Cell Calcium 2013, 53: 159–169.
111. Tvrdik P, Kearns KN, Sharifi KA, Sluzewski MF, Acton ST, Kalani MYS. Calcium imaging of microglial network activity in stroke. Methods Mol Biol 2019, 2034: 267–279.
112. Edison P, Donat CK, Sastre M. *In vivo* imaging of glial activation in Alzheimer's disease. Front Neurol 2018, 9: 625.
113. Bloomfield PS, Selvaraj S, Veronese M, Rizzo G, Bertoldo A, Owen DR, *et al.* Microglial activity in people at ultra high risk of psychosis and in schizophrenia: An [^{11}C]PBR28 PET brain imaging study. Am J Psychiatry 2016, 173: 44–52.
114. Kuil LE, Oosterhof N, Ferrero G, Mikulasova T, Hason M, Dekker J, et al. Zebrafish macrophage developmental arrest underlies depletion of microglia and reveals Csf1r-independent metaphocytes. Elife 2020, 9: e53403.
115. Orczykowski ME, Calderazzo SM, Shobin E, Pessina MA, Oblak AL, Finklestein SP, *et al.* Cell based therapy reduces secondary damage and increases extent of microglial activation following cortical injury. Brain Res 2019, 1717: 147–159.
116. Stanhope BA, Jaggard JB, Gratton M, Brown EB, Keene AC. Sleep regulates glial plasticity and expression of the engulfment receptor draper following neural injury. Curr Biol 2020, 30: 1092–1101.e3.
117. Geirsdottir L, David E, Keren-Shaul H, Weiner A, Bohlen SC, Neuber J, *et al.* Cross-species single-cell analysis reveals divergence of the primate microglia program. Cell 2019, 179: 1609–1622.e16.
118. Smith AM, Gibbons HM, Dragunow M. Valproic acid enhances microglial phagocytosis of amyloid-beta(1–42). Neuroscience 2010, 169: 505–515.
119. Gibbons HM, Smith AM, Teoh HH, Bergin PM, Mee EW, Faull RL, *et al.* Valproic acid induces microglial dysfunction, not apoptosis, in human glial cultures. Neurobiol Dis 2011, 41: 96–103.
120. Prinz M, Priller J. Microglia and brain macrophages in the molecular age: From origin to neuropsychiatric disease. Nat Rev Neurosci 2014, 15: 300–312.
121. Xu J, Zhu L, He S, Wu Y, Jin W, Yu T, *et al.* Temporal-spatial resolution fate mapping reveals distinct origins for embryonic and adult microglia in zebrafish. Dev Cell 2015, 34: 632–641.
122. Tavian M, Péault B. Embryonic development of the human hematopoietic system. Int J Dev Biol 2005, 49: 243–250.
123. Ginhoux F, Lim S, Hoeffel G, Low D, Huber T. Origin and differentiation of microglia. Front Cell Neurosci 2013, 7: 45.
124. Biffi A, Montini E, Lorioli L, Cesani M, Fumagalli F, Plati T, *et al.* Lentiviral hematopoietic stem cell gene therapy benefits metachromatic leukodystrophy. Science 2013, 341: 1233158.
125. Cartier N, Lewis CA, Zhang R, Rossi FM. The role of microglia in human disease: Therapeutic tool or target?. Acta Neuropathol 2014, 128: 363–380.
126. Janowska J, Gargas J, Ziemka-Nalecz M, Zalewska T, Buzanska L, Sypecka J. Directed glial differentiation and transdifferentiation for neural tissue regeneration. Exp Neurol 2019, 319: 112813.
127. Qian H, Kang X, Hu J, Zhang D, Liang Z, Meng F, *et al.* Reversing a model of Parkinson's disease with *in situ* converted nigral neurons. Nature 2020, 582: 550–556.
128. Kettenmann H, Banati R, Walz W. Electrophysiological behavior of microglia. Glia 1993, 7: 93–101.
129. Boucsein C, Kettenmann H, Nolte C. Electrophysiological properties of microglial cells in normal and pathologic rat brain slices. Eur J Neurosci 2000, 12: 2049–2058.
130. Plescher M, Seifert G, Hansen JN, Bedner P, Steinhäuser C, Halle A. Plaque-dependent morphological and electrophysiological heterogeneity of microglia in an Alzheimer's disease mouse model. Glia 2018, 66: 1464–1480.
131. Yi MH, Liu YU, Liu K, Chen T, Bosco DB, Zheng J, *et al.* Chemogenetic manipulation of microglia inhibits neuroinflammation and neuropathic pain in mice. Brain Behav Immun 2021, 92: 78–89.

Neurosci. Bull. August, 2021, 37(8):1234–1239
https://doi.org/10.1007/s12264-021-00704-w

www.neurosci.cn
www.springer.com/12264

LETTER TO THE EDITOR

Inhibition of PI4KIIIα as a Novel Potential Approach for Gaucher Disease Treatment

Linan Zheng[1,2] · Feng Hong[3] · Fude Huang[3,4] · Wenan Wang[1,2]

Received: 26 December 2020 / Accepted: 25 February 2021 / Published online: 21 May 2021

Dear Editor,

Gaucher disease (GD) is the most common lysosomal storage disease (LSD) caused by an insufficiency of the lysosomal enzyme glucocerebrosidase (GCase) [1]. GCase insufficiency produces the excessive lysosomal accumulation of unmetabolized glycolipid substrates including glucosylceramide (GlcCer), leading to the disruption of the structure and function of tissues and organs, including the blood system, viscera, brain, bones, and cartilage. GD was initially classified into 1–3 types based on the variation of severity and progression in neuropathic manifestation, which is early onset, most severe and acute in type 2, later onset and chronic in type 3, and not obvious in type 1. However, accumulating evidence has shown that type 1 GD is clearly associated with Parkinson's disease and related synucleinopathies [1]. Currently, there are multiple available ways of treating GD patients, including enzyme replacement therapy, substrate reduction therapy, and pharmacological chaperone therapy [2]. However, the therapeutic effect of these approaches used either alone or in combination in GD patients is unsatisfactory. New drug candidates have been studied for a long time in order to develop promising therapeutic approaches to benefit GD patients, especially those with pathological features in the central nervous system.

The pathogenesis of GD involves autophagy-lysosome pathway (ALP) defect [3]; besides, hyperactivity of the mammalian target of rapamycin complex 1 (mTORC1) has been found in GD neurons derived from induced pluripotent stem cells (iPSC), and pharmacological inhibition of glucosylceramide synthase enzyme to reduce the accumulation of unmetabolized substrates of GCase reverses mTORC1 hyperactivity [4]. Moreover, lysosomal accumulation of unmetabolized glycolipid substrates produces overload and dysfunction of lysosomes, reduces the efficiency of lysosomal digestion and recycling as well as the efficiency of lysosomal fusion with autophagosomes, affects the upstream of ALP, and even may prevent lysosome reformation, resulting in further impairment of the clearance or recycling of metabolic wastes and forming a vicious cycle. Indeed, more and more defects in the ALP have been uncovered in the cells of GD patients and animal models as well as GD cell models. Besides digesting or recycling cellular wastes, lysosomes in virtually all cell types can undergo exocytosis or secretion as a secretory compartment to release intraluminal content and exchange membrane components with the plasma membrane (PM). And facilitation of lysosomal exocytosis can ameliorate the excessive lysosomal accumulation of unmetabolized

Linan Zheng and Feng Hong contributed equally to this work.

Supplementary Information The online version contains supplementary material available at https://doi.org/10.1007/s12264-021-00704-w.

✉ Fude Huang
huangfd@nuo-beta.com

✉ Wenan Wang
13611641232@163.com

[1] Department of Neurology, Xinhua Hospital Affiliated to Shanghai Jiaotong University School of Medicine, Shanghai 200092, China

[2] Department of Neurology, Xinhua Hospital Chongming Branch, Shanghai 202150, China

[3] Nuo-Beta Pharmaceutical Technology (Shanghai) Co. Ltd, Shanghai 201210, China

[4] University of the Chinese Academy of Sciences, Sino-Danish College, Chinese Academy of Sciences, Beijing 100049, China

cellular materials in many LSDs with neuropathological changes and neural symptoms [5].

Phosphatidylinositols and their metabolizing enzymes are involved in a variety of membrane trafficking between different cellular compartments in all cell types, particularly, phosphatidylinositol-4 phosphate (PI4P) is involved in autophagolysosome formation. Four types of phosphatidylinositol-4 kinase (PI4K) generate PI4P at different compartments: PI4KIIα, PI4KIIβ, and PI4KIIIβ produce PI4P in the Golgi apparatus, whereas PI4KIIIα generates PI4P and tightly controls its level at the PM [6, 7]. Of particular relevance here, we previously reported that phenylarsine oxide (PAO), an inhibitor of PI4KIIIα [8], facilitates the exocytosis of Lyso-Tracker-labeled granules and the release of ATP from cultured microglia [9], and facilitates the cellular secretion of $A\beta_{42}$ from $A\beta_{42}$- or APP-expressing cells or tissue in association with a reduction of intraneuronal accumulation of $A\beta_{42}$, indicating that the inhibition of PI4KIIIα is a potential solution for the cellular accumulation of lysosomes with unmetabolized substrates in cells.

In this study, we investigated the effects of chemical and genetic inhibition of PI4KIIIα on the impairment of ALP and cellular accumulation of glycolipids in SH-SY5Y cells, which were treated with Conduritol B epoxide (CBE), an irreversible inhibitor of GCase [10]. We found that inhibition of PI4KIIIα had therapeutic effects on CBE-treated cells, including activation of the ALP, and the amelioration of cell death, cellular accumulation of glycolipids, and overloading of lysosomes, indicating that PI4KIIIα may be a potential therapeutic target and its inhibitors be therapeutic chemicals for treating GD, and presumably for other lyososomal storage disorders and other neurodegenerative diseases.

CBE is frequently applied to cultured cells and animals for generating *in vitro* and *in vivo* models of GD. To reveal the proper concentration of CBE for studying the effect of GCase insufficiency-induced impairment in neuronal cells, we examined the viability of SH-SY5Y cells treated at different concentrations of CBE for 48 h. As shown in Fig. 1A, CBE reduced the cell viability in a dosage-dependent manner, and the reduction became significant when the concentration of CBE was at and above 100 μmol/L. Then 100 μmol/L was chosen for inhibiting GCase in the following experiments.

Next, we examined the effect of PAO at different concentrations on the viability of CBE-treated SH-SY5Y cells. After CBE treatment for 24 h and followed by starvation treatment [removal of fetal bovine serum (FBS) from the culture medium] for 24 h, PAO was applied to the culture medium at different concentrations and co-incubated with CBE for 24 h. Then, cells were fixed for the examination of viability with MTT assays. PAO at 25 nmol/L and above increased the viability (Fig. 1B). To further determine the protective effect of PAO, we examined the permeability to propidium iodide (PI) in CBE-treated cells with and without PAO treatment. Consistently, the ratios of PI-positive cells in 25 nmol/L to 75 nmol/L PAO-treated groups significantly decreased when compared to the non-treated group (Fig. 1C, D). These data demonstrated that PAO protects neuronal cells from GCase insufficiency-induced death.

The cells with GCase deficiency typically accumulate unmetabolized glycolipids and lysosomes [1]. To further investigate the therapeutic effects of PAO on CBE-treated SH-SY5Y cells, we incubated control and CBE-treated SH-SY5Y cells with Lyso-Tracker Red DND-99 for 30 min, then the culture medium was replaced with fresh medium containing PAO at the concentrations of 0, 50, or 75 nmol/L for 10 min. In comparison with control, 100 μmol/L CBE treatment dramatically increased the Lyso-Tracker signal in cells, indicating accumulation or enlargement of lysosomes, and PAO at both concentrations greatly restored this alteration (Fig. 1E, F). We next tested whether this effect of PAO was associated with a corresponding change in the cellular accumulation of glycolipids. We measured the levels of a series of GlcCer species in cells and the culture medium by LC-MS/MS. CBE treatment for 48 h remarkably increased the level of each GlcCer in cells, with a concomitant decrease in the level of each GlcCer in the culture medium (Fig. 1G, H). Application of PAO at 50 nmol/L for 24 h reversed the CBE-induced change of glycolipids in both cells and extracellular spaces (Fig. 1G, H). These results indicated that PAO removed the cellular accumulation of glycolipids and lysosomes, and restored

Fig. 1 PAO protects SH-SY5Y cells from CBE-induced cell death and reduces the pathological accumulation of glycolipids and lysosomes in CBE-treated SH-SY5Y cells. **A** The viability of SH-SY5Y cells treated with CBE at various concentrations. Data are normalized to control, $n = 5$ per group, $^{**}P < 0.001$, $^{***}P < 0.0001$ *versus* control. One-way ANOVA followed by Dunnett's test, if not specifically indicated. **B** The effect of PAO at different concentrations on the CBE-induced reduction of viability in SH-SY5Y cells. Data are normalized to control. $n = 5$ per group, $^{\#\#\#}P < 0.0001$ *versus* control, $^{**}P < 0.001$ and $^{***}P < 0.0001$ *versus* 100 μmol/L CBE-treated alone in **B**. **C** Representative DAPI and PI staining for the nucleus and cell death respectively. Scale bar, 100 μm; $n = 3$ per group. **D** Normalized PI staining. $n = 3$ per group. $^{\#\#\#}P < 0.0001$ *versus* control, $^{*}P < 0.05$, $^{**}P < 0.001$, $^{***}P < 0.0001$ *versus* 100 μmol/L CBE-treated alone. **E, F** Representative images and normalization of Lyso-Tracker labeling in control and CBE-treated SH-SY5Y cells with or without 10 min PAO treatment. $n = 5$, $^{\#\#}P < 0.001$ *versus* control, $^{**}P < 0.001$ and $^{***}P < 0.0001$ *versus* 100 μmol/L CBE-treated alone. Scale bars, 50 μm. **G, H** The levels of GlcCer species from cell lysis (**G**) and culture medium (**H**) measured by LC-MS/MS. $n = 3$. Data were analyzed with two-way ANOVA with Turkey's multiple comparison. Data are presented as the mean ± SEM.

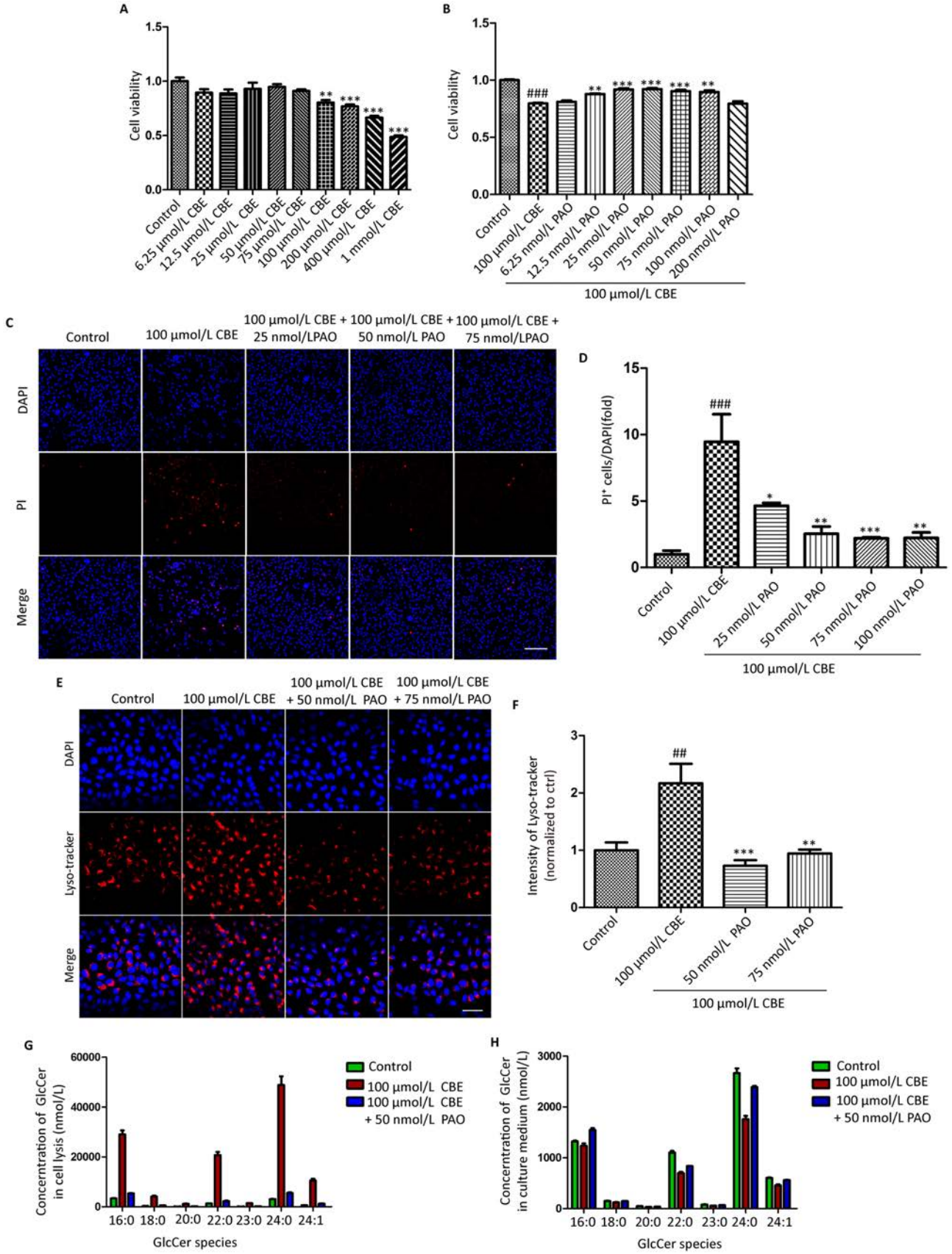
A
Cell viability
Control
6.25 μmol/L CBE
12.5 μmol/L CBE
25 μmol/L CBE
50 μmol/L CBE
75 μmol/L CBE
100 μmol/L CBE
200 μmol/L CBE
400 μmol/L CBE
1 mmol/L CBE
B
Cell viability
Control
100 μmol/L CBE
6.25 nmol/L PAO
12.5 nmol/L PAO
25 nmol/L PAO
50 nmol/L PAO
75 nmol/L PAO
100 nmol/L PAO
200 nmol/L PAO
100 μmol/L CBE
C
Control
100 μmol/L CBE
100 μmol/L CBE + 25 nmol/LPAO
100 μmol/L CBE + 50 nmol/L PAO
100 μmol/L CBE + 75 nmol/LPAO
DAPI
PI
Merge
D
PI+ cells/DAPI(fold)
Control
100 μmol/L CBE
25 nmol/L PAO
50 nmol/L PAO
75 nmol/L PAO
100 nmol/L PAO
100 μmol/L CBE
E
Control
100 μmol/L CBE
100 μmol/L CBE + 50 nmol/L PAO
100 μmol/L CBE + 75 nmol/L PAO
DAPI
Lyso-tracker
Merge
F
Intensity of Lyso-tracker (normalized to ctrl)
Control
100 μmol/L CBE
50 nmol/L PAO
75 nmol/L PAO
100 μmol/L CBE
G
Concentration of GlcCer in cell lysis (nmol/L)
16:0 18:0 20:0 22:0 23:0 24:0 24:1
GlcCer species
Control
100 μmol/L CBE
100 μmol/L CBE + 50 nmol/L PAO
H
Concentration of GlcCer in culture medium (nmol/L)
16:0 18:0 20:0 22:0 23:0 24:0 24:1
GlcCer species
Control
100 μmol/L CBE
100 μmol/L CBE + 50 nmol/L PAO

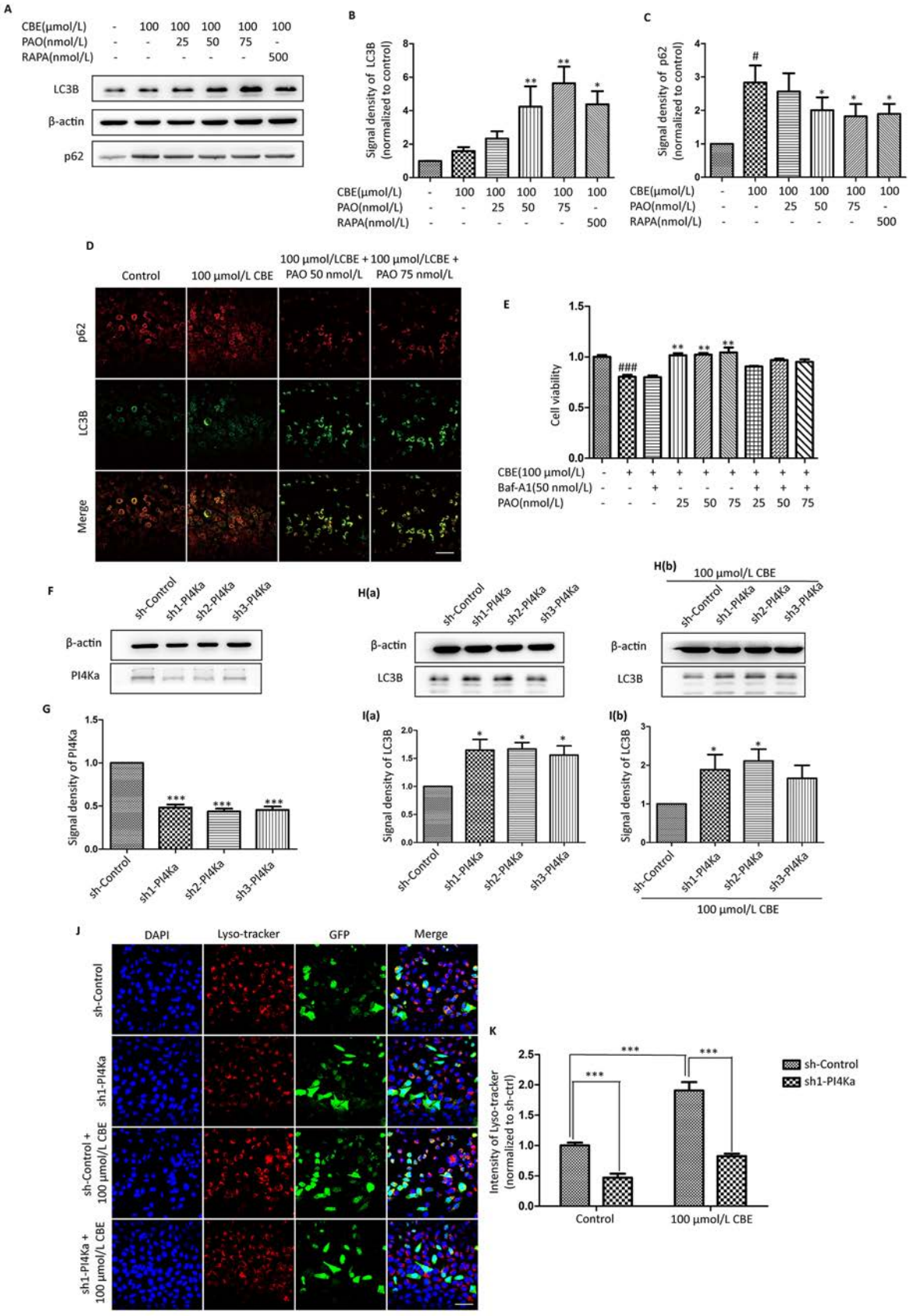
A
CBE(μmol/L) - 100 100 100 100 100
PAO(nmol/L) - - 25 50 75 -
RAPA(nmol/L) - - - - - 500
LC3B
β-actin
p62
B
Signal density of LC3B (normalized to control)
C
Signal density of p62 (normalized to control)
D
Control
100 μmol/L CBE
100 μmol/LCBE + PAO 50 nmol/L
100 μmol/LCBE + PAO 75 nmol/L
p62
LC3B
Merge
E
Cell viability
CBE(100 μmol/L)
Baf-A1(50 nmol/L)
PAO(nmol/L)
F
sh-Control
sh1-PI4Ka
sh2-PI4Ka
sh3-PI4Ka
β-actin
PI4Ka
G
Signal density of PI4Ka
H(a)
LC3B
H(b)
100 μmol/L CBE
I(a)
Signal density of LC3B
I(b)
J
DAPI
Lyso-tracker
GFP
Merge
sh-Control
sh1-PI4Ka
sh-Control + 100 μmol/L CBE
sh1-PI4Ka + 100 μmol/L CBE
K
Intensity of Lyso-tracker (normalized to sh-ctrl)
Control
100 μmol/L CBE

◀**Fig. 2** PAO activates ALP, the protective effect of PAO is blocked by Baf-A1, and knockdown of *PI4Ka* reduces the accumulation of lysosomes in CBE-treated SH-SY5Y cells. **A–C** Representative immunoblots (**A**) and quantification (**B** and **C**) of the expression of LC3B and p62 in cells under different conditions. $n = 5$, $^{\#}P < 0.05$ *versus* control, $^{*}P < 0.05$, $^{**}P < 0.001$ *versus* 100 μmol/L CBE-treated alone. **D** Representative images of LC3B and p62 immunostaining in cells under different conditions. Scale bar, 50 μm. **E** SH-SY5Y cells incubated with 100 μmol/L CBE for 48 h and then co-incubated with or without PAO or 50 nmol/L Baf-A1 for another 24 h, normalized to control. $n = 5$, data are presented as the mean ± SEM. $^{\#\#\#}P < 0.0001$ *versus* control, $^{**}P < 0.001$ *versus* 100 μmol/L CBE-treated alone. **F, G** Representative and quantification of the expression level of PI4KIIIα protein in cells with control (sh-control) or *PI4Ka*-targeting vectors (sh1-*PI4Ka*, sh2-*PI4Ka* and sh3-*PI4Ka*) expressing double-stranded RNAs against the mRNA of *PI4Ka*. **H, I** Representative and normalization of LC3B protein levels in cells with control or *PI4Ka*-targeting vectors, and without [**H(a)** and **I(a)**] or with [**H(b)** and **I(b)**] CBE treatment. $n = 5$, $^{*}P < 0.05$ *versus* sh-control group. **J, K** Representative images and normalization of Lyso-Tracker labeling in cells with or without CBE treatment, which were infected by either sh-control or sh1-*PI4Ka* (GFP). $n = 5$, mean ± SEM, $^{***}P < 0.0001$. Scale bar, 50 μm.

the morphological change in lysosomes in GD cell models by facilitating the lysosome-mediated secretion of glycolipids, confirming the previous report that PAO facilitates lysosomal exocytosis [9] and the facilitation of lysosomal exocytosis can promote clearance of unmetabolized substrates and restore the pathological changes in LSD cells [5].

To test whether the effect of PAO on lysosomal alteration in CBE-treated cells is associated with a restoration of autophagic flux, we incubated control and CBE-treated SH-SY5Y cells with PAO at different concentrations or rapamycin for 24 h, and then analyzed the most widely used autophagy biomarkers LC3B and p62 by either western blot or immunostaining. The representative immunoblots and normalized quantifications of LC3B and p62 are shown in Fig. 2A–C. Indeed, application of PAO remarkably increased the level of LC3B with a concomitant dramatic decrease in p62 in a dosage-dependent manner, which was comparable to the effect of rapamycin (the well-known activator of ALP) on both proteins. Consistently, similar effects of PAO on L3CB and p62 in CBE-treated cells were visualized by immunostaining (Fig. 2D). These results indicate that PAO did restore the autophagic flux in CBE-treated cells.

To further test that the therapeutic effects of PAO on GCase deficiency-caused pathological changes could be ascribed to the activation of ALP, we examined whether the protective effect of PAO on CBE-treated cells could be abolished by Bafilomycin A1 (Baf-A1), a specific inhibitor of vacuolar H^+-ATPase (V-ATPase), which blocks autophagosome-lysosome fusion and inhibits acidification and substrate degradation in lysosomes. MTT assay results manifested that the cell protective effect of PAO was reversed by Baf-A1 (Fig. 2E).

To test whether PAO produced the foregoing protective effect against GCase deficiency *via* inhibiting PI4KIIIα, we generated three recombinant lentiviral vectors that expressed three different double-strand RNAs to specifically knockdown the mRNA of *PI4Ka* (encoding PI4KIIIα). As shown in Fig. 2F and 2G, all of the three vectors reduced the amount of PI4KIIIα protein in SH-SY5Y cells. Then, we infected cells with control or targeting vectors, followed by vehicle- or CBE-treatment for 48 h. We found that knockdown of PI4KIIIα increased the level of LC3B (Fig. 2H, I), but reduced the cellular accumulation of lysosomes in both vehicle- and CBE-treated cells (Fig. 2J, K). Thus, reduction of PI4KIIIα expression mimicked the effect of PAO in terms of activating ALP in cells with GCase insufficiency.

Previously we reported that inhibition of PI4KIIIα by PAO facilitates lysosome exocytosis in glial cells [9] and now we found that down-regulation of PI4KIIIα restored the cellular pathological changes in neuronal cells with GCase deficiency *via* facilitating lysosome exocytosis and activating autophagic flux. Both together indicate that PI4KIIIα and its inhibitors might be a potential new therapeutic target and compounds respectively for treating GD. The exact mechanism of how inhibition of PI4KIIIα facilitates lysosome exocytosis is unknown. PAO and *PI4Ka* knockdown could have biased the conversion of phosphatidylinositol into PI3P and $PI(3,5)P_2$, in turn upregulated the activation of TRPML1 (the principal Ca^{2+} channel mediating lysosomal exocytosis), and therefore ameliorated lysosomal accumulation of the unmetabolized substrates and alteration of lysosomes. On the other hand, PAO and *PI4Ka* knockdown could have simultaneously reduced the levels of $PI(4,5)P_2$ and $PI(3,4,5)P_3$ at the PM, then the activity of the Akt-mTOR pathway, leading to the disinhibition of autophagy and the restoral of autophagy flux and the ALP in CBE-treated cells.

The ALP and lysosomes are involved in a variety of cellular activities. Accumulating evidence demonstrates that in addition to regulating the final steps of catabolic processes, lysosomes are essential up-stream modulators of autophagy and other pathways implicating lysosome [11, 12]. Therefore, lysosomal dysfunction or alteration has a profound impact on cell homeostasis, resulting in manifold pathological situations, including neurodegeneration, cancer, infectious diseases, inflammation, and aging, in addition to LSD. Aged cells and cells with either LSD or neurodegeneration display blockade of ALP flux [13]. By facilitating lysosomal exocytosis and restoring ALP to relieve the block of autophagic flux, inhibition of PI4KIIIα may provide a common therapeutic approach for treating LSD and neurodegenerative diseases *via* removal of

excessive metabolic wastes and damaged organelles. It is noteworthy that partial inhibition of PI4KIIIα could be therapeutically useful for the treatment of GD and other disorders while full inhibition of PI4KIIIα might trigger cell senescence and/or cell death [14].

In conclusion, we demonstrated that PAO, an inhibitor of PI4KIIIα produced protective effects on CBE-treated SH-SY5Y cell models with activation of ALP and lysosomal exocytosis, and reduction of the accumulation of substrates and lysosomes. In addition, our data indicate that knocking down *PI4Ka* mimicked the effects of PAO. Therefore, the evidence above suggests that down-regulation or inhibition of PI4KIIIα can be regarded as a potential therapeutic strategy for GD and other LSDs.

Acknowledgements This work was supported by the National Natural Science Foundation of China (81771416, 81650110527, and 8197100), Shanghai Municipal Commission of Health and Family Planning (201740153), and Key Discipline of Chongming District, Shanghai, China, 2018.

Conflict of interest The authors disclose no relevant conflict of interests with this research.

References

1. Dandana A, Ben Khelifa S, Chahed H, Miled A, Ferchichi S. Gaucher disease: Clinical, biological and therapeutic aspects. Pathobiology 2016, 83: 13–23.
2. Stirnemann J, Belmatoug N, Camou F, Serratrice C, Froissart R, Caillaud C. A review of gaucher disease pathophysiology, clinical presentation and treatments. Int J Mol Sci 2017, 18: 441.
3. Darios F, Stevanin G. Impairment of lysosome function and autophagy in rare neurodegenerative diseases. J Mol Biol 2020, 432: 2714–2734.
4. Brown RA, Voit A, Srikanth MP, Thayer JA, Kingsbury TJ, Jacobson MA, *et al.* mTOR hyperactivity mediates lysosomal dysfunction in Gaucher's disease iPSC-neuronal cells. Dis Model Mech 2019, 12: dmm038596.
5. Buratta S, Tancini B, Sagini K, Delo F, Chiaradia E, Urbanelli L, *et al.* Lysosomal exocytosis, exosome release and secretory autophagy: The autophagic- and endo-lysosomal systems go extracellular. Int J Mol Sci 2020, 21: 2576.
6. Balla A, Balla T. Phosphatidylinositol 4-kinases: Old enzymes with emerging functions. Trends Cell Biol 2006, 16: 351–361.
7. Clayton EL, Minogue S, Waugh MG. Phosphatidylinositol 4-kinases and PI4P metabolism in the nervous system: Roles in psychiatric and neurological diseases. Mol Neurobiol 2013, 47: 361–372.
8. Balla A, Tuymetova G, Toth B, Szentpetery Z, Zhao X, Knight ZA, *et al.* Design of drug-resistant alleles of type-III phosphatidylinositol 4-kinases using mutagenesis and molecular modeling. Biochemistry 2008, 47: 1599–1607.
9. Mu SJ, Lim NKH, Huang FD. Inhibition of phosphatidylinositol kinase-III alpha induces or facilitates lysosome exocytosis from microglia. NeuroReport 2020, 31: 697–701.
10. Marshall J, Sun Y, Bangari DS, Budman E, Park H, Nietupski JB, *et al.* CNS-accessible inhibitor of glucosylceramide synthase for substrate reduction therapy of neuronopathic gaucher disease. Mol Ther 2016, 24: 1019–1029.
11. Bonam SR, Wang F, Muller S. Lysosomes as a therapeutic target. Nat Rev Drug Discov 2019, 18: 923–948.
12. Fang Z, Feng Y, Li Y, Deng J, Nie H, Yang Q, *et al.* Neuroprotective autophagic flux induced by hyperbaric oxygen preconditioning is mediated by cystatin C. Neurosci Bull 2019, 35: 336–346.
13. Song L, Zhang L. Tau accumulation and defective autophagy: A common pathological mechanism underlying repeat-expansion-induced neurodegenerative diseases?. Neurosci Bull 2020, 36: 1411–1413.
14. Bojjireddy N, Botyanszki J, Hammond G, Creech D, Peterson R, Kemp DC, *et al.* Pharmacological and genetic targeting of the PI4KA enzyme reveals its important role in maintaining plasma membrane phosphatidylinositol 4-phosphate and phosphatidylinositol 4, 5-bisphosphate levels. J Biol Chem 2014, 289: 6120–6132.

Neurosci. Bull. August, 2021, 37(8):1240–1245
https://doi.org/10.1007/s12264-021-00707-7

www.neurosci.cn
www.springer.com/12264

LETTER TO THE EDITOR

GABA Signaling Pathway-associated Gene *PLCL1* Rare Variants May be Associated with Autism Spectrum Disorders

Fengyun Zheng[1] · Guoyuan Liu[2] · Ting Dang[1,3] · Qiaowen Chen[2] · Yu An[1] · Meng Wu[1] · Xiangxuan Kong[4] · Zilong Qiu[5,6] · Bai-Lin Wu[1,2,3,4]

Received: 20 November 2020 / Accepted: 3 February 2021 / Published online: 5 June 2021

Dear Editor,

Autism spectrum disorders (ASDs) are neurodevelopmental disorders with phenotypic and genetic heterogeneity, and are among the most heritable of neurodevelopmental disorders [1]. Rare single nucleotide variants (SNVs) of genes and/or rare copy number variants (CNVs) involving gene variants and/or genomic imbalances play an important role in ASD, but their molecular pathogenic mechanisms remain indistinct [2]. Over the decades, genetic and neurobiological studies mainly involving severe ASD comorbid with intellectual disability (ID) or developmental delay (DD) have indicated that loss of function affects neural development [3].

GABAergic signaling and impaired $GABA_A$ receptor function may contribute to the pathogenesis of multiple neuropsychiatric disorders including ASD [4]. Phospholipase C-like 1 (PLCL1), also named phospholipase C (PLC)-related inactive protein type 1 (PRIP-1), plays a central role in controlling $GABA_A$ receptor phospho-dependent modulation, and therefore, the efficacy of synaptic inhibition mediated by these receptors [5]. Several studies have focused on the mouse PLCL1 loss-of-function models. The *Plcl1*$^{-/-}$ mice exhibit altered behaviors including frequent ambulation and impaired motor coordination [6], or show an epileptic phenotype [7]. While in double knockout of *Plcl1* and *Plcl2* (compensatory to *Plcl1* function) mice, orofacial movements are affected; including reduced vertical jaw movements, tongue protrusions and movements of the head and vibrissae [8]. In humans, a pediatric specific Phenome-Wide Association Study revealed that one single nucleotide polymorphism (rs1595825) in *PLCL1* intron 1 is associated with developmental delays of speech and language [9]. Despite the relevant studies on animal models and human, the role of *PLCL1* in neural development, particularly, whether ASD patients have rare *PLCL1* variants, and whether these variants have harmful effects that may be associated with the development of ASD remains unknown.

To identify rare variants of the *PLCL1* gene in ASD, we first screened 437 American patients with ASD using array comparative genomic hybridization (array CGH), and identified 35 pathogenic CNVs (supplementary materials and methods). Among them, a 542,605 bp microdeletion (542 kb deletion) located in chromosome 2q33.1 was

Supplementary Information The online version contains supplementary material available at https://doi.org/10.1007/s12264-021-00707-7.

✉ Guoyuan Liu
gyliu@fudan.edu.cn

✉ Zilong Qiu
zqiu@ion.ac.cn

✉ Bai-Lin Wu
Bai-Lin.Wu@childrens.harvard.edu

1 Institutes of Biomedical Sciences, Fudan University, Shanghai 200032, China

2 Department of Pathology, School of Basic Medical Sciences, Fudan University, Shanghai 200032, China

3 Children's Hospital of Fudan University, Shanghai 201102, China

4 Boston Children's Hospital and NGS Collaboration, Harvard Medical School, Boston 02115, USA

5 Institute of Neuroscience, State Key Laboratory of Neuroscience, CAS Center for Excellence in Brain Science and Intelligence Technology, Chinese Academy of Sciences, Shanghai 200031, China

6 The College of Life Science, University of the Chinese Academy of Sciences, Beijing 100049, China

identified in one of the 437 patients (Table S1), which covers the exons 2–6 of the *PLCL1* gene, *LOC101927619* (long intragenic non-protein coding RNA 1923), exons 3 and 4 of *LOC105373831,* and the whole length of *LOC105373830* (two uncharacterized non-coding RNA genes). Neither of the patient's parents carried the same variant, and no similar loss was found in 8,045 non-neurological/psychiatric patients [the database of Genetic Diagnostics Lab of Boston Children's Hospital (BCH-GDL database)]. Therefore, we conclude that the 542 kb deletion found in ASD is rare and *de novo*.

We further searched several publicly available databases of CNVs or SNVs detected/submitted by clinical genetic diagnosis laboratories. In the DECIPHER database (website: decipher.Sanger.ac.uk), we found approximately 45 genomic deletions and duplications that included an overlapped region similar to the 542 kb deletion. Of them, 6 relevant smaller microdeletions were selected to compare with the 542 kb deletion (Table S1). Notably, all 6 deletions (range 2.54–6.94 Mb) were associated with DD, but were not seen in normal controls. Furthermore, the *PLCL1* deletion was the only gene shared within all 7 cases (Table S1). Most interestingly, their phenotypes were comorbid within all 7 cases: 6/7 had ID and 4/7 had delayed speech and language development, which were frequently observed in patients with ASD/ID/DD; while the 542 kb deletion only involved one coding gene, *PLCL1*. Therefore, these results strongly suggest that the 542 kb deletion/*PLCL1* gene deletion is likely a pathogenic variant associated with ASD/DD/ID. We further performed functional studies of *PLCL1* in mice.

Moreover, we screened 455 Han Chinese patients with ASD, and found four missense variants of *PLCL1* in coding sequence (c.82 G>A, c.311 A>G, c.434 G>A, and c.2922 G>T) and two non-coding region variants in the upstream regulatory region of *PLCL1* (c.−636 C>A and c.−136_−134 delGCC) by Sanger sequencing (Fig. 1A, Table S2). All the variants were heterozygous (Fig. S1) and existed in unrelated individual samples. Moreover, the variants were not present in 576 control DNA samples or in the dbSNP, Ensembl, and ExAC databases, thus we considered they may be rare variants that only present in ASD patients.

By genetic/genomic screening, it seemed that the *PLCL1* deletion and variants were not uncommon in ASD/DD/ID, and potential detrimental effects (Tables S1, S2; Fig. S2) of the above *PLCL1* variants may exist, so we subsequently investigated the role of *PLCL1* in neural development, particularly whether these rare *PLCL1* variants have loss- or gain-of-function effects.

First, we explored *Plcl1* gene expression in the early stage of mouse cerebral cortex. We examined PLCL1 protein levels in embryonic (E) and postnatal (P) cortex of mouse brains and found that PLCL1 was strongly expressed from E16 to P28 (Fig. 1B). Furthermore, human PLCL1 protein has been reported to be distributed specifically in the brain and expressed abundantly in the cerebral cortex and hippocampus [10]. Taken together, the results suggest that PLCL1 may play an important role in brain development and normal neuronal function.

The formation of protrusions and the abnormal elongation of axons and dendrites may be the structural basis for the pathogenesis of ASD [11]. To elucidate the role of PLCL1 in the growth of neuronal axons and dendrites, we specifically knocked down *Plcl1* in mouse primary cortical neurons with short hairpin RNAs (shRNAs) (Fig.1C), and found that the length of axons and dendrites were significantly decreased compared with control neurons that were transfected with nonspecific control shRNAs (NC), while the number of dendritic branches was not affected (Fig. 1D).

Since the encoded peptide chain of exon 1 of *PLCL1* does not locate in the coding region of any domain of *PLCL1* (Fig. 1A), we speculate that the deletion of exons 2–6 of the *PLCL1* gene found in ASD patients may cause loss-of-function of PLCL1 protein and affect the proper neurite development, similar to the effect of reducing PLCL1 protein. To explore whether the deletion of exons 2–6 and the four missense variants of *PLCL1* detected in ASD patients might affect the normal function of PLCL1 protein, we transfected the plasmids only expressing GFP

Fig. 1 The dosage of PLCL1 is crucial for neurite outgrowth of primary cultured mouse cortical neurons, and the deletion of *PLCL1* exons 2–6 affects the promotion of neuronal growth, while *PLCL1* missense variants have no effect. **A** The location of *PLCL1* rare variants in studied ASD patients on the *PLCL1* gene and coding protein. Colored bars represent the PLCL1 protein functional domains. **B** The PLCL1 expression pattern in mouse cerebral cortex during the embryonic and postnatal period. **C** The efficiency of endogenous *Plcl1* knockdown was verified using shRNA packaged in lentivirus by Western blot (top) or using pFUGW-H1-shRNA plasmids by qRT-PCR (bottom) in primary cultured mouse cortical neurons. **D** *Plcl1* knockdown affects mouse neuronal growth. Upper panel shows the specific cellular morphology of neurons transfected with pFUGW-H1 vector (NC, as a control), *Plcl1* shRNA1 and shRNA2. All neurons were co-labeled with DAPI (to identify nuclei), GFP (to identify overall neuronal morphology) and SMI 312 (an axonal marker). Scale bar, 20 μm. Bottom panel shows the statistical results of the axon length, total length of neurites, and the number of dendritic branches of mouse neurons with *Plcl1* knockdown. Approximately 90 cells from three independent experiments were counted and the *P*-value was determined by one-way ANOVA. $*P < 0.05$, $**P < 0.01$, $***P < 0.001$. **E** Western blot analysis of ectopic expression of PLCL1-WT, PLCL1-E1, and four missense variants in HEK-293T cells. **F** The morphology of neurons overexpressing the CAG vector (GFP, as a control), PLCL1-WT, PLCL1-E1, and four missense variants. Scale bar, 20 μm. **G** The axon length (upper), total length of neurites (middle), and the number of dendritic branches (bottom) were measured and analyzed as described above. Error bars, ± SEM.

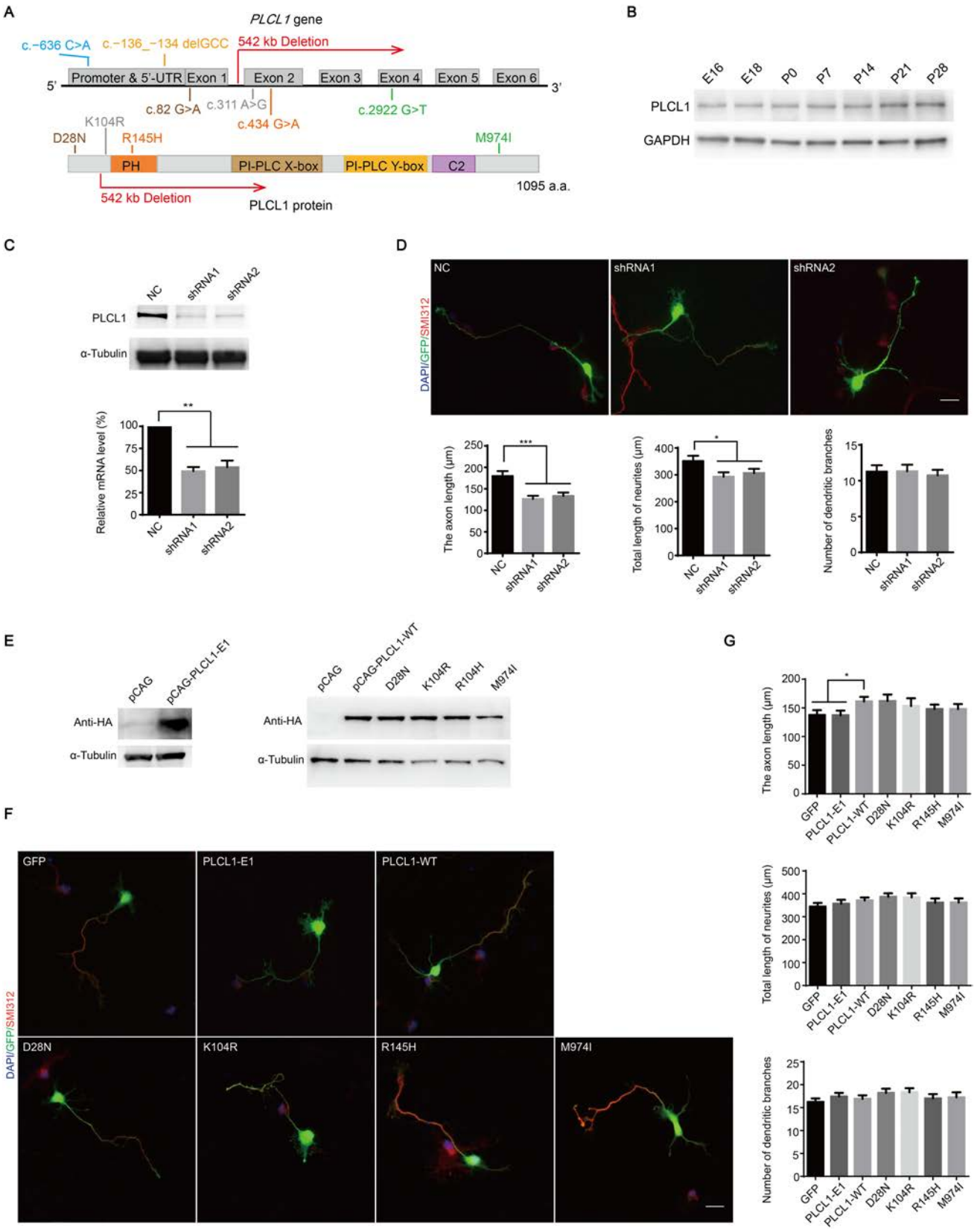
A
PLCL1 gene
c.−636 C>A
c.−136_−134 delGCC
542 kb Deletion
Promoter & 5'-UTR
Exon 1
Exon 2
Exon 3
Exon 4
Exon 5
Exon 6
5'
3'
c.82 G>A
c.311 A>G
c.434 G>A
c.2922 G>T
K104R
D28N
R145H
M974I
PH
PI-PLC X-box
PI-PLC Y-box
C2
1095 a.a.
542 kb Deletion
PLCL1 protein
B
E16
E18
P0
P7
P14
P21
P28
PLCL1
GAPDH
C
NC
shRNA1
shRNA2
PLCL1
α-Tubulin
Relative mRNA level (%)
D
DAPI/GFP/SMI312
The axon length (μm)
Total length of neurites (μm)
Number of dendritic branches
E
pCAG
pCAG-PLCL1-E1
pCAG-PLCL1-WT
D28N
K104R
R104H
M974I
Anti-HA
α-Tubulin
F
GFP
PLCL1-E1
PLCL1-WT
D28N
K104R
R145H
M974I
G
The axon length (μm)
Total length of neurites (μm)
Number of dendritic branches

(as a control), or PLCL1-wild-type (WT), or PLCL1-E1 (the recombinant plasmid only including exon 1), or the four missense variants (Fig. 1E) into mouse primary cortical neurons, considering the PLCL1 is highly conserved between human and mouse (approximately 94.4% according to protein peptide alignment). We found that overexpression of PLCL1-WT significantly increased the axon length compared with control neurons expressing GFP alone (Fig. 1F, G), while the total length of neurites and the branching number of neuronal dendrites did not change. Overexpression of PLCL1-E1 had no effect on the neuronal growth, which resembled that of control (Fig. 1F, G). The result confirmed that PLCL1-E1 lacked the normal function of PLCL1-WT. In addition, the effect of overexpression of the four missense variants in mouse neurons did not significantly differ from that of PLCL1-WT (Fig. 1F, G), indicating that the four variants did not affect the normal function of PLCL1 in neuronal growth. Taken together, the PLCL1 dosage is critical for proper neurite and axonal outgrowth, and the deletion of *PLCL1* exons 2–6 is a loss-of-function mutant, while the four missense variants are not.

Dendritic spine abnormalities have been reported to be strongly associated with various neurological and neuropsychiatric disorders [12], and dysfunction of the GABAergic pathway in early development can lead to severe excitatory/inhibitory (E/I) imbalance in the neural circuitry, which may be the cause of behavioral defects in ASD patients [13]. Vesicular glutamate transporter 1 (VGLUT1) and vesicular GABA transporter (VGAT) are excitatory and inhibitory markers of synaptic transmission. To further explore the role of PLCL1 in synaptic development, we examined the function of PLCL1 in spine formation, dendrite development, and excitatory and inhibitory synapse formation by immunostaining in mouse primary cortical neurons. We found that *Plcl1* knockdown with shRNA resulted in a decrease in both VGLUT1 and VGAT density on dendrites and spines compared with the control, but not for the spine density, length of dendrites, and brunching number (Fig. 2A, B). Thus, *Plcl1* knockdown altered the excitatory and inhibitory synapse formation. Furthermore, PLCL1-WT successfully rescued the suppression of both VGLUT1 and VGAT density in *Plcl1* knockdown mouse neurons (Fig. 2C, D). The four missense variants had no significantly different effect compared with PLCL1-WT, indicating that they did not affect the normal function of PLCL1 in excitatory and inhibitory synapse formation (Fig. 2C, D).

In addition to PLCL1 depletion, overexpression of PLCL1 also reduced VGLUT1 and VGAT density (Fig. 2C, D), while the total dendrite length, branch number, and spine density were unaffected (Fig. S3). Thus, the dosage of PLCL1 is crucial for glutamatergic and GABAergic synapse development. We speculated that the variant with deletion of exons 2–6, a loss-of-function mutant as we mentioned above, may affect glutamatergic and GABAergic synapse development as well.

Fig. 2 PLCL1 is crucial in neuronal excitability and its dosage imbalance affects glutamatergic and GABAergic synapse development *in vitro*. **A** Decreased VGLUT1 and VGAT density caused by *Plcl1* knockdown. Morphology of the VGLUT1 and VGAT density of neurons transfected with *Plcl1* shRNA and control NC vector. The skeleton represents dendrite segments and dendritic spines. Scale bar, 5 μm. **B** Statistical analysis of the total dendrite length, branching number, spine density (per 10 μm), VGLUT1 density (red puncta number per 10 μm), and VGAT density (blue puncta number per 10 μm) between NC and shRNA groups. Forty neurons from three independent experiments were measured and counted. *P*-value is determined by unpaired *t*-test. ***P <0.001. **C** PLCL1-WT and mutant variants of PLCL1 rescues (res) the phenotype of decreased VGLUT1 and VGAT density caused by *Plcl1* knockdown. The specific morphology of neurons in each condition expressing the indicated vectors. All neurons were co-labeled with VGLUT1, VGAT, and GFP. Scale bar, 5 μm. **D** Statistical results for the VGLUT1 density and VGAT density between each group. Approximately 30 cells from three independent experiments were randomly selected and counted. *P*-value was determined by one-way ANOVA. Error bars, ± SEM. *P <0.05; **P <0.01.

According to the predicted transcription factors that bind to the *PLCL1* promoter (Table S2, Fig. S4A), we selected four relatively high-scoring transcription factors E2F4, E2F6, SP1, and GATA1 to assess the effects of the two promoter variants c.−636 C>A and c.−136_−134 delGCC on *PLCL1* transcription activity and protein expression. We ectopically expressed E2F4, E2F6, SP1, and GATA1 (Fig. S4B), and co-transfected the expression plasmids with wild-type *PLCL1* promoter (pGL3-WT, c.−1 to c.−901), mutant type c.−636 C>A (pGL3−636), c.−136_−134 delGCC (pGL3−136), and the empty vector into HEK-293T cells, and used promoter luciferase assays to determine the transcription activity of the promoters. We found that the activation of pGL3−136 by ectopic expression of GATA1 was significantly lower than that of pGL3-WT (Fig. S4C), while GATA1 had a similar strong activation effect on pGL3-WT and pGL3−636. E2F4, E2F6, and SP1 had similar effects on pGL3-WT and the two mutants (Fig. S4D). Therefore, we speculated that the mutant-type pGL3−136 may affect the transcriptional activation of *PLCL1* promoter by GATA1.

Consistent with the luciferase assay results, overexpression of E2F4, E2F6, and SP1 had no significant effect on PLCL1 expression in HEK-293T cells, while overexpression of GATA1 up-regulated PLCL1 protein (Fig. S4E). Moreover, GATA1-induced PLCL1 protein expression was weakened after ectopic *GATA1* knockdown (Fig. S4F). Therefore, we further verified that GATA1 has a positive regulatory effect on the expression of PLCL1 protein. Taken together, the rare variant c.−136_−134 delGCC of the *PLCL1* promoter in ASD patients suppressed the

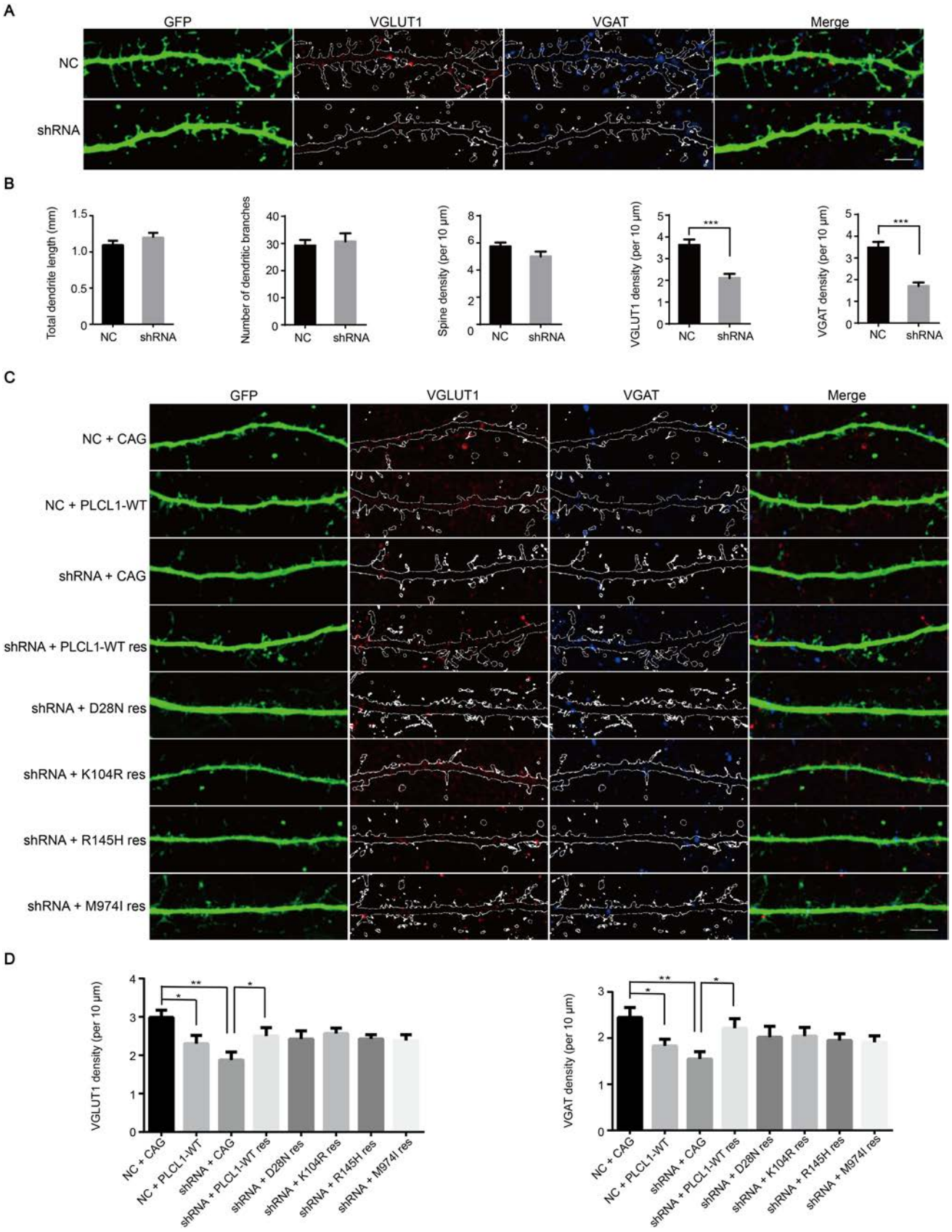
A
GFP
VGLUT1
VGAT
Merge
NC
shRNA
B
Total dendrite length (mm)
Number of dendritic branches
Spine density (per 10 μm)
VGLUT1 density (per 10 μm)
VGAT density (per 10 μm)
***
NC
shRNA
C
GFP
VGLUT1
VGAT
Merge
NC + CAG
NC + PLCL1-WT
shRNA + CAG
shRNA + PLCL1-WT res
shRNA + D28N res
shRNA + K104R res
shRNA + R145H res
shRNA + M974I res
D
VGLUT1 density (per 10 μm)
VGAT density (per 10 μm)
NC + CAG
NC + PLCL1-WT
shRNA + CAG
shRNA + PLCL1-WT res
shRNA + D28N res
shRNA + K104R res
shRNA + R145H res
shRNA + M974I res

transcription-activating effect of GATA1 on *PLCL1*, and subsequently decreased PLCL1 expression. As abnormal expression of PLCL1 leads to abnormal neurite outgrowth and glutamatergic and GABAergic synapse development, we believe that the variant may be related to the pathogenesis of ASD.

In this study, we identified one *de novo PLCL1* variant, exons 2–6 deletion (within the 542 kb genomic deletion located on chromosome 2q33.1) in American ASD cohorts, and one *PLCL1* promoter rare variant c.−136_−134 delGCC in Chinese ASD patients, which may relate to the onset of ASD. A 778 kb duplication including *PLCL1* exons 2–6 was reported in one patient diagnosed with agenesis of the corpus callosum with ASD, DD, and seizures [14], which corroborated our observation that overexpression of PLCL1 reduced VGLUT1 and VGAT density, implying that the 542 kb deletion is likely related to neuronal development. Furthermore, whether the absence of three non-coding RNAs in this 542 kb region is involved in the pathogenesis of ASD warrants further research.

The four missense variants behaved similarly to PLCL1-WT when overexpressed in regard to neurite and axon outgrowth, and all could rescue the decreased VGLUT1 and VGAT density, that was caused by *Plcl1* knockdown. However, we cannot exclude that they may affect other functions of PLCL1, such as its function in the inositol 1,4,5-trisphosphate [Ins(1,4,5)P_3]-mediated Ca^{2+} signaling pathway, which was not assessed by this study. According to a "bilineal two-hit model" [15], that is, even rare SNVs are not a direct cause of ASD, they can increase the risk of ASD, thus the possibility that variants existing on other genes may be involved in the pathogenesis of ASD in cooperation with *PLCL1* variants should not be excluded.

In summary, we report and describe rare variants of the *PLCL1* gene in American and Chinese cohorts with ASD, and provided preliminary clues for further elucidating the role of PLCL1 in neuron development. Further research is needed to identify other essential genes which are required either independently or collaboratively with *PLCL1* for the phosphorylation or clustering of $GABA_A$ receptors, and to better understand the role of PLCL1 in GABAergic signaling as well as in the pathogenesis of central nervous system diseases including ASD.

Acknowledgments This work was supported by the National Natural Science Foundation of China (31671461, 31301162, 31625013, and 81941405), 973 Program from the Ministry of Science and Technology of China (2013CB945404 and 2010CB529601), Shanghai Brain-Intelligence Project from STCSM (16JC1420501), the Strategic Priority Research Program of the Chinese Academy of Sciences (XDBS01060200 and XDA16010310), and the Shanghai Municipal Science and Technology Major Project (2018SHZDZX05). We are grateful to Dr. Yasong Du of Shanghai Mental Health Center and to Dr. Xiu Xu of Children's Hospital of Fudan University for the collection of patients' samples and clinical data. We thank Dr. Yiping Shen and Hong Shao of the Genetics Diagnostic Lab at Boston Children's Hospital for their assistance.

Conflict of interest The authors declare no conflict of interest in this work.

References

1. Iakoucheva LM, Muotri AR, Sebat J. Getting to the cores of autism. Cell 2019, 178: 1287–1298.
2. Weiss LA, Shen Y, Korn JM, Arking DE, Miller DT, Fossdal R. Association between microdeletion at 16p11.2 and autism. N Engl J Med 2008, 358: 667–675.
3. Qiu Z, Yuan B. Towards the framework of understanding autism spectrum disorders. Neurosci Bull 2019, 35: 1110–1112.
4. Kang JQ, Barnes G. A common susceptibility factor of both autism and epilepsy: functional deficiency of $GABA_A$ receptors. J Autism Dev Disord 2013, 43: 68–79.
5. Yoshimura K, Takeuchi H, Sato O, Hidaka K, Doira N, Terunuma M, *et al.* Interaction of p130 with, and consequent inhibition of, the catalytic subunit of protein phosphatase 1alpha. J Biol Chem 2001, 276: 17908–17913.
6. Kanematsu T, Jang IS, Yamaguchi T, Nagahama H, Yoshimura K, Hidaka K, *et al.* Role of the PLC-related, catalytically inactive protein p130 in $GABA_A$ receptor function. EMBO J 2002, 21: 1004–1011.
7. Zhu G, Yoshida S, Migita K, Yamada J, Mori F, Tomiyama M, *et al.* Dysfunction of extrasynaptic GABAergic transmission in phospholipase C-related, but catalytically inactive protein 1 knockout mice is associated with an epilepsy phenotype. J Pharmacol Exp Ther 2012, 340: 520–528.
8. Tomiyama K, Song L, Kobayashi M, Kinsella A, Kanematsu T, Hirata M, *et al.* Orofacial movements in phospholipase C-related catalytically inactive protein-1/2 double knockout mice: Effect of the GABAergic agent diazepam and the D_1 dopamine receptor agonist SKF 83959. Synapse 2010, 64: 714–720.
9. Namjou B, Marsolo K, Caroll RJ, Denny JC, Ritchie MD, Verma SS, *et al.* Phenome-wide association study (PheWAS) in EMR-linked pediatric cohorts, genetically links PLCL1 to speech language development and IL5-IL13 to Eosinophilic Esophagitis. Front Genet 2014, 5: 401.
10. Murakami A, Matsuda M, Nakasima A, Hirata M. Characterization of the human PRIP-1 gene structure and transcriptional regulation. Gene 2006, 382: 129–139.
11. Bakos J, Bacova Z, Grant SG, Castejon AM, Ostatnikova D. Are molecules involved in neuritogenesis and axon guidance related to autism pathogenesis? Neuromolecular Med 2015, 17: 297–304.
12. Dang T, Duan WY, Yu B, Tong DL, Cheng C, Zhang YF, *et al.* Autism-associated Dyrk1a truncation mutants impair neuronal dendritic and spine growth and interfere with postnatal cortical development. Mol Psychiatry 2018, 23: 747–758.
13. Fanelli F, Marino R, Keller F. Focusing on the interactions between the GABAergic system and neurosteroids in neurodevelopmental disorders. Curr Pharm Des 2013, 19: 6491–6498.
14. Sajan SA, Fernandez L, Nieh SE, Rider E, Bukshpun P, Wakahiro M, *et al.* Both rare and *de novo* copy number variants are prevalent in agenesis of the corpus callosum but not in cerebellar hypoplasia or polymicrogyria. PLoS Genet 2013, 9: e1003823.
15. Brandler WM, Antaki D, Gujral M, Kleiber ML, Whitney J, Maile MS, *et al.* Paternally inherited cis-regulatory structural variants are associated with autism. Science 2018, 360: 327–331.

Neurosci. Bull. August, 2021, 37(8):1246–1250
https://doi.org/10.1007/s12264-021-00725-5

www.neurosci.cn
www.springer.com/12264

LETTER TO THE EDITOR

Mitochondrial Events Determine the Status of Hippocampal Cells in the Post-Ischemic Period

Iryna Lushnikova[1] · Yelyzaveta Nikandrova[1] · Galyna Skibo[1]

Received: 9 November 2020 / Accepted: 6 March 2021 / Published online: 7 June 2021

Dear Editor,

Understanding ischemia-induced events is important for effective protective strategies in brain pathologies. Actively functioning neuronal cells, the specialization and efficiency of which were formed evolutionarily, are resistant to minor fluctuations in the extracellular environment, maintaining cell and tissue homeostasis. If the threshold for resistance is exceeded, a molecular imbalance appears, followed by a neurodegenerative process. Although the energy-supplying function of mitochondria in cellular metabolism is well known, the contribution of mitochondrial events to cell survival in extreme situations is not yet fully understood. In conditions of oxygen-glucose deficiency, the vulnerability of the brain is not identical in different cells and regions. It is known that the pyramidal neurons of the CA1 hippocampal region are most vulnerable, while interneurons and glial cells are relatively resistant to ischemia, and contribute to neuroprotection [1, 2]. The approaches in the study of mechanisms underlying neurodegeneration and/or rehabilitation are complicated by overlapping responses of functionally and structurally connected brain cells. Often, researchers focus on one type of cell in the investigation of cerebral damage. Despite numerous studies, many aspects of neuronal and glial responses to ischemia have not yet been elucidated. Deficiency of oxygen and glucose leads to systemic changes in the brain that are initially oriented towards the restoration of cellular and tissue homeostasis (adaptation), but can also trigger delayed pathological events up to irreversible neuronal degradation. In brain diseases, along with specific pathogenic mechanisms, ischemia-induced mitochondrial dysfunction is a general factor in the neurodegenerative process [3–5]. The reasons for delayed damage to hippocampal cells in a mild oxygen-glucose deficit, as well as the cellular aspects of this phenomenon, have not yet been fully elucidated. The energy supply of mammalian brain metabolism is mainly carried out by mitochondria through the aerobic oxidation of glucose. The cellular energy resource (production and buffering of ATP) is largely determined by mitochondrial activity (MA), as well as the number and morphology of mitochondria [6, 7]. This *in vitro* study presents an evaluation of the mitochondrial patterns of basic hippocampal cell types in the modeling of post-ischemic damage using slice cultures and transient oxygen-glucose deprivation (OGD) followed by normoxia. The hippocampal CA1 region that is most sensitive to OGD was analyzed. MA was determined based on a semi-quantitative analysis of mitochondrial membrane potential using a mitochondrial probe [MitoTracker Orange (MTO)] and confocal microscopy. Electron microscopic assessment of structural mitochondrial parameters was also carried out. In addition, given the standardized experimental conditions of our ischemic damage model *in vitro*, we extrapolated mitochondrial dynamics to relative parameters characterizing the state of hippocampal cells during the study period.

Double staining, namely MTO combined with immunohistochemistry, allowed us to differentiate an MTO-positive signal (MTO+) (Fig. 1, red) co-localized with specific cellular markers (Fig. 1, green). In this way, we traced the

Supplementary Information The online version contains supplementary material available at https://doi.org/10.1007/s12264-021-00725-5.

✉ Iryna Lushnikova
ivlook@ukr.net

[1] Department of Cytology, Bogomoletz Institute of Physiology, NAS of Ukraine, Kyiv 01024, Ukraine

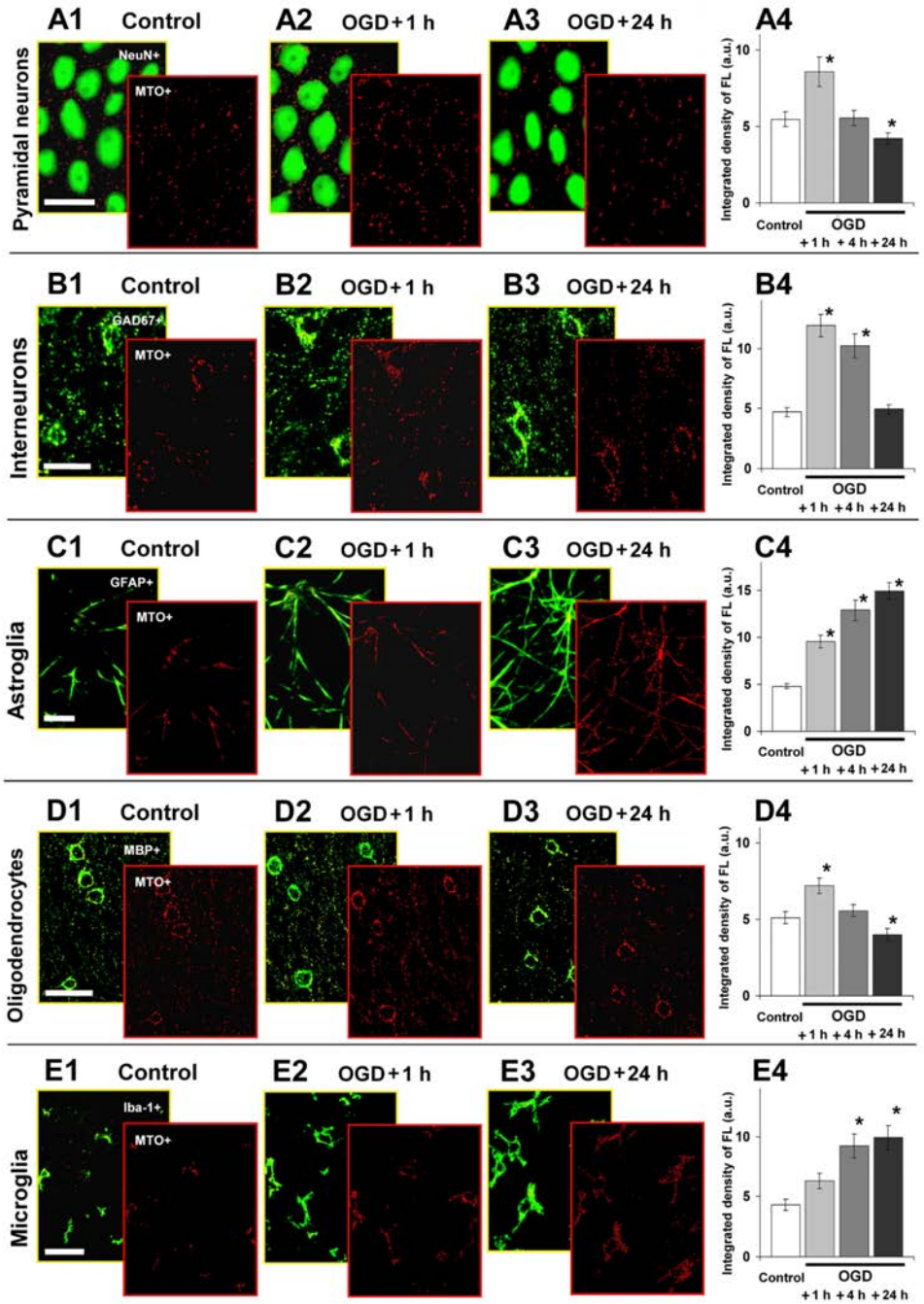

Fig. 1 Analysis of mitochondrial activity in the CA1 region of hippocampal slice cultures at 1, 4, and 24 h after 30 min OGD compared to control. Combined MitoTracker Orange (MTO; red)/immunohistochemical (green) staining of various hippocampal cell types: **A1–A3** pyramidal neurons (NeuN+); **B1–B3** interneurons (GAD67+); **C1–C3** astroglia (GFAP+); **D1–D3** oligodendroglia (MBP+); **E1–E3** microglia (Iba-1+); co-localization of markers gives yellow. Illustrations of staining in Control (**A1–E1**), 1 h (**A2–E2**), and 24 h (**A3–E3**) after 30 min OGD. Scale bars, 100 μm. **A4–E4** Diagrams of changes in the integrated density of MTO+ fluorescence (FL) characterizing mitochondrial activity in the respective immunopositive cells (*P <0.05 *vs* Control, n = 30). Data are expressed as arbitrary units (a.u.).

relative MA changes associated with pyramidal neurons (NeuN+), interneurons (GAD67+), astroglia (GFAP+), oligodendroglia (MBP+), and microglia (Iba-1+) for 24 h after 30-min OGD. When identifying cells, the singular cytoarchitectonics of the hippocampus, preserved in the cultured slices, as well as cell morphology (shape, size, density, and immunoreactivity) were taken into account. It is known that the pyramidal bodies are densely packed in the pyramidal zone [stratum pyramidale (SP)] and predominate there (up to 98% of the total number) [8, 9]. Given this, the widely used NeuN (neuronal nucleus) marker indicates the position of the pyramidal neural bodies in the CA1 region with a high probability [10]. Interneurons and glial cells are relatively evenly distributed in the CA1 region, mostly outside the pyramidal layer. The CA1 radial zone [stratum radiatum (SR)] is predominantly the closely intertwined appendages of hippocampal cells. In addition to MA, the mitochondrial ultrastructure was analyzed in the SP and SR using electron microscopy. The following parameters were assessed: (1) the ratio of the

total mitochondrial area to the corresponding cytoplasmic area of the pyramidal soma (excluding the nucleus and processes) in the SP zone, as well as the ratio of the total mitochondrial area to the corresponding area of the processes in the SR zone (in Fig. 2, "Soma" is marked with a purple dotted line); and (2) average density and optical density of mitochondria in the pyramidal soma, as well as in the SR region.

In the hippocampus, excitable pyramidal neurons are functionally dominant, but they are also the most vulnerable. The molecular mechanisms of OGD-induced pyramidal neuron neurodegeneration have been well studied. They are mainly associated with disruption of ion transport pumps resulting from ATP deficiency and glutamate excitotoxicity, as well as the accumulation of reactive oxygen species (ROS) and subsequent oxidative stress [3, 4]. The imbalance of transmembrane ionic gradients involving glutamate/calcium-mediated cascades leads to hyperactivation of excitable pyramidal neurons [7], which can initiate cell damage. There is a fine line between normal functioning and the beginning of neurodegeneration. Using an ischemic damage model, we investigated changes in some mitochondrial features and then compared the studied parameters with the status of hippocampal cells. The post-OGD effects can be differentiated into initial (reactive stage), intermediate (adaptive stage), and delayed (destructive stage) [11], which is conditionally comparable to 1, 4, or 24 h of normoxia after 30-min OGD in our experimental model (Fig. S1).

The experimental protocol we used did not produce rapid disturbances, but had signs of delayed damage that simulates post-ischemic injury events. The reactive stage

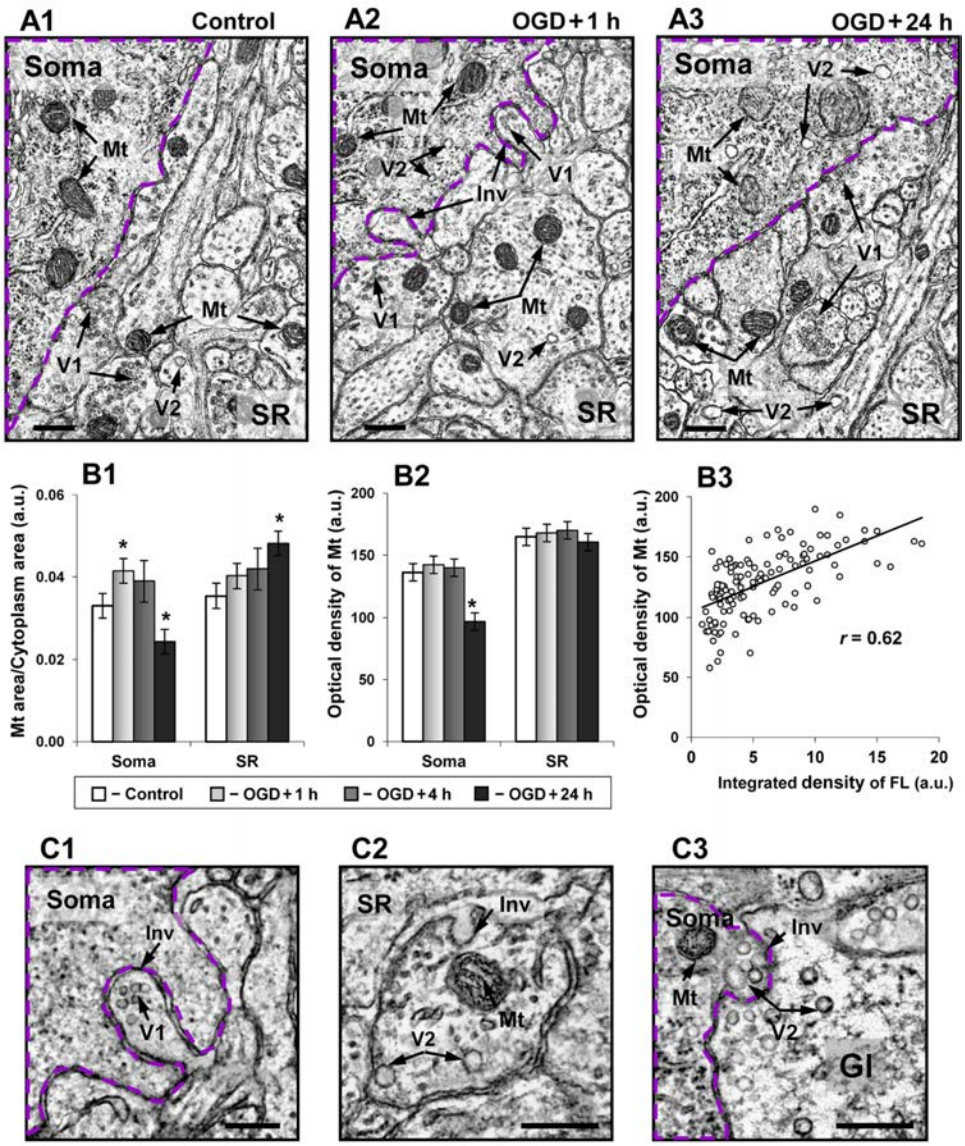

Fig. 2 Electron microscopic analysis of mitochondria in the CA1 region in hippocampal slice cultures. **A** Representative electron micrographs: control (**A1**), 1 h (**A2**), and 24 h (**A3**) after OGD. Images illustrate the transverse profile of a part of a pyramidal neuronal soma (purple dashed line) and the region of the cell processes [(stratum radiatum (SR)]. Arrows indicate: Mt, mitochondria; V1, synaptic vesicles; V2, other cellular vesicles; Inv, invaginations. Scale bars, 500 nm. **B1** Ratio of the mitochondrial area/area of the neuronal cytoplasm (marked on the graph as "Soma") and mitochondrial area/area of the measured SR region in the Control, 1 h, 4 h, and 24 h after 30 min OGD (*$P < 0.05$ *vs* Control, $n = 60$). **B2** Changes in the optical density of mitochondria in the neuronal cytoplasm and the SR region (*$P < 0.05$ *vs* Control, $n = 60$). **B3** Scatter plot showing a correlation between mitochondrial optical density and integrated density of MTO+ fluorescence (FL) in CA1 pyramidal neurons; $n = 90$, $r = 0.62$. **C** Images illustrating exocytosis/endocytosis involving: pyramidal soma and SR cell processes (**C1**), SR cell processes (**C2**), and pyramidal soma and astroglia (**C3**). The pyramidal soma is marked with a purple dashed line. Scale bars, 200 nm.

(1 h after OGD) was characterized by an increase in the integrated density of MTO fluorescence compared to the control in all types of cells (Fig. 1A1–E1, A2–E2, A4–E4; $n = 30$, $P < 0.05$), which may indicate the activation of their metabolism. The parameters that characterize the status of various hippocampal cell types (namely, relative immunoreactivity and number) remained at the control level (Fig. S2B, C; $n = 15$, $P < 0.05$). These data indicate the adequacy of the available mitochondrial resources to maintain cellular homeostasis during this period. In the reactive stage after temporary OGD, electron microscopy showed statistically significant increases in total mitochondrial area (Fig. 2B1; $n = 60$, $P < 0.05$) and density (i.e., average number of mitochondria per unit area, Table S1) just in CA1 pyramidal soma, although their shape (Fig. 2A1, A2) and the average optical density (Fig. 2B2; $n = 60$, $P < 0.05$) remained without significant changes. Thus, in the early period after OGD, along with mitochondrial activation (based on MTO staining), the number of mitochondria increases in CA1 pyramidal somata.

There are data that neuronal cells can exchange their contents. Neurons are able to release and accept mitochondria, when astrocytes can form mitochondrial fragments that can be transported to neurons through exocytosis/endocytosis [12, 13]. Delivery of neuroprotective factors and removal of reactive molecules can be carried out in the same way [14]. In this study, electron microscopy allowed us to detect morphological signs of intercellular communication in the border zone between the SP and SR of the CA1 region. CA1 pyramidal neurons were identified based on their spatial localization and morphology (characteristic shape, size, density, and features of the internal ultrastructure). In addition to regular synaptic contacts, we have found many examples of interaction through exocytosis/endocytosis with the formation of membrane invaginations and/or subcellular vesicles (Fig. 2A2, 2C), suggesting the possibility of direct exchange of cellular contents. Due to the formation of invaginations, an increase in the surface area of contacts between the pyramidal soma and inhibitory interneurons, which dominate in the zone of interest, was observed. As a result of exocytosis/endocytosis, intracellular vesicles of various sizes were formed, carrying the contents of neighboring cells, not excluding small organelles (namely, mitochondria). The GIF images well illustrate the phenomena described above (Fig. S3). The described form of intercellular communication can be one of the mechanisms for the normalization of the state of pyramidal neurons during their hyperactivation in the reactive stage after OGD.

Subsequent events (adaptive stage) showed that CA1 hippocampal cells remained viable for 4 h after OGD, but MA differed significantly in the considered cell types. Variations in MA parameters were as follows: the average MA level stabilized to control in pyramidal neurons and oligodendrocytes; and remained elevated or increased in interneurons, astroglia, and microglia (Fig. 1A4–E4; $n = 30$, $P < 0.05$). The fact that MA in pyramidal neurons and oligodendrocytes decreased (compared to OGD + 1 h) indicates a probable decrease in the adaptive potential and resistance of these cells. The ultrastructural parameters of mitochondria in the SP and SR remained stable for 4 h after OGD stress. Thus, the data indicate that in our experimental model at the adaptive stage there are sufficient resources to maintain cellular homeostasis, but the energy status is approaching a critical level.

In further studies, delayed destructive post-OGD effects became apparent and were in direct correspondence with MA dynamics. It was revealed that 24 h after OGD, the average MA level was lower than the control in pyramidal neurons and oligodendrocytes, while it significantly increased in astroglia and microglia (Fig. 1A4–E4; $n = 30$, $P < 0.05$). The described MA changes were correlated with the degradation of pyramidal neurons and oligodendrocytes and the hyperactivation of astroglia and microglia, respectively (Fig. S2). MA parameters of interneurons were similar to those in control. These data demonstrate the relatively greater resistance of the last mentioned three types of cells in the post-OGD period.

It should be noted that the basal MA level and mitochondrial morphology were largely comparable in different cell types of control hippocampal cultures. It is clear that the functional potential of mitochondria has limits. It can be assumed that when energy resources for functioning and maintaining homeostasis are depleted, cells degrade. Vulnerability/resistance varies both for different hippocampal cells and within the CA1 pyramidal cell population as well. In our experimental model, morphological abnormalities of mitochondria (membrane deformation, amorphousness, absence of cristae) were observed even in the somata of CA1 pyramidal neurons, which did not yet have pronounced signs of cellular degradation at the destructive stage, as shown in Fig. 2A3. At this stage, we evaluated the parameters of the mitochondrial ultrastructure without taking into account extremely damaged cells, when mitochondria could not be marked. It was in the pyramidal soma that a significant decrease in the total area, density, and optical density of mitochondria was found 24 h after OGD (Fig. 2B1, B2; $n = 60$, $P < 0.05$; Table S1). It should be noted that the parameters of the optical density of mitochondria in the pyramidal soma correlated with the integrated fluorescence density characterizing MA in the SP region (Fig. 2B3; $n = 90$, $r = 0.62$).

Based on the analysis of mitochondrial and cellular changes in the post-OGD period, we presume that

glutamatergic pyramidal neurons most actively spend their energy resources on glutamate/calcium-mediated events at the reactive stage (OGD + 1 h). Subsequently, to restore homeostasis at the adaptive stage (OGD + 4 h), they also consume mitochondrial resources more actively than cells of other types. At the destructive stage (OGD + 24 h), when the resistance threshold is reached, pyramidal neurons are more likely to degenerate. Since oligodendrocytes involved in signaling are in close contact with excitatory glutamatergic synapses and express glutamate receptors [15], they are very sensitive to the excitotoxicity of glutamate, as well as to other OGD-induced factors. Our data demonstrate an MA decrease and cell degradation in the oligodendrocytic population, similar to pyramidal neurons. During the post-OGD period studied, the results showed a stable state and/or activation of interneurons, as well as astroglial and microglial cells, which were more resistant and able to modulate the state of pyramidal neurons, at least in part.

The higher vulnerability of hippocampal pyramidal neurons in cerebral ischemia, which has been widely described in both *in vivo* and *in vitro* studies, can be largely due to the specific cytoarchitectonics of the hippocampus. That is, the evolutionarily formed hippocampal patterns are functionally expedient, but they are also limiting. Apparently, processes similar to those described can also occur in any brain regions in the context of the energy resources of various cellular types.

Thus, mitochondrial events largely determine the homeostatic threshold of hippocampal cells in OGD, and thus their survival. A comprehensive study of cellular and mitochondrial patterns in the hippocampus expands the understanding of the causes of the high vulnerability of CA1 pyramidal neurons in cerebral ischemia and the phenomenon of delayed neuronal death after transient cerebral ischemia. We believe that in brain diseases caused by ischemia, it is advisable to take into account both the cell specificity and the dynamics of destructive processes, which can expand the therapeutic window, as well as increase the effectiveness of neuroprotective strategies that also target mitochondria.

Acknowledgements This work was supported by the State Fund for Fundamental Researches of Ukraine (F46.2/001). We thank Kateryna Smozhanyk for technical support with electron microscopy experiments.

Conflict of interest All authors claim that there are no conflicts of interest.

References

1. Kirschen GW, Kéry R, Ge SY. The hippocampal neuro-glio-vascular network: Metabolic vulnerability and potential neurogenic regeneration in disease. Brain Plast 2018, 3: 129–144.
2. Voytenko LP, Lushnikova IV, Savotchenko AV, Isaeva EV, Skok MV, Lykhmus OY. Hippocampal GABAergic interneurons coexpressing alpha7-nicotinic receptors and connexin-36 are able to improve neuronal viability under oxygen-glucose deprivation. Brain Res 2015, 1616: 134–145.
3. Budman E, Deeb W, Martinez-Ramirez D, Pilitsis JG, Peng-Chen Z, Okun MS, *et al.* Potential indications for deep brain stimulation in neurological disorders: An evolving field. Eur J Neurol 2018, 25: 434-e30.
4. Frenguelli BG, Dale N. Purines: from diagnostic biomarkers to therapeutic agents in brain injury. Neurosci Bull 2020, 36: 1315–1326.
5. Panchal K, Tiwari AK. Mitochondrial dynamics, a key executioner in neurodegenerative diseases. Mitochondrion 2019, 47: 151–173.
6. Benaroya H. Brain energetics, mitochondria, and traumatic brain injury. Rev Neurosci 2020, 31: 363–390.
7. Garcia GC, Bartol TM, Phan S, Bushong EA, Perkins G, Sejnowski TJ, *et al.* Mitochondrial morphology provides a mechanism for energy buffering at synapses. Sci Rep 2019, 9: 18306.
8. Aika Y, Ren JQ, Kosaka K, Kosaka T. Quantitative analysis of GABA-like-immunoreactive and parvalbumin-containing neurons in the CA1 region of the rat hippocampus using a stereological method, the disector. Exp Brain Res 1994, 99: 267–276.
9. Benavides-Piccione R, Regalado-Reyes M, Fernaud-Espinosa I, Kastanauskaite A, Tapia-González S, León-Espinosa G, *et al.* Differential structure of hippocampal CA1 pyramidal neurons in the human and mouse. Cereb Cortex 2020, 30: 730–752.
10. Zhang J, Ke KF, Liu Z, Qiu YH, Peng YP. Th17 cell-mediated neuroinflammation is involved in neurodegeneration of aβ1-42-induced Alzheimer's disease model rats. PLoS One 2013, 8: e75786.
11. Sandoval KE, Witt KA. Blood-brain barrier tight junction permeability and ischemic stroke. Neurobiol Dis 2008, 32: 200–219.
12. Gao LF, Zhang Z, Lu J, Pei G. Mitochondria are dynamically transferring between human neural cells and Alexander disease-associated GFAP mutations impair the astrocytic transfer. Front Cell Neurosci 2019, 13: 316.
13. Hayakawa K, Esposito E, Wang XH, Terasaki Y, Liu Y, Xing CH, *et al.* Corrigendum: Transfer of mitochondria from astrocytes to neurons after stroke. Nature 2016, 539: 123.
14. Yin YN, Hu J, Wei YL, Li ZL, Luo ZC, Wang RQ, *et al.* Astrocyte-derived lactate modulates the passive coping response to behavioral challenge in male mice. Neurosci Bull 2021, 37: 1–14.
15. Bergles DE, Roberts JD, Somogyi P, Jahr CE. Glutamatergic synapses on oligodendrocyte precursor cells in the hippocampus. Nature 2000, 405: 187–191.

Neurosci. Bull. August, 2021, 37(8):1251–1255
https://doi.org/10.1007/s12264-021-00736-2

www.neurosci.cn
www.springer.com/12264

LETTER TO THE EDITOR

Functional Near-Infrared Spectroscopy Neurofeedback of Cortical Target Enhances Hippocampal Activation and Memory Performance

Xin Hou[1] · Xiang Xiao[1] · Yilong Gong[1] · Yihan Jiang[1] · Peipei Sun[1] · Juan Li[2] · Zheng Li[3,4] · Xiaojie Zhao[5] · Li Yao[1,5] · Antao Chen[6] · Chaozhe Zhu[1,4]

Received: 2 November 2020 / Accepted: 16 March 2021 / Published online: 24 June 2021

Dear Editor,

Neuromodulation, a rapidly expanding field attracting wide attention over recent decades, facilitates human cognition, behavior, and pathology by modifying the activity of specific neural targets. Human brain functions can be modified by exogenous brain neuromodulation techniques that deliver physical energy (e.g., electrical current or magnetic pulses) into the brain [1], such as deep brain stimulation, transcranial magnetic stimulation, and transcranial direct current stimulation. In contrast, neurofeedback is considered to be an endogenous form of neuromodulation for regulating human brain function [2], in which individuals use mental strategies to voluntarily regulate the on-going neural activity of target brain regions. Compared to exogenous brain modulation techniques, neurofeedback is relatively safe, side-effect-free, well-tolerated, and acceptable to both healthy and clinical populations (see [3] for review).

Most neurofeedback systems currently utilize electroencephalography (EEG), functional magnetic resonance imaging (fMRI), or functional near-infrared spectroscopy (fNIRS) to acquire the on-going brain activity of individuals. Among these techniques, fNIRS neurofeedback (fNIRS-NF) has several special advantages. In contrast to fMRI, fNIRS devices are much cheaper, having lower purchase and operational costs, are relatively insensitive to movement-related artifacts, have no restrictions on location, have fewer contraindications (e.g., claustrophobia and MRI-incompatible metal implants), and can be used in natural environments [4] and with special populations (e.g., patients and infants) [5, 6]. These features also make fNIRS-NF more suitable for long-term and multi-session applications than fMRI neurofeedback. Besides, fNIRS has a relatively high and acceptable spatial resolution compared to EEG, which allows fNIRS-NF to achieve more precise self-regulation of a local cortical target. Thus, fNIRS-NF is a promising brain modulation technique and has been successfully applied in many areas (see the recent review by Kohl *et al.*, 2020 [7]).

Like other transcranial techniques, fNIRS measures activity near the surface of the brain but not in deep brain regions. However, several regions located in deep areas (e.g., the hippocampus, amygdala, and subgenual cingulate cortex) are critical for brain function, and dysfunction of these regions may lead to certain neurological or psychiatric diseases. These regions usually serve as the targets of deep brain stimulation to treat related diseases but cannot

Supplementary Information The online version contains supplementary material available at https://doi.org/10.1007/s12264-021-00736-2.

✉ Chaozhe Zhu
czzhu@bnu.edu.cn

1 State Key Laboratory of Cognitive Neuroscience and Learning & IDG/McGovern Institute for Brain Research, Beijing Normal University, Beijing 100875, China

2 CAS Key Laboratory of Mental Health, Center on Aging Psychology, Institute of Psychology, Beijing 100101, China

3 State Key Laboratory of Cognitive Neuroscience and Learning, Center for Cognition and Neuroergonomics, Beijing Normal University at Zhuhai, Zhuhai 519085, China

4 Center for Collaboration and Innovation in Brain and Learning Sciences, Beijing Normal University, Beijing 100875, China

5 College of Information Science and Technology, Beijing Normal University, Beijing 100875, China

6 Key Laboratory of Cognition and Personality of the Ministry of Education, Faculty of Psychology, Southwest University, Chongqing 400715, China

be directly modulated by fNIRS-NF. This, therefore, limits the scope of application of fNIRS-NF.

Accumulating evidence has indicated that the modulatory effects of focal neurostimulation can spread from the directly-stimulated region to distant connected regions [8–10]. Fox *et al*. (2014) found that known effective cortical sites used in noninvasive brain stimulation for neurological and psychiatric diseases usually have strong resting-state functional connections with the deep sites usually targeted by invasive brain stimulation [11]. Furthermore, cortico-subcortical functional connectivity can predict the clinical efficacy of neurostimulation [12]. Transcranial magnetic stimulation of a superficial target with robust functional connections with a deep brain region—the hippocampus—selectively enhances the functional connectivity among cortical-hippocampal network regions [13], and increases task activation of the hippocampus and related regions [14]. This evidence suggests that cortico-subcortical connectivity is helpful for cortical target selection and the optimization of transcranial neuromodulation techniques, and superficial cortical regions with robust functional connectivity to key subcortical nodes might be effective targets through which to achieve indirect modulation of deep brain regions.

Here, we aimed to test the feasibility of fNIRS-NF for indirectly regulating deep brain regions. First, knowledge from functional connectomics was used to select a cortical target robustly connected with the key deep brain region. We selected the hippocampus as the deep modulation target for its importance in long-term memory, especially associative memory retrieval [15]. Our hypothesis was: fNIRS-NF of a cortical region connected to the hippocampus will improve associative memory performance by indirectly changing the neural activity of the hippocampus.

We conducted a placebo-controlled real-time multisession fNIRS-NF experiment with behavioral test and task fMRI measurement to test the hypothesis. This study was approved by the Southwest University Brain Imaging Center Institutional Review Board. In the participant screening phase, any individuals with experience in mnemonic strategies or neurofeedback were excluded. Fifty healthy college students (25 males, age range 18–25 years) were recruited to participate in this study, and all participants provided written informed consent.

An overview of the experimental design is illustrated in Fig. 1. To define the cortical target for fNIRS-NF, we first performed a resting-state functional connectivity analysis based on the open-access large sample fMRI database SLIM [16] to find the cortical regions with robust intrinsic connections to the hippocampus (Supplementary Materials). Consistent with previous studies [17], the left lateral parietal cortex (LPC, peak voxel MNI (Montreal Neurological Institute) coordinate: [−45, −69, 33]) exhibited robust positive connectivity with the left hippocampus (FDR-corrected $P < 0.005$, Fig. 1A), and was selected as the cortical feedback target. Then, 30 participants (15 males) from among the recruited participants were assigned to the experimental group and instructed to upregulate the neural activity of LPC. Control conditions are essential for neurofeedback studies to distinguish whether neuropsychological changes are due to regulation of the target region or due to placebo effects. Therefore, the other twenty participants (10 males) were assigned to the active control group and received placebo neurofeedback of activity in an irrelevant brain region (left premotor area, PMA, mean MNI [−38, −13, 60], Fig. 1A). All participants were blinded to their group allocation. The deep region and cortical targets were located in the left hemisphere (for reasons, see Supplementary Materials). The arrangement of optodes is shown in the Supplementary Materials (Fig. S1A).

The entire experiment was divided into three stages: preassessment, 8 fNIRS-NF sessions, and post-assessment (Fig. 1B). Each participant received 8 neurofeedback sessions within 9 days. Each session had ∼30 min of effective feedback time. Changes in oxyhemoglobin concentration were measured using the NIRS system (FOIRE-3000, Shimadzu Corp., Kyoto, Japan). Neurofeedback was performed on our in-house fNIRS neurofeedback platform (Fig. 1C), in which the height of the stone in an on-screen image represented the relative concentration change of oxygenated hemoglobin compared to the baseline in the target brain region (for the calculation of the neurofeedback index see Supplementary Materials). Without providing explicit strategies, participants were asked to raise the stone as high as they could use any strategy they found helpful. Post-assessment was performed on the day after the final feedback session.

To assess the behavioral and neural effects induced by fNIRS-NF, all participants performed a face-noun associative memory test while undergoing functional MRI scanning in the pre- and post-assessment sessions. The day before the first fNIRS-NF session, the face-noun associative memory task and functional MRI scanning were performed to assess the baseline behavioral performance and brain function. The entire associative memory test consisted of four parts: encoding, recognition, immediate recall, and delayed recall (Fig. 1D). The encoding phase and recognition test were performed in an MRI scanner. Participants were instructed to learn the relationships between the human faces and corresponding noun words in the encoding phase, then an 8-min structural imaging scan followed. Afterward, a 4-choice recognition test was given, and participants were asked to recollect the correct noun from four possible alternative nouns containing three distractors and make a response. After leaving the scanner

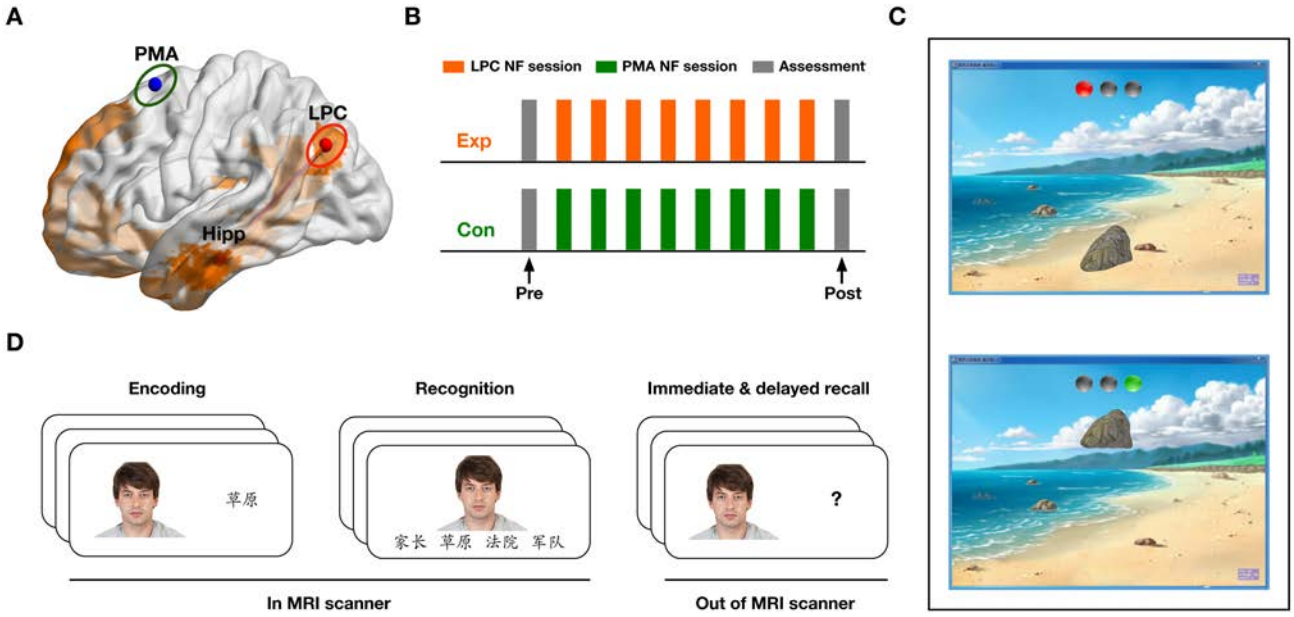

Fig. 1 Experimental design overview. **A** Neurofeedback target identification. Orange shading indicates the hippocampal (Hipp) functional connectivity mask. The experimental group's target (LPC: lateral parietal cortex) is within the hippocampal connectivity network, while the control group's target (PMA: premotor area) is outside of the connectivity network. **B** Experimental procedure. Both experimental (Exp) and control (Con) groups received 8-session neurofeedback (NF) sessions. Before and after the 8-session neurofeedback, all participants completed task fMRI scans and associative memory assessments. **C** Neurofeedback visual interface. Two sample images of the interface depict fixation (upper) and regulation (lower) blocks. **D** Associative memory test.

room, the immediate recall test was given. And the delayed recall test was performed approximately 24 h later. The face-noun associative memory task was performed again with the same procedure and different stimuli on the day after the last fNIRS-NF session. All MRI data were collected on a 3-Tesla Siemens Trio MRI scanner (Siemens Medical, Erlangen, Germany) with a 12-channel head coil.

Offline analysis of fNIRS-NF time-course data indicated that both groups succeed in up-regulating the real-time activity of their target brain regions but not non-target regions (Fig. S2 and Table S2). To determine whether fNIRS-NF could induce a neuroplastic change in hippocampal activity during memory processing, relative activation values of task-dependent fMRI within the left hippocampus during the memory recognition task were calculated and then compared between groups. The values for changes in voxel-wise task activation within the left hippocampal region of interest (3 mm radius sphere used in the feedback targeted identification phase) from the delta activation map were extracted and averaged for subsequent neural effect comparison. Though no significant group difference was found ($t_{(43)} = 1.10$, $P = 0.28$, Cohen's $d = 0.34$), a significant increase in hippocampal activation was found in the experimental group after 8 sessions of fNIRS-NF relative to the baseline in pre-assessment session ($t_{(26)} = 2.05$, $P = 0.05$, Cohen's $d = 0.39$), but not in the control group ($t_{(17)} = 0.01$, $P = 0.99$, Cohen's $d = 0.00$, Fig. 2A and Table S1). Meanwhile, no significant pre-post or group differences in task-dependent activation in the LPC and PMA were found (Table S2). Behavioral effect analyses showed that recognition memory performance significantly increased relative to the baseline in the pre-assessment session in the experimental group ($t_{(26)} = 2.83$, $P < 0.01$, Cohen's $d = 0.54$, Fig. 2B and Table S1), while the change was not found to be significant in the control group ($t_{(17)} = 0.81$, $P = 0.43$, Cohen's $d = 0.19$). The group difference of the modulation effects in recognition memory performance was significant ($t_{(43)} = 2.40$, $P = 0.02$, Cohen's $d = 0.73$). Similar results were obtained in the immediate recall test after leaving the MRI scanner room and the delayed recall test approximately 24 h later (Table S1 and Fig. S3). Correlation analysis revealed that task activation changes in the left hippocampus were significantly and positively correlated with increases in accuracy of recognition memory performance in the experimental group ($r = 0.42$, $P = 0.03$, 95% CI: [0.05, 0.69], Fig. 2C). No significant trend was found in the control group ($r = 0.13$, $P = 0.62$, 95% CI: [−0.36, 0.56], Fig. 2C).

Despite being a promising neural modulation technique with several specific advantages, its inability to modulate deep brain regions limits the application of fNIRS-NF. In the current study, we made a preliminary attempt to test whether fNIRS-NF could indirectly modulate the deep

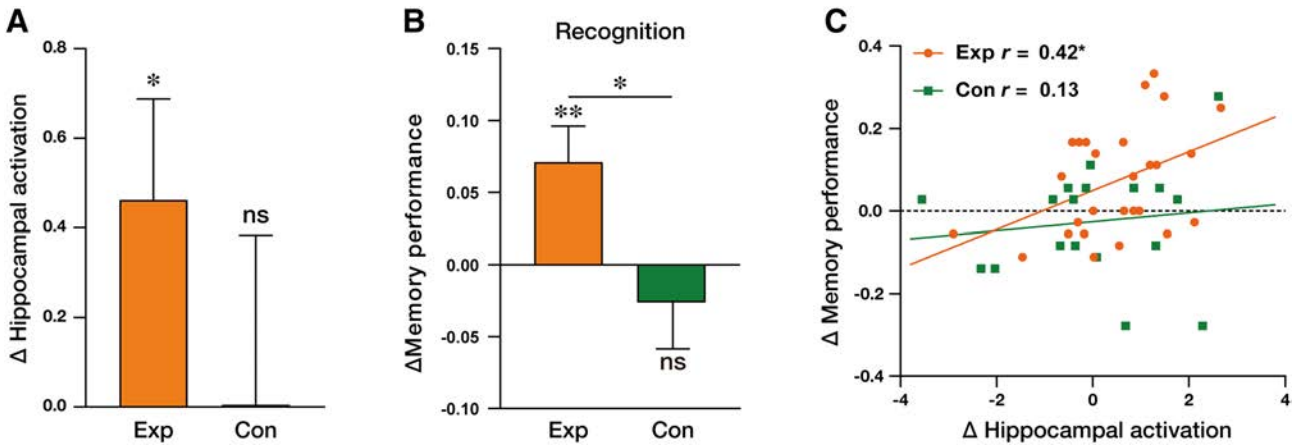

Fig. 2 Experimental results. **A** fNIRS-NF induced task activation in the hippocampus. **B** Recognition test performance of associative memory. **C** Scatter plots showing the relationships between changes in hippocampal activation and changes in memory performance. Error bars indicate SEM. *P ≤0.05; **P ≤0.01; ns, not significant.

brain region *via* directly regulating a cortical region with robust intrinsic connections with the deep region.

The LPC was selected as the direct feedback target because of its robust intrinsic functional connectivity with the hippocampus. Then, multi-session fNIRS-NF training was performed on this region with the aim of enhancing hippocampal activation and improve the subsequent memory performance. Neural effect analysis showed that the activation in the hippocampus during associative memory recognition increased after 8 self-regulation sessions. In addition to neural results, the behavioral effect analysis showed that associative memory performance also increased after training. Furthermore, increased hippocampal activation was significantly correlated with memory improvement. The underlying neural mechanisms for the remote modulation effect and subsequent behavioral improvement induced by fNIRS-NF might be explained as follows. First, self-regulation with mental strategies not only changes the neural activity of the direct target region but also affects the related deep regions within the same network (especially those having strong intrinsic connections with the direct feedback target). Long-term regulation gradually consolidates these influences and finally induces significant changes in neuroplasticity in the connected deep regions. And then the affected key deep regions play their special roles in changing cognitive or behavioral performance. In this study, though the feedback signal from the LPC was regulated directly, the hippocampus having strong functional connectivity with this cortical target could also be activated simultaneously. After 8 fNIRS-NF training sessions, the hippocampal activation was increased significantly. Enhanced hippocampal activation supports more effective associative memory processing, and increases subsequent memory performance. The hippocampus is the core component of the distributed hippocampal-cortical network [18] and plays a crucial role in associative memory processing [19]. Information from various distributed cortical modules is received by the adjacent cortical regions of the medial temporal lobe *via* respective streams, and then these independent elements are rapidly integrated and bound into coherent long-term memory traces by the hippocampus [20]. During retrieval, the presentation of a subset of the original information reactivates the hippocampus and causes the cortical network to reinstate the original pattern of activity, allowing recall of the stored information [21]. Increased hippocampal activation makes these memory processes more efficient and precise, and improves final memory performance [15, 22].

Here, we preliminarily tested the feasibility of using fNIRS-NF to indirectly modulate a deep brain region by directly regulating an accessible cortical feedback target with robust functional connectivity with the deep region. These neural and behavioral results suggested the potential for fNIRS-NF on a functionally-connected cortical region to be used to indirectly modulate the neural activity of a related deep brain regions and improve the desired cognitive functions. However, several limitations should be noted when interpreting our results, and future studies are needed to generalize our method. First, we only tested the feasibility of fNIRS-NF to indirectly modulate a single deep brain region – the hippocampus. And, the results were generated based on a healthy young adult population sample. Future studies are needed to test its feasibility for other deep brain regions (e.g., the amygdala and subgenual cingulate cortex) in different populations, especially before deployment to clinical applications. Second, in the current study, the robust functional connectivity between the superficial cerebral cortex and the hippocampus was identified by using FDR correction (P <0.005) on the

result of group-level resting-state fMRI analysis, but the criteria might be different in other specific studies. The final goal, here, was to identify an accessible cortical region with strong and stable function connectivity with a deep brain target in the same network, which is more likely to affect the deep region and achieve plastic change in that region. Besides, although distal neural modulation was found in the current study and other related research, the underlying mechanism is yet unclear, requiring further study.

In conclusion, self-regulation of a hippocampus-connected cortical region by fNIRS-NF successfully increased task-related hippocampal activation and the associative memory improvement. Furthermore, the change in hippocampal activation was correlated with the behavioral change. Our results suggest the potential of fNIRS-NF to indirectly modulate deep regions *via* regulating a functionally-connected cortical regions and improve the related cognitive functions or clinical symptoms.

Acknowledgments This work was supported by the National Natural Science Foundation of China (82071999, 61431002, 31521063, and 61273287), and the National 973 Program (2014CB846100).

Conflict of interest The authors claim that there are no conflicts of interest.

References

1. Johnson MD, Lim HH, Netoff TI, Connolly AT, Johnson N, Roy A, *et al*. Neuromodulation for brain disorders: Challenges and opportunities. IEEE Trans Biomed Eng 2013, 60: 610–624.
2. Sitaram R, Ros T, Stoeckel L, Haller S, Scharnowski F, Lewis-Peacock J, *et al*. Closed-loop brain training: The science of neurofeedback. Nat Rev Neurosci 2017, 18: 86–100.
3. Thibault RT, MacPherson A, Lifshitz M, Roth RR, Raz A. Neurofeedback with fMRI: A critical systematic review. Neuroimage 2018, 172: 786–807.
4. Ferrari M, Quaresima V. A brief review on the history of human functional near-infrared spectroscopy (fNIRS) development and fields of application. Neuroimage 2012, 63: 921–935.
5. Wang Q, Zhu GP, Yi L, Cui XX, Wang H, Wei RY, *et al*. A review of functional near-infrared spectroscopy studies of motor and cognitive function in preterm infants. Neurosci Bull 2020, 36: 321–329.
6. Wu Z, Luo Y, Gao Y, Han Y, Wu K, Li X. The role of frontal and occipital cortices in processing sustained visual attention in young adults with attention-deficit/hyperactivity disorder: A functional near-infrared spectroscopy study. Neurosci Bull 2020, 36: 659–663.
7. Kohl SH, Mehler DMA, Lührs M, Thibault RT, Konrad K, Sorger B. The potential of functional near-infrared spectroscopy-based neurofeedback-A systematic review and recommendations for best practice. Front Neurosci 2020, 14: 594.
8. Alhourani A, McDowell MM, Randazzo MJ, Wozny TA, Kondylis ED, Lipski WJ, *et al*. Network effects of deep brain stimulation. J Neurophysiol 2015, 114: 2105–2117.
9. Chen XY, Zhang CC, Li YX, Huang P, Lv Q, Yu WW, *et al*. Functional connectivity-based modelling simulates subject-specific network spreading effects of focal brain stimulation. Neurosci Bull 2018, 34: 921–938.
10. Herrington TM, Cheng JJ, Eskandar EN. Mechanisms of deep brain stimulation. J Neurophysiol 2016, 115: 19–38.
11. Fox MD, Buckner RL, Liu H, Chakravarty MM, Lozano AM, Pascual-Leone A. Resting-state networks link invasive and noninvasive brain stimulation across diverse psychiatric and neurological diseases. Proc Natl Acad Sci U S A 2014, 111: E4367–E4375.
12. Fox MD, Buckner RL, White MP, Greicius MD, Pascual-Leone A. Efficacy of transcranial magnetic stimulation targets for depression is related to intrinsic functional connectivity with the subgenual cingulate. Biol Psychiatry 2012, 72: 595–603.
13. Wang JX, Rogers LM, Gross EZ, Ryals AJ, Dokucu ME, Brandstatt KL, *et al*. Targeted enhancement of cortical-hippocampal brain networks and associative memory. Science 2014, 345: 1054–1057.
14. Kim S, Nilakantan AS, Hermiller MS, Palumbo RT, VanHaerents S, Voss JL. Selective and coherent activity increases due to stimulation indicate functional distinctions between episodic memory networks. Sci Adv 2018, 4: eaar2768.
15. Wais PE. Hippocampal signals for strong memory when associative memory is available and when it is not. Hippocampus 2011, 21: 9–21.
16. Liu W, Wei D, Chen Q, Yang W, Meng J, Wu G, *et al*. Longitudinal test-retest neuroimaging data from healthy young adults in southwest China. Sci Data 2017, 4: 170017.
17. Kahn I, Andrews-Hanna JR, Vincent JL, Snyder AZ, Buckner RL. Distinct cortical anatomy linked to subregions of the medial temporal lobe revealed by intrinsic functional connectivity. J Neurophysiol 2008, 100: 129–139.
18. Ranganath C, Ritchey M. Two cortical systems for memory-guided behaviour. Nat Rev Neurosci 2012, 13: 713–726.
19. Mayes A, Montaldi D, Migo E. Associative memory and the medial temporal lobes. Trends Cogn Sci 2007, 11: 126–135.
20. Suzuki WA. Making new memories: The role of the hippocampus in new associative learning. Ann N Y Acad Sci 2007, 1097: 1–11.
21. Ritchey M, Wing EA, LaBar KS, Cabeza R. Neural similarity between encoding and retrieval is related to memory *via* hippocampal interactions. Cereb Cortex 2013, 23: 2818–2828.
22. Addis DR, Moscovitch M, Crawley AP, McAndrews MP. Recollective qualities modulate hippocampal activation during autobiographical memory retrieval. Hippocampus 2004, 14: 752–762.

Neurosci. Bull. August, 2021, 37(8):1256–1259
https://doi.org/10.1007/s12264-021-00690-z
www.neurosci.cn
www.springer.com/12264

RESEARCH HIGHLIGHT

A Novel Phagocytic Role of Astrocytes in Activity-dependent Elimination of Mature Excitatory Synapses

Tong Luo[1] · Tian-Ming Gao[1]

Received: 18 January 2021 / Accepted: 23 February 2021 / Published online: 23 April 2021

One of the grand strategies in the development of the nervous system is to overproduce constructive elements and then selectively to prune the excess, for example, by synaptic pruning. Given limited resources, surviving synapses are nurtured and reinforced, while the unsuccessful synapses are eliminated. Synaptic pruning also persists in the mature nervous system *via* activity-dependent plasticity, which is crucial for learning and memory. To assemble refined mature neuronal circuits and maintain homeostasis, synaptic pruning must proceed in a controlled and timely manner. Aberrant synaptic pruning may lead to neurodevelopmental disorders, such as autism, schizophrenia, and epilepsy [1].

Phagocytosis is defined as the process by which phagocytes identify, engulf, and digest large particles, such as pathogens, dead cells, and cellular debris. In the central nervous system, phagocytosis functions as a defense and clearance mechanism. Glial cells are the critical effectors of synaptic pruning through phagocytosis to eliminate unnecessary synapses. Microglia are considered to be the primary phagocytes [2], which mainly use immune signaling pathways such as the classical complement pathway to remove unwanted synapses [3]. In addition to microglia, astrocytes are regarded as less-efficient phagocytes in the brain through the Multiple Epidermal Growth Factor-Like Domains Protein 10 (Megf10) and MER Proto-Oncogene, Tyrosine Kinase (Mertk) phagocytic pathways [4, 5]. Particularly, the complement component C1q binds to Megf10 in astrocytes to trigger intracellular downstream signals [6], which requires PTB Domain-Containing Engulfment Adapter Protein 1 and ATP-binding cassette subfamily A member 1. Mertk in astrocytes uses the integrin pathway to regulate phagocytosis involving CRKII/DOCK180/Rac1 [7]. Astrocyte-mediated phagocytosis is significantly reduced in $Megf10^{-/-}$ and $Mertk^{-/-}$ mice, and is further reduced in double-knockout mice, indicating that Megf10 and Mertk mediate synapse elimination in parallel [5].

Although astrocytes were initially regarded as secondary phagocytes that back up microglial phagocytic activity in the brain, recent studies indicate that microglia and astrocytes play orchestrated roles: microglia specialize in engulfing cell bodies and proximal dendrites, while astrocytes preferentially engulf distal processes and diffuse neuritic debris [8]. Nevertheless, the precise interplay between microglia and astrocytes in synapse elimination is still unknown. Specifically, the brain contains various types of synapse, including excitatory and inhibitory synapses. And a has synapse two components, the pre- and the post-synaptic compartments. It remains unexplored whether the diversity of synapses is responsible for the distinct phagocytic pathways used by different phagocytes (Fig. 1).

Using novel fluorescent phagocytosis reporters, Hyungju Park, Won-Suk Chung, and colleagues have demonstrated that astrocytes, not microglia, play a major role in constantly eliminating unnecessary adult excitatory synapses in response to brain activity. To monitor glial phagocytosis, they generated a novel molecular sensor. In a neutral pH environment, the sensor on the cell membrane

✉ Tian-Ming Gao
tgao@smu.edu.cn

[1] State Key Laboratory of Organ Failure Research, Key Laboratory of Mental Health of the Ministry of Education, Guangdong-Hong Kong-Macao Greater Bay Area Center for Brain Science and Brain-Inspired Intelligence, Guangdong Key Laboratory of Psychiatric Disorders, Collaborative Innovation Center for Brain Science, Department of Neurobiology, School of Basic Medical Sciences, Southern Medical University, Guangzhou 510515, China

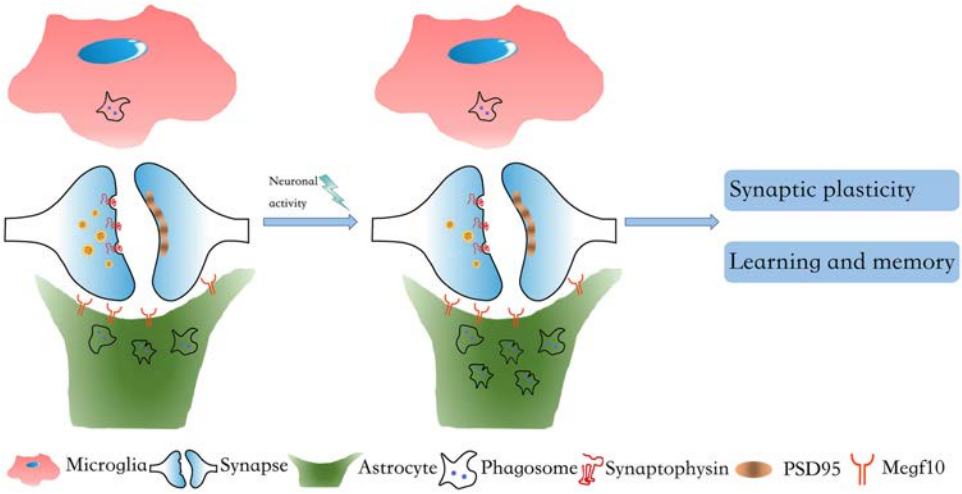

Fig. 1 Astrocytes play a major role in the neuronal activity-dependent elimination of excitatory synapses. Astrocytes (green) eliminate unwanted excitatory synapses from neurons (blue) by phagocytosing them through Megf10 receptors in adult mouse hippocampus. Neuronal activity selectively increases the Megf10-dependent astrocytic phagocytosis of excitatory synapses, which has important implications for synaptic plasticity and memory formation.

has intact fluorescent intensity of both mCherry and eGFP, while under acidic conditions, for instance after phagocytosis in the lysosome, the sensor preserves only the mCherry signal. Consequently, investigators were able to localize and quantify phagosomes by tracing the puncta with a mCherry but not an eGFP signal. Then the authors targeted the sensor into different synaptic terminals *via* linking it to pre- or post-synaptic markers driven by cell-type-specific promotors, through which they were able to separately quantify the phagocytic events of one type of synapse. Moreover, by co-localizing the phagocytic signals with microglia or astrocytic markers, they measured how often and by which type of glial cell synapses were phagocytosed. Their results revealed that in the CA1 region of the adult mouse hippocampus, although both excitatory and inhibitory synaptic terminals can be eliminated by glial phagocytosis, remarkably more excitatory synapses than inhibitory synapses were phagocytosed. Strikingly, they also found that astrocytes had more phagocytic puncta than microglia regardless of the type of synapse. Further investigation showed that only astrocytic phagocytosis of excitatory synapses increased with neuronal activity induced by environmental enrichment, while neither the uptake of inhibitory synapses by astrocytes nor the uptake of synapses by microglia were affected.

Recently, Megf10 and Mertk have been reported to be major phagocytic pathways in astrocytes. To investigate the mechanisms underlying the synapse elimination by astrocytic phagocytosis, the authors also deployed the fluorescent phagocytosis reporters in a mouse model in which Megf10 was inducibly deleted in adult astrocytes. They found that astrocytes use Megf10 specifically to engulf excitatory synapses in the adult hippocampus. Further experiments showed that astrocytic deletion of Megf10 resulted in significantly more total synapses and excitatory synapses, as well as causing abnormal synaptic plasticity. In addition, mice with hippocampus-specific astrocyte conditional Megf10-knockout displayed a significant deficit in novel object recognition and novel object location tests, suggesting a critical role of Megf10-mediated astrocytic phagocytosis in learning and memory.

Previously, astrocytes were reported to participate in synapse elimination in the developing visual system in mice [5, 9]. And human astrocytes have been demonstrated to be able to phagocytose synapses in dissociated cultures and cerebral organoids [10, 11], indicating that astrocytes prune synapses in the human CNS. Nevertheless, astrocytes were regarded as a secondary or back-up phagocyte in the CNS. Contrary to this consensus, Hyungju Park, Won-Suk Chung and their colleagues have shown that astrocytes are the dominant phagocytes. Compared with previous findings in developing brains, synapse pruning in adults may have quite distinct significance in physiological functions. This study showed that astrocytes control excitatory synapse elimination in adult mouse hippocampal CA3–CA1 circuits, and that Megf10-mediated astrocytic phagocytosis is functionally relevant to synaptic plasticity and memory formation [12]. Thus, this study proposes a possible mechanism for controlling synaptic turnover and re-patterning connectivity, which may contribute to the rapid renewal of memory traces in the adult hippocampus.

Just as it gave several answers for synapse elimination, this investigation raised more interesting questions. The authors proposed a predominant role of astrocytic phagocytosis in synapse elimination under physiological conditions. Few studies have examined astrocytic phagocytosis in pathological synaptic dysfunction following injury or nervous system degeneration in adults. In mouse models of Alzheimer's disease (AD), astrocytes have been suggested to have the capacity to clear Aβ [13]. APOE4, a strong genetic risk factor for AD, suppresses astrocytic phagocytosis, and the protective APOE allele for AD, APOE2,

remarkably promotes phagocytosis by astrocytes [14]. Overall, the phagocytic capacity of astrocytes appears to decrease during reactive astrogliosis [15, 16]. On the contrary, several publications have shown that phagocytosis by microglia is strongly implicated in neurological pathologies [17]. Inhibition or knockout of C1q, complement C3, or the microglia-specific C3 receptor (CR3), which are required for microglial phagocytosis, reduce the synapse loss in AD [18]. Similarly, mice with depleted microglia or deficiency in C3 or CR3a are protected from virus-induced synaptic loss [19]. There are other reports of microglial phagocytosis involved in the synaptic loss induced by HIV [20], by ageing [21], and in schizophrenia [22]. Given this evidence, it would be interesting to further define the possible divergent roles of astrocytic and microglial phagocytosis under pathological conditions.

Generally, all phagocytosis can be divided into 3 major steps: "find me", "eat me", and "digest me". This study left black boxes in each step. For example, what guides the astrocytes to phagocytose the unnecessary excitatory synapses after neuronal activity? This question can be addressed how neuronal activity induces unnecessary excitatory synapses to recruit astrocytes or how neuronal activity protects necessary excitatory synapses from elimination. In the brain, some examples of synapse pruning may give hints to answer this question. For instance, astrocytes secrete the glycoprotein hevin (SPARCL1), which modulates the formation of excitatory inputs in the visual cortex and regulates the elimination of these connections [23]. Accumulation of C1q and C3 on certain subsets of synapses promote microglia to engulf them. On the other hand, CD47 on the neuronal cell membrane, and its receptor in microglia, SIRPα, suppress the phagocytosis of synaptic structures [24]. Consequently, one possible mechanism is that neuronal activity triggers the relocation or regulates the expression of these "eat-me" or "don't-eat-me" signals to mediate phagocytosis by astrocytes.

In addition to the above topics, it seems that in the brain, each region has different rates of synapse elimination by microglia and astrocytes. It will be of great interest to elucidate the internal and external factors controlling these rates. Another intriguing finding of this study is that both astrocytes and microglia have significantly different levels of phagocytosis between presynaptic and postsynaptic structures. It is reasonable to speculate that there are important mechanisms of eliminating synapses other than phagocytosis, and these occur more often in postsynaptic than presynaptic structures, such as miRNA in extracellular vesicles proposed by Prada *et al.* [25]. Last but not least, since Megf10 and Mertk are major phagocytic pathways in astrocytes, the results of this investigation arouse curiosity about the role of Mertk-mediated astrocytic phagocytosis in synapse elimination. Overall, this study emphasizes the astrocyte-mediated synapse turnover in learning and memory and provides novel insight into treating various brain disorders by modulating astrocytic phagocytosis to restore synaptic connectivity.

Acknowledgements This Research Highlight was supported by Grants from the National Natural Science Foundation of China (31830033 and 82090032), the Program for Changjiang Scholars and Innovative Research Teams in University (IRT_16R37), and the Key-Area Research and Development Program of Guangdong Province, China (2018B030334001).

Conflict of interest The authors declare that they have no competing interests.

References

1. Neniskyte U, Gross CT. Errant gardeners: glial-cell-dependent synaptic pruning and neurodevelopmental disorders. Nat Rev Neurosci 2017, 18: 658–670.
2. Galloway DA, Phillips AEM, Owen DRJ, Moore CS. Phagocytosis in the Brain: Homeostasis and Disease. Front Immunol 2019, 10: 790.
3. Stephan AH, Barres BA, Stevens B. The complement system: an unexpected role in synaptic pruning during development and disease. Annu Rev Neurosci 2012, 35: 369–389.
4. Magnus T, Chan A, Linker RA, Toyka KV, Gold R. Astrocytes are less efficient in the removal of apoptotic lymphocytes than microglia cells: implications for the role of glial cells in the inflamed central nervous system. J Neuropathol Exp Neurol 2002, 61: 760–766.
5. Chung WS, Clarke LE, Wang GX, Stafford BK, Sher A, Chakraborty C. Astrocytes mediate synapse elimination through MEGF10 and MERTK pathways. Nature 2013, 504: 394–400.
6. Iram T, Ramirez-Ortiz Z, Byrne MH, Coleman UA, Kingery ND, Means TK, *et al.* Megf10 is a receptor for C1Q that mediates clearance of apoptotic cells by astrocytes. J Neurosci 2016, 36: 5185–5192.
7. Jung YJ, Chung WS. Phagocytic roles of glial cells in healthy and diseased brains. Biomol Ther (Seoul) 2018, 26: 350–357.
8. Damisah EC, Hill RA, Rai A, Chen F, Rothlin CV, Ghosh S, *et al.* Astrocytes and microglia play orchestrated roles and respect phagocytic territories during neuronal corpse removal in vivo. Sci Adv 2020, 6: eaba3239.
9. Chung WS, Allen NJ, Eroglu C. Astrocytes control synapse formation, function, and elimination. Cold Spring Harb Perspect Biol 2015, 7: a020370.
10. Zhang Y, Sloan SA, Clarke LE, Caneda C, Plaza CA, Blumenthal PD, *et al.* Purification and characterization of progenitor and mature human astrocytes reveals transcriptional and functional differences with mouse. Neuron 2016, 89: 37–53.
11. Sloan SA, Darmanis S, Huber N, Khan TA, Birey F, Caneda C, *et al.* Human astrocyte maturation captured in 3d cerebral cortical spheroids derived from pluripotent stem cells. Neuron 2017, 95(779–790): e776.
12. Lee JH, Kim JY, Noh S, Lee H, Lee SY, Mun JY, *et al.* Astrocytes phagocytose adult hippocampal synapses for circuit homeostasis. Nature 2020.
13. Wyss-Coray T, Loike JD, Brionne TC, Lu E, Anankov R, Yan F, *et al.* Adult mouse astrocytes degrade amyloid-beta in vitro and in situ. Nat Med 2003, 9: 453–457.
14. Chung WS, Verghese PB, Chakraborty C, Joung J, Hyman BT, Ulrich JD, *et al.* Novel allele-dependent role for APOE in

controlling the rate of synapse pruning by astrocytes. Proc Natl Acad Sci U S A 2016, 113: 10186–10191.
15. Hong S, Beja-Glasser VF, Nfonoyim BM, Frouin A, Li S, Ramakrishnan S, *et al.* Complement and microglia mediate early synapse loss in Alzheimer mouse models. Science 2016, 352: 712–716.
16. Liddelow SA, Guttenplan KA, Clarke LE, Bennett FC, Bohlen CJ, Schirmer L, *et al.* Neurotoxic reactive astrocytes are induced by activated microglia. Nature 2017, 541: 481–487.
17. Qin C, Zhou LQ, Ma XT, Hu ZW, Yang S, Chen M, *et al.* Dual functions of microglia in ischemic stroke. Neurosci Bull 2019, 35: 921–933.
18. Vilalta A, Brown GC. Neurophagy, the phagocytosis of live neurons and synapses by glia, contributes to brain development and disease. FEBS J 2018, 285: 3566–3575.
19. Vasek MJ, Garber C, Dorsey D, Durrant DM, Bollman B, Soung A, *et al.* A complement-microglial axis drives synapse loss during virus-induced memory impairment. Nature 2016, 534: 538–543.
20. Tremblay ME, Marker DF, Puccini JM, Muly EC, Lu SM, Gelbard HA. Ultrastructure of microglia-synapse interactions in the HIV-1 Tat-injected murine central nervous system. Commun Integr Biol 2013, 6: e27670.
21. Shi Q, Colodner KJ, Matousek SB, Merry K, Hong S, Kenison JE, *et al.* Complement C3-deficient mice fail to display age-related hippocampal decline. J Neurosci 2015, 35: 13029–13042.
22. Sekar A, Bialas AR, de Rivera H, Davis A, Hammond TR, Kamitaki N, *et al.* Schizophrenia risk from complex variation of complement component 4. Nature 2016, 530: 177–183.
23. Singh SK, Stogsdill JA, Pulimood NS, Dingsdale H, Kim YH, Pilaz LJ, *et al.* Astrocytes assemble thalamocortical synapses by bridging NRX1alpha and NL1 *via* hevin. Cell 2016, 164: 183–196.
24. Lehrman EK, Wilton DK, Litvina EY, Welsh CA, Chang ST, Frouin A, *et al.* CD47 protects synapses from excess microglia-mediated pruning during development. Neuron 2018, 100(120–134): e126.
25. Prada I, Gabrielli M, Turola E, Iorio A, D'Arrigo G, Parolisi R, *et al.* Glia-to-neuron transfer of miRNAs *via* extracellular vesicles: a new mechanism underlying inflammation-induced synaptic alterations. Acta Neuropathol 2018, 135: 529–550.

Neurosci. Bull. August, 2021, 37(8):1260–1263
https://doi.org/10.1007/s12264-021-00721-9

www.neurosci.cn
www.springer.com/12264

RESEARCH HIGHLIGHT

A Temporal Precision Approach for Deep Transcranial Optogenetics with Non-invasive Surgery

Shanshan Sun[1,2] · Jiali Shi[1,2] · Yongjie Wang[1,2] · Jun Cheng[1] · Zhihui Huang[1,2]

Received: 13 December 2020 / Accepted: 24 April 2021 / Published online: 6 June 2021

Optogenetics, an optical technique that uses light as a modality of biological control to manipulate neuronal activity, has revolutionized the understanding of individual neurons and the ability to decode neural circuit mechanisms in the nervous system [1]. Optogenetics technology has rapidly become a standard tool for understanding the mechanisms of cell types, neural circuits, and nervous systems under both normal and pathological conditions. For example, optogenetics has been developed to drive the expression of reporter proteins in specific cell types. These tools encompass gene delivery methods (e.g., biological, chemical, and viral transfection or chromosomal integration), as well as cell-type specific promoters and driver lines (e.g., GAL4/UAS or Cre-Lox systems) that have been identified or generated for various model organisms, such as worm, fly, fish, and mouse. Furthermore, optogenetics is a powerful technique to achieve precise regulation of specific cellular subtypes and circuits *in vivo*. Experiments have probed the function of brain circuits in awake and behaving animals with previously unimagined temporal and spatial resolution, revealing the complexity of behavioral control and new horizons of circuit function [2].

✉ Jun Cheng
chengjun119@hotmail.com

✉ Zhihui Huang
huang0069@hznu.edu.cn

[1] College of Pharmacy, School of Medicine, and Department of Neurosurgery, The Affiliated Hospital, Hangzhou Normal University, Hangzhou 311121, China

[2] Key Laboratory of Elemene Class Anti-Cancer Chinese Medicines, Engineering Laboratory of Development and Application of Traditional Chinese Medicines, Collaborative Innovation Center of Traditional Chinese Medicines of Zhejiang Province, Hangzhou Normal University, Hangzhou 311121, China

The key to this new experimental technique is the development of new optogenetic probes, which are continuously advancing at an accelerating rate. In 2005, Boyden *et al.* first reported the successful *in vitro* transfection and expression of functional channelrhodopsin-2 (ChR2) in mammalian neurons *via* lentiviral gene delivery [3]. ChR2 is derived from *Chlamydomonas reinhardtii* and primarily expressed in cellular membranes. It permits temporal control of neuronal activity at the millisecond scale but at the risk of a high level of desensitization [4, 5]. Currently, the application of ChR2 provides greater flexibility in experimental design in addition to more powerful and refined operations. Therefore, ChR2 is widely applied in optogenetics and has been gradually applied in exploring neurological diseases.

Apart from optogenetics, there are several other methods for the regulation of neurons: ultrasound (US), electrical deep brain stimulation (DBS), and transcranial magnetic stimulation (TMS). But each has its shortcomings. For example, US stimulation is non-invasive, and suitable for stimulating neuronal populations but might generate ion fluxes by disrupting the integrity of otherwise ion-impermeant lipid bilayers [6]. Like all brain surgery, DBS is characterized by a small risk of infection, stroke, bleeding, or seizures. Compared to DBS, TMS is more readily accepted by patients because it does not require anesthesia and is minimally invasive with fewer side-effects [7]. The shortcoming of TMS is the inaccurate positioning. Another unavoidable defect of TMS is the challenge to the depth of stimulation-TMS can only stimulate the superficial cortex; it exerts no stimulating effect on subcortical areas [8]. Inaccurate positioning of TMS is also shared by US stimulation.

By comparison, optogenetics has unparalleled advantages; it enables the almost instantaneous response of

opsins to visible light along with the benefits of pinpoint optical targeting and high spatiotemporal resolution. This highly rapid and selective neuromodulation by visible light is unachievable by other modalities [1]. However, the transmission of visible light generally requires the invasive implantation of external objects and equipment into the brain, which may cause tissue damage and increase the risk of infection and ischemia. Moreover, scattering and absorption in skull and tissues can potentially cause light decay and limit the transmission of a sufficient photon density to stimulate the neural activity in deep brain structures (Fig.1A). At present, it is urgent to develop new tools to solve these problems.

Recently, Professor Karl Deisseroth's team reported the potent fast red-shifted opsin ChRmine, which exhibits significantly larger photocurrents with hundred-fold improvement in operational light sensitivity compared to existing fast red-shifted variants and rapid off-kinetics suitable for millisecond-scale control over neural activity, which may be proper for deep transcranial optogenetics [9]. Based on these characteristics, the authors attempted to elucidate whether ChRmine can achieve rapid transcranial deep brain photoactivation under the premise of ensuring safety (Table 1). The ventral tegmental area (VTA), 4.5 mm deep from the skull surface, was chosen to examine its effect. When a 400-μm optical fiber was positioned directly above the surface of the intact skull and short pulses of 635-nm light delivered at a certain pulse duration, irradiance, and frequency, the light-responsive neurons were activated. Also, they found that the neural responsivity

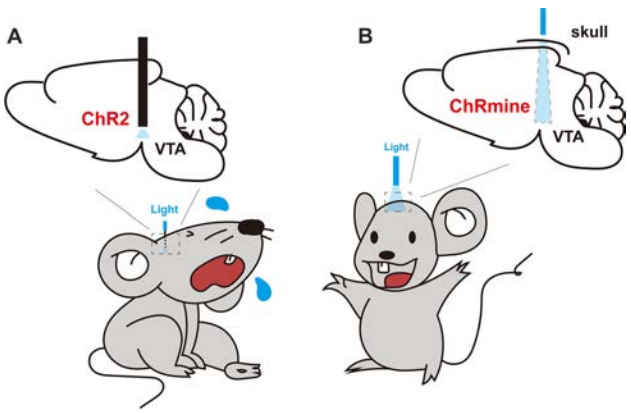

Fig. 1 Optogenetics with microbial channelrhodopsin-2 (ChR2) *vs* the potent fast red-shifted opsin ChRmine. **A** Microbial channelrhodopsins (ChRs) enable cell type-specific excitation or light inhibition of neuronal activity; however, the delivery of visible light often requires invasive implantation of foreign materials and devices into the brain, which damages tissue and increases the risk of infection and ischemia. **B** Deep transcranial photoactivation with ChRmine raises the possibility of exploring interventions for brain disorders where the light source is well-separated from the target cells with non-invasive implantation of light stimulation devices.

improved with increased pulse duration. Further, they explored whether a lower irradiance could activate cells with an extension of pulse time. The results demonstrated that, with an extended pulse time up to 100 ms, the VTA neurons were activated, even when the light delivered to the surface of the skull was as low as 40 mW/mm^2. In addition, the spike latencies shortened upon strengthening the irradiance both *in vivo* and *in vitro*.

To explore the depth limit at which ChRmine-expressing neurons can be activated by transcranial light transmission, AAV8-CamKIIα::ChRmine-oScarlet-Kv2.1 was injected into the brains of rats at different depths. Notably, they found that at a 100-ms pulse width of 400 mW/mm^2, the reliable light stimulation dropped to 7 mm, and only approximately 0.02% of the initial irradiance (400 mW /mm^2) penetrated to this depth, and this is almost the sensitivity limit of ChRmine. Amazingly, they also found that none of these conditions applied to deep transcranial optogenetics caused tissue damage, which is highly critical for its human application in future.

Can deep transcranial activation of ChRmine regulate behaviors of mice *in vivo*? By injecting AAV8-EF1α::DIO-ChRmine-oScarlet into the VTA of DAT::Cre mice, ChRmine was specifically expressed in dopamine neurons in the marginal cortex. The authors proposed to elucidate whether transcranial optical stimulation could specifically regulate appetite. The results demonstrated that mice expressing ChRmine increased the proportion of time spent in the irradiated paired area in the real-time place preference assay test at irradiance ≥200 mW/mm^2 (20 Hz, 5 ms) with minimal toxicity, whereas the control mice did not. And the same behavior was evoked even after 6 months of chronic viral expression. Also, the place preference was not affected by the power of the light stimulation, but related to its frequency.

Further, the authors examined whether this method could be adopted to treat brain diseases. With the hippocampal alginate model of temporal lobe epilepsy, ChRmine optogenetic methods were applied to target hippocampal parvalbumin (PV$^+$) inhibitory (GABAergic) interneurons to provide feedforward inhibition and stop wild-type animal seizures. By subjecting the experimental group to light stimulation (40 mW/mm^2, 50 ms on, 100 ms off, lasting 10 s) during epileptic seizures, the seizure duration was truncated by 51% ± 2%; however, when ChRmine was used to target the wider GABAergic hippocampal septal neurons (not just PV$^+$ neurons), only 27% ± 4% of epileptic seizures were inhibited. These results suggested that deep brain optogenetics with ChRmine indeed can treat brain diseases, at least epilepsy.

Finally, the authors assessed whether systemic viral delivery using ChRmine could adjust neuromodulation without brain tissue damage. Here, they administered

Table 1 Differences between ChRmine and ChRs for optogenetics.

Characteristics	ChRmine	ChRs
Provides high temporal control enabled by fast opsins	Yes	No
Requires invasive implantation of foreign materials and device into the brain	No	Yes
Limits transmission of sufficient photon densities	No	Yes
Is suitable for deep transcranial optogenetics	Yes	No

ChRs channelrhodopsins.

AAVPHPeB-Tph2::ChRmine-eYFP *via* retro-orbital injection to target serotonergic 5-HT neurons in the dorsal raphe nucleus of the brainstem in wild-type mice. After 6 weeks, they found that ChRmine-expressing mice, but not control mice, showed social preference in a three-chamber sociability task with no mood impairment after transcranial stimulation. In addition, systemic injection and intracranial injection did not differ in the photoactivation of neurons. Collectively, these results demonstrated that deep transcranial ChRmine photoactivation can promote specific adaptive behaviors without any intracranial surgery.

Notably, Karl Deisseroth and colleagues reported a new optogenetic approach, which is undoubtedly a major breakthrough in the field. Optogenetics has more unparalleled advantages than US, DBS, and TMS [10]: Optogenetics can provide opsins with the advantages of precise optical aiming, and high temporal and spatial resolution. This new discovery has improved the deficiencies of optogenetics, advancing the treatment of brain diseases such as epilepsy.

More deeply, the future applications of optogenetics may not be limited to the central nervous system, but may also be applied in non-neuronal systems, including glial, muscle, cardiac, and embryonic stem cells [11]. For instance, the heart and its associated diseases also poses a major challenge in human research. Optogenetics can bring the dawn and new options for its treatment.

However, one of the limitations is that this method can only reach 7 mm, which makes its application in humans and other non-human primates almost impossible. This warrants further in-depth research. Given that the human brain is much larger than the rodent brain, the other limitations of ChRmine is how to apply it in the clinic. Although it can be used in small brains to alter neuronal activity and behavior, it may have some difficulties in the application to large brains. In addition, the expression of exogenous genes is also a potential risk for application to human beings. In a nutshell, improving the deficiency of optogenetics will have great significance in the management of diseases. More importantly, these new breakthroughs provide new insights for the in-depth exploration of optogenetics and further advances the course of optogenetics.

In summary, Professor Karl Deisseroth and his colleagues applied the powerful rhodopsin ChRmine to achieve transcranial light activation of defined neural circuits (including midbrain and brainstem structures), reaching an unprecedented depth of 7 mm with millisecond precision. With ChRmine's systemic viral delivery, behavioral regulation can be demonstrated without surgery, enabling implant-free deep brain optogenetics (Table 1). Notably, this is a significant new achievement of optogenetics (Table 1). In summary, the researchers demonstrated a method of deep light activation of ChRmine-neurons, which can accurately control the peak time and provide an excellent in-depth manipulation of brain tissue in a completely non-invasive manner, with minimal optical power requirements (Fig. 1B, Table 1). This offers more advantages than luminous implants and intracranial surgery (Fig. 1A, Table 1). Of note, the deep-cranial optogenetics method has been applied in various behavioral environments.

Acknowledgements This Research Highlight was supported by the Natural Science Foundation of Zhejiang Province (LR18C090001), the National Natural Science Foundation of China (92049104, 81801102, and 82071230), and a Research Start-up Project by Hangzhou Normal University (4125C5021920453 and 4125C50220204109).

References

1. All AH, Zeng X, Teh DBL, Yi ZG, Prasad A, Ishizuka T. Expanding the toolbox of upconversion nanoparticles for *in vivo* optogenetics and neuromodulation. Adv Mater 2019, 31: e1803474. https://doi.org/10.1002/adma.201803474.
2. Zemelman BV, Miesenböck G. Genetic schemes and schemata in neurophysiology. Curr Opin Neurobiol 2001, 11: 409–414.
3. Boyden ES, Zhang F, Bamberg E, Nagel G, Deisseroth K. Millisecond-timescale, genetically targeted optical control of neural activity. Nat Neurosci 2005, 8: 1263–1268.
4. Nagel G, Szellas T, Huhn W, Kateriya S, Adeishvili N, Berthold P, *et al.* Channelrhodopsin-2, a directly light-gated cation-selective membrane channel. Proc Natl Acad Sci USA 2003, 100: 13940–13945.
5. Wang HX, Sugiyama Y, Hikima T, Sugano E, Tomita H, Takahashi T, *et al.* Molecular determinants differentiating photocurrent properties of two channelrhodopsins from *Chlamydomonas*. J Biol Chem 2009, 284: 5685–5696.

6. Tyler WJ. Noninvasive neuromodulation with ultrasound? A continuum mechanics hypothesis. Neuroscientist 2011, 17: 25–36.
7. Wu HC, Yan X, Tang DL, Gu WX, Luan YW, Cai HJ, *et al.* Internal states influence the representation and modulation of food intake by subthalamic neurons. Neurosci Bull 2020, 36: 1355–1368.
8. Wagner T, Gangitano M, Romero R, Théoret H, Kobayashi M, Anschel D, *et al.* Intracranial measurement of current densities induced by transcranial magnetic stimulation in the human brain. Neurosci Lett 2004, 354: 91–94.
9. Chen R, Gore F, Nguyen QA, Ramakrishnan C, Patel S, Kim SH, *et al.* Deep brain optogenetics without intracranial surgery. Nat Biotechnol 2021, 39: 161–164.
10. Li X, Li YD, Zhang JH, Zhang XH. Selective targeting of perirhinal cortex projection to hippocampal CA1 interneurons. Neurosci Bull 2019, 35: 763–765.
11. Deisseroth K. Optogenetics. Nat Methods 2011, 8: 26–29.

Neurosci. Bull. August, 2021, 37(8):1264–1266
https://doi.org/10.1007/s12264-021-00703-x

www.neurosci.cn
www.springer.com/12264

RESEARCH HIGHLIGHT

Heteromolecular Plasticity in Striatal Astrocytes

Yi-Hua Chen[1] · Tian-Ming Gao[1]

Received: 12 January 2021 / Accepted: 8 February 2021 / Published online: 2 June 2021

Astrocytes, which are at least as abundant as neurons in the central nervous system, are crucial for sustaining nearly all aspects of brain functions, including ion and neurotransmitter homeostasis, neural circuit formation, synaptic plasticity, and function as well as neurovascular coupling [1]. Astrocytes are also involved in diseases, including Huntington's disease (HD) [2]. Although astrocytes have been assumed to be a homogenous population, a growing body of evidence suggests that they exhibit high heterogeneity across and within brain regions [3]. This heterogeneity is reflected in their morphologies, gene expression profiles, and functions [4]. By using single-cell spatial transcriptomic approaches, a recent study uncovered precise molecular features of astrocytic spatial organization underlying cortical architecture that could provide insight into specialized functions in development and/ or disease [5] (Fig. 1A). Despite such progress, major open questions remain to be addressed relating to how a defined population of astrocytes responds to different challenges, whether such responses can be quantified molecularly, and whether they can be exploited for correction of disease phenotypes with contributory astrocytic roles.

To address these important issues, Yu *et al*. used single-cell sequencing to disentangle how astrocytes respond at the molecular level to multiple experimental perturbations (EPs) [6]. Given that astrocytes differ markedly between brain nuclei, the authors chose a single brain area—the adult striatum—to study their responses. The EPs comprised 14 groups encompassing striatum-relevant disease and physiology, including HD mouse models, pathology, ionic signaling, and GPCR signaling (Fig. 1B). By performing experiments to evaluate changes in the gene expression of astrocytes following each of the 14 EPs, the authors found that (1) the number of differentially-expressed genes, (2) gene networks and their associated pathways, and (3) upstream regulators of astrocyte gene expression displayed a high degree of EP specificity (Fig. 1B), indicating that astrocytes showed remarkable flexibility in response to different perturbations. Further analysis showed that there was little effect on pan-reactive neurotoxic-A1, and neuroprotective-A2 reactivity genes [7] for each EP.

On the basis of evaluations of RNA-seq datasets from 14 EPs, the authors proceeded to evaluate the potential contributions of striatal astrocytes to HD. By mapping HD mice and human gene expression data, the authors found a strong concordance between mouse and human HD striatal astrocytes, which provide further support for using an animal model to study the mechanisms of HD. Of note, disease phenotype-dependent changes included several pathways related to GPCR, Ca^{2+} signaling, and synaptic plasticity. Importantly, $G_{\alpha i}$ signaling was consistently inhibited in HD astrocytes among the top pathways that were downregulated in HD astrocytes. To explore whether the activation of astrocyte Gi-GPCRs in HD model mice would produce beneficial effects, the authors employed designer receptors exclusively activated by designer drugs (DREADDs) to express hM4DGi in striatal astrocytes and found that striatal astrocyte G_i-GPCR activation corrected

✉ Tian-Ming Gao
tgao@smu.edu.cn

[1] State Key Laboratory of Organ Failure Research, Key Laboratory of Mental Health of the Ministry of Education, Guangdong-Hong Kong-Macao Greater Bay Area Center for Brain Science and Brain-Inspired Intelligence, Guangdong Province Key Laboratory of Psychiatric Disorders, Collaborative Innovation Center for Brain Science, Department of Neurobiology, School of Basic Medical Sciences, Southern Medical University, Guangzhou 510515, China

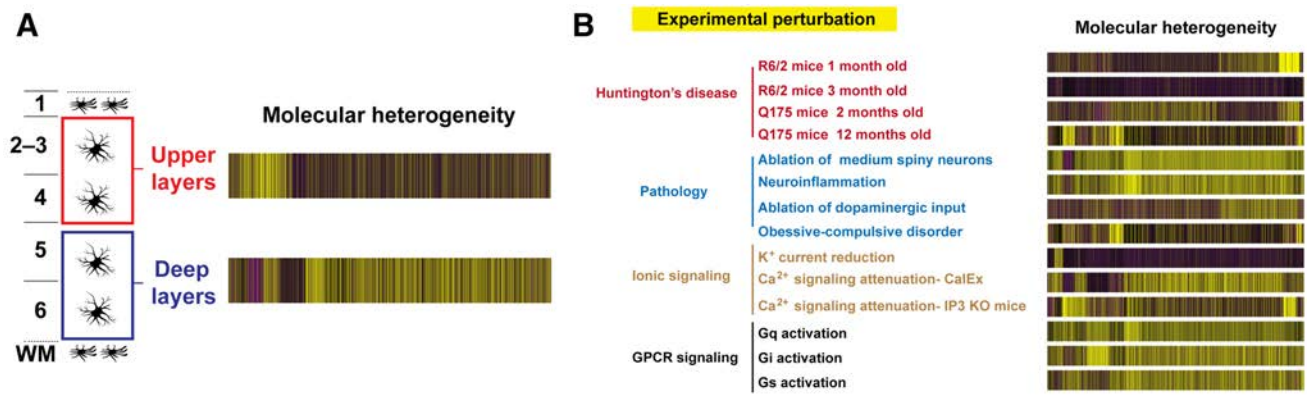

Fig. 1 Schematic of molecular heterogeneity of astrocytes in physiological and challenged brain. **A** Molecular heterogeneity of layer astrocytes identified by RNA-sequence. **B** 14 experimental perturbations from four groups, showing HD, pathology, ionic signaling, and GPCR signaling led to context-specific astrocyte molecular responses. The figure was reproduced from references [5, 6].

(1) attenuated Ca^{2+} signals, (2) reduced AMPA and NMDA EPSCs, (3) impaired motor behaviors, and (4) HD-related molecular modifications (Fig. 2). Moreover, the expression of *Thbs1*, which was previously found to promote synaptogenesis and is astrocyte-enriched, was enhanced. By blocking TSP1 (encoded by *Thbs1*) action, the authors found that hM4DGi activation in the striatal astrocytes failed to improve cellular and behavioral outcomes in HD model mice, suggesting possible downstream mechanisms of Gi-GPCR activation. The authors also identified new endogenous astrocyte GPCRs (e.g., *Gpr37l1*, *S1pr1*, and *Edenrb*) that may mimic the effects seen with Gi-GPCR activation and might represent new drug targets to correct astrocyte-dependent cellular and behavioral dysfunctions in HD.

Notably, this is the first direct experimental evaluation of heteromolecular plasticity of astrocytes in responds to multiple stimuli *in vivo* as far as we know. Just as it uncovers the heteromolecular plasticity of astrocytes, this investigation raises more interesting questions. Firstly, what makes the astrocytes so special that each EP elicits unique changes? A way that astrocytes can be specified while maintaining many of their defining functional properties is through the acquisition of sub-features during the distinct developmental time windows of gliogenesis. Alternatively, Astrocytes might also be regionally specialized to confer stimulus complexity in a defined brain region. It is reasonable to speculate whether there are special spatial distributions for each kind of EP-characterized astrocytes. Secondly, astrocytes are ubiquitous in the central nervous system, they possess thousands of individual processes, which extend out into the neuropil, interacting with neurons, other glia, and blood vessels. The degree of functional diversity begs the question of how they shape information processing and orchestrate network activity flows that underlie each EP. Thirdly, do astrocytes in different brain regions show flexibility under a defined EP and contribute to different symptoms of a defined

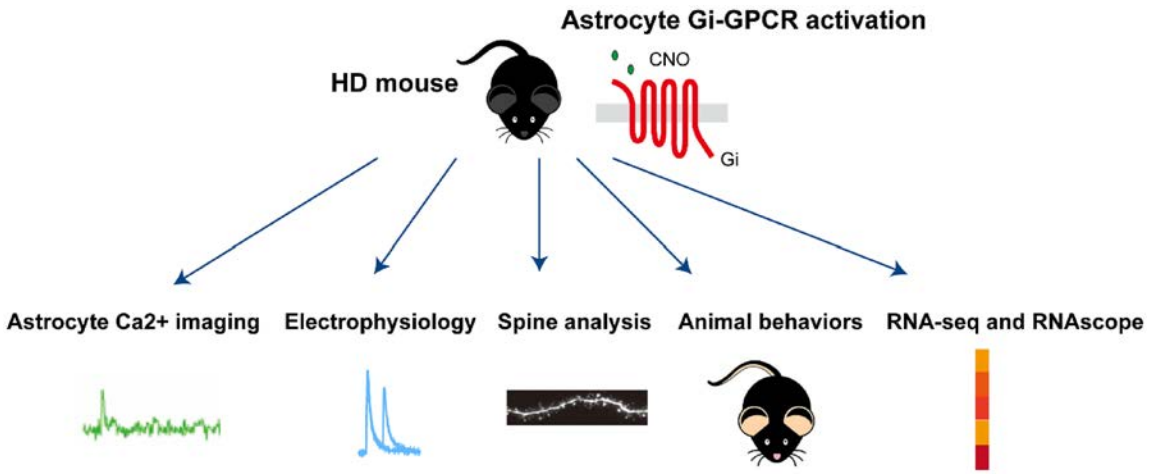

Fig. 2 Activation of astrocyte G_i-GPCR signaling *in vivo* corrects several HD-related molecular, cellular, and behavioral phenotypes.

disease? HD in this case, cognitive and psychiatric symptoms may be attributed to astrocytic dysfunctions in the cortical limbic system [8]. Last but not least, it will be of great interest to explore the heterogeneity of astrocytes and elucidate their complicated properties in healthy and diseased brain in different brain regions.

A key finding of this study is that activating Gi-DREADD can correct several HD phenotypes. Astrocyte GPCRs have been studied for more than two decades. For non-invasive stimulation of GPCR pathways in a genetically targeted manner, several typesets of DREADD have been developed: Gq-coupled hM3D, Gi-coupled hM4D, and Gs-coupled rM3D [9]. Interestingly, both the endogenous G_q or G_i GPCRs and the Gq, Gi, and Gs DREADDs all evoked Ca^{2+} signaling in astrocytes, despite the fact that they usually have separable effects on neuronal membrane potential and signaling pathways [10]. It was not surprise that this paper showed that activation of G_q, G_i, and G_s DREADDs evokes similar but non-identical molecular changes. Nevertheless, the complexity of astrocytic GPCR signaling needs to be further explored, especially if they are going to be used in therapeutic development. Overall, this study emphasizes the heteromolecular plasticity of astrocytes in response to different challenges and provides novel insight into treating HD by modulating Gi-GPCR to restore cellular and behavioral phenotypes.

Acknowledgements This Research Highlight was supported by grants from the National Natural Science Foundation of China (31430032, 81329003, 81671356, 31801007 and 81881240049), the Program for Changjiang Scholars and Innovative Research Team in University (IRT_16R37), the Science and Technology Program of Guangdong Province, China (2018B030334001), Basic and Applied Basic Research Foundation of Guangdong Province, China (2020A1515011310), Science and Technology Program of Guangzhou Municipality (201707020027), Guangdong-Hong Kong-Macao Greater Bay Area Center for Brain Science and Brain-Inspired Intelligence Fund (2019019).

Conflict of interest The authors declare no conflicts of interest.

References

1. Allen NJ, Eroglu C. Cell biology of astrocyte-synapse interactions. Neuron 2017, 96: 697–708.
2. Khakh BS, Sofroniew MV. Diversity of astrocyte functions and phenotypes in neural circuits. Nat Neurosci 2015, 18: 942–952.
3. Hu NY, Chen YT, Wang Q, Jie W, Liu YS, You QL. Expression patterns of inducible cre recombinase driven by differential astrocyte-specific promoters in transgenic mouse lines. Neurosci Bull 2020, 36: 530–544.
4. Khakh BS, Deneen B. The emerging nature of astrocyte diversity. Annu Rev Neurosci 2019, 42: 187–207.
5. Bayraktar OA, Bartels T, Holmqvist S, Kleshchevnikov V, Martirosyan A, Polioudakis D, *et al.* Astrocyte layers in the mammalian cerebral cortex revealed by a single-cell in situ transcriptomic map. Nat Neurosci 2020, 23: 500–509.
6. Yu X, Nagai J, Marti-Solano M, Soto JS, Coppola G, Babu MM, *et al.* Context-specific striatal astrocyte molecular responses are phenotypically exploitable. Neuron 2020, 108: 1146-1162.e10.
7. Liddelow SA, Guttenplan KA, Clarke LE, Bennett FC, Bohlen CJ, Schirmer L, *et al.* Neurotoxic reactive astrocytes are induced by activated microglia. Nature 2017, 541: 481–487.
8. Al-Dalahmah O, Sosunov AA, Shaik A, Ofori K, Liu Y, Vonsattel JP, *et al.* Single-nucleus RNA-seq identifies Huntington disease astrocyte states. Acta Neuropathol Commun 2020, 8: 19.
9. Yu X, Nagai J, Khakh BS. Improved tools to study astrocytes. Nat Rev Neurosci 2020, 21: 121–138.
10. Durkee CA, Covelo A, Lines J, Kofuji P, Aguilar J, Araque A. $G_{i/o}$ protein-coupled receptors inhibit neurons but activate astrocytes and stimulate gliotransmission. Glia 2019, 67: 1076–1093.

Neurosci. Bull. August, 2021, 37(8):1267–1269
https://doi.org/10.1007/s12264-021-00708-6
www.neurosci.cn
www.springer.com/12264

RESEARCH HIGHLIGHT

Naturally Occurring Parkinson's Disease Raises the Need for Nonhuman Primates in Neurodegenerative Diseases Research

Yuxuan Yao[1] · Ji Dai[1,2]

Received: 21 January 2021 / Accepted: 25 February 2021 / Published online: 26 May 2021

Parkinson's disease (PD) is a common neurodegenerative disorder that affects millions of people [1]. Typical symptoms of PD include bradykinesia, rigidity, resting tremor, and postural instability [1]. Therefore, PD severely affects the patient's daily life and mental health and imposes a tremendous burden on the medical system. In the past few decades, numerous studies have uncovered pathogenies and developed therapies for PD. However, the disease-modifying treatment of PD is still a major challenge worldwide. One of the important reasons is that most of the basic research on PD have not directly studied patients with PD but used animal models [2]. It is believed that PD is a human-exclusive disease because it has not been identified in other animals, including nonhuman primates [3]. Rodent PD models created by toxins including 6-hydroxydopamine and 1-methyl-4-phenyl-1,2,3,6-tetrahydropyridine or gene-editing only imitate some symptoms of PD but do not fully replicate the pathogenies including the neuronal loss in the substantia nigra (SN) [4]. Thus PD is considered to be a consequence of human brain evolution that the dramatic expansion of neocortex creates a significant burden on subcortical circuits [3].

Under this circumstance, from the point of view of evolution, there is another possibility: that PD is evolving concurrently in other primates (nonhuman primates, NHPs) given their genetic similarity. The fact that no NHPs with PD have been identified cannot rule out the possibility that PD is naturally occurring in a small portion of NHPs without being noticed.

To answer this question, very recently, a group of Chinese researchers, Li *et al.* carefully screened a large population of monkeys at the Kunming Primate Research Center and attempted to identify those with naturally-occurring PD [5]. By using various criteria including clinical symptoms, pharmacological responses, pathological evidence, and genetic mutations, a 10-year old male cynomolgus monkey without any operation was diagnosed as having PD. The monkey showed four lines of evidence and got a PD score over 15 out of 20 on the rating scale. The score indicated that the monkey had severe PD symptoms including bradykinesia, tremor, and postural instability, which are all typical PD symptoms. The pharmacological test on the monkey was positive, showing that the PD score decreased significantly after taking levodopa (a commonly used drug for PD). Treatment with apomorphine was also effective in lowering the PD score. Pathologically, Li *et al*. found that the monkey had a severe loss of dopaminergic neurons in the SN, which is the pathological hallmark of PD [1]. Although the study did not find Lewy bodies (another pathological hallmark of PD) in the monkey, it found alpha-synuclein, which is the early stage of the Lewy body [1]. The study also found an increased number of microglial cells and astrocytes in the monkey, which serves as further pathological evidence of PD. Besides, the study ran a sequence analysis and found that the potential cause of PD in the monkey was a missense mutation in LRRK2 [2]. These together clearly indicate that this monkey had PD. Thus, a spontaneously-occurring PD monkey has been identified.

✉ Ji Dai
ji.dai@siat.ac.cn

[1] CAS Key Laboratory of Brain Connectome and Manipulation, The Brain Cognition and Brain Disease Institute, Shenzhen Institute of Advanced Technology, Chinese Academy of Sciences; Shenzhen-Hong Kong Institute of Brain Science-Shenzhen Fundamental Research Institutions, Shenzhen 518055, China

[2] University of Chinese Academy of Sciences, Beijing 100049, China

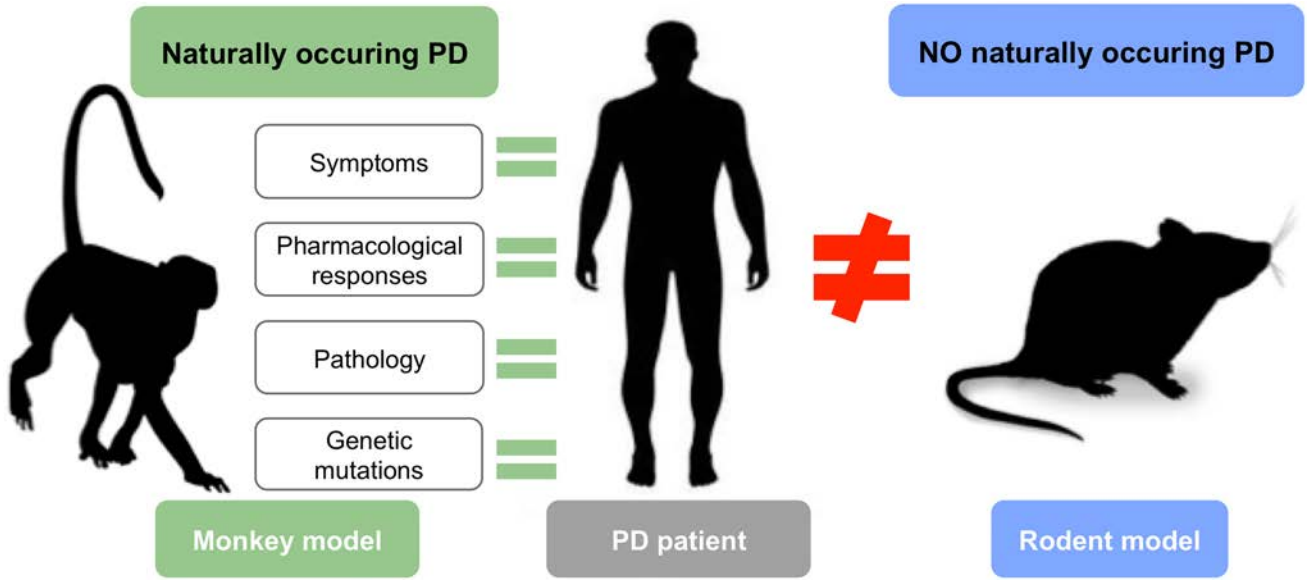

Fig. 1 The advantage of the monkey model in PD research. In addition to the similarity to PD patients in clinical symptoms, pharmacological responses, pathology, and genetic mutations, the monkey model can spontaneously develop PD, which has never been reported in rodent models.

This is the first report of a naturally-occurring PD monkey in the world. The finding indicates that PD is not a exclusively human disease but developed before the speciation of humans. As a close relative to humans, a monkey can spontaneously develop an animal version of PD that is very similar to humans in symptoms, pathology, and genetic mutations. Therefore, the monkey is an ideal candidate for PD research and therapeutic strategy development.

Previously, rodents were widely used in basic and translational studies of PD regardless of the tremendous differences between rodents and humans. However, no report has ever claimed that rodents can naturally develop PD, suggesting that the mechanism in these two species could be different (Fig. 1). Even though many strategies to treat PD have been developed based on rodent studies [6], the chance they can be successful in treating patients with PD would be low. Therefore, the focus of PD studies, including the evaluation of PD biomarkers [7], should move to NHPs given they are more genetically and anatomically close to humans, have very similar symptoms and pathogenies, and can develop PD spontaneously [5]. The successful identification of monkeys with naturally-occurring PD also suggests that other neurodegenerative disorders such as Huntington's disease (HD) [8] and Alzheimer's disease (AD) [9] may also naturally occur in NHPs. Extra screening of a large population of NHP is needed to clarify this possibility.

What was missing from Li *et al.*'s study was that the authors could not trace back the history of the PD monkey's family. Although they found the LRRK2 mutation in the PD monkey, it is still difficult to claim that PD is caused by a particular gene mutation or environment. Other than the hypothesis that PD is the consequence of human brain evolution [3], it is time to establish a new hypothesis regarding the presence of PD in humans.

In general, using NHPs as research models, there will be a higher chance of generating new theories and develop new effective therapeutic strategies for PD and other neurological disorders including HD and AD. To push the research to transmit from rodents to NHPs, a close collaboration is urgently needed across the scientific community, pharmaceutical corporations, governments, and evaluation systems including academic journals [10]. For example, research funds should shift towards NHPs, and academic journals should consider publishing more NHP-related studies. We hope to see that human patients with neurodegenerative diseases could eventually benefit from NHP research in the foreseeable future.

Acknowledgments This Research Highlight was supported by the National Natural Science Foundation of China (U20A2017), the Natural Science Foundation of Guangdong Province (2020A1515010785), the Youth Innovation Promotion Association CAS (2017120), and the Chinese Academy of Sciences International Partnership Program (172644KYSB20170004).

Conflict of interest The authors declare no competing interests.

References

1. Poewe W, Seppi K, Tanner CM, Halliday GM, Brundin P, Volkmann J, *et al.* Parkinson disease. Nat Rev Dis Primers 2017, 3: 17013.

2. Dawson TM, Ko HS, Dawson VL. Genetic animal models of Parkinson's disease. Neuron 2010, 66: 646–661.
3. Diederich NJ, James Surmeier D, Uchihara T, Grillner S, Goetz CG. Parkinson's disease: Is it a consequence of human brain evolution? Mov Disord 2019, 34: 453–459.
4. Yang W, Liu Y, Tu Z, Xiao C, Yan S, Ma X, *et al.* CRISPR/Cas9-mediated $PINK_1$ deletion leads to neurodegeneration in rhesus monkeys. Cell Res 2019, 29: 334–336.
5. Li H, Su LY, Yang LX, Li M, Liu QJ, Li ZH, *et al.* A cynomolgus monkey with naturally occurring Parkinson's disease. Natl Sci Rev 2021, 8: nwaa292.
6. Qian H, Kang X, Hu J, Zhang D, Liang Z, Meng F, *et al.* Reversing a model of Parkinson's disease with *in situ* converted nigral neurons. Nature 2020, 582: 550–556.
7. Li TB, Le WD. Biomarkers for Parkinson's disease: How good are they? Neurosci Bull 2020, 36: 183–194.
8. Glaser T, Andrejew R, Oliveira-Giacomelli Á, Ribeiro DE, Bonfim Marques L, Ye Q, *et al.* Purinergic receptors in basal Ganglia diseases: Shared molecular mechanisms between Huntington's and Parkinson's disease. Neurosci Bull 2020, 36: 1299–1314.
9. King A. The search for better animal models of Alzheimer's disease. Nature 2018, 559: S13–S15.
10. Ning B, Zhao Y. To embrace open science more closely. The Innovation 2020, 1: 100012.

Neuroscience Bulletin

Neuroscience Bulletin

Copyright Information

For Authors

As soon as an article is accepted for publication, authors will be requested to assign copyright of the article (or to grant exclusive publication and dissemination rights) to the publisher (respective the owner if other than Springer Nature). This will ensure the widest possible protection and dissemination of information under copyright laws.

More information about copyright regulations for this journal is available at www.springer.com/12264

For Readers

While the advice and information in this journal is believed to be true and accurate at the date of its publication, neither the authors, the editors, nor the publisher can accept any legal responsibility for any errors or omissions that may have been made. The publisher makes no warranty, express or implied, with respect to the material contained herein.

All articles published in this journal are protected by copyright, which covers the exclusive rights to reproduce and distribute the article (e.g., as offprints), as well as all translation rights. No material published in this journal may be reproduced photographically or stored on microfilm, in electronic data bases, on video disks, etc., without first obtaining written permission from the publisher (respective the copyright owner if other than Springer Nature). The use of general descriptive names, trade names, trademarks, etc., in this publication, even if not specifically identified, does not imply that these names are not protected by the relevant laws and regulations.

Springer Nature has partnered with Copyright Clearance Center's RightsLink service to offer a variety of options for reusing Springer Nature content. For permission to reuse our content please locate the material that you wish to use on link.springer.com or on springerimages.com and click on the permissions link or go to copyright.com and enter the title of the publication that you wish to use. For assistance in placing a permission request, Copyright Clearance Center can be contacted directly via phone: +1-855-239-3415, fax: +1-978-646-8600, or e-mail: info@copyright.com

Journal Website

www.springer.com/12264
For the actual version of record please always check the online version of the publication.

Subscription Information

Volume 37 (12 issues) will be published in 2021.

ISSN: 1673-7067 print
ISSN: 1995-8218 electronic

For information on subscription rates please contact Springer Nature Customer Service Center: customerservice@springernature.com

The Americas (North, South, Central America and the Caribbean)
Springer Nature Journal Fulfillment,
Harborside Plaza II,
200 Hudson Street, Jersey City,
NJ 07302, USA
Tel. 800-SPRINGER (777-4643);
212-460-1500 (outside North America)

Outside the Americas
Springer Nature Customer Service Center GmbH, Tiergartenstr. 15,
69121 Heidelberg, Germany
Tel.: +49-6221-345-4303

Advertisements

E-mail contact: advertising@springer.com or anzeigen@springer.com (Germany)

Disclaimer

Springer Nature publishes advertisements in this journal in reliance upon the responsibility of the advertiser to comply with all legal requirements relating to the marketing and sale of products or services advertised. Springer Nature and the editors are not responsible for claims made in the advertisements published in the journal. The appearance of advertisements in Springer Nature publications does not constitute endorsement, implied or intended, of the product advertised or the claims made for it by the advertiser.

Office of Publication

Springer Nature Singapore Pte Ltd.
152 Beach Road, #21-01/04
Gateway East, Singapore 189721,
Singapore

Impactor Factor

5.203

2020 Journal Citation Reports: Q2
(CLARIVATE ANALYTICS, 2021)

NEUROSCIENCE BULLETIN 神经科学通报 (Monthly)

Vol. 37 No. 8 August 15, 2021

Sponsored by: Center for Excellence in Brain Science and Intelligence Technology, Chinese Academy of Sciences
Chinese Neuroscience Society

Editors-in-Chief: Shunmin Duan, Ru-Rong Ji

Edited by: Editorial Board of *Neuroscience Bulletin*
319 Yueyang Road, Building 8, Room 612, Shanghai 200031, China
Phone: +86-21-64032273; 64170853; 64032696
E-mail: nsb@ion.ac.cn; http://www.neurosci.cn

Editors: Bin Wei, Fei Dong, Ting Lyu

Published by: Center for Excellence in Brain Science and Intelligence Technology, Chinese Academy of Sciences

Printed by: Shanghai Shengtong Times Printing Co.,Ltd (A6, No. 2888, Caolang Highway, Jinshan District, Shanghai)

Overseas Distributed by: Springer Nature

Home Distributed by: Local Post Offices

ISSN 1673-7067
CN 31-1975/R

Post Office Code Number: 4-608
Permit of Ad. Number: 3100420130051
Price: ¥ 100.00

ISSN 1673-7067

OLYMPUS

转盘共聚焦超分辨显微镜

SpinSR10

IXplore

兼顾分辨率和速度的
转盘共聚焦活细胞超分辨系统 SpinSR10

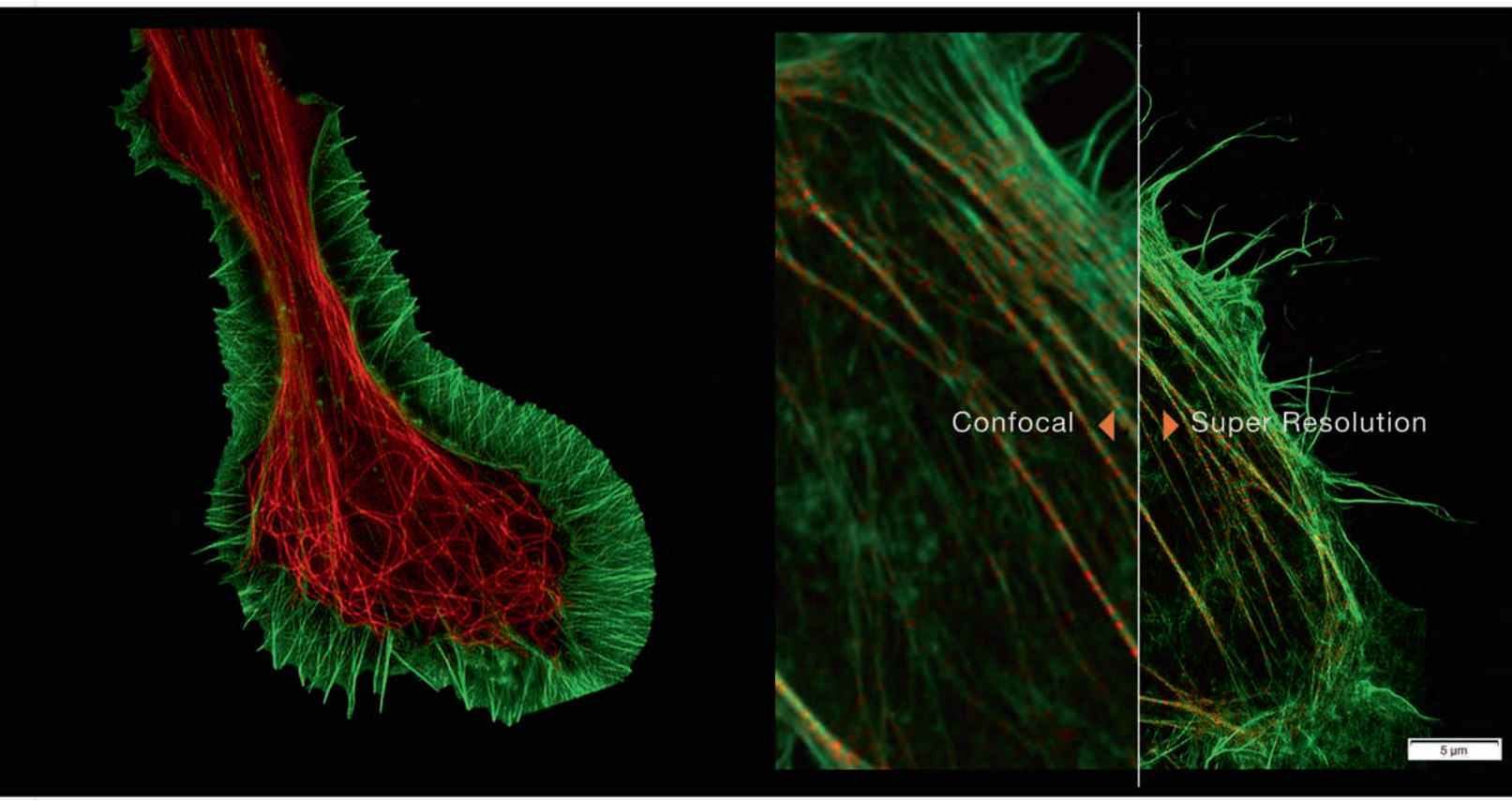

- 分辨率高达110 nm的实时超分辨率成像
- 专有反卷积算法进一步提升图像质量
- 宽视野成像，速度高达 200fps
- 特色硅油物镜可以实现活细胞深层成像
- 宽场、共聚焦、超分辨率模式自由切换
- 功能强大的智能cellSens软件平台

奥林巴斯（北京）销售服务有限公司

北京朝阳区酒仙桥路10号恒通商务园B12C座2F （北京） 010-59756006
上海市徐汇区淮海中路1010号嘉华中心11楼 （上海） 021-51582084
广州市环市东路403号广州电子大厦16楼 （广州） 020-61227171
陕西省西安市新城区尚德路85号太平洋保险大厦8F （西安） 029-87206108
湖北省武汉市江岸区中山大道1628号武汉天地企业中心5号7楼701单元 （武汉） 027-82718838
四川省成都市人民南路四段三号来福士广场T1-11楼 （成都） 028-86703700
辽宁省沈阳市沈河区友好街10号新地中心1号楼3501室 （沈阳） 024-23342084

http://www.olympus-lifescience.com.cn/zh/